SECOND INTERNATIONAL WORKSHOP

on

Discrete Time Domain Modelling of Electromagnetic Fields and Networks

Sponsored by:

The German IEEE MTT/AP Joint Chapter
The German IEEE CAS Chapter
The European Research Office of the U.S. Army
The Ferdinand-Braun-Institut für Höchstfrequenztechnik Berlin

In collaboration with the
MTT Technical Committee on Field Theory
(MTT-15)

October 28 and 29, 1993

Hotel Ambassador
Berlin, Germany

1. Program Co–Chairpersons

Prof. Dr. Peter Russer
Ferdinand–Braun–Institut
für Höchstfrequenztechnik Berlin
Rudower Chaussee 5
12489 Berlin
Germany
Tel: +49/30/6392–2601
Fax: +49/30/6392–2602

Prof. Dr. Josef A. Nossek
Lehrstuhl für Netzwerktheorie
und Schaltungstechnik
Technische Universität München
Arcisstraße 21, 80333 München
Germany
Tel: +49/89/2105–8501
Fax: +49/89/2105–8504

2. Objectives

Due to advances in different areas of microwave– and millimeter–wave techniques, demand for efficient CAD tools has grown. This statement is today as true as it was at our last workshop held two years ago in Munich on this topic. The numerical analysis in time domain is attractive since it describes the evolution of physical quantities in a natural way. The two basic concepts, the modelling of fields and networks, are more closely related than it seems at first glance. In the TLM method, for example, the network model is the basis for modelling electromagnetic fields. Another example is the application of generalized S–matrix methods and diacoptics in field theory. The purpose of this conference is to stimulate synoptic considerations of field and network theory and to promote a lively exchange between researchers engaged in these fields.

3. Organizer

The organizer of this workshop is Prof. Dr. Peter Russer.

4. Venue

The workshop will take place at the Hotel Ambassador Berlin, Bayreuther Str. 42/43, 10787 Berlin, Germany, Tel.: +49/30/21902-0, Fax: +49/30/21902-380.

5. Conference Secretary

For any questions or information about the workshop, please contact the Program Co–Chairpersons or

Michael Krumpholz, Conference Secretary
Ferdinand–Braun–Institut für Höchstfrequenztechnik Berlin
Rudower Chaussee 5, 12489 Berlin
Tel: +49/30/6392-2625, Fax: +49/30/6392-2612
e-mail: krumphol@fbh.wtza–berlin.de

6. Registration

Advance Registration may be done by the Registration Form enclosed in this Preliminary Program. On–site registration is also possible. The registration office at the Hotel Ambassador will be open at October 28, from 8:00 a.m. to 10:30 p.m..

Please note that late registration as well as on–site registration is subject to a late fee.

7. Projection Facilities

Projection equipment available will be a standard slide and an overhead projector.

8. Accommodation

Blocks of rooms have been reserved at the following hotels near or at the workshop site in Berlin at special workshop rates. Please make your reservations directly with the hotel. Refer to the Ferdinand–Braun–Institut für Höchstfrequenztechnik to obtain the special rate.

Hotel Ambassador	Bayreuther Str. 42/43
Tel.: +49/(0)30/21902-0	10787 Berlin
Fax : +49/(0)30/21902-380	205 DM single, 225 DM double
Hotel Westerland	Knesebeckstr. 10
Tel.: +49/(0)30/3121004	10623 Berlin
Fax : +49/(0)30/3136489	100 DM single, 155 DM double
Hotel Charlot	Giesebrechtstr. 17
Tel.: +49/(0)30/3234051	10629 Berlin
Fax : +49/(0)30/3240819	60/90/115 DM single, 170 DM double

Please note: **The rooms are only reserved until September 14, 1993.**

9. Transportation

Berlin is served by three airports: Berlin–Tegel, Berlin–Tempelhof and Berlin–Schönefeld. Berlin–Tegel is situated in the north–west of Berlin. You may take a taxi (about 30 DM) or the bus no. 109 directly to Berlin Zoologischer Garten (Berlin–Zoo) (35 min.). Berlin–Tempelhof located in the south–east of Berlin. You may choose a taxi (about 25 DM) or the underground (U-Bahn), U8 to Hallesches Tor and change to the U1 for going to Berlin–Zoo. If you arrive at Berlin–Schönefeld in the very south–east of Berlin, the most preferable way to get into the center is taking the S–Bahn directly to Berlin–Zoo (70 min.). A taxi will be about 60 DM. In general, public transportation in Berlin is the most preferable way of transportation within the city. During day–time, the underground and buses run every five or ten minutes.

If you are arriving by train, the trains will stop at Berlin–Zoo or Berlin–Hauptbahnhof from where you can take the S-Bahn directly to Berlin–Zoo. If you are arriving by car, leave the Autobahnring no. 10 at Autobahndreieck Drewitz to the Autobahn no. 115. At Autobahndreieck Funkturm, head towards north (look for the direction to the airport Berlin–Tegel) and get off the motorway at Kaiserdamm to arrive at Berlin–Zoo via Ernst–Reuter Platz. For your local orientation, we have enclosed two maps.

10. Program

This program consists of the invited talks and the non–invited contributions. Late contributions presented in session B2 will be accepted at the workshop.

Thursday, October 28, 1993:

8:00	Registration	
	Session A1 (Chairmen: P. Russer, W.J.R. Hoefer)	
8:30	Opening Session	
8:40	Time Domain Wave–Oriented Data Processing or: How to Extract Phenomenology from Observations	L. Felsen
9:20	Comparison of Different Field Theoretical Methods of Analysis of Distributed Microwave Circuit Elements	R. Sorrentino
10:00	-Break-	
10:20	Time Domain Electromagnetic Field Computation with Finite Difference Methods	T. Weiland
11:00	Finite Difference Time Domain Models for Coplanar Waveguide Discontinuities	V. Fouad Hanna
11:40	Enhanced FDTD Method for Active and Passive Microwave Structures	B. Houshmand, T. Itoh
12:20	-Break-	
	Session A2 (Chairmen: R. Sorrentino, J.A. Nossek)	
13:20	On the Field Theoretic Foundation of the Transmission Line Matrix Method	P. Russer, M. Krumpholz
14:00	TLM Modelling of Guiding and Radiating Microwave Structures	W.J.R. Hoefer
14:40	Modelling of Planar Microwave Structures in Frequency and Time Domain	R. Vahldieck
15:20	-Break-	
15:40	Time Domain Simulation of Non–Linear Networks Containing Distributed Interconnect Structures	M.I. Sobhy, E.A. Hosny
16:20	Transient Analysis of Large Non–Linear Networks	U. Feldmann
	Social Event	
19:00	Piano Recital: Diana Lawton Steinway–Haus, Hardenbergstr. 9	
20:30	Berlin Evening Berlin Pavillon, Straße des 17.Juni 100	

Friday, October 29, 1993:

Session B1 (Chairmen: M.I. Sobhy, T. Itoh)

8:00	Dynamic Simulation of Semiconductor Devices	R. Stenzel, W. Klix
8:40	Signal-Processing Approach to Robust Time-Domain Modelling of Electromagnetic Fields	A. Fettweis
9:20	New Results in Transient Analysis of Crystal Oszillators	Ch. Schmidt-Kreusel, W. Mathis
9:40	-Break-	
10:00	Adaptive Detection and Tracking of Active Scatterers by Cascaded Notch Filters	M. Zouak, J. Saillard
10:20	Sub-mm Wave Circuit Characterization Using the Finite Difference Time Domain Method	N.I. Dib, L.P.B. Katehi
10:40	FDTD Modelling of Wirebond Interconnects	E. Pillai, C. Bornkessel, W. Wiesbeck
11:00	Space and Time Discretization in Field Computation Using TLM	C. Christopoulos, J.L. Herring
11:20	Distributed Computing for Transmission Line Matrix Method	P.P.M. So, W.J.R. Hoefer
11:40	TLM: Order of Accuracy Enhancement	D. de Cogan, A. Soulos, P. Enders
12:00	-Break-	

Session B2 (Chairmen: L.P.B. Katehi, L. Felsen)

13:00	Rigorous and Fast Computation of Modal Johns' Responses	M. Mongiardo, M. Righi, R. Sorrentino, W.J.R. Hoefer
13:20	Transmission-Line Matrix Modelling and Huygens' Principle or The Range of Applicability of TLM	P.Enders
13:40	Towards Better Understanding of the SCN TLM Method for Inhomogenous Problems	M. Celuch-Marcysiak
14:00	Generation of Lumped Element Models of Distributed Microwave Circuits	P. Russer, M. Righi, C. Eswarappa, W.J.R. Hoefer
14:20	Towards Exactly Modelling Open/Absorbing Boundaries	P.Enders, A.J. Wlodarczyk
14:40	-Break-	

Friday, October 29, 1993:

Session B2 (Chairmen: L.P.B. Katehi, L. Felsen)

15:00	Simulation of Electromagnetic Fields in Nonlinear and *Photonic* Waveguiding Structures	D. Jaeger
15:10	Derivation of Stability Condition for the Time Domain Method of Moments Algorithms Using Functional Analysis Approach	M. Mrozowski
15:20	Convergence Criteria for Maxemol – a Numerical Scheme for the Solution of Maxwell's Equations Using the Method of Lines	W.B. Fu, R.A.C. Metaxas
15:30	Broadband Simulation of Open Waveguide Boundaries within Large Frequency Ranges	M. Dohlus, P. Thoma, T. Weiland
15:40	On the Geometrical Structure of Network Equations	St. Paul
15:50	Further Late Contributions	
16:00	Concluding Session: open forum, panel discussion, approximately finished by 17:00	

Teilnehmerliste

Invited Speakers

Dr. U. Feldmann	Siemens AG
Prof. Dr. L.B. Felsen	Polytechn. University Farmingdale
Prof. A. Fettweis	Ruhruniversität Bochum
Dr. V. Fouad Hanna	France Telecom
Prof. W. J. R. Hoefer	University of Victoria
Prof. T. Itoh	University of California, LA
Prof. J.A. Nossek	TU München
Prof. P. Russer	FBH Berlin
Prof. M. Sobhy	University of Kent at Canterbury
Prof. R. Sorrentino	Universita di Perugia
Prof. R. Stenzel	Hochschule für Technik und Wirtschaft, Dresden
Prof. R. Vahldieck	University of Victoria
Prof. T. Weiland	TH Darmstadt

Participants

St. Aidam	TU Berlin
B. Bader	FBH Berlin
Prof. H.J. Bex	FH Aachen
Dr. E. Biebl	TU München
Ch. Bornkessel	Universität Karlsruhe
M. Celuch-Marcysiak	Warsaw University
Prof. C. Christopoulos	University of Nottingham
Dr. D. De Cogan	School of Information Systems, Norwich
Dr. H. Delfs	Rohde & Schwarz
R. Doerner	FBH Berlin
Dr. P. Enders	
Dr. U. Erz	Universität Stuttgart
Dr. W. B. Fu	Cambridge University
Ch. Fuchs	Universität Karlsruhe
P. Gelin	ENST - Bretagne
R. Gillard	LCST-INSA de Rennes
Dr. R. Gründler	FBH Berlin
Dr. V. Güngerich	TU München
Dr. R. Güther	FBH Berlin
Prof. G. Härtler	FBH Berlin
Dr. J. Haase	Fraunhofer-Institut für Integrierte Schaltungen, Dresden
Dr. J. Heine	FBH Berlin
Dr. W. Heinrich	FBH Berlin
Dr. P. Heymann	FBH Berlin
Ch. Huber	FBH Berlin
B. Isele	TU München
Prof. D. Jäger	Universität Duisburg
L. P. B. Katehi	University of Michigan
M. Krumpholz	FBH Berlin
Dr. H. Kumric	Universität Stuttgart
St. Lindenmayer	TU München
Prof. W. Mathis	Bergische Universität Wuppertal
Dr. M. Michalski	TU München
Dr. M. Mrozowski	TU Gdansk

Dr. St. Müller	TU München
M. Ney	ENST - Bretagne
M. Niederhoff	FBH Berlin
A. Nonnenmacher	Universität Karlsruhe
Dr. St. Paul	TU München
E. Pillai	Universität Karlsruhe
Dr. H. Prinzler	FBH Berlin
St. Römer	FBH Berlin
M. Rudolph	TU Berlin
S. Sattler	TU München
M. Schinke	Universität Karlsruhe
Dr. F. Schnieder	FBH Berlin
M. Sihapustan	TU Berlin
P. So	University of Victoria
G. Stankus	TU Berlin
P. Thoma	TH Darmstadt
A. Wien	Kernforschungszentrum Karlsruhe
H. Wiesmann	Universität Karlsruhe
M. Witting	SIBET GmbH
F. Zinkler	FBH Berlin
M. Zouak	IRESTE Universite de Nantes
Dr. H. Zscheile	FBH Berlin

Recital Program

Berlin, Germany, October 1993

***Diana Lawton,** Piano*

I

W.A. Mozart

Sonate d-dur, KV. 311
Allegro con spirito
Andante con espressione
Rondo

II

C. Debussy

L'Isle Joyeuse

Intermission

III

F. Chopin

Sonate III h-moll, Op. 58
Allegro maestoso
Scherzo molto vivace
Largo
Finale presto, ma non tanto

Workshop sites and Hotels

1 Hotel Ambassador
2 Hotel Westerland
3 Hotel Charlot
4 Steinway-Haus
5 Berlin Pavillon
6 Bahnhof Zoo(logischer Garten)
7 Autobahndreieck Funkturm
8 Kaiserdamm
9 Ernst-Reuter Platz

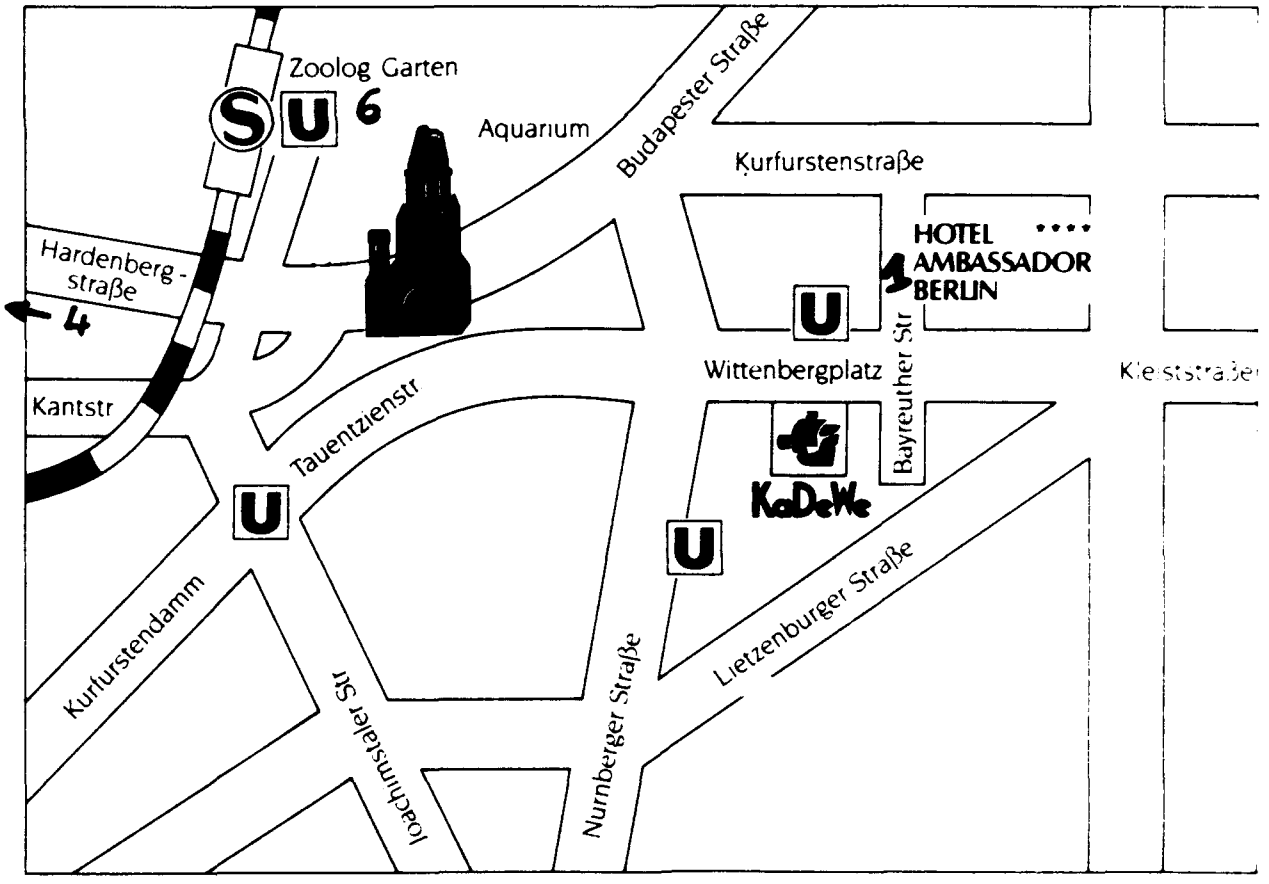

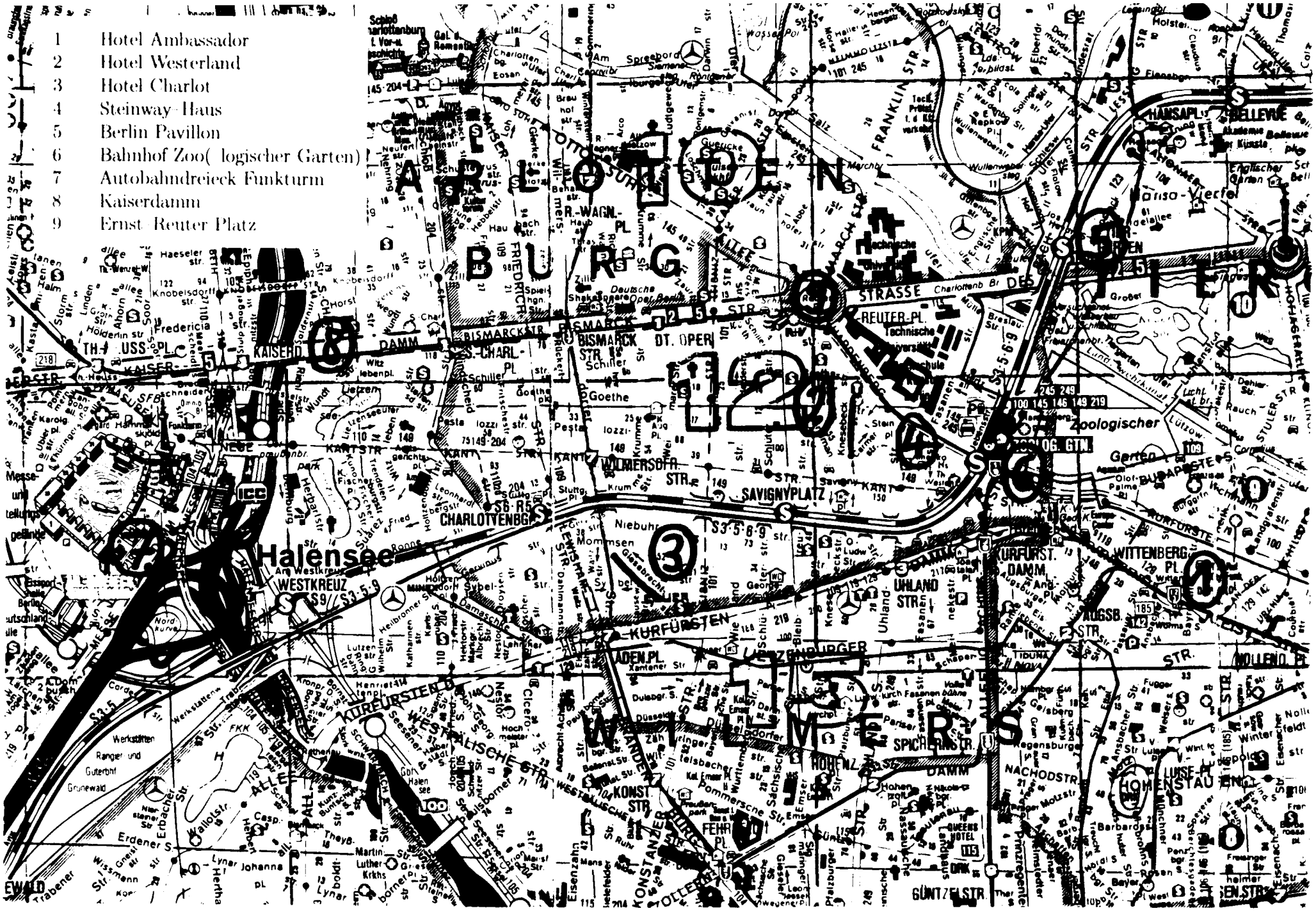

1	Hotel Ambassador
2	Hotel Westerland
3	Hotel Charlot
4	Steinway-Haus
5	Berlin Pavillon
6	Bahnhof Zoo(logischer Garten)
7	Autobahndreieck Funkturm
8	Kaiserdamm
9	Ernst-Reuter-Platz

Universita` di Perugia **Comett**

European Community program on cooperation between universities and industry regarding training in the field of technology

COMETT course on

Numerical Methods in the Modeling of Microwave Circuits

November 15-19, 1993 - Perugia - Italy

The course on "Numerical Methods in the Modeling of Microwave Circuits" has been organized within the COMETT program to provide you state-of-the-art information on computer techniques for the accurate electromagnetic analysis of microwave circuits.
A wide range of numerical techniques will be presented by internationally recognized experts in a 5 day intensive course.
One full day of presentation will be devoted to each topic.
In addition to lectures describing the numerical techniques, software demonstration on PC's and workstations will be made available to the attendees.

PROGRAM:

Monday, November 15, 1993. **9-12 a.m., 2-5 p.m.**
Microwave circuit modelling using the transmission line matrix method

Tuesday, November 16, 1993 **9-12 a.m., 2-5 p.m.**
Finite Element Method applied to the analysis of 2D and 3D microwave structures

Wednesday, November 17, 1993 **9-12 a.m., 2-5 p.m.**
MESFET and HEMT modelling for CAD

Thursday, November 18, 1993 **9-12 a.m., 2-5 p.m.**
Full wave analysis of microwave and mm-wave structures using 3D-mode matching techniques

Friday, November 19, 1993 **9-12 a.m., 2-5 p.m.**
Advanced linear and non linear modelling techniques in the framework of a commercial microwave/mmw CAD package

COORDINATORS:

Prof. P. Russer, FBH, Berlin
Germany

Prof. P. Guillon, University of Limoges
France

Prof. A. Cappy, University of Lille
France

Prof. R. Sorrentino, University of Perugia
Italy

Prof. R. H. Jansen, University of Duisburg
Germany

COURSE REGISTRATION FORM

Please fill in and return or fax this form to:

Istituto di Elettronica - Università di Perugia -
Loc. Santa Lucia
06131 PERUGIA
ITALY
Tel. +39-75-585/2669 Catena /2633 or 2659 Roselli
Fax. +39-75-585-2654

'lease register me to the COMETT course on "Numerical Methods in the Modeling of Microwave Circuits" (November 15-19,1993)

.ast name.....First name.....

ıffiliation ..... Address .....

'ountry ..... Zip ..... Telephone ..... Fax .....

Signature .....

tegistration fee: **Lit. 300.000** (please sign your way of payment), **Deadline**: 5/11/93

] money order payable to **"Consorzio TUCEP, cc n° 4430/23, Cassa di Risparmio di Perugia, Ag. n° 8, specifying for "COMETT Course n° 2"**
] cash at the registration desk

'RACTICAL INFORMATION

'he course will be given in **English** and will take place at the " Centro di Calcolo " of the University of Perugia, Loc. ;.Lucia, Perugia, Italy. The full course price is 300.000 Italian Lire, including course notes, copies of viewgraphs.

ıccommodations

ı list of possible accommodations is as following. For more detailed information you can refer directly to the Tourist Office of Perugia -Information Service-" P.za IV Novembre, Perugia, Tel. +39-75-5736458 Fax. +39-75-:736828.

Hotel La Rosetta" ★★★★	P.za Italia,19, Perugia	Tel +39-75-5720841	Fax +39-75-5720841
Hotel Fortuna" ★★★★	V. Bonazzi, 19, Perugia	Tel +39-75-5722845	Fax +39-75-5735040
Hotel Giò" ★★★★	V. d'Andreotto,19, Perugia	Tel +39-75-5731100	Fax +39-75-5731100
Hit Hotel" ★★★★	S. S. Trasimeno Ovest,159, Perugia	Tel +39-75-5179247	Fax +39-75-5178947
Hotel Rosalba" ★★	V. del Circo, 7, Perugia	Tel +39-75-5728285	

Iow to get to PERUGIA

'LIGHTS:
'rom Milan to Perugia dep. 7:05 a.m. arr. 9:05 a.m. via Ancona
dep. 6:25 p.m. arr. 7:35 p.m.

'RAINS:

'rom Rome to Perugia	dep.	6:55	a.m	arr.	9:21	a.m.	
All trains change in		7:30	a.m.		1 0:19	a.m.	
'oligno except the		1 0:05	a.m.		1 2:34	a.m.	
ntercity)		1:55	p.m		4:00	p.m.	Intercity, via Terontola
		2:50	p.m.		5:19	p.m.	
		3:25	p.m.		6:24	p.m.	
		5:25	p.m.		8:26	p.m.	
		6:45	p.m.		9:16	p.m.	
		8:30	p.m.		1 0:36	p.m.	Intercity, no on Saturday

:OADS:
'rom North exit **VALDICHIANA** from the A1 highway then about 58 Km to Perugia.
'rom South exit **ORTE** from the A1 highway then about 95 Km to Perugia.

ABOUT THE LECTURERS

Peter RUSSER was born in Vienna, Austria, in 1943. He received the Dipl. Ing. degree in 1967 and the Dr. techn. degree in 1971, both in electrical engineering and both from the Technische Universitat in Vienna, Austria. From 1968 to 1971, he has been an Assistant Professor at the Technische Universitat in Vienna. In 1971 he joined the Research Institute of AEG-Telefunken in Ulm, where he worked on fiber optic communications, high speed solid-state electronic circuits, laser modulation and fiber optic gyroscopes. In 1979 he was co-recipient of the NTG award. Since 1981 he has held the chair of Hochfrequenztechnik at the Technische Universitat Munchen. In 1990 he was Visiting Professor at the University of Ottawa. Since October 1992 he is the Director of the Ferdinand-Braun-Institut fur Hochstfrequenztechnik in Berlin. His current research interests are integrated microwave and millimeter wave circuits, electromagnetic fields, statistical noise analysis of microwave circuits, and methods for CAD of microwave circuits. Peter Russer is the author of numerous scientific papers in these areas.
He is IEEE Senior Member and member of the German Informationstechnische Gesellshaft and the Austrian and German Physical Societies.

Pierre GUILLON was born in May 1947. He received the Doctorat es Sciences degree from the University of Limoges, France, in 1978.
From 1971 to 1980 he was with the Microwave and Optical Communication Laboratory Univ[illegible] of Limoges, where he studied dielectric resonators and their applications to microwave and millimeter -wave circuits.
From 1981 to 1985, he was a Professor of Electrical Engineering at the University of Poitiers, France.
In 1985, he joined again the University of Limoges, where he is currently a Professor and head of research group in the area of microwave and millimeter-wave devices. He is a member of IEEE.

Alain CAPPY was born in Chalons sur Marne, France on January 15, 1954. In 1977 he joined the "Centre Hyperfréquence et Semiconducteurs" University of Lille, France. In 1986 he received the "Docteur es Sciences" degree from the University of Lille for his work on the modeling and the characterization of MESFET's and HEMT's. He is now Professor of Electronics at the University of Lille. His main research interests are concerned with the modeling, the realization and the characterization of low-noise devices for applications in the centimeter and millimeter wave ranges. He is the founder of the International GaAs Simulation Group.

Roberto SORRENTINO received the Doctor degree in Electronic Engineering from the University of Rome "La Sapienza", Rome, Italy in 1971. In 1971 he joined the Department of Electronics of the same University where he became an Assistant Professor in 1974, and an Associate Professor from 1982 to 1986. In 1983 and 1986 he was appointed as a Research Fellow at the University of Texas at Austin, USA. From 1986 to 1990 he was a Professor at the second University of Rome "Tor Vergata". Since November 1990 he has been a Professor at the University of Perugia, Italy where he is presently the Director of the Computer Center. His research activities has been concerned mainly with the analysis and design of microwave and millimeter-wave passive circuits. He has contributed to the planar circuit approach for the analysis of microstrip circuits and to the development of numerical techniques for the modeling of components in planar and quasi-planar configurations. Dr. Sorrentino is a Fellow of IEEE. He is a member of the editorial boards of IEEE Trans. on MTT, the Int. J. on Numerical Modeling and the Int. J. of Microwave and MM-wave Computer Aided Engineering.

Rolph H. JANSEN received the M.S. (1972) and the Ph. D. from the University of Aachen (RWTH). He continued his research work at the RWTH Aachen microwave laboratory as a Senior Research Engineer (1976-79), and since 1977 he worked for about 8 years as a research associate in radio communications for Standard Elektrik Lorenz AG (SEL) in Pforzheim, West Germany. In 1979, he became Professor of Electrical Engineering at the University of Duisburg, West Germany, with teaching and research on electromagnetic theory, microwave techniques and CAD, measurement techniques, and modelling. He is author and co-author of about 90 technical papers in the field of microwave CAD and related topics and recipient of the outstanding publications award in 1979 of the German Society of Radio Engineers.
Since the end of 1984 till early 1992, he was engaged in the development of a novel engineering CAD workstation for GaAs MMICs with Plessey Research Caswell, U.K. Since 1985 he is owner and president of a small microwave company, named Jansen Microwave at Ratingen, Germany. He served as the West Germany MTT Chapter Chairman June 1985 to May 1987 and as one of the Distinguished Lecturers of the MTT -Society in 1987-88. Also, he is an elected member of MTT-S AdCom since 1989 and Co-Chairman of the MTT-S Transnational Committee. Further he is a Fellow of the IEEE since 1989 and a member of the Electromagnetic Academy of the MIT, Boston,USA. In 1992, he co-initiated and chaired GaAs '92 at Noordwijk, The Nederlands, the first European Gallium Arsenide Applications Symposium.

TOPICS

Microwave circuit modelling using the Transmission Line Matrix (TLM) method. In TLM the space is subdivided into cells. The electromagnetic field dynamics is modeled by wave pulses propagating between adjacent cells and scattered within the cells. The main advantage of the TLM simulation resides in the capability to model circuits of arbitrary geometry and to compute and display the time evolution of the fields. The TLM method exhibits an excellent numerical stability and is also suitable for modelling of lossy, dispersive and nonlinear media. A field theoretical foundation of the TLM method is given using the Method of Moments with sectional base functions. The space discretization with regular meshes as well as with nonuniform and curved meshes and the error introduced by the mesh discretization are discussed. The modelling of lossy, dispersive, nonlinear, and active regions as well as the skin effect and absorbing boundary conditions are treated. Emphasis is put on numerous practical examples of the calculation of microwave circuit structures including:

Planar, coplanar and slot lines/Planar line discontinuities/Planar tapers/Planar filters/Planar hybrid rings/Skin effect in planar circuits/Superconducting planar circuits/Nonlinear and active circuits.

In addition to the presentations practical demonstrations of TLM calculations on the computer are given.

Finite Element Method applied to the analysis of 2D and 3D microwave structures.

1. Finite element method.
- Formulation (E and H formulation)
- Meshing
2. Applications and results concerning 2D and 3D microwave structures
3. Software utilization by participants

MESFET and HEMT modelling for CAD. For the modelling of microwave circuit using MESFETS and/or HEMTs, the linear performance of the active device is of primary importance. For some applications, the use of a FET numerical modelling can be a good alternative to the use of experimental data files. After a short description of the different FET modelling techniques, the quasi two dimensional (Q2D) approach, well suited for the CAD of microwave circuits, will be described in detail. Based on the Q2D approach the software "HELENA" will be then presented and several examples of applications will be given.

Full wave analysis of microwave and mm-wave structures using 3D mode matching techniques. Formulation of the mode matching method for isolated waveguide junctions. The Generalized Scattering Matrix and the Generalized Admittance Matrix. Application to planar and quasi planar circuits. The Transverse Resonance Method. Segmentation techniques. 3D Mode Matching Method. Full wave optimization of microwave components.

Advanced linear and non linear modelling techniques in the framework of a commercial microwave/mmw CAD package. This lecture provides detailed information and theoretical background on one of the most comprehensive European CAD solutions for layout-and-process-related microwave and millimeterwave integrated circuit design. Many portions of this CAD package are based on first principles and reflect well the enormous progress made in the respective design techniques since about mid of the 70s. The lecture is grouped into 4 sub-topics, namely:

- General framework and hierarchical model library for microwave CAD in layout and physics-related form
- Field-theory bases look-up table generation, direct 2D electromagnetic analysis and piecewise 2D representation of geometrically complex (M)MIC components.
- High speed full wave 3D electromagnetic analysis and S-parameter generation for microstrip type and coplanar waveguide (M)MIC conductor geometries
- Active device modeling, parameter extraction and simulation and associated harmonic balance based circuit design.

International Journal of Numerical Modelling, Electronic Networks, Devices and Fields

AIMS AND SCOPE

Prediction through modelling forms the basis of engineering design. The computational power at the fingertips of the professional engineer is increasing enormously and techniques for computer simulation are changing rapidly. Engineers need models which relate to their design area and which are adaptable to new design concepts. They also need efficient and friendly ways of presenting, viewing and transmitting the data associated with their models.

The International Journal of Numerical Modelling: Electronic Networks, Devices and Fields provides a communication vehicle for numerical modelling methods and data preparation methods associated with electrical and electronic circuits and fields. It concentrates on numerical modelling rather than abstract numerical mathematics.

Contributions on numerical modelling cover the entire subject of electrical and electronic engineering. They range from electrical distribution networks to integrated circuits on VLSI design, and from static electric and magnetic fields through microwaves to optical design. Also included are papers that discuss the use of electrical networks as a modelling medium.

READERSHIP

Practicing electronic and electrical engineers, researchers and educators in numerical modelling.

SUBSCRIPTION ORDER FORM

[ ] Please enter my/our subscription to
INTERNATIONAL JOURNAL OF NUMERICAL MODELLING, ELECTRONIC NETWORKS, DEVICES AND FIELDS
ISSN: 0894-3370 Volume 7 (1994) Quarterly $395.00
Personal subscribers are entitled to 25% discount. Personal subscriptions must be paid out of private funds and mailed to a private address.
(All prices include postage/air speeded delivery)

[ ] Please send me a free sample copy

METHOD OF PAYMENT

[ ] Cheque/Money order enclosed (payable to John Wiley & Sons Ltd)

[ ] Purchase order enclosed [ ] Please send me an invoice

[ ] Please charge to my credit card
[ ] American Express [ ] Diners Club [ ] Mastercard/Access [ ] Visa/Barclaycard

Card No._____ Expiry Date._____

Name (PLEASE PRINT)_____

Address_____

_____

_____

Signature_____ Date_____

Send your order to either address:
Dept AC, John Wiley & Sons Ltd, Baffins Lane, Chichester, West Sussex, PO19 1UD, England
Subscription Dept. C, John Wiley & Sons Inc, 605 Third Avenue, New York, NY 10158, USA

Wave-Oriented Processing of Scattering Data

Leopold B. Felsen and Lawrence Carin
Department of Electrical Engineering
Polytechnic University
Brooklyn, NY 11201

Abstract - Windowed transforms applied to scattering data gathered along an elevated track parallel to a scattering surface are shown to provide local plane wave spectra which can be backpropagated to synthesize distinct features of the scattering environment. The method is illustrated for plane wave scattering from a truncated array of pitched strips.

Present and emerging technologies for microwave signal generation and detection, over wide bandwidths and with short-pulse resolution, have substantially enlarged the data base available for missions pertaining to scattering from targets, terrain and other complex environments. A principal task is the extraction of information about the scattering environment from the data. Modern signal processing techniques, despite their sophistication, generally do not utilize the "wave history" of the signal as influenced by the environment during its travel from source to receiver. It is proposed here that wave-oriented data processing, which incorporates wave content into the basis functions selected for analyzing the received signal, can motivate processing strategies linked with "good physics," thereby providing a parametrization for forward and backpropagation algorithms matched to phenomenology. Since the basis functions depend on configurational (space-time) as well as spectral (wavenumber-frequency) variables, the setting is in appropriate subdomains of the eight-dimensional configuration-spectrum phase space.

For implementation, it is suggested to assemble a catalog of scattering signatures that highlight specific scattering processes. Given data from a scattering experiment could then be projected onto the phase space subdomain relevant for comparison with the catalog signatures. For illustration, we consider oblique plane wave scattering from environments which are

suspected to have quasi-periodic background over an extended or truncated interval. Examples are the surface of the ocean, the flat corrugated roof of a building, a furrowed field, etc. Data is gathered on a track parallel to the scattering surface and perpendicular to the striations. The suspected features may be invisible from the platform (shielded by clouds, for example) but accessible to the radar signal.

For the catalog prototype, we choose a finite array of perfectly reflecting strips as shown in Fig. 1. Elsewhere [1,2], we have presented (and validated against a moment-method numerical reference solution) a rigorously based hybrid ray - (Floquet mode) algorithm that parametrizes the scattering in terms of truncated Floquet modes (FM) from the bulk of the array and FM-modulated edge diffractions from the truncations. The two-dimensional numerically determined scattered field $u(x; y_o)$ along the horizontal x-track at a near zone height $y_o = 1\lambda$, as shown in the bottom of Fig. 2, represents the given data base (λ = operating wavelength). To extract wave phenomenology, this data is subjected to a windowed Fourier transform, with respect to x, in the $(x, k_x; y_o)$ phase space subdomain, where k_x is the wavenumber corresponding to x. This yields the local spectrum $u(k_x(x);y_o)$ (grey-scale plot of Fig. 2) which specifies the local plane wave strength and direction at each sampled point $(x; y_o)$. The (x, k_x) windowed transform is the spatial analog of the time-frequency transform of signal processing [3]. One notes a) five tracks extended over x with constant k_{xm} which describe m-indexed truncated collimated beams, and b) two tracks extended over x with variable k_x which describe spatially spreading waves. (The conventional global Fourier transform (left-hand plot in Fig. 2) has spectral peaks at k_{xm} and at $k_x\lambda=\pm 2\pi$ (grazing angles), but no x resolution). The local plane wave (i.e., ray) spectra can be backpropagated to the scattering surface along the directions $\theta=\sin^{-1}(k_x\lambda/2\pi)$ to identify there the local regions $(\underline{x},0)$ responsible for establishing the observed field at $(x; y_o)$. This procedure is found to yield for each backpropagated track in b) a convergence onto two scattering centers $\underline{x}_1$ and $\underline{x}_2$, and for each track in a) an interval between $\underline{x}_1$ and $\underline{x}_2$ intercepted by the θ_m-inclined parallel beam. Since constant k_{xm} implies linear phase progression $\exp(ik_{xm}\underline{x})$ along $\underline{x}$, each contribution in a) synthesizes a distinct linearly phased truncated aperture distribution, whereas each contribution in b) synthesizes cylindrical waves

emanating from the endpoints $\underline{x}_1$ and $\underline{x}_2$ of the active region on the $y = 0$ plane. These features match the hybrid ray-FM scattering model introduced in [1,2] for the truncated periodic array, since the k_{xm} phasings of the various beams are found to be consistent with the FM dispersion relation, for the <u>infinite</u> array, at the specified values of θ_i, λ and d. Thus, the windowed (x, k_x) transform extracts, <u>directly</u> from the data, the diffraction phenomenology that had been invoked to parametrize (i.e., provide the wave-oriented basis functions for) the <u>forward</u> scattering problem in [1,2].

At greater observation heights, for example, $y_o = 100\ \lambda$, the (x, k_x) plot takes on the form shown in Fig. 3. The FM beams no longer overlap completely as in Fig. 2 but their x-projected width is still approximately equal to the width of the truncated array. Upon backpropagation, each beam still converges onto the aperture region but with poorer resolution than before. Similar considerations apply to the cylindrically spreading edge contributions. Having sorted out phenomenology via the windowed Fourier transform, resolution can be selectively enhanced by other processing (e.g. multiresolution) algorithms [4-7]. When the periodicity is randomly perturbed, the (x, k_x) signature becomes fuzzier (Fig. 4) but still reveals the underlying truncated periodic array background. Other scenarios, like backscatter over various frequencies, can be analyzed by the same general scheme, as can other scattering phenomena for enlarging the catalog. For time domain applications see [7].

References

1. CARIN, L., and FELSEN, L.B. :"Time harmonic and transient scattering by finite periodic flat strip arrays: Hybrid (ray)-(Floquet mode)-(MOM) algorithm," *IEEE Trans.*, 1993, **AP-41**, (4), pp. 412-421

2. FELSEN, L.B., and CARIN, L: "Diffraction theory of frequency and time domain scattering by weakly aperiodic truncated thin wire gratings," to appear in *J. Optical Soc. Am. A.*

3. COHEN, L.: "Time-frequency distributions - A review," *Proc. IEEE,* 1989, **77**, (7), pp. 941-981

4. MOGHADDAR, A., and WALTON, E.K.:"Time-frequency distribution analysis of scattering from waveguide cavities," *IEEE Trans.*, 1993, **AP-41**, pp. 677-679

5. KIM, H., and LING, H.: "Wavelet analysis of backscattering data from an open-ended waveguide cavity," *IEEE Microwave and Guided Wave Letts.*, 1992, **2**, (4), pp. 140-142

6. KIM, H., and LING, H.:"Wavelet analysis of radar echo from finite-size targets," *IEEE Trans.* **AP-41**, 1993, (2), pp. 200-202

7. CARIN, L., FELSEN, L.B., PILLAI, S.U., KRALJ, D., LEE, W.C.:"Dispersive modes in the time domain: analysis and time-frequency representation," submitted to *IEEE Microwave and Guided Wave Letts.*

Figure Captions

Figure 1. Finite array of forty perfectly conducting strips for which scattering data is computed. Parameters: $w=\lambda$, $d=3\lambda$, $s=2.366\lambda$, $\alpha=30°$, $\theta_i=45°$, λ=wavelength.

Figure 2. Scattered field along horizontal x–track at 1λ above grating (bottom), global Fourier transform (FT) of bottom curve (left), and windowed FT with Gaussian window function having standard deviation $\sigma=4.5\lambda$ (center).

Figure 3. As in Fig. 2, observed 100λ above the grating.

Figure 4. As in Fig. 2, except the period d in Fig. 1 is selected using a Gaussian random number generator with a mean $d_{AVG}=3\lambda$ and a standard deviation $\sigma_d=0.03\lambda$.

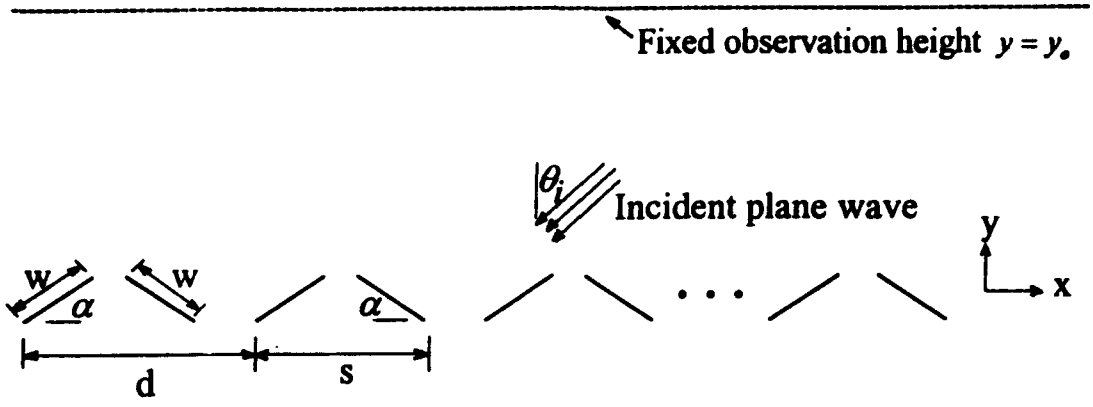
Fixed observation height $y = y_o$
θ_i
Incident plane wave
y
x
w
w
α
α
d
s

Fig. 1

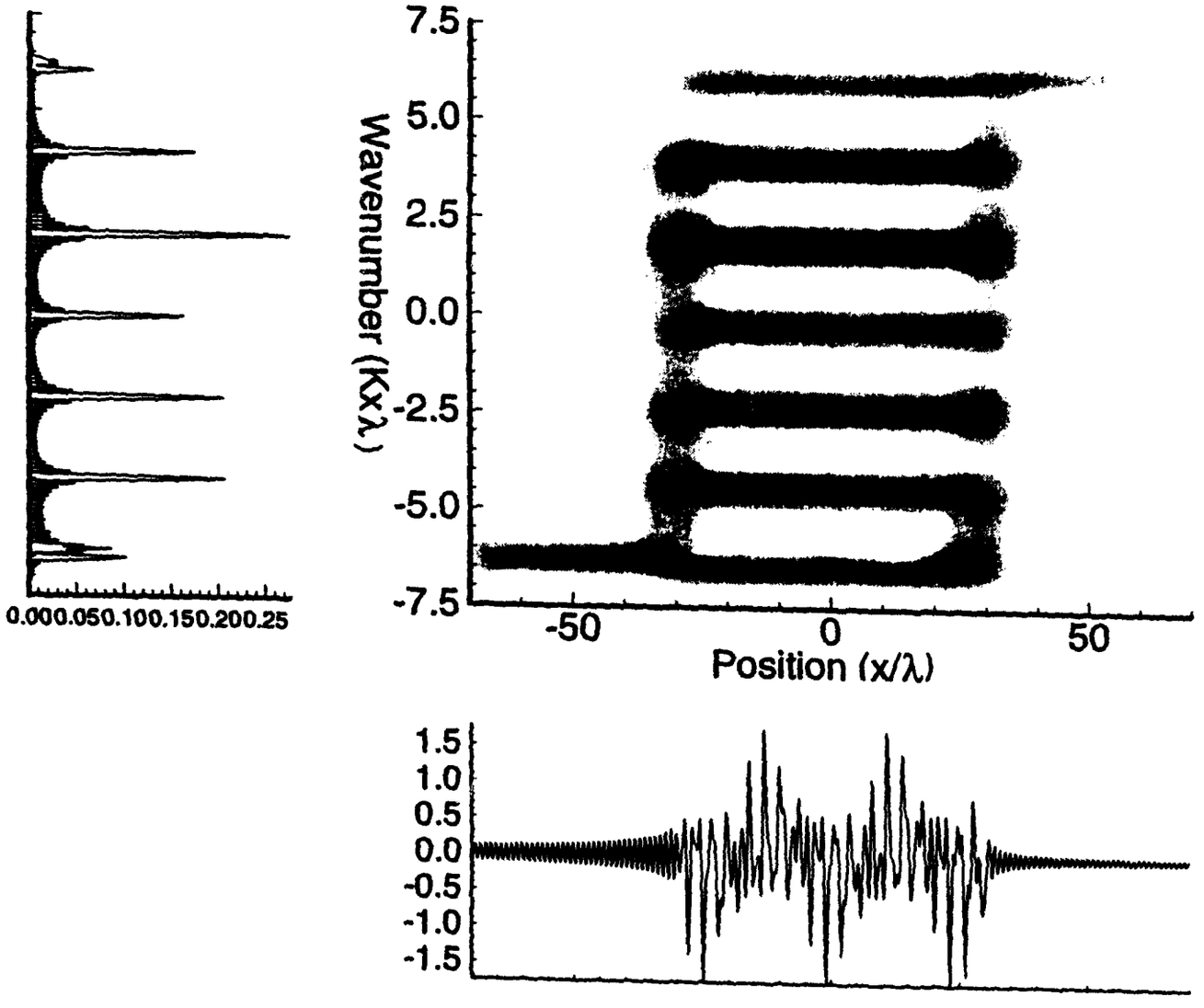
0.000.050.100.150.200.25
7.5
5.0
2.5
0.0
-2.5
-5.0
-7.5
Wavenumber (Kx/λ)
-50
0
50
Position (x/λ)
1.5
1.0
0.5
0.0
-0.5
-1.0
-1.5

Fig. 2

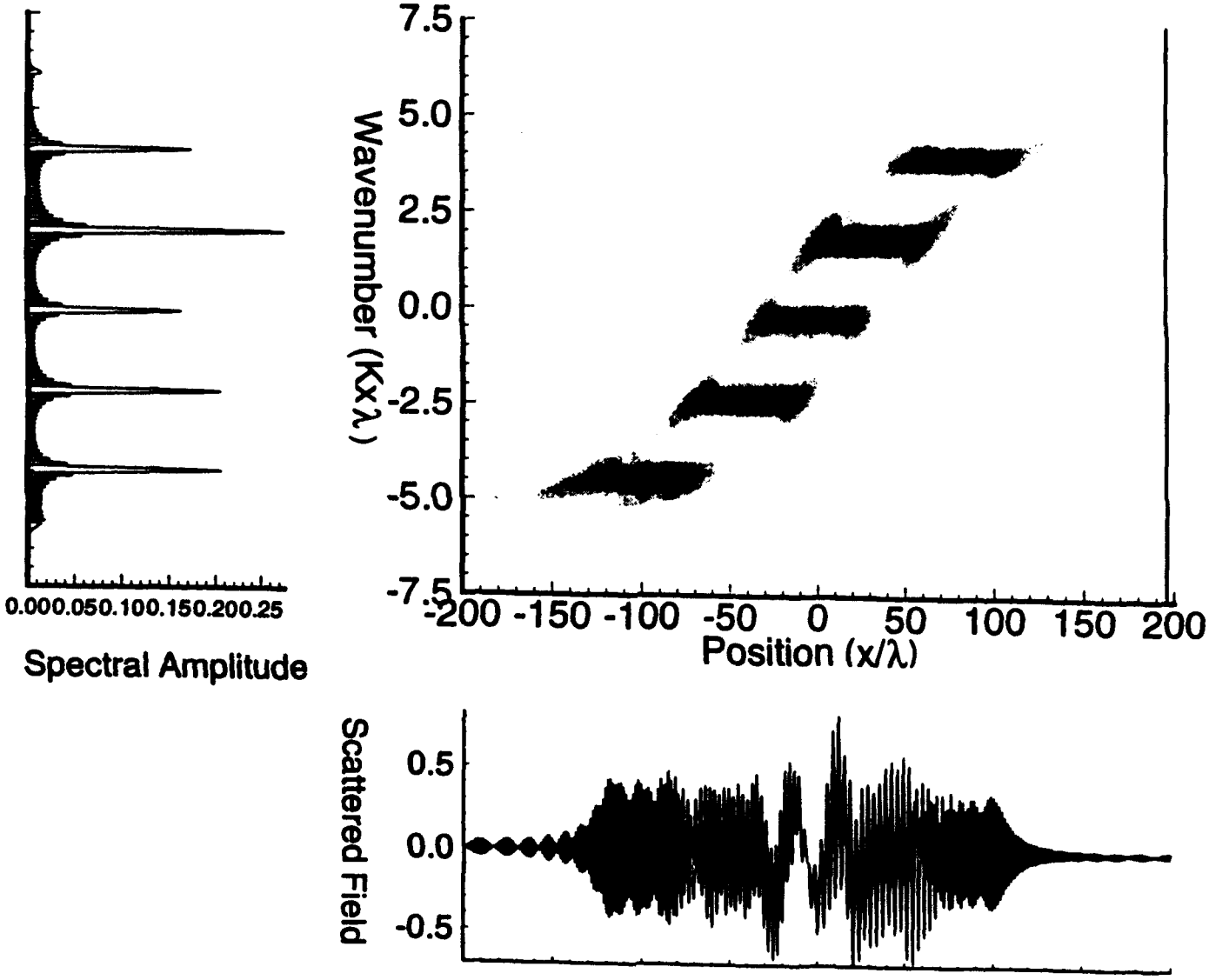
0.000.050.100.150.200.25
Spectral Amplitude
7.5
5.0
2.5
0.0
-2.5
-5.0
-7.5
Wavenumber (Kx λ)
-200 -150 -100 -50 0 50 100 150 200
Position (x/λ)
0.5
0.0
-0.5
Scattered Field

Fig. 3

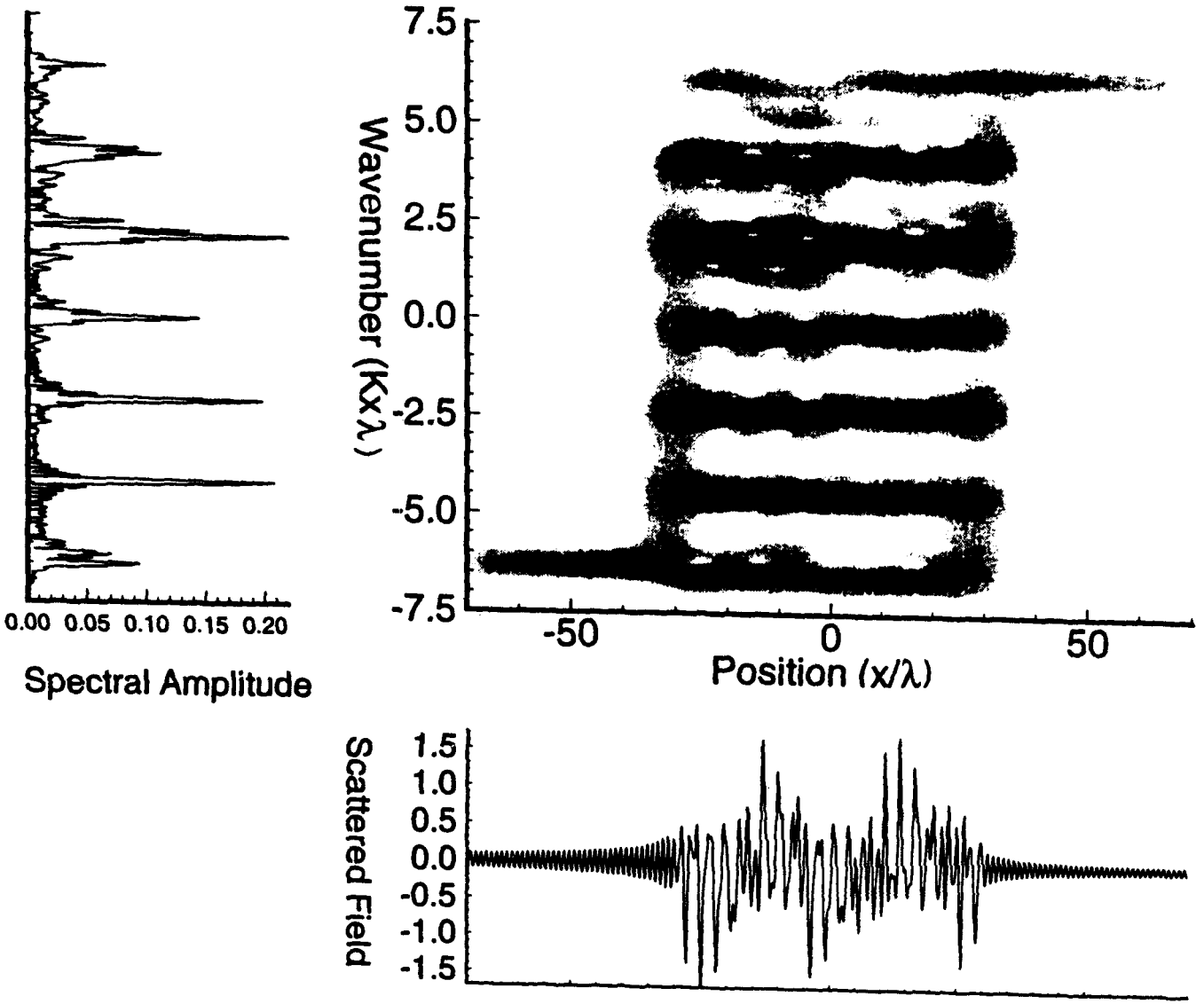
0.00 0.05 0.10 0.15 0.20
Spectral Amplitude
7.5
5.0
2.5
0.0
-2.5
-5.0
-7.5
Wavenumber (Kx/λ)
-50
0
50
Position (x/λ)
1.5
1.0
0.5
0.0
-0.5
-1.0
-1.5
Scattered Field

Fig. 4

Dispersive Modes in the Time Domain: Analysis and Time-Frequency Representation

L. Carin, L.B. Felsen, D. Kralj, S.U. Pillai, and W.C. Lee

Department of Electrical Engineering
Polytechnic University
Six MetroTech Center
Brooklyn, NY 11201

Abstract- Four algorithms for time-frequency (TF) distributions are considered for the processing and interpretation of dispersive time-domain (TD) data: the short-time Fourier transform, frequency and time domain wavelets, and a new ARMA-based representation. The TF resolutions of the various distributions are discussed and compared with reference to results for the scattered fields from a chirped finite grating excited by a pulsed plane wave. The processing in the TF phase space extracts TD phenomenology, in particular the instantaneous dispersion relation -- with its associated time-dependent frequencies -- descriptive of the local TD Floquet modes on the chirped truncated grating.

With the trend toward wideband (WB) transient waveforms, it is important to understand highly dispersive structure-induced wave phenomena directly in the time domain (TD) because the frequency-dependent scattering angles of the WB waveforms vary drastically over the bandwidth. Examples are provided by leaky modes (LM) on layered configurations [1,2] and by Floquet modes (FM) excited by gratings [3,4]. In a comprehensive study based on the high

frequency asymptotic behavior of rigorously formulated TD scattered fields, we have identified novel TD LM and FM which, although relating specifically to the layered [1,2] and grating [3,4] configurations, describe TD phenomena due to structure-induced dispersion in general. The asymptotics, due to inherent localization [5,6], parametrize the wave physics in terms of compact wave objects which can be forward and backward propagated for wave-oriented data processing in the (space-time)-(wavenumber-frequency) phase space (for space-wavenumber processing, see [7]); the accuracy of the algorithms have been verified in [1-4].

In this letter, we concentrate on the TD characteristics of FM observed at a fixed location as a function of time. The scattered TD signal is synthesized by inverting a frequency-domain FM Fourier integral asymptotically [3,4], and yields a result parametrized by one or more time-dependent frequencies localized around stationary points. Because the FM are dispersive, the instantaneous frequencies place time-dependent constraints on the modal wavenumbers through the FM dispersion relation. Thus, a TD dispersive mode is a wavetrain with varying oscillation frequency dictated by its instantaneous dispersion, inside an envelope weighted by the frequency spectrum of the input pulse [3,4]. Specifically, we consider an N-element weakly aperiodic grating of wires parallel to the y axis on the z=0 plane and located along the x axis at points x_n, for n=0, 1, 2, ..., N-1. For weak departure from strict periodicity, we have shown [4] that, by introducing the function x(v) through the replacement of the discrete index n by the continuous variable v ($n \rightarrow v$), we can define a local period $d(v)=dx(v)/dv=x'(v)$ in the vicinity of x(v). We have also shown that the instantaneous frequency associated with a $m \neq 0$ TD-FM excited by a normally incident plane wave is [4]

$$\omega_m(x,z,t)=\pm\frac{c\tau 2\pi|m|}{d_m(t)\sqrt{\tau^2-z^2}}, \quad d_m(t)=x'[v_m(t)], \quad m=\pm1,\pm2,... \tag{1}$$

Here, $\tau=ct$ with c the speed of light in vacuum, m tags the various FM that propagate away from the grating, and $x[v_m(t)]$ identifies the localized region on the grating aperture from where the rays of the mth FM, which reach the observer at (x,z) at time t, originate. The instantaneous dispersion relation [4] $\sin\theta_m(t)=m\lambda_m(t)/d_m(t)$ (λ=wavelength) reveals that <u>all</u> $m\neq0$ FM travel to the observer at the <u>same</u> time-dependent angle $\theta_m(t)=\sin^{-1}[1-(z/\tau)^2]^{1/2}$. This allows synthesis of highly resolved short-pulse (SP) scatterings from the collection of individual wires by superposition, at each instant of time, of the various interfering TD-FM wavetrains with their distinct frequencies given by (1). The analysis above has been generalized to the case of an obliquely incident pulsed plane wave [8]; the wave physics in that case is similar to that for normal incidence but with an escalation in algebraic complexity.

A useful way to display the role of time-dependent localized frequencies in scattering data is via time-frequency (TF) phase-space representations, as examined recently by several authors. Attention has been given to the Wigner transform [9], the short-time Fourier transform (STFT) [9-11], and a frequency-domain wavelet transform [10,11]. Here we look at the time-dependent frequencies and instantaneous dispersion relations by comparing four different TF processing schemes for a grating example, which comprises 20 (N=20) wire elements at $x_n=d_o(n+n^2\alpha/2)$; the aperiodicity parameter is $\alpha=.0025$, corresponding to a maximum variation of nearly 5% in the local period over the extent of the aperiodic grating.

For the problem conditions listed in its caption, Fig. 1 exhibits results for the TD scattered field (bottom plot), for its conventional global frequency spectrum (left-side plot), and for its instantaneous spectrum obtained via STFT with a Gaussian window having a standard deviation σ=0.602T (center plot). Also shown is the scattered field for the same finite unchirped grating (α=0). One observes that even a weak chirp may introduce significant departures from the periodic case. The results demonstrate nicely how the STFT parametrizes the data in terms of instantaneous physical wave processes that are hidden completely in the global FT. One discerns two distinct TF signatures: those with short time duration, broad instantaneous bandwidth and negligible dispersion (vertical bands) at the beginning and the end, and those with long time duration, narrow instantaneous bandwidth and strong dispersion (curved bands). The former represent SP wavefronts which sweep past the observer during a time interval equal to the pulse duration whereas the latter represent sustained oscillatory waves associated with TD-FM [3]. Scattering is seen to occur only over a finite time interval, implying a scatterer of finite extent, with weak body resonances. Taken together, the STFT features characterize clearly the scattering from a finite aperture whose scattering-induced equivalent excitation is the superposition of several distinct dispersive wavefields; the initial and final nondispersive pulsed events are due to diffraction at the truncations and (or) due to a nondispersive degenerate mode. This interpretation, inferred directly from the STFT, is in complete accord with the analytic model [4].

The STFT, which sorts out the basic physics, has constant TF resolution. To home in better on the modal dispersion relation (in our case the TF curve from (1)), we consider variable-width windowing via two versions of the wavelet transform. The first, implemented in the

frequency domain (FD), was developed by Ling and Kim [10,11] and is essentially a variable window STFT. The FD wavelet (in our case, a modulated Gaussian) is described in the caption of Fig. 2. Compared with the STFT (Fig. 1), the results in Fig. 2 do show narrowed definition of the instantaneous dispersion bands. However, this wavelet transform is known to require data for which the early and late time response are discernable clearly. In Fig. 3 the TD transform using the Morlet "mother wavelet" [13] also implements the high (poor) temporal-poor (high) frequency resolution tradeoff but without the restrictive *a priori* discrimination between early and late times. Since the TD wavelet transform gathers low and high frequency information by using wide and narrow time windows, respectively, the temporal resolution at low frequencies is poor (see the early-time nondispersive return) but improves at higher frequencies with correspondingly poorer frequency resolution (note that the vertical spread of the modal TF bands is wider at higher frequencies). The final TF processing scheme is based on a newly developed Auto-Regressive Moving Average (ARMA) algorithm [14] that guarantees stable spectral pole (and residue) extraction within a sliding TD Gaussian window (as was used in the STFT). The poles, weighted by their respective residues, yield the TF tracks in Fig. 4, which are seen to coincide closely with the instantaneous frequencies predicted in (1). The dispersion curves of the m=1, 2, and 3 TDFM modes are predicted very accurately with the ARMA scheme, while the predicted m=4 curve is slightly lower than that given by (1). This may be attributed to weak excitation of the m=4 mode since its time-dependent frequencies are at the upper edges of the frequency spectrum (see Fig. 1). An additional advantage of the ARMA scheme is its excellent stability even in the presence of noise.

In conclusion, we have processed numerical scattering data for a chirped truncated grating excited by a pulsed plane wave to demonstrate extraction of information pertaining to TD dispersive phenomenology. Four different TF processings have been presented and compared. The STFT, which is least beset by artifacts, provides a good first cut at the phenomenology of TD wave objects in the TF phase space. The wavelet transforms selectively resolve the STFT bands around the dispersion curves tracing out instantaneous frequencies. For the example here, the windowed-ARMA scheme provides the best TF resolution.

References

[1] F. Niu and L.B. Felsen, "Asymptotic analysis and numerical evaluation of short pulse radiation from a point dipole in a grounded dielectric layer," *IEEE Trans. Antennas and Prop.*, vol. AP-41, pp. 762-769, June 1993.

[2] F. Niu and L.B. Felsen, "Time domain leaky modes on layered media: dispersion characteristics and synthesis of pulsed radiation," *IEEE Trans. Antennas and Prop.*, vol. AP-41, pp. 755-761, June 1993.

[3] L. Carin and L.B. Felsen, "Time harmonic and transient scattering by finite periodic flat strip arrays: Hybrid (ray)-(Floquet mode)-(MOM) algorithm," *IEEE Trans. Antennas and Prop.*, vol. AP-41, pp. 412-421, April 1993.

[4] L.B. Felsen and L. Carin, "Diffraction theory of frequency and time domain scattering by weakly aperiodic truncated thin wire gratings," to appear in *J. Optical Soc. Am. A.*

[5] L.B. Felsen, "Phase-space engineering," *Ultra-Wideband Short-Pulse Electromagnetics*, (H.L. Bertoni, L. Carin, and L.B. Felsen, Eds), Plenum, New York, 1993.

[6] L.B. Felsen and N. Marcuvitz, Radiation and Scattering of Waves, Prentice-Hall, Englewood Cliffs, NJ, Ch. 4, 1973.

[7] L.B. Felsen and L. Carin, "Wave-oriented processing of scattering data," to appear in *Elect. Letts.*

[8] L.B. Felsen and P. Borderies, "Time harmonic and transient scattering by an infinite periodic flat strip array," *Ultra-Wideband Short-Pulse Electromagnetics*, (H.L. Bertoni, L. Carin, and L.B. Felsen, Eds), Plenum, New York, 1993.

[9] A. Moghaddar and E.K. Walton, "Time-frequency distribution analysis of scattering from waveguide cavities," *IEEE Trans. Antennas and Prop.*, vol. AP-41, pp. 677-679,

[10] H. Kim and H. Ling, "Wavelet analysis of backscattering data from an open-ended waveguide cavity," *IEEE Microwave and Guided Wave Letts.*, vol. 2, pp. 140-142, April 1992.

[11] H. Kim and H. Ling, "Wavelet analysis of radar echo from finite-size targets," *IEEE Trans. Antennas and Prop.*, vol. AP-41, pp. 200-207, Feb. 1993.

[12] P. Hubral and M. Tygel, "Analysis of the Raleigh pulse," *Geophysics*, vol. 54, pp. 654-658, 1989.

[13] I. Daubechies, "The wavelet transform, time-frequency localization and signal analysis," *IEEE Trans. Info. Theory*, vol. 36, p. 964, Sept. 1990.

[14] S.U. Pillai, T.I. Shim, and D.C. Youla, "A new technique for ARMA-system identification and rational approximation," *IEEE Trans. Sig. Proc.*, vol. 41, pp. 1281-1304, March 1993.

Figure Captions

Figure 1. Scattering data and processing (see text) for a 20 (N=20) element grating of thin wires parallel to the y axis at z=0 and located along the x-axis at $x_n=d_o(n+n^2\alpha/2)$ for n=0, 1, 2,..., N-1; the aperiodicity parameter is α=.0025. The normally incident pulsed plane wave is described by a Raleigh wavelet [2,3,12] with center wavelength $\lambda_c=d_o/2$, and the scattered field is observed at a distance of $20\lambda_c$ directly above the right-most wire. Time is normalized to $T=d_o/c$, where c is the speed of light in vacuum. The TD scattered field and the global frequency spectrum for the same finite unchirped grating (α=0) are shown dashed.

Figure 2. FD wavelet transform [10,11] of scattering data in Fig. 1 from aperiodic grating. The FD wavelet is adjusted such that in the early time the STFT Gaussian window is narrow and provides high temporal resolution; as the window is moved to the late time, it widens and provides good frequency (poor temporal) resolution. The standard deviation of the Gaussian window is σ=0.481T at 9.872T and grows to 1.333T at the end of TD waveform.

Figure 3. Time domain Morlet [13] wavelet transform of scattering data in Fig. 1 corresponding to the aperiodic finite grating. The wavelet has 2.5 periods of a sine wave within the 3db point of the Gaussian envelope; the Gaussian envelope has a standard deviation of σ=2.15T at frequency 0.69fT and a standard deviation of σ=0.32T at frequency 5.67fT.

Figure 4. ARMA processing of scattering data in Fig. 1 corresponding to the aperiodic finite grating. ARMA processing is performed to extract resonant frequencies and their residues over windowed portions of the time-domain data. A sliding Gaussian window is used as in Fig. 1, with a standard deviation of σ=0.602T. For each window position, the poles associated with models ARMA(8,1) through ARMA(12,12) are calculated along with their residues. Each dot in this figure represents a pole from one of the ARMA models and its intensity is indicated by the grey scale. The curves represent the time-dependent dispersion curves of the TDFM as given by (1).

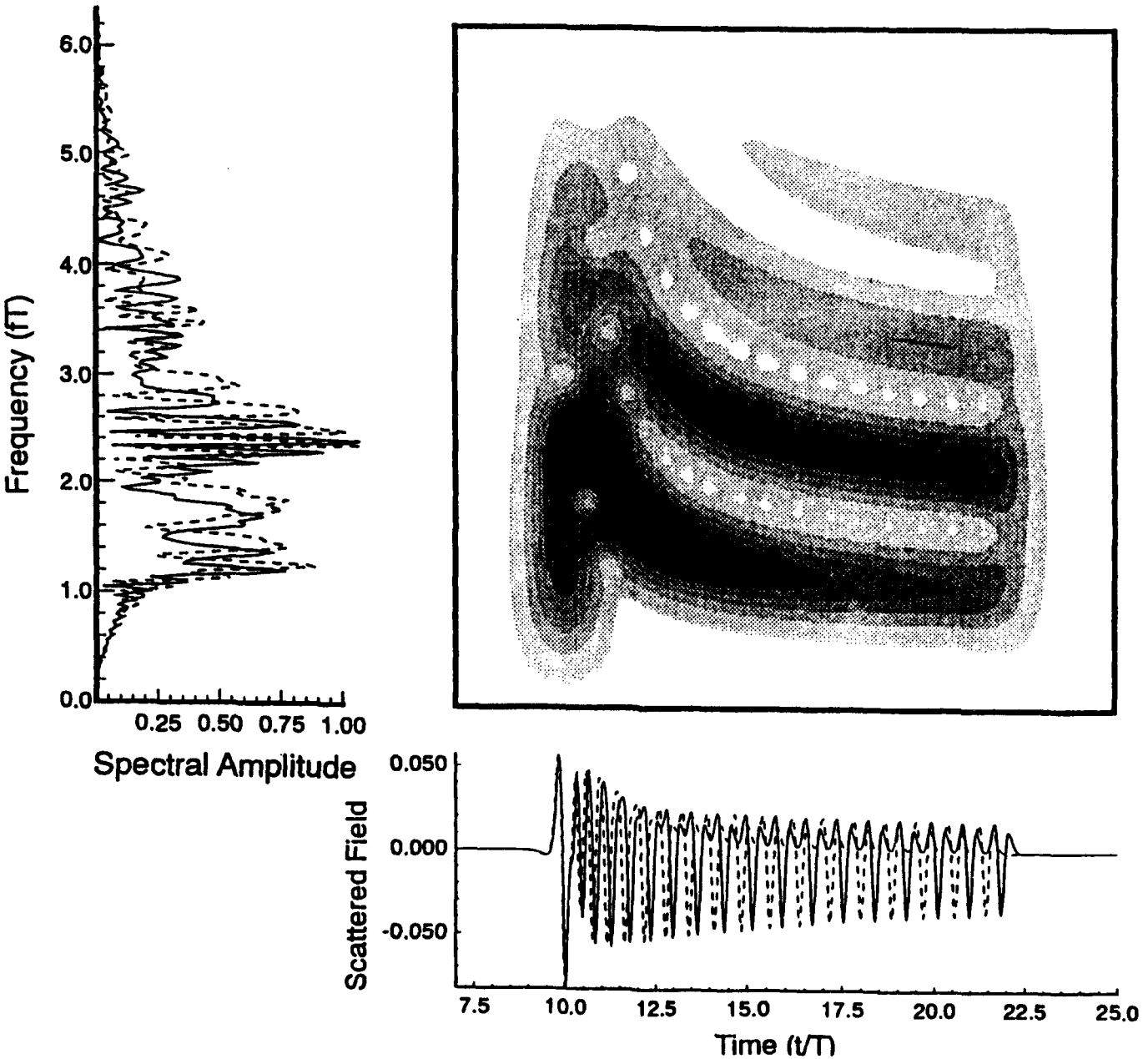
Frequency (fT)
6.0
5.0
4.0
3.0
2.0
1.0
0.0
0.25 0.50 0.75 1.00
Spectral Amplitude
Amplitude
1.0
0.9
0.8
0.7
0.6
0.5
0.4
0.3
0.2
0.1
0.0
Scattered Field
0.050
0.000
-0.050
7.5 10.0 12.5 15.0 17.5 20.0 22.5 25.0
Time (t/T)

Fig. 1

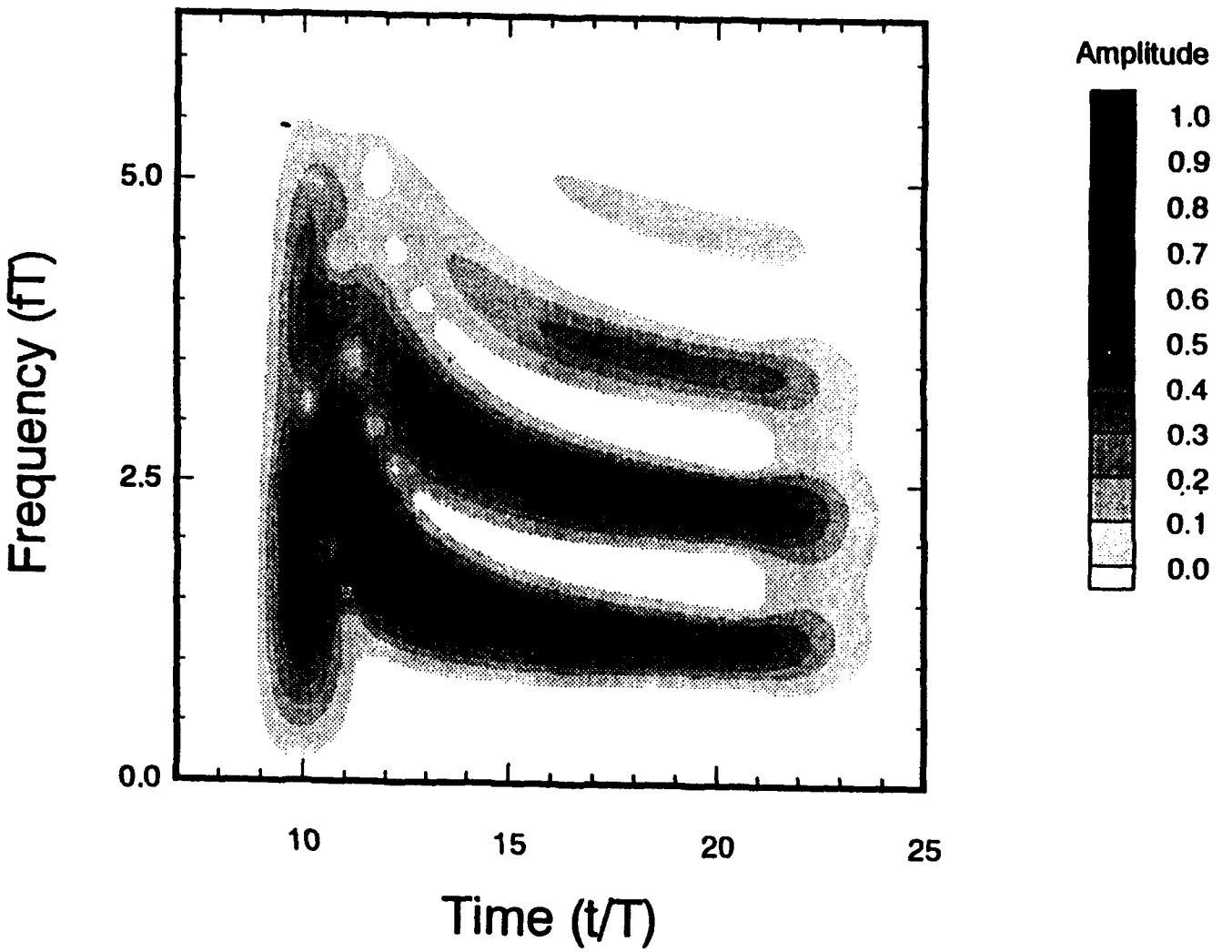
Amplitude
1.0
0.9
0.8
0.7
0.6
0.5
0.4
0.3
0.2
0.1
0.0
Frequency (fT)
5.0
2.5
0.0
10
15
20
25
Time (t/T)

Fig.

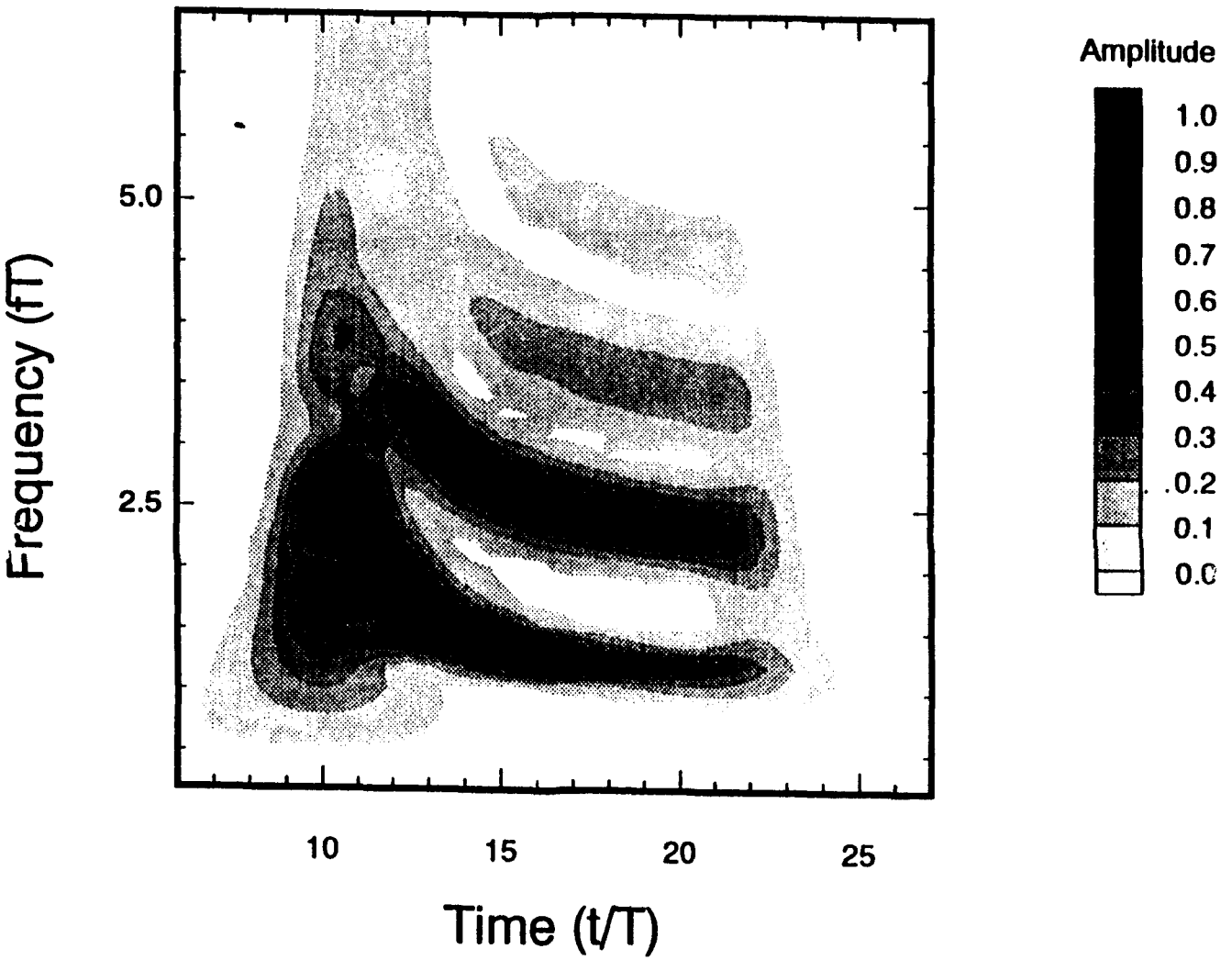
Frequency (fT)
5.0
2.5
10
15
20
25
Time (t/T)
Amplitude
1.0
0.9
0.8
0.7
0.6
0.5
0.4
0.3
.0.2
0.1
0.0

Fig. 3

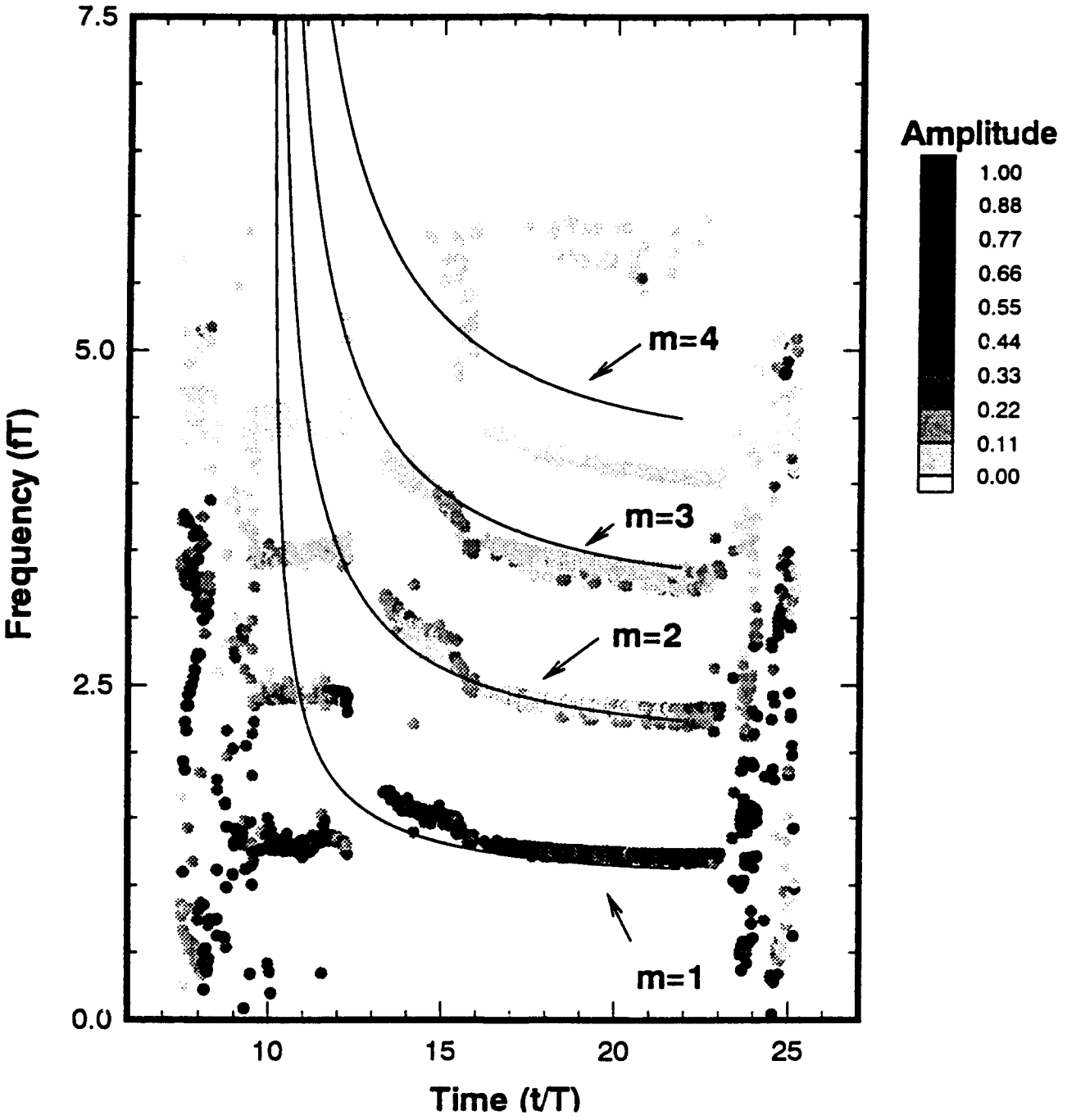
7.5
5.0
2.5
0.0
Frequency (fT)
10
15
20
25
Time (t/T)
m=4
m=3
m=2
m=1
Amplitude
1.00
0.88
0.77
0.66
0.55
0.44
0.33
0.22
0.11
0.00

Comparison of Different Field Theoretical Methods of Analysis of Distributed Microwave Circuit Elements

Roberto Sorrentino,
Mauro Mongiardo, Luca Roselli, Paolo Mezzanotte and Ferdinando Alessandri

Istituto di Elettronica, University of Perugia, I-06100, Perugia, Italy
Fax +39-75-5852658

Abstract
Mode matching method and Finite Difference Time Domain method are taken as representative field-theoretical methods for the modelling of microwave circuits. MM represents analytically oriented (or integral) frequency domain methods, while FDTD represents numerically oriented (or differential) time domain methods. A number of test cases have been run on an IBM RISC 365 workstation to compare the accuracy and efficiency of both methods.

1. Introduction

Numerical methods for the analysis of microwave structures belong basically to two categories corresponding to the numerical formulation of Maxwell's equations in differential or integral form. Strictly numerical methods, on the one hand, are based on the discretization of Maxwell's equations, (e.g. Finite Element, Finite Difference (in frequency or time domain)) or on the implementation of Huygen's principle (Transmission Line Matrix (TLM) method). Thanks to their high flexibility, they are well suited for problems with irregular geometries. On the other hand, methods requiring a high degree of mathematical preprocessing, such as Spectral Domain Approach (SDA) and Mode Matching (MM) method, are based on a continuous rather than discrete representation of the field quantities. They lead to very efficient computer codes, but are limited to problems with simple geometries.

Another important categorization of numerical methods concerns the use of frequency or time domains. Dramatic advances in computing resources have recently made it possible the practical implementation of time domain techniques for the simulation and even the optimization of microwave circuits. Not may years ago, because of their huge memory and CPU requirements, methods such as Transmission Line Matrix (TLM) and Finite Difference Time Domain (FDTD) were considered essentially as academic exercises. Instead, we are now facing an era where such techniques are becoming increasingly popular and of practical utility.

While differential methods have been used both in frequency and time domains, integral methods have been used in practice only in frequency domain. This paper is an attempt to make a comparison between two very popular numerical methods, FDTD and Mode Matching (MM) illustrating the respective advantages and disadvantages. Such methods are typical representatives of frequency and time domain techniques, on the one hand, and of differential and

integral methods on the other hand. The aim is to help the researcher to make a sound choice of the technique most appropriate for the problem at hand.

The comparison will be unavoidably biased by the personal views and specific experience of the authors. Additional and more extensive investigations are needed. We nevertheless hope the results presented here, although partial and preliminary, have some degree of general validity.

2. Classification of Field Theoretical Methods

The electromagnetic (EM) modeling of microwave circuits can be viewed as a process consisting of the following steps (Fig.1):

- Description of the problem (geometry, electrical parameters, etc.) (INPUT)
- Excitation of the structure
- Computation of the EM field in the structure by solution of Maxwell's equations
- Extraction of terminal parameters (e.g. S-parameters) (OUTPUT)

Our attention here focuses on the third step, i.e. the solution of Maxwell's equations. The Maxwell's equation solver can operate either in time domain (TD) or frequency domain(FD). Correspondingly, adopting Miller's point of view [1], it can be defined as a

- field propagator : time-domain solver, where the initial value boundary value problem is updated in time;
- field solver: frequency domain solver requiring matrix inversion or system solution

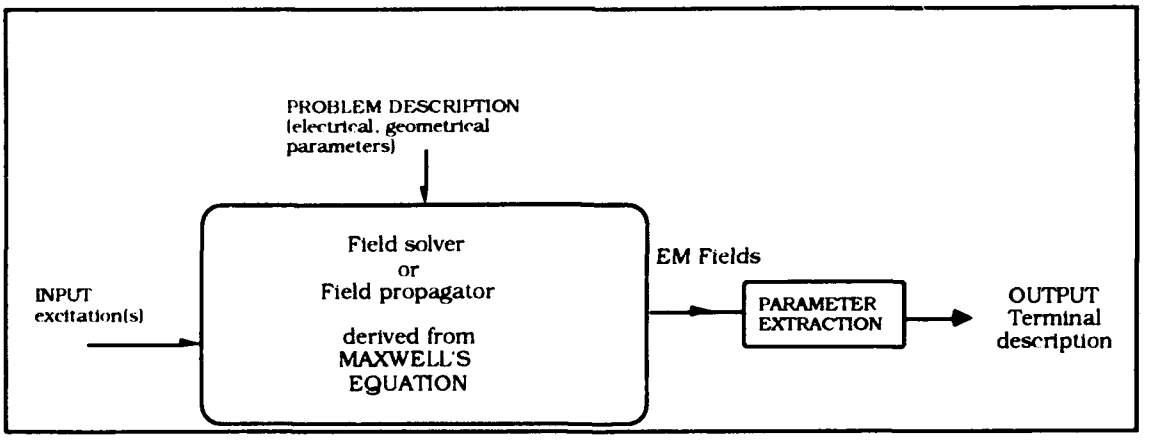

Fig. 1 The direct problem

The inverse or synthesis problem (Fig. 2) consists of finding (some) geometrical parameters that give a desired output (terminal description) from a specified input. The synthesis is usually performed in FD using proper iterative algorithms. Essentially the synthesis results from a large number (100-1000) of repeated analyses according to some search strategy. Attempts to synthesize

microwave structures directly in TD, however, have been reported recently using a time reversal technique [2] or a hybrid frequency/time domain [3].

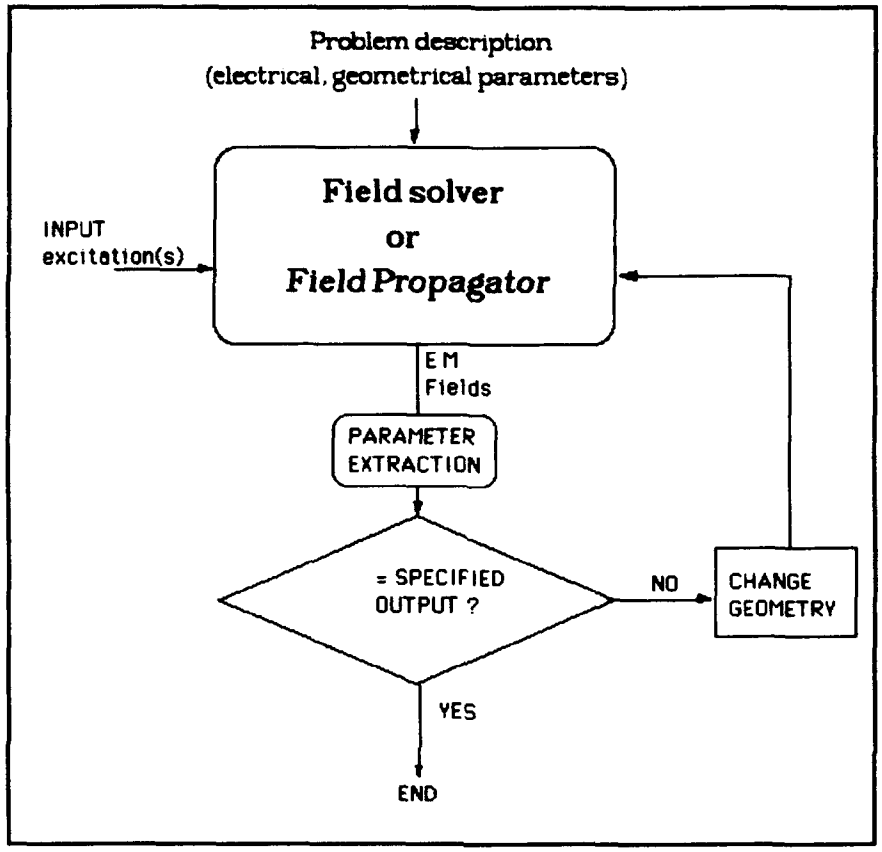

Fig. 2. The synthesis (inverse) problem

A variety of numerical techniques can be employed for building up a field solver or propagator. Among the most common are the following:

Integral Equation (IE) techniques, including the Spectral Domain Approach (SDA)
Mode Matching (MM) Method
Finite Element and Boundary Element Methods (FEM, BEM)
Finite Difference (FD) Method
TLM Method (and Spatial Network Method, SNM)

	Frequency Domain	Time Domain
Differencial Method	FD FDTLM FEM	FDTD TLM
Integral Method	MM SDA EFIE, MPIE	

Tab. I Classification of Numerical Methods

These techniques can operate in frequency or time domains (Tab. I). It is interesting to note that some techniques originally developed and typically operating in one domain are currently being transferred into the complementary domain (e.g. FDTLM [4]. Also, the Finite Element Method, conventionally applied in frequency domain, can be implemented in time domain). Integral methods in Time Domain have not been implemented for microwave circuit modelling, except in connection with wave scattering [5].

Step	Activity	MM	FDTD
Formulation	Translating the elementary description into a complete mathematical representation	Apply appropriate segmentation Use appropriate bases for field representations. (Green's functions). This step requires educated people and has to be adjusted each time.	Adoption of Yee's algorithm, the appropriate graded mesh, ABC, etc. Simple, broadly applicable in the basic formulation. More elaborate for higher performances (edge condition, graded mesh)
Numerical Implementation	Transforming into a computer algorithm using various numerical techniques	A new code must be assembled each time (problem dependent). Some building blocks can be re-used	Relatively easy. The code is problem independent
Computation	Obtaining quantitative results	Fast	Lengthy
Validation	Determining the numerical and physical credibility of the computed results	A new validation is required for any new problem, but computation is not time consuming (experimental results generally available in frequency domain)	Since the code is problem independent it must not be validated each time; but running computation is time consuming

Tab.II. Steps in developing a computer model with MM and FDTD

This paper is not intended to provide a comparative analysis of all numerical methods, but rather to focus our attention to two of the most consolidated and representative methods, such as FDTD and MM methods. Such methods represent, on the one hand, methods operating in time and frequency domains . On the other hand, they also represent the two categories of differential methods or numerically oriented methods (based on discretized space representation) and integral or analytically oriented methods (using continuous space representation)[1]. Most of the conclusions drawn here in connection with FDTD and MM can be extended to other methods such as TLM and SDA.

[1]It must be noted that we refer here to a generalized Mode Matching technique that includes a 3D formulation. Accordingly, MM consists of the segmentation of a 3D structure into simple volume elements (boxes) where the EM fields are expanded in terms of modal series or in terms of Green's function. At the apertures connecting contiguous boxes, the tangential fields are expanded into suitable 2D basis functions (usually waveguide modes). The boundary conditions at the apertures are manipulated so as to obtain a linear system of equations in the expansion coefficient of the 2D series.

Attribute	Definition	MM	FDTD
Accuracy	The quantitative degree to which the computed results conform to the mathematical and physical reality being modeled; accuracy, preferably of known and, better, yet, selectable, value is the most important model attribute	The accuracy attained is quantified by using some convergence test. The cost (simulation time) of performing this step is considerably less than with FDTD	The accuracy attained is quantified by using some convergence test. The cost (simulation time) of performing this step is considerably higher than with MM
Efficiency	The relative cost of obtaining the needed results; determined by the human effort required to develop the computer input and interpret the output, and by associated computer cost of running the model	A user front-end which allows an easy input of the data as well as an easy intepretation of the output has not been realized yet. This is partially due to the lack of generality of MM codes. The cost of running the model is generally less than for FDTD	User front ends are under development and are very encouraging. The easy access to the fields helps to develop a basic understanding of what is going on. The cost of running the model is quite high.
Utility and flexibility	The applicability of the computer model in terms of problem size and complexity; utility also relates to ease of use, reliability of results obtained, etc.	The code is usually strictly problem-dependent. As such, using the code for a slightly different application is almost impossible. Problem size and complexity are rather large since the method use as unknowns the fields on surfaces and not on volumes. Reliability is also excellent.	The code is applicable to almost any geometry. With proper modifications can also be used in conjunction with non linear solvers. The complexity and problem size are strictly related to the computer performances. At the moment even the analysis of small regions can exceeds normal workstation capability. Reliability tests can be very expensive.

Tab. III. Attributes of computer codes based on MM and FDTD

2. Terms of Comparison

It is widely recognized that FDTD has the advantage of high versatility and easiness of implementation but has poor numerical efficiency compared to MM. The latter is numerically efficient, but has limited versatility and requires more analytical work to be implemented.

We try now to establish a comparison between the two methods on a more quantitative basis using the following criteria:

a. A "conceptual" approach based on the analysis of the methodology
b. Accuracy of the computed results:
   - source of errors
   - convergence of the solution

c. Computation time
d. Memory requirements

3. Analysis of methodologies

We use here with slight modifications Miller's point [1] to analyze both MM and FDTD methodologies in the process of developing a computer code for the analysis of 3D structures.
Tab. II synthesizes the main steps required in this process. Specific comments, added to both methods, illustrate the respective advantages and disadvantages.
Based again on Miller's paper, Tab. III. identifies the desirable attributes of a computer code and tries to specify in what measure they are possessed by MM and FDTD.

4 Accuracy of the computed results

Error sources in MM are essentially due to two types of approximations. One is the truncation error in the computation of the Green's function in the volume, the other is the truncation error in the field representation on the apertures connecting adjacent volume elements. Both errors can be viewed as due to the limited spatial resolution of the two field representations. It is interesting to observe that, in many cases, because of the variational properties of the MM formulation, the two errors tend to compensate. As a consequence, even with a modest approximation of the field distributions, very accurate results can be obtained by a proper choice of the two truncations [6].

The application of MM method to structures with non canonical boundaries (e.g. curved boundaries in rectangular coordinated, etc.) involves additional errors due to boundary approximation.

Error source	Description	Countermeasures
Green's function approximation	Series truncation in the field representation in the volume	Asimptotic evaluations
Aperture field approximation	Series truncation in the field representation on the apertures	Incorporation of edge conditions
Non conformal boundaries	Boundaries are approximated by staircase approximation	Use different segmentation. Use conformal coordinates

Tab. IV. Error sources in MM

Other error sources associated with typical numerical procedures, such as the numerical solution of linear systems, are of standard nature and have a relative negligible impact.
Some of the most common error sources in FDTD are listed and described in Tab. V. Possible countermeasures to decrease the associated errors are also suggested.
In both MM and FDTD error decreases with increasing spatial resolution.

For a quantitative comparison of both methods in terms of accuracy vs. efficiency we have performed a number of numerical experiments performed on an IBM RISC 6000 -365.

Error source	Description	Countermeasures
Spatial discretization	Coarseness of the spatial mesh	Increase spatial resolution
Spatial quantization	Geometrical dimensions not fitted by the mesh	Graded mesh
Time record truncation	Truncation of the time iteration affects Fourier transform evaluation	Add more iterations. Use spectrum estimation techniques
Non conformal contours	Contours are staircase approximated	Use a conformal coordinate system

Tab. V. Error sources in FDTD

A square TEM line has been chosen as a test case.
Results of FDTD computations of the characteristic impedance for different space resolutions are shown in Fig. 3a. The relative error has been evaluated with reference to an extrapolated value for Zo. In the present case, for a spatial resolution decreasing by a factor of 10 (from 1mm down to 0.1 mm) the error decreases by a factor 14 (from 0.7% down to about 0.05%), while the computation time increases by a factor of 634 (from 7s to 4440s).
The same problem has been solved by MM method (in this case the method can also be referred to as Field Matching method). Computed results are shown in Fig. 4a. The spatial resolution here is defined as one half of the smallest spatial wavelength. When the spatial resolution is increased to 0.3mm, the error becomes negligible. On the opposite, when the spatial resolution is 3.3 mm, the CPU time becomes negligible. It is also observed that the convergence of the MM solution is not as smooth as that of FDTD.
Another test case is illustrated in Figs. 3b, 4b. The center conductor of the line has been replaced by a metal strip. The higher field singularity produces an increase of the coarseness error that can be observed in both methods.
The results of Figs. 3 and 4 show that MM is extremely more efficient than FDTD. This is due also to the choice of the geometries considered that are perfectly suited for MM. On the other hand, even simple modifications of the geometries require a new MM code to be set up, while the same FDTD code can be used in all cases.
Quantization error is a typical phenomenon occurring when using space discretization. This type of error and the effect of using graded meshes are illustrated in Fig. 5. A square coaxial line with sizes a=10.25 mm and a'=4.25 mm is considered. Fig. 5a shows the results of FDTD analyses when the mesh does not fit with the metal boundaries (mesh size=0.5mm). In such a case the sizes of the line must be adjusted by $\pm\Delta$ in order to fit the mesh. The computed data exhibit an error varying from 4.26 to 11.90 %. For the same mesh size, the error in Fig. 3 was only 0.37%. To reduce the error one can reduce the mesh size or introduce a variable mesh. The first option involves additional memory storage and CPU

requirements. Fig. 5b shows that the use of a simple graded mesh to fit the metal boundaries reduces the error again down to 0.37%.
A finer mesh is useful to reduce the discretization error by better resolving the field distribution. It is essential however that the mesh refinement be properly located. Fig. 5c shows that a mesh refinement in the center of the structure does not have any significant effect (err=0.44%). On the contrary, a denser mesh at the corners reduces the error almost to zero (Fig. 5d).

5. A 3D MMIC discontinuity

As a final example we have analyzed both by MM and FDTD a via hole ground in a packaged microstrip line. Fig. 6a shows the segmentation adopted for implementing the MM analysis. Fig. 6b shows the model adopted with the FDTD simulator. Fig. 6c shows the computed behaviors of the via compared with our measurements. A good agreement is observed between theories and experiment. In particular both theories predict the effect of package resonances.

Nx * Ny * Nz	mesh dimension	CPU time mS per Δt DEC 12000	CPU time mS per Δt RISC 6000-375
65 * 65 * 100	422500	1100	-
64 64 * 100	409600	630	3950
10 * 10 * 100	10000	480	80
51*55*105	294525	650	-

Table VI. CPU time per Δt versus mesh size.

Tab. VI describes the discretization used in FDTD. To run the FDTD code in a reasonable amount of time (hours), it has been necessary to use the DEC 12000 Massive Parallel computer of Ferdinand Braun Institute (FBH).
The MM code was again extremely faster. One analysis required about 5 minutes per frequency point on the IBM RISC 6000 workstation. The MM analysis involves the solution of a system of equation of the order of less than 500 variables, corresponding to the number of modes used in the field expansions.
It must be observed, however, that the presence of the transitions could be taken into account only with the FDTD code. In addition, the latter could be used to modify the the shape of the microstrip package and to introduce samples of damping materials to choke the resonances off. With the MM code, only the parameters of the rectangular subregions can be changed. Any variation in the shape of the regions would require a new code to be built up.

6. Conclusions

Mode matching method and Finite Difference Time Domain method have been taken as representative field-theoretical methods for the modelling of microwave circuits. MM represents analytically oriented (or integral) frequency domain methods, while FDTD represents numerically oriented (or differential) time domain methods. A number of test cases have been run on an IBM RISC 365 workstation to compare the accuracy, efficiency and versatility of both methods..

The MM code was shown to be extremely faster than the FDTD code. The latter however have extremely higher flexibility to model structures with various and different shapes, such as microstrip interconnections.

ACNOWLEDGMENT
Professor P. Russer and his co-workers at FBH are gratefully acknowledged for the support given to the authors with the use of the DEC 12000 masspar.

REFERENCES

[1] E.K. Miller, "Aselective survey of computational electromagnetics", IEEE Trans. AP, vol. AP-36, No. 9, pp. 1281-1305, Sept. 1988.

[2] R. Sorrentino, Poman So, and W.J.R. Hoefer, "Numerical microwave synthesis by inversion of the TLM process", Proc. 21st Eu. Microwave Conf., Stuttgart, Sept. 1991, pp. 1273-1277.

[3] P.P.M. So, W.J.R. Hoefer, J.W. Bandler, R.M. Biernacki, and S.H. Chen, "Hybrid frequency/time domain field theory based CAD of microwave circuits", in Proc. 23rd Eu. Microwave Conf., Madrid (Spain) 1993, pp. 218-219.

[4] H. Jin and R. Vahldieck, "The frequency domain TLM method- A new concept", IEEE Trans. MTT, vol. MTT-40, pp. 2207-2218, Dec. 1992.

[5] H. Mieras and C.L. Bennet, "Space-time integral equation approach to dielectric targets", IEEE Trans. AP, vol. AP-30, pp. 2-9, 1982.

[6] R. Sorrentino, M. Mongiardo, F. Alessandri, and G. Schiavon, "An investigation of the numerical properties of the mode-matching technique", Int. J. Numerical Modelling, vol. 4, pp. 19-43, 1991.

FDTD Computations

50 ohm RCL

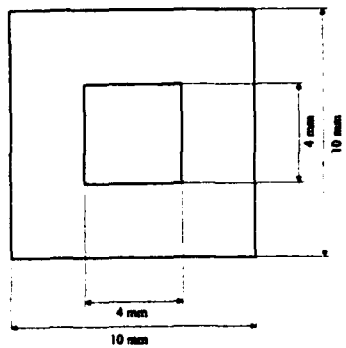

ds (mm)	Computed Z_n	CPU time (IBM RISC 6000-375)	err %
1	49.410	7 s	0.7
.5	49.582	40 s	0.37
.2	49.711	8 m 30 s	0.11
.1	49.745	1 h 14 m	0.051
$1x10^{-2}$	49.769 (extrapolated)		
$1x10^{-3}$	49.771 "		

Error versus space step

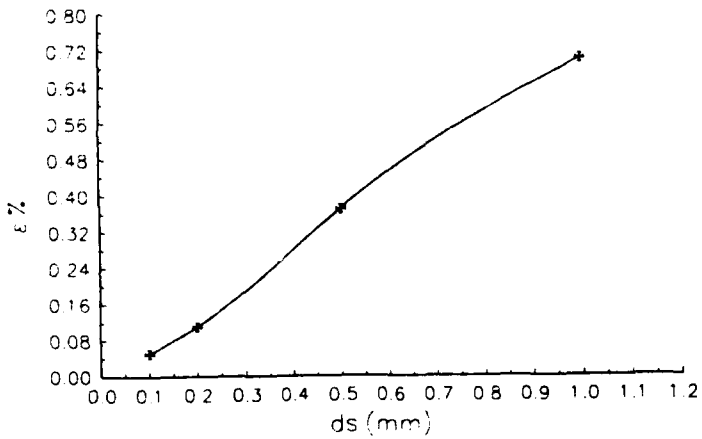

Fig. 3a

Homogeneous stripline

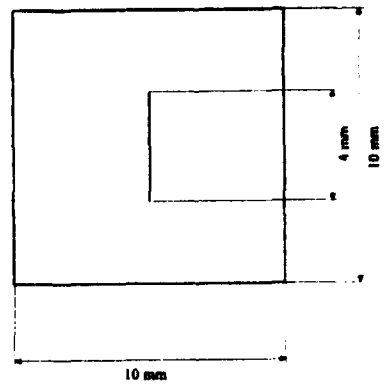

ds (mm)	Computed Z_n	CPU time (IBM RISC 6000-375)	err %
1	96.009	7 s	4.23
.5	98.167	40 s	2.08
.2	99.649	8 m 30 s	0.60
.1	100.162	1 h 14 m	0.09
$1x10^{-2}$	100.169 (Extrapolated)		
$1x10^{-3}$	100.190 "		
$1x10^{-4}$	100.210 "		
$1x10^{-5}$	100.256 "		

Error versus space step

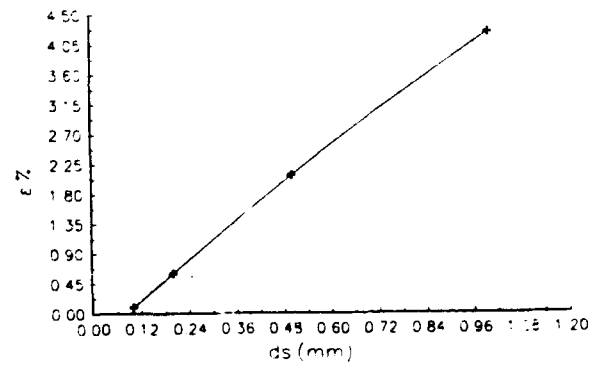

Fig.3b

MM Computations

50 ohm RCL

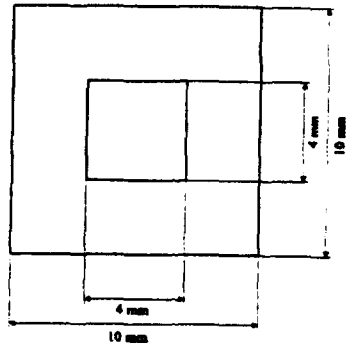

spatial resolution (mm)	Computed Z_0	CPU time (IBM RISC 6000-375)	err %
3.33	48.40	< .01 s	2.83
2	49.50	< .01 s	.62
1.11	49.70	< .01 s	.22
.77	49.76	< .01 s	.1
.66	49.77	.01 s	.08
.4	49.80	.02 s	.02
.34	49.81	.02 s	0

Error versus spatial resolution

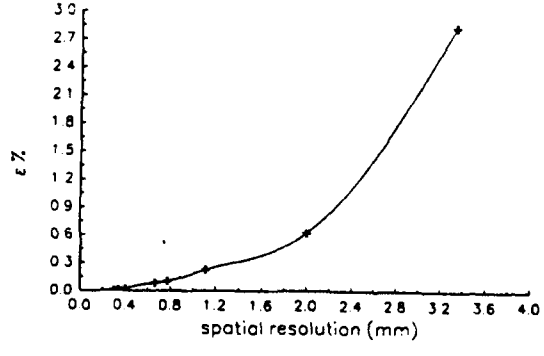

Fig. 4a

Homogeneous stripline

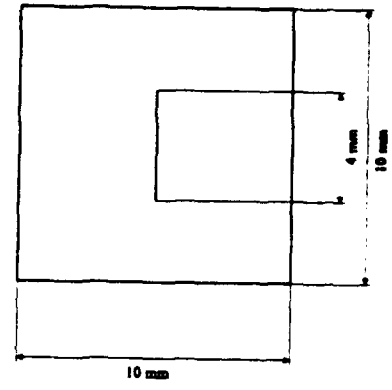

spatial resolution (mm)	Computed Z_0	CPU time (IBM RISC 6000-375)	err %
10	85.50	< .01 s	14.7
3.33	96.37	< .01 s	3.91
2	98.42	< .01 s	1.87
1.42	99.23	.01 s	1.06
1.11	99.64	.01 s	.65
1.08	99.88	.01 s	.41
.91	100	.01 s	.29
.66	100.2	.02 s	.09
.58	100.3	.02 s	0

Error versus spatial resolution

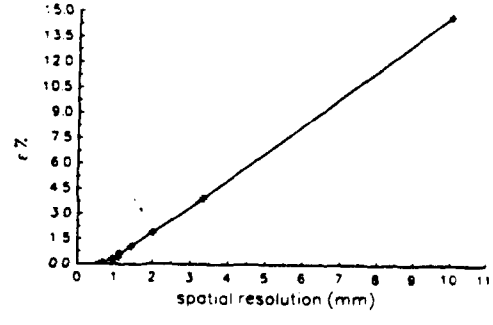

Fig. 4b

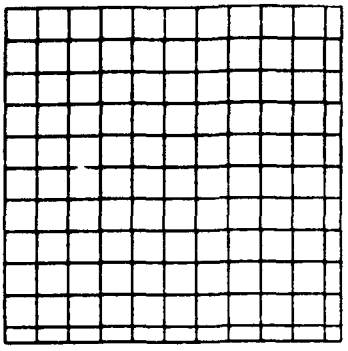

ds=.5 mm

Δ=.25 mm

	g+Δ	g−Δ	g'+Δ	g'−Δ		
case 1	*		*		45.56	4.26
case 2		*		*	49.58	4.18
case 3	*			*	42.34	11.03
case 4		*	*		42.40	11.90

Z_0=47.59 ohm

CPU time (RISC IBM 6000-365): 50 s

Fig. 5a

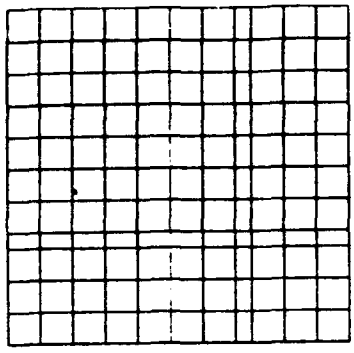

ds=.5 mm

ds'=.25 mm

impedance = 47.41 ohm

err%= .37

CPU time (RISC IBM 6000-365): 1 m 35 s

Fig. 5b

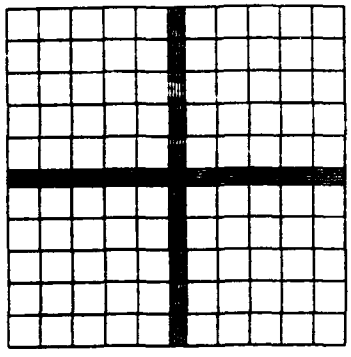

ds=.5 mm

ds'=.05 mm

impedance = 47.38 ohm

err% = .44

CPU time (RISC IBM 6000-365): 10 m

Fig. 5c

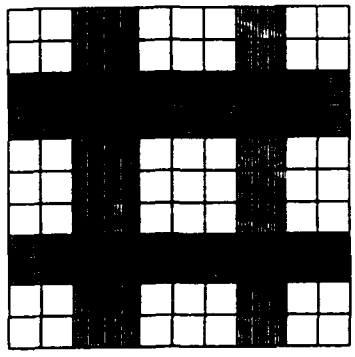

ds=.5 mm

ds'=.05 mm

impedance = 47.59 ohm

err% = 0

CPU time (RISC IBM 6000-365): 29 m

Fig. 5d

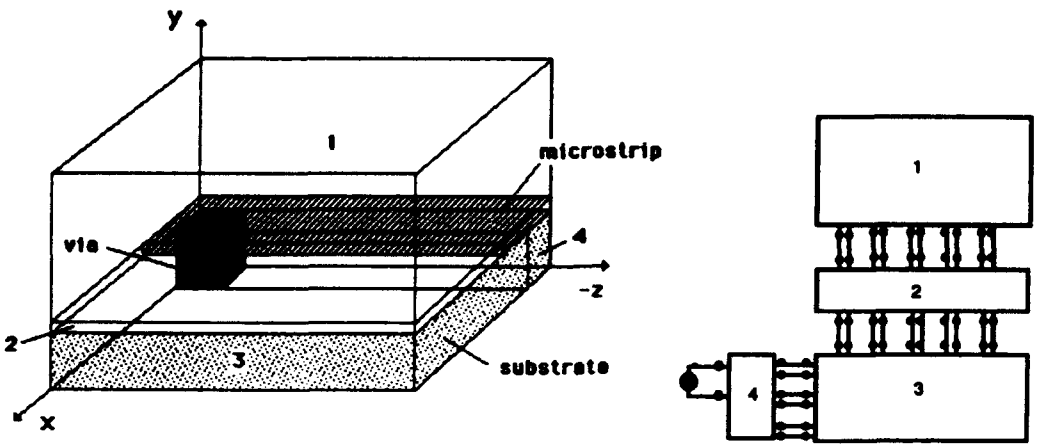

Fig. 6a The packaged microstrip via and the MM segmentation

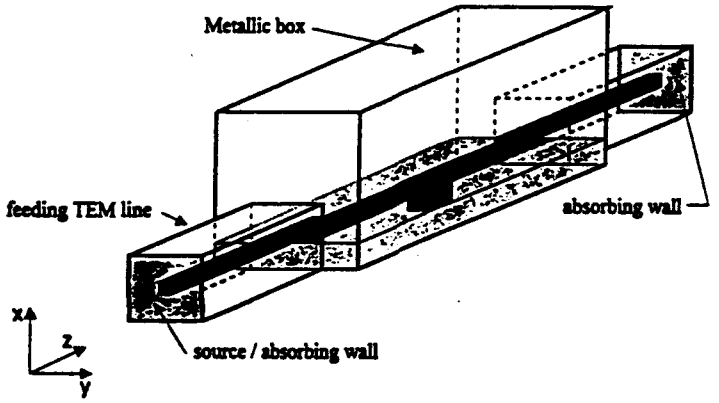

Fig. 6b The packaged microstrip via in the FDTD simulation

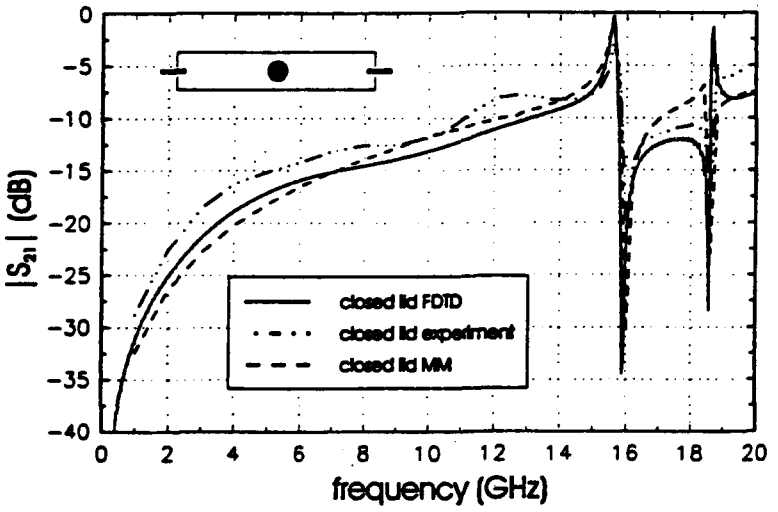

Fig. 6c Computed and measured behaviors of the via

Time Domain Electromagnetic Field Computation with Finite Difference Methods

T. Weiland [1]

Technische Hochschule Darmstadt

Fachbereich 18, Fachgebiet Theorie Elektromagnetischer Felder

Schloßgartenstr. 8, D6100 Darmstadt, Germany

ABSTRACT

The solution of Maxwell's equations in time domain is now being used since almost three decades and has had great success in many different applications. The main attraction of the time domain approach, originating in a paper of Yee [1], is its simplicity. It takes only marginal effort to write a computer code for solving a simple scattering problem compared with conventional frequency domain methods. However, when applying the time domain approach in a general way to arbitrarily complex problems, many seemingly simple additional problems add up.

We describe a theoretical framework for solving Maxwell's equations in integral from, resulting in a set of matrix equations, each of which is the discrete analogon to one of the original Maxwell equations. This approach is called Finite Integration Theory and was first developed for frequency domain problems starting about two decades ago. The key point in this formulation is that it can be applied to static, harmonic and time dependent fields, mainly because it is nothing but a computer-compatible re-formulation of Maxwell's equations in integral form. When specialized to time domain fields, the method actually contains Yee's algorithm as a subset. Further additions include lossy materials and fields of moving charges, even including fully relativistic analysis.

For many practical problems the pure time domain algorithm is not sufficient. For instance a wave guide transition analysis requires the knowledge of the incoming and outgoing mode patterns for proper excitation in time domain. This is a typical example where both frequency and time domain analysis are essential and only the combination yields the successful result.

Typical engineers may wonder why at all one applies time domain analysis to basically monochromatic field problems. The answer is simple: it is much faster, needs less computer memory, is more general and typically more accurate. Speed up factors of over 200 have been reached for realistic problems in filter and wave guide design.

The small core space requirement makes time domain methods applicable on desktop computers using millions of cells, and six unknowns per cell - a dimension that has not yet been reached by frequency domain approaches. This enormous amount of mesh cells is absolutely necessary when complex structures or structures with spatial dimensions of many wavelengths are to be studied. Our personal record so far is a wave guide problem in which we used 72.000.000 unknowns.

As result of the efficiency of time domain methods it is now possible to move from analysis type of computations to the wide area of automatic optimization, requiring hundreds of analysis runs for one target. We present a number of conventional examples from electrical engineering and the forefront reasearch in high power rf generation to demonstrate that time domain methods are 'better by design' and that there is no pure frequency domain method around that can reach the same generality and practicability.

INTRODUCTION

The theory (and the related software) of Maxwell's Grid Equations (MGE) was originally developed for frequency domain applications [2, 3, 4] and later from the need for solving many different problems including static, low frequency, high frequency and transient fields for designing large scale accelerators [5]. Thus the goal was to solve all of Maxwell's equations rather

[1] spokesman of the MAFIA collaboration: M.Bartsch, U.Becker, M.Dehler, M.Dohlus, X.Du, S.Gutschling, P.Hahne, R.Klatt, A.Langstroff, M.Marx, Z.Min, U.van Rienen, D.Schmitt, A.Schulz, B.Steffen, P.Thoma, B.Wagner, T.Weiland, S.Wipf, H.Wolter

than only a specific subset as one usually is concerned with. The basics of the theory and the computer codes are so well published that we refer here to the literature (e.g. [6] [7]) and start directly with writing down the MGE:

Maxwell's Grid-Equations - I (regular coordinate grids)

Integral Form	Matrix Representation
$\iint_A -\frac{\partial}{\partial t}\vec{B}\cdot d\vec{A} = \oint_{\partial A}\vec{E}\cdot d\vec{r}$	$-\mathbf{D_A}\dot{\mathbf{b}} = \mathbf{D_s e}$
$\iint_{\partial V}\vec{B}\cdot d\vec{A} = 0$	$\mathbf{D_A b} = \mathbf{0}$
$\iint_{\tilde{A}}\left(\vec{J}+\frac{\partial}{\partial t}\vec{D}\right)\cdot d\vec{\tilde{A}} = \oint_{\partial\tilde{A}}\vec{H}\cdot d\vec{\tilde{r}}$	$\tilde{\mathbf{D}}_\mathbf{A}(\mathbf{i}+\mathbf{D}_\epsilon\dot{\mathbf{e}}) = \tilde{\mathbf{C}}\,\tilde{\mathbf{D}}_\mathbf{s}\mathbf{D}_\mu^{-1}\mathbf{b}$
$\int_{\partial\tilde{V}}\vec{D}\cdot d\vec{\tilde{A}} = \iiint_{\tilde{V}}\varrho\, d\tilde{V}$	$\tilde{\mathbf{S}}\,\tilde{\mathbf{D}}_\mathbf{A}\mathbf{D}_\epsilon\mathbf{e} = \mathbf{q}$
$\vec{D} = \epsilon\vec{E}$	$\mathbf{d} = \mathbf{D}_\epsilon\,\mathbf{e}$
$\vec{B} = \mu\vec{H}$	$\mathbf{b} = \mathbf{D}_\mu\,\mathbf{h}$
$\vec{J}_L = \kappa\vec{E}$	$\mathbf{i_L} = \mathbf{D}_\kappa\,\mathbf{e}$

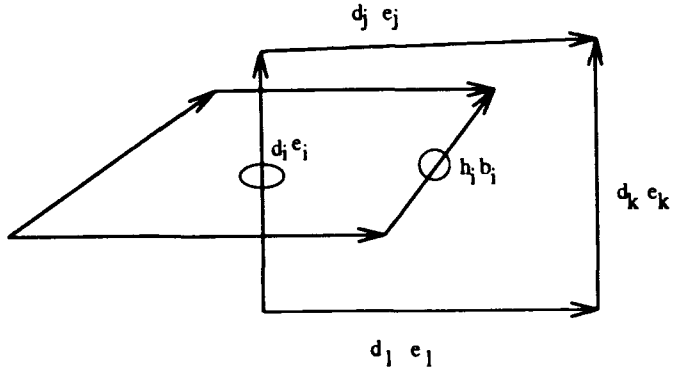

One cell of the grid **G** and the dual grid $\tilde{\mathbf{G}}$. The allocation of the electric field and flux components are shown as well as the allocations of the corresponding magnetic quantities.

This set of matrix equations is a one-to-one translation of Maxwell's equations to a grid space doublet $G-\tilde{G}$ and represents the only known theory that not only allows practical solution on a computer but also maintains all analytical properties of electromagnetic fields when changing from R^3 to the grid space.

In this formulation the grids are orthogonal coordinate grids in one of the usual coordinate systems such as $(x-y-z),(x-y),(r-\phi-z),(r-\phi),(r-z)$.

Grid-fields represent not only a large bunch of numbers but also have analytical, algebraic properties that ensure accurate numerical results and enable an algebraically exact self-testing of numerical results.

So far this theory is state of the art and the basis for existing computer codes solving problems in time domain, frequency domain and in statics [8].

In order to avoid the restriction to coordinate grids and to improve the capability of a grid to approximate curved boundaries, extensions to non-regular grids have been discussed by many authors in recent years, see for instance [9] [10] [11]. Here we present a generalization of the normal Maxwell-Grid-Equations to non-coordinate grids having the same properties as they will be discussed below. One can define a general grid doublet $\{\mathbf{G}-\tilde{\mathbf{G}}\}$:

- The solution volume **G** is simply connected and contained in R^3 (or R^2).
- **G** is a finite set of non-empty sub-volumes:

$$\mathbf{V} = \{V_1 \dots V_{n_V}\};\ \cap V_i = \{A_i\};\ \cup V_i = \mathbf{G}$$

- The non-empty areas A_i are defined as the intersections of two volumes:

$$\mathbf{A} = \{A_1 \dots A_{n_A}\},$$

- Lines L_i are defined by the intersection of areas:

$$\mathbf{L} = \{L_1 \dots L_{n_L}\}$$

- Points P_i are defined by the intersections of lines:

$$\mathbf{P} = \{P_1 \dots P_{n_P}\}.$$

On such a grid **G** it is more convienient to use integrated fields as state variables rather than directly the field components (for convienience we use from here on e no longer as electric field but as *voltage* and similarly we proceed with all other field vectors in order to avoid the introduction of a whole new set of variables).

If we define a grid *voltage* along a grid line L_i and magnetic flux quantity by:

$$e_i = \int_{L_i} \vec{E} \cdot d\vec{s}\ ;\ b_i = \int_{A_i} \vec{B} \cdot d\vec{A} \tag{1}$$

we can rewrite the first Maxwell equation on **G**:

$$\oint \vec{E} \cdot \vec{ds} = -\int \frac{\partial \vec{B}}{\partial t} \cdot \vec{dA} \tag{2}$$

in *exact* representation as:

$$\sum_k c_{ik} e_k = -\frac{\partial b_i}{\partial t} \tag{3}$$

So far no approximation and no discretization is applied. The only step from the orginal field equation to the latter one was to replace field components by their exact integrals along lines or over areas.

Similarly we continue with replacing the second Maxwell equation but on $\tilde{\mathbf{G}}$ rather than on **G**, where $\tilde{\mathbf{G}}$ is defined such that each point $\tilde{P}_i$ of $\tilde{\mathbf{G}}$ is located somewhere inside V_i of **G**. On this dual grid $\tilde{\mathbf{G}} = \{\tilde{V}_{n_V}\}$ we introduce magnetic voltages h_i, electric fluxes d_i and currents i_i as:

$$h_i = \int_{\tilde{L}_i} \vec{H} \cdot d\vec{s}\ ;\ \ , d_i = \int_{\tilde{A}_i} \vec{D} \cdot d\vec{A}\ ;\ i_i = \int_{\tilde{A}_i} \vec{J} \cdot d\vec{A} \tag{4}$$

With these new variables we again can exactly map the original equation:

$$\oint \vec{H} \cdot \vec{ds} = \int (\frac{\partial \vec{D}}{\partial t} + \vec{J}) \cdot \vec{dA} \tag{5}$$

to a grid equation:

$$\sum_k \tilde{c}_{ik} h_k = \frac{\partial d_i}{\partial t} + i_i \tag{6}$$

The third and fourth Maxwell equation is similarly turned into:

$$\sum_k \tilde{s}_{ik} d_k = q_i\ ;\ \sum_k s_{ik} b_k = 0\ ;\ with\ q_i = \int_{V_i} \rho\, dV \tag{7}$$

So far we have mapped all Maxwell equations to a grid space doublet without any specialization. The final discretization comes into the procedure only now that we have somehow to relate electric voltages and fluxes, and magnetic voltages and fluxes as well. In the above derivation the magnetic voltage is one variable and the magnetic flux another independent one. The relation f must be of the form:

$$f(\vec{B},\vec{H}) = \frac{\int_{A_i} \vec{B}\cdot d\vec{A}}{\int_{\tilde{L}_i} \vec{H}\cdot d\vec{s}} \approx D_{\mu,i}$$

The matrix $\mathbf{D}_\mu$ is now the discrete representation of the permeability. Thus in this derivation the approximation comes in through the material relations rather than difference expressions for derivatives.

In general this matrix is not diagonal but sparse with some dialgonals of nonzero elements. Furthermore $\mathbf{D}_\mu$ is symmetric for reciprocal materials. In the case of coordinate grids as well as for a few other orthogonal grid doublets (such as the one of URMEL-T, see further down) the discretization of the material equation has a second order accuracy and the material matrices are true diagonal if the material tensors are diagonal or isotrope.

The same arguments lead to the discrete permittivity and conductivity as (in general not diagonal) matrices:

$$\mathbf{d} = \mathbf{D}_\epsilon \mathbf{e} \;;\; \mathbf{i} = \mathbf{D}_\kappa \mathbf{e} \tag{8}$$

Summarizing this derivation yields a dual set of equations where the discrete equations correspond *one-to-one* to analytical ones on any non-regular grid doublet obeying the above definitions.

Maxwell's Grid-Equations - II (iregular grids)

Integral Form		Matrix Representation		
$\iint_A -\frac{\partial}{\partial t}\vec{B}\cdot d\vec{A}$	$= \oint_{\partial A} \vec{E}\cdot d\vec{r}$	$-\dot{\mathbf{b}}$	$=$	$\mathbf{C}\,\mathbf{e}$
$\iint_{\partial V} \vec{B}\cdot d\vec{A}$	$= 0$	$\mathbf{S}\,\mathbf{b}$	$=$	$\mathbf{0}$
$\iint_{\tilde{A}} \left(\vec{J}+\frac{\partial}{\partial t}\vec{D}\right)\cdot d\tilde{\vec{A}}$	$= \oint_{\partial \tilde{A}} \vec{H}\cdot d\vec{\tilde{r}}$	$\mathbf{i}+\dot{\mathbf{d}}$	$=$	$\tilde{\mathbf{C}}\,\mathbf{h}$
$\int_{\partial \tilde{V}} \vec{D}\cdot d\tilde{\vec{A}}$	$= \iiint_{\tilde{V}} \varrho\, d\tilde{V}$	$\tilde{\mathbf{S}}\,\mathbf{d}$	$=$	$\mathbf{q}$
$\vec{D}$	$= \epsilon\vec{E}$	$\mathbf{d}$	$=$	$\mathbf{D}_\epsilon\,\mathbf{e}$
$\vec{B}$	$= \mu\vec{H}$	$\mathbf{b}$	$=$	$\mathbf{D}_\mu\,\mathbf{h}$
$\vec{J}_L$	$= \kappa\vec{E}$	$\mathbf{i}_L$	$=$	$\mathbf{D}_\kappa\,\mathbf{e}$

This discrete form of Maxwell's equations is very general and not restricted to regular coordinate grids. However, most practical implementations do not use iregluar grids as the coding is by far more complicated as it is already for coordinate grids. However, to show that such non-coordinate grid doublets do exist we show one example with a 2D $(r-z)$ geometry where the grid $\mathbf{G}$ is made of triangles and the dual grid $\tilde{\mathbf{G}}$ of hexagons [11]. In this grid the material matrices are diagonal for isotrope material.

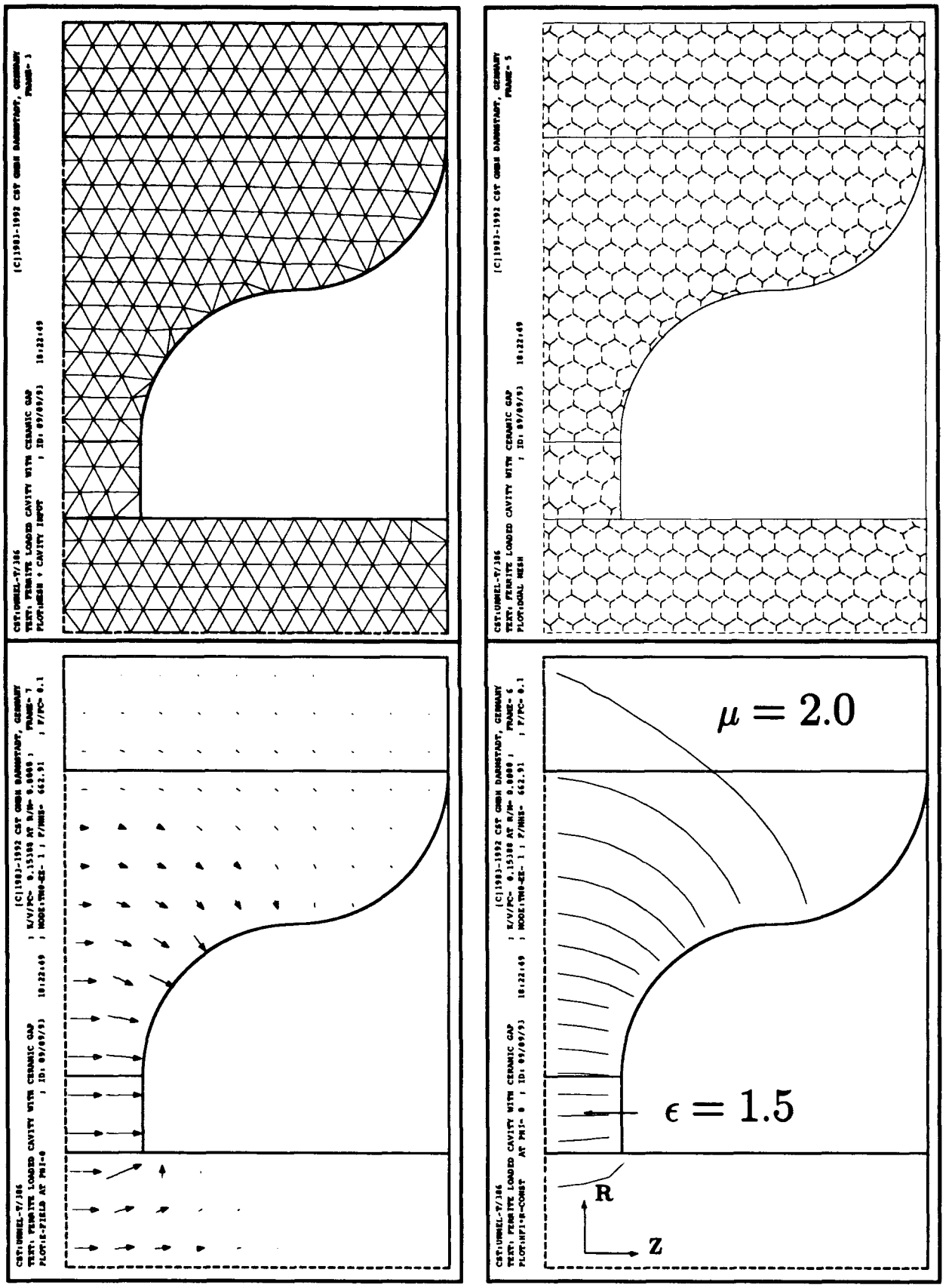

These plots show a two dimensional example of a non-regular grid doublet made of a triangluar and hexagonal set of meshes. The structure is a cylindrically symmetric resonator. The lower two plots show the electric field of the fundamental resonant mode as vector and field lines. This results were obtained from **URMEL-T** *[11].*

ALGEBRAIC PROPERTIES OF MAXWELL'S GRID EQUATIONS

Although this paper is supposed to deal mainly with time domain solutions, we will consider here field solutions also in time harmonic form as only the combination of frequency and time domain methods opens an almost unlimited area of possible applications.

The outstanding feature of Maxwell's Grid Equations (MGE) when compared with other numerical methods for solving field problems is that this set of matrix equations is a consistent discrete representation of the original field equations in that sense that basic properties of analytical fields are maintained when moving from $\mathbf{R^3}$ to $\{\mathbf{G}, \tilde{\mathbf{G}}\}$.

These properties may be considered useful in two ways. One aspect is that many numerical problems are a priori eliminated, such as spurious modes and parasitic charges. Furthermore numerical solution no longer are only a *bunch of numbers* but vectors with exact algebraic properties enabling an independent cross check of accuracy.

Another aspect is that the matrix theory can be used instead of the analytical equations to study properties of fields in an algebraic manner, without actually solving the equations numerically.

For grid doublets there exists a dual index system such that the point $\tilde{P}_i$ is located inside V_i and vice versa P_i inside $\tilde{V}_i$. All other elements of $\mathbf{G}, \tilde{\mathbf{G}}$ receive an index defined by this system as well. This numbering scheme ensures that the following key properties hold [6] [12] [13] [14]:

$$\mathbf{C} = \tilde{\mathbf{C}}^{\mathbf{T}} \tag{9}$$

$$\mathbf{S}\,\mathbf{C} = \mathbf{0} \tag{10}$$

Both equations represent a topological property resulting from the duality of the two grids. The analytical and algebraic properties resulting from these basic equations are [6]:

$$\mathbf{C}\,\mathbf{S} = \mathbf{0} \;\leftrightarrow\; \mathbf{curl\,grad} = \mathbf{0} \tag{11}$$

$$\mathbf{S}\,\mathbf{C} = \mathbf{0} \;\leftrightarrow\; \mathbf{div\,curl} = \mathbf{0} \tag{12}$$

and similarly for the dual grid operators:

$$\tilde{\mathbf{C}}\,\tilde{\mathbf{S}} = \mathbf{0} \;\leftrightarrow\; \mathbf{curl\,grad} = \mathbf{0} \tag{13}$$

$$\tilde{\mathbf{S}}\,\tilde{\mathbf{C}} = \mathbf{0} \;\leftrightarrow\; \mathbf{div\,curl} = \mathbf{0} \tag{14}$$

As an example for a proof using algebra we consider the (well known) fact, that resonant fields in loss free structures can have only real eigen frequencies. For the case of MGE it requires only a few lines to proove this. We rewrite the MGE in frequency domain as:

$$\mathbf{Ce} = -i\omega\mathbf{b} \tag{15}$$

$$\tilde{\mathbf{C}}\mathbf{D}_\mu^{-1}\mathbf{b} = +i\omega\mathbf{D}_\epsilon\mathbf{e} \tag{16}$$

We combine both equations to:

$$\tilde{\mathbf{C}}\mathbf{D}_\mu^{-1}\mathbf{Ce} = \omega^2\mathbf{D}_\epsilon\mathbf{e} \tag{17}$$

We introduce an energy density normalization by

$$\tilde{\mathbf{e}} = \mathbf{D}_\epsilon^{1/2}\,\mathbf{e} \tag{18}$$

and finally obtain:

$$(\mathbf{D}_\epsilon^{-1/2}\tilde{\mathbf{C}}\mathbf{D}_\mu^{-1/2})\,(\mathbf{D}_\epsilon^{-1/2}\tilde{\mathbf{C}}\mathbf{D}_\mu^{-1/2})^{\mathbf{t}}\,\tilde{\mathbf{e}} = \omega^2\,\tilde{\mathbf{e}} \tag{19}$$

This equation is a simple, algebraic, linear eigenvalue problem with an (obviously) symmetric and real matrix of the form A^tA. Thus one knows from algebra that all eigenvalues ω^2 are real and positive, q.e.d.

Another property of resonant fields is similarly easy to proove, namely that the average energy in the magnetic field equals the average energy in the electric field. To show this we write the MGE equations in frequency domain without sources and for loss free materials:

$$\mathbf{C}\,\mathbf{e} = -i\omega\mathbf{b} \tag{20}$$
$$\tilde{\mathbf{C}}\mathbf{h} = +i\omega\mathbf{d} \tag{21}$$

We multiply the first equation from the left with $\mathbf{h}^{*t}$ and the second one with $\mathbf{e}^{*t}$:

$$\mathbf{h}^{*t}\,\mathbf{C}\,\mathbf{e} = -i\omega\mathbf{h}^{*t}\mathbf{b} \tag{22}$$
$$\mathbf{e}^{*t}\tilde{\mathbf{C}}\,\mathbf{h} = +i\omega\mathbf{e}^{*t}\mathbf{d} \tag{23}$$

Transposing the last equation and taking the complex conjugate yields:

$$\mathbf{h}^{*t}\,\mathbf{C}\,\mathbf{e} = -i\omega\mathbf{h}^{*t}\mathbf{b} \tag{24}$$
$$\mathbf{h}^{*t}\,\mathbf{C}\,\mathbf{e} = -i\omega\mathbf{e}^{*t}\mathbf{d} \tag{25}$$

As $1/4\,\mathbf{h}^{*t}\mathbf{b}$ is the total magnetic field energy in $\mathbf{G}$ and $1/4\,\mathbf{e}^{*t}\mathbf{d}$ the electric energy in $\mathbf{G}$, we find that both are equal, q.e.d.

The same fact can be shown in a different way. Within the MGE one can show that the total change of energy within $\mathbf{G}$ in the presence of currents is given by [14]:

$$\frac{\partial W}{\partial t} = \frac{\partial W_e}{\partial t} + \frac{\partial W_m}{\partial t} = -\mathbf{i}^t\,\mathbf{e}^* \tag{26}$$

From this equation it also follows immediately that for $\mathbf{i} = \mathbf{0}$ and time harmonic fields that $W_e = W_m$.

The time idependent energy in $\mathbf{G}$ resulting from constant potentials and currents is given by expressions which can easily be identified as the corresponding analytical expressions, namely:

$$W_{e,static} = 1/2\,\mathbf{q}^t\varphi \;\left(\leftrightarrow W_{e,static} = \int_V \rho\Phi dV\right) \tag{27}$$

$$W_{m,static} = 1/2\,\mathbf{i}^t\mathbf{a} \;\left(\leftrightarrow W_{m,static} = \int_V \vec{A}\cdot\vec{J}dV\right) \tag{28}$$

where

$$\mathbf{e} = \tilde{\mathbf{S}}^t\varphi \;(\leftrightarrow \vec{\mathbf{E}} = -\mathbf{grad}\Phi) \tag{29}$$
$$\mathbf{b} = \mathbf{C}\mathbf{a} \quad (\leftrightarrow \vec{\mathbf{B}} = \mathbf{curl}\vec{\mathbf{A}}) \tag{30}$$

φ is the scalar grid-potential and $\mathbf{a}$ is the grid-vector-potential.

Back to time harmonic fields there is another very important property that follows from the *curlcurl* equation, written down here without energy normalization as:

$$\tilde{\mathbf{C}}\mathbf{D}_\mu^{-1}\mathbf{C}\mathbf{e} = \omega^2\tilde{\mathbf{D}}_\epsilon\mathbf{e} \tag{31}$$

We multiply this equation from the left with $\tilde{\mathbf{S}}$:

$$\tilde{\mathbf{S}}\tilde{\mathbf{C}}\mathbf{D}_\mu^{-1}\mathbf{C}\mathbf{e} = \omega^2\tilde{\mathbf{S}}\tilde{\mathbf{D}}_\epsilon\mathbf{e} \tag{32}$$

As the left hand side vanishes due to $\tilde{\mathbf{S}}\tilde{\mathbf{C}} = \mathbf{0}$ we are left with:

$$0 = \omega^2\tilde{\mathbf{S}}\tilde{\mathbf{D}}_\epsilon\mathbf{e} \tag{33}$$

This equation allows only two distinct cases for the solutions { **e,d** } :

$$\mathbf{e,d}: \begin{cases} \omega^2 = 0 & \tilde{\mathbf{S}}\mathbf{d} \neq \mathbf{0} \\ \omega^2 \neq 0 & \tilde{\mathbf{S}}\mathbf{d} = \mathbf{0} \end{cases}$$

As the original eigenvalue problem is real and symmetric we can create a set of orthonormal eigenmodes $\mathbf{e_n}$ such that

$$\mathbf{e}_i^t \mathbf{e}_j = \delta_{ij} \tag{34}$$

Thus the solution space $\mathbf{\Omega}$ of equation of Equ. 19 is made of two orthogonal sub spaces:

$$\mathbf{\Omega} = \mathbf{\Omega_0} \oplus \mathbf{\Omega}_\omega \tag{35}$$

This relation is in so far essential as one is only interested in solutions of $\mathbf{\Omega}_\omega$ and not in static fields contained in $\mathbf{\Omega_0}$. However, as the eigenvalue problem contains both at a time, this fact also is responsible for a significant problem: for N grid nodes there are approximately N zero and $2N$ nonzero eigenvalues. This almost excludes a numerical approach with iterative methods as it is almost impossible for large N to compute the $N+1$ th eigenvalue and vector. The solution to this problem is found by transforming the **curl-curl** equation into a discrete Helmholtz-like equation in analogy to the analytical step:

$$\mathbf{curl\,curl} \;=\; \mathbf{grad\,div} \;-\; \nabla^2 \tag{36}$$

This transition to ∇^2 is not possible in a one-to-one manner as it implies a constant material property function. Thus a similar transition with MGE will be more general as there is no restriction to constant material properties. The generalized Helmholtz-Grid-Equation reads as [6] [13]:

$$(\tilde{\mathbf{C}}\mathbf{D}_\mu^{-1}\mathbf{C} + \mathbf{D_1}\tilde{\mathbf{S}}^t\mathbf{D_2}\tilde{\mathbf{S}}\mathbf{D_3})\mathbf{e} = \omega^2\mathbf{e} \tag{37}$$

where the term $\mathbf{D_1}\tilde{\mathbf{S}}^t\mathbf{D_2}\tilde{\mathbf{S}}\mathbf{D_3}$ corresponds to the **grad-div** operator and $\mathbf{D_1, D_2, D_3}$ are diagnoal matrices which can be constructed in such a way that the Helmholtz-Grid-Equation in homogeneous regions turns into a normal discretization on the ∇^2 operator. However, this form is valid for any non constant material distribution. This is one of the rare cases where the grid equation is more general than the commonly used analytical one.

The solution space $\mathbf{\Omega}_{\nabla 2}$ is again a set of two distinct orthogonal sub spaces:

$$\mathbf{\Omega}_{\nabla 2} = \mathbf{\Omega}_\gamma \oplus \mathbf{\Omega}_\omega \tag{38}$$

where the $\mathbf{\Omega}_\omega$ has not been altered. All static solutions with eigenvalue zero in $\mathbf{\Omega_0}$ are turned into eigen solutions of

$$\mathbf{D_1}\tilde{\mathbf{S}}^t\mathbf{D_2}\tilde{\mathbf{S}}\mathbf{D_3}\mathbf{e} = \omega^2\mathbf{e} \tag{39}$$

These eigenmodes are **not** solution of Maxwell's equations. However, the advantadge of this transformation is that the eigenvalues of $\mathbf{\Omega}_\gamma$ are also positive and real. The disadvantadge on the other hand is that these solutions are naturally obtained together with Maxwellian solutions. Historically these solutions have probably observed first by simply discretizing the wave equation with a conventional 6-star operator and investigating the obtained fields. As solutions in $\mathbf{\Omega}_\gamma$ can be often identified by a trained user as non-Maxwellian ones, the were named *ghost* modes, *spurious* modes or simply *unphysical* solutions. With the exact relations shown above this *contamination* can be exactly taken care of within the MGE. Thus the widespread problem of *spurious modes*, which are subject to enormous effort in e.g. Finite Element studies, is simply a non-problem for MGE [2] [3] [4] [6].

More as a side remark for the reader interested in physics beyond Maxwell's equations it shall be pointed out here that the solutions in $\mathbf{\Omega}_\gamma$ are **not at all** unphysical. It is true that they are not electromagnetic solutions but they are in fact solutions of the Schroedinger equation.

For the case of quasi-two-dimensional problems as they are set by the evaluation of wave guide properties the situation is in fact more complicated than in 3D. Here one can restrict the discretization to a 2D mesh only and use the ansatz for the z-dependance:

$$\vec{\mathbf{E}}(\mathbf{x},\mathbf{y},\mathbf{z}+\delta\mathbf{z}) \;=\; \vec{\mathbf{E}}(\mathbf{x},\mathbf{y},\mathbf{z})\mathbf{e}^{ik\delta z} \tag{40}$$

If one uses as state variable only transverse components of the 3D vectors, one can implement here (in contrast to the 3D case) a priori the condition $\mathbf{div}\vec{\mathbf{D}} = \mathbf{0}, \tilde{\mathbf{S}}\mathbf{d} = \mathbf{0}$ and totally remove any non-Maxwellian solution from the algebraic system [2, 3, 4]. The derivation however is to long to be repeated here and we show only the final equations in the two possible forms as:

$$\mathbf{A}\,\mathbf{e_{tr}} \;=\; \omega^2\mathbf{e_{tr}}\;;\; k^2 : \mathit{specified value} \tag{41}$$

$$\mathbf{A}\mathbf{e_{tr}} \;=\; k^2\mathbf{e_{tr}}\;;\; \omega^2 : \mathit{specified value} \tag{42}$$

In the latter case one finds that although $\mathbf{A}$ is real for loss free materials that $\mathbf{A}$ is **not** symmetric. Thus linear algebra tells us that there can exist complex conjugate solutions of this linear and real eigenvalue problem - a simple proof of existence for *complex modes.*

For the rather specialized but important case of cylindrically symmetric structures described in $(r-\phi-z)$ coordinates one can derive an eigenvalue equation for the modes using $e_{tr} = (e_r, e_z)$ as the state variables [22, 11]. The resulting eigenvalue problem is also linear and simple and the algebraic eigenvalues are equal ω^2. By defining a proper scalar product it has been shown that in this case **no** complex solutions exist [14].

MAXWELL's GRID EQUATIONS IN TIME DOMAIN

When practically solving MGE in time domain one first has to discetrize the time axis, which so far was untouched. There are of course numerous approaches to time integrate such systems and here we only want to describe the three basic (canonical) methods.

Given a function $f(t)$ for $t \geq 0$ we first break the time coordinate (here for simplicity) in equal intervals δt with $t^i = i\delta t$ and $f^i := f(t^i)$.

The discretization of $\frac{\partial f}{\partial t}(t)$ can be performed primarily by forward or backwards oriented operators:

$$\frac{\partial f(t^i)}{\partial t} \;\cong\; (f^{i+1} - f^i)/\delta t \tag{43}$$

$$\frac{\partial f(t^i)}{\partial t} \;\cong\; (f^i - f^{i-1})/\delta t \tag{44}$$

Introducing these schemes into MGE we first rewrite MGE as a single matrix equation:

$$\mathbf{M}\,\mathbf{f} = \mathbf{D_m}\,\dot{\mathbf{f}} + \mathbf{s} \tag{45}$$

with the definitions:

$$Z_0 \;=\; \sqrt{\mu_0/\epsilon_0} \tag{46}$$

$$\mathbf{M} \;=\; \begin{pmatrix} \mathbf{0} & \tilde{\mathbf{C}} \\ -\mathbf{C}^t & \mathbf{0} \end{pmatrix} \tag{47}$$

$$\mathbf{D_m} \;=\; \begin{pmatrix} Z_0^{-1}\mathbf{D}_\epsilon & \mathbf{0} \\ \mathbf{0} & Z_0\mathbf{D}_\mu \end{pmatrix} \tag{48}$$

$$\mathbf{f} \;=\; \begin{pmatrix} Z_0^{-1/2}\mathbf{e} \\ Z_0^{+1/2}\mathbf{h} \end{pmatrix} \tag{49}$$

$$\mathbf{s} \;=\; \begin{pmatrix} Z_0^{+1/2}\mathbf{i} \\ \mathbf{0} \end{pmatrix} \tag{50}$$

The forward discretization yields the recursion formula:

$$\mathbf{f}^{i+1} = (\mathbf{I} + \delta t\, \mathbf{D}_{\mathbf{m}}^{-1}\, \mathbf{M})\, \mathbf{f}^{i} - \delta t\, \mathbf{D}_{\mathbf{m}}^{-1}\, \mathbf{s}^{i} \tag{51}$$

which is known to be unstable for any value of δt.

The backwards discretization yields the implicit recursion formula:

$$(\mathbf{I} - \delta t\, \mathbf{D}_{\mathbf{m}}^{-1}\, \mathbf{M})\, \mathbf{f}^{i+1} = \mathbf{f}^{i} + \delta t\, \mathbf{D}_{\mathbf{m}}^{-1}\, \mathbf{s}^{i} \tag{52}$$

which can be rewritten as recursion using an inverse matrix as:

$$\mathbf{f}^{i+1} = (\mathbf{I} - \delta t\, \mathbf{D}_{\mathbf{m}}^{-1}\, \mathbf{M})^{-1}\, (\mathbf{f}^{i} + \delta t\, \mathbf{D}_{\mathbf{m}}^{-1}\, \mathbf{s}^{i}) \tag{53}$$

This formula is known to be stable for any value of δt but the major draw back is that the inverse matrix cannot be computed nor stored for large problems and thus each time step requires the solution of a (large) linear system of equations.

A third scheme employs so a so called leap-frog scheme which samples values of **e** and **b** at times separated by half a time step. With $f^{i+1/2} := f(t = (i + 1/2)\delta t)$ one can rewrite the MGE as a set of two recursion formula:

$$\mathbf{b}^{i+1} = \mathbf{b}^{i} - \delta t \mathbf{C} \mathbf{e}^{i+1/2} \tag{54}$$

$$\mathbf{e}^{i+3/2} = \mathbf{e}^{i+1/2} + \delta t \mathbf{D}_{\epsilon}^{-1} (\tilde{\mathbf{C}} \mathbf{D}_{\mu}^{-1} \mathbf{b}^{i+1} - \mathbf{j}^{i+1}) \tag{55}$$

This recursion when applied to regular $(x - y - z)$ coordinate grids is a matrix formulation of the local discretization algorithm of Yee [1]. In order to determine the stability of the recursion one first has to rewrite it in such a way that only one single system matrix multiplication is left. We first define

$$\mathbf{A} = \begin{pmatrix} \mathbf{I} & -\delta t \mathbf{C} \\ \delta t \mathbf{D}_{\epsilon}^{-1} \tilde{\mathbf{C}} \mathbf{D}_{\mu}^{-1} & \mathbf{I} + \delta t^2 \mathbf{D}_{\epsilon}^{-1} \tilde{\mathbf{C}} \mathbf{D}_{\mu}^{-1} \mathbf{C} \end{pmatrix} \tag{56}$$

$$\mathbf{f}^{i} = \begin{pmatrix} \mathbf{b}^{i} \\ \mathbf{e}^{+1/2} \end{pmatrix} \tag{57}$$

$$\mathbf{s}^{i} = \begin{pmatrix} \mathbf{0} \\ -\delta t \mathbf{D}_{\epsilon}^{-1} \mathbf{j}^{i} \end{pmatrix} \tag{58}$$

and obtain the recursion formula:

$$\mathbf{f}^{i+1} = \mathbf{A} \mathbf{f}^{i} + \mathbf{s}^{i} \tag{59}$$

This resurcion is stable if all eigenvalues λ_j of **A** lie within the unit circle in the complex plane. The advantadge of this *leap frog* scheme is that only simple matrix multiplications are required for proceeding one step in time while the solution of a large linear system of equations was employed by the backward difference scheme.

The drawback here is that the eigenvalues of **A** become greater than 1 for time steps larger than a critical time step determined by the above relations. In practice it turns out that the time step limit is in fact rather stringent.

In order to avoid the effort of actually computing the largest eigenvalue of **A** one can employ the well known Courant condition, which however is equivalent to the eigenvalue limit for the case of regular equidistant coordinate grids with homogeneous material only:

$$\Delta t \leq \left(c \sqrt{\frac{1}{\Delta x^2} + \frac{1}{\Delta y^2} + \frac{1}{\Delta z^2}} \right)^{-1}$$

Thus in the case of generalized MGE the evaluation of the largest eigenvalues of **A** is necessary, but does not represent a serious drawback as the eigenvalue calculation of large sparse matrices is well developed and routinely used in the frequency formulation of MGE.

This relation, shown here for x-y-z coordinate grids, must be valid for each cell with the local value for the speed of light. It is much easier to find the time step limit by this approximation despite the fact that this limit turns out to be too small compared to the exact one.

For material with a conductivity in a range such that the skin depth is larger than the smallest mesh step, the above recursion formula can be extended at only little extra expense to [12]:

$$\mathbf{b}^{i+1} = \mathbf{b}^{i} - \delta t \mathbf{C}\mathbf{e}^{i+1/2} \tag{60}$$

$$\mathbf{e}^{i+3/2} = \mathbf{e}^{\mathbf{D}_\epsilon^{-1}\mathbf{D}_\kappa \delta t}\,\mathbf{e}^{i+1/2} + \mathbf{D}_\kappa^{-1}(\mathbf{I} - \mathbf{e}^{\mathbf{D}_\epsilon^{-1}\mathbf{D}_\kappa \delta t})(\tilde{\mathbf{C}}\mathbf{D}_\mu^{-1}\mathbf{b}^{i+1} - \mathbf{j}^{i+1}) \tag{61}$$

If the skin depth is smaller than the smallest mesh step size a surface impedance model is employed which assumes local plane waves and the known dependance of plane waves in conducting material. Thus with the two latter extensions the time domain algorithm covers quite easily the wide and important range of lossy materials, which are by far more difficult to handle in a frequency domain approach.

Comparing the two time integration schemes shows that the leap frog scheme is appropriate for computation with a time scale in the order of the spatial dimension of the solution space divided by the speed of light, whereas the implicit scheme is favourable for *slowly* varying functions and large time scales.

As simple illustrative example we consider a space of the size $1m \times 1m \times 1m$, a frequency of 3 GHz, a spatial step of $1cm$ in each direction. To compute the penetration of a wave through the entire volume we have to execute about 300 time steps only, which is a resonably small number.

Consider the same volume but as problem the evaluation of the transient field of an AC-transformer running at $50Hz$ for the first ten periods, we end up with 10^{10} necessary time steps, which is certainly out of any reasonable limit.

Thus we find that *both* time discretization schemes are needed when solving a wide range of electric engineering field problems.

Before considering more practical problems we should check the charge conservation of both time stepping algorithms. Therefor we multiply the recursion formulae from the left with the grid-divergence operators:

$$\mathbf{S}\mathbf{b}^{i+1} = \mathbf{S}\mathbf{b}^{i} - \delta t \mathbf{S}\mathbf{C}\mathbf{e}^{i+1/2} \tag{62}$$

$$\equiv \mathbf{S}\mathbf{b}^{i} \tag{63}$$

$$\tilde{\mathbf{S}}\mathbf{D}_\epsilon \mathbf{e}^{i+3/2} = \tilde{\mathbf{S}}\mathbf{D}_\epsilon \mathbf{e}^{i+1/2} + \delta t \tilde{\mathbf{S}}\mathbf{D}_\epsilon \mathbf{D}_\epsilon^{-1}(\tilde{\mathbf{C}}\mathbf{D}_\mu^{-1}\mathbf{b}^{i+1} - \mathbf{j}^{i+1}) \tag{64}$$

$$\equiv \tilde{\mathbf{S}}(\mathbf{D}_\epsilon \mathbf{e}^{i+1/2} + \mathbf{j}^{i+1}) \tag{65}$$

Due to the basic relation **SC=0** we find that the charge conservation is explicitly built-in this recursion for all times. The same property can be shown for the implicit time integration scheme. The rounding errors nevertheless will introduce parasitic charges as all matrix vector multiplication are of finite accuracy. We immediatley find that the leap frog scheme is much less sensitive to round-off erros than the implicit integration scheme, which requires many more floating operations per time step.

Now that we found the charge conservation in the time integration scheme it is worthwhile to point out that the continuity equation is also an implicit property of MGE. To show this we multiply the second MG equation from the left with the dual grid divergence operator:

$$\tilde{\mathbf{S}}\,(\tilde{\mathbf{C}}\mathbf{h} = \dot{\mathbf{d}} + \mathbf{j}) \tag{66}$$

and immediately obtain, again due to $\tilde{\mathbf{S}}\tilde{\mathbf{C}} = \mathbf{0}$, the continuity equation for the grid fields:

$$\tilde{\mathbf{S}}\mathbf{i} = -\dot{\mathbf{q}} \leftrightarrow \mathbf{div}\,\vec{\mathbf{J}} = -\dot{\rho} \tag{67}$$

The only condition to be met is that all driving sources i must be such that they are charge conserving, which becomes quite important when adding free moving charges to the field computation. Thus for field computations including free moving charges further conditions must be implied on the driving terms. The origin of this additional problem is that free moving charges are not grid-bound and thus do not produce a priori consistent grid currents and charges.

In practice there are three regions of interest:

- **slow** particles: slow means here that the particle velocity $v = \beta c_0$ is small compared to the speed of light and the mechanics can be treated as classical mechanics.
- **fast** particles: fast means here that the particle velocity $v = \beta c_0$ is not small compared to the speed of light and the mechanics must be treated relativistically.
- **ultra relativistic** particles such as electrons at a few GeV energy have a speed which is very close to the speed of light. Here we can neglect the difference to infinite energy and set $\beta = 1$. The mechanics in the ultrarelativistic case is decoupled from the electromagnetic forces in the sense that the immediate reaction of particle motion can be neglected due to their inifinte energy.

Fully relativistic treatment of free charges adds to the leap frog algorithm a second parallel iteration for solving the mechanics at each time step. This is in practice much more complicated and time consuming so that the field computation becomes the smaller part of the full problem. By learning from early work in plasma physics one can treat the particles in a way such that charge conservation remains fulfilled for all times [15]. For ultra relativistic simulation the charged particle beam represents a current term in the field equation. By choosing the time step in a proper way, one can here also a priori satisfy the charge conservation [16, 17].

The fully relativistic self-consistent simulation is a typical area where pure time domain calculations do not suffice. In order to simulate a high power klystron for instance, one needs

- **electrostatic** fields in the electron source region
- **magnetostatic** fields of coils generating the electron beam guiding field
- **RF resonant** fields for the modes in the gain and output cavities
- **time domain** fields with the three above mentioned fields as starting condition

The whole area of field analysis including the mechanics of free charges is a very wide subject, too wide to be explored here in more detail, for further reading see [15]and references therein.

The last item to be adressed in discussing time domain analysis is the field excitation from various sources. Typical driving terms are:

- **incident plane paves,**
- **incident waves in cables, microstrip lines, etc..**
- **dipole radiators,**
- **electric currents and**
- **free moving charges**

Plane waves can be implemented as inhomogeneous boundary condition where there realization of *open* boundary conditions is a wide area of possible mathematics (and instabilities). The proper realization of stable low-reflection open boundaries is rather complicated [12] [14].

Electric currents are taken care of by the appropriate terms in the recursion formula.

Also quite complicated are wave guide boundary conditions. First one needs a proper mesh-consistent eigen mode solution of the wave port. This can be obtained by the frequency domain version of the MGE. For each mode one knows the propagation constants and thus can express the total field at a boundary as a sum of all wave guide modes. For transversely homogeneously loaded wave guides it is sufficient to know the eigenmodes at one frequency only. For this case a broad band excitation is possible. In case of non-homogeneous wave guides, such as microstrip lines, broad band excitation is only an approximation. Broad band wave guide boundary condition boosts up the usefulness of time domain analysis versus frequency domain methods by orders of magnitude: Basically at the cost of obtaining one result for one single frequency one obtains results for a large number of frequencies at a time. This feature becomes extremely vital for instance when searching narrow resonances in a filter structure. For further details on this subject see [18].

SOLVING MAXWELL'S GRID EQUATIONS WITH THE MAFIA CODE

The coordinate-grid version of the MGE has been implemented in various computer codes over the last 20 years. Staring with 2D frequency domain codes in 1977 [2] [3] [4], followed by the first time domain codes for relativistic particle beams [17], the first fully three dimensional implementation was realized for 3D eddy current solvers in 1978 [19] [20] [21]. Later a new 3D code family for 3D resonators and transient fields was developed, named MAFIA [8], released in the first version in 1983. The first non-coordinate grid implementation was performed for the resonator code URMEL-T [11]. Following the first release of MAFIA in 1983 the code was improved significantly. Meanwhile the MAFIA family of codes covers a wide range of applications such as

- electro static fields
- magneto static fields
- low frequency eddy current fields
- high frequency eddy current fields (including displacment current)
- high frequency resonators and wave guides
- transient fields
- fully self-consistent transient fields including free moving charges

MAFIA and the 2D earlier codes TBCI [17], URMEL [22] and URMEL-T [11] are now in worldwide use since more than 10 years in more than 25 countries. Applications documented in several hundred publications by users have proven their accuracy and reliability in numerous practical projects.

All examples presented here have been obtained from using MAFIA on workstations, such as SUN-Sparc, HP7xx or IBM RISC.

EXAMPLES

We present here a series of practical applications of the MAFIA software. The description of each example is contained in the figure captions. The examples were intentionally generated with the currently available version 3.2 of MAFIA and not with software still being developed.

The examples are taken from practical applications in research and industry. They give a short insight in what is possible to achieve today by anyone and not only by the authors.

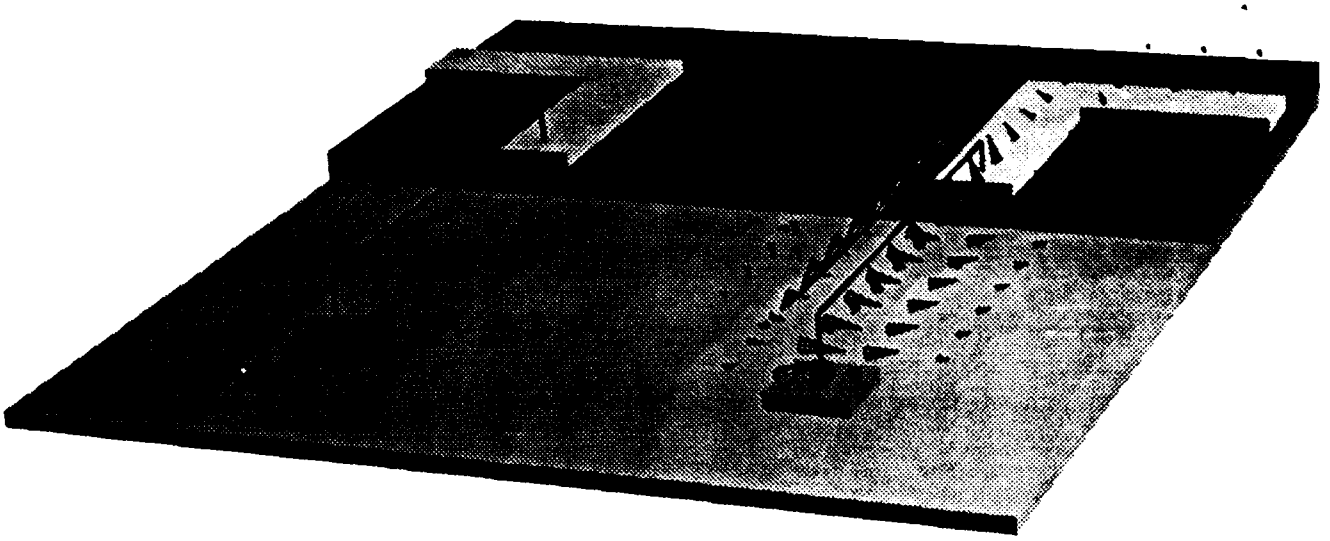

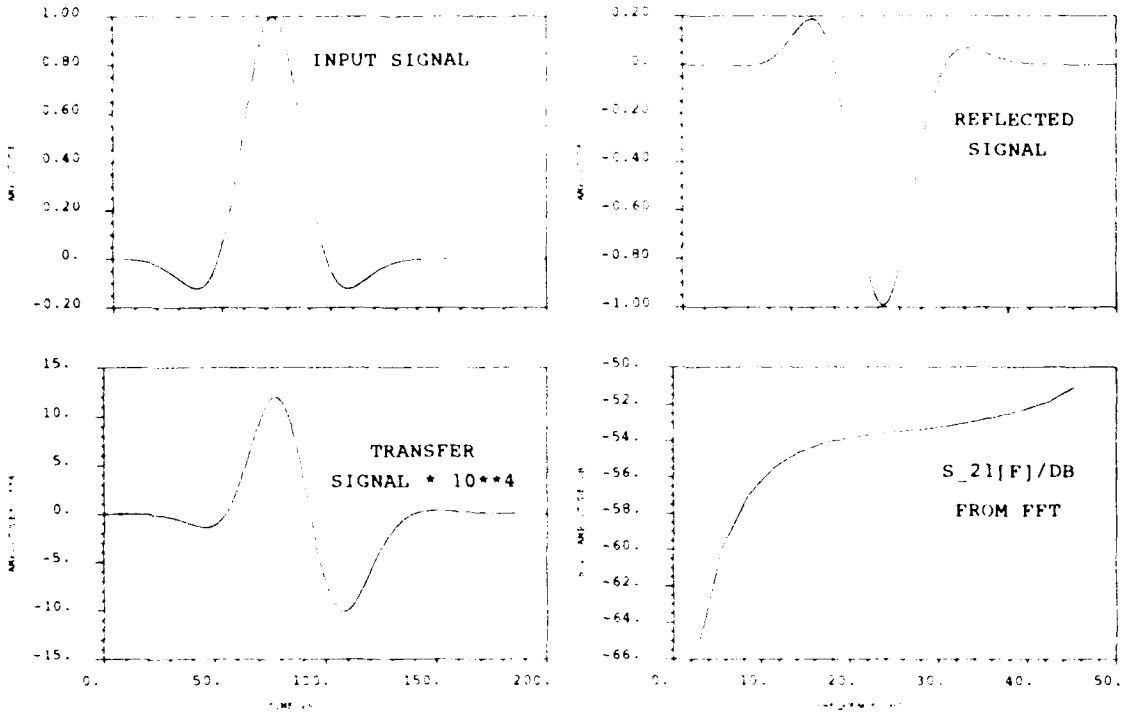

This example shall serve a prototype for explaining the steps towards a broad-band computation of S-parameters. The structure is a piece of a chip showing two micro strip ports and two thin wires connecting the strips with resistive blocks on the chip material. The resistive blocks have a conductivity $\kappa = 13000 S/m$*, the substrate a permittivty* $\epsilon = 9.0$*.*
The geometrical extensions are about $700\mu m \times 300\mu m$*. The problem here was to determine the cross talk from one wire to the other within a frequency range of* $0 - 50GHz$*.*
The procedure is as follows: After calculating the proper eigen modes in the micro strip lines, these modes are loaded and driven with a time dependent envelope shown above as Input Signal. The output signals at both ports are recorded in terms of wave amplitudes. After the output signal has decayed, both input and output signal are transformed to frequency domain by FFT. A division of both Fourier transforms yields the desired S-parameter in a very wide range of frequencies, much wider than shown here.
The key advantadge of this procedure is that an entire range of frequencies can be obtained roughly at the same cost as required for one single point in frequency when either applying frequency domain analysis or monochromatic time domain analysis.

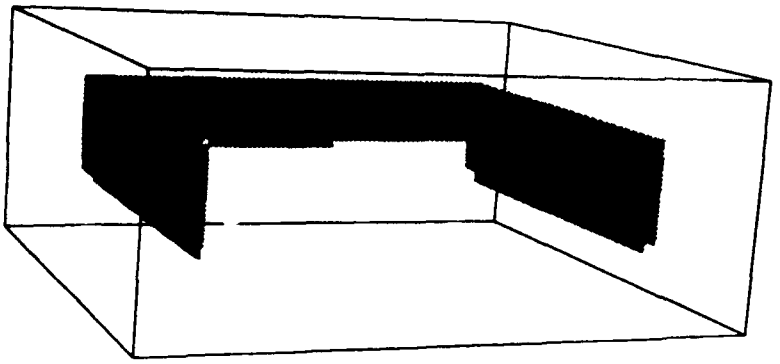

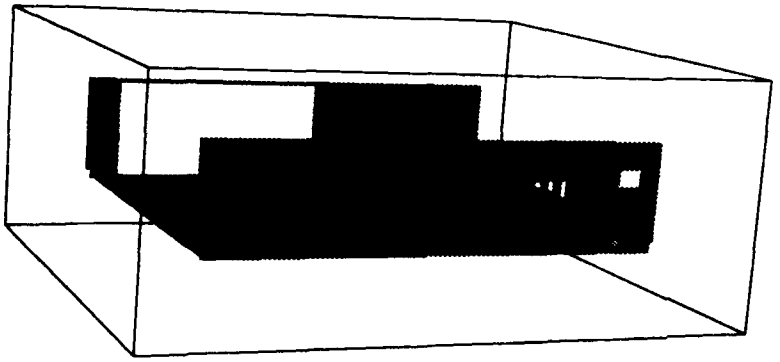

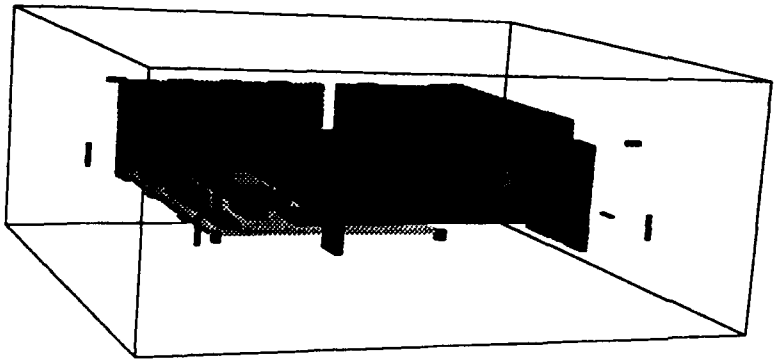

These plots show an IBM PC (model PS/2-30286) used for demonstrating the possibilities to study rf radiation caused from the inner circuits. The top plot shows the metallic cover with many ventilation slots on the left hand side (which are probably hard to see at this resolution). The second plot shows the metallic frame with the disk slot and the rectangular hole at the rear for the slot card access. The third plot shows all innere pieces such as power supply, cpu board, floppy drive, hard disc drive, rf-cealing springs etc.

This PC was analyzed in both frequency and time domain. Frequency domain analysis allows easy identification of inner resonances and eigen fields. In time domain both broadband and monochromatic excitation was employed, represented by current on the cpu board. The plots here show the results of a monochromatic excitation in time domain. From the steady state field near the outer mesh boundary one obtains by far field transformation the according patterns as known from antenna design.

Such a far field diagram is shown on the bottom right hand side plot in the horizontal plane. The left plot on the bottom shows an (unusual) three dimensional contour surface plot of the 3D farfield pattern.

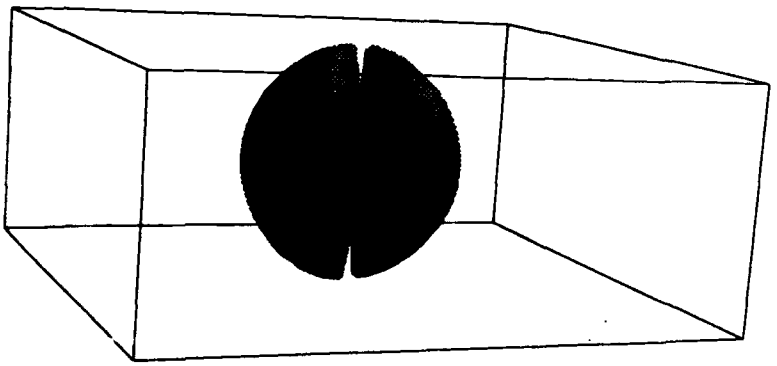

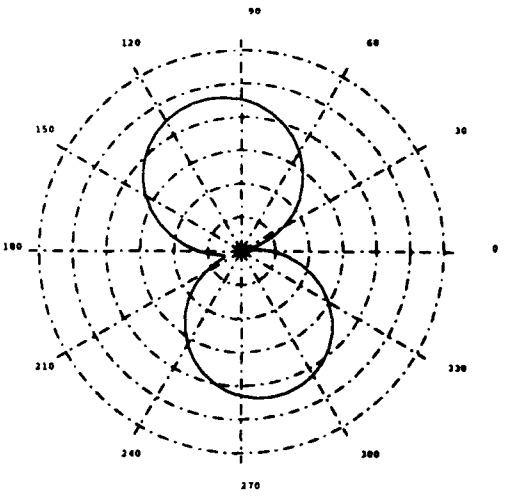

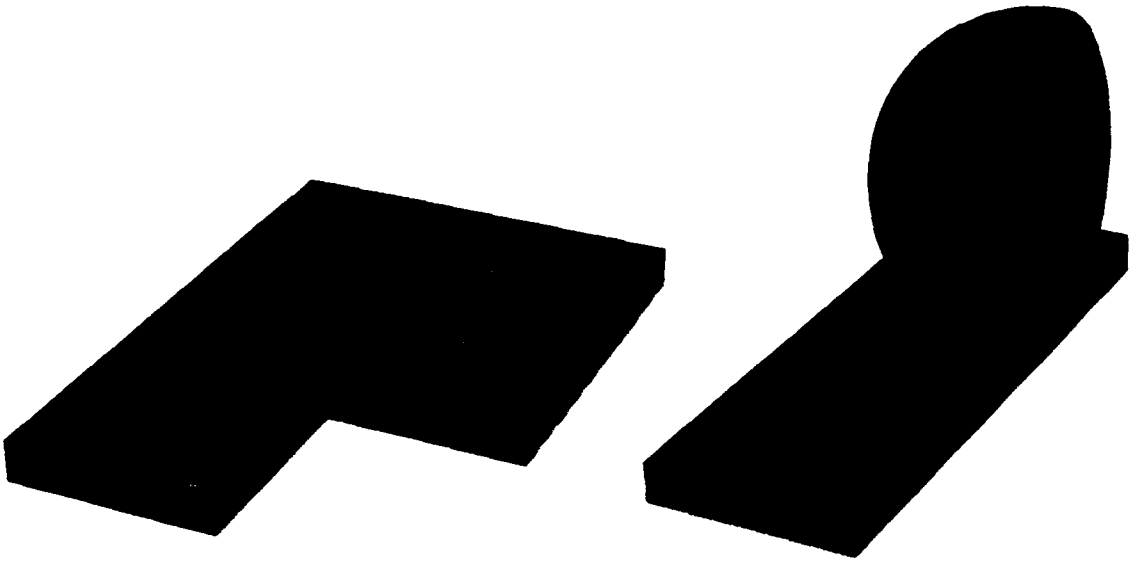

The left plot shows a patch antenna on a dielectric layer with a coaxial feed underneath. In order to find the frequency with the lowest reflection coefficient at the feed the structure was first excited by a broad band signal. The resulting $S_{11}(\omega)$ showed a minimum at $3.85GHz$. At this frequency a monochromatic signal was injected in a second calculation. The farfield pattern is shown in the right hand side plot as three dimensional contourplot and was obtained by a farfield transformation of the near field [24]. The total number of mesh cells used is 100.000, corresponding to 600.000 unknowns.

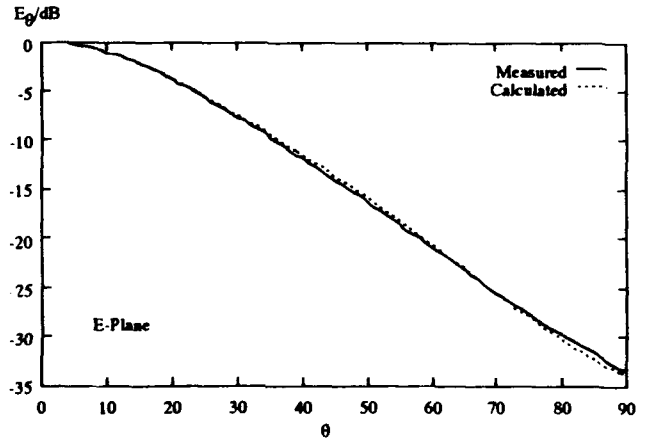

These plots show a cylindrically symmetric horn antenna radiating at $f = 10.4GHz$ developed by the DEUTSCHE TELEKOM [23]. The excitation is represented by a H_{11} wave. The upper plot shows the lines of constant radial component of the electric field. The lower plot shows the measured (courtesy of TELEKOM [23]) and computed values for the E-plane far field pattern. A total of 64.000 cells was used, corresponding to 384.000 unknown field components.

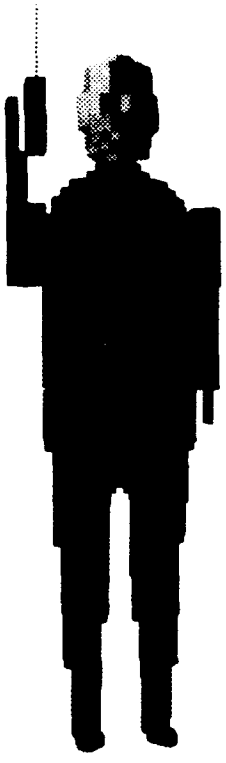

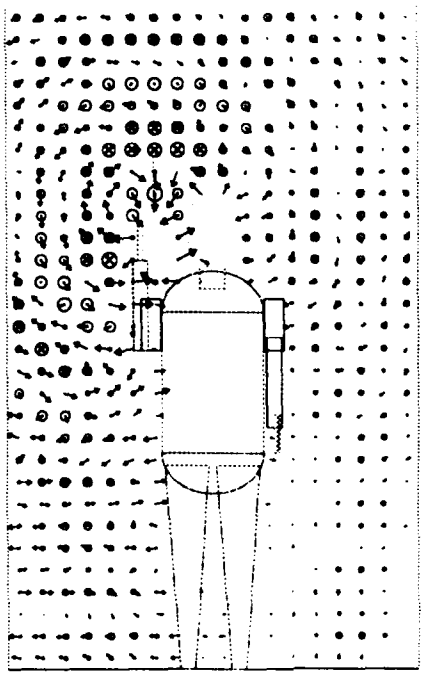

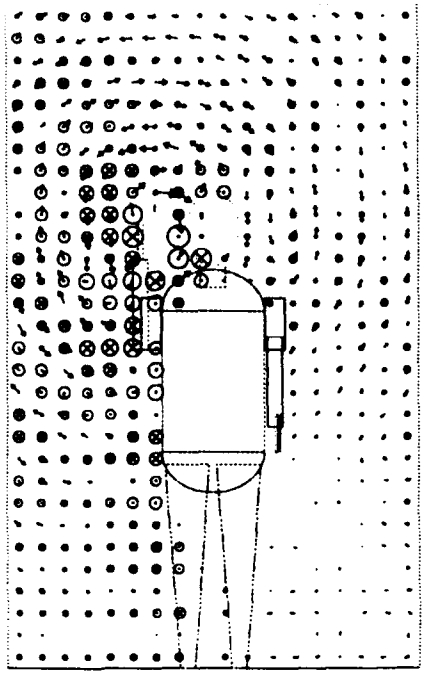

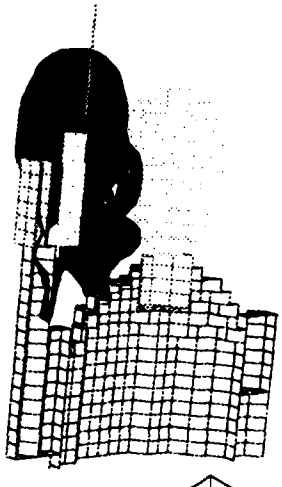

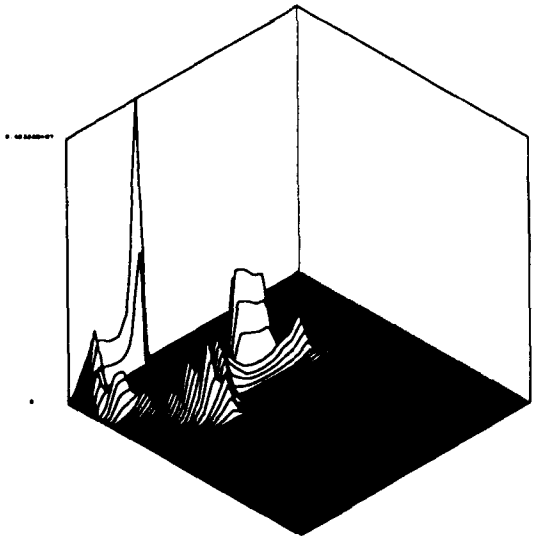

This example is a simulation of a full size person with a cellular phone in his hand. The body material is modelled as human tissue ($\epsilon_r el = 40, \kappa = 1.5 S/m \mu_r el = 1$). As this example was set up as proof of principle there is no internal structure of the body - but this is only a question of getting more detailed data. There is no problem in defining a different material property (ϵ, μ, κ) for each cell.

The top left plot shows the 3D geometry. The two arrow plots show the electric and magnetic field vectors for a frequency of $750 MHz$ in a cut plane. Circles show the vector components perpendicular to the cut plane.

The middle plot shows a 3D contour surface plot of constant electric field energy in a cut-away plot of the head region.

The bottom plot shows the SAR pattern ($(1/2)\vec{\mathbf{E}} \cdot \vec{\mathbf{J}}^*$) in a cut plane through the head. The highest peak is located at the hand. The second highest peak near the ear.

The total number of mesh cells used is 508.000, corresponding to roughly 3.000.000 unknowns. The necessary cpu time for this simulation on a SPARC station is of the order of one hour only. The memory required is 30 Mega Bytes.

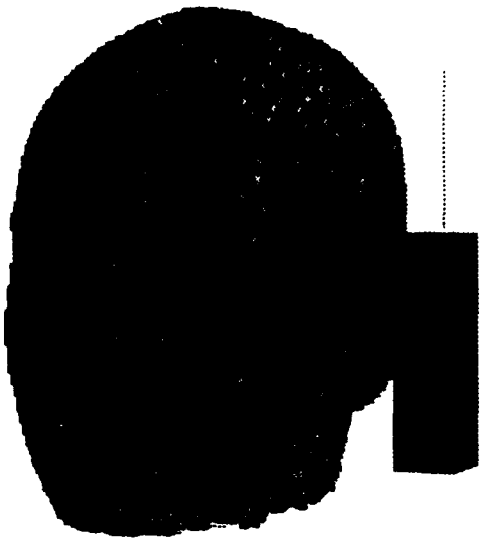

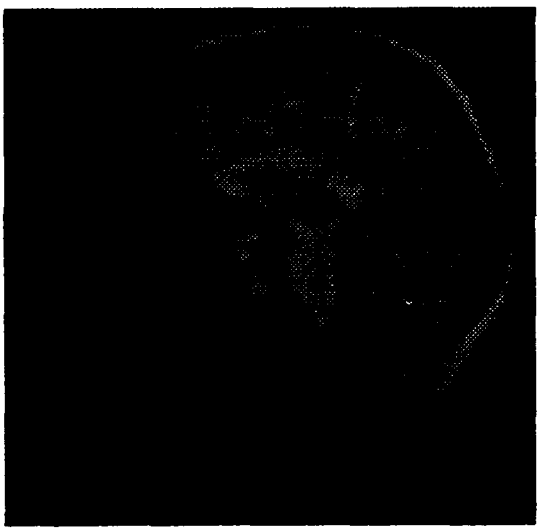

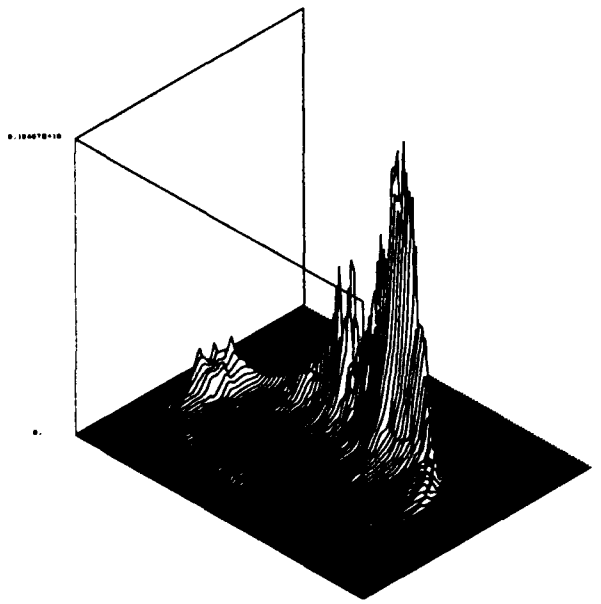

The computation of fields from cellular phones inside a human body are today a problem of great interest. From the analysis point of view this is a rather difficult case. The material properties of a human body are unusual for theorists normally assuming loss-free dielectric or inifinitely conducting materials. On top of the material property the material distribution is very complex. The major difficulty to analyze such an example was at the first point to obtain good data for a human head and to feed these data into the mesh generator.

The left pictures show the generated mesh using 1.200.000 cells for a human head. Each cell of the mesh is filled with a material according to the scan data. Next to the head is a cellular phone with an antenna, fed at 915MHz from the inside of the phone.

As the amount of data is so large, we were not able to produce better plots for this paper as POSTSCRIPT files exceed several tens of mega bytes for a good 3D picture. The top plot shows a 3D view of the head model, the middle plot a cut through the head showing the complex internal material structure exactly as it is modelled in the code (this is not a plot of scanned data but a plot of mesh cells filled with material!).

The computation with 7.200.000 degrees of freedom turns out to be no problem in terms of cpu time. Such an analysis requires roughly 100 MBytes memory and a few hours of cpu time - the real problem is how to display such an incredible amount of data in 3D.

If the same model were analyzed with a surface method and a resolution of 60 different materials, such as moment methods, it would require about 1.000.000 surface elements, which is to our knowledge out of reach.

The lowest plot shows the Joule loss density (SAR pattern) in a center cut plane through the head. One clearly sees the maximum heat near the ear next to the phone.

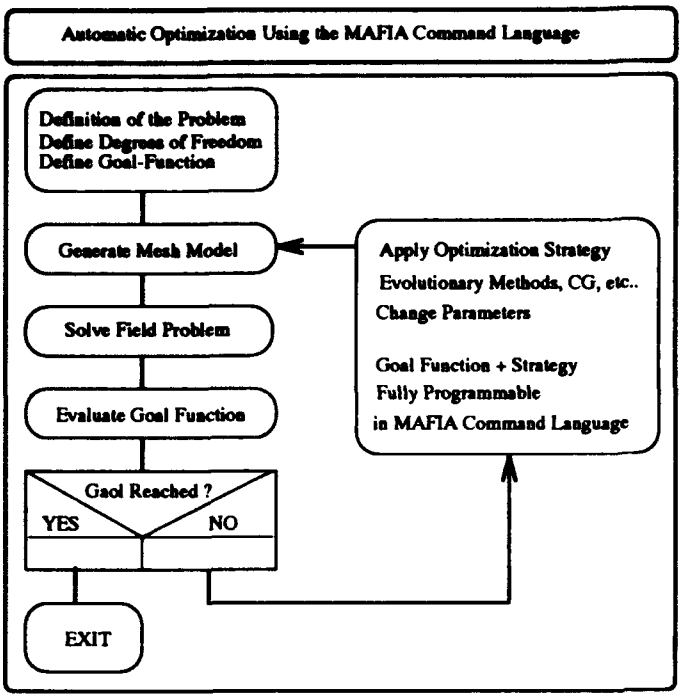

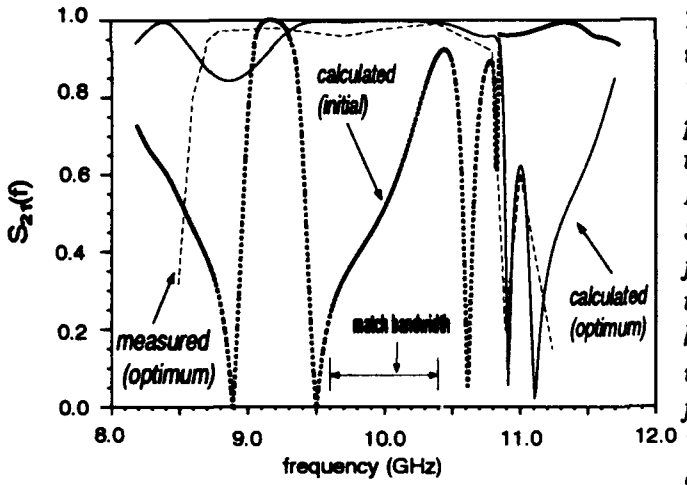

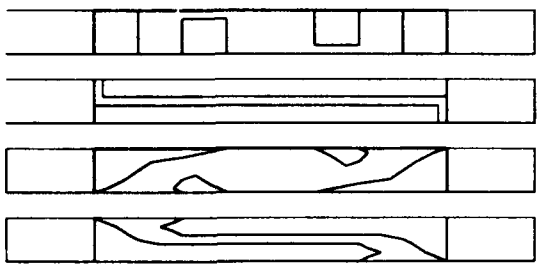

As time domain computation are extremely effective and accurate it is practically possible to implement time domain solvers into optimization codes. If a structure is not too complicated, such as wave guide transitions and simple antennas, the total cpu time for a single analysis can be down to a few minutes on modern workstations. Thus it is within reach to run several hundred jobs within a few days and to apply some strategy to reach a specific goal by changing geometric parameters from run to run.

The example here demonstrates such an automatic optimization with the optimizer module OO of MAFIA-3.2. It is a transition from a rectangular wave guide to a micro strip line. To ease the measurement the transition was doubled and the micro strip is in fact in the center of the structure. The goal was to obtain a flat S_{21} for frequencies of 10GHz+/-0.4GHz.

This example was solved by MAFIA-OO invoking the modules M(mesh generator), T3(3D time domain solver) and P(post processor) and took about 4.3 days cpu time on an IBM RISC/6000-550.

During the optimization OO performed 350 runs optimizing with 30 degrees of freedom for the shape of the bottom and top layer. The mesh model had 40.000 unknowns. Each of these 350 runs resulted in over 100 values for S_{21} in the desired frequency range of $9.6GHz$ to $10.4GHz$.

The outcome of the optimization was such a strange looking shape that we wanted to verify the results by measurements. The middle plot shows S_{21} versus frequency for the initial shape, the optimized shape and the measured results. The agreement between measured and calculated data is very good.

The bottom plot shows the top and bottom layer shapes for the initial transition and the final optimized shape.

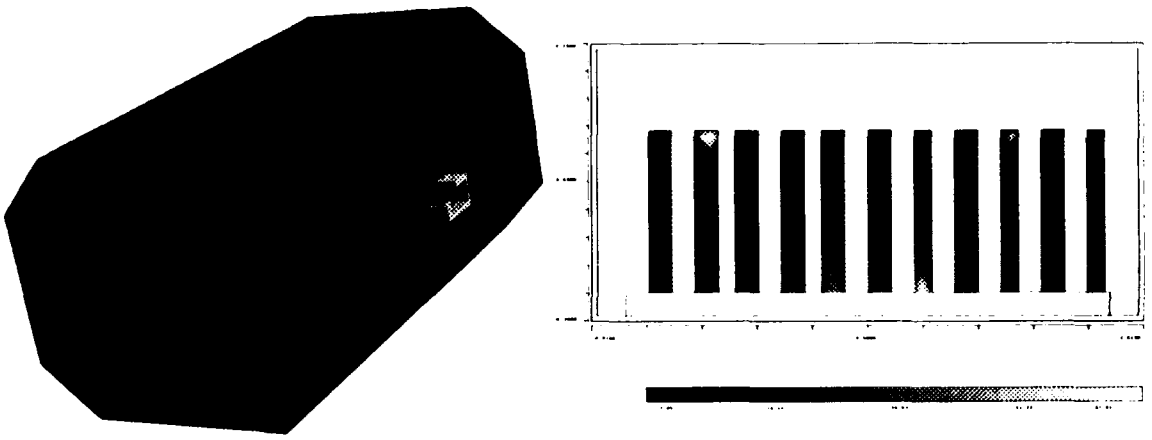

This plot shows a micro wave oven driven by a 2.45 GHz source. The power is fed through a standard rectangular wave guide into the box. On a support there is a row of wet books (or similar objects). The purpose of this device is to dry these objects. This case was simulated in time domain. For the excitation we used the 2D frequency domain solver in oder to determine the field distribution in the feed. The eigenmode field is used as incoming time harmonic boundary condition field with a transition envelope slowly increasing the amplitude to its steady state value. The total number of mesh cells used is 300.000, corresponding to 1.800.000 unknowns. The left plot shows a three dimensional arrow plot distribution of the real part of the electric field vector. The right hand side plot shows the heat source distribution within a cut plane through the wet books.

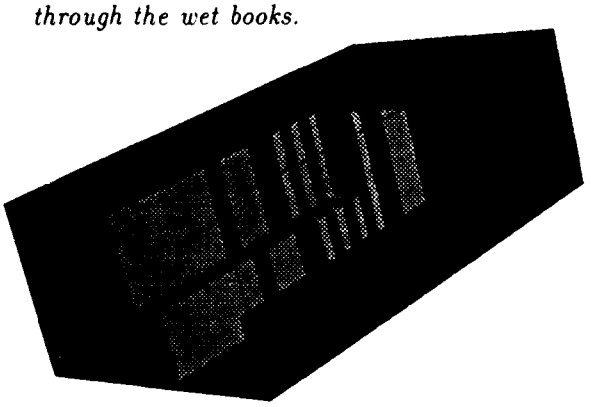

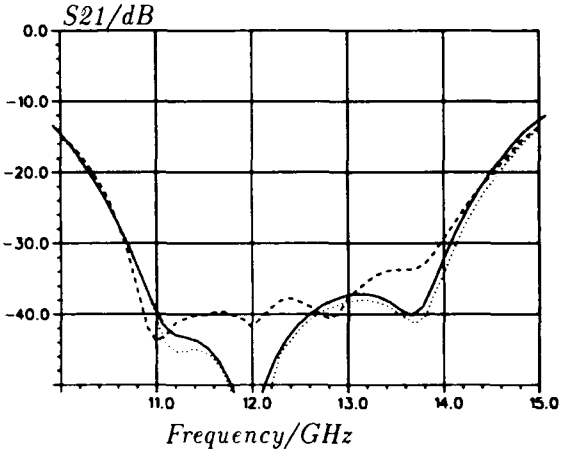

The left figure shows a 3D view of a 3dB rectangular waveguide coupler with four ports built by MBB (DASA). There are a number of slots adjusted such that a desired broadband behaviour is reached. The right hand side plot shows S_{11} versus frequency together with measured results and results obtained from mode matching technique. This example was again analyzed with time and frequency domain solvers. Frequency domain was used for computing the proper port modes, time domain for computing the S-parameters. By means of a braod band technique the entire frequency range can be analyzed with one single run. The excitation is set such that a pulse with given band width is fed in such that it covers the desired frequency range. The cpu time per S-parameter was as small as 5 seconds on an IBM550 RISC workstation, using roughly 18.000 cells (or 120.000 unknowns). The accuracy compared with measurements by MBB showed agreement better than 0.1 dB in transmission (S_{21}) over the desired frequency range. This is compared to pure frequency domain approaches almost an unbelievable value in terms of accuracy and speed.

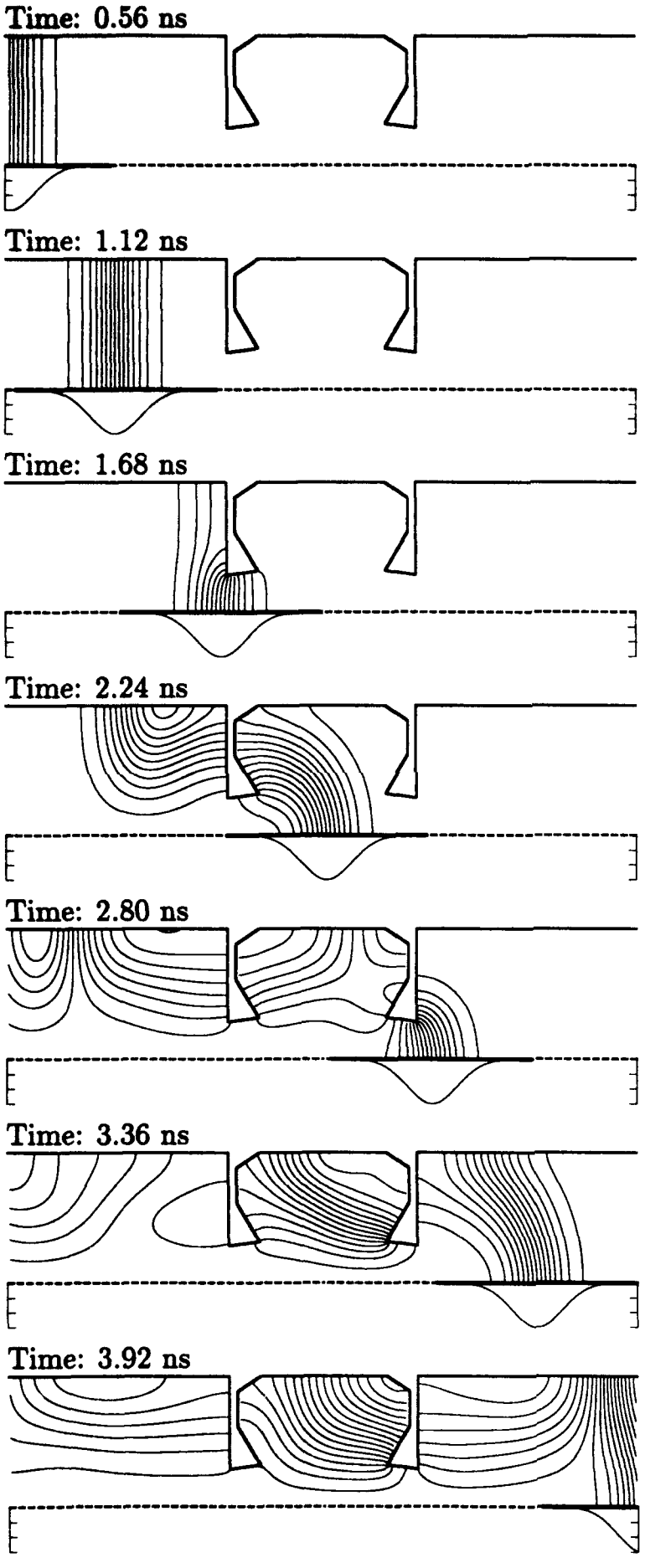

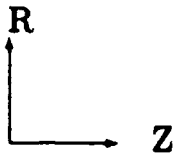

The left plot shows a sequence of plots for a bunch of electrons travelling along a cylindrically symmetric structure at the speed of light. All figures show only the upper portion for $r > 0$. The lines are equipotential lines of the time dependent time integrated vector potential and are thus proportional to $r\vec{E}$. Below the axis downwards the time dependent current density of the travelling electrons is plotted.

The bunch of particles has a longitudinally Gaussian distribution with an rms width of $\sigma = 4cm$. The vacuum chamber with a central resonator has a radius of 21.0cm.

It is clearly observed that the field lines are purely radial before the electrons approach the disk in the waveguide - a consequence of the fact that the electrons travel exactly at the speed of light. This approximation is arbitrarily well fulfilled for high energy electrons, which actually are closer to speed of light than $\delta\beta = 1e-7$ above some 10 GeV of energy. Later the disks produce scattered fields that start to interact with the electrons. This interaction produces a change of momentum of the elctrons and constitutes the main collective (current dependent) limitation for almost any accelerator.

These longitudinal and transverse transient fields are called wake fields. These plot have been obtained from TBCI [17].

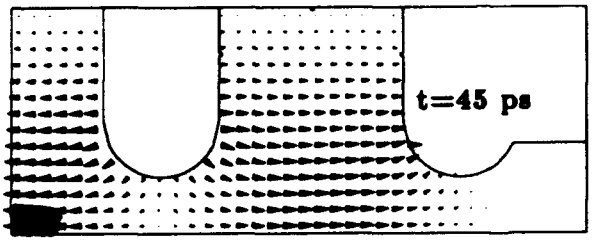

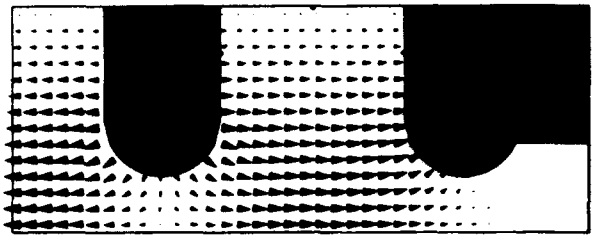

$\vec{E}_{harmonic}$

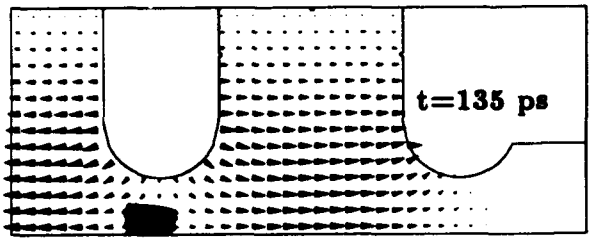

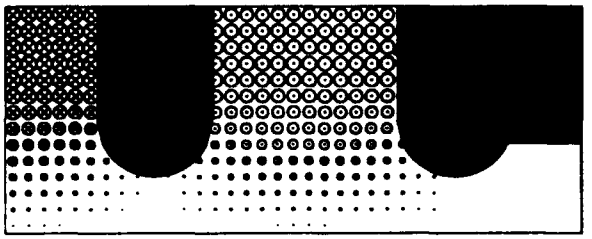

$\vec{B}_{harmonic}$

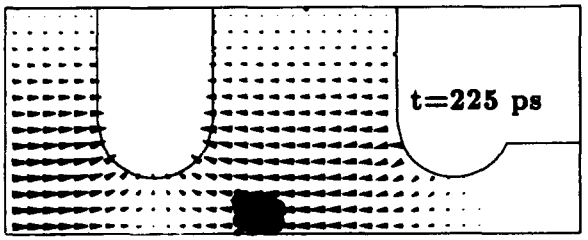

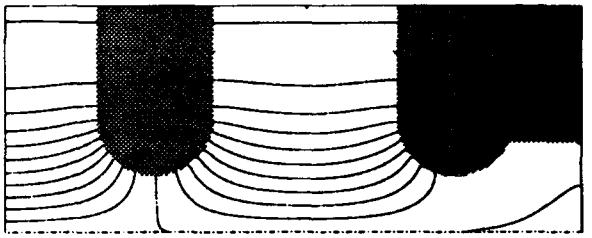

$r\vec{B}_{harmonic} = const.$

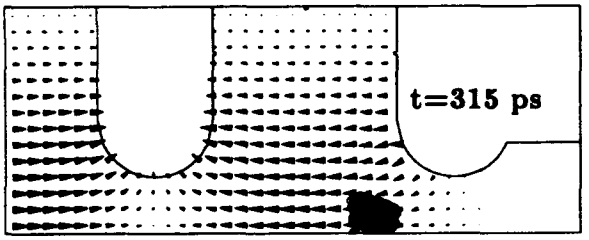

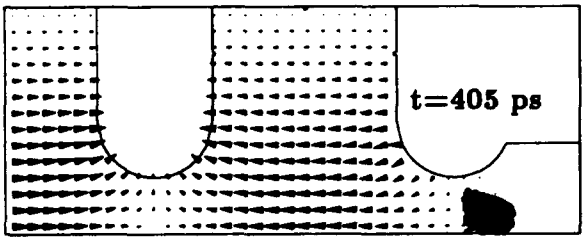

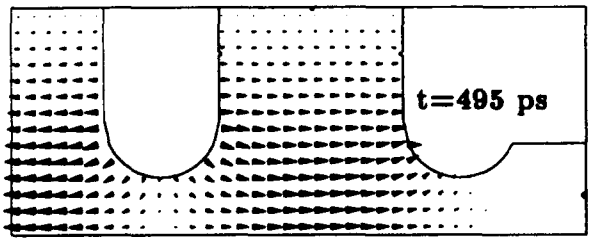

This device is a high brigthness electron source developed at CERN and BNL(New York) and works similar to a klystron. The simulation shows a cylindrically symmetric 1-1/2 cavity resonant at $3GHz$. The cavity mode (TM_{010}) is computed first in frequency domain as eigen value problem and then loaded (after proper amplitude scaling) into the time domain self-consistent simulator. On the left there is a photo emission cathode illuminated by a short laser pulse. Electron bunches are emitted and accelerated by the rf field of the mode with a strenght of $100MV/m$. This simulation includes the full set of Maxwell's equations and the fully relativistic equation of motion for the electrons. Thus all effects such as space charge, transient fields and interaction with the resonant fields are included. As result of the interaction the electron bunches blow up.

The left hand side series of plots show the electron bunch traversing the cavity at several time instances. The right column shows the starting solution obtained from frequency domain analysis.

References

[1] Yee K. S., *Numerical Solution of Initial Boundary Value Problems Involving Maxwell's Equations in Isotropic Media*, IEEE, AP-14, S. 302-307, (1966).

[2] Weiland T., *A Discretization Method for the Solution of Maxwell's Equations for Six-Component Fields*, Electronics and Communication (AEÜ), Vol.31(1977), pp.116

[3] Weiland T., *A Numerical Method for the Solution of the Eigenwave Problem of Longitudinally Homogeneous Waveguides*, Electronics and Communication (AEÜ), Vol.31(1977), pp.308

[4] Weiland T., *Lossy Waveguides with an Arbitrary Boundary Contour and Distribution of Material*, Electronics and Communication (AEÜ), Vol.33(1979), pp.170

[5] Weiland T., *On the Numerical Solution of Maxwell's Equations and Applications in Accelerator Physics*, Particle Accelerators Vol.15(1984), pp. 245-291

[6] Weiland T., *On the Unique Solution of Maxwellian Eigenvalueproblems in Three Dimensions*, Particle Accelerators Vol.17(1985), pp. 227-242

[7] Bartsch M. et al. *Solutions of Maxwell's Equations*, Computer Physics Comm. 72 (1992) 22-39

[8] The MAFIA collaboration, *User's Guide MAFIA Version 3.x*, CST GmbH, Lauteschlägerstr.38, D6100 Darmstadt.

[9] Feltz F., *Differenzenverfahren zur Berechnung elektromagnetischer Felder*, Dipl.Thesis, TH Darmstadt, 1978

[10] Holland R., *Finite Difference Solution of Maxwell's Equations in Generalized Nonorthogonal Grids*, IEEE Trans.Nucl.Sci.Vol NS30, No 6. 4589-4591, 1983

[11] van Rienen U., ,Weiland T., "Triangular Discretization Method for the Evaluation of RF-Fields in Cylindrically Symmetric Cavities" Particle Accelerators, Vol.20(1987), 239-267

[12] Dohlus M., *Ein Beitrag zur numerischen Berechnung elektromagnetischer Felder im Zeitbereich*, Technische Hochschule Darmstadt D17 (1992).

[13] Hahne P., *Zur numerischen Berechnung zeitharmonischer elektromagnetischer Felder*, Technische Hochschule Darmstadt D17 (1992).

[14] Dehler M., *Numerische Lösung der Maxwell'schen Gleichungen auf zylindrischen Gittern*, Technische Hochschule Darmstadt D17 (1993).

[15] Schütt P., *Zur Dynamik eines Elektron-Hohlstrahls*, Dissertation Hamburg, DESY M-88-03 (1988).

[16] Weiland T., *Transient Electromagnetic Fields Excited by Bunches of Charged Particles in Cavities of Arbitrary Shape*, Proceedings of the XI-th International Conference on High Energy Accelerators, Geneva 1980,Birkhauser Verlag, Basel,edited by W.S.Newman,pp.570

[17] Weiland T., *Transverse Beam Cavity Interaction, Part I: Short Range Forces*, Nuclear Instruments and Methods (NIM), Vol.212(1983), pp.13-34

[18] Thoma P., Dohlus M., Weiland T., this conference.

[19] Weiland T., *On the Calculation of Eddy Current in Arbitrarily Shaped, Three Dimensional, Laminated Iron Cores, Part I: The Method*, Archiv für Elektrotechnik (AfE), Vol.60(1978), pp.345

[20] Euler H. and Weiland T., *On the Calculation of Eddy Current in Arbitrarily Shaped, Three Dimensional, Laminated Iron Cores, Part II: Applications*, Archiv für Elektrotechnik (AfE), Vol.61(1979), pp.103

[21] Weiland T., *On the Calculation of Eddy Currents in Arbitrarily Shaped, Three Dimensional, Solid Iron Cores*, Archiv für elektrische Energietechnik, etz, Vol.1(1979), pp.263

[22] Weiland T., *On the computation of resonant modes in cylindrically symmetric cavities*, Nuclear Instruments and Methods, North Holland Publishing Company, Vol. 216, S. 329-348 (1983).

[23] Kühn E. und V. Hombach, *Computer Aided Analysis of Corrugated Horns with Axial or Ring-Loaded Slots*, Third International Conference on Antennas and Propagation ICAP 83, IEE Conf. Publ. No. 219, S. 127ff. (1983).

[24] Dehler M., Dohlus M., Weiland T., *Calculation of Frequency Domain Parameters by Time Domain Methods*, IEEE Trans. on Magn., Vol.28, No.2, 1992, p.1797

FINITE DIFFERENCE TIME DOMAIN MODELS FOR COPLANAR WAVEGUIDE DISCONTINUITIES

Victor FOUAD HANNA. Silviu VISAN. Odile PICON
FRANCE TELECOM
Centre National d'Etudes des Télécommunications - Centre Paris B
38, rue du Général Leclerc 92131 Issy les Moulineaux FRANCE

ABSTRACT

This paper assembles various models that were developped using Finite Difference Time Domain (FDTD) Method to characterise coplanar waveguide (CPW) uniaxial discontinuities (step in width, gap, short circuit, open circuit) and multiaxial ones (T junction, bend). Comparaison of these models with those developped using other general purpose methods will be presented whenever possible. Models for other possible CPW discontinuities used for monolithic applications like air bridges and via holes for conductor backed CPW will be given also. For CAD purposes, these discontinuities will be modeled between predefined reference planes either by an equivalent electric circuit or a scattering matrix.

WHY

	CPW	Microstrip
series connection	easy	easy
shunt connection	easy	difficult
dispersion	low	high
radiation losses	low	high
CAD facilities	inadequate	adequate

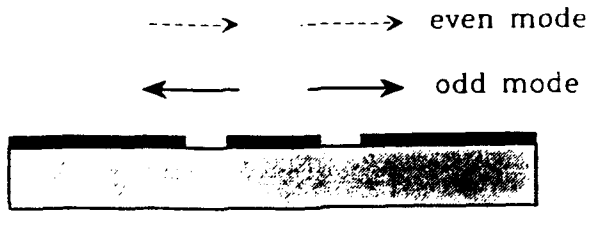

Advantages of the FDTD method :

- General 3D method, not limited by any assumption concerning the boundaries or the configuration of the structure to be studied.

- Wide band characterization of the circuits after a single computation (the frequency domain methods compute a single frequency point at each simulation).

- Direct physical interpretation.

- Analysis of problems where the shape of signals is needed (e.g. logical circuits).

- Well adapted for the insertion of lumped non-linear elements.

- This method can fully benefit from the possibilities of new parallel and vectorial computers.

Characterization of a microwave circuit using the 3D Finite Difference Time Domain Method

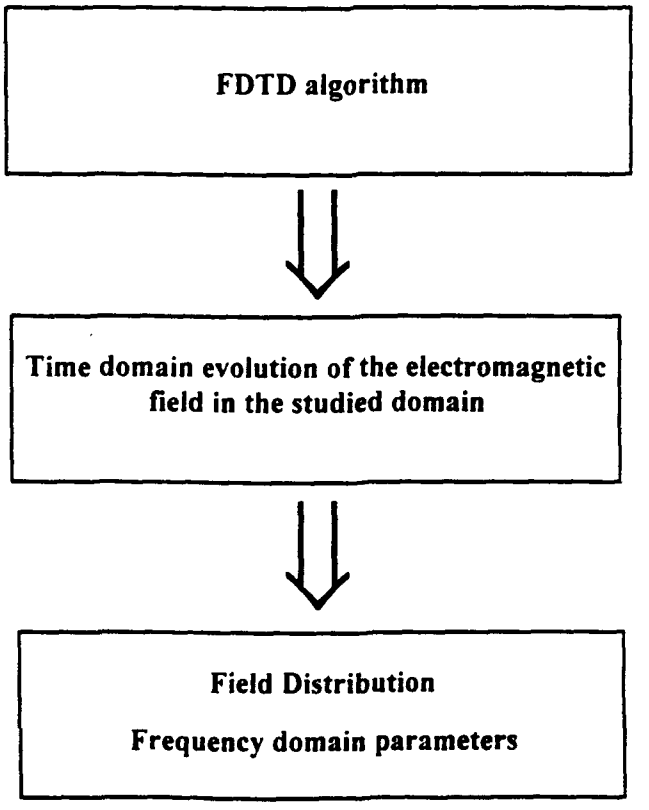

Maxwell's equations :

$$\frac{\partial H}{\partial t} = -\frac{1}{\mu}\nabla \times E \tag{1}$$

$$\frac{\partial E}{\partial t} = \frac{1}{\varepsilon}\nabla \times H \tag{2}$$

We have to discretize : $\frac{\partial}{\partial x}, \frac{\partial}{\partial y}, \frac{\partial}{\partial z}, \frac{\partial}{\partial t}$

$$\left.\frac{\partial f}{\partial u}\right|_{u+\frac{\Delta u}{2}} = \frac{f(u+\Delta u)-f(u)}{\Delta u} \tag{3}$$

It is a double discretization, in time and in space :

1. In time :

$2n\frac{dt}{2} \rightarrow$ Electric field calculation

$(2n+1)\frac{dt}{2} \rightarrow$ Magnetic field calculation

Stability condition :

$$dt \leq \frac{1}{v}\frac{1}{\sqrt{\frac{1}{dx^2}+\frac{1}{dy^2}+\frac{1}{dz^2}}} \tag{4}$$

2. In space : rectangular mesh.

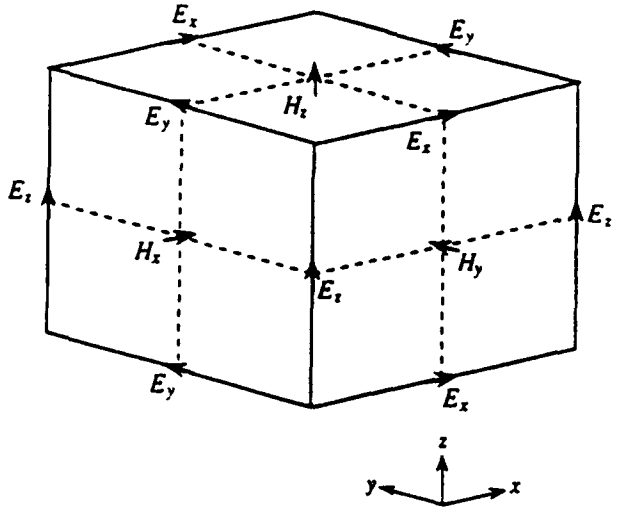

Field components in the unit mesh

$$H_x^{n+\frac{1}{2}}(i,j,k) = H_x^{n-\frac{1}{2}}(i,j,k) - \frac{dt}{\mu dy}[E_z^n(i,j+1,k) - E_z^n(i,j,k)] + \frac{dt}{\mu dz}[E_y^n(i,j,k+1) - E_y^n(i,j,k)]$$

$$H_y^{n+\frac{1}{2}}(i,j,k) = H_y^{n-\frac{1}{2}}(i,j,k) - \frac{dt}{\mu dz}[E_x^n(i,j,k+1) - E_x^n(i,j,k)] + \frac{dt}{\mu dx}[E_z^n(i+1,j,k) - E_z^n(i,j,k)]$$

$$H_z^{n+\frac{1}{2}}(i,j,k) = H_z^{n-\frac{1}{2}}(i,j,k) - \frac{dt}{\mu dx}[E_y^n(i+1,j,k) - E_y^n(i,j,k)] + \frac{dt}{\mu dy}[E_x^n(i,j+1,k) - E_x^n(i,j,k)]$$

$$E_x^{n+1}(i,j,k) = E_x^n(i,j,k) + \frac{dt}{\varepsilon dy}\left[H_z^{n+\frac{1}{2}}(i,j,k) - H_z^{n+\frac{1}{2}}(i,j-1,k)\right] - \frac{dt}{\varepsilon dz}\left[H_y^{n+\frac{1}{2}}(i,j,k) - H_y^{n+\frac{1}{2}}(i,j,k-1)\right]$$

$$E_y^{n+1}(i,j,k) = E_y^n(i,j,k) + \frac{dt}{\varepsilon dz}\left[H_x^{n+\frac{1}{2}}(i,j,k) - H_x^{n+\frac{1}{2}}(i,j,k-1)\right] - \frac{dt}{\varepsilon dx}\left[H_z^{n+\frac{1}{2}}(i,j,k) - H_z^{n+\frac{1}{2}}(i-1,j,k)\right]$$

$$E_z^{n+1}(i,j,k) = E_z^n(i,j,k) + \frac{dt}{\varepsilon dx}\left[H_y^{n+\frac{1}{2}}(i,j,k) - H_y^{n+\frac{1}{2}}(i-1,j,k)\right] - \frac{dt}{\varepsilon dy}\left[H_x^{n+\frac{1}{2}}(i,j,k) - H_x^{n+\frac{1}{2}}(i,j-1,k)\right]$$

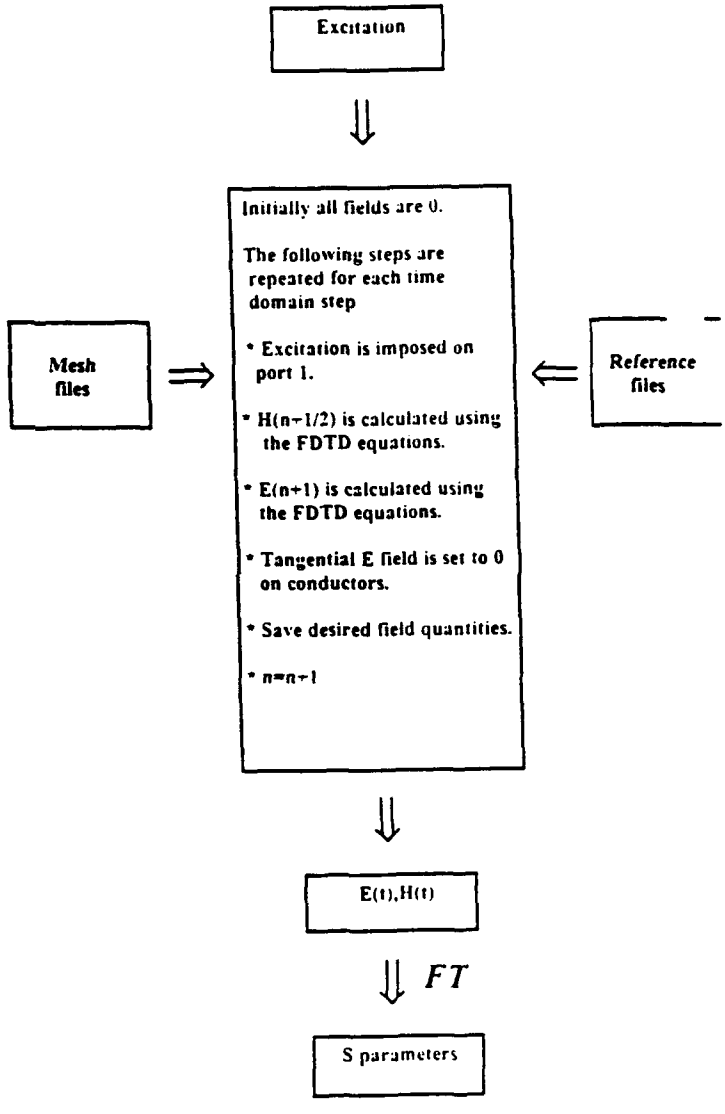

Determination of β(ω) for uniform CPW

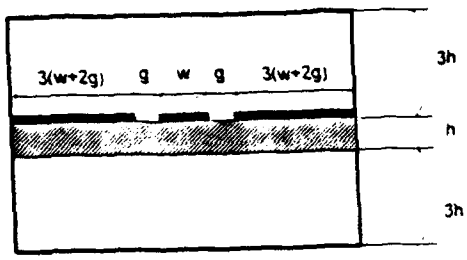

Coplanar Waveguide
h=0.635 mm eps=9.8
w=0.343 mm g=0.147 mm

$$Ez(\omega, y1) = F[Ez(t, y1)]$$

$$Ez(\omega, y1 + dy) = F[Ez(t, y1 + dy)]$$

$$Ez(\omega, y1 + dy) = Ez(\omega, y1)e^{-j\beta(\omega)dy}$$

$$e^{j\beta(\omega)dy} = \frac{Ez(\omega, y1)}{Ez(\omega, y1+dy)}$$

$$\beta(\omega) = \frac{1}{jdy} \ln\left[\frac{Ez(\omega, y1)}{Ez(\omega, y1+dy)}\right]$$

$$\lambda(\omega) = \frac{2\pi}{\beta(\omega)}$$

$$v(\omega) = \lambda(\omega)f = \frac{2\pi f}{\beta(\omega)} = \frac{\omega}{\beta(\omega)}$$

$$\varepsilon_{eff}(\omega) = \left[\frac{c}{v(\omega)}\right]^2 = \left[\frac{c\beta(\omega)}{\omega}\right]^2$$

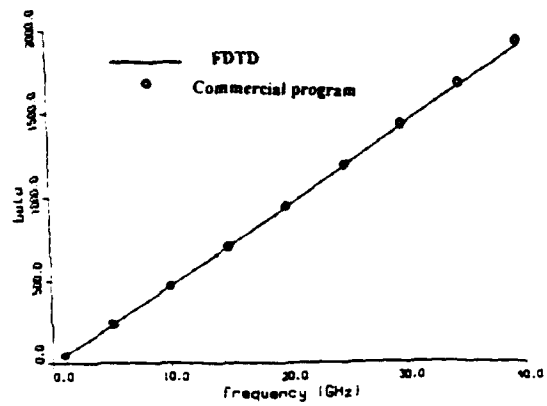

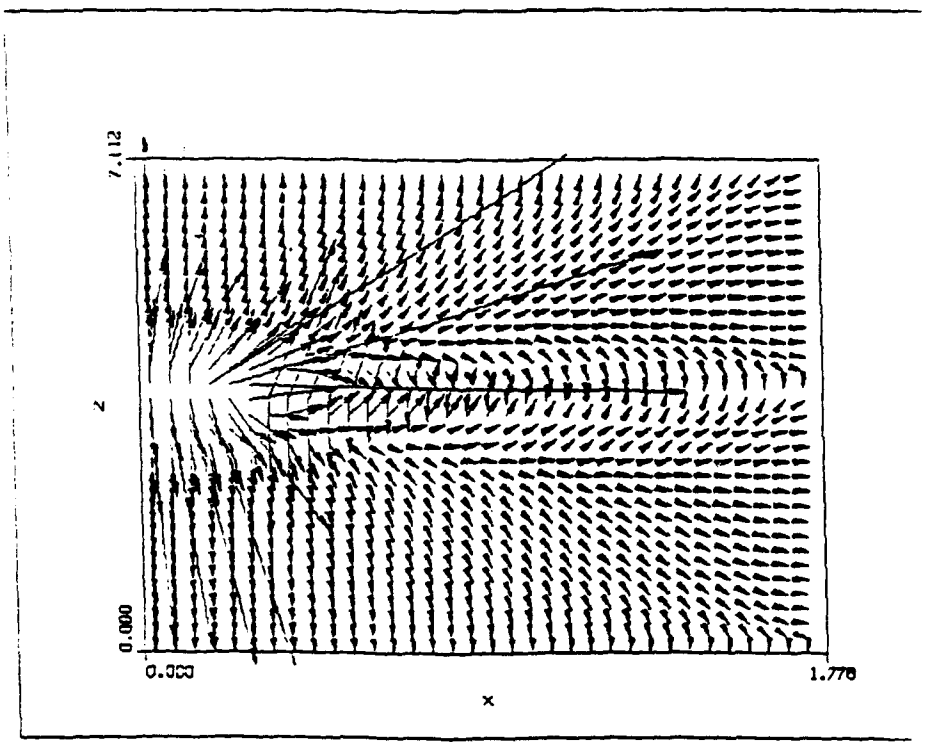

CPW transverse field pattern at the reference plane y1

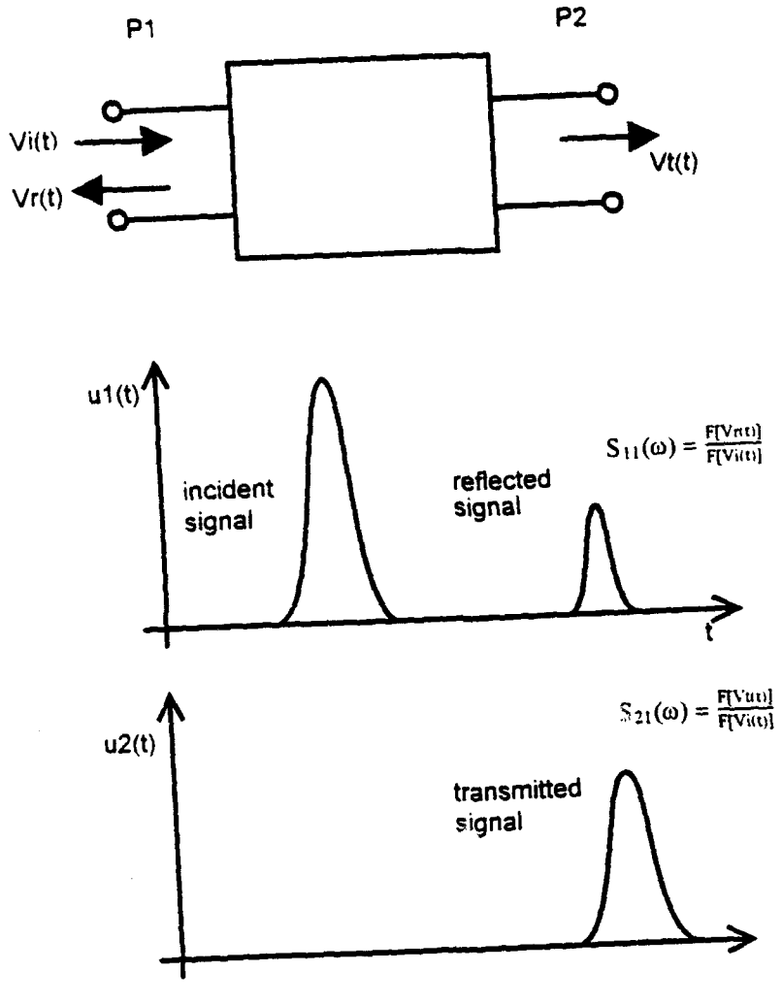

Scattering matrix parameters for a quadripole

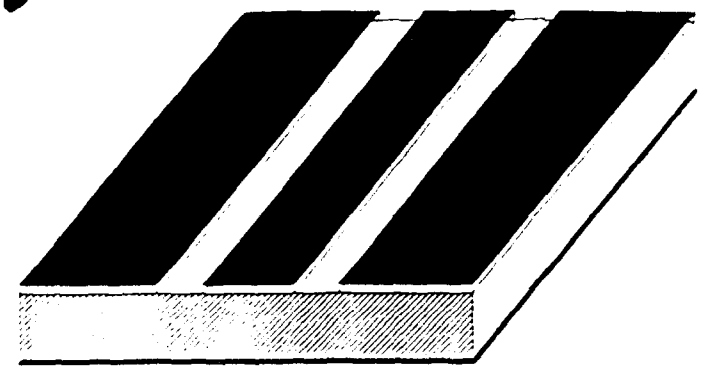

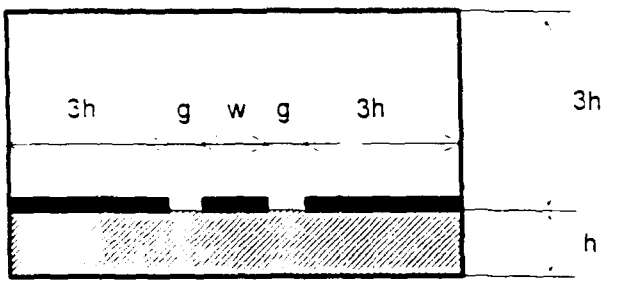

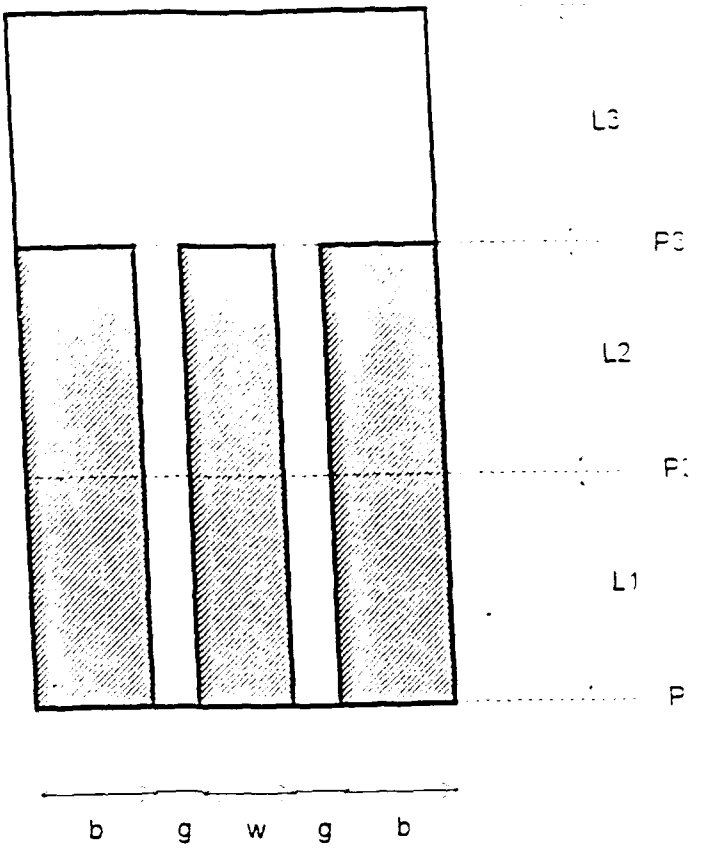

w=80 µm g=40 µm h=100 µm ε_r = 12.8

CPW open circuit discontinuity

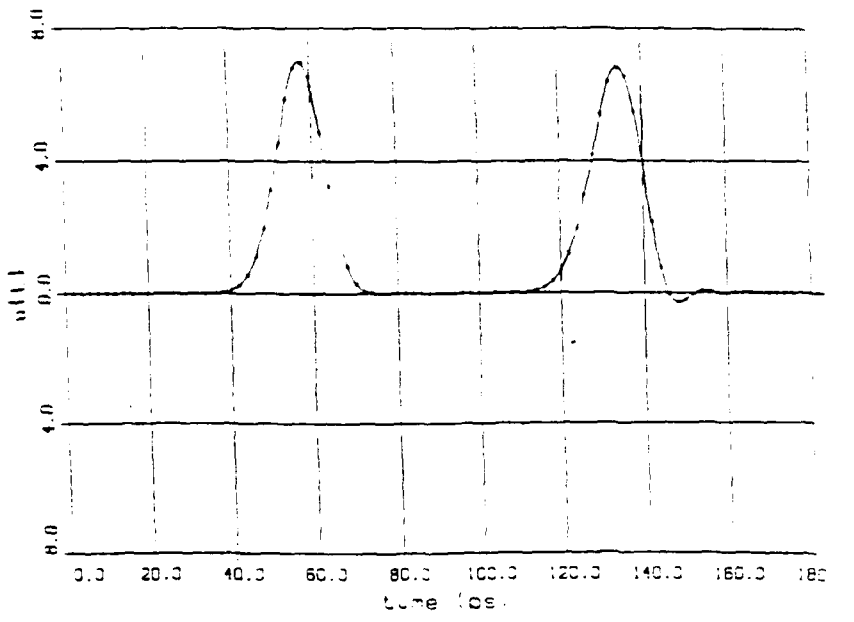

Time domain signal at the reference plane P2

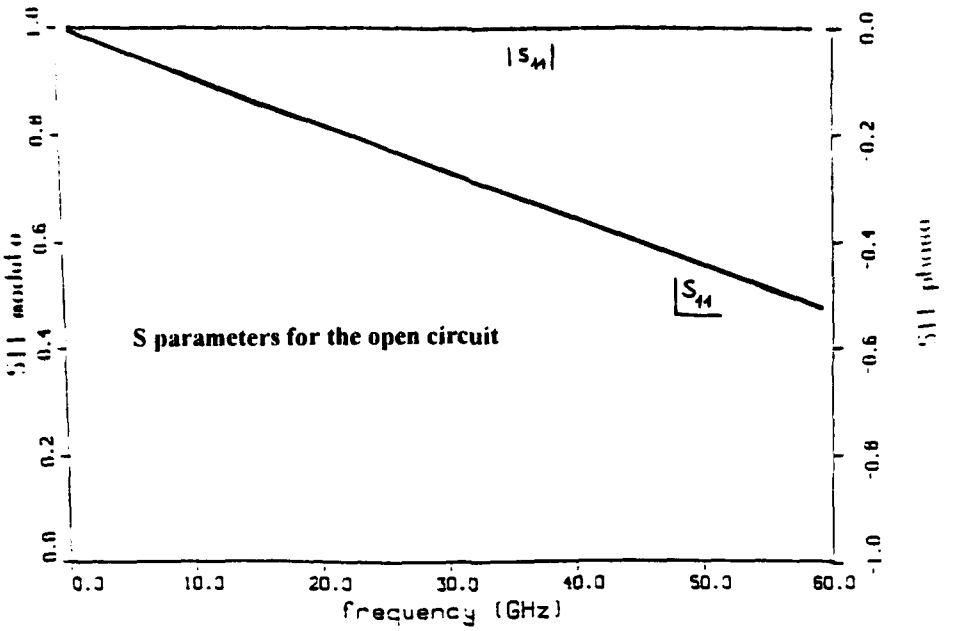

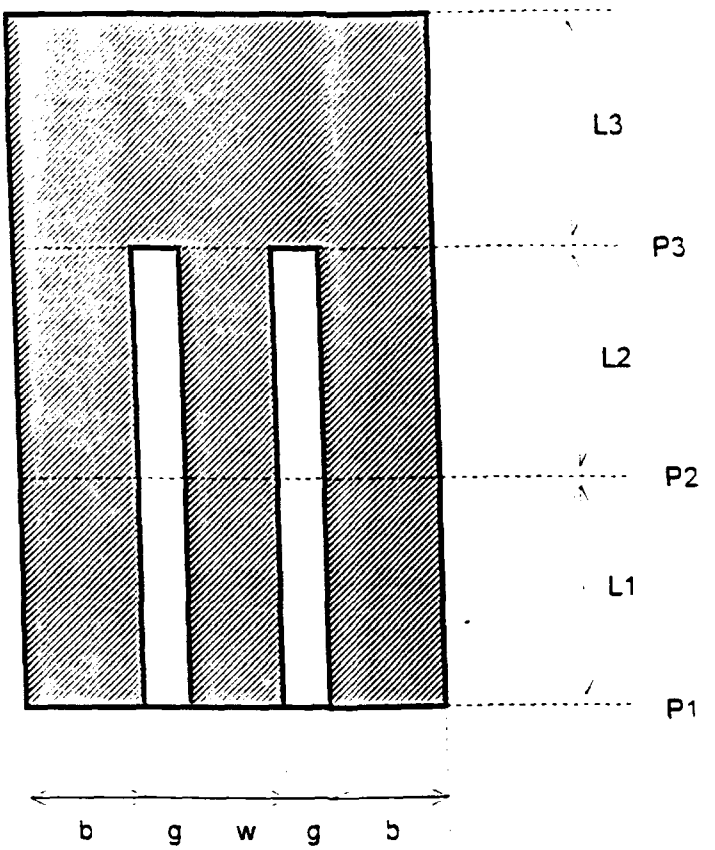

CPW short circuit discontinuity

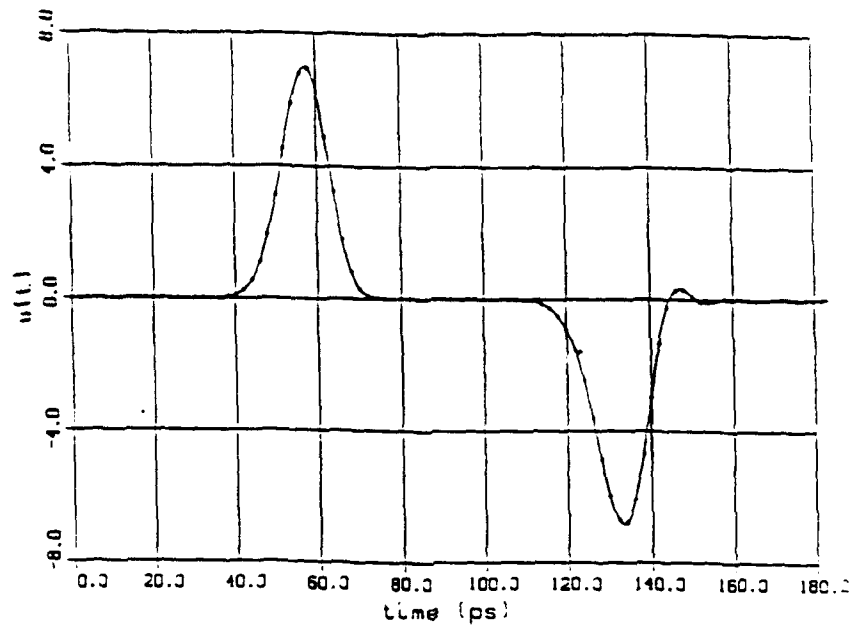

Time domain signal at the reference plane P2

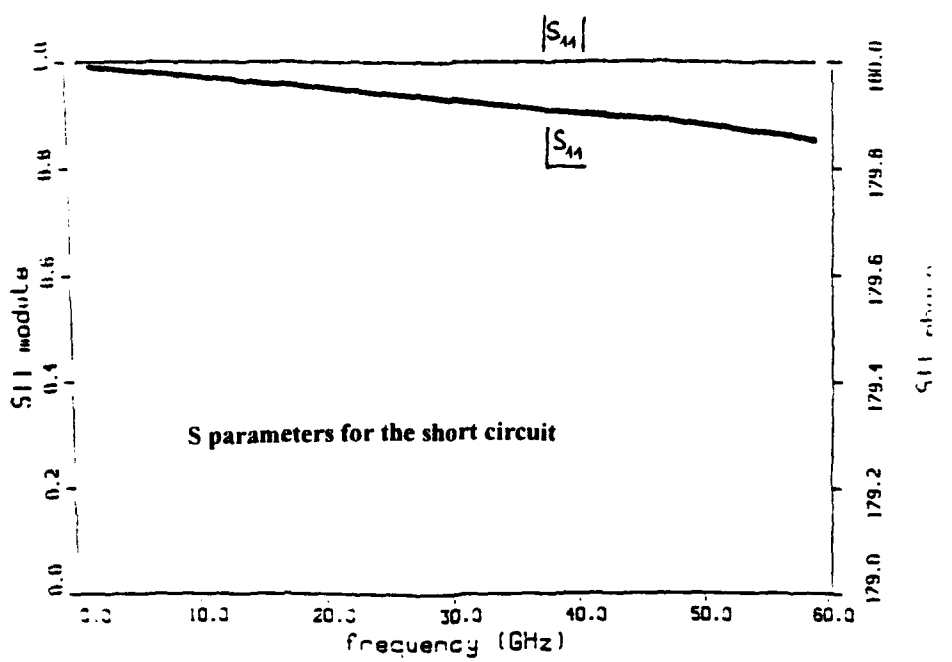

S parameters for the short circuit

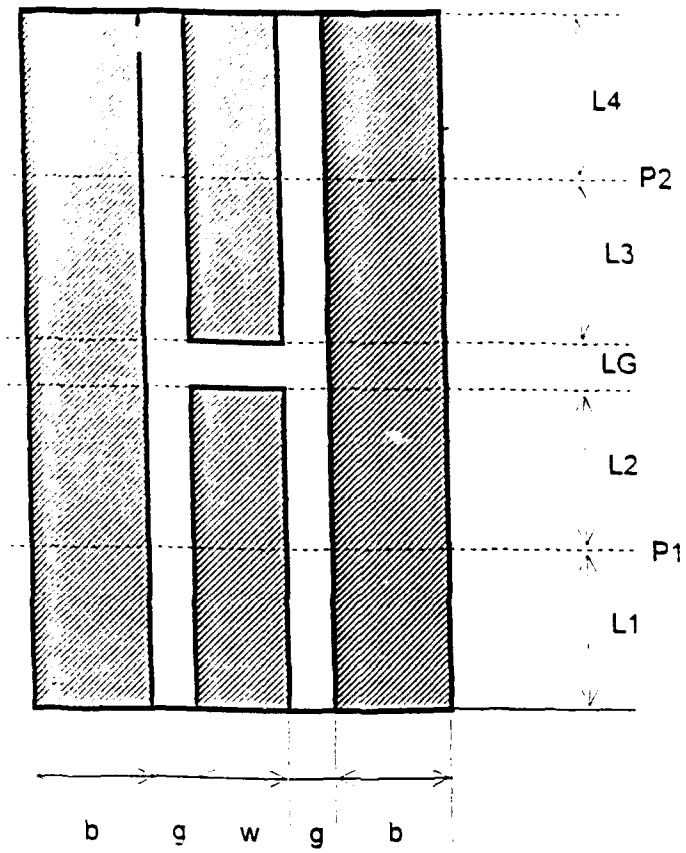

CPW gap discontinuity

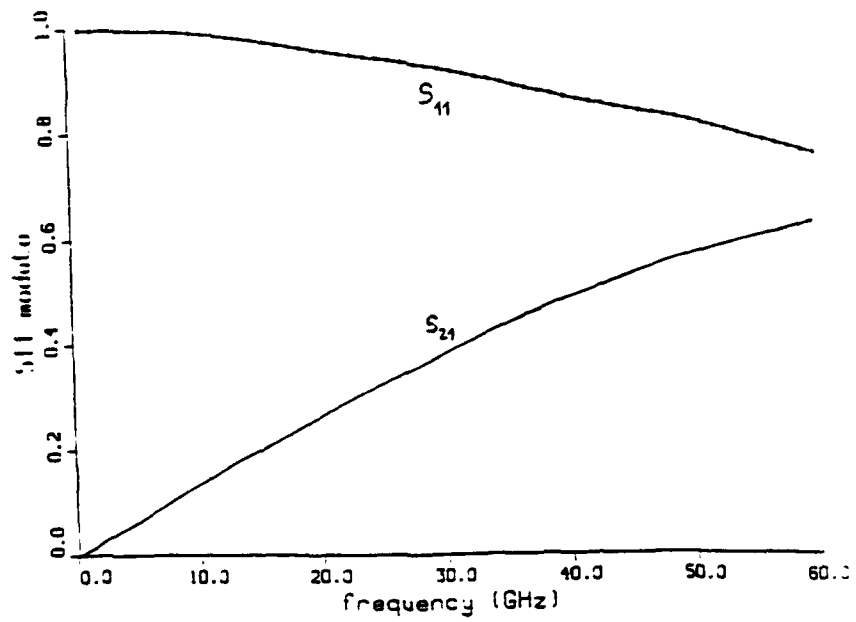

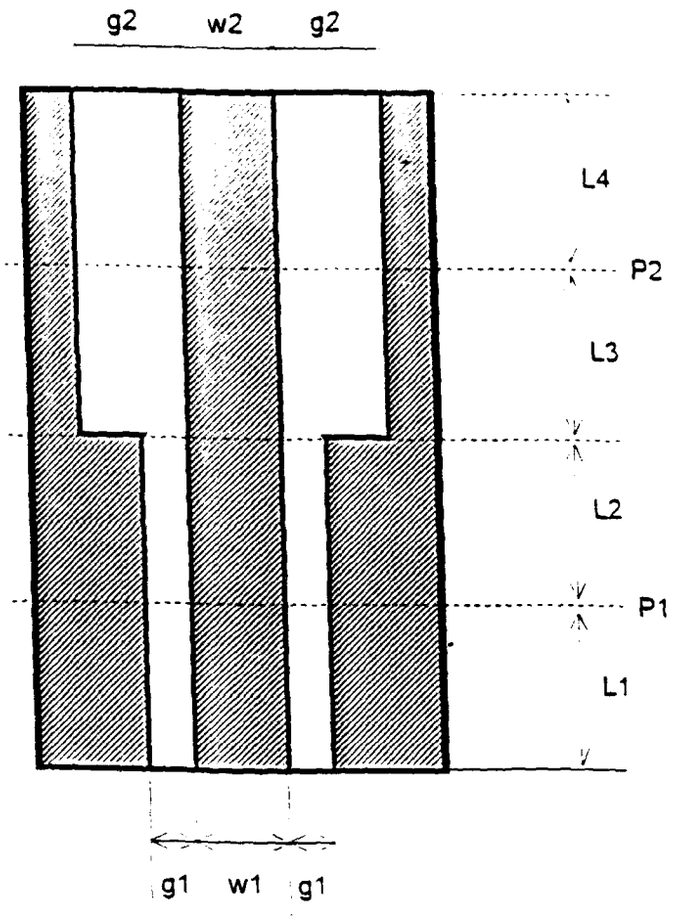

CPW step in width discontinuity

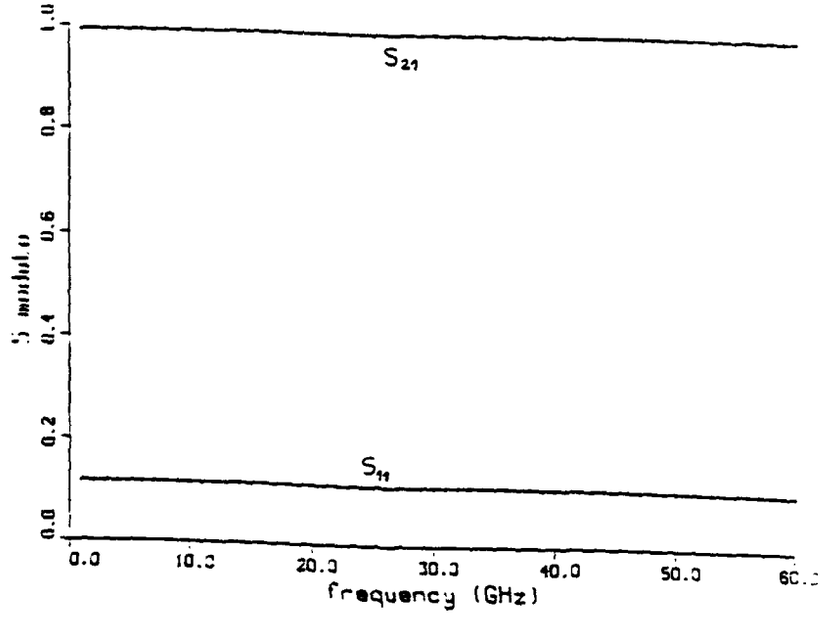

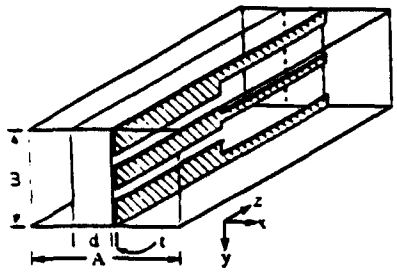

(a)

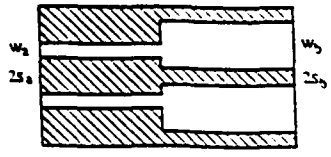

(b)

WR-28
$\epsilon_r = 9.6$
$d = 0.254$ mm
$w_a = 0.1$ mm
$s_a = 0.4$ mm
$w_b = 0.6$ mm
$s_b = 0.1$ mm

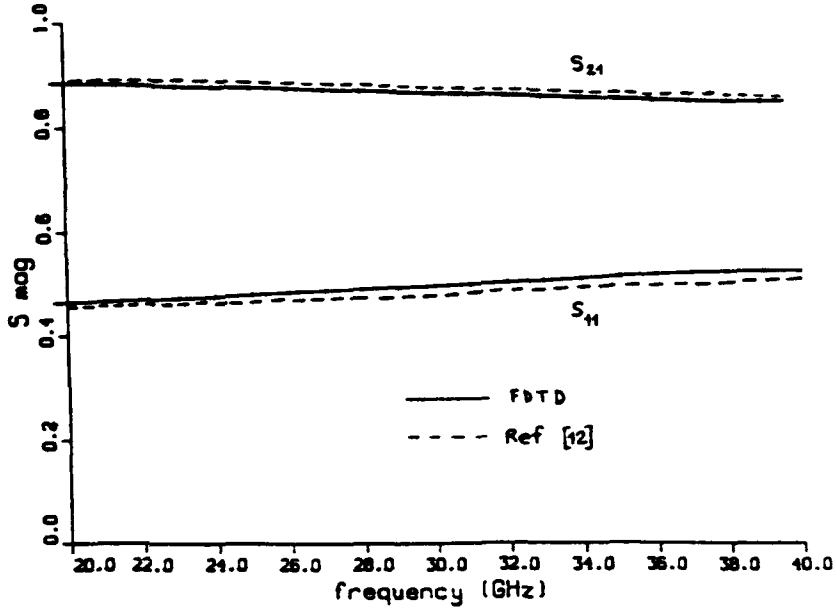

Equivalent circuits for studied discontinuities

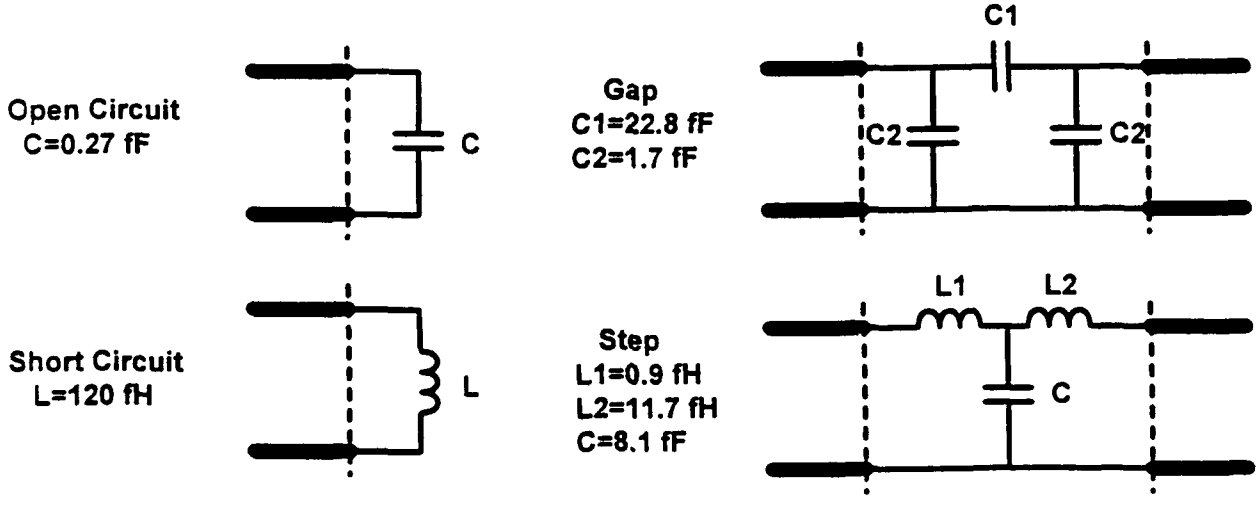

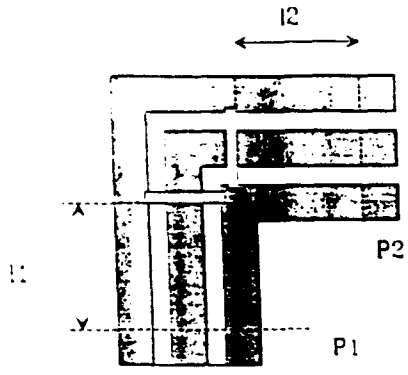

Right angle CPW bend
including two air bridges

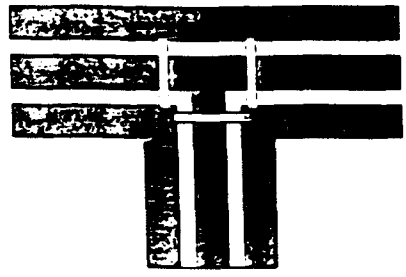

CPW T junction
including three air bridges

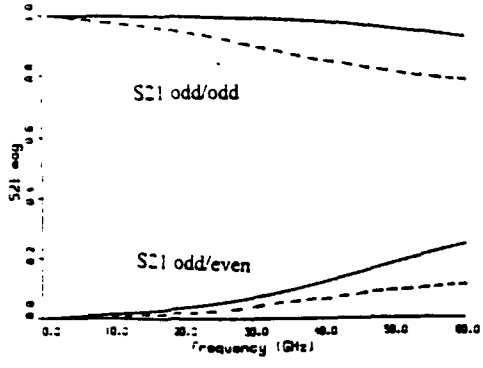

Variation of the scattering parameters S21 as a function of frequency for the right angle CPW bend

——— without air bridges
- - - - - - with air bridges

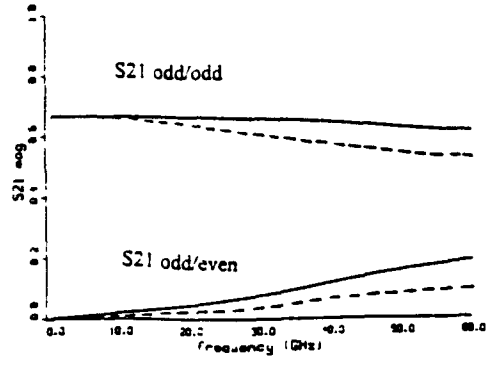

Variation of the scattering parameters S21 as a function of frequency for the CPW T junction

——— without air bridges
- - - - - - with air bridges

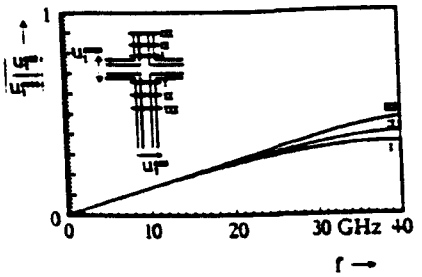

Mode conversion with different bond wire positions.

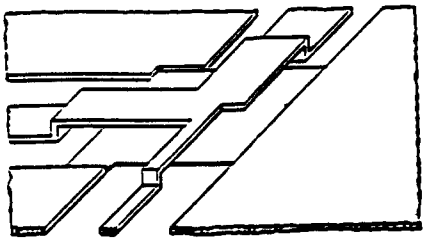

The air bridge T-junction

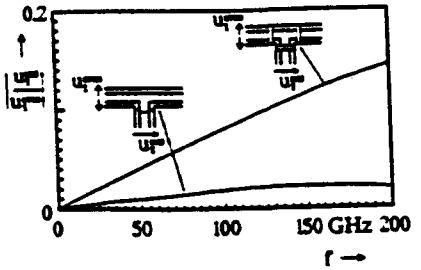

Mode conversion for different T-junctions. $w = 15\mu m$, $s = 10\mu m$, $\varepsilon_r = 12.9$.

Effect of position and geometry of air bridges Ref [10]

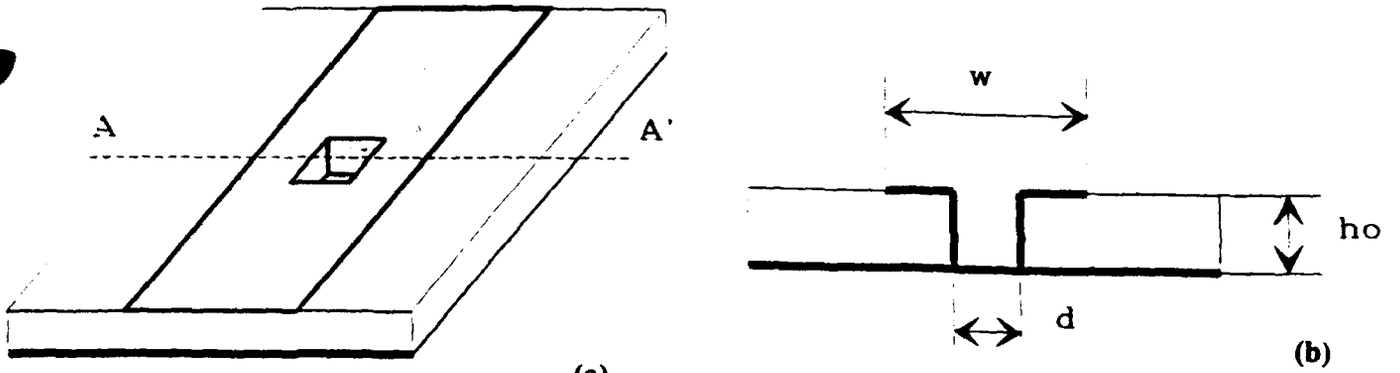

Via hole ground in microstrip
(a) Geometry of the via hole
(b) Cross sectional view through the via hole

w=2.3 mm, h0=0.794 mm, d=0.6 mm, εr=2.32

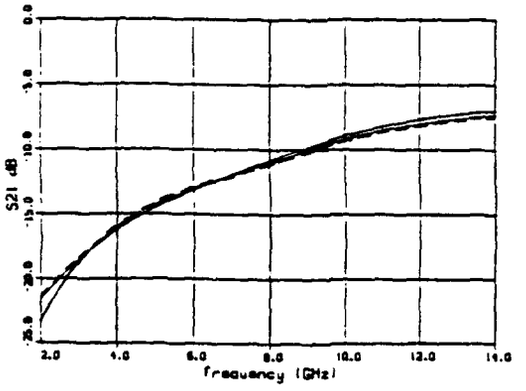

Variation of |S21| for a via hole in microstrip as a function of frequency

——— **our results**
- - - - - - **experimental results of Mr. Sorrentino** [13]

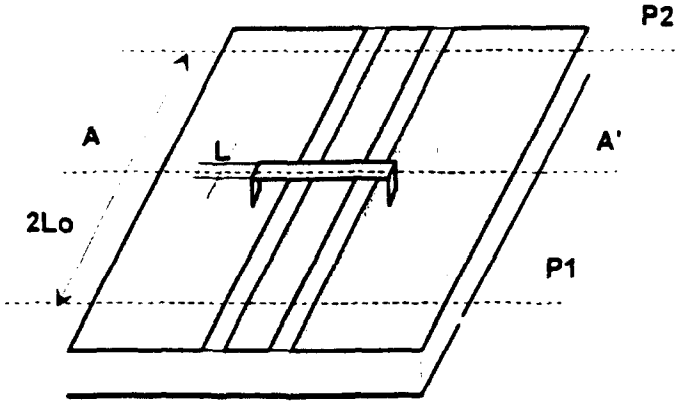

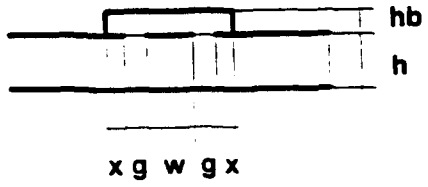

L=5 μm hb=5 μm

Air bridge on a conductor backed CPW

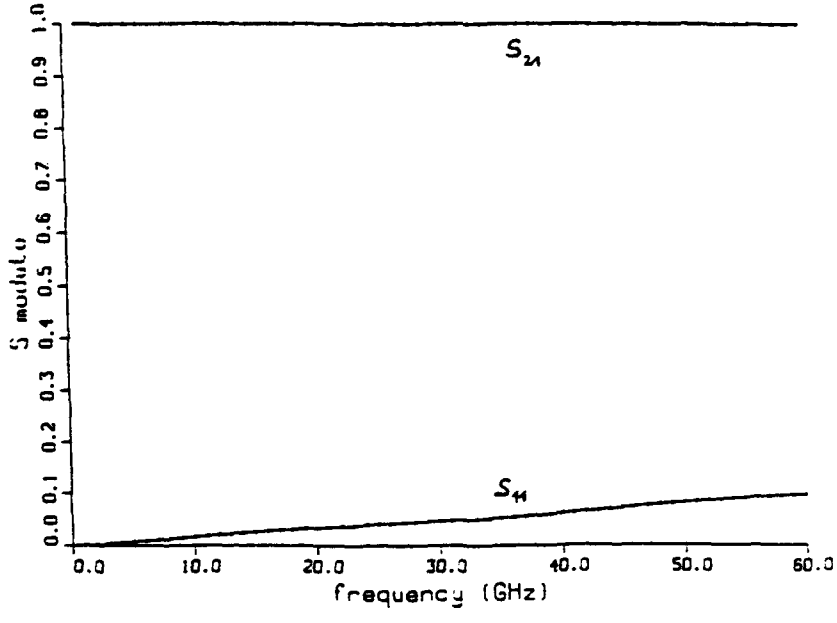

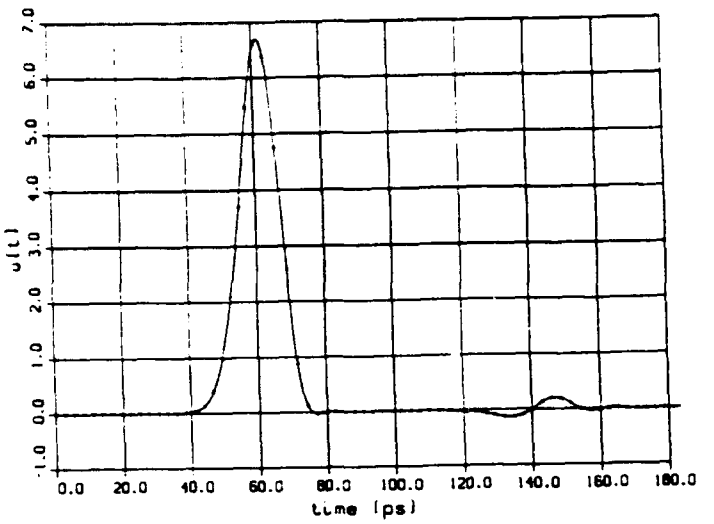

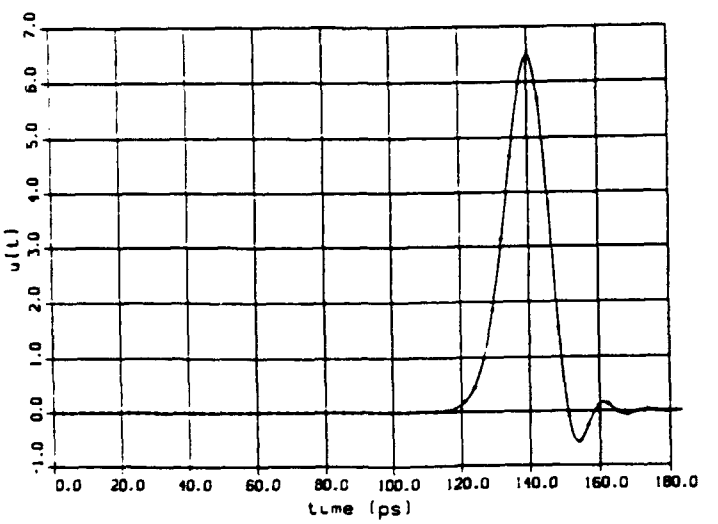

Time domain signals at reference planes P1 and P2

Equivalent circuit for an air bridge

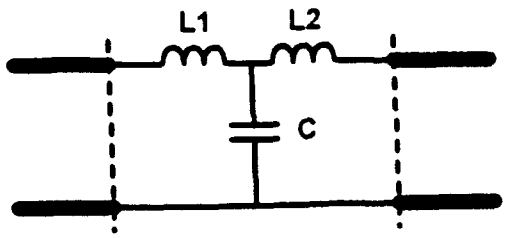

Air bridge on a CPW
L=15.71 pH C=1.46 fF

Air bridge on a conductor backed CPW
L=12.48 pH C=1.21 fF

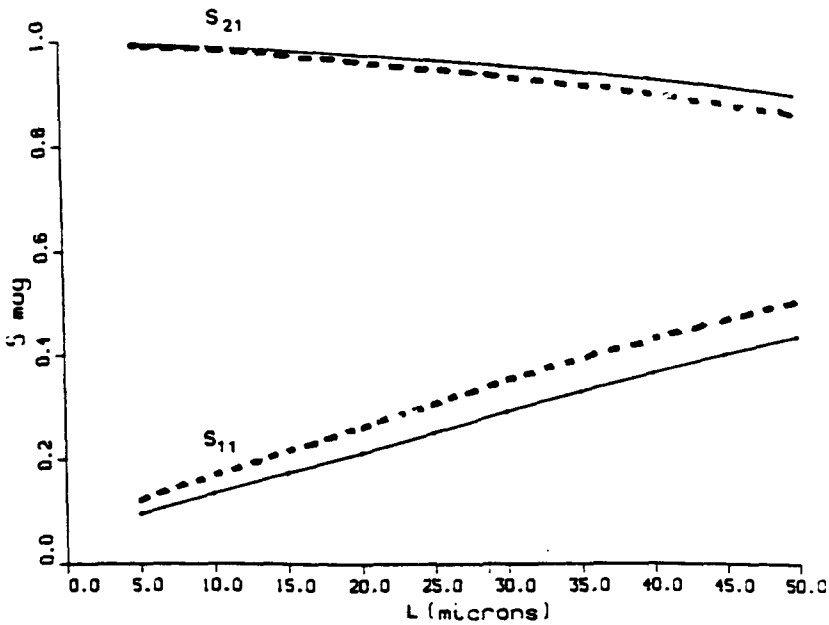

Variation of S parameters as a function of the air bridge width, at f=60 GHz

(——— conductor backed CPW, - - - - CPW)

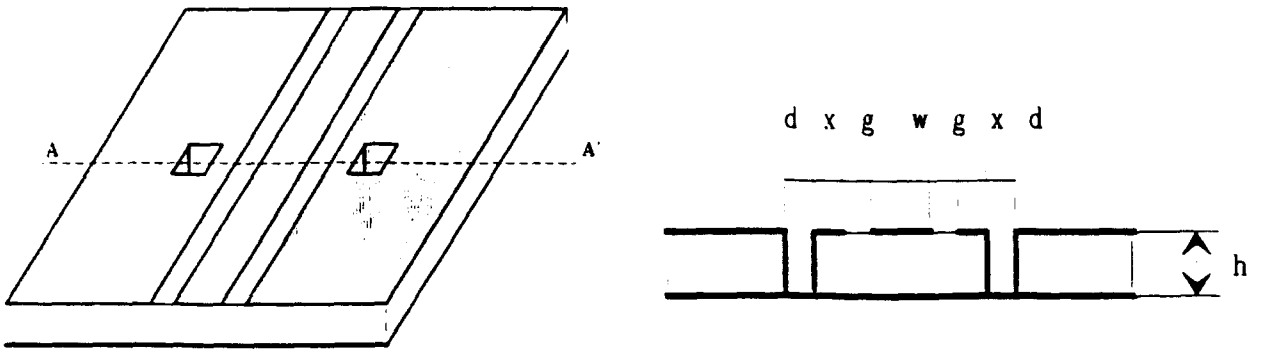

(a) (b)

Via holes in coplanar waveguide
(a) Geometry of the via holes
(b) Cross sectional view through the via holes
w=66 μm, g=40 μm, εr=12.8
d=80 μm, x=20 μm

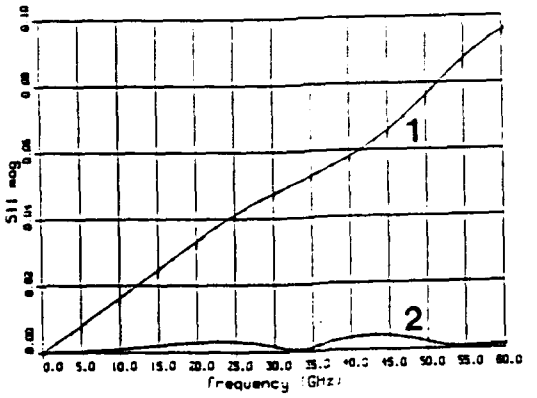

Variation of |S11| as a function of frequency

1 - air bridge + conductor backed CPW
2 - via holes + conductor backed CPW

CONCLUSION

- **Adaptability of FDTD Method for characterisation of CPW structures**
- **Complete control of CPW characterisation using FDTD Method :**
  - **Uniform line**
  - **Planar axial and multiaxial discontinuities**
  - **3D discontinuities (air bridges, via holes)**

REFERENCES

[1] S Visan, O Picon, V Fouad Hanna, "3D characterization of air bridges and via holes in conductor backed coplanar waveguides", 1993 IEEE MTT-S Digest, pp 709-712

[2] S Visan, O Picon, V Fouad Hanna, "Characterization of coplanar discontinuities including air bridges", 1993 MIOP Sindelfingen

[3] S Visan, O Picon, V Fouad Hanna, "Modelisation d'un pont a air sur une ligne coplanaire avec ou sans plan de masse utilisee pour des applications monolithiques", Journees Nationales Microondes, Brest 1993

[4] G C. Liang, Y W Liu, K.K. Mei, "Analysis of coplanar waveguide by the time domain finite difference method", 1989 IEEE MTT-S Digest, pp. 1005-1008

[5] T Shibata, H. Kimura, "Computer aided engineering for microwave and millimeter wave circuits using the FDTD technique of field simulations", International Journal of Microwave and Millimeter Wave Computer Aided Engineering, vol. 3, no. 3, 1993, pp 238-250

[6] D M. Sheen, S. M. Ali, M. D Abouzahra, J. A. Kong, "Application of the three-dimensional finite-difference time-domain method to the analysis of planar microstrip circuits", IEEE Trans. on MTT, vol. MTT-38, July 1990, pp. 849-857

[7] X. Zhang, K. Mei, "Time domain finite difference approach to the calculation of the frequency dependent characteristics of microstrip discontinuities", IEEE Trans. on MTT, vol. MTT-36, dec. 1988, pp. 1775-1787

[8] J. Moore, H. Ling, "Characterization of a 90° microstrip bend with arbitrary miter via the time domain finite difference method", IEEE Trans. on MTT, vol. MTT-38, april 1990, pp. 405-410.

[9] N H. L. Koster, S Koblowski, R. Bertenburg, S Heinen, I. Wolff, "Investigations on air bridges used for MMICs in CPW technique", 1989 EMC Digest, pp. 666-671.

[10] M. Rittweger, M. Abdo, I. Wolff, "Full wave analysis of coplanar discontinuities considering three-dimensional bond wires", 1991 IEEE MTT-S Digest, pp. 465-468

[11] W Hoefer, "The transmission line matrix method - theory and applications", IEEE Trans. on MTT, vol. MTT-33, oct. 1985, pp. 882-893

[12] C W Kuo, T. Itoh, "Characterization of shielded coplanar type transmission line junction discontinuities incorporating the finite metallization thickness effect", IEEE Tr. on MTT, january 1992, pp 73-80

[13] F Alessandri, M. Mongiardo, R. Sorrentino, "Full-Wave Modeling of Via Hole Grounds in Microstrip by Three-Dimensional Mode Matching Technique", in 1992 IEEE MTT-S International Microwave Symposium Digest, pp 1237-1240.

Enhanced Finite Difference Time Domain (FDTD) Method for Active and Passive Structures

B. Houshmand and T. Itoh
Department of Electrical Engineering
University of California, Los Angeles
Los Angeles, CA 90024-1594
U. S. A.

ABSTRACT

The Finite-Difference Time-Domain algorithm is a powerful method for analyzing the electromagnetic wave behavior in a complicated geometry. This method, however, is a memory intensive and time consuming operation due to spatial and temporal discretization. Here the FDTD is augmented with Diakoptics and System Identification algorithms in order to reduce the computational cost. Furthermore, the FDTD algorithm is extended to include the analysis of nonlinear and active regions. Theoretical development and numerical examples are presented. A comparison of the nonlinear FDTD algorithm and measurement results demonstrate the versatility of this algorithm.

I. Introduction

It is well known that the Finite-Difference Time-Domain (FDTD) is a powerful method for analyzing the electromagnetic wave behavior in a complicated geometry. This method, however, is a memory intensive and time consuming operation. Recently, we have utilized several techniques to alleviate these deficiencies. Specifically, we have implemented the FDTD Diakoptics method to use numerical Green's function to replace large computational volume with its impulse response. Hence, the memory requirement is drastically reduced. For reducing the computational time, we have implemented a method based on the system identification (SI) technique. A reduction of computation time of a factor of ten can readily be attained. In addition, we have analyzed large volumes containing active and nonlinear regions (or devices, plasmas, etc.) by means of FDTD environment.

In this paper, an overview of the FDTD Diakoptics, application of system identification to the FDTD algorithm, and application of FDTD to nonlinear and active regions are presented. Several examples which illustrate these methods are included.

II. FDTD Diakoptics

Analysis of a computationally large circuit can be accomplished by dividing the circuit structure into several small modules. Each module can be analyzed separately, and the

mutual interaction of the modules can be included by proper treatment of the circuit boundaries. Based on this methodology, the time-domain Diakoptics method has been developed in TLM [1], [2], and in FDTD [3], [4]. The time domain Diakoptics can include all the mutual interactions among modules through a convolution interface without invoking any approximations.

The time-domain Diakoptics uses time-domain convolution for connecting modules. This convolution requires the knowledge of the impulse responses of the circuit segments. These impulse responses are in effect the numerical Green's functions.

II.1 Theory

Time-Domain Diakoptics originates from the linear circuit theory. Once input and output ports are identified, the system output Y(n) of a passive structure can be determined from the convolution of the system impulse response h(n) and the input X(n). This indicates that the complete two-port linear passive structure can be replaced by its impulse response h(n). Similarly, multi-port linear passive region in the field calculation can be replaced by an impulse response matrix [g], see Figure 1. This operation is similar to the method used in [5]. The multi-port convolution is defined

$$Y_m(k)=\sum_{n=1}^{N}\sum_{k'=0}^{K} g(m,n,k-k')X_n(k') \qquad (1)$$

where g(m,n,k') is the impulse response (or the time-domain Green's function) at port "m" at time t=k' due to the unit excitation at port "n" at t=0.

The computation of the numerical Green's function is performed by applying an impulsive source at the input port of the passive structure. If the impulse response over a limited frequency range is required, the frequency band-limited response can be computed by applying a deconvolution process between the structure output and the input signal which spans the frequency range of interest [6].

II.2 Results

The numerical behavior of the FDTD Diakoptics is demonstrated by applying it to a one-dimensional circuit . Figure (2) shows an infinitely long parallel-plate transmission line loaded with lumped elements and material discontinuity. Only the TEM mode of operation is considered due to the dimensions of the problem. As such, the results produced by the time-domain Diakoptics can be directly compared with those produce by conventional time-domain circuit simulators, like Microwave SPICE (MWSPICE). Figure (3) shows the agreement between the MWSPICE and the FDTD Diakoptics method.

III. System Identification

The Finite-Difference Time-Domain algorithm is an effective computational method for full vector analysis of microwave structures [7]. The theoretical formulation directly follows the Maxwell's equations, and algorithm implementation is simple and flexible for general structures of interest. The computation requirements, however, is excessive due to the spatial-temporal discretization. Recently, digital signal processing methods have been used to reduce the computational requirements of the time-domain methods [8-11]. For example, The Prony's method is used to estimate the time signal in terms of the previously computed values [8], also a covariance based system identification (SI) algorithm has been used to reduce the computation cost of the Transmission Line and FDTD Methods by employing a stochastic ARMA model [9-10]. In this paper a Least-Squares based system identification projection algorithm for a deterministic Auto-Regressive Moving Average model is applied to the FDTD algorithm [12]. The application of this algorithm to the partially filled rectangular cavity has demonstrated excellent numerical results. Savings in the computation requirements are achieved by replacing the computationally intensive FDTD algorithm by the ARMA model for output signal computation, after the system parameters converge to their final values. In addition, the frequency response is evaluated directly from the computed system parameters, thus eliminating the need for Fourier Transformation.

III.1 THEORY

The computed time signal at an appropriate location in the computational volume and the corresponding input signal can be interpreted as the input and output signals of a discrete linear system. This linear system description is

$$y(n) = -\sum_{k=1}^{K} a_k\, y(n-k) + \sum_{m=0}^{M} b_m\, x(n-m) \qquad (2)$$

The output signal is completely known when the model parameters (a_k, b_m) are computed. The parameter space is taken to be large enough to allow the convergence of the model output to the FDTD simulated field values. Equation (2) can be written in a compact form

$$y(n) = \Phi^T(n-1)\,\Theta_0 \tag{3}$$

where T stands for Transpose, and Φ is a vector containing the present and past values of the input and output which can be considered as data. The vector Θ_0 contains the system parameters and uniquely defines the properties of the linear system such as the resonance frequencies. Equation (3) represents the output of a linear system as the inner product of the Φ and the parameter vector. Using the available data vector Φ, the output signal can be estimated in terms of the estimated system parameters

$$\hat{y}(n) = \Phi(n-1)^T\,\hat{\Theta}(n-1) \tag{4}$$

The difference in Equations (3) and (4) is minimized with respect to the system parameters to arrive at a parameter update law

$$\hat{\Theta}(n) = \hat{\Theta}(n-1) + \frac{P(n-1)\,\Phi(n-1)}{\Phi(n-1)^T\,P(n-1)\,\Phi(n-1)}\,[e(n)] \tag{5}$$

$$P(n) = P(n-1) - \frac{P(n-1)\,\Phi(n-1)\,\Phi(n-1)^T\,P(n-1)}{\Phi(n-1)^T\,P(n-1)\,\Phi(n-1)},\ P(0) = I \tag{6}$$

where P(n) provides an orthogonal projection search in the parameter space which results in rapid parameter convergence [12], $\Theta(n)$ is the computed parameter vector, and e(n) is the discrepancy between the estimated output and the FDTD computed field value. Computation of Equations (5) and (6) requires only vector addition and multiplication, and results in minimal additional cost to the FDTD computation. We note that the system parameters converge to their final values when the output error is sufficiently small.

III.2 RESULTS

The numerical behavior of this method is demonstrated by applying it to the cavity problem. An ARMA model with system parameters K=40, M=40, see Equation (2), is used to obtain the resonance frequencies of a rectangular cavity. The cavity is excited at the

center plane by imposing a TE_{10} mode distribution with impulsive temporal dependence. Figure 4 shows the parameter convergence for a number of system coefficients. The initial condition for the parameters is set to the origin of the parameter space, and the parameter values are updated at each sampled interval.

The resonance frequencies of the cavity can be derived directly from the poles of the ARMA model. They can also be recovered from the spectrum of the output signal. This spectrum is computed by the Fourier Transform of the output signal, or directly by evaluation of the Z-Transform of Equation (2) on the unit circle which is defined in terms of the system parameters. Figure 5 shows the spectrum of the output signal using the system parameters and the Fourier Transformation of the output signal. The recovered resonance frequencies of the first three odd modes are illustrated. The location of the observation point coincides with the null position of the even modes as the result these modes can not be recovered form this time signal. In this example, the ARMA based spectrum is computed using 140 output samples. Similar spectrum is obtained by applying the Fourier Transformation to 500 output samples. Figure 5 also shows the Fourier Transform of the 140 output samples which are augmented with zero padding to provide sufficient spectral resolution for locating the spectrum peaks. This spectrum, while qualitatively locates the resonance frequencies, is distorted and might not provide sufficient resolution where the resonance frequency separation is small. We note that the first two resonance frequencies are predicted accurately for this example, while higher order modes are underestimated due to frequency dispersion of the FDTD spatial grid. This method is used to obtain the resonant frequencies of a partially filled rectangular cavity. Figure 6 shows the shift in the resonant frequency as the permittivity is gradually changed from $\varepsilon=1$ to $\varepsilon=2$.

IV. Modeling of Nonlinear and Active regions with the FDTD method

The FDTD method can be extended to include nonlinear and active regions embedded in distributed circuits. Recently, the two dimensional FDTD was extended to include active, passive and possibly nonlinear lumped circuit elements [13]. In that work the incorporation of the lumped elements into the FDTD algorithm is described, and transmission lines with various lumped element loads were simulated. In [13] only one active load was modeled, which was linear, and the modelling follow the same procedure as the passive lumped elements. The inclusion of active nonlinear regions, however,

requires additional procedures in order to preserve the numerical stability of the FDTD algorithm.

This effect is observed in [14] where the TLM method was used to model active nonlinear subregions of distributed circuits, and it was noted that regions of negative conductivity may cause spurious oscillations at the TLM mesh cut-off frequencies. To circumvent this problem, the TLM mesh cut-off is chosen to be well above the active device cut-off frequency. Similar condition holds for the FDTD algorithm. In addition, we have found that in many cases the FDTD algorithm will become unstable unless some care is taken in incorporating the active device model. This is due to the fact that realistic active devices can produce extremely large local currents. These local currents, in turn, produce large fields that are fed back into the device model which can create unstable behavior.

Here we describe the steps we have implemented to produce a stable algorithm, and we use this algorithm to simulate an active antenna. This method is used to simulate a three-dimensional microwave circuit containing an active and nonlinear device. Figure 7 shows a two element active antenna which is examined. Each patch is excited by a separate Gunn Diode and therefore the circuit really consists of two oscillators. However, the two oscillators are strongly coupled through a length of transmission line and there are several possible modes of operation for the entire coupled circuit. In [15] an extensive model analysis, which determines the most stable mode of operation, has been described. We will demonstrate here that the FDTD is able to correctly predict this model as well, with the additional advantage that the complete electromagnetic behavior of the circuit is obtained. It is important to note that while a frequency domain analysis can be used to determine the possible circuit modes, the frequency domain analysis alone cannot predict which is the most stable mode and hence cannot predict the steady state behavior of the circuit.

IV.1 Theory

As mentioned above, special care must be taken to simulate nonlinear and active elements in the FDTD or TLM. First, it is necessary that the cut-off frequency of the active device be well below the mesh cut-off frequency to prevent the unstable oscillations at these frequencies. We therefore model each Gunn diode by the equivalent circuit shown in Figure 8. The active current is given by the polynomial

$$F(V_s) = -G_1 V_s + G_3 V_s^3 \qquad (7)$$

The coefficients were determined experimentally from measurements at 10.48 GHz (the patch resonance frequency) to be G1 = 0.0252 ohm^{-1} and G3 = 0.0265 ohm^{-1} V^{-2}, and the capacitance was determined to be C= 0.2 pF. The series resistance was estimated to be R=1.0 ohm. Note the instead of using complicated model for Gunn diode which would incorporate the correct dispersive behavior, we are using a simplified model which is approximately correct over a narrow frequency range and ensures that the active device cut-off frequency is bellow the mesh cut-off frequency. This simplification is justified by the highly resonant nature of the circuit, which limits the possible frequencies of interest.

To incorporate the package diodes into the FDTD mesh, we use an equivalent active region which extends over three vertical cells between the microstrip and the ground plane (Figure 7), and occupies only one cell in the horizontal or x-y plane. Note that we cannot assume each mesh cell in the active region is dependent only on the local field at the cell, as was done in [13], [14], and [16]. This is because each cell will then act as a separate diode, with aggregate effect of tree diodes in series. Instead, we model the entire active region as a single diode. The total voltage across this diode is given by

$$V_z(t) = \frac{V^{n+1} + V^n}{2} = \frac{\Delta z}{2} \sum_{k=1}^{3} [E_z^{n+1}(i_s, j_s, k) + E_z^n(i_s, j_s, k)] \qquad (8)$$

Here n represents the time step increment, and (i_s, j_s) are indices in the x, y plane for the two active regions (s= 1, 2). This time average voltage is then fed into our active device model (Figure 8) which then calculates the total current by

$$A_0 I^{n+1} = A_1 I^n - A_2 F(V_s^n) - A_3 V^{n-1} - A_4 V^n + A_5 V^{n+1} \qquad (9)$$

with

$$A_0 = 2RC + \Delta t + R\,\Delta t\,\dot{F}(V_s^n),\ A_1 = 2RC - \Delta t + R\,\Delta t\,\dot{F}(V_s^n),\ A_2 = 2\,\Delta t,$$

$$A_3 = C,\ A_4 = \Delta t\,\dot{F}(V_s^n),\ A_5 = C + \Delta t\,\dot{F}(V_s^n)$$

where (.) denotes the derivative of the dependent current source with respect to the voltage. A forward differencing scheme with time averaging has been used in order to produce

stable oscillations. This process is described in more detail in [17]. The current is then fed back as a source into the FDTD cells in the active regions. For each active region (s= 1, 2),

$$\frac{\varepsilon}{\Delta t}E_z^{n+1}(i_s, j_s, k) = \frac{\varepsilon}{\Delta t}E_z^{n}(i_s, j_s, k) + L[H_x, H_y] - \frac{I^{n+1} + I^{n}}{2\Delta x\, \Delta y} \qquad (10)$$

The term $L[H_x, H_y]$ is

$$\frac{H_x^{n+\frac{1}{2}}(i_s, j_s-1, k) - H_x^{n+\frac{1}{2}}(i_s, j_s, k)}{\Delta y} + \frac{H_y^{n+\frac{1}{2}}(i_s, j_s, k) - H_y^{n+\frac{1}{2}}(i_s-1, j_s, k)}{\Delta x} \qquad (11)$$

Equations (8) and (9) are then used in (10) in order to obtain a stable FDTD algorithm in the active region [17]. This algorithm is stable for circuits embedded with nonlinear active regions which we have considered.

IV.2 RESULTS

By using the modified FDTD algorithm described above, we have simulated the two element active antenna shown in Figure 1. A small amount of numerical noise is introduced into the FDTD mesh, and oscillations build up until a steady state frequency of 12.4 GHz is achieved (Figure 9). The measured frequency is 11.8 GHz and the frequency predicted by the modal analysis [18] is 12.2 GHz. The 5 percent discrepancy in the predicted frequency can be attributed to modelling errors in the geometry description and measurement of the Gunn diode parameters. What is more significant is that the FDTD simulation has predicted the same stable mode of operation as was observed in the measurement (there are three possibilities [18]). This cannot be done with a frequency domain simulation. The stable mode is an odd mode which can be seen clearly in Figure 10, where we show the steady state voltage across each diode as a function of time. Figure 11 shows the distribution of the z component of the electric field at the dielectric-air interface.

V. CONCLUSION

In this paper an enhanced Finite-Difference Time-Domain algorithm is presented. The Diakoptics and System identification algorithms have the potential of reducing the computational cost effectively through reducing the memory requirements and simulation

time, respectively. The FDTD algorithm is also applied to problems which include nonlinear and active properties. It is noted that care must be taken in order to insure the stability of the algorithm. The modified FDTD algorithm is used to analyze a two element active antenna. The simulation has remarkably produced the proper steady state behavior which is indicated through measurements.

REFERENCES

[1] P. B. Johns, and K. Akhtarzad, "The use of time domain diakoptics in time discrete models of fields," Int. J. Num. Methods Eng., vol. 17, pp. 1-14, 1981.

[2] W.J.R. Hoefer, "The discrete time-domain Green's function or Johns matrix - a new powerful concept in transmission line modeling (TLM), " Int. J. Num. Modelling, vol. 2, pp. 215-225, 1989.

[3] T.W. Huang, B. Houshmand, and T. Itoh, "THe FDTD Diakoptics Method," IEEE MTT-S Int. Microwave Symp. Digest, 1993, pp. 1435-1438.

[4] T.W. Huang, B. Houshmand, and T. Itoh, "The Sequential FDTD Diakoptics method for modular computation" Asia-Pacific Microwave Conference Proceeding, Oct. 1993.

[5] C.W. Huo, and T. Itoh, "A new time-domain transverse resonance method in solving guided wave problems," Int. J. Num. Modelling, vol. 3, pp. 229-234, 1990.

[6] T.W. Huang, B. Houshmand, and T. Itoh, "The Implementation of Time-Domain Diakoptics in the FDTD Method," Submitted to the IEEE Trans. Microwave Theory Tech.

[7] X. Zhang and K.K. Mei, "Time-Domain finite-difference approach to the calculation of frequency dependent characteristics of microstrip discontinuities", *IEEE Trans. Microwave Theory Tech., vol. MTT-36, no. 12, pp.* 1775-1787, Dec. 1988.

[8] J.L. Dubard, D. Pompei, J. Le Roux and A. Papiernik, "Characterization of Microstrip antennas using the TLM simulation associated with a Prony-Pisarenko Method," Int. J. of Numerical Modeling: Electronic Networks, Devices and Fields, Vol. 3, 269-285, 1990.

[9] W. Kuempel and I. Wolff, "Digital signal processing of time domain field simulation results using the system identification method", IEEE MTT-S Digest, June 1992.

[10] W. Kuempel and I. Wolff, "System Identification Method for Transient Analysis of (M)MIC-Components Using Time Iterative Methods," 22ND European Microwave conference, Finland, 24-27 August 1992.

[11] B. Houshmand, and T. Itoh, "Parameter estimation for characterization of microwave structures," presented at the National Radio Science Meeting, Jan. 5-8, 1993.

[12] P. Strobach, Linear Prediction Theory: A Mathematical Basis for Adaptive Systems, Springer Verlag, Berlin, 1990.

[13] W. Sui, D.A. Christensen, and C.H. Durney, "Extending the two dimensional FDTD method to hybrid electromagnetic systems with active and passive lumped

elements," IEEE Trans. Microwave Theory Tech., vol. MTT-40, no. 4, pp. 724-730, April 1992.

[14] P. Russer, P.M. So, and W.J.R. Hoefer, "Modeling of nonlinear active regions in TLM," IEEE Microwave and Guided Wave Letters, vol. 1, no. 1, pp. 10-13, Jan. 1991.

[15] S. Nogi, J. Lin, and T. Itoh, "Mode analysis and stabilization of a spatial power-combining array with strongly coupled oscillators," to be published in the special issue on Quasi-optical Technidues of the IEEE Trans. Microwave Theory Tech., Oct. 1993.

[16] B. Toland, B. Houshmand, and T. Itoh," Modeling of nonlinear active regions with FDTD Method," to be published in the IEEE Microwave and Guided Wave Letters.

[17] B. Toland, J. Lin, B. Houshmand, and T. Itoh," FDTD Analysis of an Active Antenna," to be published in the IEEE Microwave and Guided Wave Letters.

[18] C.C. Yang and D.S. Pan, " Theoretical investigations of a proposed series integration of resonant Tunneling Diodes for millimeter-wave power generation," IEEE Trans. Microwave Theory Tech., vol. MTT-40, no. 3, pp.434-441, March 1992.

Figure 1. A multi-port linear passive region is replaced by its impulse response matrix.

Figure 2. A multi-layered circuit is analyzed by the FDTD diakoptics. The impulse response of segmentations are combined sequentially.

Figure 3. Comparison of the transient current flow through the circuit resistor. The FDTD diakoptics compare well with the MWSPICE simulation.

Figure 4. Parameter convergence of the ARMA model with 80 coefficients. The evolution of the first four output coefficients is demonstrated.

Figure 5. FDTD generated spectrum. 140 samples (at a rate of 1 sample per 5 FDTD output values) are used to obtain the spectrum by the SI method. Similar spectrum is obtained by Fourier Transformation of 500 samples. The Fourier Transform of 140 samples with zero padding is distorted.

Figure 6. Resonance frequency computation of a partially filled rectangular cavity using the ARMA model. The first resonance frequency shifts at the permittivity is changed gradually from 1 to 2.

Figure 7. The layout of the two element patch array.

Figure 8. Circuit model of Gunn Diode.

Figure 9. The time development of the total voltage across one oscillator.

Figure 10. The steady state time variations of total voltage across each oscillator.

Figure 11. The steady state electric field distribution (z component) at one instant in time.

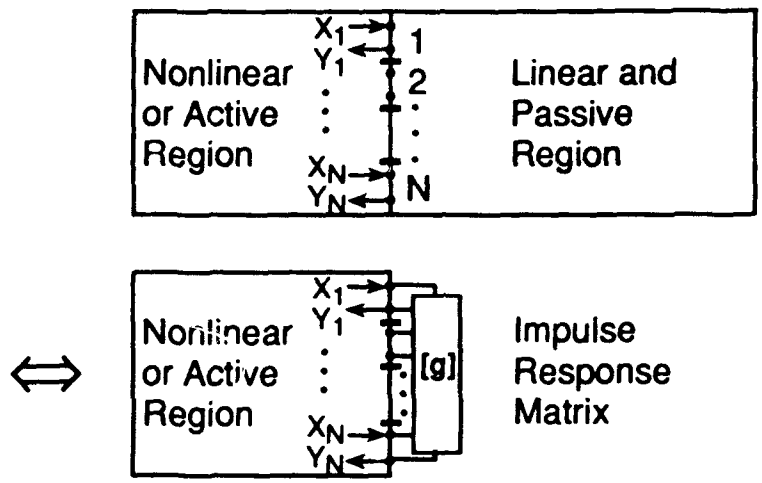
Nonlinear
or Active
Region
X_1
Y_1
X_N
Y_N
1
2
N
Linear and
Passive
Region
$\Leftrightarrow$
Nonlinear
or Active
Region
X_1
Y_1
X_N
Y_N
[g]
Impulse
Response
Matrix

Fig. 1.

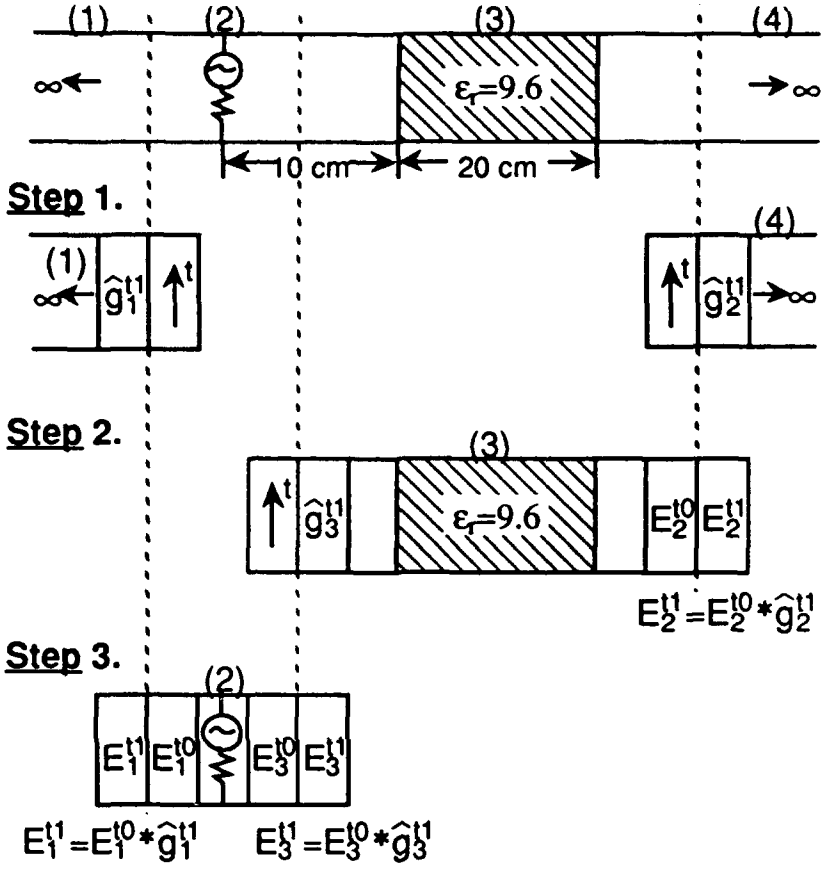
(1)
(2)
(3)
(4)
ε_r=9.6
10 cm
20 cm
Step 1.
Step 2.
Step 3.
$E_2^{t1}=E_2^{t0}*\hat{g}_2^{t1}$
$E_1^{t1}=E_1^{t0}*\hat{g}_1^{t1}$
$E_3^{t1}=E_3^{t0}*\hat{g}_3^{t1}$

Fig 2.

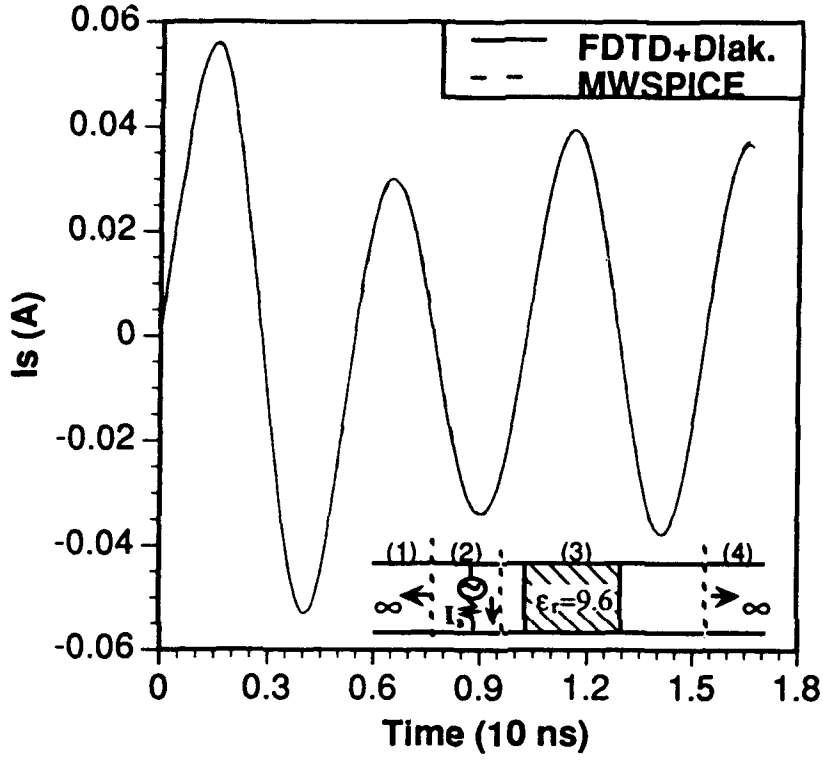
FDTD+Diak.
MWSPICE
0.06
0.04
0.02
0
-0.02
-0.04
-0.06
Is (A)
0
0.3
0.6
0.9
1.2
1.5
1.8
Time (10 ns)
(1)
(2)
(3)
(4)
∞
Is
εr=9.6
∞

Fig. 3.

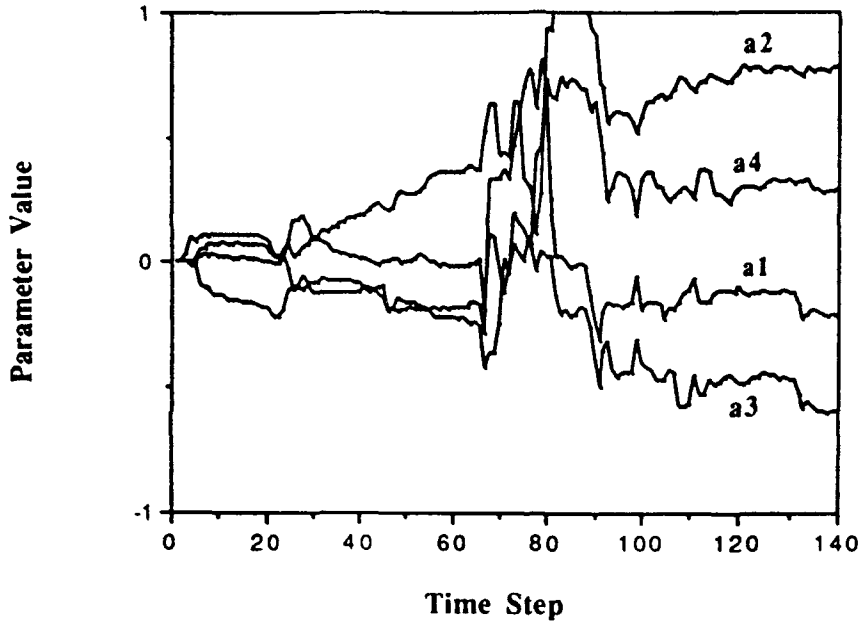
Parameter Value
1
0
-1
0
20
40
60
80
100
120
140
Time Step
a2
a4
a1
a3

Fig. 4

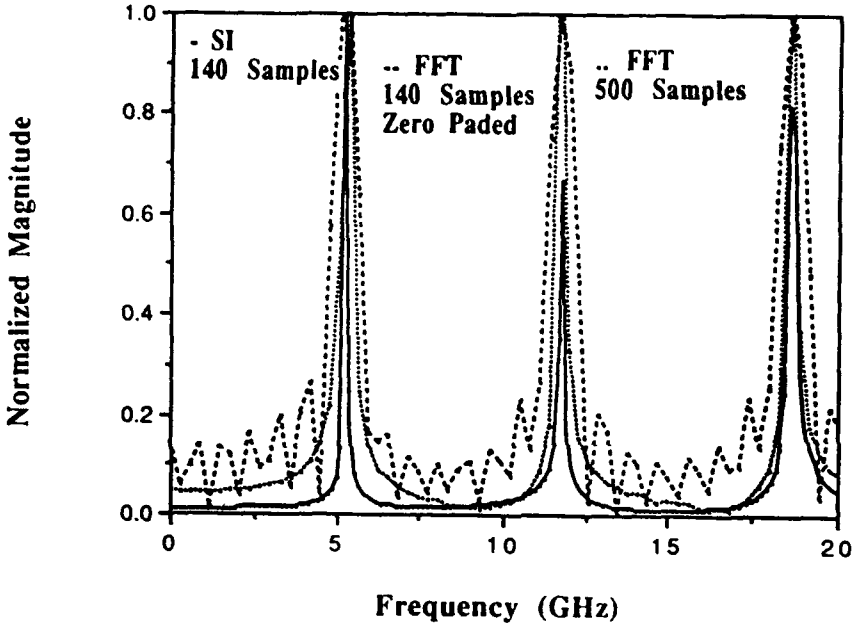
- SI
140 Samples
-- FFT
140 Samples
Zero Paded
.. FFT
500 Samples
Normalized Magnitude
1.0
0.8
0.6
0.4
0.2
0.0
0
5
10
15
20
Frequency (GHz)

Fig. 5.

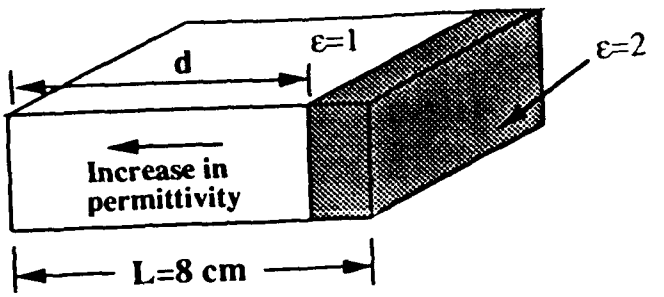
d
ε=1
ε=2
Increase in
permittivity
L=8 cm

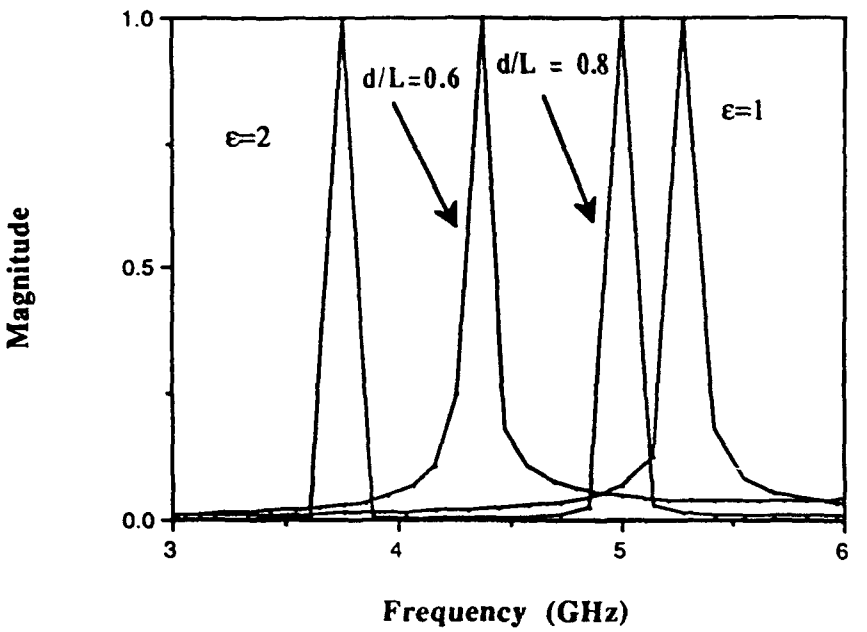
1.0
0.5
0.0
3
4
5
6
Magnitude
Frequency (GHz)
ε=2
d/L=0.6
d/L = 0.8
ε=1

Fig. 6.

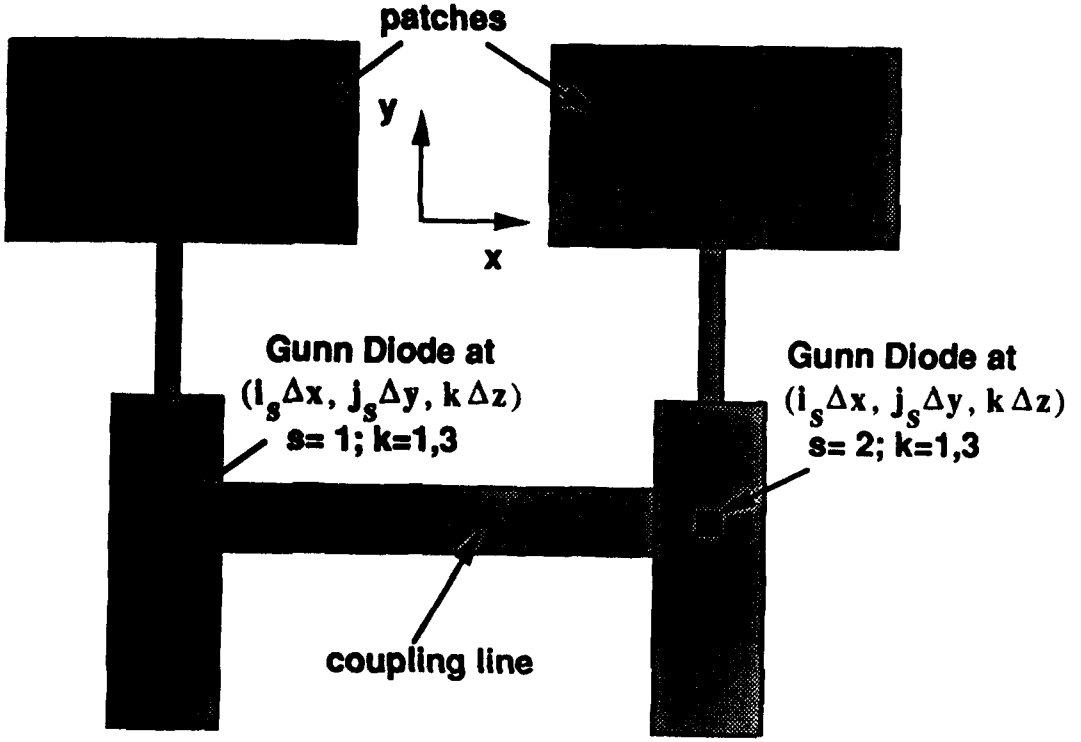

Metallization on dielectric subtstrate ($\varepsilon = 2.33$). Gunn Osc. are between strip and groundplane ($H = 3\Delta z$).

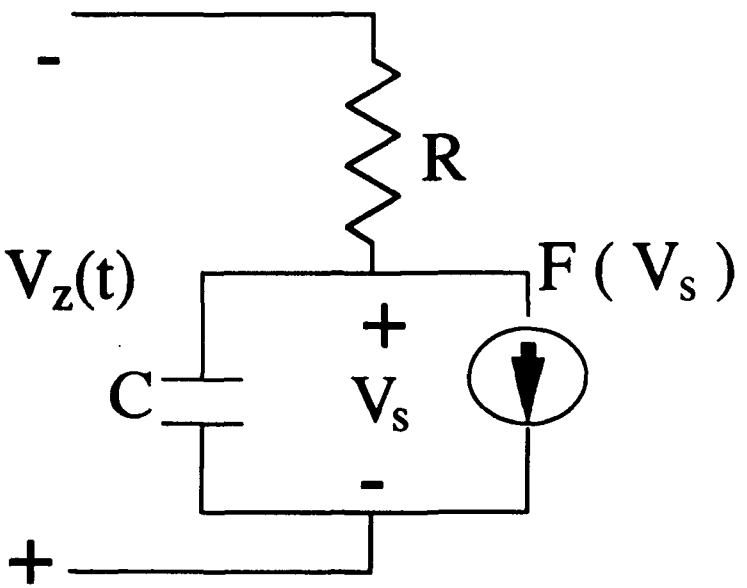

Fig. 8.

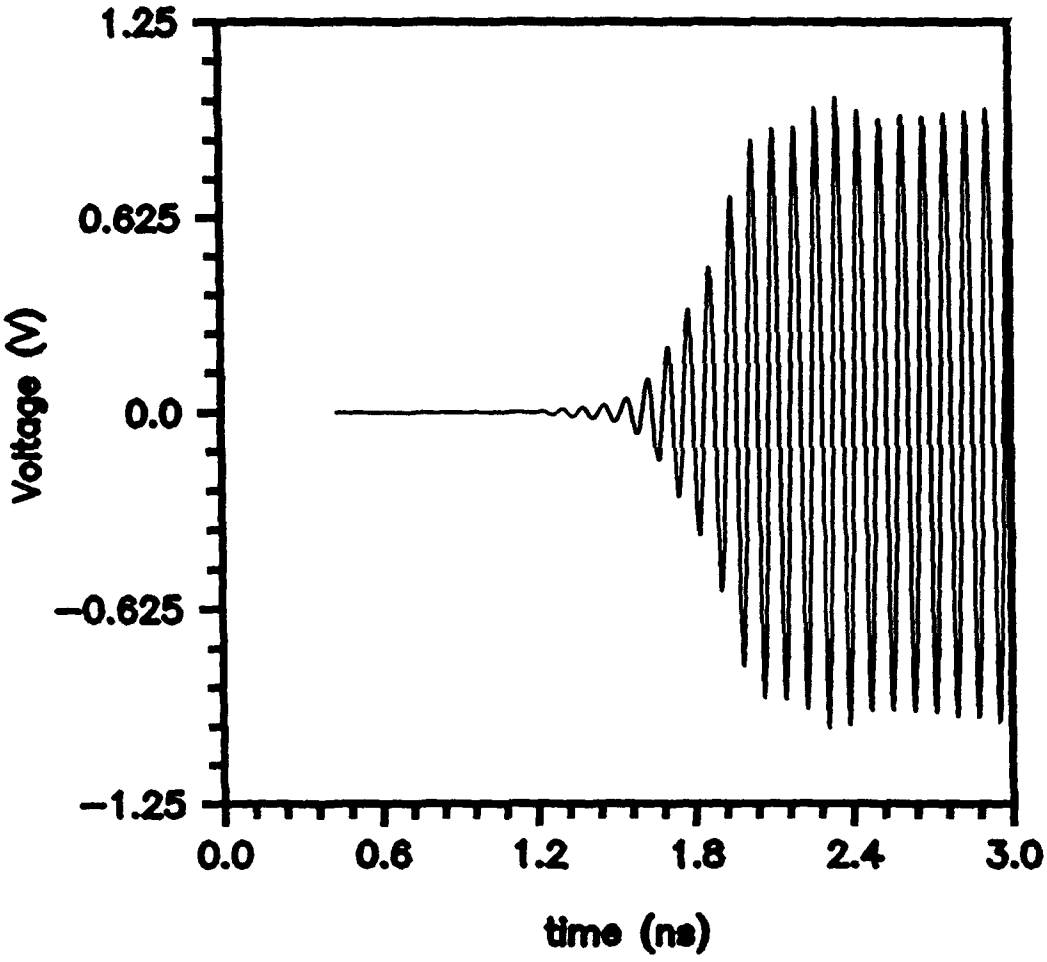

Fig. 9.

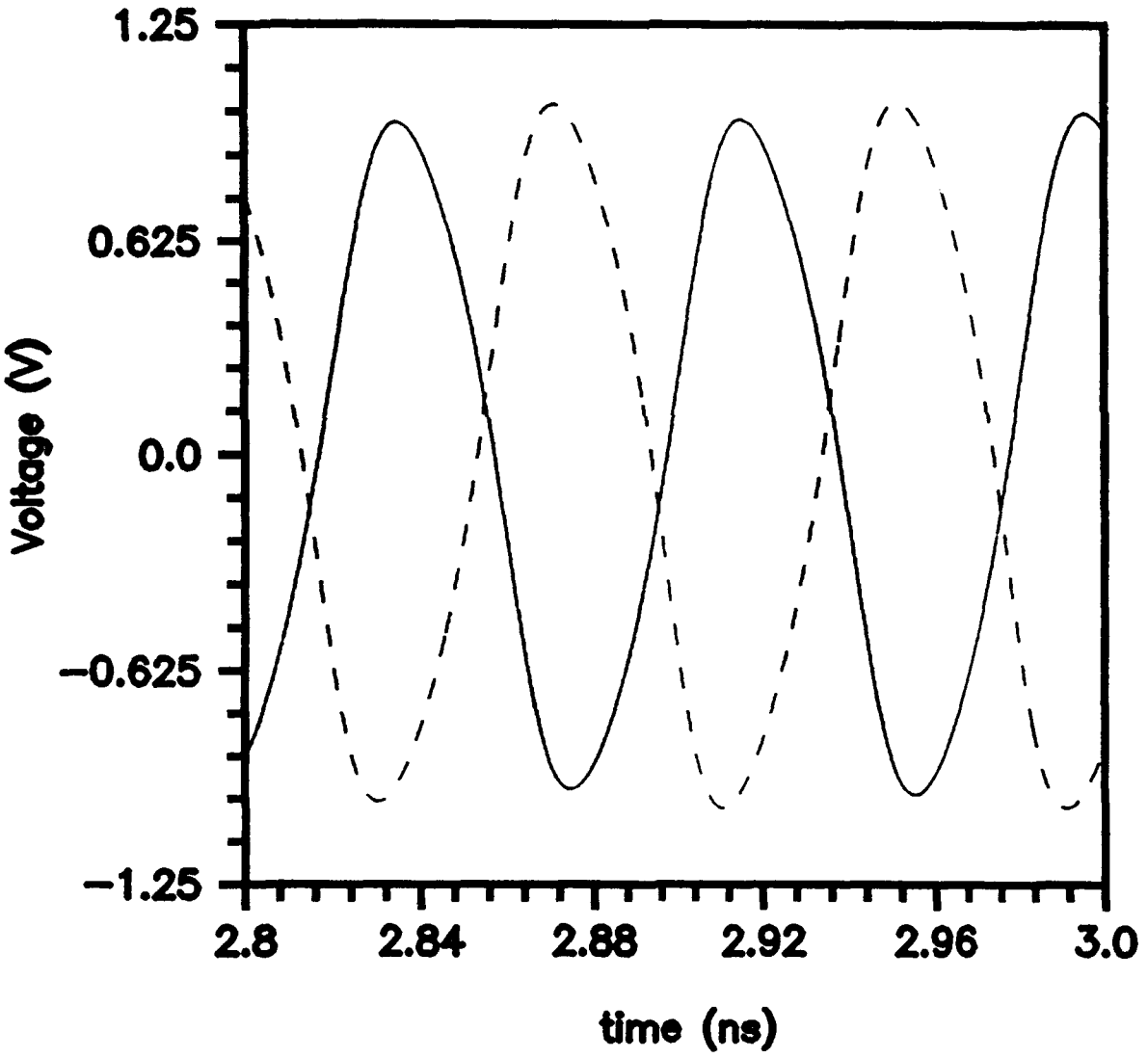

Fig. 10

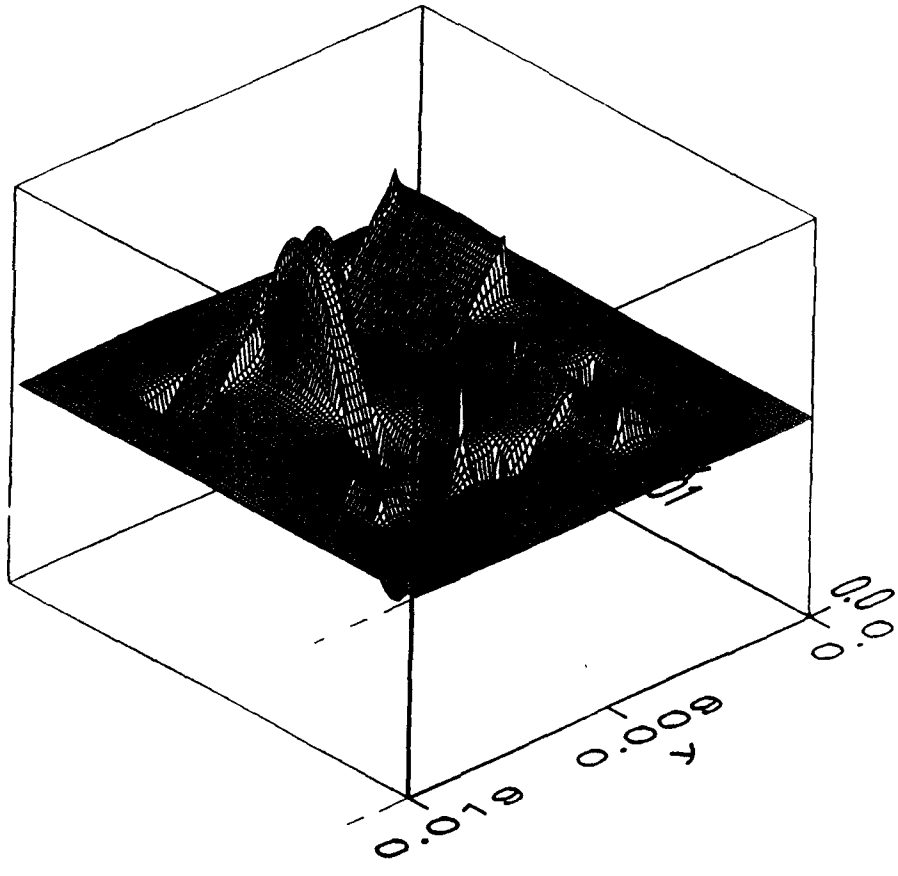

Fig. 11

On the Field Theoretical Foundation of the Transmission Line Matrix Method

Peter Russer and Michael Krumpholz

Ferdinand-Braun-Institut für Höchstfrequenztechnik, Berlin
Lehrstuhl für Hochfrequenztechnik, Technische Universität München

Abstract

Field theoretical foundations of the two-dimensional TLM method and the three-dimensional TLM method with condensed node are given using the method of moments with sectional base functions. Introducing the Hilbert space representation for the field state, the description of geometrical structures and the field evolution is performed algebraically. It is shown that the sampling of the tangential electric and magnetic field components in the cell boundary surfaces yields a correct bijective mapping between electromagnetic field components and TLM wave amplitudes. The same method is applied to derive the two-dimensional and three-dimensional FDTD schemes. For the calculation of the TLM and FDTDM dispersion relations, we use a new generalized method. A critical comparison of two-dimensional and three-dimensional TLM with Yee's finite difference time domain method is given.

1 Introduction

Although the TLM method has proven to be a very powerful method of field computation [1], there have been only a few investigations about its theoretical foundations. Originally TLM is based on the analogy between the electromagnetic field and a mesh of transmission lines [2]. In this paper we derive the two-dimensional TLM-method [1] and the three-dimensional TLM method with condensed symmetric node introduced by Johns [3] directly from Maxwell's equations using the Method of Moments [4] and the Hilbert space representation of the TLM method [5, 6]. For comparison of TLM with FDTD we also apply the Method of Moments to derive Yee's two-dimensional and three-dimensional FDTD schemes [7, 8, 9].

In TLM, the continuous space is discretized by introducing a TLM mesh with the TLM nodes as the elementary element. The electromagnetic field is represented by wave pulses scattered in the nodes and propagating in transmission lines between neighbouring nodes. This picture of TLM stresses the analogy to the network concept. However, the introduction of wave amplitudes has to be related to transverse electric and magnetic field components. Therefore, in contrast to the one-dimensional case where the introduction of wave amplitudes is a formal substitution of variables, the introduction of wave amplitudes in two- or three-dimensional space requires at first the introduction of any set of curves of reference (for two-dimensional TLM) or planes of reference (for three-dimensional TLM) defining tangential planes. The transverse electromagnetic field components are defined with respect to these tangential planes and the wave amplitudes are normal to these tangential planes. The boundary of an elementary TLM cell is formed by the boundary curves or planes of reference. In each boundary plane seperating two TLM cells, a sampling point for the tangential electric and magnetic field components is chosen. In the network model of TLM, in each sampling point, one port is assigned to each polarization. By this way, we assign an elementary multiport to each TLM cell. In the literature, this multiport is called the TLM node. In the following, we use the term TLM *cell* for the geometrical object we have defined in the continuous space, whereas the term TLM *node* is used for the abstract network model representing the relations between the wave amplitudes in the sampling points of a TLM cell.

The definition of all six electric and magnetic field components at the center of the TLM cell [1, 3] causes serious problems because the mapping between the field components and the wave amplitudes is not bijective. However, introducing the wave amplitudes with respect to the TLM cell boundaries yields a bijective one-to-one mapping between the electric and magnetic field components and the wave amplitudes. We use this cell boundary mapping to obtain the fundamental TLM equations for wave amplitudes from

the discretized field equations for the electric and magnetic field components. In this way, the TLM method with condensed symmetric node is derived from first principles of field theory.

For the derivation of the two–dimensional TLM method, sampling Maxwell's equations with rectangular pulse functions yields three discretized field equations for the three electric and magnetic field components at the center of a TLM cell. For the field components at the cell boundary, the mean values of the field components in the two neighbouring TLM cells are taken. We call these mean values the cell boundary mean (CBM) values. Introducing the CBM values of the electric and magnetic field components yields four discretized field equations per TLM cell. Applying the cell boundary mapping, we obtain four discretized field equations for wave amplitudes which determine the scattering matrix of the two–dimensional TLM method uniquely. In two–dimensional TLM as well as in two–dimensional FDTD, there are three linearly independent electric and magnetic field components per unit cell. Introducing the mean values of the electric and magnetic field components, an additional degree of freedom, which corresponds to an additional solution in the two–dimensional TLM method, is introduced. This becomes clear by investigating the eigenvalues of both methods.

Due to the spatial discretization, the TLM and the FDTD method exhibit a cutoff frequency and deviations from the linear dispersion relations for frequencies approaching the cutoff frequency. In order to estimate the error introduced into the calculations by these deviations, the dispersion relation of the discrete mesh has to be known. The dispersion in FDTD has been investigated intensively. The method for the calculation of the dispersion relation for different FDTD schemes is well-known [10, 11]. In contrast to FDTD, only a few TLM dispersion relations are known in closed algebraic forms. The usual approach for the calculation of TLM dispersion relations is based on network considerations [1]. The approach fails if the TLM node cannot be represented by an equivalent circuit as e.g. the three–dimensional condensed symmetric TLM node introduced by Johns [3]. Nielsen has calculated numerically the dispersion relation of the three–dimensional condensed symmetric TLM node [12, 13]. Based on his approach, we calculate the TLM dispersion relations algebraically [14, 15]. This method for the calculation of TLM dispersion relations may be applied to any kind of TLM nodes described by square scattering and propagation matrices of equal dimension.

2 Three–Dimensional TLM with Condensed Node

To derive the three-dimensional TLM method with condensed symmetric node, we apply the Method of Moments [4] to Maxwell's equations

$$\nabla \times \mathbf{H} = \frac{1}{Z_0 c}\frac{\partial \mathbf{E}}{\partial t} \tag{1}$$

$$\nabla \times \mathbf{E} = -\frac{Z_0}{c}\frac{\partial \mathbf{H}}{\partial t} \tag{2}$$

with the wave propagation velocity $c = 1/\sqrt{\mu_0\epsilon_0}$ and the wave impedance for the free space $Z_0 = \sqrt{\mu_0/\epsilon_0}$. We expand the electric fields in

$$\begin{aligned} E_x(\vec{x},t) &= \sum_{k,l,m,n=-\infty}^{+\infty} {}_{k+1/2}E^x_{l,m+1/2,n}\; F^x_{l,m+1/2,n}(\vec{x})\; T_{k+1/2}(t) \;+ \\ &\quad + \sum_{k,l,m,n=-\infty}^{+\infty} {}_{k+1/2}E^x_{l,m,n+1/2}\; F^x_{l,m,n+1/2}(\vec{x})\; T_{k+1/2}(t) \\ E_y(\vec{x},t) &= \sum_{k,l,m,n=-\infty}^{+\infty} {}_{k+1/2}E^y_{l+1/2,m,n}\; F^y_{l+1/2,m,n}(\vec{x})\; T_{k+1/2}(t) \;+ \\ &\quad + \sum_{k,l,m,n=-\infty}^{+\infty} {}_{k+1/2}E^y_{l,m,n+1/2}\; F^y_{l,m,n+1/2}(\vec{x})\; T_{k+1/2}(t) \end{aligned}$$

$$E_z(\vec{x},t) = \sum_{k,l,m,n=-\infty}^{+\infty} {}_{k+1/2}E^z_{l+1/2,m,n}\, F^z_{l+1/2,m,n}(\vec{x})\, T_{k+1/2}(t) + \sum_{k,l,m,n=-\infty}^{+\infty} {}_{k+1/2}E^z_{l,m+1/2,n}\, F^z_{l,m+1/2,n}(\vec{x})\, T_{k+1/2}(t) \tag{3}$$

where ${}_{k+1/2}E^{\mu}_{l,m,n}$ and ${}_{k+1/2}H^{\mu}_{l,m,n}$ with $\mu = x, y, z$ are the expansion coefficients. The index k denotes the discrete time coordinate related to the time coordinate via $t = k\Delta t$, where Δt represents the unit time interval. The indices l, m and n denote the three discrete space coordinates in x–, y– and z–direction related to the space coordinates via $x = l\Delta l$, $y = m\Delta l$ and $z = n\Delta l$, where Δl represents the unit space interval. For the magnetic field components $H_x(\vec{x},t)$, $H_y(\vec{x},t)$ and $H_z(\vec{x},t)$, we proceed in the same way. The base functions in time $T_{k\pm1/2}$ are given by

$$T_{k\pm1/2}(t) = g\left(\frac{t}{\Delta t} - k \mp 1/2\right) \tag{4}$$

where the triangle function $g(x)$, see Fig 1, is defined by

$$g(x) = \begin{cases} 1-|x| & \text{for } |x| < 1 \\ 0 & \text{for } |x| \geq 1 \end{cases} \tag{5}$$

The use of the functions $T_{k\pm1/2}$ provides a piecewise linear approximation [4] of the exact solution of

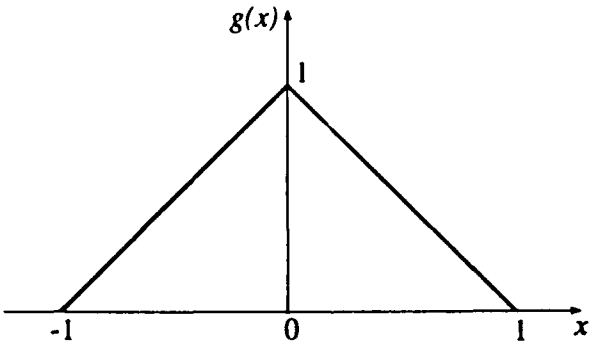

Figure 1: The triangle function $g(x)$.

Maxwell's equations with respect to the time coordinate. The base functions $F^{\mu}_{l,m,n}(\vec{x})$ with $\mu = x, y, z$ are given by

$$\begin{aligned} F^x_{l,m,n}(\vec{x}) &= H(\frac{x}{\Delta x} - l)\; F_{m,n}(y,z) \\ F^y_{l,m,n}(\vec{x}) &= H(\frac{y}{\Delta y} - m)\; F_{l,n}(x,z) \\ F^z_{l,m,n}(\vec{x}) &= H(\frac{z}{\Delta z} - n)\; F_{l,m}(x,y) \end{aligned} \tag{6}$$

with the rectangular pulse function depicted in Fig. 2

$$H(x) = \begin{cases} 1 & \text{for } |x| < 1/2 \\ 1/2 & \text{for } |x| = 1/2 \\ 0 & \text{for } |x| > 1/2 \end{cases} \tag{7}$$

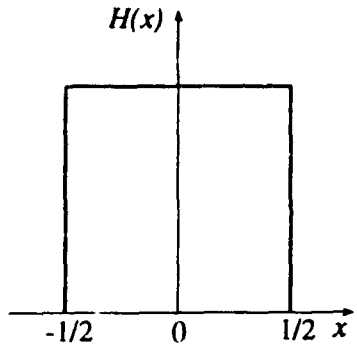

Figure 2: The pulse function $H(x)$.

and the two–dimensional triangle base functions

$$F_{l,m}(x,y) = w(\frac{x}{\Delta x} - l, \frac{y}{\Delta y} - m) \tag{8}$$

where

$$w(x,y) = g(x-y)\ g(x+y) \quad . \tag{9}$$

The function $g(x)\ g(y)$ is depicted in Fig. 3. Expanding the electric and magnetic field components using the functions $F^{\mu}_{l,m,n}(\vec{x})$ provides a step approximation [4] in μ–direction and a piecewise linear approximation in the diagonal directions of the plane perpendicular to the μ–direction.

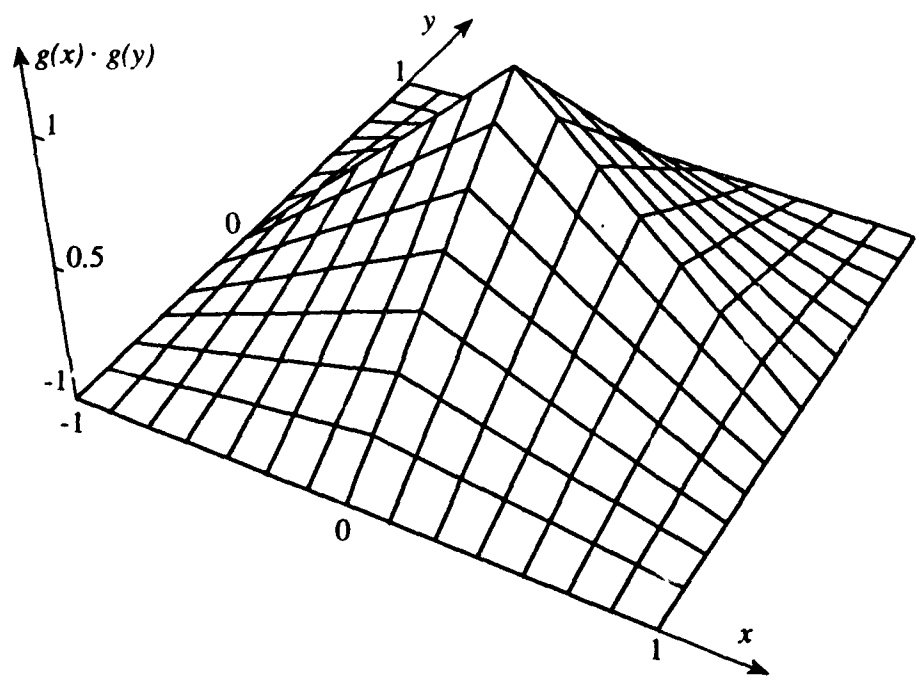

Figure 3: The function $g(x)\ g(y)$.

Sampling $\partial E_z/\partial y$ yields

$$\iiint\!\!\int \frac{\partial E_z}{\partial y}\ \delta(t - k\Delta t)\ \delta(x - l\Delta x)\ \delta(y - m\Delta y)\ \delta(z - n\Delta y)\ dx\ dy\ dz\ dt\ =$$

$$= \frac{1}{2\Delta y}\left({}_{k+1/2}E^{z}_{l,m+1/2,n} - {}_{k+1/2}E^{z}_{l,m-1/2,n} + {}_{k-1/2}E^{z}_{l,m+1/2,n} - {}_{k-1/2}E^{z}_{l,m-1/2,n}\right)$$

Sampling $\partial E_y/\partial z$ and $\partial H_x/\partial t$, we obtain

$$\begin{aligned}
&{}_{k+1/2}H^{x}_{l,m+1/2,n} + {}_{k+1/2}H^{x}_{l,m-1/2,n} + {}_{k+1/2}H^{x}_{l,m,n+1/2} + {}_{k+1/2}H^{x}_{l,m,n-1/2} - \\
&-{}_{k-1/2}H^{x}_{l,m+1/2,n} - {}_{k-1/2}H^{x}_{l,m-1/2,n} - {}_{k-1/2}H^{x}_{l,m,n+1/2} - {}_{k-1/2}H^{x}_{l,m,n-1/2} = \\
&= \frac{2\Delta t c}{Z_0 \Delta y}\left({}_{k+1/2}E^{z}_{l,m-1/2,n} - {}_{k+1/2}E^{z}_{l,m+1/2,n} + {}_{k-1/2}E^{z}_{l,m-1/2,n} - {}_{k-1/2}E^{z}_{l,m+1/2,n}\right) + \\
&+ \frac{2\Delta t c}{Z_0 \Delta z}\left({}_{k+1/2}E^{y}_{l,m,n+1/2} - {}_{k+1/2}E^{y}_{l,m,n-1/2} + {}_{k-1/2}E^{y}_{l,m,n+1/2} - {}_{k-1/2}E^{y}_{l,m,n-1/2}\right) \qquad (10)
\end{aligned}$$

Sampling the dual equation yields

$$\begin{aligned}
&{}_{k+1/2}E^{x}_{l,m+1/2,n} + {}_{k+1/2}E^{x}_{l,m-1/2,n} + {}_{k+1/2}E^{x}_{l,m,n+1/2} + {}_{k+1/2}E^{x}_{l,m,n-1/2} - \\
&-{}_{k-1/2}E^{x}_{l,m+1/2,n} - {}_{k-1/2}E^{x}_{l,m-1/2,n} - {}_{k-1/2}E^{x}_{l,m,n+1/2} - {}_{k-1/2}E^{x}_{l,m,n-1/2} = \\
&= \frac{2\Delta t Z_0 c}{\Delta y}\left({}_{k+1/2}H^{z}_{l,m+1/2,n} - {}_{k+1/2}H^{z}_{l,m-1/2,n} + {}_{k-1/2}H^{z}_{l,m+1/2,n} - {}_{k-1/2}H^{z}_{l,m-1/2,n}\right) + \\
&+ \frac{2\Delta t Z_0 c}{\Delta z}\left({}_{k+1/2}H^{y}_{l,m,n-1/2} - {}_{k+1/2}H^{y}_{l,m,n+1/2} + {}_{k-1/2}H^{y}_{l,m,n-1/2} - {}_{k-1/2}H^{y}_{l,m,n+1/2}\right) \qquad (11)
\end{aligned}$$

We rewrite these discretized field equations using the TLM Hilbert space representation [5]. We define the electric field vector $|F_E\rangle$ and the magnetic field vector $|F_M\rangle$ in the Hilbert space $\mathcal{H}_W$ given by the cartesian product of $\mathcal{C}^{12}$, $\mathcal{H}_m$ and $\mathcal{H}_t$:

$$\mathcal{H}_W = \mathcal{C}^{12} \otimes \mathcal{H}_m \otimes \mathcal{H}_t \qquad (12)$$

The electric field vector $|F_E\rangle$ combines all electric field components of the whole discretized space. It is given by

$$|F_E\rangle = \sum_{k,l,m,n=-\infty}^{+\infty} \begin{bmatrix} {}_k|E_y|_{l-1/2,m,n} \\ {}_k|E_y|_{l+1/2,m,n} \\ {}_k|E_z|_{l-1/2,m,n} \\ {}_k|E_z|_{l+1/2,m,n} \\ {}_k|E_z|_{l,m-1/2,n} \\ {}_k|E_z|_{l,m+1/2,n} \\ {}_k|E_x|_{l,m-1/2,n} \\ {}_k|E_x|_{l,m+1/2,n} \\ {}_k|E_x|_{l,m,n-1/2} \\ {}_k|E_x|_{l,m,n+1/2} \\ {}_k|E_y|_{l,m,n-1/2} \\ {}_k|E_y|_{l,m,n+1/2} \end{bmatrix} |k; l, m, n\rangle \qquad (13)$$

The magnetic field vector $|F_M\rangle$, defined by

$$|F_M\rangle = Z \sum_{k,l,m,n=-\infty}^{+\infty} \begin{bmatrix} k\,[H_z]_{l-1/2,m,n} \\ k\,[H_z]_{l+1/2,m,n} \\ k\,[H_y]_{l-1/2,m,n} \\ k\,[H_y]_{l+1/2,m,n} \\ k\,[H_x]_{l,m-1/2,n} \\ k\,[H_x]_{l,m+1/2,n} \\ k\,[H_z]_{l,m-1/2,n} \\ k\,[H_z]_{l,m+1/2,n} \\ k\,[H_y]_{l,m,n-1/2} \\ k\,[H_y]_{l,m,n+1/2} \\ k\,[H_x]_{l,m,n-1/2} \\ k\,[H_x]_{l,m,n+1/2} \end{bmatrix} |k;l,m,n\rangle \tag{14}$$

summarizes all magnetic field components of the discretized space. The twelve–dimensional complex vector space $\mathcal{C}^{12}$ is the space of the vectors combining the twelve electric or twelve magnetic field components of the TLM cell with the center at the discrete coordinates (l,m,n) at the discrete time coordinate k. Using Dirac's bra–ket notation [16], a system of orthonormal space domain base vectors $|l,m,n\rangle$ in the Hilbert space $\mathcal{H}_m$ is introduced. To each node with the discrete coordinates (l,m,n), a base vector $|l,m,n\rangle$ is assigned. In the Hilbert space $\mathcal{H}_t$, the base vector $|k\rangle$ corresponds to the discrete time coordinate k.

The product space $\mathcal{H}_W$ allows to describe the complete sequence of the discretized field by a single vector. The orthonormal base vectors of $\mathcal{H}_m \otimes \mathcal{H}_t$ are given by the ket–vectors $|k;l,m,n\rangle$. The bra–vector $\langle k;l,m,n|$ is the Hermitian conjugate of $|k;l,m,n\rangle$. The orthogonality relations are given by

$$\langle k_1;l_1,m_1,n_1|k_2;l_2,m_2,n_2\rangle = \delta_{k_1,k_2}\,\delta_{l_1,l_2}\,\delta_{m_1,m_2}\,\delta_{n_1,n_2} \tag{15}$$

We define the time shift operator T which increments k by 1 i.e. it shifts the field state by Δt in the positive time direction. Applying the time shift operator to a vector $|k;l,m,n\rangle$, we obtain

$$T\ |k;l,m,n\rangle = |k+1;l,m,n\rangle \tag{16}$$

Choosing equidistant discretization in all three spatial directions

$$\Delta x = \Delta y = \Delta z = \Delta l \quad . \tag{17}$$

and using the Hilbert space formulation, eqs. (10) and (11) may now be written as

$$\begin{aligned} &[0,0,0,0,1,1,0,0,0,0,1,1]\ (1-T)\ |F_M\rangle\ = \\ &=\ [0,0,0,0,1,-1,0,0,0,0,-1,1]\ (1+T)\ \tfrac{2Z\Delta tc}{Z_0\Delta l}\,|F_E\rangle \end{aligned} \tag{18}$$

and

$$\begin{aligned} &[0,0,0,0,0,0,1,1,1,1,0,0]\ (1-T)\ |F_E\rangle\ = \\ &=\ [0,0,0,0,0,0,-1,1,1,-1,0,0]\ (1+T)\ \tfrac{2Z_0\Delta tc}{Z\Delta l}\,|F_M\rangle \end{aligned} \tag{19}$$

Applying the traditional mapping between the wave amplitudes and the electric and magnetic field components leads to wrong results [17, 18]. To overcome these problems, we introduce the TLM waves with respect to the TLM cell boundary surfaces. In each boundary plane seperating two TLM cells, a sampling point for the tangential electric and magnetic field components is chosen. As this mapping relates the wave amplitudes and the electric and magnetic field components at the cell boundary, this mapping is called

the cell boundary mapping. The cell boundary mapping provides a bijective one–to–one mapping between the twenty–four electric and magnetic field components and the twenty–four incident and scattered wave amplitudes at one condensed symmetric TLM node.

To describe the relationship between the tangential electric and magnetic field components and the wave amplitudes [19], we introduce the local scattered wave vectors $\vec{b}_i$. The vectors $\vec{b}_i$ are defined in a sampling point in each boundary plane seperating two TLM cells. In the network model of TLM, this definition corresponds to a definition of the vectors $\vec{b}_i$ at the end of the arm i of the condensed symmetric TLM node. The vectors $\vec{b}_i$ are perpendicular to the local outward directed vectors $\vec{n}_i$ which denote the unit vectors in the propagation direction of the scattered plane waves. Therefore the cartesian component of $\vec{b}_i$ in the direction of $\vec{n}_i$ is zero. The two nonzero cartesian components of $\vec{b}_i$ are the two scattered wave amplitudes of one arm of the TLM node. They are directed according to Fig. 4.

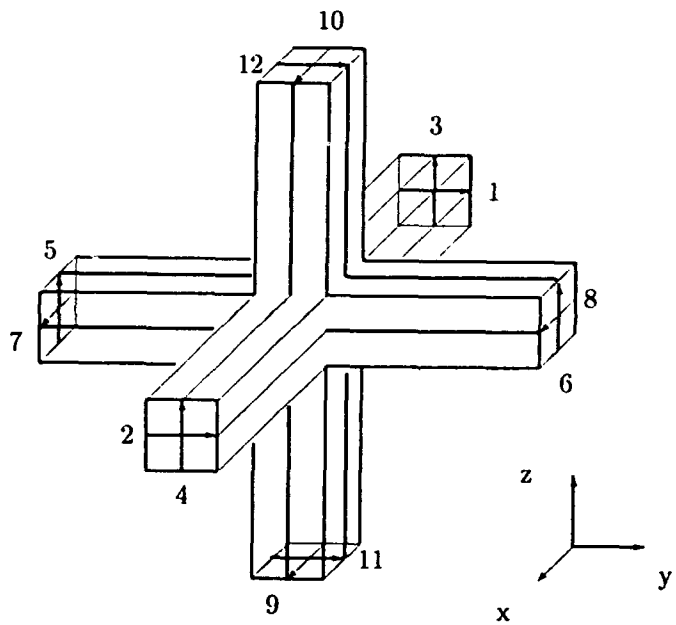

Figure 4: A three–dimensional condensed symmetric TLM node.

With the local scattered wave vectors, the cell boundary mapping is determined by

$$\vec{b}_i = -1/2 \left(\vec{n}_i \times \vec{n}_i \times \vec{E} + Z \, \vec{n}_i \times \vec{H} \right) \tag{20}$$

with $i = 1, 2, \ldots 6$. In the same way, we introduce the local incident wave vectors $\vec{a}_i$. The cell boundary mapping between the electric and magnetic field components and the incident wave amplitudes is determined by

$$\vec{a}_i = 1/2 \left(-\vec{n}_i \times \vec{n}_i \times \vec{E} + Z \, \vec{n}_i \times \vec{H} \right) \tag{21}$$

As an example, we consider the arm 2 of the condensed TLM node l, m, n at time k with the ports two and four, Fig. 4. The local wave vectors are given by $\vec{a}_2 = [0, a_2, a_4]^T$ and $\vec{b}_2 = [0, b_2, b_4]^T$, the vector $\vec{n}_2$ by $\vec{n}_2 = [1, 0, 0]^T$. With

$$\vec{E} = \begin{bmatrix} {}_k[E_x]_{l+1/2,m,n} \\ {}_k[E_y]_{l+1/2,m,n} \\ {}_k[E_z]_{l+1/2,m,n} \end{bmatrix} \quad \text{and} \quad \vec{H} = \begin{bmatrix} {}_k[H_x]_{l+1/2,m,n} \\ {}_k[H_y]_{l+1/2,m,n} \\ {}_k[H_z]_{l+1/2,m,n} \end{bmatrix} \tag{22}$$

we obtain from eqs. (20) and (21)

$$\begin{aligned} {}_k[a_2]_{l,m,n} &= 1/2 \left({}_k[E_y]_{l+1/2,m,n} - Z \; {}_k[H_z]_{l+1/2,m,n} \right) \\ {}_k[a_4]_{l,m,n} &= 1/2 \left({}_k[E_z]_{l+1/2,m,n} + Z \; {}_k[H_y]_{l+1/2,m,n} \right) \\ {}_k[b_2]_{l,m,n} &= 1/2 \left({}_k[E_y]_{l+1/2,m,n} + Z \; {}_k[H_z]_{l+1/2,m,n} \right) \\ {}_k[b_4]_{l,m,n} &= 1/2 \left({}_k[E_z]_{l+1/2,m,n} - Z \; {}_k[H_y]_{l+1/2,m,n} \right) \end{aligned} \tag{23}$$

and

$$\begin{aligned} {}_k[E_y]_{l+1/2,m,n} &= {}_k[a_2 + b_2]_{l,m,n} & {}_k[H_y]_{l+1/2,m,n} &= 1/Z \; {}_k[a_4 - b_4]_{l,m,n} \\ {}_k[E_z]_{l+1/2,m,n} &= {}_k[a_4 + b_4]_{l,m,n} & {}_k[H_z]_{l+1/2,m,n} &= 1/Z \; {}_k[b_2 - a_2]_{l,m,n} \end{aligned} \tag{24}$$

respectively.

Evaluating eqs. (20) and (21) yields

$$\begin{aligned} |a\rangle &= 1/2 \; (\; |F_E\rangle + P \; |F_M\rangle \;) \\ |b\rangle &= 1/2 \; (\; |F_E\rangle - P \; |F_M\rangle \;) \end{aligned} \tag{25}$$

and

$$\begin{aligned} |F_E\rangle &= |a\rangle + |b\rangle \\ |F_M\rangle &= P \; (\; |a\rangle - |b\rangle \;) \end{aligned} \tag{26}$$

where we have introduced the matrix

$$P = \begin{bmatrix} B & 0 & 0 \\ 0 & B & 0 \\ 0 & 0 & B \end{bmatrix} \tag{27}$$

with

$$B = \begin{bmatrix} 1 & 0 & 0 & 0 \\ 0 & -1 & 0 & 0 \\ 0 & 0 & -1 & 0 \\ 0 & 0 & 0 & 1 \end{bmatrix} \tag{28}$$

The property $P^2 = 1$ ensures that the cell boundary mapping is a bijective one–to–one mapping between the twenty–four electric and magnetic field components and the twenty–four incident and scattered wave amplitudes at one condensed symmetric TLM node.

The vector of all incident wave amplitudes

$$|a\rangle = \sum_{k,l,m,n=-\infty}^{+\infty} {}_k a_{l,m,n} \; |k; l, m, n\rangle \tag{29}$$

with

$$ {}_k a_{l,m,n} \;=\; {}_k\,[a_1, a_2, a_3, a_4, a_5, a_6, a_7, a_8, a_9, a_{10}, a_{11}, a_{12}]^T_{l,m,n} \tag{30} $$

combines all incident wave amplitudes of the TLM mesh. In the same way, we introduce the vector of all scattered wave amplitudes

$$ |b\rangle = \sum_{k,l,m,n=-\infty}^{+\infty} {}_k b_{l,m,n}\ |k;l,m,n\rangle \tag{31} $$

with

$$ {}_k b_{l,m,n} \;=\; {}_k\,[b_1, b_2, b_3, b_4, b_5, b_6, b_7, b_8, b_9, b_{10}, b_{11}, b_{12}]^T_{l,m,n} \tag{32} $$

The vectors $|a\rangle$ and $|b\rangle$ are vectors in the Hilbert space $\mathcal{H}_W$.

Since all tangential electric and magnetic field components in each cell boundary surface are also specified in the neighbouring cell boundary surfaces, only twelve field components per TLM cell are linearly independent. Specifying e.g. all twelve incident wave amplitudes per TLM cell yields a complete description of the field state. For each boundary surface, the wave amplitudes incident into one TLM cell are identical with the wave amplitudes scattered from the neighbouring TLM cells. This relation is expressed by

$$ |a\rangle = \boldsymbol{\Gamma}\ |b\rangle \qquad \text{and} \qquad |b\rangle = \boldsymbol{\Gamma}\ |a\rangle \tag{33} $$

where we have introduced the connection operator $\boldsymbol{\Gamma}$ given by

$$ \begin{aligned} \boldsymbol{\Gamma} \;=\; & \boldsymbol{X}(\boldsymbol{\Delta}_{1,2} + \boldsymbol{\Delta}_{3,4}) + \boldsymbol{X}^\dagger(\boldsymbol{\Delta}_{2,1} + \boldsymbol{\Delta}_{4,3}) + \boldsymbol{Y}(\boldsymbol{\Delta}_{5,6} + \boldsymbol{\Delta}_{7,8}) \\ + \; & \boldsymbol{Y}^\dagger(\boldsymbol{\Delta}_{6,5} + \boldsymbol{\Delta}_{8,7}) + \boldsymbol{Z}(\boldsymbol{\Delta}_{9,10} + \boldsymbol{\Delta}_{11,12}) + \boldsymbol{Z}^\dagger(\boldsymbol{\Delta}_{10,9} + \boldsymbol{\Delta}_{12,11}) \end{aligned} \tag{34} $$

with the 12×12 (m,n)-matrix $(\boldsymbol{\Delta}_{i,j})_{m,n} = \delta_{i,m}\,\delta_{j,n}$.

The shift operators $\boldsymbol{X}$, $\boldsymbol{Y}$, $\boldsymbol{Z}$ and their Hermitian conjugates $\boldsymbol{X}^\dagger$, $\boldsymbol{Y}^\dagger$ and $\boldsymbol{Z}^\dagger$ are defined by

$$ \begin{aligned} \boldsymbol{X}\,|k;l,m,n\rangle &= |k;l+1,m,n\rangle \\ \boldsymbol{X}^\dagger\,|k;l,m,n\rangle &= |k;l-1,m,n\rangle \\ \boldsymbol{Y}\,|k;l,m,n\rangle &= |k;l,m+1,n\rangle \\ \boldsymbol{Y}^\dagger\,|k;l,m,n\rangle &= |k;l,m-1,n\rangle \\ \boldsymbol{Z}\,|k;l,m,n\rangle &= |k;l,m,n+1\rangle \\ \boldsymbol{Z}^\dagger\,|k;l,m,n\rangle &= |k;l,m,n-1\rangle \end{aligned} \tag{35} $$

The operators $\boldsymbol{X}$, $\boldsymbol{Y}$ and $\boldsymbol{Z}$ shift the field state by one unit space interval Δl in the positive l-, m- and n-direction, respectively. Their Hermitian conjugates $\boldsymbol{X}^\dagger$, $\boldsymbol{Y}^\dagger$ and $\boldsymbol{Z}^\dagger$ shift the field state in the opposite direction.

The connection operator $\boldsymbol{\Gamma}$ is hermitian and unitary:

$$ \boldsymbol{\Gamma} = \boldsymbol{\Gamma}^\dagger = \boldsymbol{\Gamma}^{-1} \tag{36} $$

As we have already shown for two-dimensional TLM, regions with different material parameters may be taken into consideration by the scattering operator $\boldsymbol{S}$, boundary conditions may be considered via the propagation operator $\boldsymbol{\Gamma}$ [5].

We apply the cell boundary mapping to obtain the discretized field equations for wave amplitudes and the fundamental TLM equations, respectively. Choosing

$$ \frac{2Z\Delta tc}{Z_0\Delta l} = 1 \qquad \text{as well as} \qquad \frac{2Z_0\Delta tc}{Z\Delta l} = 1 \tag{37} $$

and introducing the mesh pulse velocity $c_m = \Delta l/\Delta t$ yields

$$Z_0 = Z \qquad \text{and} \qquad \frac{c}{c_m} = \frac{1}{2} \tag{38}$$

which is well-known from literature [3]. Eqs. (18) and (19) yield two fundamental TLM equations for the condensed symmetric node:

$$\begin{aligned} &|0,0,0,0,1,-1,0,0,0,0,-1,1|\ |b\rangle\ = \\ &=\ |0,0,0,0,-1,1,0,0,0,0,1,-1|\ \boldsymbol{T}\ |a\rangle \end{aligned} \tag{39}$$

and

$$\begin{aligned} &|0,0,0,0,0,0,1,1,1,1,0,0|\ |b\rangle\ = \\ &=\ |0,0,0,0,0,0,1,1,1,1,0,0|\ \boldsymbol{T}\ |a\rangle \end{aligned} \tag{40}$$

In the same way, we proceed with the other four cartesian components of Maxwell's equations and obtain another four fundamental TLM equations for the condensed symmetric node. With eqs. (10) and (37), the six fundamental TLM equations are given by

$$\boldsymbol{P}_b\ |b\rangle = \boldsymbol{T}\ \boldsymbol{P}_a\ |a\rangle \tag{41}$$

The scattering matrix of the three-dimensional condensed symmetric TLM node, eqs. (48) and (49), is a 12×12-matrix. Therefore we need twelve fundamental TLM equations to determine the scattering matrix uniquely. The six missing fundamental TLM equations for the condensed symmetric node are calculated by using the derivatives of the spatial delta function as test functions.

Proceeding in the same way as demonstrated above yields the other six fundamental TLM equations for the condensed symmetric node

$$\boldsymbol{P}_1\ |b\rangle = \boldsymbol{T}\ \boldsymbol{P}_2\ |a\rangle \tag{42}$$

where we have introduced the operators

$$\boldsymbol{P}_1 = \begin{bmatrix} 0 & 0 & 0 & 0 & 0 & 0 & 1 & 1 & -1 & -1 & 0 & 0 \\ 1 & 1 & 0 & 0 & 0 & 0 & 0 & 0 & 0 & 0 & -1 & -1 \\ 0 & 0 & 1 & 1 & -1 & -1 & 0 & 0 & 0 & 0 & 0 & 0 \\ 0 & 0 & 0 & 0 & 1 & -1 & 0 & 0 & 0 & 0 & 1 & -1 \\ 0 & 0 & -1 & 1 & 0 & 0 & 0 & 0 & -1 & 1 & 0 & 0 \\ 1 & -1 & 0 & 0 & 0 & 0 & 1 & -1 & 0 & 0 & 0 & 0 \end{bmatrix} \tag{43}$$

and

$$\boldsymbol{P}_2 = \begin{bmatrix} 0 & 0 & 0 & 0 & 0 & 0 & -1 & -1 & 1 & 1 & 0 & 0 \\ -1 & -1 & 0 & 0 & 0 & 0 & 0 & 0 & 0 & 0 & 1 & 1 \\ 0 & 0 & -1 & -1 & 1 & 1 & 0 & 0 & 0 & 0 & 0 & 0 \\ 0 & 0 & 0 & 0 & 1 & -1 & 0 & 0 & 0 & 0 & 1 & -1 \\ 0 & 0 & -1 & 1 & 0 & 0 & 0 & 0 & -1 & 1 & 0 & 0 \\ 1 & -1 & 0 & 0 & 0 & 0 & 1 & -1 & 0 & 0 & 0 & 0 \end{bmatrix} \tag{44}$$

Eqs. (41) and (42) may be written in the form

$$\boldsymbol{M}_1\ |b\rangle = \boldsymbol{T}\ \boldsymbol{M}_2\ |a\rangle \tag{45}$$

with

$$\boldsymbol{M}_1 = \begin{bmatrix} \boldsymbol{P}_b \\ \boldsymbol{P}_1 \end{bmatrix} \qquad \text{and} \qquad \boldsymbol{M}_2 = \begin{bmatrix} \boldsymbol{P}_a \\ \boldsymbol{P}_2 \end{bmatrix} \tag{46}$$

Multiplying eq. (45) by M_1^T, we obtain

$$|b) = \boldsymbol{T}\ \boldsymbol{S}\ |a) \tag{47}$$

with the scattering matrix $\boldsymbol{S}$ given by

$$\boldsymbol{S} = \begin{bmatrix} 0 & \mathbf{S_0} & \mathbf{S_0}^T \\ \mathbf{S_0}^T & 0 & \mathbf{S_0} \\ \mathbf{S_0} & \mathbf{S_0}^T & 0 \end{bmatrix} \tag{48}$$

where we have introduced

$$\mathbf{S_0} = \begin{bmatrix} 0 & 0 & \frac{1}{2} & -\frac{1}{2} \\ 0 & 0 & -\frac{1}{2} & \frac{1}{2} \\ \frac{1}{2} & \frac{1}{2} & 0 & 0 \\ \frac{1}{2} & \frac{1}{2} & 0 & 0 \end{bmatrix} \tag{49}$$

The operator $\boldsymbol{S}$ is real, symmetric, hermitian and unitary. The scattering at all TLM mesh nodes is connected with a time delay Δt.

3 Two–dimensional TLM

With $\partial/\partial z = 0$, Maxwell's equations are seperated in two independent systems of partial differential equations for E_x, E_y, H_z and H_x, H_y, E_z, respectively. The partial differential equations for H_x, H_y and E_z are given by

$$\frac{\partial H_y}{\partial x} - \frac{\partial H_x}{\partial y} = \frac{1}{Z_0 c}\frac{\partial E_z}{\partial t} \tag{50}$$

$$-\frac{\partial E_z}{\partial y} = \frac{Z_0}{c}\frac{\partial H_x}{\partial t} \tag{51}$$

$$\frac{\partial E_z}{\partial x} = \frac{Z_0}{c}\frac{\partial H_y}{\partial t} \tag{52}$$

For the derivation of the two–dimensional TLM method with shunt node, we expand the fields in

$$\begin{aligned} E_z(x,y,t) &= \sum_{k,m,n=-\infty}^{+\infty} {}_kE^z_{m,n}\ H_k(t)\ K_{m,n}(x,y) \\ H_x(x,y,t) &= \sum_{k,m,n=-\infty}^{+\infty} {}_kH^x_{m,n}\ H_k(t)\ K_{m,n}(x,y) \\ H_y(x,y,t) &= \sum_{k,m,n=-\infty}^{+\infty} {}_kH^y_{m,n}\ H_k(t)\ K_{m,n}(x,y) \end{aligned} \tag{53}$$

with the expansion coefficients ${}_kE^z_{m,n}$, ${}_kH^x_{m,n}$ and ${}_kH^y_{m,n}$. The indices m, n and k are the discrete space and time coordinates related to the space and time coordinates via $x = m\Delta x$, $y = n\Delta y$ and $t = k\Delta t$, where Δx, Δy and Δt represent the unit space interval in x–, y–direction and the unit time interval, respectively. The rectangular pulse function $H_k(t)$ is given by

$$H_k(t) = H(\frac{t}{\Delta t} - k) \tag{54}$$

and the two–dimensional rectangular pulse function $K_{m,n}(x,y)$ shown in fig. 5 by

$$K_{m,n}(x,y) = H(\frac{x}{\Delta x} - m)\ H(\frac{y}{\Delta y} - n) \tag{55}$$

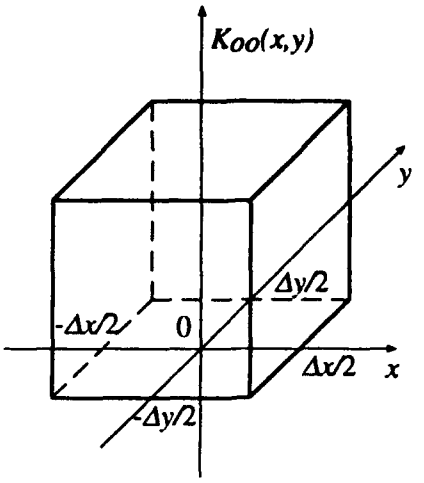

Figure 5: The two–dimensional pulse function $K_{0,0}(x, y)$.

At first, we insert the field expansions in eq. (50) and sample the field components with respect to space using the function

$$L_{m,n}(x,y) = H(\frac{x}{2\Delta x} + \frac{y}{2\Delta y} - \frac{m+n}{2})\ H(\frac{x}{2\Delta x} - \frac{y}{2\Delta y} - \frac{m-n}{2}) \tag{56}$$

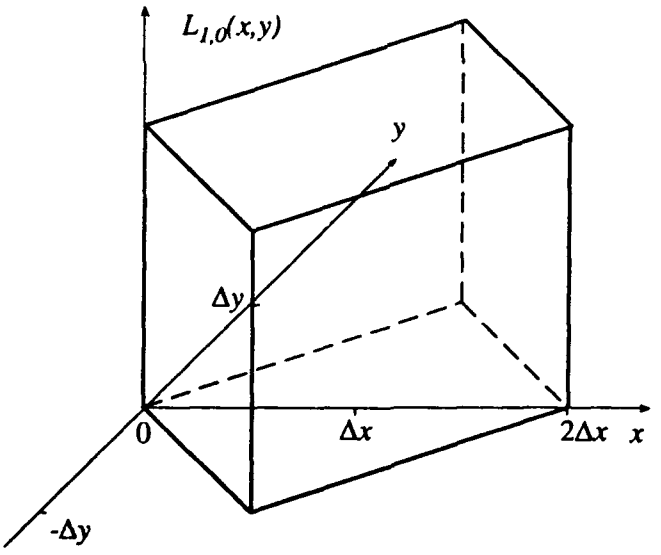

Figure 6: The two–dimensional pulse function $L_{1,0}(x, y)$.

The functions $L_{m,n}(x, y)$, shown in fig. 6, are squares in the x–y plane rotated by 45° around the z–axis with respect to the functions $K_{m,n}(x, y)$. Sampling the field expansions using the test functions $H_k(t)$ with respect to time, we obtain

$$4\,{}_{k+1}E^z_{m,n} + {}_{k+1}E^z_{m+1,n} + {}_{k+1}E^z_{m-1,n} + {}_{k+1}E^z_{m,n+1} + {}_{k+1}E^z_{m,n-1} -$$

$$-4\,{}_{k}E^z_{m,n} - {}_{k}E^z_{m+1,n} - {}_{k}E^z_{m-1,n} - {}_{k}E^z_{m,n+1} - {}_{k}E^z_{m,n-1} =$$

$$= \frac{2\Delta t Z_0 c}{\Delta x}\left({}_{k+1}H^y_{m+1,n} + {}_kH^y_{m+1,n} - {}_{k+1}H^y_{m-1,n} - {}_kH^y_{m-1,n}\right) +$$

$$+ \frac{2\Delta t Z_0 c}{\Delta y}\left({}_{k+1}H^x_{m,n-1} + {}_kH^x_{m,n-1} - {}_{k+1}H^x_{m,n+1} - {}_kH^x_{m,n+1}\right) \tag{57}$$

We insert the field expansions in eqs. (51) and (52) and sample the field components with respect to space using the functions $K_{m,n}(x,y)$ as test functions. We obtain

$${}_{k+1}E^z_{m,n+1} + {}_kE^z_{m,n+1} - {}_{k+1}E^z_{m,n} - {}_kE^z_{m,n} =$$

$$= \frac{\Delta y Z_0}{\Delta t c}\left({}_kH^x_{m,n+1} + {}_kH^x_{m,n} - {}_{k+1}H^x_{m,n+1} - {}_{k+1}H^x_{m,n}\right) \tag{58}$$

and

$${}_{k+1}E^z_{m+1,n} + {}_kE^z_{m+1,n} - {}_{k+1}E^z_{m,n} - {}_kE^z_{m,n} =$$

$$= \frac{\Delta x Z_0}{\Delta t c}\left({}_{k+1}H^y_{m+1,n} - {}_kH^y_{m+1,n} + {}_{k+1}H^y_{m,n} - {}_kH^y_{m,n}\right) \tag{59}$$

All electric and magnetic field components of the TLM mesh at all time sampling points $k\Delta t$ are summarized in the Hilbert space vector [5, 14]

$$|F\rangle = \sum_{k,m,n=-\infty}^{+\infty} {}_k[E_z, Z_0 H_x, Z_0 H_y]^T_{m,n}\ |k;m,n\rangle \tag{60}$$

where Z is a wave impedance different from the wave impedance Z_0 of the free space. The complete electromagnetic field state is represented by a single vector $|F\rangle$ in the Hilbert space $\mathcal{H}_F = \mathcal{C}^3 \otimes \mathcal{H}_m \otimes \mathcal{H}_t$. In the three-dimensional complex vector space $\mathcal{C}^3$, the three electric and magnetic field components at the discrete space coordinates (m,n) at the discrete time coordinate k are summarized in the vector ${}_k[E_z, Z_0 H_x, Z_0 H_y]^T_{m,n}$. To each space sampling point with the discrete coordinates (m,n), we assign a base vector $|m,n\rangle$. The set of vectors $|m,n\rangle$ is an orthonormal base of the Hilbert space $\mathcal{H}_m$. The time states $|k\rangle$ are the base vectors of the Hilbert space $\mathcal{H}_t$. The base vectors $|k;m,n\rangle = |k\rangle \otimes |m,n\rangle$ fulfill the orthogonality relations

$$\langle k_1;m_1,n_1|k_2;m_2,n_2\rangle = \delta_{k_1,k_2}\ \delta_{m_1,m_2}\ \delta_{n_1,n_2} \tag{61}$$

Assuming a quadratic mesh with

$$\Delta x = \Delta y = \Delta l \tag{62}$$

and defining the shift operator $\boldsymbol{X}$ and its Hermitian conjugate $\boldsymbol{X}^\dagger$ by

$$\boldsymbol{X}\,|k;m,n\rangle = |k;m+1,n\rangle \qquad \text{and} \qquad \boldsymbol{X}^\dagger|k;m,n\rangle = |k;m-1,n\rangle \tag{63}$$

as well as in an analogous way, the shift operators $\boldsymbol{Y}$ and $\boldsymbol{Y}^\dagger$ for the discrete space coordinate n and the time shift operators $\boldsymbol{T}$ and $\boldsymbol{T}^\dagger$ for the discrete time coordinate k, we obtain the operator equation

$$\boldsymbol{M}_2(\boldsymbol{T},\boldsymbol{X},\boldsymbol{Y})\ |F\rangle = 0 \tag{64}$$

with

$$\boldsymbol{M}_2(\boldsymbol{T},\boldsymbol{X},\boldsymbol{Y}) = \begin{bmatrix} 4(1-\boldsymbol{T})(1+\boldsymbol{C}_1) & (1+\boldsymbol{T})(\boldsymbol{Y}^\dagger-\boldsymbol{Y}) & (1+\boldsymbol{T})(\boldsymbol{X}-\boldsymbol{X}^\dagger) \\ (1+\boldsymbol{T})(\boldsymbol{Y}^\dagger-1) & (1-\boldsymbol{T})(\boldsymbol{Y}^\dagger+1) & 0 \\ (1+\boldsymbol{T})(\boldsymbol{X}^\dagger-1) & 0 & (\boldsymbol{T}-1)(\boldsymbol{X}^\dagger+1) \end{bmatrix} \tag{65}$$

where we have introduced

$$C_1 = \frac{1}{4}\left(X + Y + X^\dagger + Y^\dagger\right) \tag{66}$$

For the three–dimensional TLM method with condensed symmetric node, the cell boundary mapping [17, 18] is the correct mapping between the wave amplitudes and the electric and magnetic field components. The cell boundary mapping relates the TLM wave amplitudes with the tangential electric and magnetic field components in the tangential planes seperating the TLM cells. For the field components at the cell boundary, we introduce the CBM values of the electric and magnetic field components. The CBM value of a field component is defined at the cell boundary between two neighbouring space sampling points as the mean value of the field components at these space sampling points. E.g. the CBM value $E^z_{m,n+1/2}$ is given by

$$E^z_{m,n+1/2} = \frac{1}{2}\left(E^z_{m,n+1} + E^z_{m,n}\right) \tag{67}$$

The error introduced by this approximation as well as the error introduced by the discretization of Maxwell's equations is of second order since both approximations are linear.

Following [14], we define the electric field vector $|F_E\rangle$ and the magnetic field vector $|F_M\rangle$ as vectors in the Hilbert space $\mathcal{H}_W = \mathcal{C}^4 \otimes \mathcal{H}_m \otimes \mathcal{H}_t$. The electric field vector $|F_E\rangle$ combining all CBM values of the electric field components of the two–dimensional discrete space at all time sampling points $k\Delta t$ is given by

$$|F_E\rangle = \sum_{k,m,n=-\infty}^{+\infty} \begin{bmatrix} {}^k[E_z]_{m-1/2,n} \\ {}^k[E_z]_{m+1/2,n} \\ {}^k[E_z]_{m,n-1/2} \\ {}^k[E_z]_{m,n+1/2} \end{bmatrix} |k;m,n\rangle \tag{68}$$

$|F_M\rangle$, defined by

$$|F_M\rangle = Z \sum_{k,m,n=-\infty}^{+\infty} \begin{bmatrix} {}^k[H_y]_{m-1/2,n} \\ {}^k[H_y]_{m+1/2,n} \\ {}^k[H_x]_{m,n-1/2} \\ {}^k[H_x]_{m,n+1/2} \end{bmatrix} |k;m,n\rangle \tag{69}$$

summarizes all CBM values of the magnetic field components of the two–dimensional discrete space at all time sampling points $k\Delta t$. As the impedance Z, the wave impedance of one of the four identical arms of a TLM node is choosen. The relationship between the field components at the center of a TLM cell and the CBM values of the field components may be written as

$$|F_E\rangle = \frac{1}{2}\begin{bmatrix} X+1 & 0 & 0 \\ X^\dagger+1 & 0 & 0 \\ Y+1 & 0 & 0 \\ Y^\dagger+1 & 0 & 0 \end{bmatrix} |F'\rangle \tag{70}$$

and

$$|F_M\rangle = \frac{1}{2}\begin{bmatrix} 0 & 0 & X+1 \\ 0 & 0 & X^\dagger+1 \\ 0 & Y+1 & 0 \\ 0 & Y^\dagger+1 & 0 \end{bmatrix} |F'\rangle \tag{71}$$

Inserting eqs. (70) and (71) in eq. (57) we obtain

$$[1,1,1,1]\ (1-T)\ |F_E\rangle = [-1,1,1,-1]\ (1+T)\ \frac{2Z_0\Delta tc}{Z\Delta l}\ |F_M\rangle \tag{72}$$

Multiplying eq. (58) by $(1 + \boldsymbol{Y})$ and inserting eqs. (70) and (71) yields

$$\begin{bmatrix} 0 & 0 & -1 & 1 \end{bmatrix} (1+\boldsymbol{T}) \; |F_E\rangle = \begin{bmatrix} 0 & 0 & -1 & -1 \end{bmatrix} (1-\boldsymbol{T}) \; \frac{Z_0 \Delta l}{Z \Delta t c} \; |F_M\rangle \tag{73}$$

Multiplying eq. (59) by $(1 + \boldsymbol{X})$ and inserting eqs. (70) and (71) yields

$$\begin{bmatrix} -1 & 1 & 0 & 0 \end{bmatrix} (1+\boldsymbol{T}) \; |F_E\rangle = \begin{bmatrix} 1 & 1 & 0 & 0 \end{bmatrix} (1-\boldsymbol{T}) \; \frac{Z_0 \Delta l}{Z \Delta t c} \; |F_M\rangle \tag{74}$$

Adding eq. (58) multiplied by $(\boldsymbol{Y} - 1)$ and eq. (59) multiplied by $(1 - \boldsymbol{X})$, we obtain

$$\begin{bmatrix} 1 & 1 & -1 & -1 \end{bmatrix} (1+\boldsymbol{T}) \; |F_E\rangle = \begin{bmatrix} 1 & -1 & 1 & -1 \end{bmatrix} (1-\boldsymbol{T}) \; \frac{Z_0 \Delta l}{Z \Delta t c} \; |F_M\rangle \tag{75}$$

The mapping between the wave amplitudes and the CBM values of the electric and magnetic field components is defined at the cell boundary and therefore called cell boundary mapping. It is given by [20]

$$\begin{aligned} |a\rangle &= \tfrac{1}{2} \left(|F_E\rangle - P \; |F_M\rangle \right) \\ |b\rangle &= \tfrac{1}{2} \left(|F_E\rangle + P \; |F_M\rangle \right) \end{aligned} \tag{76}$$

and

$$\begin{aligned} |F_E\rangle &= |a\rangle + |b\rangle \\ |F_M\rangle &= P \left(|b\rangle - |a\rangle \right) \end{aligned} \tag{77}$$

with the operator

$$P = \begin{bmatrix} 1 & 0 & 0 & 0 \\ 0 & -1 & 0 & 0 \\ 0 & 0 & -1 & 0 \\ 0 & 0 & 0 & 1 \end{bmatrix} \tag{78}$$

and the Hilbert space vectors

$$|a\rangle = \sum_{k,m,n=-\infty}^{+\infty} {}_k[a_1, a_2, a_3, a_4]^T{}_{m,n} \; |k; l, m, n\rangle \tag{79}$$

and

$$|b\rangle = \sum_{k,m,n=-\infty}^{+\infty} {}_k[b_1, b_2, b_3, b_4]^T{}_{m,n} \; |k; m, n\rangle \tag{80}$$

in the Hilbert space $\mathcal{H}_W$. The vectors $|a\rangle$ and $|b\rangle$ summarize all incident and scattered wave amplitudes of the TLM mesh at all discrete time sampling points $k\Delta t$. The property $P^2 = 1$ ensures that the cell boundary mapping is a bijective one–to–one mapping between the eight CBM values of the electric and magnetic field components and the eight incident and scattered wave amplitudes at one two–dimensional TLM shunt node. At each boundary surface, the wave amplitudes incident into one TLM cell are identical with the wave amplitudes scattered from the neighbouring TLM cell. This relation is expressed by the connection operator [5] via

$$|a\rangle = \boldsymbol{\Gamma} \; |b\rangle \qquad \text{and} \qquad |b\rangle = \boldsymbol{\Gamma} \; |a\rangle \tag{81}$$

where $\boldsymbol{\Gamma}$ is given by

$$\boldsymbol{\Gamma} = \begin{bmatrix} 0 & \boldsymbol{X} & 0 & 0 \\ \boldsymbol{X}^\dagger & 0 & 0 & 0 \\ 0 & 0 & 0 & \boldsymbol{Y} \\ 0 & 0 & \boldsymbol{Y}^\dagger & 0 \end{bmatrix} \tag{82}$$

Applying the cell boundary mapping, we obtain the discretized field equations for the wave amplitudes. We choose

$$\frac{2Z_0\Delta tc}{Z\Delta l} = 1 \qquad \text{as well as} \qquad \frac{Z_0\Delta l}{Z\Delta tc} = 1 \tag{83}$$

With the mesh pulse velocity $c_m = \Delta l/\Delta t$, eq. (83) yields

$$Z_0 = \frac{Z}{\sqrt{2}} \qquad \text{and} \qquad \frac{c}{c_m} = \frac{1}{\sqrt{2}} \tag{84}$$

which is well-known from literature [1]. Now, eqs. (72) - (75) yield

$$\boldsymbol{P}_1 \; |b\rangle \; = \; \boldsymbol{P}_2 \, \boldsymbol{T} \; |a\rangle \tag{85}$$

with

$$\boldsymbol{P}_1 = \begin{bmatrix} 1 & 1 & 1 & 1 \\ 0 & 0 & -1 & 1 \\ -1 & 1 & 0 & 0 \\ -1 & -1 & 1 & 1 \end{bmatrix}, \quad \boldsymbol{P}_2 = \begin{bmatrix} 1 & 1 & 1 & 1 \\ 0 & 0 & 1 & -1 \\ 1 & -1 & 0 & 0 \\ 1 & 1 & -1 & -1 \end{bmatrix} \tag{86}$$

Multiplying eq. (85) by $\boldsymbol{P}_1^{-1}$ we obtain

$$|b\rangle = \boldsymbol{T}\,\boldsymbol{S} \; |a\rangle \tag{87}$$

with the scattering matrix of the two-dimensional TLM shunt node

$$\boldsymbol{S} = \begin{bmatrix} -\frac{1}{2} & \frac{1}{2} & \frac{1}{2} & \frac{1}{2} \\ \frac{1}{2} & -\frac{1}{2} & \frac{1}{2} & \frac{1}{2} \\ \frac{1}{2} & \frac{1}{2} & -\frac{1}{2} & \frac{1}{2} \\ \frac{1}{2} & \frac{1}{2} & \frac{1}{2} & -\frac{1}{2} \end{bmatrix} \tag{88}$$

Note that the two-dimensional TLM series node can be derived in the same way by the priciple of duality [21].

4 Yee's FDTD Scheme

The finite-difference time domain (FDTD) method is the mathematical approach for the solution of partial differential equations [22]. The partial derivatives are simply replaced by finite differences. In 1966, Yee has first given a finite-difference time-domain scheme for solution of the Maxwell equations [7, 8, 9]. In the FDTD method space and time are discretized with increments Δl and Δt, respectively. The field component placement in the FDTD unit cell is shown in Fig. 7. The side length of a unit cell in our notation is $2\Delta l$.

In this section, we derive Yee's FDTD scheme with central difference approximations [7] by applying the Method of Moments to Maxwell's equations. As expansion functions, we use pulse functions in space and time. The field expansions of the magnetic field components are shifted by half an interval in space and time with respect to the field expansions of the electric field components. As test functions, we use pulse functions in space and time, too, which is equivalent to applying Galerkin's method [4]. For simplicity, we restrict our considerations to the free space. We expand the fields in

$$\begin{aligned} E_x(\vec{x},t) &= \sum_{k,l,m,n=-\infty}^{+\infty} {}_kE^x_{l+1/2,m,n}\; H_k(t)\; H_{l+1/2}(x)\; H_m(y)\; H_n(z) \\ H_x(\vec{x},t) &= \sum_{k,l,m,n=-\infty}^{+\infty} {}_{k+1/2}H^x_{l,m+1/2,n+1/2}\; H_{k+1/2}(t)\; H_l(x)\; H_{m+1/2}(y)\; H_{n+1/2}(z) \end{aligned} \tag{89}$$

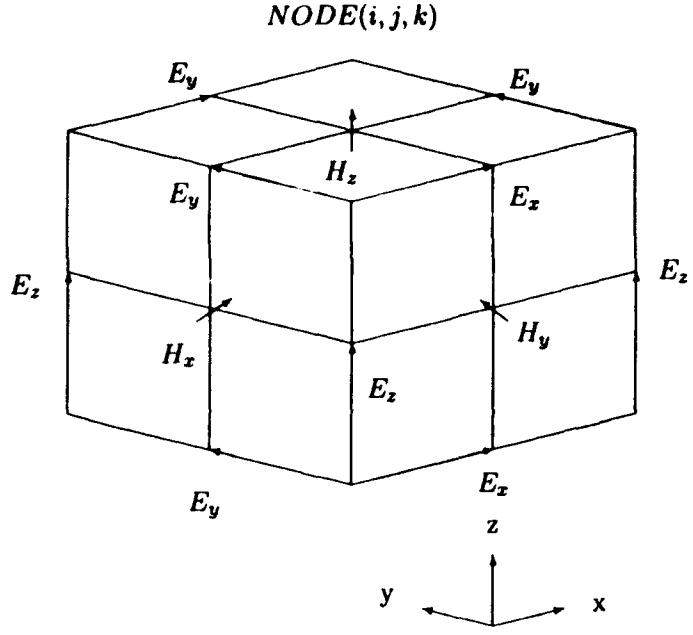

Figure 7: Field components in the FDTD unit cell.

${}_kE^{\mu}_{l,m,n}$ and ${}_kH^{\mu}_{l,m,n}$ with $\mu = x, y, z$ are constant expansion coefficients. We obtain the expansions for $E_y(\vec{x}, t)$, $E_z(\vec{x}, t)$ and $H_y(\vec{x}, t)$, $H_z(\vec{x}, t)$, respectively, by cyclic permutation of x, y, z and Δx, Δy, Δz.

Choosing $\Delta x = \Delta y = \Delta z = \Delta l$ and proceeding in the same way as above with all components of Maxwell's equations yields Yee's FDTD scheme with central difference approximations [7]:

$$
\begin{aligned}
&{}_{k+1}E^{x}_{l+1/2,m,n} - {}_kE^{x}_{l+1/2,m,n} = \\
&= sZ_0 \left({}_{k+1/2}H^{z}_{l+1/2,m+1/2,n} - {}_{k+1/2}H^{z}_{l+1/2,m-1/2,n} + {}_{k+1/2}H^{y}_{l+1/2,m,n-1/2} - {}_{k+1/2}H^{y}_{l+1/2,m,n+1/2} \right)
\end{aligned}
$$

$$
\begin{aligned}
&{}_{k+1}E^{y}_{l,m+1/2,n} - {}_kE^{y}_{l,m+1/2,n} = \\
&= sZ_0 \left({}_{k+1/2}H^{x}_{l,m+1/2,n+1/2} - {}_{k+1/2}H^{x}_{l,m+1/2,n-1/2} + {}_{k+1/2}H^{z}_{l-1/2,m+1/2,n} - {}_{k+1/2}H^{z}_{l+1/2,m+1/2,n} \right)
\end{aligned}
$$

$$
\begin{aligned}
&{}_{k+1}E^{z}_{l,m,n+1/2} - {}_kE^{z}_{l,m,n+1/2} = \\
&= sZ_0 \left({}_{k+1/2}H^{x}_{l,m-1/2,n+1/2} - {}_{k+1/2}H^{x}_{l,m+1/2,n+1/2} + {}_{k+1/2}H^{y}_{l+1/2,m,n+1/2} - {}_{k+1/2}H^{y}_{l-1/2,m,n+1/2} \right)
\end{aligned}
$$

$$
\begin{aligned}
&{}_{k+1/2}H^{x}_{l,m+1/2,n+1/2} - {}_{k-1/2}H^{x}_{l,m+1/2,n+1/2} = \\
&= \frac{s}{Z_0} \left({}_kE^{y}_{l,m+1/2,n+1} - {}_kE^{y}_{l,m+1/2,n} + {}_kE^{z}_{l,m,n+1/2} - {}_kE^{z}_{l,m+1,n+1/2} \right)
\end{aligned}
$$

$$
\begin{aligned}
&{}_{k+1/2}H^{y}_{l+1/2,m,n+1/2} - {}_{k-1/2}H^{y}_{l+1/2,m,n+1/2} = \\
&= \frac{s}{Z_0} \left({}_kE^{x}_{l+1/2,m,n} - {}_kE^{x}_{l+1/2,m,n+1} + {}_kE^{z}_{l+1,m,n+1/2} - {}_kE^{z}_{l,m,n+1/2} \right)
\end{aligned}
$$

$$
\begin{aligned}
&{}_{k+1/2}H^{z}_{l+1/2,m+1/2,n} - {}_{k-1/2}H^{z}_{l+1/2,m+1/2,n} = \\
&= \frac{s}{Z_0} \left({}_kE^{x}_{l+1/2,m+1,n} - {}_kE^{x}_{l+1/2,m,n} + {}_kE^{y}_{l,m+1/2,n} - {}_kE^{y}_{l+1,m+1/2,n} \right)
\end{aligned}
\tag{90}
$$

where we have introduced the stability factor $s = c\Delta t/\Delta l$.

We define the field vector $|F\rangle$ in the Hilbert space $\mathcal{H}_W = \mathcal{C}^4 \otimes \mathcal{H}_m \otimes \mathcal{H}_t$:

$$|F\rangle = \sum_{k,l,m,n=-\infty}^{+\infty} {}_k|E_x, E_y, E_z, Z_0H_x, Z_0H_y, Z_0H_z|^T_{l,m,n} \; |k;l,m,n\rangle \tag{91}$$

We define the half shift operators $\boldsymbol{X}_h$ and its Hermitian conjugate $\boldsymbol{X}_h^\dagger$ by

$$\boldsymbol{X}_h\,|k;l,m,n\rangle = |k;l+1/2,m,n\rangle \qquad \text{and} \qquad \boldsymbol{X}_h^\dagger\,|k;l,m,n\rangle = |k;l-1/2,m,n\rangle \tag{92}$$

and in an analogous way, the shift operators $\boldsymbol{Y}_h$, $\boldsymbol{Y}_h^\dagger$, $\boldsymbol{Z}_h$ and $\boldsymbol{Z}_h^\dagger$ for the spatial coordinates m and n. In the same way, we introduce the half time shift operators $\boldsymbol{T}_h$ and its Hermitian conjugate $\boldsymbol{T}_h^\dagger$. From eq. (90), we obtain the FDTD equation

$$\boldsymbol{M}_1\;|F\rangle = 0 \tag{93}$$

with

$$\boldsymbol{M}_1 = \begin{bmatrix} \frac{1}{s}\boldsymbol{X}_h^\dagger \boldsymbol{T}_h^\dagger \boldsymbol{D}_t^\dagger & 0 & 0 & 0 & \boldsymbol{T}_h^\dagger \boldsymbol{X}_h^\dagger \boldsymbol{D}_z^\dagger & \boldsymbol{T}_h^\dagger \boldsymbol{X}_h^\dagger \boldsymbol{D}_y \\ 0 & \frac{1}{s}\boldsymbol{Y}_h^\dagger \boldsymbol{T}_h^\dagger \boldsymbol{D}_t^\dagger & 0 & \boldsymbol{T}_h^\dagger \boldsymbol{Y}_h^\dagger \boldsymbol{D}_z & 0 & \boldsymbol{T}_h^\dagger \boldsymbol{Y}_h^\dagger \boldsymbol{D}_x^\dagger \\ 0 & 0 & \frac{1}{s}\boldsymbol{Z}_h^\dagger \boldsymbol{T}_h^\dagger \boldsymbol{D}_t^\dagger & \boldsymbol{T}_h^\dagger \boldsymbol{Z}_h^\dagger \boldsymbol{D}_y^\dagger & 0 & \boldsymbol{T}_h^\dagger \boldsymbol{Z}_h^\dagger \boldsymbol{D}_x \\ 0 & \boldsymbol{Y}_h^\dagger \boldsymbol{Z}_h^\dagger \boldsymbol{D}_z & \boldsymbol{Y}_h^\dagger \boldsymbol{Z}_h^\dagger \boldsymbol{D}_y^\dagger & \frac{1}{s}\boldsymbol{Y}_h^\dagger \boldsymbol{Z}_h^\dagger \boldsymbol{D}_t^\dagger & 0 & 0 \\ \boldsymbol{X}_h^\dagger \boldsymbol{Z}_h^\dagger \boldsymbol{D}_z^\dagger & 0 & \boldsymbol{X}_h^\dagger \boldsymbol{Z}_h^\dagger \boldsymbol{D}_x & 0 & \frac{1}{s}\boldsymbol{X}_h^\dagger \boldsymbol{Z}_h^\dagger \boldsymbol{D}_t^\dagger & 0 \\ \boldsymbol{X}_h^\dagger \boldsymbol{Y}_h^\dagger \boldsymbol{D}_y & \boldsymbol{X}_h^\dagger \boldsymbol{Y}_h^\dagger \boldsymbol{D}_x^\dagger & 0 & 0 & 0 & \frac{1}{s}\boldsymbol{X}_h^\dagger \boldsymbol{Y}_h^\dagger \boldsymbol{D}_t^\dagger \end{bmatrix} \tag{94}$$

where we have used the abbreviations

$$\boldsymbol{D}_x = \boldsymbol{X}_h^\dagger - \boldsymbol{X}_h \qquad \boldsymbol{D}_y = \boldsymbol{Y}_h^\dagger - \boldsymbol{Y}_h \qquad \boldsymbol{D}_z = \boldsymbol{Z}_h^\dagger - \boldsymbol{Z}_h \qquad \boldsymbol{D}_t = \boldsymbol{T}_h^\dagger - \boldsymbol{T}_h \tag{95}$$

For two-dimensional FDTD, with $\partial/\partial z = 0$, eq. (90) yields

$${}_{k+1}E^z_{m,n} - {}_kE^z_{m,n} = sZ_0\left({}_{k+1/2}H^x_{m,n-1/2} - {}_{k+1/2}H^x_{m,n+1/2} + {}_{k+1/2}H^y_{m+1/2,n} - {}_{k+1/2}H^y_{m-1/2,n}\right)$$

$$\begin{aligned} {}_{k+1/2}H^x_{m,n+1/2} - {}_{k-1/2}H^x_{m,n+1/2} &= \frac{s}{Z_0}\left({}_kE^z_{m,n} - {}_kE^z_{m,n+1}\right) \\ {}_{k+1/2}H^y_{m+1/2,n} - {}_{k-1/2}H^y_{m+1/2,n} &= \frac{s}{Z_0}\left({}_kE^z_{m+1,n} - {}_kE^z_{m,n}\right) \end{aligned} \tag{96}$$

for the system of partial differential equations for H_x, H_y and E_z if we choose a quadratic mesh with $\Delta x = \Delta y = \Delta l$.

We introduce the Hilbert space vector [5, 14]

$$|F'\rangle = \sum_{k,m,n=-\infty}^{+\infty} {}_k|E_z, Z_0H_x, Z_0H_y|^T_{m,n} \; |k;m,n\rangle \tag{97}$$

to represent the complete electromagnetic field state in the Hilbert space $\mathcal{H}_F = \mathcal{C}^3 \otimes \mathcal{H}_m \otimes \mathcal{H}_t$. Eq. (96) may be expressed by the operator equation

$$\boldsymbol{M}_1(\boldsymbol{T}_h, \boldsymbol{X}_h, \boldsymbol{Y}_h)\;|F'\rangle = 0 \tag{98}$$

with

$$\boldsymbol{M}_1(\boldsymbol{T}_h, \boldsymbol{X}_h, \boldsymbol{Y}_h) = \begin{bmatrix} \frac{1}{3}\boldsymbol{T}_h^{\dagger}\left(\boldsymbol{T}_h - \boldsymbol{T}_h^{\dagger}\right) & \boldsymbol{T}_h^{\dagger}\left(\boldsymbol{Y}_h - \boldsymbol{Y}_h^{\dagger}\right) & \boldsymbol{T}_h^{\dagger}\left(\boldsymbol{X}_h^{\dagger} - \boldsymbol{X}_h\right) \\ \boldsymbol{Y}_h^{\dagger}\left(\boldsymbol{Y}_h - \boldsymbol{Y}_h^{\dagger}\right) & \frac{1}{3}\boldsymbol{Y}_h^{\dagger}\left(\boldsymbol{T}_h - \boldsymbol{T}_h^{\dagger}\right) & 0 \\ \boldsymbol{X}_h^{\dagger}\left(\boldsymbol{X}_h^{\dagger} - \boldsymbol{X}_h\right) & 0 & \frac{1}{3}\boldsymbol{X}_h^{\dagger}\left(\boldsymbol{T}_h - \boldsymbol{T}_h^{\dagger}\right) \end{bmatrix} \tag{99}$$

5 The Dispersion Relations of FDTD and TLM

5.1 The General Dispersion Relation of TLM

Eliminating the scattered wave amplitudes from eqs. (33) and (47), we obtain the eigenvalue equation

$$(\boldsymbol{\Gamma}\,\boldsymbol{T}\,\boldsymbol{S} - 1)\,|a\rangle = 0 \tag{100}$$

The TLM algorithm and the properties of the discrete mesh are completely described by the scattering matrix and the propagation matrix. Diagonalizing $\boldsymbol{\Gamma S}$, this information is contained in the eigenvalues and the eigenvectors of $\boldsymbol{\Gamma S}$. Therefore we may calculate the dispersion relation of the discrete TLM mesh from the eigenvalues.

We calculate the eigenvalue equation in frequency domain. The field state vector $|a\rangle$ in the Hilbert space $\mathcal{H}_W$ describes the complete time evolution of the electromagnetic field in dicretized space and time. Calculating the scalar product of the vector $|a\rangle$ and the base vector $|k\rangle$ of $\mathcal{H}_t$ yields the complete field state $|a(k)\rangle_m = {}_t\langle k\,|a\rangle_{m\otimes t}$ at the time $k\Delta t$. The subscripts t and m of the Hilbert space vectors indicate that the vectors are an element of the Hilbert space $\mathcal{H}_t$ and $\mathcal{H}_m$, respectively. If it is obvious to which space the vectors are belonging, these indices will be omitted.

To calculate the complete field state in frequency domain, we introduce the base vectors

$$|\Omega\rangle_t = \sum_{k=-\infty}^{+\infty} e^{\jmath k\Omega}\,|k\rangle_t \tag{101}$$

with the normalized frequency $\Omega = 2\pi\Delta t f$ where f represents the frequency. For the scalar product of $|a\rangle_{m\otimes t}$ and $|\Omega\rangle_t$, we obtain

$$|a(\Omega)\rangle_m = {}_t\langle\Omega\,|a\rangle_{m\otimes t} = \sum_{k=-\infty}^{+\infty} e^{-\jmath k\Omega}\,{}_t\langle k\,|a\rangle_{m\otimes t} = \sum_{k,l,m,n=-\infty}^{+\infty} {}_k a_{l,m,n}\; e^{-\jmath k\Omega}\,|l,m,n\rangle_m \tag{102}$$

The vectors $|a(\Omega)\rangle_m$ and $|a(k)\rangle_m$ are connected by a Fourier series. Multiplying eq. (100) with the Hilbert space vector $|\Omega\rangle$, we obtain

$$\left(\boldsymbol{\Gamma}\,\boldsymbol{S} - e^{\jmath\Omega}\right)|a(\Omega)\rangle_m = 0 \tag{103}$$

representing the general dispersion relation of TLM. The eigenvectors $|a(\Omega)\rangle_m$ are the harmonic field solutions for the normalized eigenfrequencies Ω. The eigenvalues of $\boldsymbol{\Gamma S}$ are calculated by

$$det\left(\boldsymbol{\Gamma}\,\boldsymbol{S} - e^{\jmath\Omega}\right) = 0 \tag{104}$$

This result is also contained in a different representation in the work of Nielsen [12, 13]. However, Nielsen gives numerical solutions of eq. (104), whereas we calculate the dispersion relations algebraically. As the mapping between the electric and magnetic field components and the wave amplitudes has not beeing used in the derivation of the general dispersion relation, the method may be applied to any TLM method provided it is possible to diagonalize the matrix $\boldsymbol{\Gamma S}$.

5.2 2D–TLM and 2D–FDTD

We have shown that in two–dimensional TLM as well as in two–dimensional FDTD, there are three linearly independent field components per TLM cell. To apply the cell boundary mapping, we have introduced four CBM values of the electric and magnetic field components per TLM cell. This corresponds to the introduction of an additional degree of freedom and an additional solution for the two–dimensional TLM method, respectively. We demonstrate this by investigating the dispersion characteristics of two–dimensional FDTD and TLM.

In order to investigate the dispersion characteristics of FDTD, we calculate eq. (98) in frequency domain. Forming the inner product of $\langle\Omega|$ and eq. (98) and considering

$$\boldsymbol{T}_h\,|\Omega;m,n\rangle = e^{-\jmath\Omega/2}\;|\Omega;m,n\rangle \tag{105}$$

we obtain

$$\boldsymbol{M}_1(e^{\jmath\Omega/2},\boldsymbol{X}_h,\boldsymbol{Y}_h)\;\langle\Omega\,|F'\rangle = 0 \tag{106}$$

This procedure corresponds to a seperation of variables, which is justified because $|\Omega\rangle$ represents a maximal orthonormal set for the Hilbert space $\mathcal{H}_t$ [23]. Eq. (106) implies

$$det\boldsymbol{M}_1(e^{\jmath\Omega/2},\boldsymbol{X}_h,\boldsymbol{Y}_h) = 0 \tag{107}$$

for any non–trivial solution of FDTD. As demonstrated in [14], the solutions of eq. (107) may be calculated as

$$\boldsymbol{\lambda}_1 = \boldsymbol{C} + \sqrt{\boldsymbol{C}^2-1} \qquad \boldsymbol{\lambda}_2 = \boldsymbol{C} - \sqrt{\boldsymbol{C}^2-1} \qquad \boldsymbol{\lambda}_3 = 1 \tag{108}$$

with

$$\boldsymbol{C} = \frac{s^2}{2}\left(\boldsymbol{X}+\boldsymbol{Y}+\boldsymbol{X}^\dagger+\boldsymbol{Y}^\dagger-4\right)+1 \tag{109}$$

The solutions of eq. (107), the eigenvalues $\boldsymbol{\lambda}_i = e^{\jmath\Omega_i}$ are operators in $\mathcal{H}_m$. These operators represent the three possible non–trivial FDTD solutions: $\boldsymbol{\lambda}_1$ and $\boldsymbol{\lambda}_2$ contain the dispersion relation of the propagating solutions of a FDTD mesh, a wave propagating in positive and negative space direction. $\boldsymbol{\lambda}_3$ represents the non–propagating solution of a FDTD mesh: $\boldsymbol{\lambda}_3 = 1$ implies $\Omega = 0$ which corresponds to a stationary solution representing the magnetostatic case.

For the two–dimensional TLM method, eq. (104) yields

$$\begin{aligned} \boldsymbol{\lambda}_1 &= \boldsymbol{C}_1 + \sqrt{\boldsymbol{C}_1^2-1} & \boldsymbol{\lambda}_2 &= \boldsymbol{C}_1 - \sqrt{\boldsymbol{C}_1^2-1} \\ \boldsymbol{\lambda}_3 &= 1 & \boldsymbol{\lambda}_4 &= -1 \end{aligned} \tag{110}$$

with $\boldsymbol{C}_1$ according to eq. (66). The eigenvalues $\boldsymbol{\lambda}_i$ represent the four possible non–trivial TLM solutions: $\boldsymbol{\lambda}_1$ and $\boldsymbol{\lambda}_2$ again contain the dispersion relation of the physical solutions of a TLM mesh, a wave propagating in positive and negative space direction, for which we obtain the dispersion relation by calculating $\boldsymbol{\lambda}_1$ and $\boldsymbol{\lambda}_2$ in the wave vector domain. We introduce the base vectors

$$|\chi,\eta\rangle_m = \sum_{m,n=-\infty}^{+\infty} e^{\jmath(\chi m+\eta n)}\;|m,n\rangle_m \tag{111}$$

with the normalized wave vector components $\chi = 2\pi\Delta l k_x$ and $\eta = 2\pi\Delta l k_y$. The wave vector $\vec{k}$ has the x– and y–components k_x and k_y. $\langle\chi,\eta|a(\Omega)\rangle$ and $\langle m,n|a(\Omega)\rangle$ are connected by the Fourier series

$$\langle\chi,\eta|a(\Omega)\rangle = \sum_{m,n=-\infty}^{+\infty} e^{-\jmath(\chi m+\eta n)}\;\langle m,n|a(\Omega)\rangle \tag{112}$$

From eq. (110), we obtain the dispersion relation

$$\cos(\Omega) = \frac{1}{2}\Big(\cos(\chi) + \cos(\eta)\Big) \tag{113}$$

Note that for the two–dimensional TLM method with series nodes, we obtain the same four operators λ_i and thus the same dispersion relation. For small arguments, using $\cos x \approx 1 - x^2/2$ yields

$$2\frac{\Delta t^2}{\Delta l^2} f^2 = {k_x}^2 + {k_y}^2 \tag{114}$$

This is the dispersion relation of a two–dimensional wave equation with the wave propagation velocity $c = c_m/\sqrt{2}$. The mesh pulse velocity $c_m = \Delta l/\Delta t$ represents the propagation velocity of the TLM wave amplitudes in the mesh. The mesh pulse velocity has no physical interpretation. Only the waves resulting from the superposition of the mesh pulses give an image of the physical reality.

Since $\lambda_3 = 1$ implies $\Omega = 0$, λ_3 corresponds to a non–propagating, stationary solution representing the magnetostatic case. Note that choosing $s = 1/\sqrt{2}$ for two–dimensional FDTD, the eigenvalues λ_1, λ_2 and λ_3 are identical for two–dimensional FDTD and TLM. $\lambda_4 = -1$ implies $\Omega = \pi$: The eigenvalue λ_4 corresponds to an oscillating spurious solution.

We investigate the discrete field equations for the electric and magnetic field components at the center of a TLM cell used in the derivation of two–dimensional TLM. Eq. (64) implies

$$det\boldsymbol{M}_2(e^{\mathcal{N}\Omega}, \boldsymbol{X}, \boldsymbol{Y}) = 0 \tag{115}$$

for any non–trivial solution. We calculate the solutions of eq. (115) and obtain the eigenvalues λ_1, λ_2 and λ_3 as in eq. (110). Choosing $s = 1/\sqrt{2}$, the discretized field equations, eqs. (64) and (65) have the same eigenvalues as two–dimensional FDTD. Since two linear mapping algorithms are equivalent if the transformation matrices describing the mapping algorithms exhibit the same diagonal form, we conclude the equivalence of two–dimensional FDTD for $s = 1/\sqrt{2}$ and the linear mapping algorithm described by eqs. (64) and (65). The mapping of the three field components at the center of a TLM cell on the four CBM values per TLM cell introduces an additional degree of freedom and a spurious solution, respectivly.

5.3 3D–TLM and 3D–FDTD

For the three–dimensional TLM method with condensed symmetric node, we obtain the operators [15]

$$\begin{aligned} \lambda_1 &= \sqrt{A + \sqrt{B}} & \lambda_2 &= -\sqrt{A + \sqrt{B}} \\ \lambda_3 &= \sqrt{A - \sqrt{B}} & \lambda_4 &= -\sqrt{A - \sqrt{B}} \\ \lambda_5 &= 1 & \lambda_6 &= -1 \end{aligned} \tag{116}$$

with

$$\begin{aligned} \boldsymbol{A} &= \frac{1}{8}\Big(\boldsymbol{XY} + \boldsymbol{XZ} + \boldsymbol{YZ} + \boldsymbol{X}^\dagger\boldsymbol{Y}^\dagger + \boldsymbol{X}^\dagger\boldsymbol{Z}^\dagger + \boldsymbol{Y}^\dagger\boldsymbol{Z}^\dagger - 4\Big) \\ &+ \frac{1}{8}\Big(\boldsymbol{XY}^\dagger + \boldsymbol{XZ}^\dagger + \boldsymbol{YX}^\dagger + \boldsymbol{YZ}^\dagger + \boldsymbol{ZX}^\dagger + \boldsymbol{ZY}^\dagger\Big) \end{aligned} \tag{117}$$

and

$$\boldsymbol{B} = \frac{1}{8}\Big(\boldsymbol{XYZ} + \boldsymbol{X} + \boldsymbol{Y} + \boldsymbol{Z}\Big)\Big(\boldsymbol{X}^\dagger + \boldsymbol{Y}^\dagger + \boldsymbol{Z}^\dagger + \boldsymbol{X}^\dagger\boldsymbol{Y}^\dagger\boldsymbol{Z}^\dagger\Big)\Big(\boldsymbol{A} - 1\Big) \tag{118}$$

The operators λ_7 to λ_{12} are identical with λ_1 to λ_6. The operator λ_6 corresponds to a non–propagating, oscillating spurious solution, the operator λ_5 to a non–propagating, stationary solution representing the

electromagnetic and magnetostatic case, respectively. The operators λ_1 to λ_4 correspond to the propagating solutions of a mesh of condensed symmetric TLM nodes. We calculate the dispersion relation for the propagating solutions and introduce

$$|\chi,\eta,\xi\rangle_m = \sum_{l,m,n=-\infty}^{+\infty} e^{j(\chi l+\eta m+\xi n)}\ |l,m,n\rangle_m \tag{119}$$

with the normalized wave vector components $\chi = 2\pi\Delta l k_x$, $\eta = 2\pi\Delta l k_y$ and $\xi = 2\pi\Delta l k_z$. The normalized wave vector $\vec{k}$ has the x–, y– and z–components k_x, k_y and k_z. Again, $\langle\chi,\eta,\xi|a(\Omega)\rangle$ and $\langle l,m,n|a(\Omega)\rangle$ are connected by a Fourier series. In the wave vector domain, eq. (116) yields

$$\cos^2(\Omega) = \frac{1}{4}\Big(\cos(\chi)\cos(\eta) + \cos(\chi)\cos(\xi) + \cos(\eta)\cos(\xi) + 1\Big) \tag{120}$$

For small arguments, using $\cos x \approx 1 - x^2/2$ yields

$$4\frac{\Delta t^2}{\Delta l^2} f^2 = {k_x}^2 + {k_y}^2 + {k_z}^2 \tag{121}$$

which is equivalent to the dispersion relation of a three–dimensional wave equation with the wave propagation velocity $c = c_m/2$. The dispersion relation of the three–dimensional condensed node has another solution for small frequencies. We use $\cos x \approx 1 - x^2/2$ to approximate the left side and $\cos(x+\pi) \approx -1 + x^2/2$ to approximate the right side of eq. (120). In this way, we calculate the low–frequency dispersion relation of the spurious modes propagating in a mesh with condensed symmetric TLM nodes [12]. Again, we obtain eq. (121): The spurious modes have the same low–frequency propagation characteristics as the physical modes.

In the two–dimensional case, we have no propagation in z–direction. With $\xi = 0$ eq. (120) yields

$$\cos(\Omega) = \frac{1}{2}\Big(\cos(\frac{\chi-\eta}{2}) + \cos(\frac{\chi+\eta}{2})\Big) \tag{122}$$

which is different from the dispersion relation of the two-dimensional TLM method. With $\cos x \approx 1 - x^2/2$, we obtain

$$4\frac{\Delta t^2}{\Delta l^2} f^2 = {k_x}^2 + {k_y}^2 \tag{123}$$

This is the dispersion relation of a two–dimensional wave equation with the wave propagation velocity $c = c_m/2$. In contrast to the three–dimensional dispersion relation, eq. (120), the two–dimensional dispersion relation, eq. (122) has no other solution for small frequencies so that no spurious modes occur.

The FDTD equation implies

$$det\boldsymbol{M}_1 = 0 \tag{124}$$

for any non–trivial solution of FDTD. The solution of eq. (124) yields the dispersion relations of all non–trivial solutions in a FDTD mesh. The calculation of the dispersion relation in FDTD is performed in the same way as in TLM where we calculate the eigenvalues from eq. (104).

Calculating eq. (124) in frequency– and wave vector–domain in the same way as described above yields the dispersion relation for the propagating FDTD solutions:

$$\cos(\Omega) = s^2\Big(\cos(\chi) + \cos(\eta) + \cos(\xi)\Big) + 1 - 3s^2 \tag{125}$$

which may be rewritten in the form [10]

$$\sin^2(\Omega/2) = s^2\Big(\sin^2(\chi/2) + \sin^2(\eta/2) + \sin^2(\xi/2)\Big) \tag{126}$$

Eq. (125) has a solution for all χ, η and ξ if

$$\left|s^2\Big(\sin^2(\chi/2)+\sin^2(\eta/2)+\sin^2(\xi/2)\Big)\right| \leq 1 \tag{127}$$

is satisfied. This yields the stability condition

$$s \leq \frac{1}{\sqrt{3}} \tag{128}$$

To compare the FDTD dispersion relation with the dispersion relation of the three–dimensional TLM method with condensed symmetric node, we choose $s = 1/2$. From eq. (125), we obtain

$$\cos(\Omega) = \frac{1}{4}\Big(\cos(\chi)+\cos(\eta)+\cos(\xi)+1\Big) \tag{129}$$

The low–frequency approximation yields the dispersion relation of a three–dimensional wave equation with the wave propagation velocity $c = c_m/2$. In contrast to the three–dimensional TLM method with condensed symmetric node, no other low–frequency solution exists.

To compare the FDTD dispersion relation with the dispersion relation of the two–dimensional TLM method, we have to choose $s = 1/\sqrt{2}$ and $\xi = 0$. In this case, we obtain the same dispersion relation for the two–dimensional FDTD and the two–dimensional TLM method. This fact has already been proved by Simons and Bridges [24].

6 Conclusion

In the case of cell boundary mapping, the three–dimensional TLM method with condensed symmetric node uses twelve wave amplitudes and twelve linearly independent field components per TLM cell, respectively. In this case, the number of wave amplitudes per TLM cell corresponds to the number of degrees of freedom per TLM cell. Three–dimensional FDTD method, the discretization scheme contains only six linearly independent field components per unit cell [7]. If we are comparing the two methods, we have to use discretizations with the length interval ratios $1 : \sqrt[3]{2}$ between FDTD and TLM in order to obtain the same number of degrees of freedom for a given problem.

As in the two–dimensional FDTD method, in the two–dimensional TLM method, there are three linearly independent field components per unit cell. However, the two–dimensional TLM method uses four wave amplitudes and four field components per TLM cell, respectively, in the simulation of a two–dimensional scalar wave equation. The additional degree of freedom in the two–dimensional TLM method compared with the two–dimensional FDTD method corresponds to a spurious solution. This spurious solution is a non–propagating solution oscillating with the frequency $1/2\Delta t$.

The dispersion analysis of TLM and FDTD prooves that the propagation characteristics of the two–dimensional TLM method and the two–dimensional FDTD method with central difference approximation are indentical. The dispersion relation of the three–dimensional TLM method with condensed symmetric node and of the three–dimensional FDTD method with central difference approximation are different.

In the FDTD mesh, only one low–frequency solution is propagating. In the three–dimensional TLM method with condensed symmetric node, two low–frequency solutions of the dispersion relation corresponding to $\vec{k} = [k_x, k_y, k_z]^T$ and $\vec{k} = [\pi/(2\Delta l) - k_x, \pi/(2\Delta l) - k_y, \pi/(2\Delta l) - k_z]^T$ exist. Spurious modes with a wavelength in the neighbourhood of $2\Delta l$ have the same propagation characteristics as the physical modes. Due to the ambiguity of the low–frequency solution in TLM with condensed symmetric node, the three–dimensional FDTD method exhibits advantages over the TLM method with condensed symmetric node with respect to the dispersion characteristics.

Calculating a two–dimensional problem in a three–dimensional TLM mesh with condensed symmetric nodes, the three–dimensional mesh can be replaced by a two–dimensional TLM mesh with nodes which have short–circuited stubs of the length $\Delta l/2$ in the direction of the third dimension [1]. These stubs compensate for the higher mesh pulse velocity in the three–dimensional mesh in comparison with the mesh pulse velocity of the two–dimensional TLM method. At low frequencies, the three–dimensional mesh for two–dimensional problems with a mesh pulse velocity $c_m = 2\,c$ behaves in the same way as a two–dimensional mesh with $c_m = \sqrt{2}\,c$. However, the dispersion characteristics of the three–dimensional mesh with condensed symmetric nodes differs also for two–dimensional problems from the dispersion characteristics of the two–dimensional mesh. This fact indicates that two–dimensional TLM and three–dimensional TLM with condensed symmetric node are numerical methods with a different relationship to Maxwell's equations.

This work has been supported by the Deutsche Forschungsgemeinschaft.

References

[1] W.J.R. Hoefer, "The Transmission Line Matrix (TLM) Method", Chapter 8 in "Numerical Techniques for Microwave and Millimeter Wave Passive Structures", edited by T. Itoh, J. Wiley, New York, 1989, pp. 496-591.

[2] G. Kron, "Equivalent Circuit of the Field Equations of Maxwell I", Proc. IRE, vol. 32, pp. 289 - 299, May 1944.

[3] P.B. Johns, "A Symmetrical Condensed Node for the TLM–Method", IEEE Trans. Microwave Theory Tech., vol. MTT-35, no. 4, pp. 370-377, April 1987.

[4] R.F. Harrington, "Field Computation by Moment Methods", Krieger Publishing Company, Inc., Malabar, Florida, 1982.

[5] P. Russer, M. Krumpholz, "The Hilbert Space Formulation of the TLM Method", International Journal of Numerical Modelling : Electronic Networks, Devices and Fields, vol. 6, issue no. 1, pp. 29-45, February 1993.

[6] M. Krumpholz, P. Russer, "Discrete Time–Domain Green's Functions for Three–dimensional TLM Modelling of the Radiating Boundary Conditions", ACES 1993, Monterey, CA, pp. 458-466, March 1993.

[7] K.S. Yee, "Numerical Solution of Initial Boundary Value Problems Involving Maxwell's Equations in Isotropic Media", IEEE Trans. on Antennas and Propagation, vol. AP-14, no.3, pp. 302-307, May 1966.

[8] D.H. Choi, W.J.R. Hoefer, "The Finite–Difference Time–Domain Method and its Applications to Eigenvalue Problems", *IEEE Trans. Microwave Theory Tech.*, vol. MTT–34, no. 12, pp.1464–1470, 1986.

[9] D.M. Sheen, S.M. Ali, M.D. AAbouzahra, J.A. Kong "Application of the Three–Dimensional Finite–Difference Time–Domain Method to the Analysis of Planar Microstrip Circuits", *IEEE Trans. Microwave Theory Tech.*, vol. MTT–34, no. 12, pp.1464–1470, 1986.

[10] L.N. Trefethen "Group Velocity in Finite Difference Schemes", SIAM Review, vol.24, no.2, April 1982.

[11] D.R. Lynch, K.D. Paulsen, "Origin of Vector Parasites in Numerical Maxwell Solution", IEEE Trans. Microwave Theory Tech., vol. MTT-39, no.3, pp. 383-394, March 1991.

[12] J.S. Nielsen, "TLM Analysis of Microwave and Millimetre Wave Structures with Embedded Nonlinear Devices", Ph.D. dissertation, University of Ottawa, 1992.

[13] J.S. Nielsen, W.J.R. Hoefer, "A Complete Dispersion Analysis of the Condensed Node TLM Mesh", IEEE Trans. Magnetics, vol. 27, no.5, pp. 3982-3985, September 1991.

[14] M. Krumpholz, P. Russer, "On the Dispersion in TLM and FDTD", to be published in the IEEE MTT.

[15] M. Krumpholz, P. Russer, "A Generalized Method for the Calculation of TLM Dispersion Relations", proceedings of the 23th EMC, Madrid, September 1993.

[16] P.A.M. Dirac, "Quantum Mechanics", fourth edition, Oxford University Press, Oxford.

[17] M. Krumpholz, P. Russer, "A Field Theoretical Derivation of TLM", to be published in the IEEE MTT.

[18] M. Krumpholz, P. Russer, H. Zscheile, "The Derivation of the Condensed Symmetric TLM Node from Maxwell's Equations", PIERS 1993, Pasadena, CA, p. 150, July 1993.

[19] R.E. Collin, "Field Theory of Guided Waves", second edition, IEEE Press, Inc., New York, 1991, pp. 184-192.

[20] M. Krumpholz, P. Russer, "Two-dimensional FDTD and TLM", submitted to the International Journal of Numerical Modelling.

[21] J.A. Kong, "Electromagnetic Wave Theory", J.Wiley, New York, 1986, p. 368.

[22] J.C.Strikwerda, "Finite Difference Schemes and Partial Differential Equations", *Wadsworth & Brooks, Pacific Grove*, 1989.

[23] K.E. Gustafson, "Partial Differential Equations and Hilbert Space Methods", second edition, J. Wiley, New York, 1987, pp. 176.

[24] N.R.S. Simons, E. Bridges, "Equivalence of Propagation Characteristics for the TLM and FDTD Methods in Two Dimensions", IEEE Trans. Microwave Theory Tech., vol. MTT-39, no.2, pp. 354-357, February 1991.

TLM MODELLING OF GUIDING AND RADIATING MICROWAVE STRUCTURES

Wolfgang J.R. Hoefer

NSERC/MPR Teltech Research Chair in RF Engineering,
Department of Electrical and Computer Engineering,
University of Victoria, Victoria, B.C., Canada V8W 3P6
Tel: (604) 721-6030, Fax: -6230, E-Mail: WHoefer@ece.uvic.ca

ABSTRACT

This paper provides an overview of new developments, recent progress, and future trends in modelling and simulation of electromagnetic structures with the TLM method. The following aspects are featured: New theoretical developments, high performance absorbing boundaries, computer implementation and validation, and design and optimisation techniques using TLM.

1 INTRODUCTION

In recent years, discrete time domain modelling of electromagnetic fields has reached a high level of sophistication. The prominence of time domain methods is due partly to the increasing number and complexity of problems that have been successfully solved with this approach, and partly to the rapid growth in computer power available to practitioners. These developments have attracted a large constituency of researchers eager to join this exciting new field, a trend that has resulted in a rising tide of new ideas, publications, and computer software. The present Workshop is a case in point.

Finite Difference - Time Domain (FD-TD) methods are extremely popular because they are obtained by directly discretizing Maxwell's or Helmholtz's equations and thus, evolve naturally from classical electromagnetic theory. Among them, the approach formulated by Yee in 1966 [1] is very popular among practitioners in the areas of electromagnetic scattering and propagation. It is based on a discretization of Maxwell's two curl equations which are solved stepwise in a leapfrog fashion. In contrast, Transmission Line Modelling (TLM) - invented by Johns and Beurle in 1974 [2] - employs a spatial transmission line network or mesh, ie. another physical system; its wave properties emulate those of continuous space as the mesh discretization approaches the infinitesimal limit. Time domain modelling is performed by exciting the TLM network with Dirac-like voltage impulses and tracking their scattering throughout the network on a computer.

In all time domain methods, frequency domain characteristics are extracted from the time response by Fourier transform.

There are many similarities between FD-TD and TLM methods, but the main difference is that FD-TD schemes employ discretized differential (or integral) equations, while TLM algorithms are based on a scattering formulation.

TLM algorithms have been described extensively in the literature. In the following, we will thus focus on more recent generalizations of TLM algorithms, on the computer

implementation and validation of TLM, on absorbing boundaries and finally, on microwave design and optimisation techniques using TLM.

2 NEW THEORETICAL DEVELOPMENTS IN TLM

2.1 Rectangular Mesh TLM Algorithms

One of the limitations of traditional mesh algorithms is their restriction to square (in the 2D case) or cubic elementary cells. The aspect ratio of cells can, of course, be changed within limits by introducing impulse-delaying techniques in the form of stubs or impulse storage, but these techniques require additional computer resources and introduce unwanted dispersion errors. This is a drawback when modeling guiding structures in which the transversal and longitudinal components of the propagation vector differ considerably in magnitude. When discretizing such structures for numerical modelling one would thus prefer a scheme which allows for different discretization steps which are commensurate with the required resolution of the fields. Consider, for example, a microstrip line with rather small transverse dimensions and fine features such as finite metallizaton thickness and thin dielectric layers. In such a case the discretization must be much finer in the transverse than in the longitudinal directions. Traditional TLM schemes which are based on square mesh size [2], [3] become very uneconomical in such cases because they impose essentially the same mesh dimensions in both transversal and longitudinal direction.

This has motivated the development of new TLM models with mesh cells of arbitrary aspect ratio [4]. In two space dimensions, isotropic propagation space can thus be modeled by a rectangular anisotropic mesh as well as by a square mesh. To illustrate this point, Fig. 1 shows equivalent square and rectangular 2D TLM shunt meshes side-by-side (aspect ratios $\alpha = 1$ and $\alpha = \frac{1}{2}$, respectively). The same ideas have been applied to 3D TLM schemes and will be published shortly.

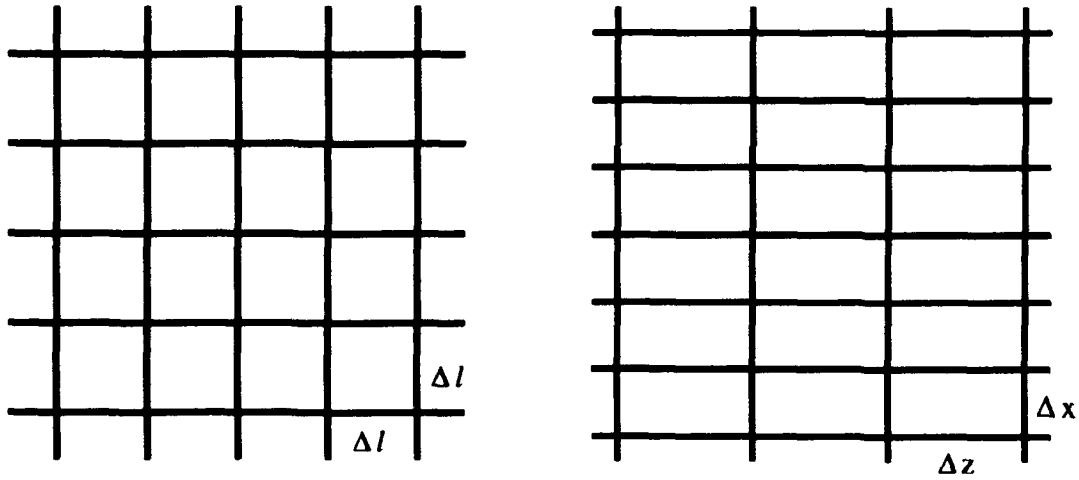

Fig. 1 Square mesh ($\alpha = 1$) and equivalent rectangular TLM mesh ($\alpha = \frac{1}{2}$). The aspect ratio is defined as $\alpha = \Delta x/\Delta z$

The desired properties of the rectangular mesh are the following:

Property 1: Impulse Synchronism:

The velocities of impulses on the dispersionless link lines must be such that the transit time Δt is the same for all lines. This implies that the line velocities must be proportional to the line lengths:

$$\frac{v_x}{v_z} = \frac{k_z}{k_x} = \frac{\Delta x}{\Delta z} = \alpha \tag{1}$$

where α is the aspect ratio of the rectangular cell.

Property 2: Isotropic Wave Properties:

In the infinitesimal limit ($\Delta x,\ \Delta z \ll \lambda$), the plane wave network velocity v_n must be the same in x and z-directions (as opposed to the line velocities v_x and v_z which are different in view of the synchronism requirement). This implies:

$$v_{nx} = v_{nz} \quad and \quad k_{nx} = k_{nz} \tag{2}$$

This property must hold for all aspect ratios α. (At higher frequencies where $\Delta x,\ \Delta z$ are no longer very small compared to λ, these equalities fail due to dispersion errors which occur as a result of the finite mesh size).

It can be shown that both conditions are satisfied if the inductances and capacitances per unit length, and the characteristic impedances of the mesh lines have the following ratios:

$$\frac{L_x}{L_z} = \alpha \quad ; \quad \frac{C_x}{C_z} = \frac{1}{\alpha^3} \quad ; \quad \frac{Z_{0x}}{Z_{0z}} = \frac{Y_{0z}}{Y_{0x}} = \frac{\sqrt{L_x C_z}}{\sqrt{L_z C_x}} = \alpha^2 \tag{3}$$

The general dispersion relation which governs the relationship between the propagation vectors in the network ($k_{nx},\ k_{nz}$) and in free space (k_0), is

$$cos(k_{nx}\Delta x) + \alpha^2 cos(k_{nz}\Delta z) = 2cos(k_0 \Delta l) \tag{4}$$

where Δl is the equivalent square mesh parameter defined as

$$\Delta l = \Delta x \sqrt{\frac{2}{1+\alpha^2}} = \Delta z \sqrt{\frac{2}{1+\frac{1}{\alpha^2}}} \tag{5}$$

The dispersion for arbitrary propagation directions is illustrated in Fig. 2 (dispersion circle). The magnitude of the normalized propagation vector is plotted vs. the angle it forms with the z-axis. In the infinitesimal limit, the locus described by this vector is the unit circle. However, for a rather coarse discretization of $\Delta z/\lambda = 0.15$ the vector becomes larger in the axial directions, and more so along the longer mesh dimension Δz. For comparison, the same function has been plotted for the *"equivalent square mesh"* defined in Eq. (5) above. Note that there is no dispersion when the propagation vector forms an angle $\phi = arc\ tan\ \frac{1}{\alpha}$ with the z-axis. This can be verified by analyzing Eq.(4). For a square mesh ($\alpha = 1$) this angle becomes 45° as expected.

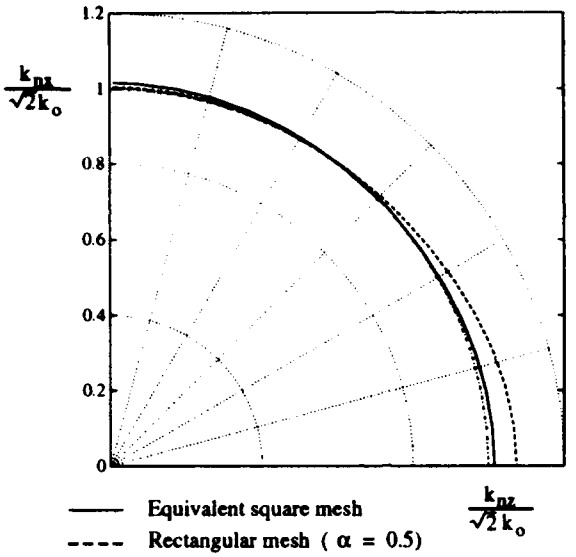

Fig. 2 Dispersion in arbitrary direction in a square and in a rectangular mesh ($\alpha = 0.5$, $\Delta z/\lambda_0 = 0.15$)

It is thus possible to define a family of rectangular mesh elements which all have the same impulse transit time and identical phase velocity in all directions. Their dimensions all satisfy Eq. 5. Fig. 3 shows such a family of equivalent mesh elements. Unfortunately, only one of these elements can be used at a time to discretize a homogeneous structure, because different elements do not fit together geometrically. This leads to the need for additional stubs to equalize phase velocities in elements of different aspect ratios, as discussed by Al-Mukhtar and Sitch [5], which have either the same width or the same length so that they can be connected together.

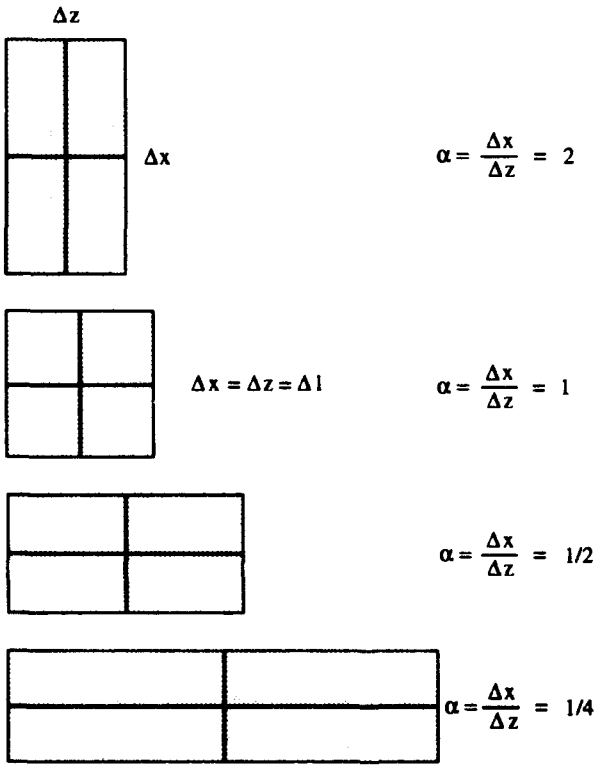

Fig. 3 Family of rectangular mesh elements having identical impulse transit time and phase velocity

2.2 Modelling of Layered Inhomogeneous Dielectrics

So far we have only considered the modelling of homogeneous media by a uniform rectangular mesh. We will now extend these concepts to inhomogeneous structures. In particular, we consider guiding structures which are uniform in propagation direction, but contain two or more dielectric layers. In such structures, the propagation vector tangential to the dielectric interface is the same in all subregions, but different in normal direction. It follows that the discretization in tangential direction should be the same in both media, while the normal discretization should be finer in the higher permittivity region.

Consider, as an example, the two-layer structure in Fig. 4.

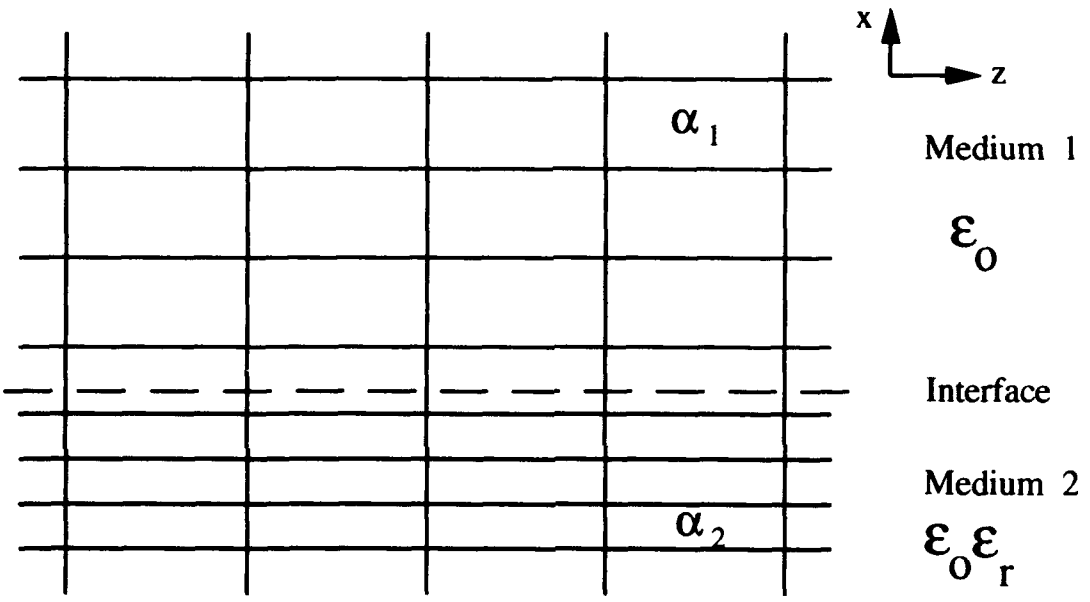

Fig. 4 Rectangular mesh discretization of a two-layered dielectric

We will now determine the required mesh aspect ratio α_2 in medium 2 as a function of the aspect ratio α_1 in medium 1 and the relative dielectric constants in both media.

Again we want to ensure that the network velocity is isotropic in both sub-meshes and equal to $c/\sqrt{2}$ and $c/\sqrt{2\epsilon_r}$, respectively. Thus, for propagation in x-direction we have:

$$\textit{in medium 1}: \quad v_{nx_1} = v_{x_1}\frac{1}{\sqrt{1+\alpha_1^2}} = \frac{c}{\sqrt{2}} \tag{6}$$

$$\textit{in medium 2}: \quad v_{nx_2} = v_{x_2}\frac{1}{\sqrt{1+\alpha_2^2}} = \frac{c}{\sqrt{2\epsilon_r}} \tag{7}$$

Similarly, for propagation in z-direction we have:

$$\textit{in medium 1}: \quad v_{nz_1} = v_{z_1}\frac{1}{\sqrt{1+\frac{1}{\alpha_1^2}}} = \frac{c}{\sqrt{2}} \tag{8}$$

$$\textit{in medium 2}: \quad v_{nz_2} = v_{z_2}\frac{1}{\sqrt{1+\frac{1}{\alpha_2^2}}} = \frac{c}{\sqrt{2\epsilon_r}} \tag{9}$$

As Fig. 4 indicates, the line velocities v_{x_1} and v_{x_2} must be equal in order to preserve the impulse synchronism. Thus, Eqs. (8) and (9) yield

$$\frac{1+\frac{1}{\alpha_2^2}}{1+\frac{1}{\alpha_1^2}} = \epsilon_r \tag{10}$$

Hence, the relative permittivity of the dielectric determines the aspect ratio α_2 in the dielectric once α_1 has been selected, and vice versa. Note that this approach permits us to model inhomogeneous layered dielectrics without the use of stubs. Furthermore, since the transverse mesh size is reduced in the electrically denser medium, dispersion normal to the interface is reduced accordingly.

We still must ensure that the interface condition is satisfied by this model as well. This amounts to determining the characteristic impedances of the x-directed mesh lines, Z_{0x_1} and Z_{0x_2}, in such a way that the network intrinsic impedances Z_{nx_1} and Z_{nx_2} have a ratio

$$\frac{Z_{nx_1}}{Z_{nx_2}} = \sqrt{\epsilon_r} \tag{11}$$

where we have assumed that both subregions have the same permeability μ_0, and subregion 1 is free space. Since these impedances are defined in both regions as follows [4]:

$$Z_{0x} = \sqrt{\frac{L_x}{C_x}} \tag{12}$$

and

$$Z_{nx} = \sqrt{\frac{L_x}{C_x(1+\alpha^2)}} \tag{13}$$

we can write in view of Eq. 10 that

$$\frac{Z_{0x_1}}{Z_{0x_2}} = \frac{\alpha_1}{\alpha_2} \tag{14}$$

which means that the impulse scattering at the interface must be accounted for in the algorithm in a way similar to that described in [6] for dual modelling of inhomogeneous structures.

3 HIGH PERFORMANCE ABSORBING BOUNDARY CONDITIONS

In order to exploit the full inherent bandwidth of a TLM simulation, high performance absorbing boundary conditions are crucial. "High performance" means that such boundaries must be numerically stable, and capable of absorbing hybrid fields over a very wide frequency range with a very low return loss. Two types of boundary conditions have been developed and tested extensively for TLM applications: a) Multi-modal Johns matrix absorbing boundaries for separable structures such as homogeneous waveguides [7]; b) Second and third-order one-way boundary conditions based on Higdon's scheme for non-separable structures [8],[9]. Examples are inhomogeneous waveguides such as microstrip, finline and coplanar lines, or antenna problems.

3.1 Multi-Modal Johns Matrix Absorbing Boundaries

The method of absorbing the dominant mode in a waveguide using the numerical convolution of the incident impulses at the center of the waveguide with a modal impulse response of a semi-infinite waveguide has been described in detail in [6],[10], and implemented in the 2D-TLM simulator software included in [6]. This is possible because in uniform waveguides with homogeneous dielectric the transverse field distribution is independent of frequency and hence, of the time behaviour of an electromagnetic signal. This approach can be extended to higher order modes as well. In a linear environment, an overmoded signal can therefore be separated into modes which may be absorbed individually by an appropriate boundary condition. The dominant and higher order modal impulse responses (modal Johns matrices) are determined either by a recursive TLM analysis of a waveguide slice [10], or by discretizing the analytical Green's function of the structure (if it is known). The latter approach will be discussed in more detail later in this Workshop [11]. To this end the field incident upon the boundary is spatially Fourier transformed to obtain the amplitudes of the modes contained in it. Each modal impulse stream is then convolved numerically with its corresponding Johns matrix term, and the result is recombined and injected back into the TLM computational domain at the boundary [7]. The process is schematically represented in Fig. 5.

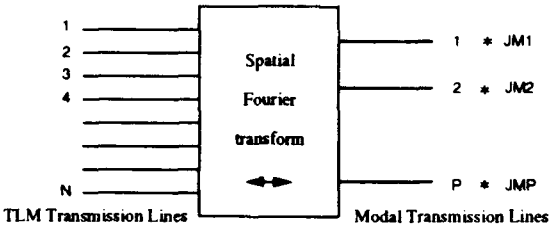

Fig. 5 Network representation of the transformations between the TLM transmission lines in the physical structure and the fictitious uncoupled modal transmission lines which are terminated by modal Johns matrices

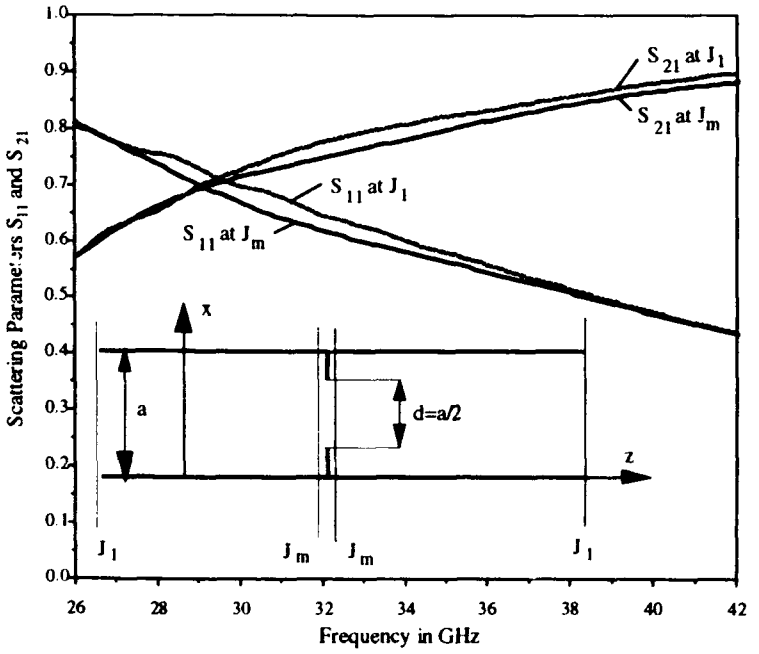

Fig. 6 Scattering parameters of an inductive iris in rectangular waveguide using single-mode Johns matrix ABC's at reference planes J_1 and multi-mode Johns matrix ABC's at J_m.

Since the modal Johns matrix is diagonal, this procedure is extremely efficient. Furthermore, such a boundary may be placed very near a discontinuity since it absorbs higher order modes even if they are below cutoff. In this way the computational domain can be dramatically reduced (typically by a factor ten) in return for inclusion of a few higher order modes in the boundary model. Fig. 6 demonstrates such an arrangement and shows S-parameters computed for an inductive iris in a rectangular waveguide [7].

3.2 One-Way Absorbing Boundary Conditions

Structures with inhomogeneous cross-sections such as partially dielectric-filled transmission lines cannot be terminated in this way since the modal transverse field distributions are frequency dependent. Structures of this type are best terminated with absorbing boundaries modelled by one-way equations known from Finite Difference - Time Domain models. We have adapted Higdon's scheme [12] for TLM applications. However, we apply the boundary operators to the reflected impulses rather than the total field values in front of the boundary. In the 3D Condensed Symmetrical Node scheme, it can be applied simultaneously to both polarizations of the boundary arm, resulting in the boundary condition being imposed simultaneously on the tangential electric and magnetic fields (similar to the principle of superabsorption known from FD-TD approaches). One of the principal problems affecting one-way boundary conditions in Symmetrical Condensed Node TLM is the presence of low-frequency spurious modes which are excited at discontinuities and which are amplified by the boundary operators due to their high spatial frequency. We have found that the numerical stability of the differential boundaries could be considerably improved by a judicious determination of their characteristic parameters [8].

The performance of a third-order Higdon-type absorbing boundary in a microstrip line is demonstrated in Fig. 7.

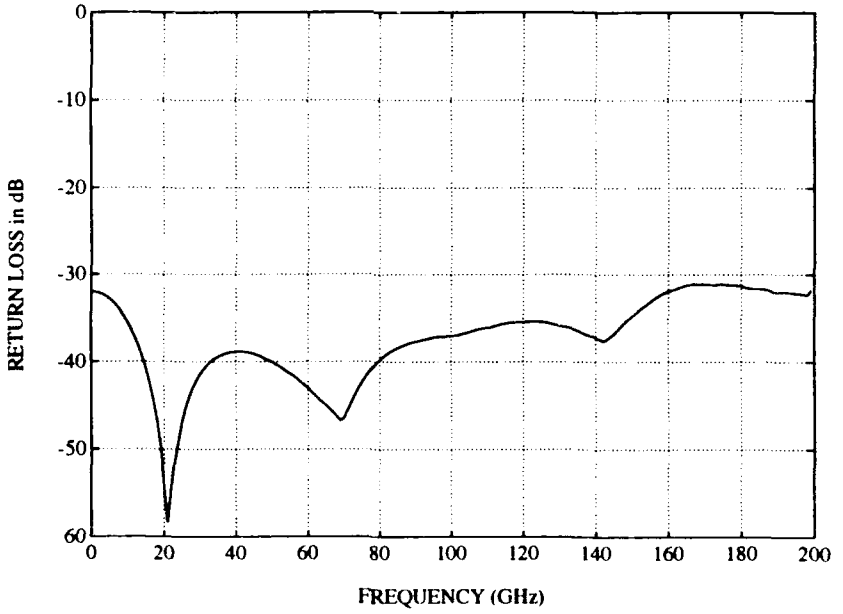

Fig. 7 Return loss of a third-order Higdon absorbing boundary condition in an open microstrip with the following characteristics: ϵ_r = 10.2, w = 0.508 mm, h = 0.635 mm).

The boundary has a return loss better than 30 dB from 0 to 200 GHz, a range that exceeds by far the dominant operating range of the line. It is thus appropriate for absorbing very

short transients and for nonlinar modelling where higher harmonic frequencies must be properly terminated. Such boundaries also work well in waveguides of homogeneous cross-section, and they may be used as free-space radiating boundaries in antenna modelling [9]. Fig. 8 shows the return loss of a microstrip patch antenna computed with variable-mesh SCN 3D-TLM and employing a stabilized second order Higdon absorbing boundary (see [9] for details of the computation]. The TLM result is in good agreement with results obtained by Wu et al. [13] with the spectral domain technique.

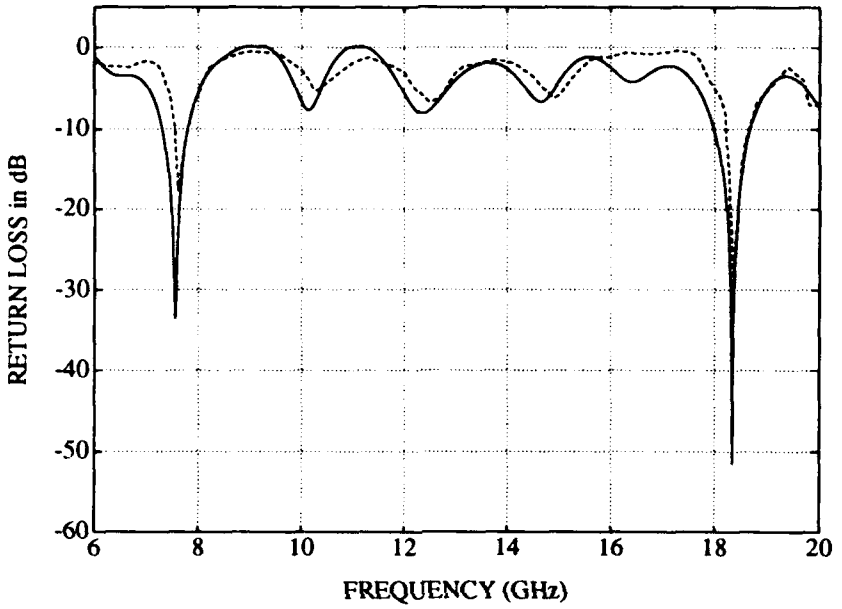

Fig. 8 Return loss of a microstrip patch antenna using second-order Higdon absorbing boundary conditions in the microstrip feed line and the remaining walls [9]. TLM results compare well with spectral domain results (dotted line) published by Wu et al. [13].

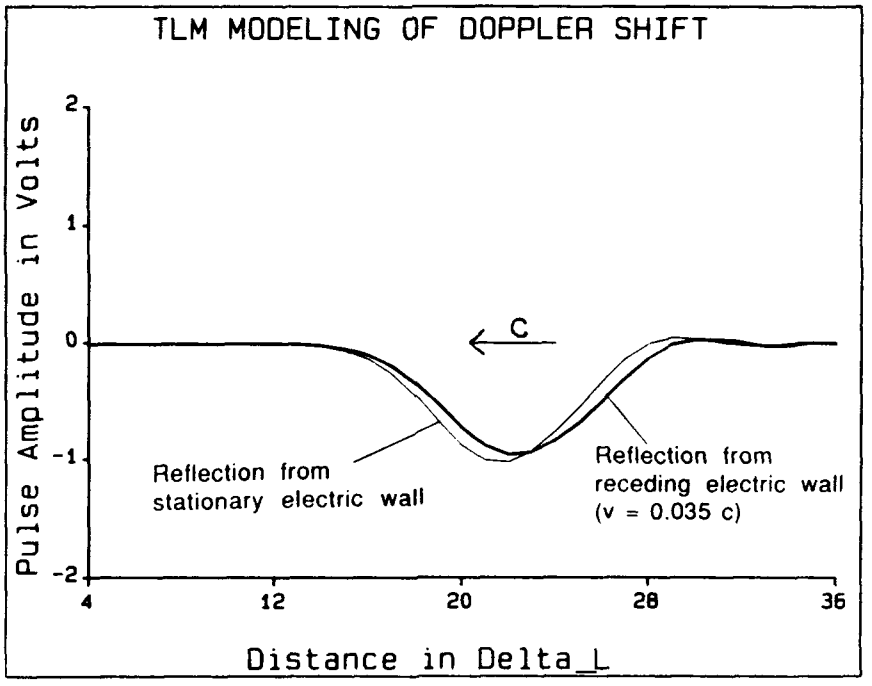

Fig. 9 Reflection of a Gaussian pulse from a moving (receding) electric wall, simulated with TLM.

4 REFINEMENTS IN BOUNDARY MODELLING

Since the dispersion of the three-dimensional condensed node mesh is almost negligible, it is preferable to maintain a uniform Cartesian grid throughout the computational domain and modify the properties of the mesh only in the vicinity of features that create strong local non-uniformities, or that are not conformal to the grid. Examples are sharp corners, edges, and slanted or curved boundaries. A number of techniques for local mesh modification have been developed recently. They include special cornernodes and edge nodes [14]-[16], or extension of boundary positions using signal processing [17],[18]. In the first approach, the impulse scattering parameters of boundary nodes are modified to account for the modification in the boundary position. The second approach is implemented by processing the signal reflected by the boundary. Since these modifications can be updated at every time step, they allow also the modelling of moving boundaries. Fig. 9 shows the delay and broadening of a Gaussian pulse reflected by a conducting boundary that is moving away from the source at a speed of 0.035c. The modification of the pulse shape results in the Doppler shift of its spectrum. These techniques of modifying wall positions during a TLM simulation can be used for boundary adjustments in optimization problems.

5 COMPUTER IMPLEMENTATION AND VALIDATION OF TLM

TLM being a computationally intensive numerical technique, proper implementation of algorithms is essential to ensure optimal use of computational resources. Furthermore, a user-friendly interface and compatibility with other CAD tools are important aspects. Programming is therefore performed preferably in C++ language on computers which incorporate special graphic processing hardware in order to free the main memory for TLM computation. Particularly impressive computational speeds can be obtained with SIMD-type massively parallel processors such as the Connection Machine or the DEC 12000 (MasPar). In 2D simulations, each processor can be associated with one TLM node, and all nodes are updated simultaneously, while in 3D the computer can process one vertical or horizontal slice of the structure at a time. Typically, a parallel computer with 8K processors is able to perform 250,000 three-dimensional scatterings per second. Table 1 compares the performance of various well-known computer platforms when solving a 2D problem with 128x64 mesh cells and 4,000 iterations.

Computers	CPU time in seconds	2D scatterings/second
Toshiba PC, Model T5200/100	6,500	5,000
IBM Model 90 XP486	1,250	26,000
DEC RISC, Model 5100	352	93,000
IBM RS6000, Model 350	117	280,000
HP 9000, Series 7000, Model 755	88	370,000
DECmpp 12000 with 8K processors	12	2,730,000

Table 1 Execution time and scatterings per second for a 2D-TLM simulation on various computers. The problem comprizes 128 x 64 mesh cells and 4000 iterations.

Validation of computer codes is an important issue. To demonstrate the accuracy that can be achieved with TLM, Fig. 10 shows the S-Parameters of a waveguide filter computed with TLM, together with results computed with two different mode-matching methods [19]. These results are in excellent agreement. More validation results will be shown during the Workshop presentation.

6 CIRCUIT DESIGN AND SYNTHESIS WITH TLM

Design and synthesis of electromagnetic structures are the ultimate engineering applications of a modelling technique. Two possible approaches to this theme have been demonstrated with TLM. The first - more classical - approach combines time domain field analysis controlled by an optimization program. By using datapipe techniques the TLM analysis can be performed on a powerful processor such as MasPar or the Connection Machine [20], or the task can be divided among several workstations, as will be discussed in another Workshop paper [21].

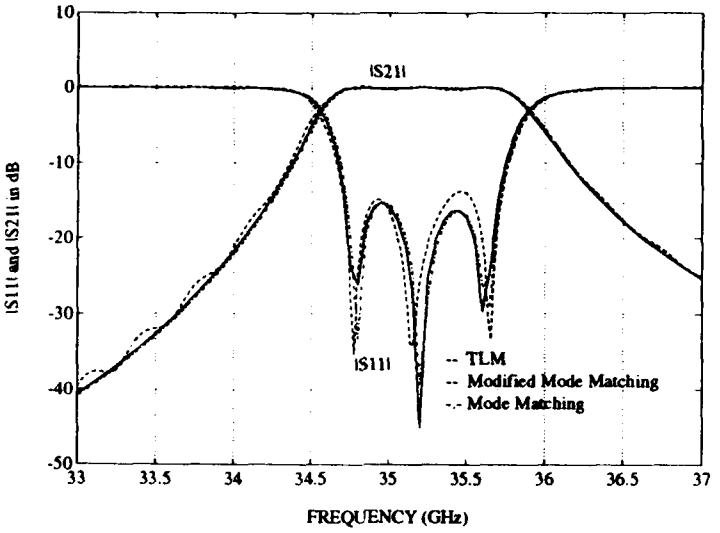

Fig. 10 S-Parameters of a waveguide filter computed with TLM and with mode matching methods

Fig. 11 sketches an arrangement which combines OSA90/hope with a TLM Electromagnetic Field Simulator [20]. The optimization is performed on a workstation which pipes updated geometrical data to a massively parallel computer. The new structure is then analyzed in the time domain with TLM, S-parameters are extracted by Fourier transform and piped back to the optimizer. This process permits design without the need for equivalent circuit representation and includes all parasitic effects. It is also much more flexible as far as geometrical complexity is concerned.

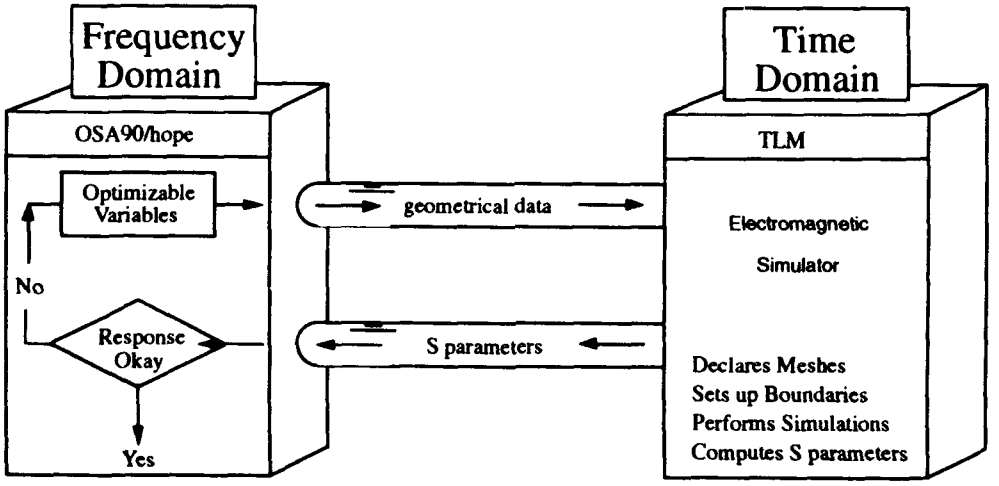

Fig. 11 Design by TLM electromagnetic field analysis controled by an optimization program: OSA90/hope and TLM communicate through UNIX high speed datapipe

The other approach makes use of time reversal to synthesize a structure geometry directly from its desired frequency response. This process is similar to inverse time domain scattering.

The reconstruction of a scatterer from the known scattered field is demonstrated in Fig. 12 by a simple example. A diamond-shaped conducting obstacle is placed in a parallel plate waveguide. A uniform plane wave excitation with a Gaussian time profile is injected into the structure from the left side. The time response is picked up at all points of the absorbing walls at the left and the right. From this response (total field solution) is subtracted the response of the empty guide to the same excitation (homogeneous solution), yielding the scattered field (particular solution). The latter is then re-injected in reverse time sequence at these boundaries into the empty waveguide, and the resulting field distribution in the guide is is processed, for example by finding the minimum of the Pointing vector profile in the computational domain. We can thus reconstruct the exact shape of the scatterer within the resolution of the TLM grid, as shown in Fig. 12.b.

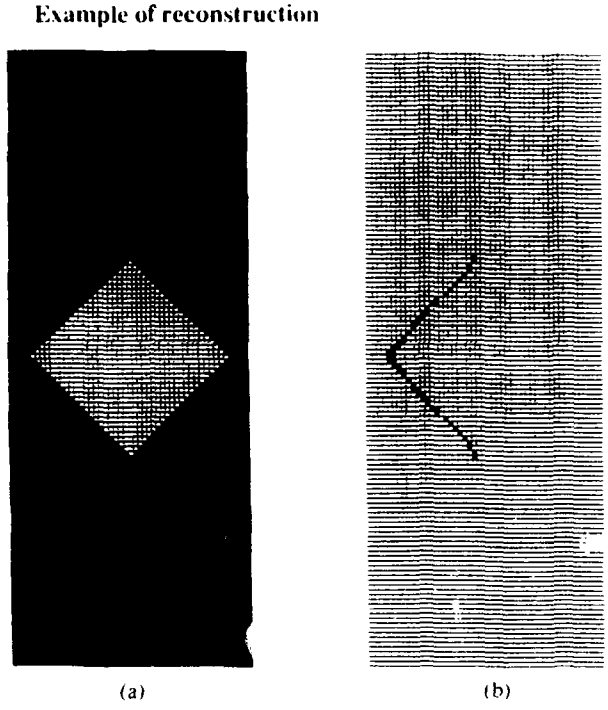

Fig. 12 Example of shape reconstruction of a metallic obstacle in a parallel plate waveguide through time inversion. (a) Shape of the scatterer, (b) reconstructed shape of left side of the obstacle. The electric field is perpendicular to the paper.

The principle of synthesis of electromagnetic structures by time inversion is the following: Since the sources of a scattered field reside on the surface of the scatterer, this reverse process allows us to construct the geometry of scatterers from a desired scattered field response. This procedure is not unique, but the difficulties associated with the non-unicity of the inverse problem can be removed by selecting *a priori* an approximate topology which has the desired geometrical features of the structure we want to design. These features are then mapped into the time domain by a forward TLM analysis. The Fourier transform of this response is subsequently modified in the lower frequency range (operating range) of the structure, while the high frequency content (which defines

the shape of the structure) is preserved. The updated and processed time response is then injected back in reverse time sequence into the computational domain to yield an improved topology. The analysis-synthesis cycle can be repeated until the desired response is achieved. Experience has shown that such a process converges very quickly, typically after two or three cycles only [21],[22].

The flowchart of this process is given in Fig. 13. It is much faster und more efficient than optimization by repeated forward analysis.

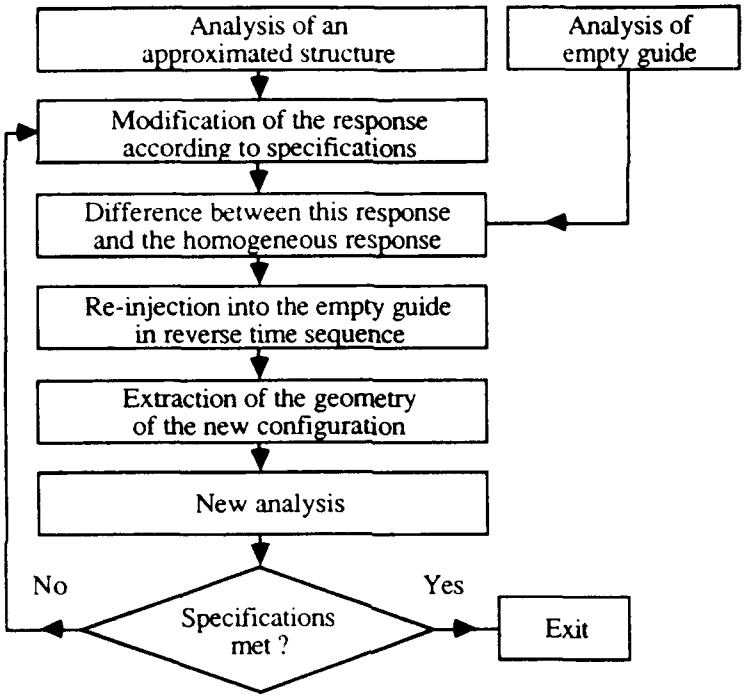

Fig. 13 Algorithm of the synthesis method using alternate forward and backward-in-time TLM processes.

The process is best clarified by means of a simple example. Suppose we want to synthesize a shunt inductance in a parallel plate waveguide. The specification given to us are then the S-Parameters of a shunt inductance in the frequency domain (Fig. 14.a)

There are many ways of realizing a shunt inductance in a waveguide - the solution is not unique. We must choose a basic topology. We select a centered thin transverse septum and guess its width required to yield the desired inductance, say 41 Δl (Fig. 14.b). The approximate dimensions can be found in many cases from closed-form expressions, given in the literature, which link the dimensions of discontinuities to their equivalent lumped element circuits. An educated guess is also fine.

The approximate structure is then analyzed forward-in-time, and the dominant mode content of the first response is extracted (Fig. 14.c). We see that S_{11} is already quite close to specifications, but S_{21} is not. We thus replace the low-frequency part of S_{21} by the desired (green) characteristic and keep the high frequency content the same. The modified total reponse is then converted back into the time domain and, reduced by the homogeneous response of the empty waveguide, re-injected into the computational domain in the inverse time sequence. The resulting synthesized scatterer geometry is an obstacle of width 31 Δl.

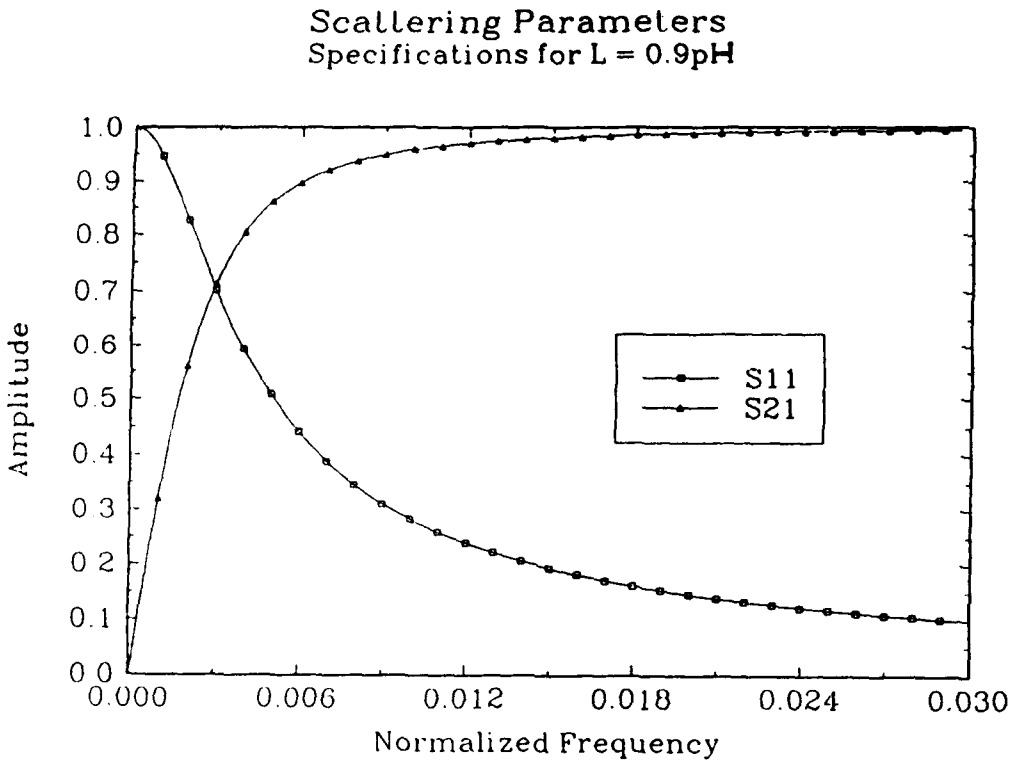

Synthesis of an inductive obstacle in a parallel plate waveguide

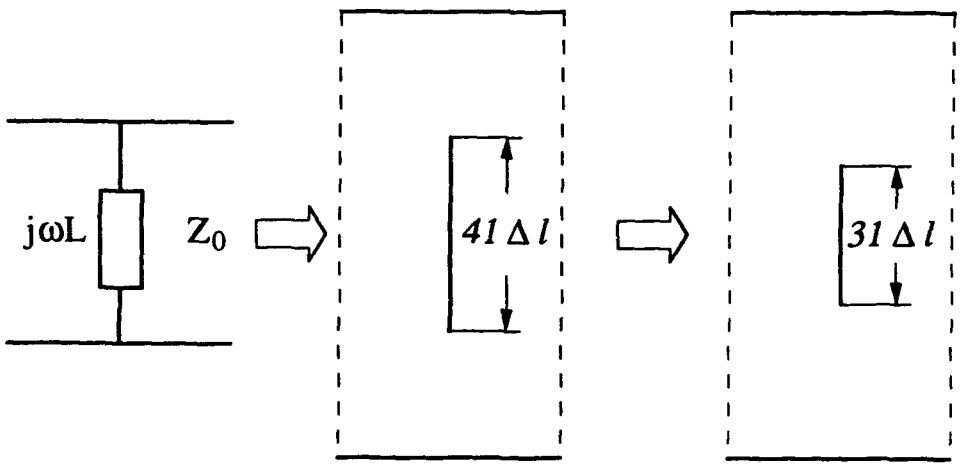

Fig. 12 (a) Desired S-parameters of a shunt inductance in a parallel plate waveguide; (b) possible topology for its practical realization.

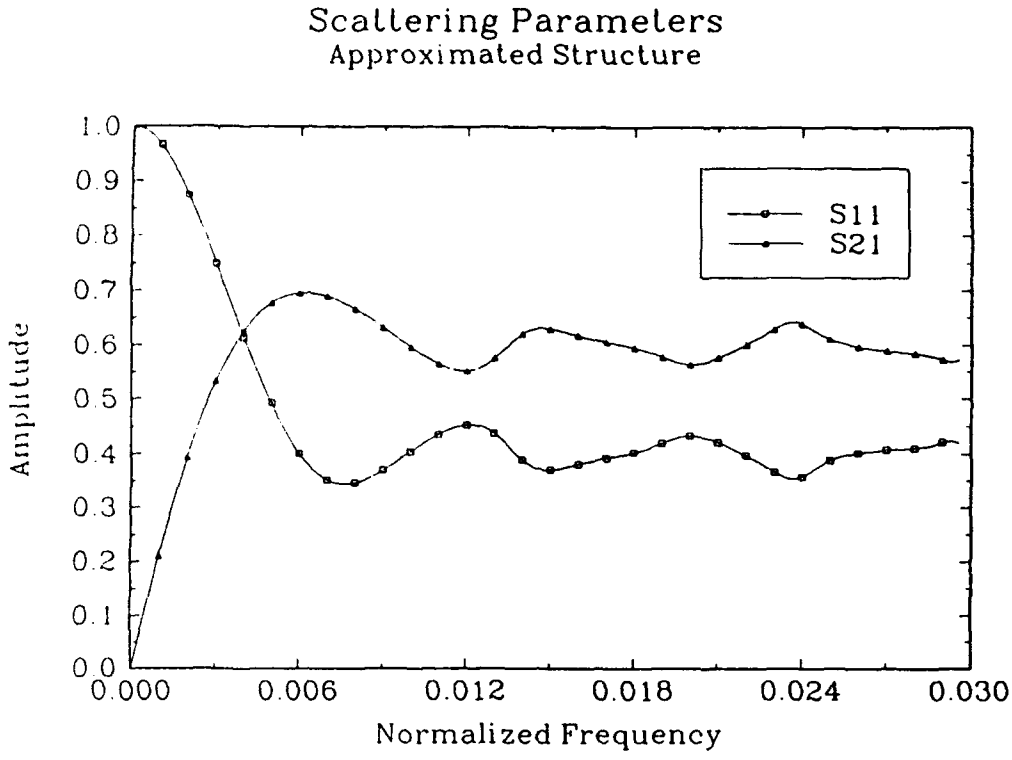

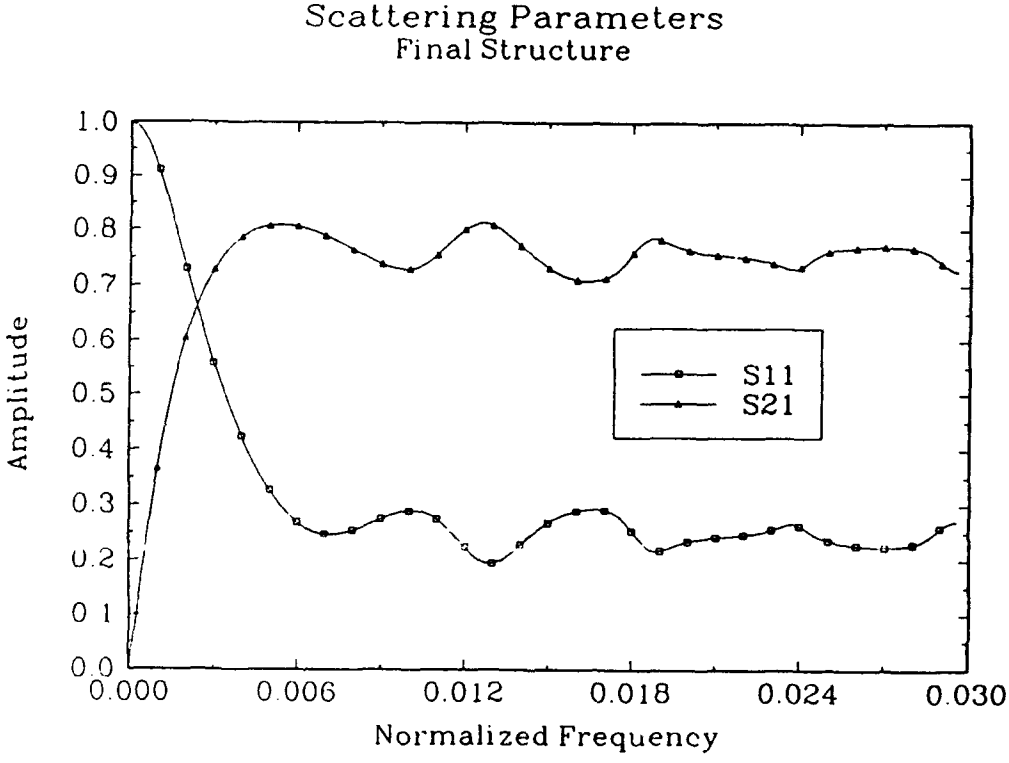

Fig. 12 continued (c) S-parameters obtained by analysis of the first guess of width 41 Δl ; (d) S-parameters obtained by analysis of the new geometry obtained by inverse time synthesis from the combination of the characteristics in Fig. 12.a and 12.c

A new analysis of this obstacle yields the S-Parameters shown in Fig. 14.d. Obviously, the result is much better for S_{21} now. If we are still not satisfied, we may repeat the synthesis cycle again.

7 CONCLUSION AND FUTURE TRENDS

While the important issues and numerous recent developments in TLM modeling could only be scanned very briefly in this Workshop paper, it is obvious that TLM has evolved into a powerful, accurate and numerically efficient tool for general purpose electromagnetic analysis, design and synthesis. However progress is still being made on many fronts. The most dynamic areas of development are: improvements in the basic TLM algorithms, refinement of high performance boundary modelling, implementation on massively parallel computers, combination of TLM with optimizers for direct geometry/field based CAD, and synthesis of structures by time reversal. Other important developments which have not been discussed in this Workshop paper include signal processing to reduce the required number of computation steps, and modelling of nonlinear and dispersive materials as well as of semiconductors. Given the rapid growth in computer performance and the increasing sophistication of TLM modelling it seems likely that TLM based electromagnetic simulators will soon become highly versatile and powerful engineering design tools indeed.

ACKNOWLEDGEMENTS

This work has been financially supported by the Natural Science and Engineering Research Council of Canada, MPR Teltech, and the Science Council of British Columbia.

REFERENCES

[1] K.S. Yee, "Numerical solution of initial boundary value problems involving Maxwell's equations in isotropic media", *IEEE Trans. Antennas Propagation*, vol. AP-14, no. 5, pp. 302-307, May 1966.

[2] P.B. Johns, and R.L. Beurle, "Numerical solution of 2-dimensional scattering problems using a transmission-line matrix", *Proc. IEE*, vol.118, no.9, pp. 1203-1208, Sept. 1971.

[3] W.J.R. Hoefer, "The Transmission Line Matrix (TLM) Method", Chapter 8 of "Numerical Techniques for Passive Microwave and Millimeter-Wave Structures," edited by T. Itoh, John Wiley & Sons, New York 1989, pp. 496-591.

[4] W.J.R. Hoefer, and P. Sautier, "Characteristics of the General Rectangular 2D-TLM Network", *International Journal of Numerical Modelling*, (Submitted).

[5] D. Al-Mukhtar, and J.E. Sitch, "Transmission line matrix method with irregularly graded space," *IEE Proc., Part H: Microwaves, Opt., Antennas*, vol. 128, pp. 299-305, Dec. 1981.

[6] W.J.R. Hoefer, and P.P.M. So, "The Electromagnetic Wave Simulator, A Visual Electromagnetics Laboratory based on the 2D TLM Method", *John Wiley & Sons*, Chichester, U.K., 1991.

[7]. M. Mongiardo, M. Righi, R. Sorrentino, and W.J.R. Hoefer, "Efficient TLM diakoptics for separable structures", *in 1993 IEEE Intl. Microwave Symp. Dig.*, pp. 425-428, Atlanta, Ga, June 14-18, 1993.

[8] C. Eswarappa, W.J.R. Hoefer, "Wideband absorbing boundary conditions using third order boundary operators for time domain TLM analysis", *in 1993 IEEE AP/S Symposium and URSI Meeting Dig.*, pp. 10-13, Ann Arbor, MI, June 27 - July 2, 1993.

[9] C. Eswarappa, W.J.R. Hoefer, "Absorbing boundaries for 3D-TLM modelling of microstrip patch antennas",*in 23rd European Microwave Conference Dig.*, pp. 291-292, Madrid, Spain, 6-9 Sept. 1993.

[10] P.P.M. So, C. Eswarappa, and W.J.R. Hoefer, "A two-dimensional TLM microwave field simulator using new concepts and procedures", *IEEE Trans. Microwave Theory Techniques*, vol. MTT-37, no. 12, pp. 1877-1884, Dec. 1989.

[11] M. Mongiardo, M. Righi, R. Sorrentino, and W.J.R. Hoefer, Rigorous and Fast Computation of Modal Johns Responses, *Second International Workshop on Time Domain Modelling of Fields and Networks* (this Digest), Berlin, October 28-29, 1993.

[12] R.L. Higdon, "Numerical absorbing boundary conditions for the wave equation," *Math. Comp.*, vol. 49, no. 179, pp. 65-91, July 1987.

[13] S. Wu, N.G. Alexopoulos, and O. Fordham, "Feeding structure contribution to radiation by patch antennas with rectangular boundaries", *IEEE Trans. on Antennas and Propagation*, vol. 40, no. 10, pp. 1245-1249, Oct. 1992.

[14] P.B. Johns, and G.F. Slater"Transient Analysis of Waveguides with Curved Boundaries," *Electronics Letters*, vol. 9, no. 21, 18th Oct. 1973.

[15] U. Mueller, P.P.M. So, and W.J.R. Hoefer, "The compensation of coarseness error in 2D TLM modeling of microwave structures", *in 1992 IEEE Intl. Microwave Symp. Dig.*, pp. 373-376, Albuquerque, NM, June 1-5, 1992.

[16] F.J. German , "Infinitesimally adjustable boundaries in symmetrical condensed node TLM simulations",*in 9th Annual Review of Progress in Applied Computational Electromagnetics Dig.*, pp. 482-490, Monterey, CA., 22-26 March, 1993.

[17] U. Mueller, A. Beyer, and W.J.R. Hoefer, "The implementation of smoothly moving boundaries in 2D and 3D TLM simulations", *in 1992 IEEE Intl. Microwave Symp. Dig.*, pp. 791-792, Albuquerque, NM, June 1-5, 1992.

[18] U. Mueller, A. Beyer, and W.J.R. Hoefer, "Moving Boundaries in 2D and 3D TLM Simulations Realized by Recursive Formulas", *IEEE Trans. Microwave Theory Techniques*, Vol. MTT-40, No. 12, pp. 2267-2271, Dec. 1992.

[19] W. Menzel, R. Sorrentino, C. Eswarappa, P.P.M. So, and W.J.R. Hoefer, "Analysis of a millimeter-wave filter using transmission line matrix and mode matching methods and comparison with measurements",*in 9th Annual Review of Progress in Applied Computational Electromagnetics Dig.*, pp. 289-296, Monterey, Ca, March 22-26, 1993.

[20] P.P.M. So, W.J.R. Hoefer, J.W. Bandler, R.M. Biernacki, and S.H. Chen, "Hybrid frequency/ time domain field theory based CAD of microwave circuits", *in 23rd European Microwave Conference Dig.*, pp. 218-219, Madrid, Spain, 6-9 Sept. 1993.

[21] P.P.M. So, and W.J.R. Hoefer, "Distributed Computing for Transmission Line Matrix Method", *Second International Workshop on Time Domain Modelling of Fields and Networks*, (this Digest), Berlin, October 28-29, 1993.

[22] M. Forest and W.J.R. Hoefer, "TLM synthesis of microwave structures using time reversal",*in 1992 IEEE Intl. Microwave Symp. Dig.*, pp. 779-782, Albuquerque, NM, June 1-5, 1992.

[23] W.J.R. Hoefer, and M. Forest, "TLM modelling of electromagnetic scattering in forward and inverse time sequence", *in 1992 International Symposium on Antennas and Propagation (ISAP) Dig.*. pp. 733-736, Sapporo, Japan, Sept. 22 - 25, 1992.

Modelling of Planar Microwave Structures in Frequency- and Time-Domain

R.Vahldieck

Laboratory for Lightwave Electronics, Microwaves and Communications (LLiMiC)
Dept. of Electrical and Computer Engineering
University of Victoria
Canada V8W 3P6

Abstract

This paper presents an overview of modelling microwave circuits in the time- and frequency-domain. The emphasis will be on modelling approaches which can be applied in the time-and frequency-domain without leaving the framework of one technique. This leaves only two pairs of methods: The finite difference (FD) method in the frequency domain with its time-domain counterpart, the time-domain FD (TDFD) method, and the transmission line matrix method in the time-domain (TDTLM) with its frequency-domain counterpart, the frequency-domain TLM (FDTLM). The latter method has been developed very recently and, in conjunction with a novel s-parameter extraction technique, represents a computationally very efficient numerical tool for frequency-domain analysis of microwave circuits. The discussion presented in this paper focusses on new developments in the FDTD method and the FDTLM.

Introduction

Time- and frequency-domain techniques are complementary tools in the analysis and design of microwave and optical integrated circuits. While time-domain methods are very useful for wideband applications like transient problems as well as for nonlinear analysis, frequency-domain techniques are computationally more efficient for the majority of microwave design problems, which are of comparatively narrow band nature.
To address the different design problems using the framework of essentially one analysis technique was possible in the past only with the finite difference method (FD) in the frequency domain or its time domain counterpart, the finite-difference time-domain (FDTD) method [1].
For another well known time-domain technique, the transmission line matrix method (TLM) [21],[22], no frequency-domain counterpart existed so far. Hence, if someone was interested not only in time-domain analysis of field problems, but also in frequency-domain results, he was forced to either apply the Fourier transform to the TLM time-domain response or leave the frame work of the TLM method alltogether and use one of the many different frequency-domain approaches. Neither of these alternatives is very satisfactory. On one hand, accurate frequency-domain data obtained from a Fourier transform of the TLM impulse response requires, in some cases, long iteration times. This can result in excessive computation time and may not be suitable for the problem at hand (design, optimization). On the other hand, to use a frequency-domain method instead, which may lead to much shorter computation time, may not be attractive either. Firstly, because of the additional effort necessary to learn the technique and, secondly, because of the possibility to find out after long hours of studies and programming that the normally unpublished problems of this particular technique produce uncertain results in exactly the case one is interested in (....).

These difficulties can be circumvented by using the FD and FDTD method. Firstly, the basic principles known from the FD method (in the frequency-domain) can readily be extended into the FDTD method and vice versa. Therefore, the knowledge of one technique (its pros and cons) can be used as a basis to extend the method to tackle another set of problems. Secondly, frequency-domain modelling using a time-domain detour with the FDTD is not necessary, the FD approach can be used instead.
Although frequency- and time-domain problems can be handled within the framework of one method, both the FD and FDTD are not without problems either. For example, a graded mesh necessary to resolve fine circuit details leads typically to a first order error. Although a solution to this problem has been proposed recently [ ], large memory space requirements and computation times are still the limiting factors in both techniques. This is mainly due to the problem of not being able to use the diakoptics technique effectively in the FDTD.
Some of the above mentioned problems are not present in the TLM approach. For example, using the symmetric condensed node in the TLM always produces a second order accuracy, even if a graded mesh arrangement is used. This is so because the node scattering parameters are calculated at the center of each TLM cell from the voltages and currents at the boundary of the cell. Hence, neighboring cells of different size have no effect on the accuracy of the discretization. Another advantage of the TLM is the potential to use diakoptics techniques. Complex structures can be divided into simpler sub-structures and are analysed separately before the individual solutions are combined. This approach saves computer memory space and computation time.
To avoid using the Fourier transform of the TLM response when frequency-domain data is required, but to stay within the framework of the TLM method, a TLM node has been developed recently which works entirely in the frequency-domain. In conjunction with a novel s-parameter extraction technique, a very powerful and flexible numerical modelling tool has been developed for frequency-domain design problems. Its computational efficiency and flexibility is better than most frequency-domain techniques known today. Since the space is discretized by using the same transmission line nodes as in the time-domain TLM (TDTLM) method, the frequency-domain TLM (FDTLM) represents a true frequency-domain counterpart to the time-domain TLM.
Before outlining the basic principles of the FDTLM approach, some new developments in the FDTD method will be discussed and new results are presented. A discussion focussing on the FDTLM follows. Results will be presented to illustrate the flexibility of this new method.

The Finite Difference Time Domain (FDTD)

The Finite Difference Time Domain (FDTD)was first introduced by Yee in 1966 [1] by discretizing Maxwell's equations directly using the central finite differences in time and space. Since then the FDTD has been further developed by many researchers [i.e. 2-6] and is now well established as a versatile technique to solve electromagnetic field problems. However, a commonly known problem in the use of the FDTD is the need for large computer memory, in particular for circuits in which the ratio of dimensions between subsections is large. Normally the smallest section to be resolved determines the mesh ratio to be used to discretize the overall circuit space. Since the mesh size and computer memory is inversely proportional and depend on the structural details to be resolved, a small mesh size leads naturaly to long iteration times for an impulse to become stable. Only then a Fourier transform can be performed to provide accurate frequency-domain information.
To alleviate these problems, two improvements have been introduced recently. The first allows a very fast frequency-domain hybrid mode analysis of complex circuits. This is possible by using a phase shift $\beta\Delta z$ along the z-direction (propagation direction). The

propagation constant of hybrid modes can then be calculated by using a two-dimensional mesh with a truly two-dimensional grid size. Furthermore, by appropriately arranging variables, only a real impulse response is involved. In contrast to the conventional FDTD analyses, which requires a three-dimensional mesh with a three-dimensional grid for this type of problems, the new technique improves the computational efficiency significantly. The basic idea to this approach was first published in [15] and at about the same time independent from the work in [15], was applied to the TLM method by the author and his group [11]. Subsequent work in his group has led to the application of this principle to the FDTD.

The second improvement is concerned with a graded lattice scheme which can be continuously adjusted along any space direction with arbitrary lattice ratio. The ratio need not be an integer number. The important contribution here is that a second-order accuracy is maintained by eliminating the first-order errors without the use of additional wave equations or space interpolations.

Two-Dimensional FDTD

The conventional time-domain analysis of hybrid modes in guide wave structures requires a three-dimensional mesh with three-dimensional space grids. Different techniques are used to determine the hybrid modes. One of those uses a Gaussian pulse as excitation in a shielded microstrip line. Typically 160 space meshes are required in propagation direction and about 5 to 7 time steps for any one mesh to satisfy the stability condition. Another approach is to resonate a section of the guided structure by placing two short-circuited planes along the z-axis a distance L apart. The length L corresponds to half a guided wavelength of the mode of interest. The resonance frequency of the cavity corresponds to the frequency at which this particular propagation constant is valid. The relationship between the propagation constant and L is then $\beta=2\pi/L$. By changing L also β changes. Repeating the calculation of the resonant frequency of the resonator for each β, the dispersion characteristic of the guided structure can be obtained. Obviously this approach involves easily thousends of iteration steps.

To avoid long iteration times in the computation of hybrid mode propagation constants, a phase shift $\beta.\Delta z$ is introduced in the propagation direction . This effectively replaces the space variable z. Since the propagation direction is replaced by the propagation constant as input parameter, the impulse needs to propagate only in the transverse direction and therefore stability is reached much faster than if a three-dimensional mesh is used.

As shown in [11,12], when the modes have been established a period of time after the excitation, only a phase shift $exp\{-j\beta z\}$ is involved at any adjacent nodes for any specific propagation constant β. This modal knowledge is used to simplify the scheme. It is easy to see that any incident or reflected impulse for any propagation constant β satisfies

$$E_x^n,\ E_y^n,\ H_z^n = \{E_x^n(x,y),\ E_y^n(x,y),\ H_z^n(x,y)\}\, j \exp\{\mp j\beta z\} \qquad (1a)$$

$$H_x^n,\ H_y^n,\ E_z^n = \{H_x^n(x,y),\ H_y^n(x,y),\ E_z^n(x,y)\} \exp\{\mp j\beta z\} \qquad (1b)$$

The factor j in (1a) is introduced to obtain a real-variable impulse response. The discretized Maxwell's equations now yield:

$$H_x^{n+0.5}(i,j) = H_x^{n-0.5}(i,j) - \frac{\Delta t}{\mu}\{[E_z^n(i,j+1) - E_z^n(i,j)]/\Delta y - \beta E_y^n(i,j)\}$$

$$H_y^{n+0.5}(i,j) = H_y^{n-0.5}(i,j) - \frac{\Delta t}{\mu}\{[E_z^n(i,j) - E_z^n(i+1,j)]/\Delta x + \beta E_x^n(i,j)\}$$

$$H_z^{n+0.5}(i,j) = H_z^{n-0.5}(i,j) - \frac{\Delta t}{\mu}\{[E_y^n(i+1,j) - E_y^n(i,j)]/\Delta x - [E_x^n(i,j+1) - E_x^n(i,j)]/\Delta y\}$$

$$E_x^{n+1}(i,j) = E_x^n(i,j) + \frac{\Delta t}{\varepsilon}\{[H_z^{n+0.5}(i,j+1) - H_z^{n+0.5}(i,j)]/\Delta y + \beta H_y^{n+0.5}(i,j+1)\}$$

$$E_y^{n+1}(i,j) = E_y^n(i,j) + \frac{\Delta t}{\varepsilon}\{[H_z^{n+0.5}(i,j) - H_z^{n+0.5}(i+1,j)]/\Delta x - \beta H_x^{n+0.5}(i,j+1)\}$$

$$E_z^{n+1}(i,j) = E_z^n(i,j) + \frac{\Delta t}{\varepsilon}\{[H_y^{n+0.5}(i+1,j) - H_y^{n+0.5}(i,j)]/\Delta x - [H_x^{n+0.5}(i,j+1) - H_x^{n+0.5}(i,j)]/\Delta y\} \quad (2)$$

Where Δt , Δx, and Δy are, respectively, the time step and the space steps in the x- and y-direction. The central finite difference scheme has been used to discretize the space as well as the time axis t.

Consideration on Conductor and Dielectric Losses

Losses can be easily taken into account in this technique. Using a self-consistent approach, losses for metallization dimensions smaller, comparable or larger than the skin depth can be considered. The loss factor is calculated from the Fourier transformation of the impulse at a specific space point and at different time steps after mode stability has been reached. In a lossy structure, the fields will decay with time due to absorption. For instance, at time $k\Delta t$, the electric field Ei of the i-th mode (operating frequency ω_i at a given β) can be written as

$$E^i(k\Delta t) = E^i(0)\exp(j\omega_i k\Delta t)\exp(-\frac{\omega_i}{2Q_i}k\Delta t) \quad (3)$$

where Q_i is the quality factor of the transmission line. When a mode has been established, the Fourier transform of the total field $E(k\Delta t)$ at the frequency ω_i is given as

$$\sum_{k=0}^{\tilde{}} E^i(k\Delta t)\exp(j\omega_i k\Delta t)\exp(-\frac{\omega_i}{2Q_i}k\Delta t) \quad (4)$$

By chosing different values of N and applying curve fitting, the quality factor Q_i or ω_i/Q_i can be obtained from the above equation. The attenuation coefficient α_i for the lossy guiding structure is directly given by [13]:

$$\alpha_i = \frac{\omega_i}{2Q_i V_{gi}} = \frac{\omega_i}{2Q_i(\partial\omega/\partial\beta)_i} \quad (5)$$

where V_{gi} is the group velocity of the i-th mode, which can be obtained by the mode dispersion relationship.

Graded Lattice

A continuously variable lattice size (Fig.1) instead of a fixed lattice ratio is an important feature to improve the computational efficiency of the FDTD technique. The option to use a fine but variable lattice size around metal corners where field changes are significant and to use a continuously growing lattice size with greater distance from that corner allows greater

computation accuracy with less computer memory. Although several attempts have been made in the past to achieve such a graded lattice, the remaining error term was always of first-order. In other words, the larger the mesh ratio, the higher the time-domain error. As a consequence, if the time-domain response is used to compute frequency-domain data via a Fourier transform, significant errors can occur. If one remains in the time-domain, this error is in most cases marginal.

Xiao and Vahldieck [14] have introduced a new universal grading scheme with continously variable lattice size in all 3 space dimensions. The second-order accuracy is maintained by eliminating the first order errors analytically. No additional wave equations are necessary at the interface between neighboring lattices. In developing the new algorithm we look first at the problem of the first-order error in the variable lattice scheme. Using the Ex-field at the boundary of two neighboring lattices as an example

$$E_x^n(i,j,k) = E_x^n(i,j,k) + \frac{\Delta t}{\varepsilon_x}\left[\frac{\partial H_z^{n+0.5}(i,j,k)}{\partial x} - \frac{\partial H_y^{n+0.5}(i,j,k)}{\partial z}\right] \tag{6}$$

we find that by developing the x-dependent term in this equation by a Taylor series yields:

$$\frac{\partial H_z^{n+0.5}(i,j,k)}{\partial x} = \frac{H_z^{n+0.5}(i,j+1,k) - H_z^{n+0.5}(i,j,k)}{\Delta h(q_j + q_{j+1})/2} + o((q_{j+1} - q_j)\Delta h) \tag{7}$$

Equ. (7) clearly shows that normally a variable grading scheme provides only a first-order accuracy. However, by appropriately arranging the lattices a second-order error can be obtained. There are two possible techniques: the first provides a second-order accuracy only for integer mesh ratios without changing the uniform mesh algorithm [14] and the second provides second-order accuracy for any non-integer mesh ratio. The latter technique however requires a modification to the algorithm in that the three neighboring lattice cells are combined.

Variable Grading SchemeWith Non-Integer Mesh Ratio and Second-Order Accuracy

Considering first the lattice arrangement shown in Fig.1a, the electric field components left and right from the boundary between the two mesh sizes (point D in Fig.1) can be always arranged in the middle of the magnetic field components or vice versa. Therefore, calculating the electric (or magnetic) field components from the magnetic (or electric) field components provides automatically a second-order accuracy since the central finite difference is maintained. The problem arises at the boundary between the two regions where the E-field (point D) is not located exactly in the middle between C and E and therefore calculating the E-field from the H-field leads to a first-order error. We found however, that a compensation factor can always be found to cancel the first-order error terms and therefore maintaining a second-order accuracy. To find this compensation factor three neighboring lattice cells must be used. To illustrate this procedure consider Fig.1b. Using the central finite difference scheme to calculate the electric field components from the magnetic field components introduces an error. A Taylor series analysis yields:

$$E_y^{\Delta_{i+1}}(i+1) = \frac{H_x(i+1) - H_x(i)}{(p_{i+1} + p_i)/2} + o(h^2) \tag{8a}$$

$$E_y^{\Delta_i}(i) = \frac{H_x(i) - H_x(i-1)}{(p_i + p_{i-1})/2} + o(h^2) \tag{8b}$$

$$E_y^{\Delta_{i-1}}(i-1) = \frac{H_x(i-1) - H_x(i-2)}{(p_{i-1} + p_{i-2})/2} + o(h^2) \tag{8c}$$

As we can see $E_y^{\Delta_{i+1}}(i+1)$, $E_y^{\Delta_i}(i)$, and $E_y^{\Delta_{i-1}}(i-1)$ are Δi+1, Δi, and Δi-1 away from the electric field nodes Ey(i+1), Ey(i), and Ey(i-1), respectively. Δi+1, Δi, and Δi-1 are given as follows

$$\Delta_{i+1} = \frac{h}{4}(p_{i+1} - p_i) \tag{9a}$$

$$\Delta_i = \frac{h}{4}(p_i - p_{i-1}) \tag{9b}$$

$$\Delta_{i-1} = \frac{h}{4}(p_{i-1} - p_{i-2}) \tag{9c}$$

The other dimensions in Fig.1b may be expressed as

$$l_i = (p_{i-1} + p_i)h + \Delta_{i+1} - \Delta_{i-1} = \frac{h}{4}[p_{i-1} + p_i + p_{i+1} + p_{i+2}] \tag{10a}$$

$$\delta_i = \frac{l_i}{2} - (p_i h - \Delta_{i-1}) - \Delta_i = \frac{h}{8}[p_{i+1} + p_{i+2} - p_{i-1} - p_i] \tag{10b}$$

Developing the electric field components at the electric field nodes in Fig.1b in a Taylor series

$$E_y(i) = E_y^{\Delta_i}(i) + \Delta_i \frac{\partial E_y^{\Delta_i}(i)}{\partial x} + o(h^2) \tag{11}$$

shows a first order partial differential term. This may be expressed by using the first order partial differential expansion at the electric nodes as follows

$$\frac{\partial E_y^{\Delta_i}(i)}{\partial x} = \frac{\partial E_y(i)}{\partial x} + \delta_i \frac{\partial^2 E_y(i)}{\partial x^2} + o(h^2) \tag{12}$$

and therefore, equ.11 can be written as

$$E_y(i) = E_y^{\Delta_i}(i) + \Delta_i[\frac{\partial E_y(i)}{\partial x} + \delta_i \frac{\partial^2 E_y(i)}{\partial x^2}] + o(h^2) \tag{13}$$

or

$$E_y(i) = E_y^{\Delta_i}(i) + \Delta_i[\frac{E_y(i+1) - E_y(i-1)}{l^i}] + o(h^2) \tag{14}$$

where, li (i=1, 2,...,N) is time independent and fixed for a specific mesh arrangement. The compensation terms in the bracket of the right side of the above equation have been calculated in the neighboring equations and therefore the new algorithm requires not much more computations. Hence, a variable mesh scheme with arbitrary lattice ratio and a second-order accuracy is always feasible if neighboring mesh field components are combined. This holds also for the other field components and is generally applicable to all three space dimensions.

Several results concerning the effectiveness of the grading scheme are shown in Fig.'s 2 and 3. Fig.2 illustrates the CPU time savings for different grading ratios in case of the two-dimensional FDTD described before. As shown for a microstrip line, the CPU time decreases but at the same time the relative error increases. Fig.3 provides an indication of

the maximum grading ratio that can be used without degrading the accuracy of the solution too much. Typically a grading ration of 1:2 provides essentially the same accuracy as a uniform grading scheme.

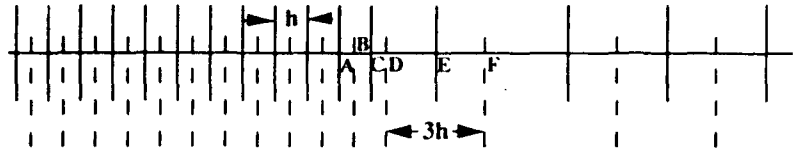

Fig.1a Variable grading scheme

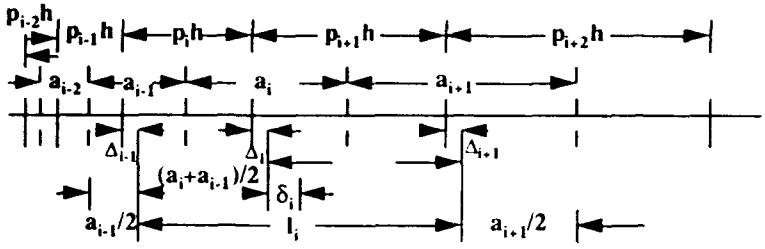

Fig.1b A generalized variable mesh.

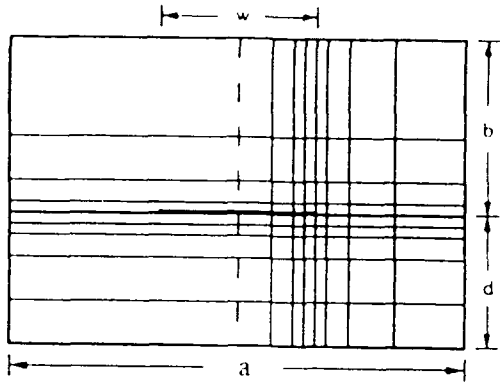

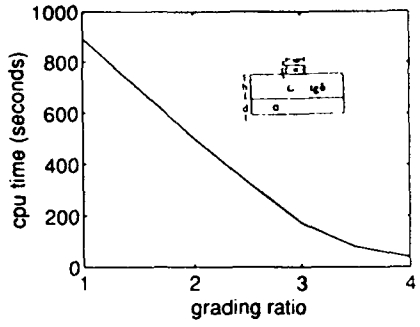

Fig.2a CPU time comparison between different mesh sizes of grading schemes, microstrip dispersion, h=100 µm, w=8 µm, ε_r=12.8, tgδ=4.10^{-4}, σ=4.1 10^7, t=4 µm, d=8 µm, normalized frequency f=0.065.

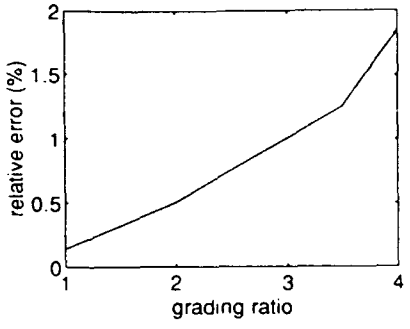

Fig.2b Relative error comparison between different mesh sizes of grading schemes, microstrip dispersion, h=100 µm, w=8 µm, ε_r=12.8, tgδ=4.10^{-4}, σ=4.1 10^7, t=4 µm, d=8 µm, normalized frequency f=0.065.

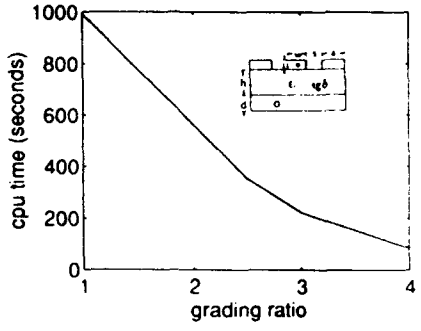

Fig.2c CPU time comparison between different mesh sizes of grading schemes, CPW dispersion, h=200 µm, w=8 µm, s=8 µm, ε_r=12.8, tgδ=4.10^{-4}, σ=4.1 10^7, t=4 µm, d=8 µm, normalized frequency f=0.065.

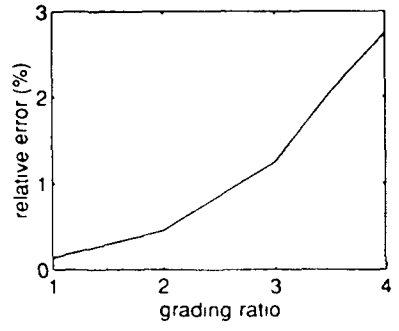

Fig.2d Relative error comparison between different mesh sizes of grading schemes, CPW dispersion, h=200 µm, w=8 µm, s=8 µm, ε_r=12.8, tgδ=4.10^{-4}, σ=4.1 10^7, t=4 µm, d=8 µm, normalized frequency f=0.065.

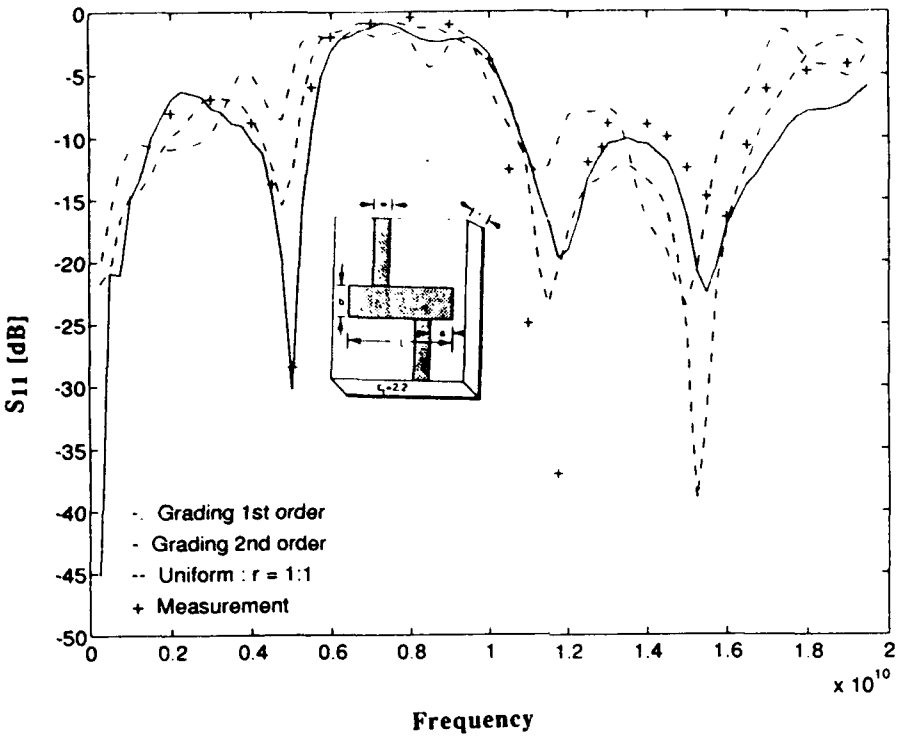

Fig.3 Comparison of different grading schemes

The Frequency-Domain TLM Method

The time-domain TLM (TDTLM) method is a time iteration procedure which requires synchronism of the impulses travelling on the transmission lines. To accommodate locally varying electrical properties or a graded mesh, transmission line stubs need to be added to the nodes. For small mesh sizes or for large mesh ratios the time step required to reach stability may be very small and the number of time samples to satisfy steady-state conditions may become large [16].This problem leads to significant computer run-time and, in cases like the one shown in Fig.9, may require the use of a supercomputer. On the other hand, the circuit discontinuity illustrated in Fig.9 is becoming a more and more typical problem in the design of MMIC's, in that fine circuit details with small dimensions exist in close neighborhood with areas of relatively large dimensions. Structures of this type are difficult to analyze with any time-domain technique because of the above mentioned problems. Furthermore, if the time-domain algorithm is only used to extract the frequency-

domain response of the circuit and the transient solution is of no interest, then it is a very inefficient way to accomplish this.

To alleviate this problem without leaving the framework of the TLM method (FDTLM), Jin and Vahldieck [17] have recently introduced a frequency-domain TLM method which works entirely in the frequency-domain.

In the FDTLM the space domain is discretized by the same transmission line network known from the conventional time-domain TLM (TDTLM) method. However, instead of exciting the network with a single impulse, an impulse train with its magnitude sinusoidally modulated is assumed. At any time step this new excitation retains the form of an impulse, but its modulated amplitude varies sinusoidally with time as $e^{j\omega N\Delta t}$, where ω is the modulation frequency, N the time step, and Δt the time interval between impulses. In practical computation, the FDTLM algorithm operates at any time instance and the common time-dependent factor $e^{j\omega N\Delta t}$ is omitted. Therefore, no time iteration procedure is needed. The assumption of an impulse train excitation is only meant to establish the relationship between the TDTLM and FDTLM and to transform the TDTLM algorithm into the frequency-domain whenever necessary. It has been demonstrated in previous work (i.e.[17]) that the FDTLM is as flexible as the TDTLM while its computational efficiency is better than most frequency-domain techniques.

In the original paper [17], in which the concept of the FDTLM was first introduced, the algorithm was derived directly from the time domain nodes (including stubs). The following paragraph describes some new developments. It will be illustrated that the nodes can also be derived directly in the frequency domain [20]. Coincidentally, parallel to our work on this subject, Christopoulos and co-workers [16] have introduced a frequency-domain TLM node and called it the steady-state TLM technique. For the special case of equal characteristic impedance on all lines, the final result of [16] is the same as the one presented in [20].

Since the FDTLM algorithm operates within one time step at an arbitrary time instance, the common time-dependent factor $e^{j\omega N\Delta t}$ can be omitted. This is in analogy to other frequency domain methods where a sinusoidal excitation is assumed. The only difference in comparison to ordinary frequency domain methods is that the time-dependent factor is a continuous function of time ($e^{j\omega t}$) , while for the FDTLM it is a discrete function ($e^{j\omega N\Delta t}$) of time. This leads to a slightly different representation for Maxwell's equation in the FDTLM where the time axis is discretized on the right hand side of the equation:

$$\nabla \times E e^{j\omega N\Delta t} = -\mu \frac{e^{j\omega(N+1)\Delta t} - e^{j\omega N\Delta t}}{\Delta t} H$$

$$\nabla \times H e^{j\omega N\Delta t} = \varepsilon \frac{e^{j\omega(N+1)\Delta t} - e^{j\omega N\Delta t}}{\Delta t} E \qquad (15)$$

By omitting the common factor $e^{j\omega N\Delta t}$ on both sides of (1) yields:

$$\nabla \times E = -j\omega\mu \frac{e^{j\omega\Delta t} - 1}{j\omega\Delta t} H$$

$$\nabla \times H = j\omega\varepsilon \frac{e^{j\omega\Delta t} - 1}{j\omega\Delta t} E \qquad (16)$$

Comparing (16) with the time harmonic representation of Maxwell's equations[17], we find that there is an additional factor on the right hand side of (16). This additional factor approaches unity if $\omega\Delta t$ approaches zero. It is obvious from (16) that the additional factor

from the time discretization leads to the dispersion problem in the TLM network. In the FDTLM, this dispersion problem can be easily eliminated by modifying the material permittivity and permeability in the following way:

$$\nabla \times E = -\bar{\mu}\frac{\partial H}{\partial t}$$
$$\nabla \times H = \bar{\varepsilon}\frac{\partial E}{\partial t} \qquad (17)$$

with $\bar{\mu} = \mu\frac{j\omega\Delta t}{e^{j\omega\Delta t}-1}$ and $\bar{\varepsilon} = \varepsilon\frac{j\omega\Delta t}{e^{j\omega\Delta t}-1}$. Hence, after the time axis is discretized, (17) becomes identical to the time harmonic representation of Maxwell's equations[13].

FDTLM nodes derived from existing TDTLM nodes

There are numerous types of nodes that can be used in the TDTLM method. Each type of node contains several main branches and stubs. The stubs are necessary to maintain the time synchronism. The number of main branches and stubs depends on the type of node. For example, for a symmetrical condensed node, there are 12 main branches and 6 stubs; while for a hybrid symmetrical condensed node, there are 12 main branches and 3 stubs. Without losing generality, we may write the scattering equation for the TDTLM (symmetrical condesed node) node as follows:

$$\begin{bmatrix} V_m^r \\ V_s^r \end{bmatrix} = [S]\cdot\begin{bmatrix} V_m^i \\ V_s^i \end{bmatrix} = \begin{bmatrix} S_{mm} & S_{ms} \\ S_{sm} & S_{ss} \end{bmatrix}\cdot\begin{bmatrix} V_m^i \\ V_s^i \end{bmatrix} \qquad (18)$$

where S is the symbolic scattering matrix. The matrix coefficients are given in [18,19]. V_m^r, V_s^r are the vectors of the reflected voltages at the main branches and stubs, respectively. while V_m^i, V_s^i denote the vectors of the incident voltages.

Assuming that d is the smallest of all node dimensions throughout the mesh, the propagation factor is defined as $e^{-jk_o d}$, where k_o is the wave number of free space. Therefore, for the stubs, the reflected voltages are related to the incident voltages at the center of the nodes in the following way:

$$V_s^i = e^{-jk_o d}\cdot\Gamma_s\cdot V_s^r \qquad (19)$$

where Γ_s is a diagonal matrix with the i^{th} element being either 1 or -1, depending on whether the i^{th} stub is open or short circuited. From equations (18) and (19), the relationship between the incident and reflected voltages at the main branches can be obtained as

$$V_m^r = \underbrace{\left[S_{mm} + e^{-jk_o d}\cdot S_{ms}\cdot\Gamma_s\cdot(I - e^{-jk_o d}\cdot S_{ss}\cdot\Gamma_s)^{-1}\cdot S_{sm}\right]}_{P}\cdot V_m^i \qquad (20)$$

Equation (20) relates the reflected and incident voltages of the main branches at the center of the node. Moving the reference plane from the center of the node to the boundary of the node, *i.e.* the ports of the main branches, yields

$$_pV_m^r = e^{-jk_o d}\cdot P\cdot V_m^i \qquad (21)$$

Equation. (21) provides an explicit expression for the scattering matrix of the symmetrical condensed FDTLM node. The scattering matrix relates the reflected and incident voltages at

the ports of the main branches of the node and its property is completely dependent upon both the propagation factor and the symbolic scattering matrix.

Any kind of nodes used in the TDTLM algorithm can be readily used for the FDTLM method, with some slight modifications. The main procedure of constructing the frequency-domain algorithm from the existing node is firstly to eliminate the stubs and then move the reference planes from the center of the node to the boundary of the node. Thus, any full-wave three-dimensional TLM node can be expressed explicitly in the frequency-domain by a (12X12) scattering matrix.

FDTLM node derived directly in the frequency-domain

To preserve the time synchronism in the TDTLM nodes, the choice of values of the distributed inductances and capacitances on the main branches is limited. Therefore, whenever necessary, stubs are added for compensation. In the frequency-domain, time synchronism is not required and therefore an extra degree of freedom is added to choose freely the distributed inductances and capacitances or propagation constants and characteristic impedances on the transmission lines so as to present the properties of the discretized space correctly. Thus stubs are no longer needed in the FDTLM node. This has been shown in a paper by Christopoulos and co-workers [16] and by Huang, Jin and Vahldieck [20]. Since the information given in [20] is quite brief, more details are provided in the following.

$$
S = \begin{array}{|cccccccccccc|c}
+xy & +xz & -xy & -xz & +yz & +yx & -yz & -yx & +zx & +zy & -zx & -zy & \\
a_1 & & c_1 & & & d_4 & & -d_4 & & b_6 & & b_6 & +xy \\
& a_2 & & c_2 & b_3 & & b_3 & & d_5 & & -d_5 & & +xz \\
c_1 & & a_1 & & & -d_4 & & d_4 & & b_6 & & b_6 & -xy \\
& c_2 & & a_2 & b_3 & & b_3 & & -d_5 & & d_5 & & -xz \\
& b_2 & & b_2 & a_3 & & c_3 & & & d_6 & & -d_6 & +yz \\
d_1 & & -d_1 & & & a_4 & & c_4 & b_5 & & b_5 & & +yx \\
& b_2 & & b_2 & c_3 & & a_3 & & & -d_6 & & d_6 & -yz \\
-d_1 & & d_1 & & & c_4 & & a_4 & b_5 & & b_5 & & -yx \\
& d_2 & & -d_2 & & b_4 & & b_4 & a_5 & & c_5 & & +zx \\
b_1 & & b_1 & & d_3 & & -d_3 & & & a_6 & & c_6 & +zy \\
& -d_2 & & d_2 & & b_4 & & b_4 & c_5 & & a_5 & & -zx \\
b_1 & & b_1 & & -d_3 & & d_3 & & & c_6 & & a_6 & -zy
\end{array}
$$

Fig.4 New symbolic scattering matrix

For the symmetrical condensed node the corresponding symbolic scattering matrix is shown in Fig.4. The matrix coefficients are derived using the principle of power conservation which leads to the well-known unitary relation:

$$S^T \cdot Y \cdot S^* = Y \tag{22}$$

where Y denotes the diagonal admittance matrix consisting of the characteristic admittance of each transmission line branch. S is the symbolic scattering matrix of the node. For simplicity we assume that the characteristic admittance of each transmission line branch is the same. Then the diagonal admittance matrix is reduced to a unit matrix and the coefficients of the symbolic scattering matrix for the condensed node are reduced to $a_n = c_n = 0$, $b_n = d_n = 0.5$, $n = 1 \sim 6$, which is found to be identical to Johns' node matrix without stubs [18].

Assuming the characteristic admittance of each branch equal to the intrinsic impedance of the medium and the propagation constant on each branch to be the same for both orthogonal polarisations, then the propagation constants in each space direction yield:

$$\gamma_x = \frac{k}{2}\left(\frac{v^2+w^2}{vw} - \frac{vw}{u^2}\right)$$
$$\gamma_y = \frac{k}{2}\left(\frac{u^2+w^2}{uw} - \frac{uw}{v^2}\right) \qquad (23)$$
$$\gamma_z = \frac{k}{2}\left(\frac{u^2+v^2}{uv} - \frac{uv}{w^2}\right)$$

where $\gamma_x, \gamma_y, \gamma_z$ are the propagation constants for the branches in x, y, and z directions, respectively. k is the wave number, u,v ,and w are the corresponding node dimensions.

Knowing the propagation constants of all transmission line branches, we now move the reference plane from the center of the node to the ports of the node and obtain, similar to equation (21):

$${}_pV^r = [S_p] \cdot {}_pV^i \qquad (24)$$

where ${}_pV^r, {}_pV^i$ are , respectively, the vectors of the reflected and incident voltages at the ports of all 12 branches. S_p is called the scattering matrix of the symmetrical condensed FDTLM node. The coefficients of the matrix are shown in Fig.5.

$$S_p = \frac{1}{2}\begin{vmatrix}
+xy & +xz & -xy & -xz & +yz & +yx & -yz & -yx & +zx & +zy & -zx & -zy & \\
 & & & & & \lambda_{xy} & & -\lambda_{xy} & & \lambda_{xz} & & \lambda_{xz} & +xy \\
 & & & & \lambda_{xy} & & \lambda_{xy} & & \lambda_{xz} & & -\lambda_{xz} & & +xz \\
 & & & & & -\lambda_{xy} & & \lambda_{xy} & & \lambda_{xz} & & \lambda_{xz} & -xy \\
 & & & & \lambda_{xy} & & \lambda_{xy} & & -\lambda_{xz} & & \lambda_{xz} & & -xz \\
 & \lambda_{xy} & & \lambda_{xy} & & & & & & \lambda_{yz} & & -\lambda_{yz} & +yz \\
\lambda_{xy} & & -\lambda_{xy} & & & & & & \lambda_{yz} & & \lambda_{yz} & & +yx \\
 & \lambda_{xy} & & \lambda_{xy} & & & & & & -\lambda_{yz} & & \lambda_{yz} & -yz \\
-\lambda_{xy} & & \lambda_{xy} & & & & & & \lambda_{yz} & & \lambda_{yz} & & -yx \\
 & \lambda_{xz} & & -\lambda_{xz} & & \lambda_{yz} & & \lambda_{yz} & & & & & +zx \\
\lambda_{xz} & & \lambda_{xz} & & \lambda_{yz} & & -\lambda_{yz} & & & & & & +zy \\
 & -\lambda_{xz} & & \lambda_{xz} & & \lambda_{yz} & & \lambda_{yz} & & & & & -zx \\
\lambda_{xz} & & \lambda_{xz} & & -\lambda_{yz} & & \lambda_{yz} & & & & & & -zy
\end{vmatrix}$$

Fig.5 Frequency-domain s-matrix for the symmetrical condensed node

where

$$\lambda_{xy} = e^{-j(\gamma_x \cdot u/2 + \gamma_y \cdot v/2)}$$
$$\lambda_{xz} = e^{-j(\gamma_x \cdot u/2 + \gamma_z \cdot w/2)} \qquad (25)$$
$$\lambda_{yz} = e^{-j(\gamma_y \cdot v/2 + \gamma_z \cdot w/2)}$$

Compared to the original approach [17] where the FDTLM algorithm was derived by modifying the existing time-domain nodes, the construction of the FDTLM node directly in the frequency-domain is somewhat more straightforward and leads to a simpler explicit algorithm.

Intrinsic Scattering Matrix

As described in [17] the FDTLM algorithm is based on the concept of the intrinsic scattering matrix (ISM), which is defined as the coefficient matrix relating the reflected and incident waves at the exterior branches of a TLM network. The exterior branches are the ones that point into the propagation direction of the wave. By establishing the ISM, the general TLM network matrix is transformed into a matrix of significantly reduced size. This matrix contains all the properties of the structure which can be computed through matrix operations. This allows one to use numerous advanced techniques in matrix algebra to enhance the computational efficiency of the FDTLM algorithm. Furthermore, the diakoptics technique may be easily implemented in the algorithm. The entire structure may be broken up into several sub-structures. The ISM for each sub-structure is calculated and the one for the entire structure is obtained through simple matrix operations. Due to this property of the FDTLM algorithm, the computer resources required in the computation are only linear proportional to the volume of the structure. This makes the FDTLM method very attractive and efficient in handling structures with complex configurations and large volumes.

In order to solve the two-dimensional (2-D) waveguide eigenvalue problem or the scattering parameters of a spatial three-dimensional (3-D) waveguide discontinuity problem, the ISM must be formulated. To do this, the coordinate z -axis is defined as the propagation direction of the wave. The main branches of the symmetrical condensed FDTLM node (Fig.6) are classified into two types:

exterior branches:	+zx, +zy, -zx, -zy.
interior branches:	+xy, +xz, -xy, -xz;
	+yz, +yx, -yz, -yx.

The exterior branches point into the propagation direction of the wave, while the interior branches between neighboring nodes are connected through the following relationship

$$V_x^i = C_x \cdot V_x^r$$
$$V_y^i = C_y \cdot V_y^r \qquad (26)$$

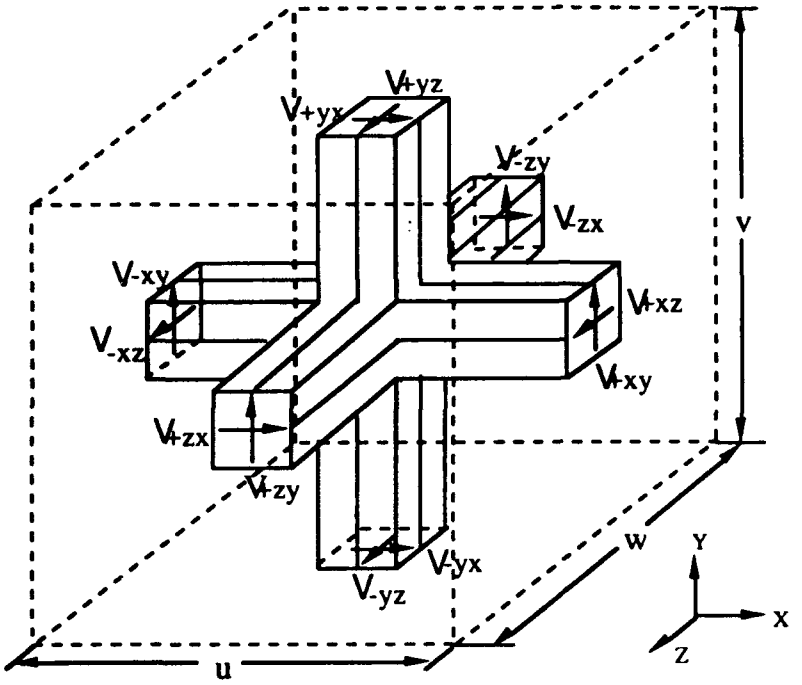

Fig.6 Symmetrical condensed node

Where C_x and C_y are the connection matrices which connect the neighboring branches in the x and y directions, respectively. $V^i_{x,y}$, $V^r_{x,y}$ are the incident and reflected voltages between neighboring nodes. Therefore, a so-called intrinsic scattering matrix can be defined as follows:

$$\begin{bmatrix} V_z^r \\ V_x^r \\ V_y^r \end{bmatrix} = \begin{bmatrix} S_{zz} & S_{zx} & S_{zy} \\ S_{xz} & S_{xx} & S_{xy} \\ S_{yz} & S_{yx} & S_{yy} \end{bmatrix} \cdot \begin{bmatrix} V_z^i \\ V_x^i \\ V_y^i \end{bmatrix} \tag{27}$$

From equations (26) and (27), we can now find a relationship between incident and reflected voltages of exterior branches, that are the branches which point in propagation direction:

$$V_z^r = [S_{ISM}] \cdot V_z^i \tag{28}$$

where

$$S_{ISM} = S_{zz} + S_{zx} \cdot C_x \cdot P \cdot (M \cdot S_{xz} + M \cdot S_{xy} \cdot C_y \cdot N \cdot S_{yz}) + S_{zy} \cdot C_y \cdot Q \cdot (N \cdot S_{yz} + N \cdot S_{yx} \cdot C_x \cdot M \cdot S_{xz})$$

$$M = (I - S_{xx} \cdot C_x)^{-1}$$

$$N = (I - S_{yy} \cdot C_y)^{-1}$$

$$P = (I - M \cdot S_{xy} \cdot C_y \cdot N \cdot S_{yx} \cdot C_x)^{-1}$$

$$Q = (I - N \cdot S_{yx} \cdot C_x \cdot M \cdot S_{xy} \cdot C_y)^{-1}$$

Equation (28) provides an explicit expression for the intrinsic scattering matrix S_{ISM} in terms of the scattering and connection matrices of the network. Once equation (28) is obtained, the eigenvalues of a guiding structure can be determined and the scattering parameters for two guiding structures connected through a discontinuity can be computed. Details of this procedure for 2-D and 3-D problems will be described in the following,

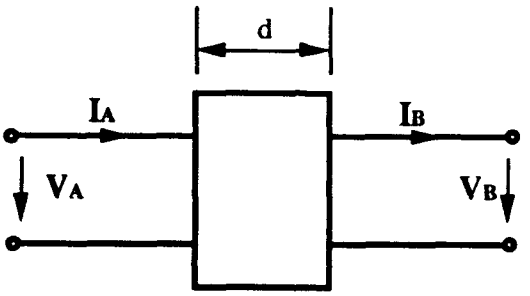

Fig. 7 A slice of waveguiding structure

The FDTLM discretizes any guiding structure as infinitely long periodic network with a structural periodicity of d in the propagation direction (along the z-axis). Therefore, the ISM is constructed from only one slice of waveguide. For simplicity we assume only one node with branches pointing in propagation direction as shown in Fig.7. For this case the ISM of the unit cell reads:

$$\begin{bmatrix} V_A^r \\ V_B^r \end{bmatrix} = \begin{bmatrix} S_{AA} & S_{AB} \\ S_{AB} & S_{BB} \end{bmatrix} \cdot \begin{bmatrix} V_A^i \\ V_B^i \end{bmatrix} \tag{29}$$

where $V_{A,B}^i$ denotes the incident voltage vector and $V_{A,B}^r$ the reflected voltage vector. To determine propagation constants and the transverse mode distribution in the guide a transfer matrix which is related to the scattering matrix is obtained as follow:

$$\begin{bmatrix} V_A \\ I_A \end{bmatrix} = A \cdot \begin{bmatrix} V_B \\ I_B \end{bmatrix} = \begin{bmatrix} SR^{-1} & SR^{-1}S - R \\ R^{-1} & R^{-1}S \end{bmatrix} \cdot \begin{bmatrix} V_B \\ I_B \end{bmatrix} \tag{30}$$

where

$$S = [(I - S_{AA}) - S_{AB}(I - S_{AA})^{-1} S_{AB}]^{-1}(I + S_{AA})$$
$$\quad -[(I - S_{AA})S_{AB}^{-1}(I - S_{AA}) - S_{AB}]^{-1} S_{AB}$$
$$R = [(I - S_{AA}) - S_{AB}(I - S_{AA})^{-1} S_{AB}]^{-1} S_{AB}$$
$$\quad -[(I - S_{AA})S_{AB}^{-1}(I - S_{AA}) - S_{AB}]^{-1}(I + S_{AA})$$

Let the propagation constant in z-direction be θ, then the periodic boundary conditions based on Floquet's theorem imply that

$$\begin{bmatrix} V_B \\ I_B \end{bmatrix} = e^{\theta d} \cdot \begin{bmatrix} V_A \\ I_A \end{bmatrix} \tag{31}$$

Thus, the transfer matrix of the unit cell must satisfy the eigenvalue equation

$$A \cdot \begin{bmatrix} V \\ I \end{bmatrix} = e^{\theta d} \cdot \begin{bmatrix} V \\ I \end{bmatrix} \tag{32}$$

The solution of the eigenvalue equation (32) is simplified if we consider the analytical properties of the matrix A. We observe first of all that if (32) is satisfied, then the following eigenvalue equation is also satisfied.

$$\frac{1}{2}(A + A^{-1}) \cdot \begin{bmatrix} V \\ I \end{bmatrix} = \frac{1}{2}(e^{\theta d} + e^{-\theta d}) \cdot \begin{bmatrix} V \\ I \end{bmatrix} = \cosh(\theta d) \cdot \begin{bmatrix} V \\ I \end{bmatrix} \tag{33}$$

The above equation proves the physically intuitive fact that if θ is a propagation constant of the structure, then $-\theta$ is also a propagation constant. Inspection of equation (30) shows that the inverse matrix of A can be easily obtained by

$$A^{-1} = \begin{bmatrix} SR^{-1} & R - SR^{-1}S \\ -R^{-1} & R^{-1}S \end{bmatrix} \tag{34}$$

So that

$$\frac{1}{2}(A + A^{-1}) = \begin{bmatrix} SR^{-1} & 0 \\ 0 & R^{-1}S \end{bmatrix} \tag{35}$$

Thus, it is sufficient to consider the reduced eigenvalue equation

$$(SR^{-1}) \cdot V = \cosh(\theta d) \cdot V \tag{36}$$

Equation (36) is the standard form of an eigenvalue problem to be solved for the propagation constants of the waveguide modes. The eigenvectors correspond to the transverse mode distributions.

ISM algorithm for 3-D discontinuities

The calculation of the scattering parameters for 3-D discontinuities using the ISM involves the following steps [17]. Firstly, any 3-D discontinuity is divided into two areas: the region containing the discontinuity and the transmission line structures attached to the discontinuity as the input and output ports. The intrinsic scattering matrices for the discontinuity region and the transmission lines attached to it are determined. Secondly, a 2-D analysis is performed for the connected transmission lines to find the field distribution for the propagating modes. Thirdly, one of the ports is then excited by its modal field. From the reflected and the transmitted field amplitudes the scattering parameters can be found.

For the case of a two port waveguide discontinuity problem, the method for evaluation of the s-parameters has been described extensively in [17], and is repeated here only briefly.

The intrinsic scattering matrices for the discontinuity region and the two attached semi-infinity waveguides are denoted as $\boldsymbol{M}$, $\boldsymbol{M_L}$ and $\boldsymbol{M_R}$ respectively. The incident and reflected modes at the interfaces to the discontinuity region and the attached waveguides are related as follows:

$$\begin{bmatrix} V_L^r \\ V_R^r \end{bmatrix} = M \cdot \begin{bmatrix} V_L^i \\ V_R^i \end{bmatrix} = \begin{bmatrix} m_{LL} & m_{LR} \\ m_{RL} & m_{RR} \end{bmatrix} \cdot \begin{bmatrix} V_L^i \\ V_R^i \end{bmatrix} \tag{37}$$

where V_L^i, V_L^r are the incident and reflected mode vectors at the interface of the left-hand waveguide and the discontinuity region; while V_R^i, V_R^r are the incident and reflected mode vectors at the interface of the right-hand waveguide and the discontinuity region (each element of these vectors corresponds to one branch of the network). The excitation of the system, V_{L0}^i and V_{L0}^r, which is obtained from a 2-D analysis, is incident at the interface between the left-hand waveguide and the discontinuity region (Fig.8). It should be noted that vector V_{L0}^i and V_{L0}^r describe the field distribution over the cross-section of the left-hand waveguide. The reflected waves, V_L^i, V_L^r of the left-hand waveguide are then given by

$$V_L^i = M_L \cdot V_L^r \tag{38}$$

$$V_L^r = (I - M_R^i \cdot M_L)^{-1} \cdot (M_R^i - M_L) \cdot V_{L0}^i \tag{39}$$

where M_R^i:

$$M_R^i = m_{LL} + m_{LR} \cdot M_R \cdot (I - m_{RR} \cdot M_R)^{-1} \cdot m_{RL} \tag{40}$$

V_R^i, V_R^r of the right-hand waveguide are obtained from:

$$V_R^i = M_R \cdot V_R^r \tag{41}$$

$$V_R^r = (I - m_{RR} \cdot M_R)^{-1} \cdot m_{RL} \cdot (M_L \cdot V_L^i + V_{L0}^i) \tag{42}$$

From (39)~(42), the corresponding scattering parameters can be obtained.

Some examples for the numerical efficiency of the FDTLM are shown in Fig.'s 9 to 11.

Fig.9 shows a CPW discontinuity on a 400µm thick GaAs substrate with a thin insulating layer SiO2 layer. Structures like this are either impossible to model with time-domain techniques or require supercomputer power. Using the FDTLM the structure is discretized with an irregular mesh of 9 nodes in x-direction and 11 in y-direction. A total of 4 subsections has been cascaded. The typical computation time on a IBM RS 6000 (530) is approximately 2 minutes per frequency point. Fig.10 shows a comparatively simple structure: An E-Plane filter. Here the computation time is approx. 0.2 seconds per frequency sample. Fig.11 illustrates the complexity of circuits that can be modelled with the FDTLM. In this case a modul interconnect is analyzed using a bonding wire to connect a microstrip motherboard with a CPW transmission line on a different substrate carrier.

Conclusion

Some new developments in time-and frequency-domain modelling of microwave circuits have been discussed. The emphasis was on the FDTD method and the frequency-domain TLM method. It has been shown that a variable grading scheme for the FDTD with second order accuracy is possible and that significant improvements in CPU-time and memory space can be achieved. For the frequency-domain TLM method is has been shown that the dispersion error due to the time discretization can be eliminated and that the frequency-domain node can be either derived from the time domain node or directly in the frequency-domain.

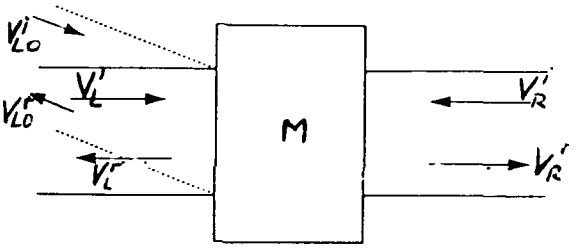

Fig. 8

Excitation and resulting incident and reflected voltage amplitudes for a two-port network.

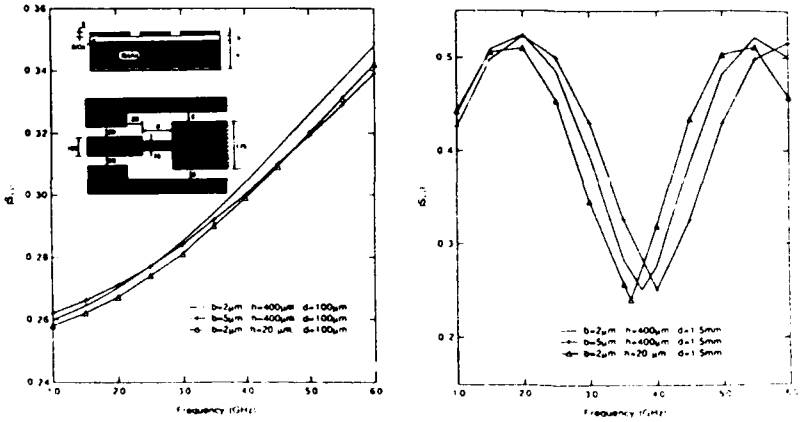

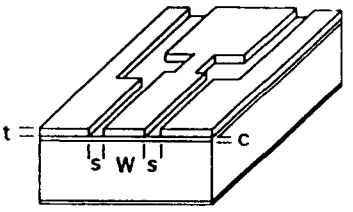

Fig.9

Cascaded double step CPW discontinuity on GaAs with thin insulating layer.

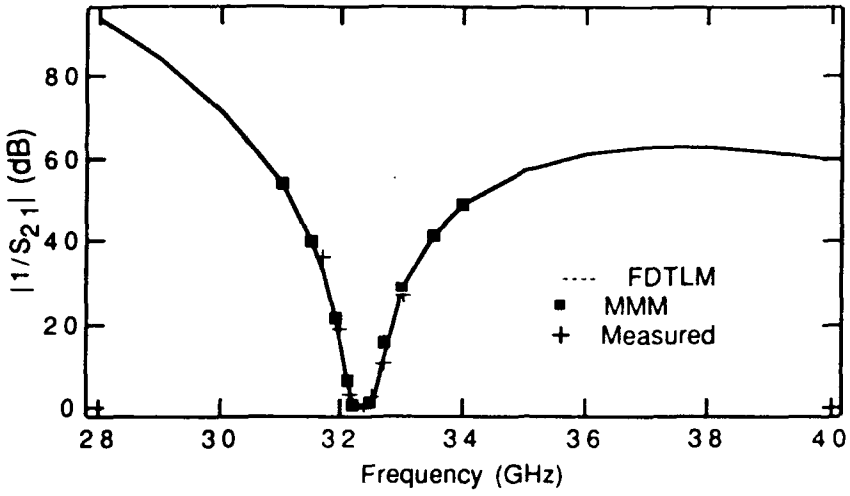

Fig. 10 Calculated and measured insertion-loss as a function of frequency of a Ka-band 3 resonator E-plane filter (waveguide housing: WR-28, insert metal thickness: t=0.51, l_1=l_7=1.009, l_2=l_6=4.778, l_3=l_5=3.87, l_4=4.796 mm).

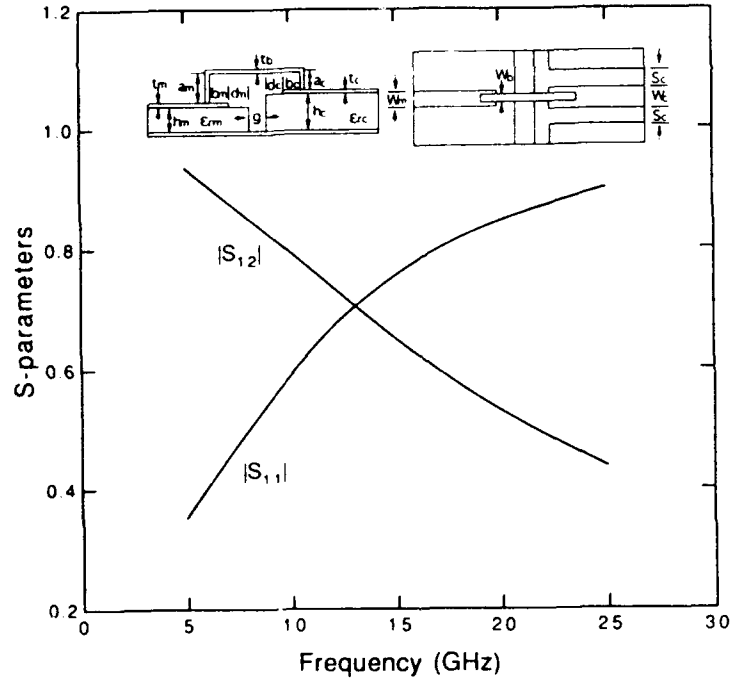

Fig 11 Frequency-dependent s parameters of interconnect assembly (b_m=b_c=d_m=d_c=0.1mm, h_m=h_c=0.2mm, g=0.3mm, a_m=a_c=0.25mm, w_m=w_c=0.2mm w_h=0.1mm, s_c=0.2mm, t_c=t_m=t_h=0, ε_{rc}=12.9, ε_{rm}=9.8)

References

[1] K.S. Yee, "Numerical solution of initial boundary value problems involving Maxwell'sequations in isotropic media", *IEEE Trans. Antennas Propagat.*, vol.AP-14, pp.302-307, May 1966.

[2] C.D.Taylor, D.H.Lam, "Electromagnetic Pulse scattering in time-varying inhomogeous media," *IEEE Trans. Antenna Prop.*, vol.AP-17, No.5, pp.585-589, Sept. 1969.

[3] D.E.Merewether, "Transient current induced on a metallic body of revolution by an electromagnetic pulse," *IEEE Trans. Electromagnetic Compatibility*, vol.EMC-13, No.2, pp.41-44, May 1971.

[4] A.Taflove and M.E.Brodwin, "Numerical solution of steady state electromagnetic scattering problems using the time-dependant Maxwell's equations," *IEEE Trans. Microwave Theory Tech.*, vol.MTT-23, pp.623-630, 1975.

[5] G.Mur, 'The modeling of singularities in the finite difference approximation of the time domain electromagnetic field equation," *IEEE Trans. Microwave Theory Tech.*, vol.MTT-29, No.10, pp.1073-1077, Oct. 1981..

[6] A.Taflove and K.R.Umashankar, "Finite difference-time domain (FDTD) modeling of electromagnetic wave scattering and interactive problems", *IEEE AP-S NewsLetter*, pp.5-19, April 1988.

[7] D.H. Choi and W.J.R. Hoefer, "The finite difference time domain method and its application to eigenvalue problems", *IEEE Trans. Microwave Theory* Tech., vol.MTT-34, pp.1464-1470, 1986.

[8] M. Rittweger and I. Wolff, "Analysis of complex passive (M)MIC-components using the finite difference time-domain approach", pp.1147-1150, *1990 IEEE-S Internatinal Microwave Symposium Digest*, Long Beach, CA, Jun. 1990.

[9] I.Wolf, "Digital signal processing of time domain simulation results by system identification method", pp.793-796 *1992 IEEE MTT MTT-S Internatinal Microwave Symposium Digest*, Albuquerque, NM, Jun. 1992.

[10] F.Arndt, V.J.Brankovic, and D.V.Krupezevic, "An improved FDTD full-wave analysis for arbitrary guiding structures using 2-D mesh," pp.389-392, *1992 IEEE MTT-S Internatinal Microwave Symposium Digest*, Albuquerque, NM, Jun. 1992.

[11] H. Jin, R. Vahldieck and S. Xiao, "An improved TLM full-wave analysis using two dimensional mesh", pp.675-677, *1991 IEEE-S Internatinal Microwave Symposium Digest*, Boston, MA, Jun. 1991.

[12] S.Xiao, R.Vahldieck, and H.Jin, "A fast 2-D FDTD full wave analyzer for arbitrary guided wave structures," *IEEE Guide Wave Letters*, pp.165-167, May 1992.

[13] H. Jin, R. Vahldieck and S. Xiao, "A full-wave analysis of arbitrary guiding structure using 2-D TLM mesh", *21th European Microwave Conference Digest*, pp.205-210, German, Sept., 1991.

[14] S.Xiao and R. Vahldieck "An Improved 2D-FDTD Algorithm for Hybrid Mode Analysis of Quasi-Planar Transmission Lines", *IEEE MTT-S Symposium Digest*, Atlanta, pp421-424, 1993.

[15] Zheng, G.W. and K.S. Chen "Effects of Substrate Anisotropy on the Dispersion of Transient Signals in Microstrip Lines" International Journal of Infrared and Millimeter Waves, Vol. 11. No.4 1990, pp.489-498.

[16] D.P.Johns and C. Christopoulos "Lossy Dielectrric and Thin Lossy Film Models for 3D Steady-State TLM" Electronics Letters, 18th Febr. 1993, vol. 29, No.4, pp. 348-349.

[17] H. Jin and R. Vahldieck, " The frequency-domain TLM method - A new concept ", *IEEE Trans.Microwave Theory and Tech.* vol. 40, No. 12, Dec. 1992, PP. 2207-2218.

[18] P. B. Johns, " A symmetrical condensed node for the TLM method," *IEEE Trans. Microwave Theory Tech.*, vol. MTT-35, pp. 370-377, April 1987.

[19] R. scaramuzza and A. J. Lowery, " Hybrid symmetrical condensed node for the TLM method," *Electron. Lett.*, vol. 26, 1990, pp. 1947-1948.

[20] J. Huang, R. Vahldieck and H. Jin, " Fast frequency-domain TLM analysis of 3D circuit discontinuities," *In the 9th Annual Review of Progress in Applied Computational Electromagnetics Symposium*, Monterey, CA, March 22-26, 1993.\

[21] P. B. Johns and R. L. Beurle, " Numerical solution of two dimensional scattering problems using a transmission line matrix," *Proc. IEE*, vol. 118, pp.1203-1208, Sept. 1971.

[22] W. J. R. Hoefer, " The transmission-line matrix method: Theory and applications," *IEEE Trans. Microwave Theory Tech.*, vol. MTT-33, pp. 882-893, Oct. 1985.

[23] H.Jin and R. Vahldieck "Full-Wave Analysis of Coplanar Waveguide Discontinuites Using the Frequency-Domain TLM Method", appears in IEEE Transaction on Microwave Theory and Techn. Vol.41, No.9 Sept. 1993

Time Domain Simulation of Non-Linear Networks Containing Distributed Interconnect Structures

M. I. Sobhy, E. A. Hosny, and K. W. Royer.

Electronic Engineering Laboratories,
University of Kent at Canterbury,
Canterbury, Kent, UK.

Tel:+(44)227 764000, *Fax:*+(44)227 456084.

Abstract

The performance of interconnects is becoming one of the main limitations in high speed digital circuits and microwave networks. It is important to be able to characterise interconnects and predict their effects in circuits for such applications. Any analysis procedure must include non-linear elements and perform analysis in the time domain. This paper describes a method of calculating the properties of interconnect structures using electromagnetic simulators and the determination of electrical circuit models. The second part of the paper describes how interconnect models are used in a circuit simulator to predict the effect of interconnects in high speed digital circuits and microwave networks.

1 Introduction

Transmission properties of interconnects such as signal delay, reflection, attenuation, dispersion and crosstalk must be taken into consideration in the analysis and design procedures of high speed digital circuits and microwave systems. It is important to include the transmission line behavior of interconnects between the system components, if the behavior of the overall system is to be accurately simulated. In general the system can be divided into lumped, non-linear subnetworks and distributed interconnect structures. The distributed interconnects can be represented by a number of basic models of transmission lines.

In this paper different approaches are described to characterise interconnects using time-domain or frequency domain procedures. Each interconnect structure can be represented by a circuit block described by its terminal relations. In the simple case, if the interconnect is a lossless non-dispersive transmission line structure, the terminal relations can be represented by a set of difference equations. In all other cases the terminal relations can be derived by using calculated or measured scattering parameters of the interconnect structure in the time domain. which can be generated directly in the time domain of by transforming frequency domain data to the time domain.

If the interconnect is modelled as a lossy quasi-static transmission line, modal time domain analysis can be applied to obtain directly the impulse responses. However, in the case of frequency dependent transmission line parameters or when coupling between the transmission line is not limited to adjacent lines the time domain modal approach does not apply. In the general case of lossy and dispersive transmission line structures, the impulse responses can be obtained directly by using time domain full-wave analysis (TLM and FD-TD) or frequency domain analysis to obtain frequency domain scattering parameters which can be transformed to the time domain. The "Method of Lines" (MoL) can be applied in this case.

Finally we have a set of lumped non-linear subnetworks, all modelled by their time domain terminal relations. A general procedure based on the state space approach has been developed to obtain the time domain performance of the whole network.

The transient responses of many examples have been obtained by using the proposed analysis procedure. These examples include different types of interconnect structures in high speed digital circuits and high frequency analogue circuits. The advantages of the proposed method are the high computational stability and efficient numerical accuracy.

The paper is in two main parts. The first part describes how the MoL can be modified to account for substrate losses, conductor losses and finite conductor thickness. The modified MoL generates the electrical parameters that are required to develop electrical models of interconnects. The second part describes how these models can be incorporated in a circuit simulator in order to predict the performance of entire high speed digital circuits and microwave circuits in the time domain.

2 MoL modelling of IC interconnects

The modelling of IC interconnects, as compared to the modelling of microstrip circuits, is complicated by the following;

- multilayer substrates with varying effective permittivity and some substrates may be anisotropic,
- conductor thicknesses are finite,
- conductor losses are significant (often greater than 100dB/m),
- the substrates can be very lossy in Si structures (the loss tangent can be greater than 0.1),
- the physical size of interconnect metalisations are very small, and have a high aspect ratio. A typical cross-sectional size is $1\mu m \times 1\mu m$.

To overcome these problems a modified MoL (Method of Lines) modelling technique has been used to model accurately the electromagnetic fields of such structures and yield the frequency dependent electrical parameters. Modern digital circuits are designed to operate at increasingly higher frequencies and the upper operating speed has become limited by interconnect performance. To overcome this limitation it is necessary to model accurately interconnects at high frequencies using electromagnetic simulation and then by using time-domain circuit simulation, the behavior of real digital circuits are accurately determined.

The "Method of Lines" (MoL) is a hybrid differential-difference scheme where a one-dimensional finite difference method is applied in the plane of the electrodes, and an associated matrix decoupling transformation allows the field equations, expressed in terms of Helmholtz potentials, to be solved in the transformed domain. Using this technique a one-dimensional discretisation need only by applied to model an arbitrary structure cross-section.

Earlier MoL modelling techniques assumed conductors to be lossless and thin, the new technique considers each conductor to be a dielectric with a large loss tangent. For example

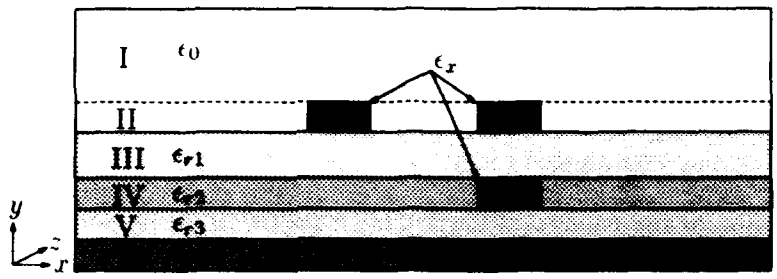

Figure 1: Example structure: $\epsilon_{r1} = 3.6, \epsilon_{r2} = 3.6, \epsilon_{r3} = 6.0$, $\epsilon_{r4} = 12.6 - 0.003j$, $\epsilon_x = 1.0 - j\frac{\sigma}{\omega\epsilon_0}$

an aluminium conductor with a conductivity of 2.5×10^7 S/m at a frequency of $1GHz$ is considered as a dielectric with a relative dielectric constant of,

$$\epsilon_r = 1.0 - j\frac{\sigma}{\omega\epsilon_0} = 1.0 - 4.494 \times 10^7 j$$

Using this technique, it is possible to model a structure as shown in figure 1 by considering it as five dielectric layers. The model is solved by first applying a finite difference discretisation in the x-direction, this is then used to form an eigen-problem involving the partial Helmholtz potentials $\underline{\Psi}_e$ and $\underline{\Psi}_h$. A wave, in a lossy structure has a complex propagation constant $\underline{\gamma} = \beta - j\alpha$. The structure then has an associated effective permittivity given by,

$$\underline{\epsilon}_{re} = \left(\frac{\underline{\gamma}}{k_0}\right)^2 \ , \ k_0 = \omega\sqrt{\mu_0\epsilon_0} \tag{1}$$

The fields $\underline{\Psi}_e$ and $\underline{\Psi}_h$ can then be scaled accordingly,

$$\Pi_e = \underline{\Psi}_e \cdot e^{-j\underline{\gamma}z} \cdot \vec{e_x} \quad , \quad \Pi_h = \underline{\Psi}_h \cdot e^{-j\underline{\gamma}z} \cdot \vec{e_x} \tag{2}$$

Maxwell's eqns. can then be discretised and written in the form,

$$\begin{aligned} \left(\underline{\epsilon}_e \hat{D} \underline{\epsilon}_h^{-1} \hat{D}^T - \hat{h}^2 \underline{\epsilon}_e\right) \underline{\psi}_e - \underline{\lambda}_e^2 \underline{\psi}_e &= 0 \\ \left(\hat{D}^T \hat{D} - \hat{h}^2 \underline{\epsilon}_h\right) \underline{\psi}_h - \underline{\lambda}_h^2 \underline{\psi}_h &= 0 \end{aligned} \tag{3}$$

Where,

$$\begin{aligned} \underline{\lambda}_e^2 &= \hat{h}^2 diag\left[\frac{\partial^2}{\partial\hat{y}^2} - \underline{\epsilon}_{re}\right] \quad , \quad \underline{\lambda}_h^2 = \hat{h}^2 diag\left[\frac{\partial^2}{\partial\hat{y}^2} - \underline{\epsilon}_{re}\right] \\ \underline{\epsilon}_e &= Effective\ Permittivity\ on\ electric\ discretisation\ lines. \\ \underline{\epsilon}_h &= Effective\ Permittivity\ on\ magnetic\ discretisation\ lines. \\ \hat{\underline{D}} &= is\ the\ \frac{\partial}{\partial x}\ operator\ for\ magnetic\ lines. \\ \hat{\underline{D}}^T &= is\ the\ \frac{\partial}{\partial x}\ operator\ for\ electric\ lines. \end{aligned}$$

By solving this eigen-problem it is possible to solve the 2nd-order differential equations in terms of y. From here it is easy to relate potentials on matching layers by applying the top and bottom boundary conditions. This procedure is simplified for layers without discontinuities in the x-direction since matrix symmetries can be applied, and the process can be streamlined.

The problems with this modelling technique are:

- the large change in the order of magnitude of the effective permittivities in the x-direction on the boundary between a conductor and the surrounding dielectric,
- the location of the dominant propagating modes for the structure for small conductor geometries (lossy conductors result in complex roots),
- the extraction of the conductor electrical properties from the field distribution of dominant propagation modes,
- the choice of a discretisation scheme that is numerically stable yet has good resolution on the conductor edges.

The vast difference between the substrate effective permittivity and the conductor effective permittivity makes the matrices ill-conditioned. This introduces inaccuracies into the eigen-values and eigen-vectors used to uncoupled the 2nd-order equations. Since the solution of these equations involves exponential terms, the relative magnitudes of the numbers vary by 10^9, this means that standard double precision computer arithmetic may not be adequately accurate. The mathematics has to be rewritten to recast simple equations into more complex but numerically stable forms.

The solution of the interface equations involves solving the eigenvalue problem,

$$[Z]\,\underline{H_B} \;=\; \underline{0} \tag{4}$$

Where $\underline{E_B}$ is the potential on a particular interface (for example between layer I and II). The matrix $[Y]$ depends upon two parameters, the frequency ω and the effective permittivity ϵ_e. By fixing the value of ω it is then necessary to locate a value for ϵ_e for which,

$$Det.\,[Z] = 0 \tag{5}$$

The solution of this problem in not trivial, since there may be more propagating modes than conductors at high frequencies. To overcome this, approximate guesses are made to the dominant mode root positions and the roots are located by gradually introducing the losses, until the actual roots are found. This procedure is outlined in the following steps,

1. The substrates are initially assumed lossless and the interconnects are infinitely thin and lossless. This yields real valued effective permittivities $\underline{\epsilon_{re}}$. At a suitable starting frequency the real roots are located using *singular value decomposition* [1].
2. Substrate losses are gradually introduced. The movement of the roots away from the real-axis is tracked until the substrate losses are included in entirety. If during this procedure the root position moves sharply, the substrate losses are decreased until the root can be tracked accurately.
3. The conductor thickness is introduced using a surface impedance model [2, 3]. This model allows the conductor surface to be replaced by a resistance that can be subtracted from the diagonal terms of the $\underline{Z}$ matrix.
4. The surface impedance model is replaced by the full MoL representation and the roots located using a complex *Newton Raphson* technique. This root location technique is reliable if the starting point is reasonably well known and the equations forming $\underline{Z}$ are

analytic which implies that $\underline{Z}$ is analytic [8]. The root located is normally surrounded by numerous poles and zeros corresponding to non-propagating modes. Stages 1 to 3 above, vastly improve root location and automate the modelling procedure.

5. Finally, the frequency is swept to yield the frequency dependent electrical parameters, tracking the movement of the roots.

Using this technique it becomes possible to locate reliably the dominant roots and characterise the structure.

3 Extraction of the stripline impedances

Once the effective permittivities for each of the fundamental propagating modes (equal to the number of conductors) and the electromagnetic field distributions have been found, further work is required to get the electrical strip impedances for the structure. The characteristic impedance matrix can be found by using the denormalised voltage, and current matrices V_m and I_m,

$$[Z_c] = [V_m] \cdot [I_m]^{-1} \tag{6}$$

These matrices can be found using on of two techniques:

1. Calculating each of the conductor voltages and currents, for each mode, by using line integrals.

2. Integrating the power and currents over the cavity area, for each of the propagating modes.

The preferred technique proceeds by integrating the power and currents. In our case, however, the problem is further complicated by multlistripline structures. For multistripline structures, it is necessary to know the individual strip currents for each mode. In symmetric models the total current flow, over the cavity cross-section for the odd propagating mode would be zero. In this case it is not possible to get the modal stripline currents. To overcome this problem, it is necessary to divide the structure into smaller sections, each containing one conductor. The power and current flows within each section are integrated to give a modal characteristic impedance and current matrix given by

$$V_{c(m,s)} = \frac{P_{c(m,s)}}{I_{c(m,s)}} \quad where \begin{cases} s = strip\ number \\ m = mode\ number \end{cases} \tag{7}$$

Using eqn 6 strip impedances for all structures can be calculated. The division of a structure is shown in figure 2. In this figure region A and B are individually integrated to yield the total power and current flowing in the 'z' direction. This technique is problematic because a large proportion of the currents flow is in the substrate, if the substrate is lossy. The substrate currents need to be partitioned into components that belong to each conductor. To minimise errors, we split the structure at the points directly between the conductors where an electric wall exists. This technique assumes that the electric wall is vertically straight through this point but, for asymmetric structures, the electric wall is a curve through this point as represented by the dotted line in figure 2.

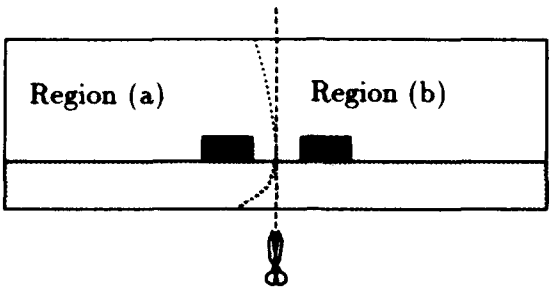

Figure 2: Division of conducting cavity for integration of current and power flows.

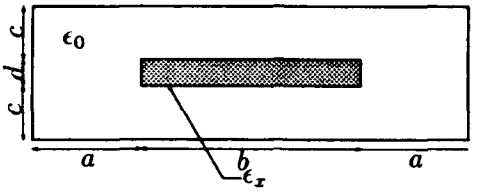

Figure 3: 3dB coupler arm of example 4.1: Constructed in brass, $\epsilon_r = 1.0 \times 10^8$ S/m, $a = 25.5$mm, $b = 52.2$mm, $c = 12.7$mm, $d = 6.35$mm.

By using the first technique of integrating the electric field from the cavity wall to the centre of each conductor, to get the modal conductor voltages, the partitioning is simplified. The modal conductor currents are found by a loop integration around each conductor. This loop integration can be enlarged to take into account the substrate currents and yield an accurate result.

The two techniques give different results, the line integral technique gives a good model of the stripline impedance seen by a wave being launched onto the stripline, the area power/current integral result is an accurate model of the stripline once a wave is propagating freely (after an infinite distance). Using both of these results it would be possible to model the coupling into the interconnect and the propagation over considerable distances.

4 MoL Results

4.1 Bar Line Example

The first structure modelled is shown in figure 3 and shows the limitations of the classical formula in calculating the characteristic impedance of a 3dB bar-line coupler arm. The MoL code was used to get accurate impedances for components of the 3dB coupler. The coupler was to be used in a power application where accurate knowledge of the losses and impedance were required. The MoL code took 7:43 minutes to run on a Sun4/75 and produced full plots of the distribution of the electric and magnetic fields, current and power densities. If field plots are not required then the program is considerably faster and the solution takes 4 minutes.

The program gives a characteristic impedance of $34.0 - 7.39 \times 10^{-4} j\Omega$ compared to 33 Ω using classical techniques [9]. The attenuation of the structure was 8.03 mdB/m. This result is useful in assessing the operating temperature of such a transmission line in high power

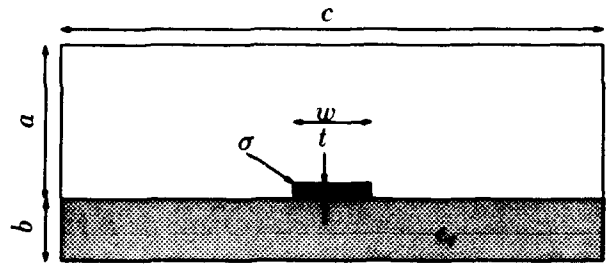

Figure 4: Simple interconnect type structure of example 4.2. $\sigma = 4.1 \times 10^7$ S/m, $\epsilon_r = 12.9$ Tan $\alpha = 0.0003$, $a = 2$mm, $b = 0.1$mm, $c = 6$mm.

applications. The power flow is plotted in figure 5 and shows the large power concentrations on the metal vertices. The small "curtaining" type effect in the x-direction along the edge of the metal is due to interpolation errors in the plotting package used.

4.2 Interconnect Example

The second example, shown in figure 4, is a large interconnect structure ($3um \times 70um$) supported on a simple single layer lossy substrate. The graph in figure 6 shows the attenuation constant for the stripline versus frequency. The attenuation factor α can be extracted directly from the calculated effective permittivity for the structure,

$$\alpha = -\Re\sqrt{k_0{}^2 \underline{\epsilon}_{re}} \tag{8}$$

$$\text{where} \quad \underline{\epsilon}_{re} = \left(\frac{\beta - j\alpha}{k_0}\right)^2$$

The characteristic impedance has been calculated by integrating the currents flowing in the structure and the conductor voltage. The real and imaginary part of the characteristic impedance are given in figures 7 and 8.

5 Equivalent circuit representation of the interconnect structures

Numerous analytical and numerical techniques have been proposed to investigate interconnect structure models in the time domain and their implementation in circuit simulators. The most common approach is to characterise the interconnect structure by its impulse responses [10–20]. These impulse responses should be as short as possible to achieve fast simulation algorithm and small memory requirements.

In this paper the integral equation method [10, 11] and an efficient scattering parameter approach [20, 21] were chosen to characterise different types of interconnects with short impulse responses. Simple circuit representations of the interconnects are introduced in the following subsections. Each equivalent circuit consists of only a resistance and a time varying source and represents one port of the interconnect structure. For brevity the mathematical details of the formulation of terminal relations for the transmission line structures are omitted and only short descriptions are given.

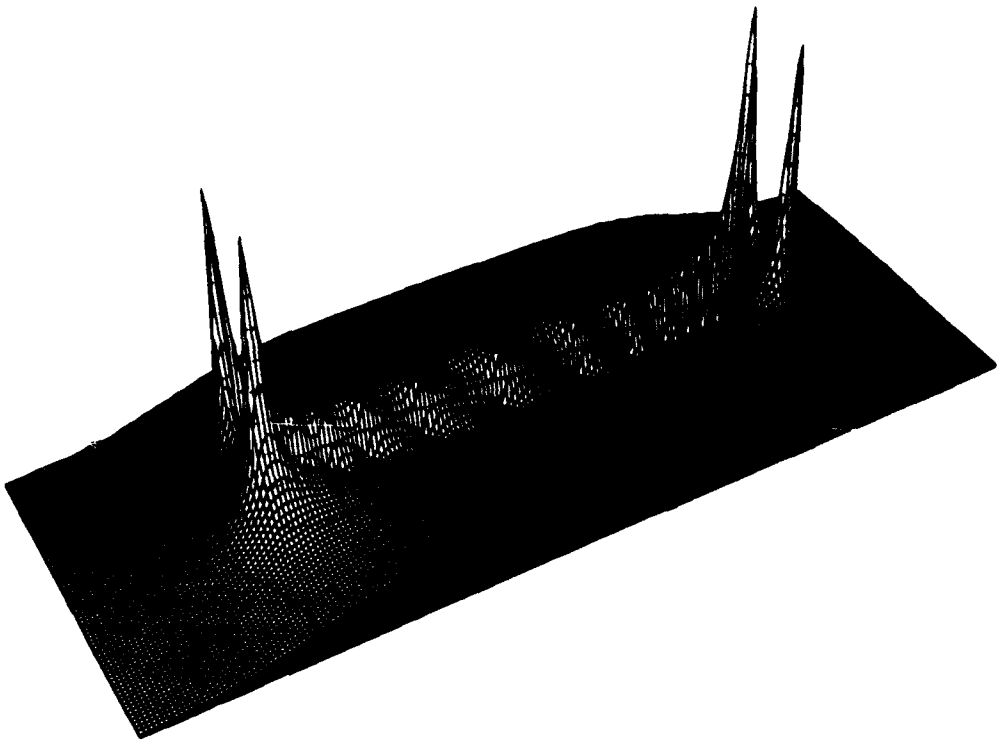

Figure 5: Surface plot of z-directed power flow of example 4.1

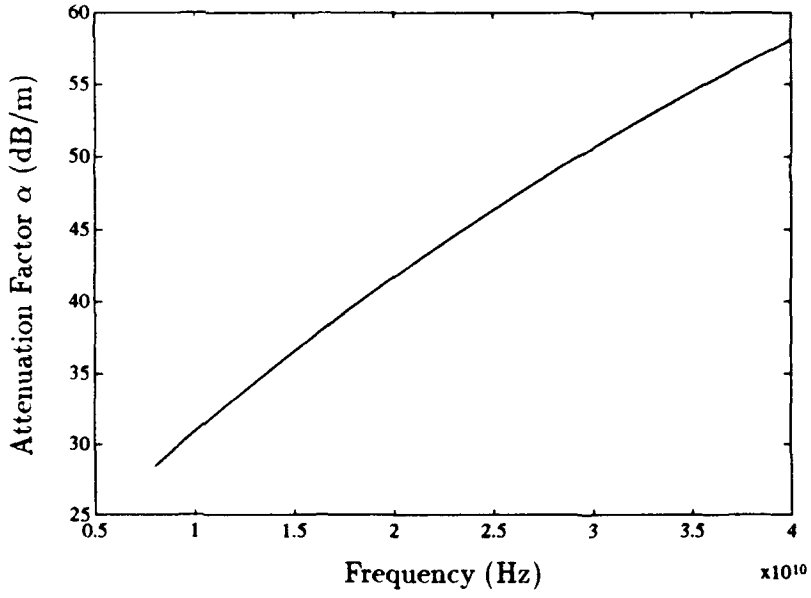

Figure 6: Attenuation vs Frequency of example 4.2.

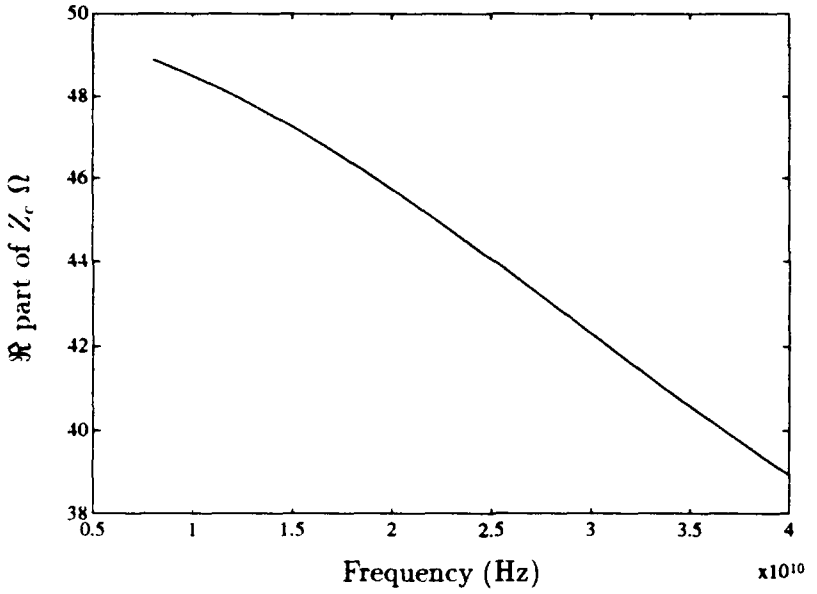

Figure 7: Characteristic Impedance (real part) vs Frequency of example 4.2.

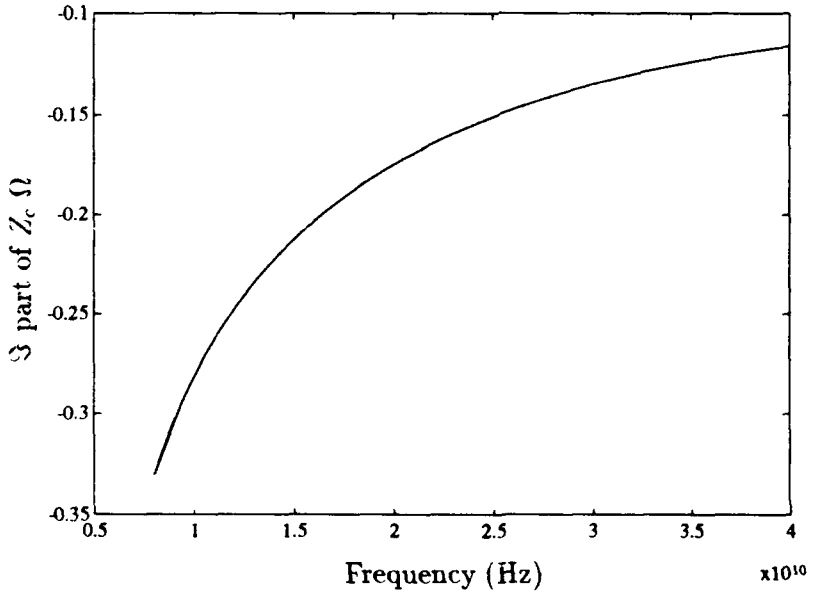

Figure 8: Characteristic Impedance (imaj part) vs Frequency of example 4.2.

5.1 Uniform lossy transmission lines with constant parameters

A simple single uniform lossy transmission line can be characterised by frequency independent resistance, inductance, conductance and capacitance per unit length. The *Telegrapher Equations* describing the electrical behavior for this type of lossy lines are,

$$\begin{aligned} \frac{\partial v}{\partial x} &= -Ri - L\frac{\partial i}{\partial t} \\ \frac{\partial i}{\partial x} &= -Gv - C\frac{\partial v}{\partial t} \end{aligned} \tag{9}$$

Taking Laplace transforms of eqn. 9, the relation between the transformed terminal voltages and currents can be easily derived [10]. We define,

$$\begin{aligned} H_1(s) &= Z_c(s) - r_0, \\ H_2(s) &= e^{-\gamma l}, \\ and \quad H_3(s) &= Z_c(s)e^{-\gamma l} \end{aligned} \tag{10}$$

where,

$$\begin{aligned} Z_c(s) &= \sqrt{\frac{R+sL}{G+sC}} \quad , \quad r_0 = \sqrt{\frac{L}{C}} \quad , \\ and \quad \gamma &= \sqrt{(R+sL)(G+sC)} \end{aligned}$$

In the time domain the explicit forms of eqn. 10 are,

$$\begin{aligned} h_1(t) &= r_0 e^{-\beta_1 t}\left\{-\beta_2 I_0(\beta_2 t) + \frac{\partial}{\partial t} I_0(\beta_2 t)\right\} \\ h_2(t) &= e^{-\alpha l}\delta(t-t_d) + \sigma l e^{-\beta_1 t}\frac{I_1(\beta_2\sqrt{t^2-t_d^2})}{\sqrt{t^2-t_d^2}}u(t-t_d) \\ h_3(t) &= r_0 e^{-\alpha l}\delta(t-t_d) + r_0 e^{-\beta_1 t}\left\{-\beta_2 I_0(\beta_2\sqrt{t^2-t_d^2}) + \frac{\partial}{\partial t} I_0(\beta_2\sqrt{t^2-t_d^2})\right\}u(t-t_d) \end{aligned} \tag{11}$$

where,

$$\begin{aligned} \beta_1 &= \frac{1}{2}\left(\frac{G}{C}+\frac{R}{L}\right) \quad , \quad \beta_2 = \frac{1}{2}\left(\frac{G}{C}-\frac{R}{L}\right) \quad , \quad t_d = \frac{l}{v} \quad , \\ v &= \frac{1}{\sqrt{LC}} \quad , \quad \alpha = \frac{\beta_1}{v} \quad , \quad \sigma = \frac{\beta_2}{v} \end{aligned}$$

$\delta(t)$ and $u(t)$ are the delta and unit step functions respectively, I_0 and I_1 are the modified Bessel functions of zero and first orders.

The relations between the instantaneous terminal voltages and currents can be obtained from the s-domain solution of the *Telegrapher* equations,

$$\begin{aligned} v_1(t) &= r_0 i_1(t) + u_{d1}(t) \\ v_2(t) &= r_0 i_2(t) + u_{d2}(t) \end{aligned} \tag{12}$$

where,

$$\begin{aligned} u_{d1}(t) &= h_1(t) \star i_1(t) + h_2(t) \star v_2(t) + h_3(t) \star i_2(t) \\ u_{d2}(t) &= h_1(t) \star i_2(t) + h_2(t) \star v_1(t) + h_3(t) \star i_1(t) \end{aligned}$$

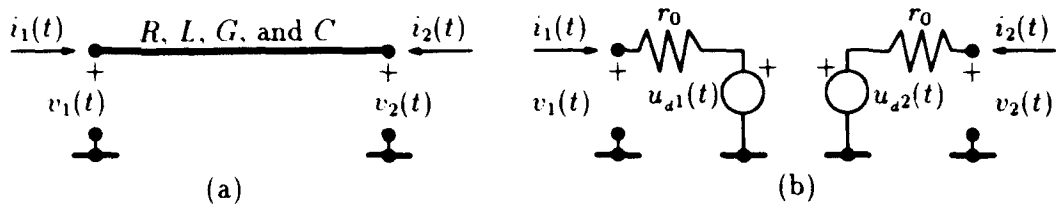

Figure 9: Lossy transmission line

Where $\star$ is the convolution operator. Each port of the transmission line is represented by an equivalent circuit which contains only a resistor and time varying source, shown in figure 9.

Coupled lossy transmission lines can be characterised by a coupled system of *Telegrapher* equations. In this case some or all of the transmission line constants, R, L, G, and C are non-diagonal matrices. Time domain modal analysis can be applied to decouple the system of equations into a set of independent *Telegrapher* equations by a linear transformation [11]. This can only occur when the coupling effects are assumed to be restricted only to the adjacent lines, and the lines are identical, equal spaced and end effects are negligible. This special case is still applicable to many integrated circuit applications, hence it is worthy of study.

The instantaneous terminal voltages/currents are related to the modal voltages/currents by the linear relation,

$$\boldsymbol{v} = \boldsymbol{M}\ \boldsymbol{v}_m \quad , \quad \boldsymbol{i} = \boldsymbol{M}\ \boldsymbol{i}_m \tag{13}$$

where,

$$\boldsymbol{M} = \text{linear transformation matrix, and } \boldsymbol{M}^{-1} = \boldsymbol{M}^T$$

The relations between modal voltages and currents are,

$$\boldsymbol{v}_m(t) = \boldsymbol{r}_{0m}\ \boldsymbol{i}_m(t) + \boldsymbol{u}_{dm}(t) \tag{14}$$

where,

$\boldsymbol{r}_{0m}$ = Diagonal matrix representing the equivalent modal characteristic impedances.

$\boldsymbol{u}_{dm}$ = Vector representing equivalent modal sources.

The terminal voltage and current relations can be obtained from eqn. 13 and 14,

$$\boldsymbol{v}(t) = \boldsymbol{R}_0\ \boldsymbol{i}(t) + \boldsymbol{u}_d(t) \tag{15}$$

where,

$$\begin{aligned} \boldsymbol{R}_0 &= \boldsymbol{M}\ \boldsymbol{r}_{0m}\ \boldsymbol{M}^T, \\ \boldsymbol{u}_d(t) &= \boldsymbol{M}\ \boldsymbol{u}_{dm} \end{aligned}$$

The $\boldsymbol{R}_0$ matrix is a non-diagonal matrix. Eqn. 15 can be rearranged such that each port of the coupled structure can be represented by an equivalent circuit similar to a single line.,

$$\boldsymbol{v}(t) = \boldsymbol{r}_0\ \boldsymbol{i}(t) + \boldsymbol{u}_d^* \tag{16}$$

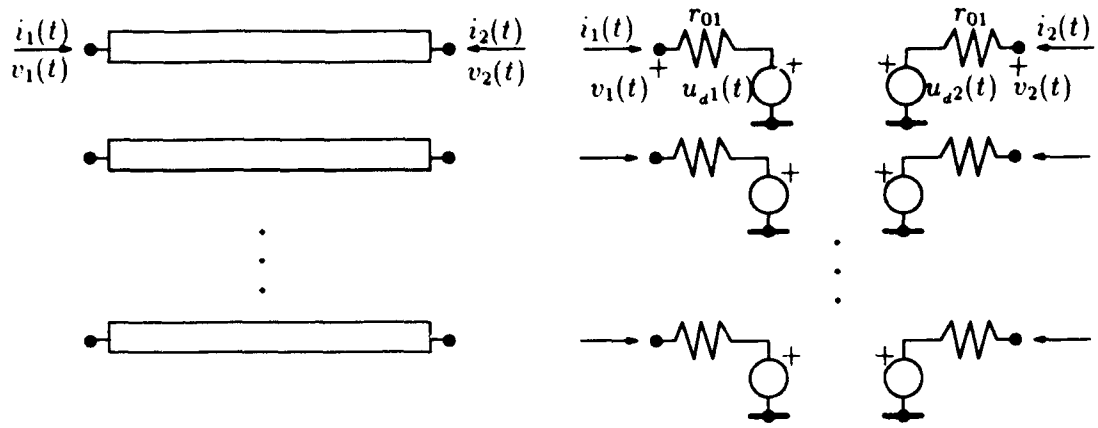

(a) Coupled transmission line structure (b) Equivalent circuit block

Figure 10: Uniform coupled transmission line structure

where,

$$\begin{aligned} \boldsymbol{r}_0 &= \text{diagonal matrix, } \boldsymbol{r}_0 = diag\{\ \boldsymbol{R}_0\}\ , \\ \boldsymbol{u}_d^* &= \boldsymbol{R}_{0c}\ \boldsymbol{i}(t) + \ \boldsymbol{u}_d(t)\ , \\ \boldsymbol{R}_{0c} &= \boldsymbol{R}_0 - \ \boldsymbol{r}_0 = \text{diagonal matrix with zero diagonal elements.} \end{aligned}$$

In fact the term $\boldsymbol{R}_{oc}\ \boldsymbol{i}(t)$ is the part of the equivalent source $\boldsymbol{u}_d^*(t)$ which represents the coupling between lines. For an uncoupled transmission line structure $\boldsymbol{u}_d^*(t) = \boldsymbol{u}_d(t)$. The equivalent circuit representation of the lossy coupled transmission line structure is shown in figure 10(b).

5.2 Uniform lossy transmission lines structures with frequency dependent parameters

Since the transmission line parameters are frequency dependent, the *Telegrapher* equations can only describe the electrical behavior of the transmission line structure in the frequency domain . A Frequency domain modal approach can be applied to decouple the *Telegrapher* equations in the case of coupled line structures. The most common approach to deal with lossy dispersive transmission line structures is by using scattering parameter techniques [12-21] . This approach offers good stability and efficiency [16].

If the reference impedance matrix is chosen identical to the frequency dependent characteristic impedance, the relation between the terminal incident and reflected voltages are,

$$\begin{bmatrix} \boldsymbol{B}_1 \\ \boldsymbol{B}_2 \end{bmatrix} = \begin{bmatrix} \boldsymbol{S}_{11}(w) & \boldsymbol{S}_{12}(w) \\ \boldsymbol{S}_{21}(w) & \boldsymbol{S}_{22}(w) \end{bmatrix} \begin{bmatrix} \boldsymbol{A}_1 \\ \boldsymbol{A}_2 \end{bmatrix} \tag{17}$$

where,

$$\begin{aligned} \boldsymbol{A}_{1,2} &= \text{Incident voltage wave vectors} \\ &\quad \text{at input or output,} \\ \boldsymbol{B}_{1,2} &= \text{Reflected voltage wave vectors} \\ &\quad \text{at input or output,} \end{aligned}$$

$$
\begin{aligned}
\boldsymbol{S}_{11}(w) &= \boldsymbol{S}_{22}(w) = 0 \\
\boldsymbol{S}_{12}(w) &= \boldsymbol{S}_{21}(w) = M_v E M_v^{-1} \\
\boldsymbol{M}_v &= \text{Matrix of eigenvectors of } \boldsymbol{Z}\,\boldsymbol{Y} \\
\boldsymbol{E} &= \begin{bmatrix} e^{-\alpha_1 l} & & \\ & \ddots & \\ & & e^{-\alpha_n l} \end{bmatrix} \\
\alpha_i &= i\text{th eigenvalue of } \boldsymbol{Z}\,\boldsymbol{Y} \\
\boldsymbol{Z} &= \boldsymbol{R}(w) + j\,\boldsymbol{L}(w) \quad \textit{and} \quad \boldsymbol{Y} = \boldsymbol{G}(w) + j\,\boldsymbol{L}(w)
\end{aligned}
$$

The transformed voltage and current relation can be written in the form,

$$
\begin{aligned}
\boldsymbol{V}_1 &= \boldsymbol{Z}_c\,\boldsymbol{I}_1 + 2\,\boldsymbol{S}_{21}\,\boldsymbol{A}_2 \\
\boldsymbol{V}_2 &= \boldsymbol{Z}_c\,\boldsymbol{I}_1 + 2\,\boldsymbol{S}_{21}\,\boldsymbol{A}_1
\end{aligned} \tag{18}
$$

where,

$$
\begin{aligned}
\boldsymbol{A}_1 &= \frac{1}{2}(\,\boldsymbol{V}_1 + \boldsymbol{Z}_c\,\boldsymbol{I}_1) \\
\boldsymbol{A}_2 &= \frac{1}{2}(\,\boldsymbol{V}_2 + \boldsymbol{Z}_c\,\boldsymbol{I}_2)
\end{aligned}
$$

Since the characteristic impedance $\boldsymbol{Z}_c$ is frequency dependent (and is also complex for lossy transmission lines structure), it can not be used in the time domain equivalent circuit. The initial-value theorem of transform analysis [20] show that,

$$
\lim_{\omega \to \infty} \boldsymbol{Z}_c(w) = \boldsymbol{R}_0
$$

where,

$$
\boldsymbol{R}_0 = \text{Real and constant matrix.}
$$

If the matrix $\boldsymbol{R}_0$ is chosen as a reference impedance, then the impulse responses, $\boldsymbol{s}_{11}(t)$ and $\boldsymbol{s}_{22}(t)$ (inverse Fourier transform of $\boldsymbol{S}_{11}(w)$ and $\boldsymbol{S}_{22}(w)$), wi'' have short durations.

The terminal voltage-current relations are,

$$
\begin{aligned}
\boldsymbol{V}_1 &= \boldsymbol{R}_0\,\boldsymbol{I}_1 + 2\,\boldsymbol{S}_{11}\,\boldsymbol{A}_1 + 2\,\boldsymbol{S}_{12}\,\boldsymbol{A}_2 \\
\boldsymbol{V}_2 &= \boldsymbol{R}_0\,\boldsymbol{I}_2 + 2\,\boldsymbol{S}_{22}\,\boldsymbol{A}_2 + 2\,\boldsymbol{S}_{21}\,\boldsymbol{A}_1
\end{aligned} \tag{19}
$$

Hence the terminal voltage-current relations in the time domain are,

$$
\begin{aligned}
\boldsymbol{v}_1(t) &= \boldsymbol{r}_0\,\boldsymbol{i}_1(t) + \boldsymbol{u}^*_{d1}(t) \\
\boldsymbol{v}_2(t) &= \boldsymbol{r}_0\,\boldsymbol{i}_2(t) + \boldsymbol{u}^*_{d2}(t)
\end{aligned} \tag{20}
$$

where,

$$
\begin{aligned}
\boldsymbol{r}_0 &= \text{Diagonal matrix , } \boldsymbol{r}_0 = diag\{\,\boldsymbol{R}_0\}\ , \\
\boldsymbol{R}_{0c} &= \boldsymbol{R}_0 - \boldsymbol{r}_0\ , \\
\boldsymbol{u}^*_{d1}(t) &= \boldsymbol{R}_{0c}\,\boldsymbol{i}_1(t) + \boldsymbol{u}_{d1}(t)\ , \\
\boldsymbol{u}^*_{d2}(t) &= \boldsymbol{R}_{0c}\,\boldsymbol{i}_2(t) + \boldsymbol{u}_{d2}(t)\ , \\
\boldsymbol{u}_{d1}(t) &= 2\,\boldsymbol{s}_{11}(t) \star \boldsymbol{a}_1(t) + 2\,\boldsymbol{s}_{12}(t) \star \boldsymbol{a}_2(t)\ , \\
\boldsymbol{u}_{d2}(t) &= 2\,\boldsymbol{s}_{22}(t) \star \boldsymbol{a}_1(t) + 2\,\boldsymbol{s}_{21}(t) \star \boldsymbol{a}_2(t)\ , \\
\boldsymbol{a}_1(t) &= \frac{1}{2}(\,\boldsymbol{v}_1(t) + \boldsymbol{R}_0\,\boldsymbol{i}_1(t))\ , \\
\textit{and}\quad \boldsymbol{a}_2(t) &= \frac{1}{2}(\,\boldsymbol{v}_2(t) + \boldsymbol{R}_0\,\boldsymbol{i}_2(t))\ .
\end{aligned}
$$

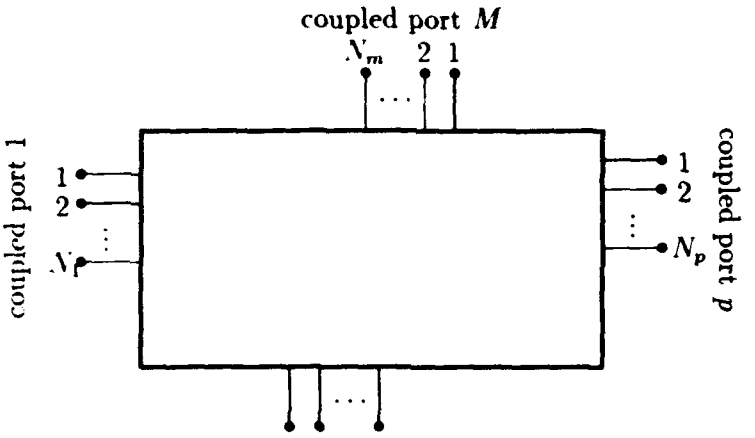

Figure 11: General interconnect structure.

From eqn. 20, each port of a lossy transmission line structure with frequency dependent parameters can be represented by a simple equivalent circuit shown in figure 9.

5.3 Non-uniform interconnect structures

Non-uniform interconnect structures are quite often used in microwave systems and in high-speed electronics [21-26]. The transient analysis of general interconnect structures terminated by arbitrary load is efficiently performed by using the scattering parameters approach [21]. The scattering parameters can by obtained by simulation or measurement. Full wave analysis provides the frequency dependent propagation constants, the characteristic impedance matrix and the eigen-voltage and eigen-current matrices needed to generate the non-TEM scattering parameters $\boldsymbol{S}(w)$.

A general interconnect structure is shown in figure 11, where the single ports are grouped into sets of coupled ports. Each coupled port p ($p = 1, \cdots, m$) consists of a set of coupled ports. The whole interconnect structure is described by the overall scattering matrix $\boldsymbol{S}(w)$,

$$\begin{bmatrix} \boldsymbol{B}_1(w) \\ \vdots \\ \boldsymbol{B}_m(w) \end{bmatrix} = \begin{bmatrix} \boldsymbol{S}_{11}(w) & \cdots & \boldsymbol{S}_{1m}(w) \\ \vdots & \ddots & \vdots \\ \boldsymbol{S}_{m1}(w) & \cdots & \boldsymbol{S}_{mm}(w) \end{bmatrix} \cdot \begin{bmatrix} \boldsymbol{A}_1(w) \\ \vdots \\ \boldsymbol{A}_m(w) \end{bmatrix} \tag{21}$$

The voltage-current relationship of port p is,

$$\boldsymbol{V}_p(w) = \boldsymbol{R}_p \, \boldsymbol{I}_p(w) + 2 \sum_{q=1}^{m} \boldsymbol{S}_{pq}(w) \, \boldsymbol{A}_q \tag{22}$$

where,

$\boldsymbol{V}_p(w)$ = Voltage vector of the coupled port p,
$\boldsymbol{I}_p(w)$ = Current vector of the coupled port p,
and $\boldsymbol{R}_p$ = Reference impedance matrix associated with coupled port p.

A local instantaneous characteristic impedance matrix is defined [21],

$$\boldsymbol{R}'_p = \left[\boldsymbol{I} - \boldsymbol{S}_{pp}^{\lim} \right]^{-1} \cdot \left[\boldsymbol{I} + \boldsymbol{S}_{pp}^{\lim} \right] \boldsymbol{R}_p$$

where,

$$\boldsymbol{S}_{pp}^{\lim} = \lim_{w \to \infty} \boldsymbol{S}_{pp}(w)$$

The matrices $\boldsymbol{R}'_p$ $(p = 1, \cdots, m)$ are real and non-diagonal. If $\boldsymbol{R}'_p$ are used as reference impedances instead of $\boldsymbol{R}_p$, the corresponding modified scattering matrix $\boldsymbol{S}'(w)$ can be calculated.

$$\boldsymbol{S}'(w) = [(\boldsymbol{I} - \boldsymbol{T}) + (\boldsymbol{I} + \boldsymbol{T})\ \boldsymbol{S}(w)] \cdot [(\boldsymbol{I} + \boldsymbol{T}) + (\boldsymbol{I} - \boldsymbol{T})\ \boldsymbol{S}(w)]^{-1} \tag{23}$$

where,

$$\begin{aligned} \boldsymbol{T} &= \left[\boldsymbol{R}'_p\right] \cdot [\boldsymbol{R}_p]^{-1}\ , \\ \boldsymbol{I} &= \text{Unit matrix}\ . \end{aligned}$$

The impulse functions $\boldsymbol{s}'(t)$ (inverse Fourier transform of $\boldsymbol{S}'(w)$) is characterized by $\boldsymbol{s}'(0) = 0$ and have a relatively short durations. Short impulse responses are important for the stability and accuracy of the solution . The instantaneous voltage-current relation of port p can be written in the form,

$$\boldsymbol{v}_p(t) = \boldsymbol{R}'_p\ \boldsymbol{i}_p(t) + \boldsymbol{u}_{dp}(t)\ ,\ p = 1, \cdots, m \tag{24}$$

where.

$$\boldsymbol{u}_{dp}(t) = 2 \sum_{q=1}^{m} \boldsymbol{s}'_{pq}(t) \star \boldsymbol{a}_q(t)$$

Eqn. 24 can be rearranged in the form,

$$\boldsymbol{v}_p(t) = \boldsymbol{r}_{op}\ \boldsymbol{i}_p(t) + \boldsymbol{u}^*_{dp}(t)\ ,\ p = 1, \cdots, m \tag{25}$$

where,

$$\begin{aligned} \boldsymbol{r}_{op} &= \text{Diagonal matrix} = diag\left\{\boldsymbol{R}'_p\right\}, \\ \boldsymbol{u}^*_{dp} &= \boldsymbol{R}_{cp}\ \boldsymbol{i}_p(t) + \boldsymbol{u}_{dp}(t), \\ \text{and}\ \boldsymbol{R}_{cp} &= \boldsymbol{R}'_p - \boldsymbol{r}_{op} \end{aligned}$$

It can be shown from eqn. 25 that each port can be represented by an equivalent circuit which contains only a resistance and a time varying source as in previous cases. In some cases the time domain scattering parameters $\boldsymbol{s}(t)$ can be directly generated from a field simulator using a time domain approach such as FD-TD and TLM methods.In these cases $\boldsymbol{s}(t)$ can be modified to obtain the equivalent circuit representations of the structure in a similar procedure as described above.

6 The network formulation

In general the network is consisting of an arbitrary number of interconnect structures which are terminated by an arbitrary number of nonlinear subnetworks (as shown in figure 12(a)). The interconnects are modelled by circuit blocks such that each port can be represented by an equivalent circuit consisting of a resistance and a time varying source (as explained in

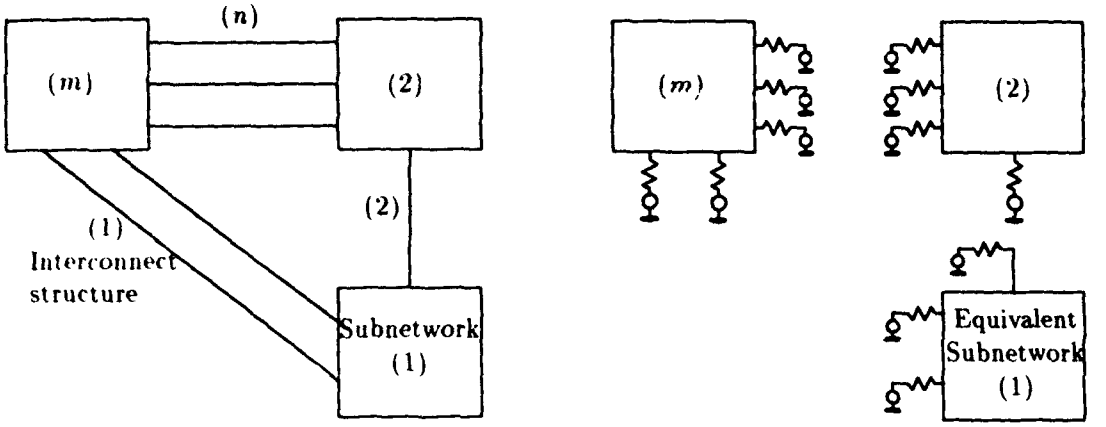

(a) The whole network (b) The equivalent subnetwork

Figure 12: General network composed of subnetworks and interconnect structures

section 1). Hence the whole network can be replaced by a set of equivalent subnetworks as shown in figure 12(b).

The electric behavior of each subnetwork can be described by the state space equations,

$$\frac{\partial \boldsymbol{x}(t)}{\partial t} = \boldsymbol{A}\,\boldsymbol{x}(t) + \boldsymbol{B}_s\,\boldsymbol{u}_s(t) + \boldsymbol{B}_n\,\boldsymbol{u}_n(t) + \boldsymbol{B}_d\,\boldsymbol{u}_d(t) \tag{26}$$

$$\boldsymbol{F}_n = \boldsymbol{H}\,\boldsymbol{x}(t) + \boldsymbol{W}_s\,\boldsymbol{u}_s(t) + \boldsymbol{W}_n\,\boldsymbol{u}_n(t) + \boldsymbol{W}_d\,\boldsymbol{u}_d(t) \tag{27}$$

$$\boldsymbol{y} = \boldsymbol{C}\,\boldsymbol{x}(t) + \boldsymbol{D}_s\,\boldsymbol{u}_s(t) + \boldsymbol{D}_n\,\boldsymbol{u}_n(t) + \boldsymbol{D}_d\,\boldsymbol{u}_d(t) \tag{28}$$

where,

$\boldsymbol{x}$ = the state variable vector,
$\boldsymbol{u}_s$ = the independent source vector,
$\boldsymbol{u}_n$ = the non-linear source vector,
$\boldsymbol{u}_d$ = the interconnect source vector.

The formulation of these equations can be obtained by a hierarchical development procedure using a topological approach similar to the one described in [27,28]. At the lowest level of hierarchy the subnetwork equations can be developed from the basic circuit elements. If the network is composed of m subnetworks and n interconnects, we can define n interconnect matrices, $N_j, (j = 1, \cdots, n)$, such that,

$$\boldsymbol{u}_d^j(t) = \boldsymbol{N}_j\,\boldsymbol{u}_d^s(t) \tag{29}$$

where,

$\boldsymbol{u}_d^s(t)$ = $\left[\boldsymbol{u}_d^{s_1} \cdots \boldsymbol{u}_d^{s_m}\right]^T$,
vector of all equivalent voltage sources
of the interconnect structures, $s_1, \cdots, s_m$,
$\boldsymbol{N}_j$ = interconnection matrix of the jth subnetwork which
has only one non-zero entry (equals one)
$\boldsymbol{u}_d^j(t)$ = the subset of source vector $\boldsymbol{u}_d^s(t)$ which are
connected to the jth subnetwork.

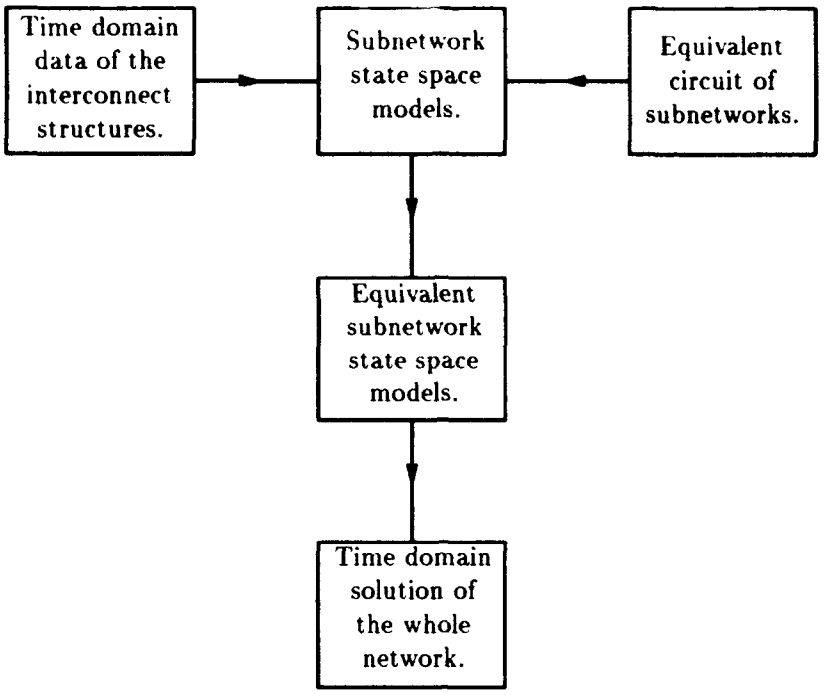

Figure 13: Block diagram of solution procedure

The interconnect matrix N_j assigns subset ports which are connected to the the jth subnetwork from all ports of the interconnects of the overall network.

7 Analysis procedure

The analysis procedure starts by finding the equivalent circuit representations of the interconnect structures as described in section 2. The unconnected equivalent subnetworks are established from the lumped subnetworks and equivalent circuits of the interconnect. Finally the time response of the whole network is obtained by solving the set of equations 26, 27,and 28 describing each equivalent subnetwork.

The values of the sources $\boldsymbol{u}_s(t)$, $\boldsymbol{u}_n(t)$ and $\boldsymbol{u}_d(t)$, are needed to solve the system of differential equations 26. The input sources $\boldsymbol{u}_s(t)$ are defined at any time and the non-linear sources $\boldsymbol{u}_n(t)$ are obtained by solving the system of non-linear equations 27 by using an iterative procedure (such as the *Newton Raphson* algorithm). The values of the sources $\boldsymbol{u}_d(t)$ are obtained by convolving the time domain data of the interconnect structures with the terminal voltages and currents. It should be noted that the disconnected equivalent subnetworks are coupled to each other through the time varying sources $\boldsymbol{u}_d(t)$. Therefore all the subnetworks are solved simultaneously at each time step. The main features of the analysis procedure is shown in figure 13.

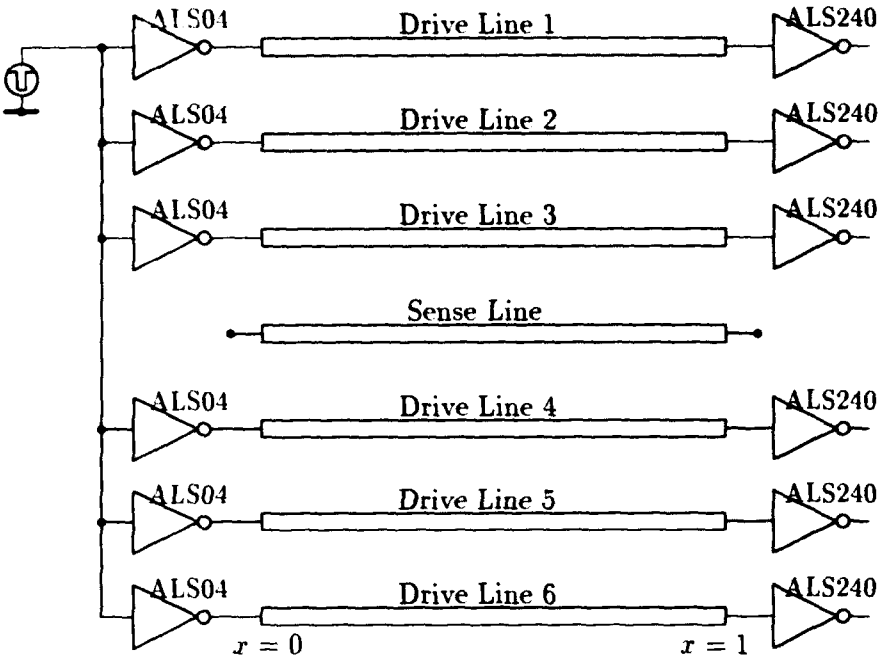

Figure 14: Schematic diagram of example 8.1

8 Time Domain Results

Illustrative examples containing different types of interconnection structures were analyzed by using the proposed approach.

8.1 Digital Circuit Example

A network used for the simulation of crosstalk on a microstrip array connected to nonlinear loads is shown in figure 14 [15]. The interconnection structure consists of six drive lines and one sense line. Each drive line is connected to the output of (ALS04) TLL, inverter at the near end and input of an ALS240 inverter at the far end. The sense line is left floating at both ends. The coupling between non-adjacent lines was neglected. Impulse responses were generated by using the modal time domain approach. The time responses obtained from simulation at the terminals of drive line 3 and sense line are shown in figures 15, 16, 17 and 18.

8.2 Microwave Circuit Example

An asymmetric two-line microstrip configuration supported by a lossy substrate is shown in figure 19 [21]. The frequency-dependent line parameter matrices $\boldsymbol{L}(w)$, $\boldsymbol{C}(w)$,and $\boldsymbol{G}(w)$ were calculated in the frequency range 0-100 GHz, see figures 21, 22 and 23. This coupled lossy dispersive transmission line structure was connected with nonlinear loads as shown in figure 20.

The scattering parameters $\boldsymbol{S}(w)$ were generated by using modal frequency domain approach and then transformed to the time domain to obtain equivalent circuits of the interconnects. The transient simulation results are represented in figures 24 and 25

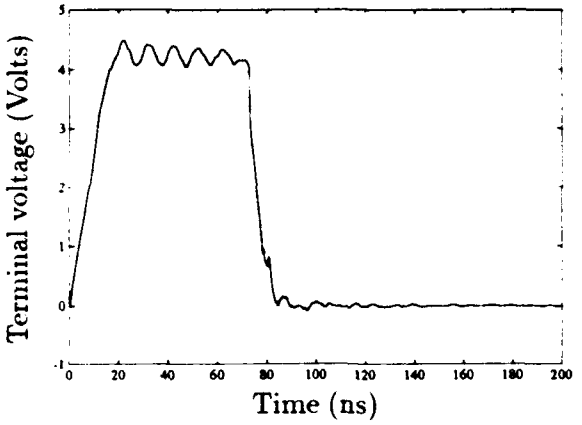

Figure 15: Drive Line 3 at near end of example 8.1.

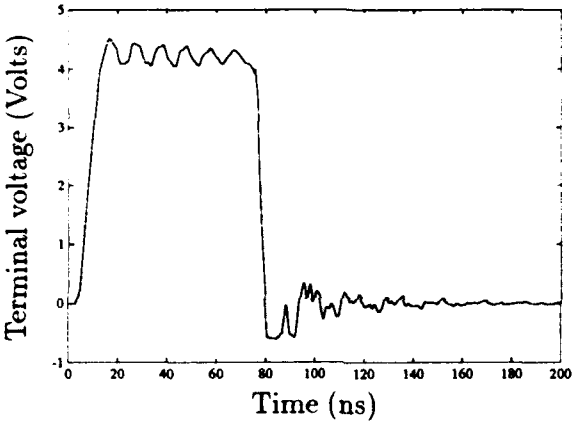

Figure 16: Drive Line 3 at far end of example 8.1.

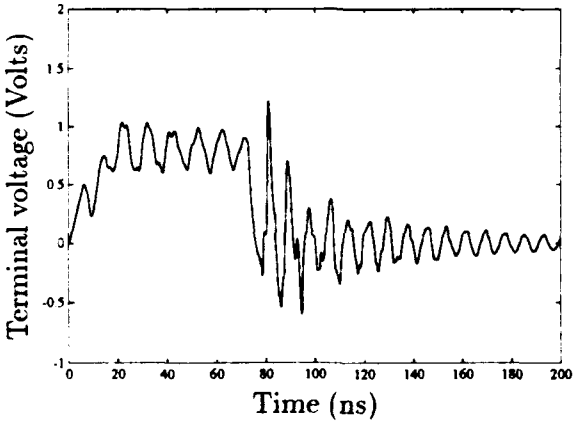

Figure 17: Sense Line 4 at near end of example 8.1.

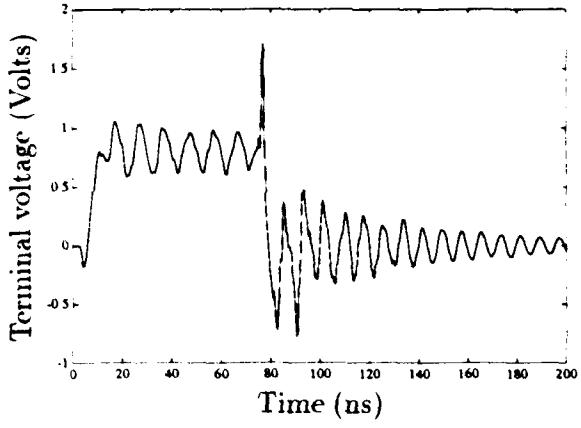

Figure 18: Sense Line 4 at far end of example 8.1.

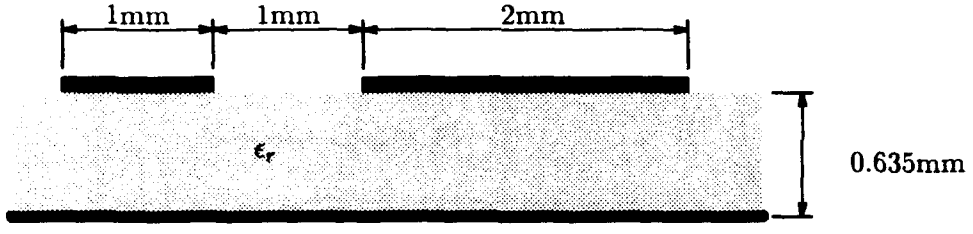

Figure 19: Assymetric two-line microstrip configuration of example 8.2. $\epsilon_r = 9.8, Tan\,\delta = 0.05$.

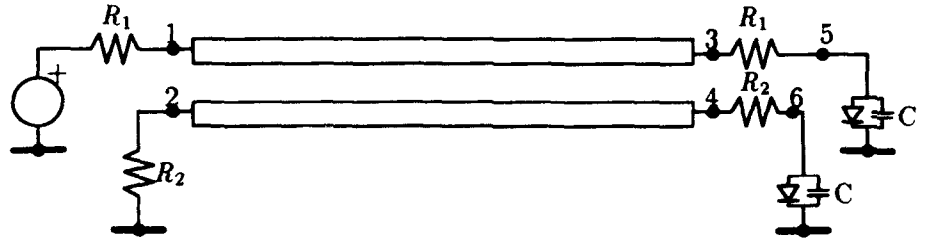

Figure 20: Coupled dispersive lossy transmission line structure of example 8.2. $R_1 = 40\Omega$, $R_2 = 25\Omega$, $C = 10$pF.

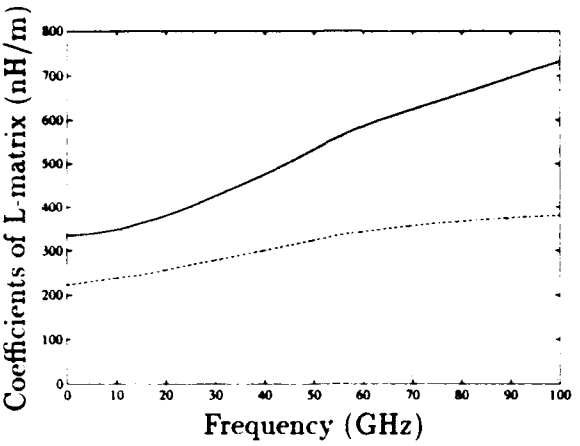

Figure 21: $L(\omega)$ of example 8.2: L_{11} —, L_{22} - - -, and $L_{12/21}$ $\cdots$.

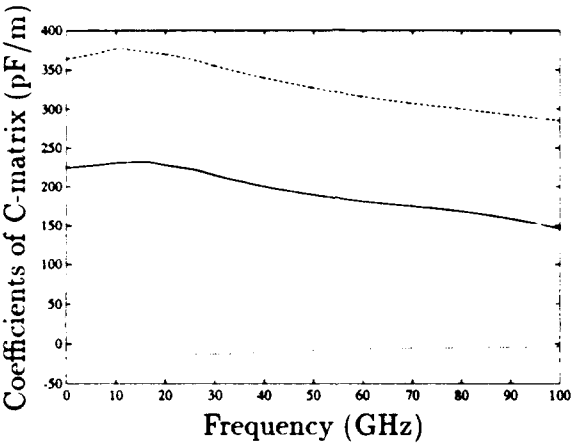

Figure 22: $C(\omega)$ of example 8.2: C_{11} —, C_{22} - - -, and $C_{12/21}$ $\cdots$.

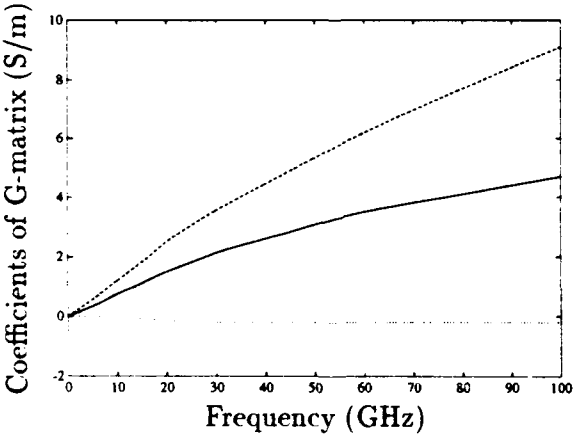

Figure 23: $G(\omega)$ of example 8.2: G_{11} —, G_{22} - - -, and $G_{12/21}$ $\cdots$.

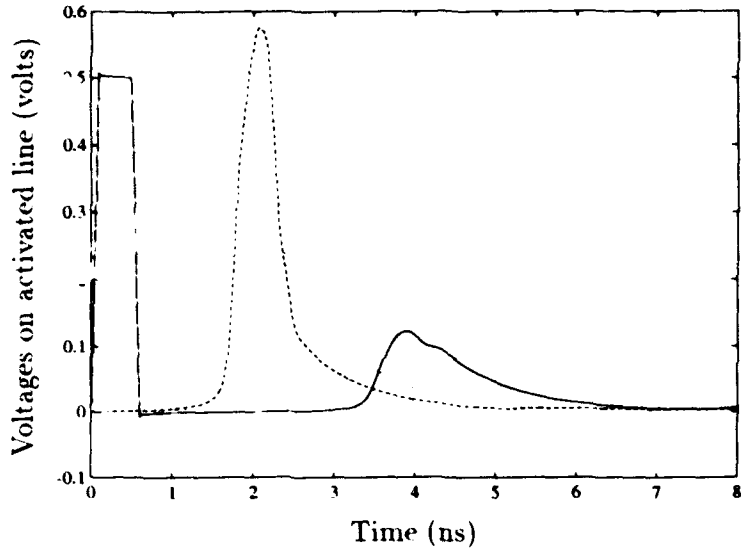

Figure 24: Time responses of example 8.2: $v_1(t)$ —, $v_3(t)$ - - -, and $v_5(t)$ $\cdots$.

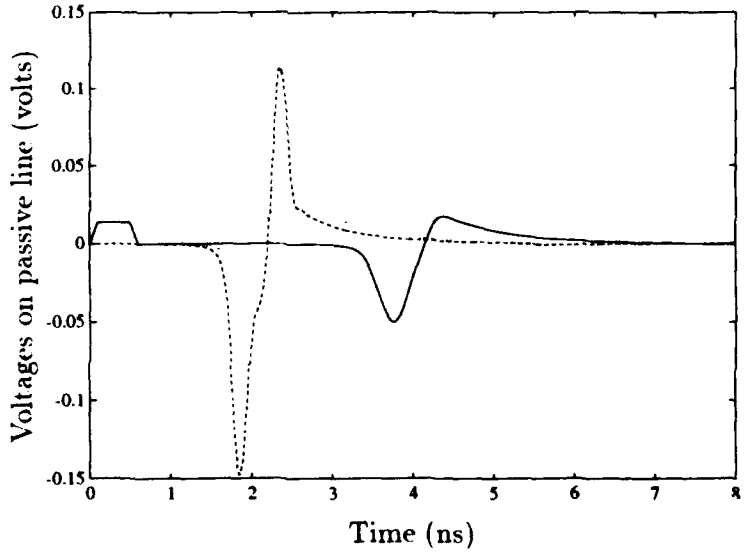

Figure 25: Time responses of example 8.2: $v_2(t)$ —, $v_4(t)$ - - -, and $v_6(t)$ $\cdots$.

9 Conclusion

High speed digital circuits and microwave circuits share the same problem of requiring accurate modelling of interconnects or microstrips. However, there are also a number of differences in the structures used for these two categories of circuits to warrant significant modifications on the modelling techniques. In digital circuits the dimensions of interconnects are small and hence, conductor losses are significant. Substrate losses are also significant in digital structures. Electromagnetic simulations used to analyse digital structures have to cope with both conductor and substate losses. For digital interconnects, circuit simulation has to be performed in the time domain due to the non-harmonic nature of the signals used. This necessitates developing interconnect models in the time domain to include losses and dispersion. The circuit simulation technique will also have to include non-linear elements in order to simulate switching devices.

In this paper we have described how the Method of Lines can be modified to model interconnects with lossy conductor and substrate losses and how circuit models of these structures can be derived. In the second half of the paper, a time domain analysis procedure has been described in order to simulate entire non-linear networks including interconnects. Several results have been given to illustrate the validity of the procedure.

References

[1] V. A. Labay, and J. Bornemann, "Matrix Singular Value Decomposition for Pole-Free Solutions of Homogeneous Matrix Equations as Applied to Numerical Modeling Methods", *IEEE Microwave and Guided Wave Letters, Vol. 2, No. 2, pp. 49-51, February 1992.*

[2] A. G. Keen, "Quasi-Static Analysis of Electro-optic Modulators by the MoL", *Journal of Lightwave Technology, Vol 8 No.1 pp. 42-50, 1990.*

[3] Kinowski D., Huret F., Seguinot C., Pribetich P., and Kennis P, "Performance of Superconducting Interconnects", *Microwave and Optical Technology, Vol.3, No.10, pp. 338-341, 1990.*

[4] Jochen Geisel, Karl-Heinz Muth and Wolfgang Heinrich, "The Behavior of the Electromagnetic Field at Edges of Media with Finite Conductivity", *IEEE Trans. on MTT, Vol.40, No.1, pp. 158-161, January 1992.*

[5] GEC Marconi Materials Technology Ltd., "Design Rules for 1.5μm High Speed Digital Process".

[6] F. J. Schmückle, and R. Pregla, "The Method of Lines for the Analysis of Lossy Planar Waveguides", *IEEE Trans. on MTT, Vol. 38, No. 10, pp. 1473-1479.*

[7] Toshihide Kitazawa, "Loss Calculation of Single and Coupled Strip Lines by Extended Spectral Domain Approach", *IEEE Microwave and Guided Letters, Vol. 3, No. 7, pp. 221-213, July 1993.*

[8] D. O. Tall, "Functions of a Complex Variable", *Routledge & Kegan Paul plc, ISBN 0 7100 8655 5, pp. 22.*

[9] G. L. Matthaei, L. Young, and E. M. T. Jones , "Microwave Filters, Impedance-Matching Networks and Coupling Structures", *McGraw Hill Book Company, Ref. 64-7937, Ch. 13, Sect. 11, pp 819.*

[10] K. Araki and Y. Naito, "Computer-Aided Analysis of Coupled Lossy Transmission Lines",*Proc. Int. Symp. on Circuits and Systems, pp. 423-426,1985.*

[11] D. S. Gao, etal, "Modelling and Simulation of Interconnection Delays and Crosstalks in High-Speed Integrated Circuits",*IEEE Trans. on Circuits and Systems, Vol. 37, No.1, January 1990.*

[12] A. R. Djordjevic, et al. "Analysis of Lossy Transmission Lines with Arbitrary Non-linear Terminal Networks",*IEEE Trans. MTT, Vol. 34, pp. 660-666, June 1986.*

[13] G. Gu, et al. "Transient Analysis of Frequency-Dependent Transmission Line Systems Terminated with Non-linear Loads",*Journal of El. Waves and Appl., Vol. 3, No. 3, pp. 183-197, 1989.*

[14] J. E. Schutt-Aine and R. Mittra, "Scattering Parameter Transient Analysis of Transmission Line Loaded with Non-linear Terminations",*IEEE Trans. MTT, Vol. 36, pp.529-536, March 1988.*

[15] J. E. Schutt-Aine and R. Mittra, "Nonlinear Transient Analysis of Coupled Lossy Transmission Lines with Arbitrary Loads",*IEEE Trans. MTT, Vol. 36, pp 959-967, July 1989.*

[16] D. Winklestein, et al, "Simulation of Arbitrary Transmission Line Networks with Nonlinear Terminations",*IEEE Trans. on Circuits and Systems, Vol. 38, No. 4, pp. 418-422, April 1991.*

[17] D. Winklestein, et al, "Corrections to Simulation of Arbitrary Transmission Line Networks with Nonlinear Terminations",*IEEE Trans. on Circuits and Systems, Vol. 38, No. 10, pp. 1238, October 1991.*

[18] G. Gordon, T. Blazeck and R. Mittra, "Time-Domain Simulation of Multiconductor Transmission Lines with Frequency-Dependent Losses",*IEEE Trans. Computer Aided Design, Vol. 11, No. 11, pp 1372-1378, November 1992.*

[19] G. W. Pan, G. Wang and B. K. Gilbert, "Analysis of Nonlinear Termination Networks for Coupled Lossy Dispersive Transmission Lines",*IEEE Trans. MTT, Vol. MTT-41, pp 531-535, March 1993.*

[20] T. Dhaene and D. De Zutter, "Time Domain Analysis of Uniformly Coupled Lossy Transmission Lines with Arbitrary Loads",*IEEE International Symp. on Circuits and Systems, San Diego (California), May 1992.*

[21] T. Dhaene, L. Martin,and D. De Zutter, "Transient Simulation of Arbitrary Nonuniform Interconnection Structures Characterized by Scattering Parameters",*IEEE Trans. on Circuits & Systems, vol CAS 39, No11, pp 928-937, November 1992.*

[22] Y.C. Yang, et al , "Time Domain Perturbational Analysis of Nonuniformly Coupled Transmission Lines",*IEEE Trans. Microwave Theory Tech., vol. 33, no. 11, pp. 1120-1130, November 1985.*

[23] Q. Gu, et al , "Time Domain Analysis of Nonuniformly Coupled Line Systems",*Journal of El. Waves and Appl., vol. 1, no. 2, pp. 109-132, 1987.*

[24] O.A. Palusinski and A. Lee, "Analysis of Transients in Nonuniform and Uniform Multiconductor Transmission Lines",*IEEE Trans. Microwave Theory Tech., vol. 37, no. 1, pp. 127-138, January 1989.*

[25] N. Orhanovic and V.K. Tripathi, "Time Domain Simulation of Uniform and Nonuniform Multiconductor Lossy Lines by the Method of Characteristics", *IEEE MTT-S: International Microwave Symposium, Dallas, pp. 1191-1194, 1990.*

[26] Q. Gu, D.M. Sheen, S.M. Ali , "Analysis of Transients in Frequency-Dependent Interconnections and Planar Circuits with Nonlinear Loads",*IEE Proceedings-H, vol. 139, no. 1, pp. 38-44, February 1992.*

[27] E.A. Hosny and M.I. Sobhy, "Computer-Aided Analysis of Nonlinear Lumped- Distributed Multiport Networks",*1990 IEEE International Symposium on Circuits and Systems, New Orleans, Louisiana, USA, May 1990.*

[28] M.I. Sobhy and E.A. Hosny, "Multiport Approach For The Analysis of Microwave Nonlinear Networks", *International Journal of Numerical Modelling : Electronic Networks, Devices and Fields,vol. 6, pp. 67-81, February 1993.*

SIEMENS

Transient Analysis of Large Nonlinear Networks

U. Feldmann, U. Wever, Q. Zheng, Siemens AG

R. Schultz, Siemens-Nixdorf

- Motivation
- Standard Algorithm of Circuit Simulation
- Exploitation of Latency
- Adaption to Parallel Hardware
- Conclusion

What is a large circuit?

1980	1000 transistors
1984	3000 transistors
1987	7000 transistors
1990	15000 transistors
1993	50000 - 100000 transistors
	25000 - 150000 equations

Why analyse large circuits?

- get reliable data for extrapolation to even larger circuits
- save human resources:
  extraction of the really critical path is difficult, time consuming and liable to errors
  (1 - 3 manmonth for critical path of 16 Mbit dram)

* classical algorithms

* exploit latency
  - Newton loop: bypass evaluation of element equations
  - time loop: multirate integration, local timestep control

* adaption to parallel hardware
  - vectorization for
    vector supercomputers like CRAY, SIEMENS/FUJITSU
    superscalar RISC workstations like HP7xx, IBM RS6000
  - distributed simulation on workstation cluster

Speedup of circuit analysis

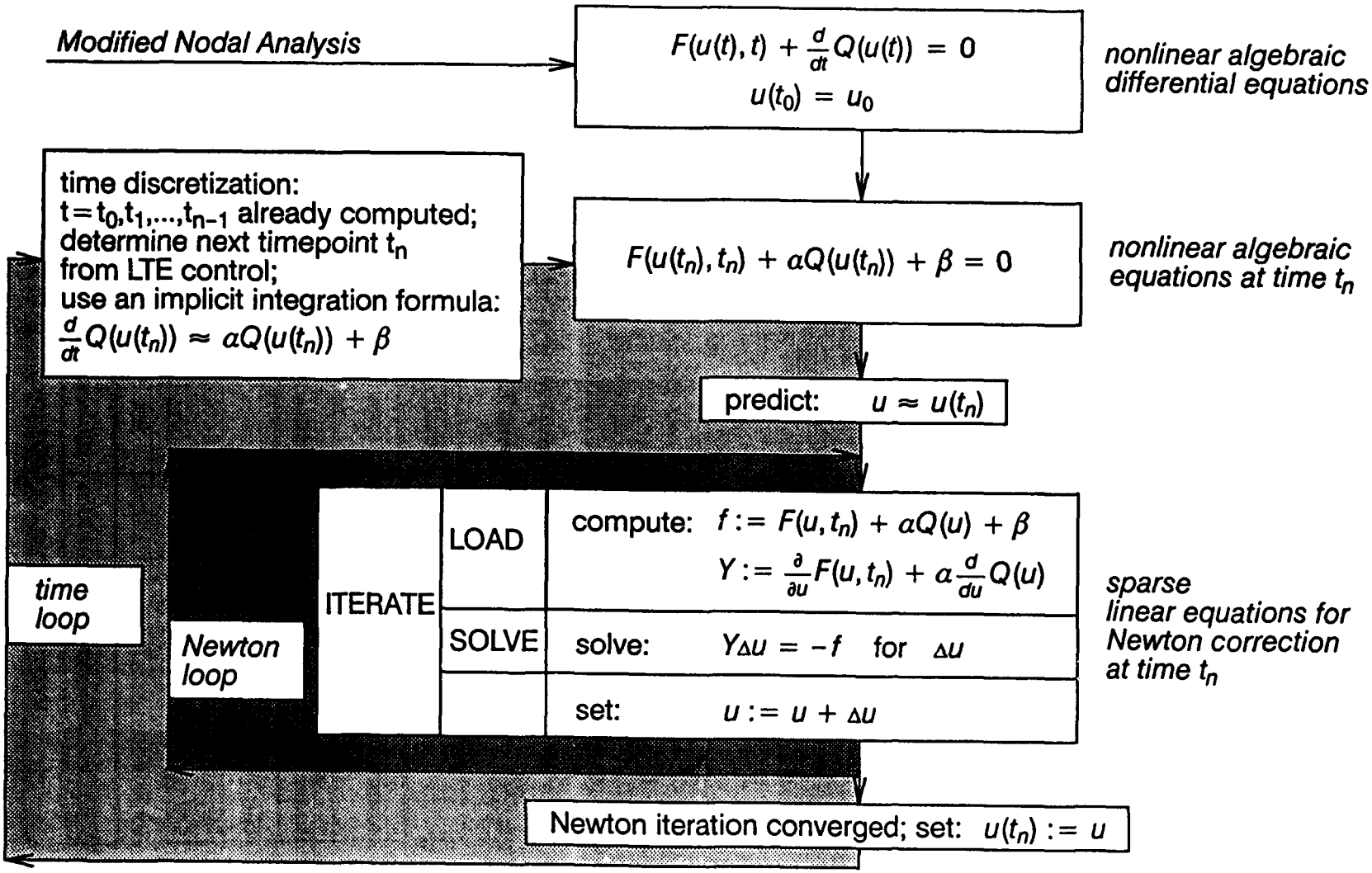

The classical direct algorithm of circuit simulation in the time domain

3.5 CPU-Times and Memory Needs

Dependence of circuit size N

cpu-time ~N for the LOAD part
~N$^{\alpha}$ for the SOLVE part α = 1.2 ... 1.8
~N for the overhead

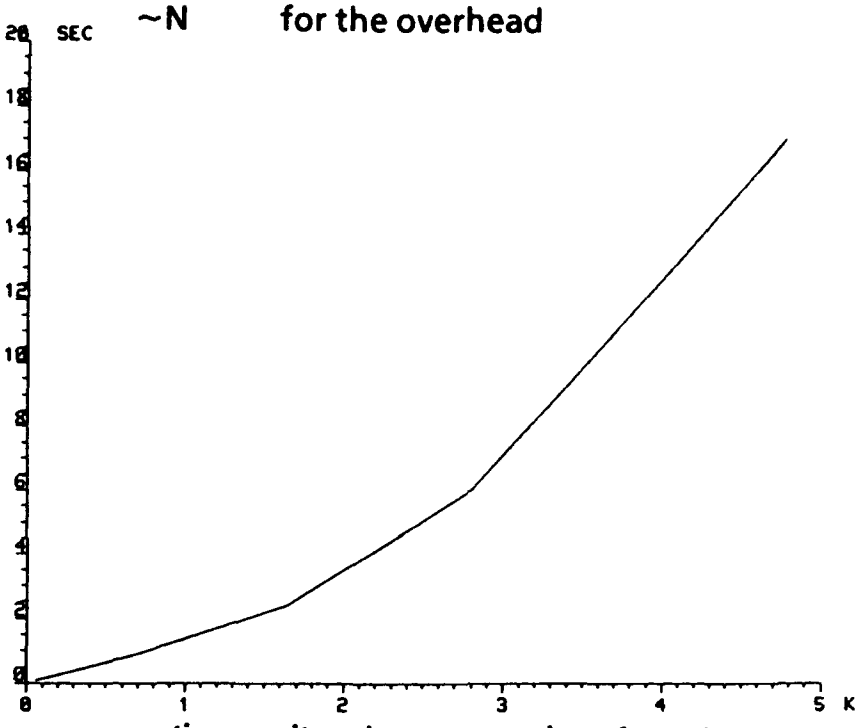

cpu-time per iteration over number of transistors
(Siemens 7571)

circuit	ex 1	ex 2	ex 3	ex 4	ex 5	ex 6
number of transistors	58	231	642	828	1895	4822
number of equations	157	70	342	376	1040	2027
sparsity	96%	86%	97%	97%	99%	99%
cpu-times						
LOAD	69%	84%	72%	80%	51%	29%
SOLVE	19%	7%	16%	18%	43%	71%
overhead	12%	9%	12%	2%	6%	0.3%
transient analysis	100%	100%	100%	100%	100%	100%

transient analysis of MOS circuits with SPICE2-S

Basic idea:

* compute only those parts of the circuit which really change
* substitute "dormant" parts of the circuit by simpler ones

Newton loop:

* "bypass" evaluation of device equations

Time loop:

* multirate integration, local timestep control

General principle:

* check a priori, whether latency condition is fulfilled
* compute solution under latency assumption
* check a posteriori, whether latency assumption was valid

Exploitation of latency

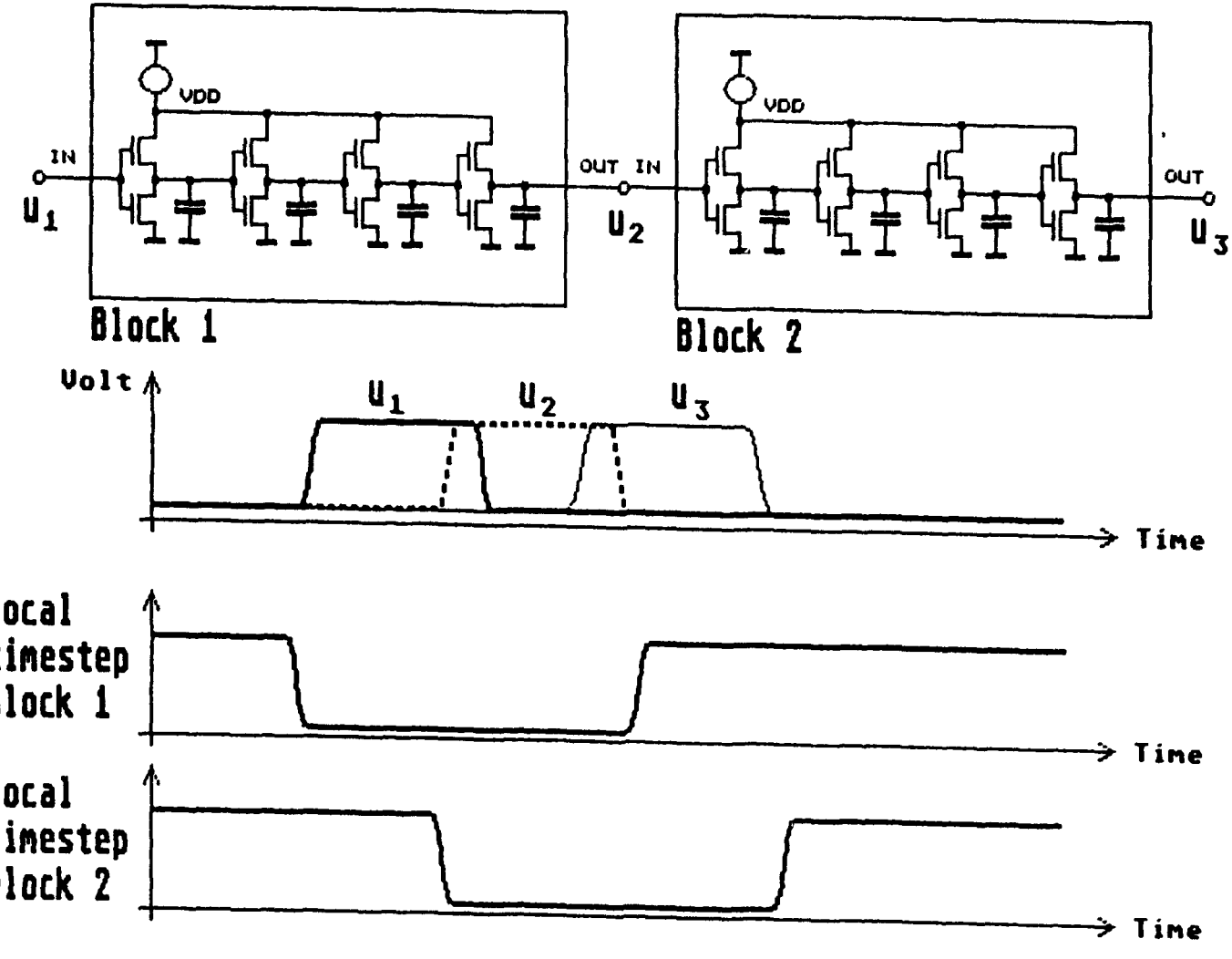
VDD
IN
U1
OUT IN
U2
VDD
OUT
U3
Block 1
Block 2
Volt
U1
U2
U3
Time
local
timestep
block 1
Time
local
timestep
block 2
Time

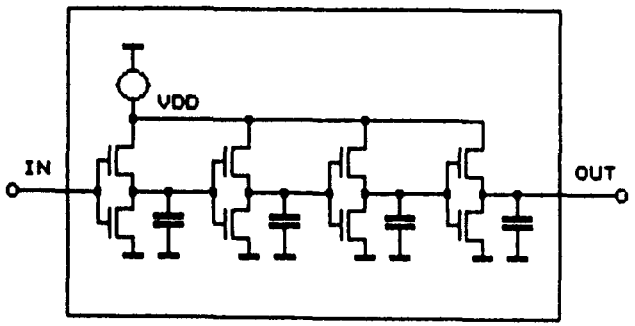

Block with four inverters

Physical Mode:

Evaluation of the physical model for each circuit element

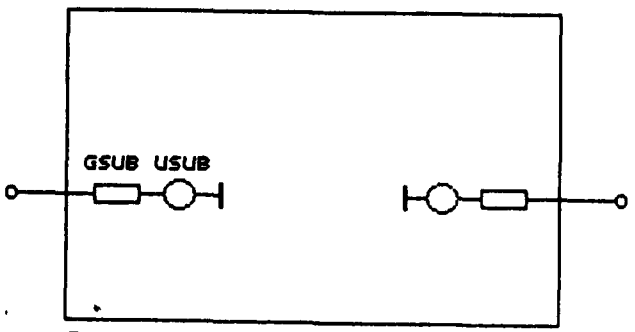

Substitute Circuit

Extrapolation Mode:

Application of a simple substitute circuit with extrapolated characteristics

EEE

External Extrapolation Error

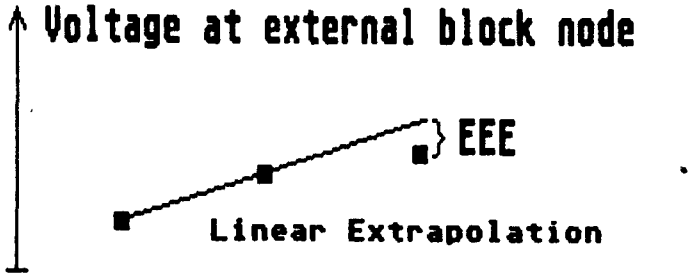

DEE

Domain-end Extrapolation Error

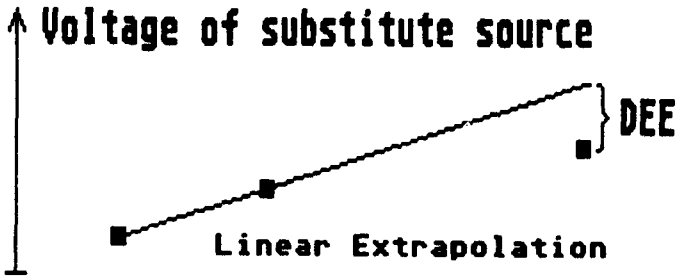

LTE

Local Truncation Error
of Integration

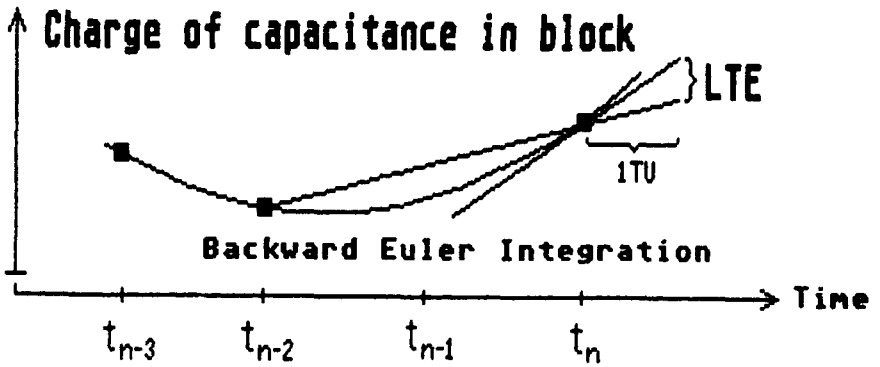

Block mode: phys. phys. extrap. phys.

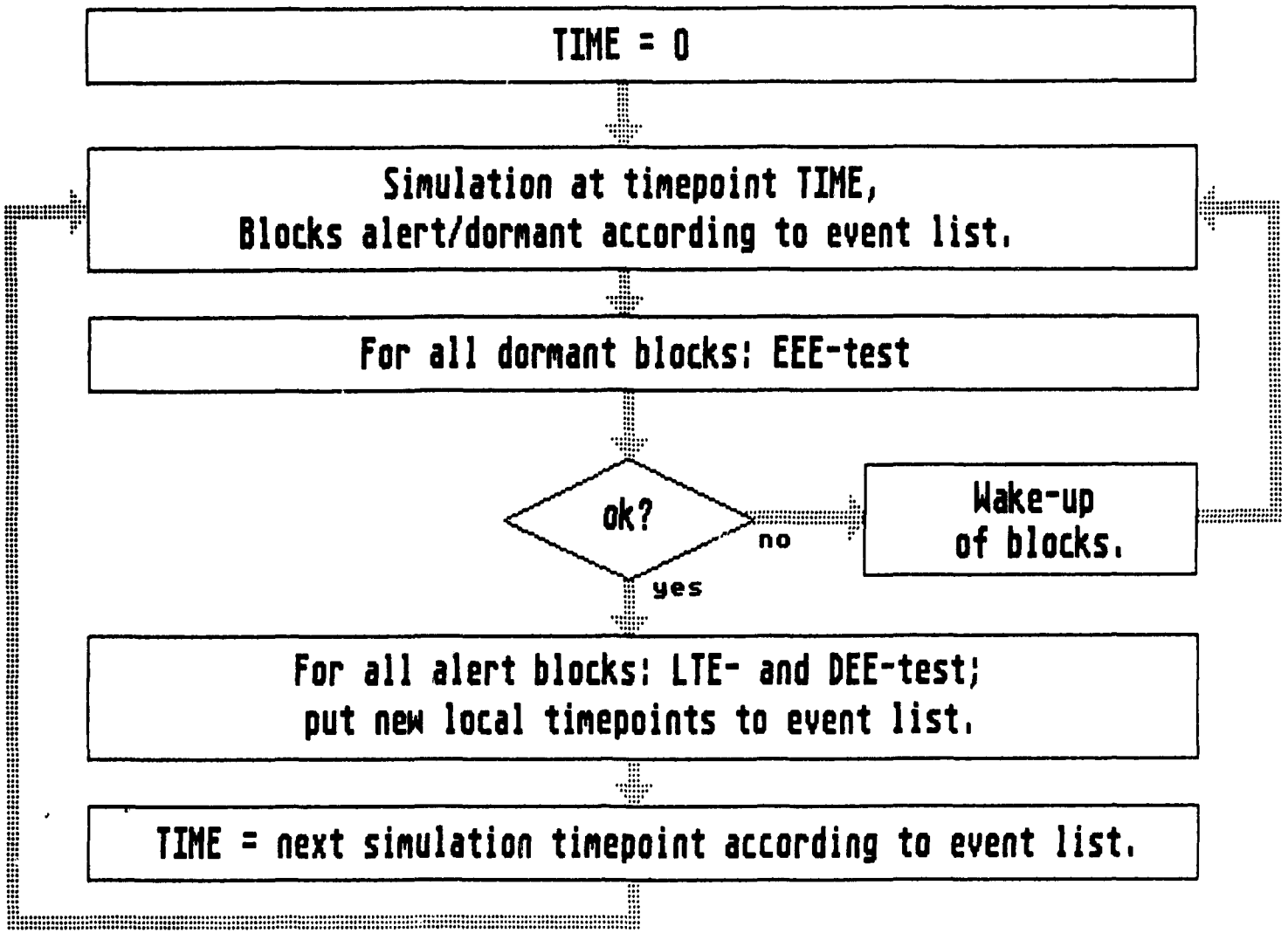
TIME = 0
Simulation at timepoint TIME,
Blocks alert/dormant according to event list.
For all dormant blocks: EEE-test
ok?
no
yes
Wake-up
of blocks.
For all alert blocks: LTE- and DEE-test;
put new local timepoints to event list.
TIME = next simulation timepoint according to event list.

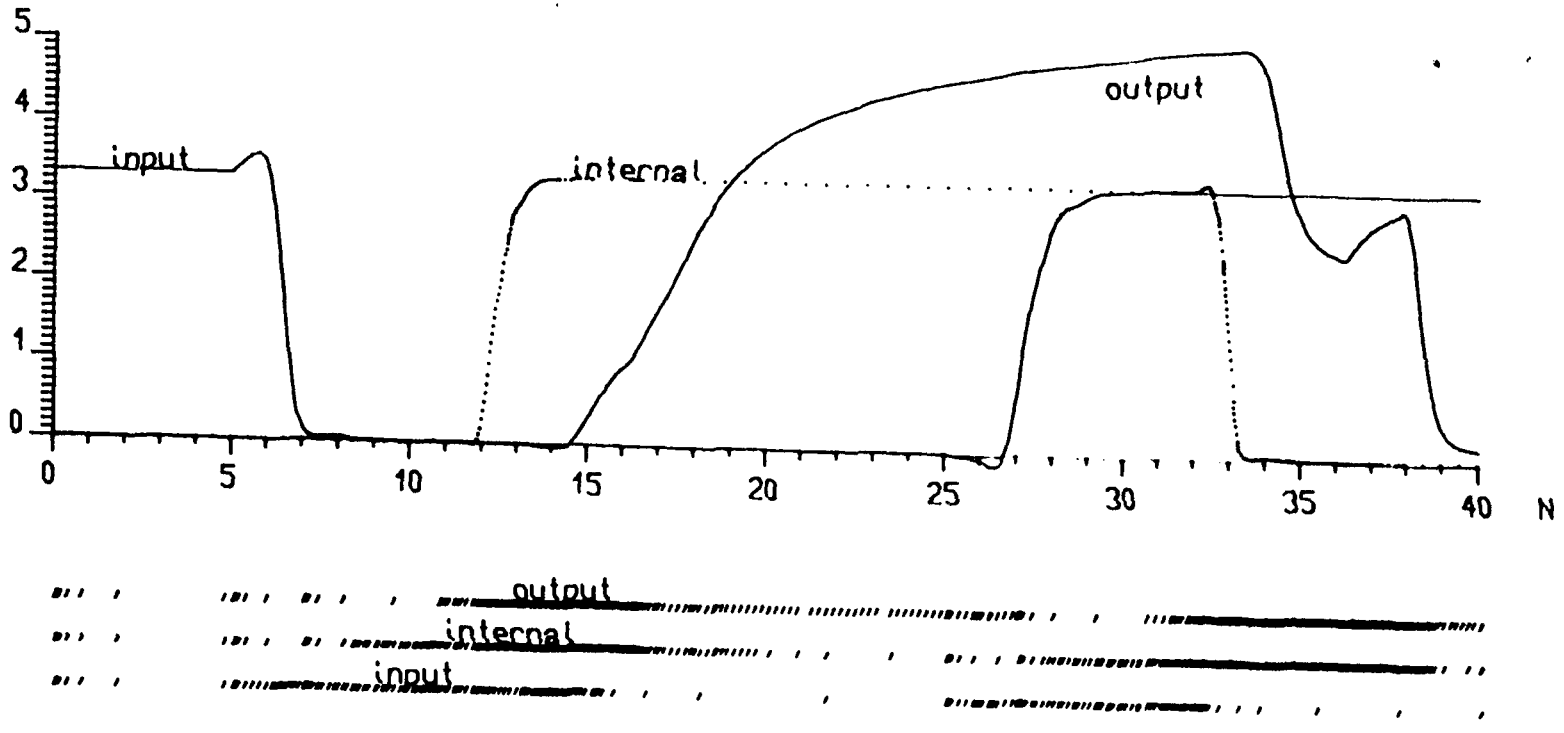
5
4
3
2
1
0
input
internal
output
0
5
10
15
20
25
30
35
40
N
output
internal
input

	global	global + bypass	local	local + bypass
timepoints:				
accepted	453	453	456	456
wake up + refused	0	0	25	26
cpu times:				
LOAD	41	34	18	17
total tr-analysis	64	56	45	44

bipolar ringoscillator
(132 transistors, 761 equations)

	global	global + bypass	local	local + bypass
timepoints:				
accepted	2100	2100	2094	2129
wake up + refused	39	50	331	320
cpu times:				
LOAD	2164	1161	451	334
total tr-analysis	2401	1393	813	701

64 bit adder
(2176 MOSFETs, 1096 equations)

Numerical results with local timestep control (Siemens S200-20 in scalar mode)

# of MOS transistors	544	1088	2176
average cpu-time per transistor evaluation	0.21 msec	0.15 msec	0.09 msec

increasing latency with increasing circuit size

tolerance (integrator)	standard * 5	standard	standard / 5
average cpu-time per transistor evaluation	0.22 ~~0.21~~ msec	0.15 msec	0.13 ~~0.09~~ msec

increasing latency with increasing accuracy (1088 transistor circuit)

method	trapez	gear	trbdf
average cpu-time per transistor evaluation	0.18 msec	0.14 msec	0.15 msec
total transient time	560 sec	573 sec	503 sec

latency versus integration method (1088 transistor circuit)

Numerical results with local timestep control (SUN 4 SPARC 2)

functions to be vectorized

* evaluation of element equations
* loading of matrix coefficients and right hand side
* LU decomposition and FB substitution
* timestep control
* preprocessing: Markowitz ordering scheme and setup of matrix

problems

* branched structure of element equations
* vector conflict when loading matrix and right hand side: update of same element in one vector instruction
* sparse structure of matrix
* latency

speedup

* factor 10 and higher on vector supercomputers
* factor 2 ...? on superscalar workstations

circuit	16M dram	8k sram	8k sram	8k sram
# of transistors	15061	52531	52531	85299
# of equations	8272	18096	123158	34480
# of timesteps	1081	497	487	497
# of iterations	3836	1414	1442	1417
cpu-times in sec				
setup	999	995	7452	1763
load	1957	5984	8284	12139
solve	198	95	1060	113
total tr-analysis	2358	6157	9487	12368

Simulation data of large circuits (Siemens S200-20 in vector mode)

SIEMENS

step 1: Harmonic Balance (nonlinear frequency analysis)

* linear solver takes more than 98%
* memory request 200 Mbyte
* distribution of cpu and of memory
* cooperation with TU München (Prof. Zenger)
* UNIX workstations and mainframes
* evaluation of distributed platforms

step 2: time domain analysis

* several functions contribute significantly to cpu and memory
* apply master slave principle
* alternatives:
  - multilevel Newton (less communication, higher computational expense)
  - single level direct approach (more communication, lower computational expense)
* software platform: PVM

Distributed simulation on workstation cluster

Master

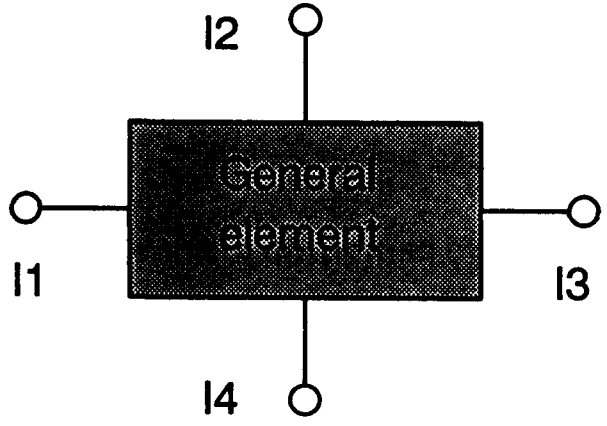

master > slave : (V1, V2, V3, V4)

Slave

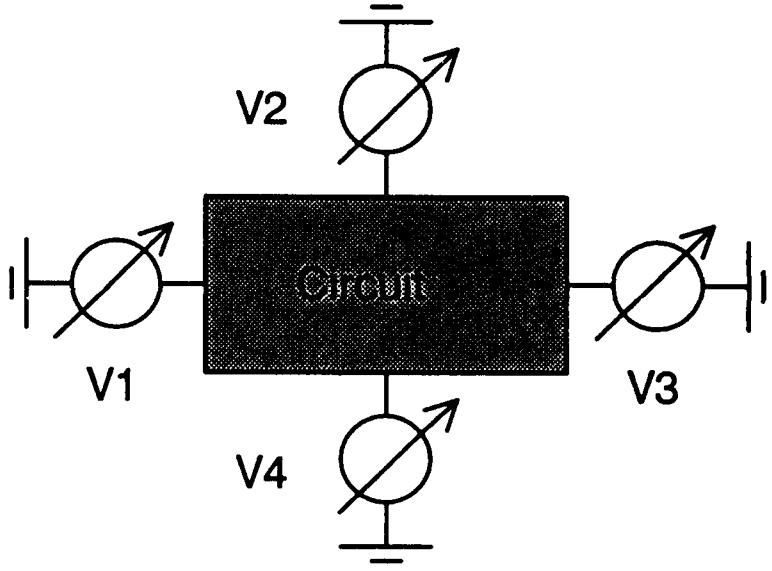

slave > master : (I1, I2, I3, I4)

$$\left(\frac{\partial I1}{\partial V1}, \ \cdots, \frac{\partial I4}{\partial V4}\right)$$

	# of transistors	# of workstations
ringoscillator	366 MOS	4 + 1
ringoscillator	132 bipolar	4 + 1
1 M dram	2005 MOS	8 + 1
artificial test circuit	4860 MOS	9 + 1
4 M dram	6104 MOS	4 + 1
artificial test circuit	135000 MOS	27 + 1

Test circuits for distributed simulation on workstation cluster

summary

* analysis of 100k transistor circuits is possible in reasonable time
* local timestep control has a good potential for speedups esp. for large circuits
* vector effects can be exploited even on modern workstations
* distributed simulation on workstation cluster will (partially) substitute simulation on supercomputers

further work

* improve data structures for local timestep control
* improve vector effect on workstation
* drive distributed simulation into productive use
* investigate partitioning strategies

Conclusion

DYNAMIC SIMULATION OF SEMICONDUCTOR DEVICES

Roland Stenzel
Hochschule für Technik und Wirtschaft Dresden
Fachbereich Elektrotechnik
Friedrich-List-Platz 1
D-01069 Dresden

Wilfried Klix
Technische Universität Dresden
Institut für Grundlagen der Elektrotechnik/Elektronik
Mommsenstr. 13
D-01062 Dresden

1. Introduction

The development and optimization of novel semiconductor devices demand the use of two (2D)- and three (3D)- dimensional simulation methods because of the rapidly rising development costs for new technologies and simultaneously the demand for shorter development times.
Objectives of the device simulation are:

- Calculation of device characteristics before the technological realization
- Optimization of technology dependent device parameters
- *Understanding of internal electronic processes*
- Determination of internal electronic quantities, which are either unmeasurable or not easily measurable
- Determination of equivalent circuit parameters of the devices

The shrinkage of device features and novel devices with significant three-dimensional effects requires an increasing use of 3D-simulation methods.
For the modeling and simulation of semiconductor devices, three basic levels can be distinguished [1]:

(1) Microscopic simulation:
Analysis of elementary processes of single carriers with the variants
   (a) Real quantum models with carrier properties described by wave functions (coupled solution of Schrödinger equation and Poisson equation) [2]
   (b) Particle models with carriers described by particles (solution of Boltzmann transport equation) [3]
   (c) Mixed models [4].

(2) Macroscopic simulation:
Use of average values with the variants
   (a) Complete hydrodynamic models consisting of balance equations for carrier-, momentum- and energy density resulting from approximations of microscopic models [5]
   (b) Simplified hydrodynamic models (drift-diffusion models) [6].

(3) Mixed microscopic-macroscopic simulation:

Combination of the advantages of both methods, e.g. spatial mixed microscopic-macroscopic description of devices [7] or microscopic treatment of electrons and macroscopic treatment of holes [8].

Microscopic methods are an essential basis for the simulation of novel semiconductor devices, but they are more expensive and therefore, now as before, macroscopic models are more widespread [9].

2. 2D- and 3D-device simulation at Dresden Universities

2.1. Overview

At the University of Technology Dresden (TUD) and the Polytechnic University of Technology and Economics Dresden (HTW) a lot of software for the simulation of semiconductor problems has been written in the last 20 years. Most of these programs are working together in a system for designing and optimizing semiconductor devices. However, they can also be used in stand alone mode. A general overview of these programs is given in Fig. 1.

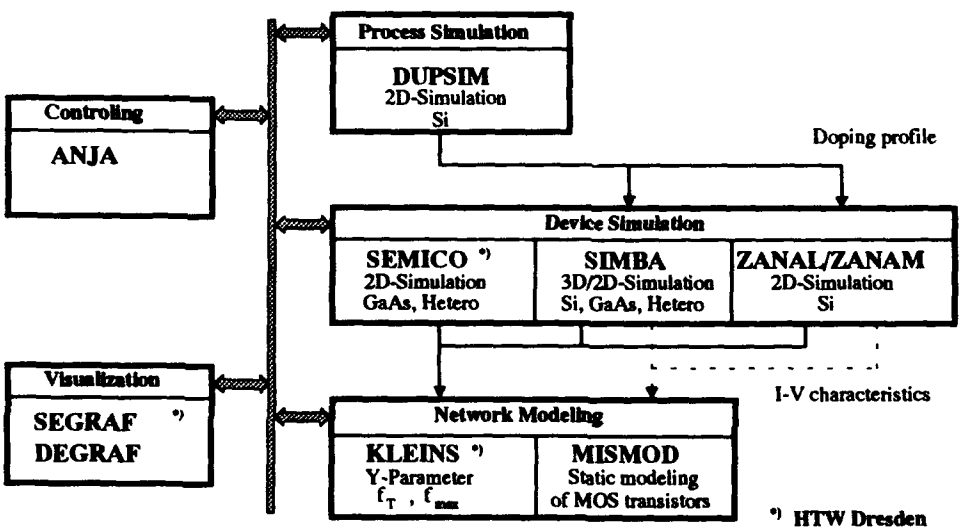

Fig. 1. Simulation tools at Dresden Universities

Following, we will only take into consideration the programs SEMICO and SIMBA, because only these programs are able to simulate heterojunction devices.

2.2. Physical models

The simulation of semiconductor devices is based on the numerical solution of a drift-diffusion model. Using the electrostatic potential φ, the hole density p and the electron density n as the vector of unknowns, these equations can be written as follows:

- Poisson equation:

$$\operatorname{div}(\varepsilon \cdot \operatorname{grad}\varphi) = -e \cdot \left(p - n + N_D^+ - N_A^-\right) \tag{1}$$

- Continuity equations for hole and electron current density:

$$\operatorname{div}\vec{S}_p = -e \cdot \left(R - G + \frac{\partial p}{\partial t}\right) \qquad \operatorname{div}\vec{S}_n = e \cdot \left(R - G + \frac{\partial n}{\partial t}\right) \tag{2,3}$$

- The corresponding transport equations:

$$\vec{S}_p = -e \cdot \mu_p \cdot p \cdot \operatorname{grad}\left(\varphi - \Theta_p\right) + k \cdot T \cdot \mu_p \cdot \operatorname{grad} p \tag{4}$$

$$\vec{S}_n = -e \cdot \mu_n \cdot n \cdot \operatorname{grad}\left(\varphi + \Theta_n\right) + k \cdot T \cdot \mu_n \cdot \operatorname{grad} n \tag{5}$$

It is necessary to take additional relations into consideration. Especially, the so-called band parameters Θ_p and Θ_n must be included to modify the carrier transport with respect to heterojunctions [10]:

$$\Theta_p = \frac{W_{EAref} - W_{EA}}{e} + \frac{W_{gref} - W_g}{e} + \frac{k \cdot T}{e} \cdot \ln\left(\frac{N_V}{N_{Vref}}\right) \tag{6}$$

$$\Theta_n = \frac{W_{EA} - W_{EAref}}{e} + \frac{k \cdot T}{e} \cdot \ln\left(\frac{N_C}{N_{Cref}}\right) \tag{7}$$

The carrier mobilities μ_p and μ_n arising in (4,5) are depending from the total impurity density, temperature and the electric field [11], [6]:

$$\mu(N_D + N_A) = \mu_{min} + \frac{\mu_D}{1 + \left(\frac{N_D + N_A}{N_{ref}}\right)^{\alpha}} \tag{8}$$

$$\mu(N_D + N_A, T) = \mu(N_D + N_A) \cdot \left(\frac{T}{T_0}\right)^{-\gamma} \tag{9}$$

$$\mu(N_D + N_A, T, \vec{E}) = \frac{\mu(N_D + N_A, T)}{\left[1 + \left(\frac{|\vec{E}|}{E_p}\right)^{\alpha}\right]^{\beta}} \tag{10}$$

Several recombination and generation effects (Shockley/Read/Hall recombination, Auger recombination, avalanche and alpha-particle generation, etc.) must be also included in the physical model. For simplification, in the next lines there are only given the relations for the Auger recombination and the SRH recombination:

$$R_{AUG} = (C_n \cdot n + C_p \cdot p) \cdot (n \cdot p - n_i^2) \tag{11}$$

$$R_{SRH} = \frac{p \cdot n - n_i^2}{(p + p_0) \cdot \tau_n + (n + n_0) \cdot \tau_p} \tag{12}$$

with $p_0 = n_0 = n_i$ in most cases.

The carrier lifetimes τ_p and τ_n in (12) are piecewise constant or functions of the total impurity density [6]:

$$\tau_{p,n} = \frac{\tau_{p0,n0}}{1 + \frac{N_D + N_A}{N_{pref,nref}}} \tag{13}$$

A lot of other models can be included in the simulation. The presence of all these mobility and recombination-generation models and the use of technological relevant model parameters influence the efficiency of a simulation program greatly.

With the help of the programs SEMICO and SIMBA, it is possible to simulate semiconductor devices, consisting of one or more of the following materials:

- Si (standard material for SIMBA)
- Ge
- $In_xGa_{1-x}As$
- $In_xGa_{1-x}As_yP_{1-y}$
- $Ga_xIn_{1-x}P$
- SiGe
- GaAs (standard material for SEMICO)
- $Al_xGa_{1-x}As$
- $Al_xIn_{1-x}As$
- InP
- AlAs
- Oxide or insulating regions

Among the above mentioned models the boundary conditions must be specified. In both programs the same types of boundaries are used:

- Ohmic contacts: - Type: Dirichlet conditions
  - Thermodynamic equilibrium

$$\varphi_0 = \operatorname{arsinh}\frac{N_D - N_A}{2\sqrt{\exp(\Theta_p + \Theta_n)}} + \frac{\Theta_p - \Theta_n}{2} \tag{14}$$

$$p_0 = \exp(\Theta_p - \varphi_0) \qquad n_0 = \exp(\Theta_n + \varphi_0) \tag{15,16}$$

- Schottky contacts: - Type: Dirichlet conditions
  - Thermodynamic Equilibrium

$$\varphi_0 = \frac{W_g}{2\cdot e} - U_B + \frac{\Theta_p - \Theta_n}{2} \tag{17}$$

$$p_0 = \exp(\Theta_p - \varphi_0) \qquad n_0 = \exp(\Theta_n + \varphi_0) \tag{18,19}$$

- MOS-contacts: - Type: Neumann Conditions
  - Constancy of the normal component

$$\varphi_{GATE} = \frac{W_g}{2\cdot e} + \frac{W_{EA} - W_M}{e} + \frac{\Theta_p - \Theta_n}{2} \tag{20}$$

$$\varepsilon_{OX}\frac{\partial\varphi}{\partial\nu}\Big|_{\text{Oxide boundary}} = \varepsilon_{SC}\frac{\partial\varphi}{\partial\nu}\Big|_{\text{Semiconductor boundary}} - \rho_S \tag{21}$$

$$S_{pv} = -S_{nv} = -e\cdot R_S \tag{22}$$

- Oxide boundary: - Type: Neumann Conditions

$$\varepsilon_{SC}\frac{\partial\varphi}{\partial\nu}\Big|_{\text{Semiconductor boundary}} = \rho_S \tag{23}$$

$$S_{pv} = -S_{nv} = -e\cdot R_S \tag{24}$$

- Symmetry: - Type: Neumann Conditions

  (Artificial boundary condition to restrict the area of the simulation. It is equivalent to an oxide boundary without any surface charge and surface recombination.)

2.3. Numerical methods

A large variety of numerical methods can be used to solve the semiconductor equations (1-5). A schematic overview and simple classification is given in Fig. 2.

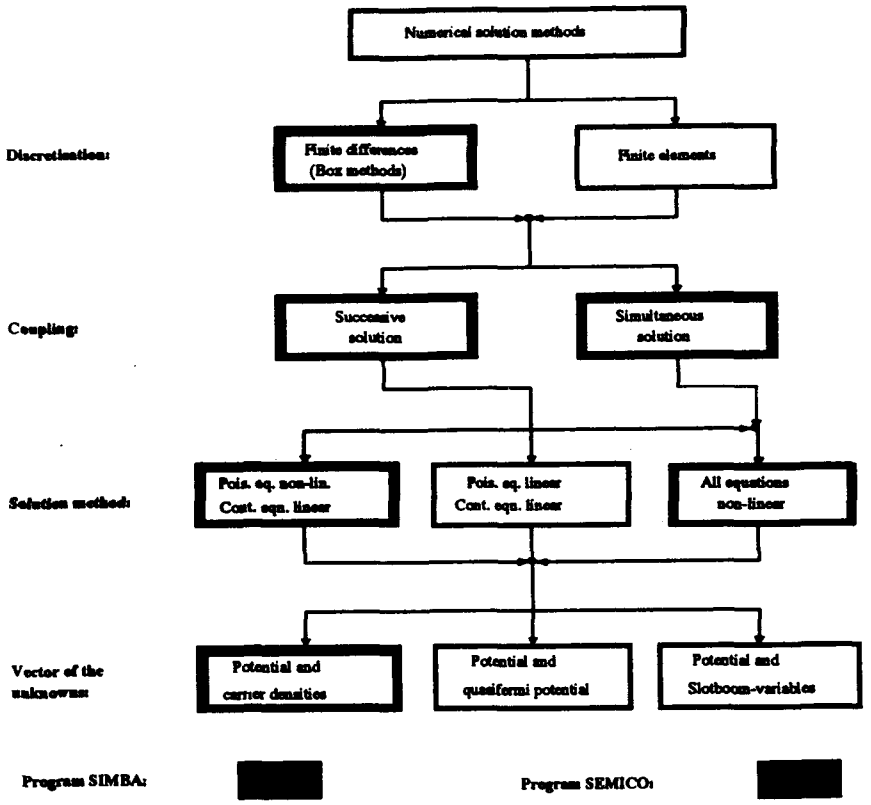

Fig.2. Classification of several numerical simulation methods for the drift-diffusion model

The spatial discretization of the equations (1-3) will be done by using an orthogonal, nonequidistant grid and applying a box method (see Fig. 3).

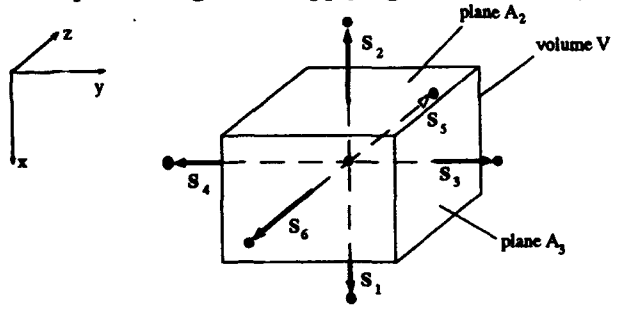

By using this box method it is also possible to include non-planar surfaces into the simulated region.

Fig. 3. Box method for the spatial discretization

The GUMMEL/SCHARFETTER approach [12] is used to handle the transport equations (4,5) before including them into (2,3):

- Constant current density between the grid points:
  - Mobility is constant between the grid points
  - Recombination and generation are located in the grid points

- Constant electrical field strength between the grid points:
  - Impurities are located in the grid points
  - Charges are located in the grid points.

The discretized form (e.g. the continuity equation for the hole current) becomes now:

$$\oint_A \vec{S}_p \cdot d\vec{A} = -e \int_V \left(R + \frac{\partial p}{\partial t} \right) \cdot dV \quad \rightarrow \quad \sum_{i=1}^{6} S_{pi} \cdot A_i = -e \left(R + \frac{\Delta p}{\Delta t} \right) \cdot V \qquad (25)$$

for each grid box.

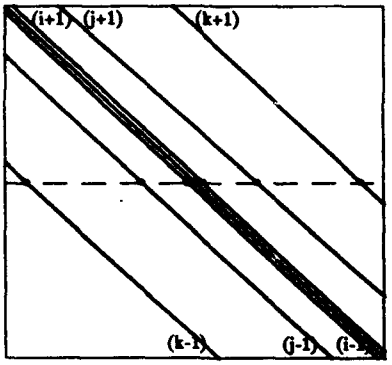

By ordering the unknowns in the natural manner the arising systems of (non) linear equations have a banded (Jacobian) matrix (see Fig. 4).

- **Dimensions:**
  - 3D-simulation: 10.000 up to several 100.000 eqn.
  - 2D-simulation: 1.000 up to several 10.000 eqn. (5 diagonals)

Fig. 4. Matrix structure of the discretized equations

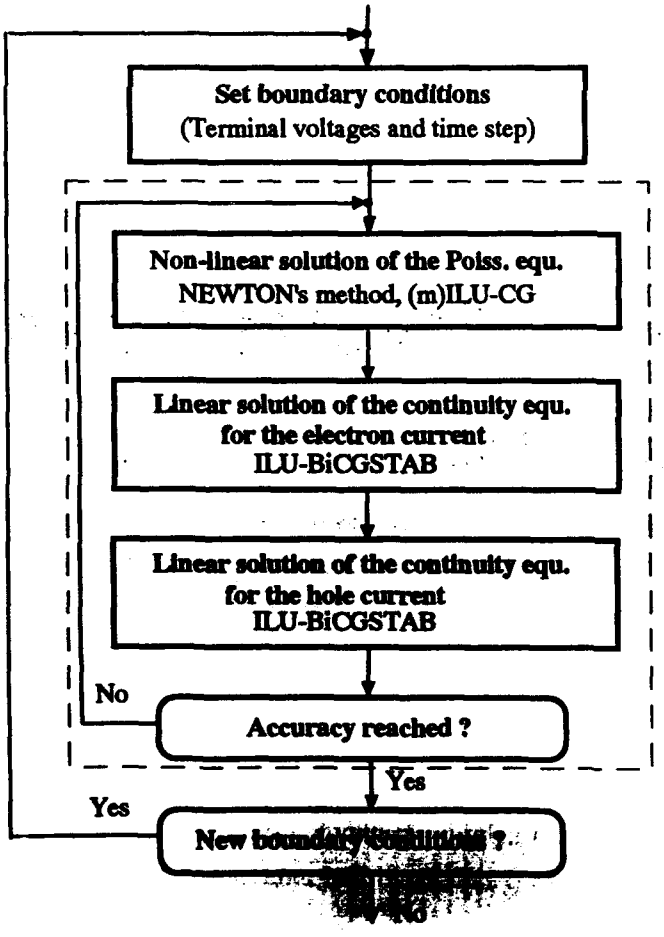

Whereas in SEMICO the simultaneous solution method is prefered (that is, one large non-linear system for all the unknowns φ, p, n is created and handled using NEWTON's method), in SIMBA the semiconductor equations will be solved by a successive method (GUMMEL's algorithm [13]), which is a blockwise non-linear Gauss/Seidel iteration (see Fig. 5).

The Poisson equation is solved nonlinearly by doing the approach, that p, resp. n are non-linear functions of the potential φ:

$$p = n_i \cdot \exp\left[\frac{\Phi_p - \varphi}{U_T} \right] \qquad (26)$$

$$n = n_i \cdot \exp\left[\frac{\varphi - \Phi_n}{U_T} \right] \qquad (27)$$

Fig. 5: Successive solution method (GUMMEL's algorithm)

The time integration in both programs SEMICO and SIMBA is done by a simple implicit EULER-scheme:

$$Y_{ti} = Y_{ti-1} + \Delta t_i \cdot f(Y_{ti}, t_i) \tag{28}$$

A better initial guess is generated by a predictor method. According to our experience it is not practicable to use an algorithm with higher degree for the time integration.

One of the most important parts of the simulation programs is the solution of the large linear systems of equations. This is very time consuming, especially in the case of 3D-simulation. As a typical example the CPU time distribution measurements from 3D-simulation of a MOS transistor on the IBM 3090/VF are shown in Fig. 6.

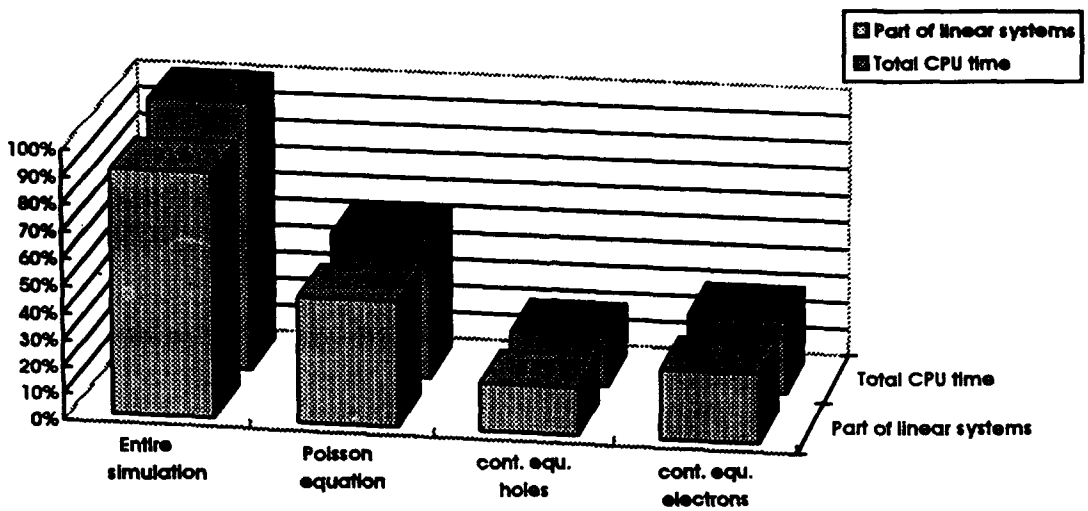

Fig. 6. CPU time distribution for a 3D-simulation of a MOS transistor on the IBM3090/VF

The arising matrixes of the linear systems of equations in the successive solution method are all very large and sparse (see Fig. 4.), but strongly different in their properties:

- Poisson equation.: (Jacobian)
  - "nearly" symmetric matrixes
  - main diagonal dominance
- Continuity eqn.:
  - strongly unsymmetric
  - no main diagonal dominance

To find an optimal solver (fast and stable) seems to be impossible. We have obtained the best results with solvers from the class of preconditioned CG-methods. From all of the tested preconditioners (Jacobi preconditioning, Diagonal scaling, Incomplete LU-Decomposition) acceptable results can be reached only with ILU [14]. Now for the Poisson equation we use a simple CG method [15] in combination with an ILU preconditioner, modified accordingly to GUSTAFFSON [16]. For the continuity equations, which are much more difficult, ILU-BCG or ILU-BiCGSTAB is used [17], [18].

Because of the large CPU time, the numerical solution methods, especially the solution of the large linear systems, should be vectorized and/or parallelized. For more results see [14].

2.4. Postprocessing

From the results of static and dynamic simulation a calculation of small-signal parameter is possible. At the interesting operation point a dynamic simulation of a small voltage jump at the input and output terminal of the device will be done. With the recursive relations [19]

$$Re\left\{\underline{y}^{i+1}(\omega)\right\} = Re\left\{\underline{y}^{i}(\omega)\right\} + \frac{\Delta I}{\Delta U}\left[cos\left(\omega T^{i}\right)\cdot\frac{sin(\omega\,\Delta t)}{\omega\,\Delta t} + sin\left(\omega T^{i}\right)\cdot\frac{cos(\omega\,\Delta t)-1}{\omega\,\Delta t}\right] \tag{29}$$

$$Im\left\{\underline{y}^{i+1}(\omega)\right\} = Im\left\{\underline{y}^{i}(\omega)\right\} - \frac{\Delta I}{\Delta U}\left[sin\left(\omega T^{i}\right)\cdot\frac{sin(\omega\,\Delta t)}{\omega\,\Delta t} - cos\left(\omega T^{i}\right)\cdot\frac{cos(\omega\,\Delta t)-1}{\omega\,\Delta t}\right] \tag{30}$$

(T^i: time step i, Δt: time step size, ΔI: current variation, ΔU: voltage jump)

the y-parameters as a function of frequency can be calculated. From this the high-frequency parameters h_{21} (small-signal current gain), MSG (maximum stable gain) and MAG (maximum available gain) can be derived [20]:

$$h_{21} = \left|\frac{\underline{y}_{21}}{\underline{y}_{11}}\right| \tag{31}$$

$$MSG = \left|\frac{\underline{y}_{21}}{\underline{y}_{12}}\right| \tag{32}$$

$$MAG = \left|\frac{\underline{y}_{21}}{\underline{y}_{12}}\right|\cdot\left(k-\sqrt{k^2-1}\right) \qquad k = \frac{2\,Re\{\underline{y}_{11}\}Re\{\underline{y}_{22}\} - Re\{\underline{y}_{12}\}Re\{\underline{y}_{21}\}}{\left|\underline{y}_{12}\underline{y}_{21}\right|} \tag{33}$$

Furthermore, a determination of scattering parameters and of a small-signal equivalent circuit of the internal transistor is possible [21].

For the visualization of the results from the numerical simulation (internal electronic parameters, terminal currents) several graphic tools are available (SEGRAF, DEGRAF).

3. Numerical simulation of heterojunction devices

3.1. High electron mobility transistor (HEMT)

HEMTs with InGaAs-channels have demonstrated excellent performance for high-speed devices. To compare the static and dynamic behaviour of HEMT-structures of different material we carried out 2D-simulations of conventional AlGaAs/GaAs-HEMTs and of AlGaAs/InGaAs/GaAs-pseudomorphic HEMTs and lattice-matched AlInAs/InGaAs/InP-HEMTs of the same size and doping levels. Fig. 7 shows the HEMT-structures used in the simulations. The gate length and the gate-source spacing are 0.1 μm, respectively. The undoped layer between substrate and channel acts as a barrier to avoid parasitic currents into the substrate and prevents the penetration of impurities into the channel region. Contact resistances were neglected. For the Schottky-contact a barrier voltage of 1 V was assumed.

The results of static calculations are represented in Fig. 8, 9 and 10. The Figures show the higher drain saturation currents and the higher transconductances of the InGaAs channel devices, especially for the $Al_{0.48}InAs/In_{0.53}GaAs$-system due to the greater conduction band discontinuity of 0.55 eV in comparison to 0.33 eV for $Al_{0.3}GaAs/GaAs$ and 0.29 eV for $Al_{0.15}GaAs/In_{0.15}GaAs$. The current density distribution of the AlGaAs/GaAs-HEMT represented in Fig. 11 shows the 2D-current flow (2DEG) within the channel and the barrier effect of the bottom heterojunction.

As a result of dynamic simulation Fig. 12 shows the power gains (MSG/MAG) versus frequency. The cutoff frequency f_{max} amounts 480 GHz, 520 GHz and 700 GHz, respectively. The switch-on characteristics of the devices are represented in Fig. 13. From this and from the corresponding switch-off characteristics we obtain the switch-off and the switch-on times. All values are summarized in Table I.

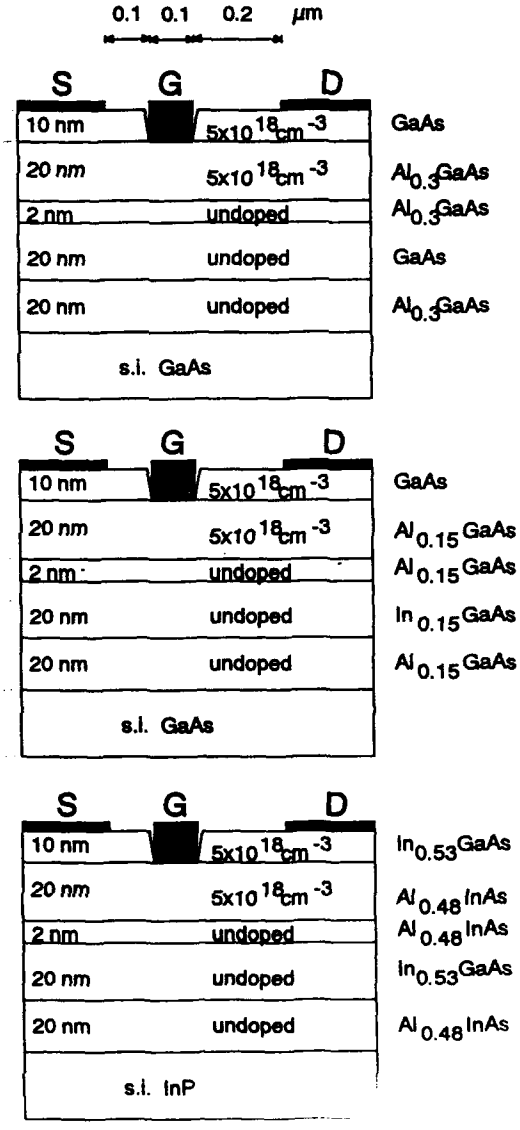

Fig. 7 HEMT-structures

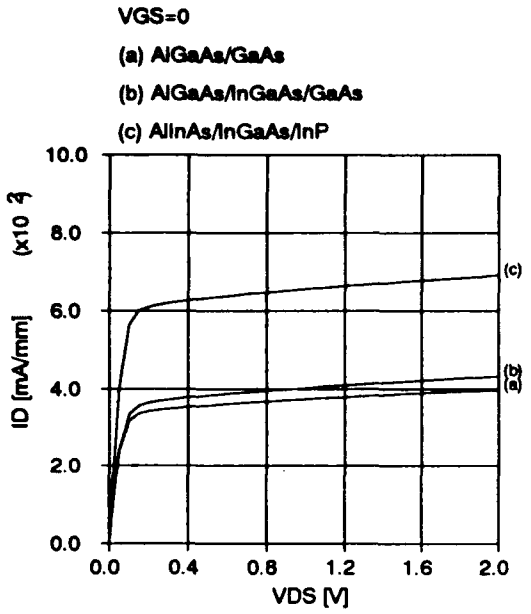

Fig. 8. Output characteristics

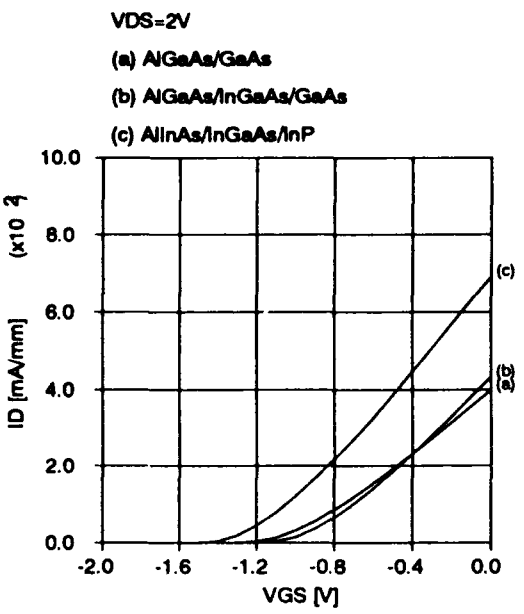

Fig. 9. Transfer characteristics

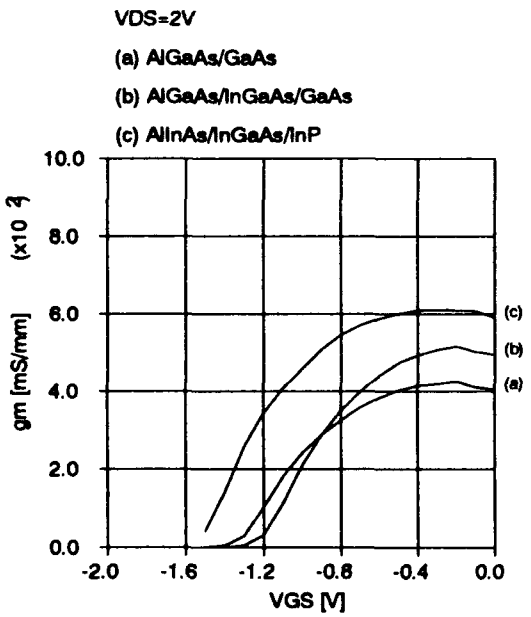

Fig.10. Transconductance versus gate-source-voltage

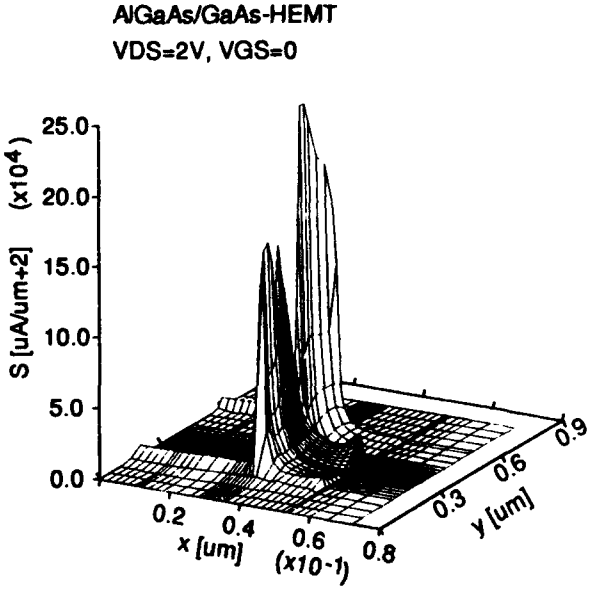

Fig.11. Current density distribution

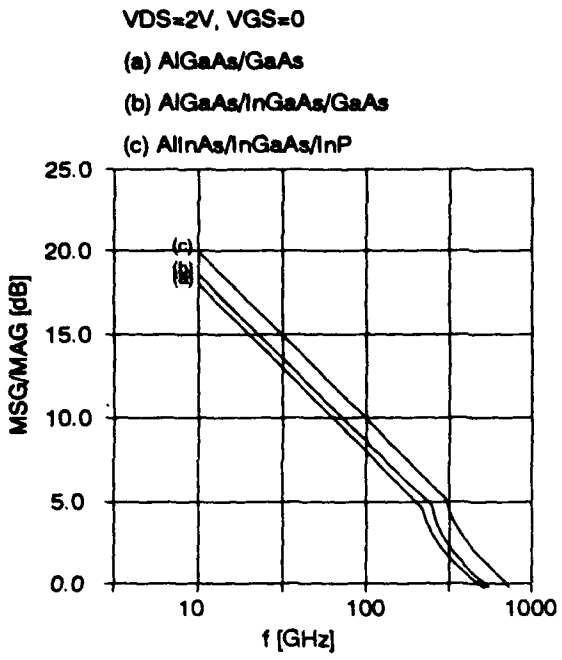

Fig.12. Power gains versus frequency

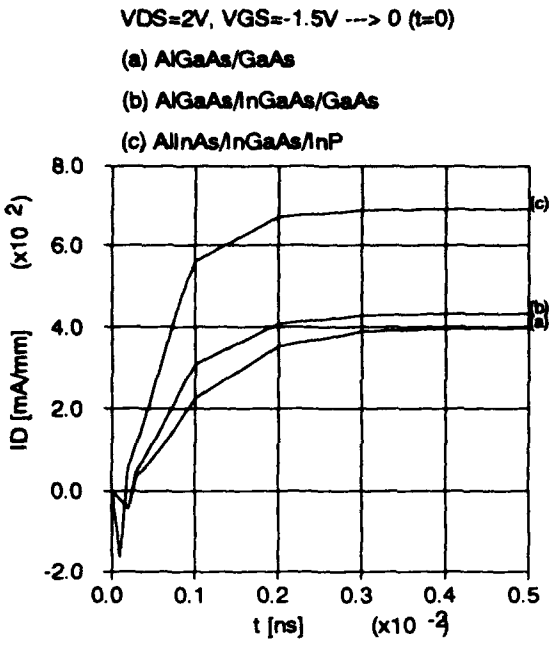

Fig.13. Switch-on characteristics

Table I. Calculated device parameters

	I_{Dmax} [mA/mm]	V_{th} [V]	g_{mmax} [mS/mm]	f_T [GHz]	f_{max} [GHz]	t_{off} [ps]	t_{on} [ps]
AlGaAs/ GaAs	398	-1.4	420	90	480	2.1	1.6
AlGaAs/ InGaAs	432	-1.3	510	110	520	1.8	1.4
AlInAs/ InGaAs	691	-1.7	610	130	700	1.5	1.0

3.2. Heterojunction bipolar transistor (HBT)

HBTs have received great interest for application to high-speed and high-frequency devices. To achieve higher cutoff frequencies we carried out an optmization of base and collector doping and thickness by 2D-simulations. Fig. 14 shows the device cross section of the initial AlGaAs/GaAs-HBT [22]. The doping levels are: $3 \cdot 10^{18}$ cm^{-3} (cap layer), $1 \cdot 10^{18}$ cm^{-3} (emitter grading), $5 \cdot 10^{17}$ cm^{-3} (emitter), $4 \cdot 10^{19}$ cm^{-3} (base), $6 \cdot 10^{16}$ cm^{-3} (collector), $3 \cdot 10^{18}$ cm^{-3} (subcollector). The dynamic simulations yielded maximum cutoff frequencies at a operation point of $V_{DS} = 2$ V, $V_{GS} = 1.65$ V (emitter current density: $6.4 \cdot 10^4$ A/cm^2). The corresponding gains as a function of the frequency are represented in Fig. 15. The cutoff frequencies of current gain and power gain are $f_T = 61$ GHz and $f_{max} = 98$ GHz, respectively.

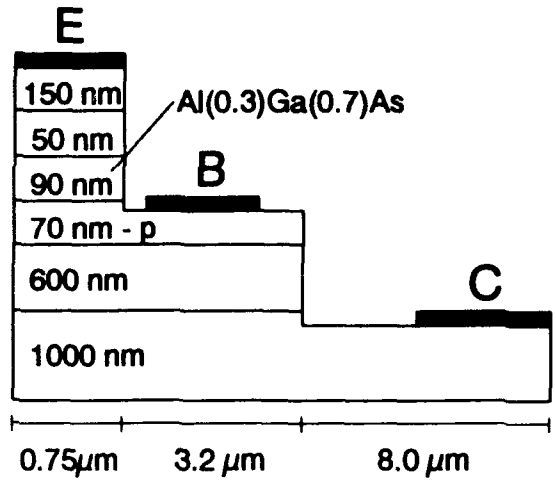

Fig. 14. HBT-cross section

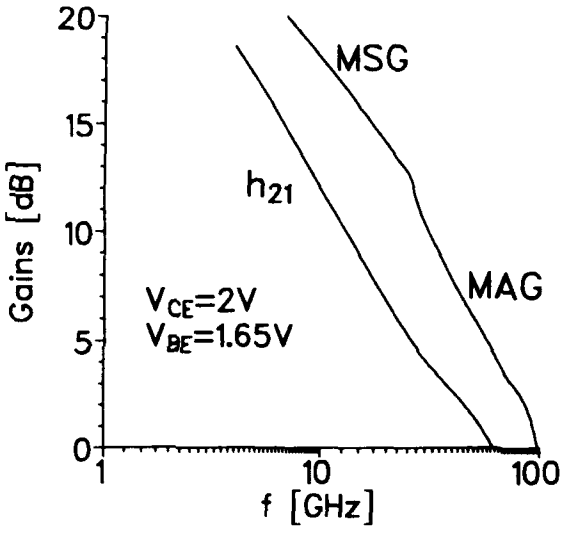

Fig. 15. Current and power gains

The results in Fig. 16 and 17 show the influence of base doping and thickness on the cutoff frequencies. With increasing base doping the base bulk resistance decreases and f_{max} rises slightly. On the other hand an increasing base doping causes a decrease of current gain and carrier mobilities and a rise of junction capacitances. Therefore the transit frequency f_T goes down. The increasing base thickness causes first of all a rise of base transit time and consequently a decrease of the transit frequency. The cutoff frequency f_{max} is nearly independent of the base thickness because of the compensation of the base transit time increasing by the reduction of base bulk resistance with increasing base thickness.

The influence of the collector layer parameters on the cutoff frequencies is represented in Fig. 18 and 19. A high collector doping decreases the collector transit time due to the smaller collector space charge region; therefore, f_T and f_{max} rise. Because of the increase of junction capacitance f_{max} decreases at higher doping levels. At a higher collector layer thickness (greater than space charge region), the junction capacitance and the transit time, and therefore f_T and f_{max} are nearly constant. If the collector layer is thinner than the space charge region, f_T rises due to the smaller transit time, and f_{max} decreases because of the increase of the junction capacitance.

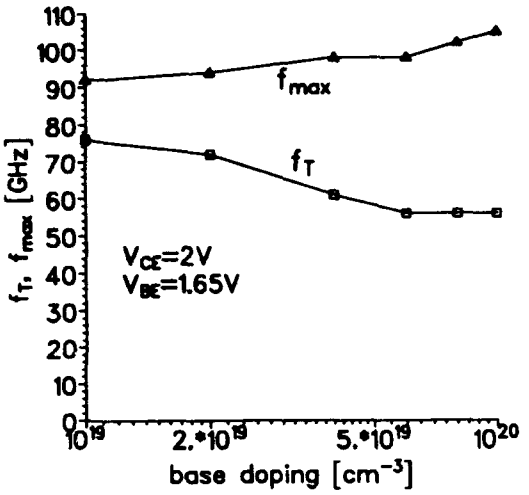

Fig. 16. Cutoff frequencies versus base doping

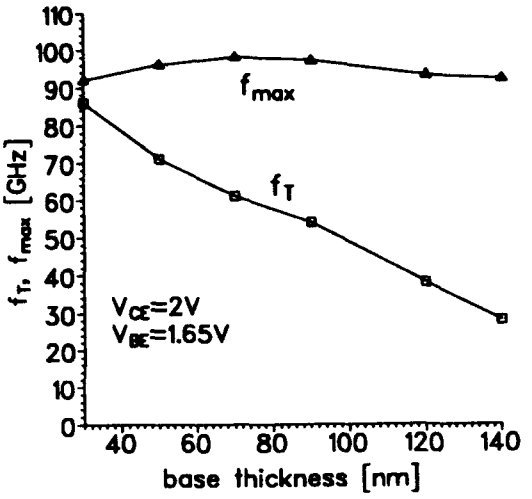

Fig.17. Cutoff frequencies versus base thickness

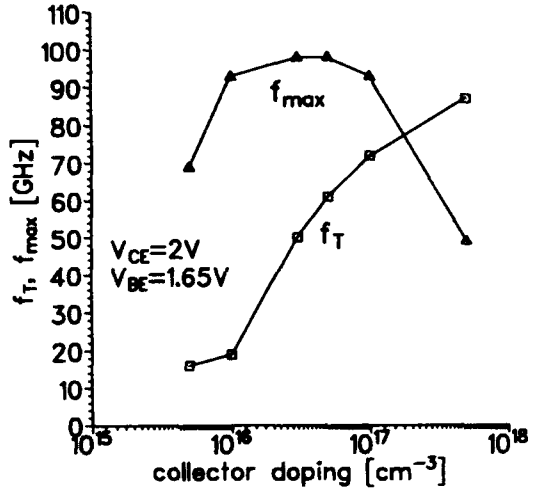

Fig.18. Cuttoff frequencies versus collector doping

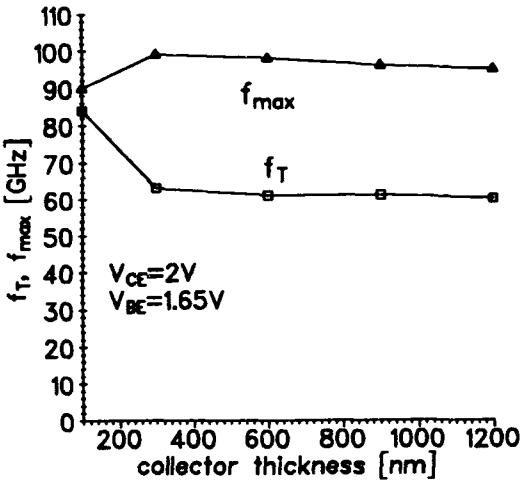

Fig.19.Cuttoff frequencies versus collector thickness

3.3. In-plane-gated field effect transistor (IPG-FET)

A new concept of a novel in-plane-gated (IPG) field-effect-transistor (FET) device was reported by A.D. Wieck and K. Ploog [23]. Based on a standard modulation-doped FET structure with a high mobility two-dimensional electron gas, they used a focused ion beam (FIB) technique to fabricate a quasi one-dimensional electron gas (1DEG) and demonstrated device operation.

We carried out 3D-simulation of IPG-FETs to obtain design rules for this new type of device structure [24]. Fig. 20 shows a view of the intrinsic part of the device used for the simulation with the isolation barrier (shaded region) of width w_i and depth d between the gate electrode (left side) and the 1D current channel (right side). The original 2DEG of a MODFET layer sequence is separated into four electrode regions and a quasi one-dimensional (1D) current channel, which is defined by two thin trapezoidal insulating lines. The functional principle of the device is fully three dimensional because of the lateral control of the 1 DEG charge density and the small length of the quasi 1D current channel. Therefore a 3D-analysis for calculating electrical device properties is useful. The layered MODFET structure used for the simulation consists of a modulation-doped $Al_{0.25}Ga_{0.75}As/GaAs$ heterostructure with a 2DEG pseudomorphic $In_{0.21}Ga_{0.79}As$ quantum well layer. Three-dimensional effects appear because of heterojunctions in x-direction, the control action of the gate in y-direction and the current flow between drain and source in z-direction.

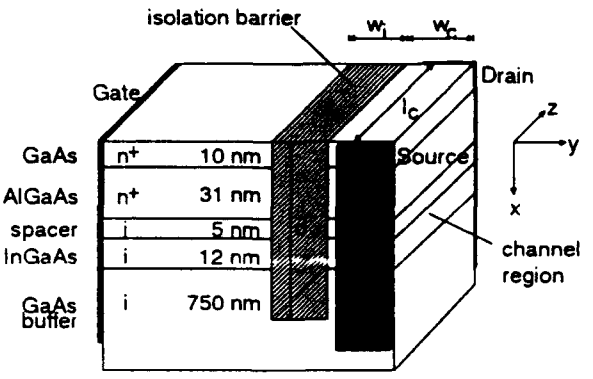

Fig. 20. IPG-structure

The layer sequence is as follows (from surface to bottom): 10 nm GaAs ($2.5x10^{18}$ cm^{-3}), 21 nm $Al_{0.25}Ga_{0.75}As$ ($3x10^{17}$ cm^{-3}), 10 nm $Al_{0.25}Ga_{0.75}As$ ($4x10^{18}$ cm^{-3}). All the following layers are intentionally undoped (a background doping of 10^{14} cm^{-3} was assumed in the calculation). The spacer consists of 2 nm $Al_{0.25}Ga_{0.75}As$ and 3 nm GaAs. A 12 nm thick $In_{0.21}Ga_{0.79}As$ layer contains the high density 2DEG. The implanted isolation barriers are considered as a highly compensated material with p-type background doping ($5 \cdot 10^{15}$ cm^{-3}). Because of the symmetric gate arrangement the numerical analysis is performed for one half of the device. Source, drain and also gate regions are ohmic contacts. Because of the high doping concentration of the cap layer, we neglect contact resistances. Simulations with a realistic surface charge density of $-2x10^{12}$ cm^{-2} yielded a surface depletion length of about 35 nm but a strong increase of computation time. Therefore we simply considered a recess region of 35 nm in the calculation instead of surface charges.

The geometrical dimensions of the isolation lines used in the simulation are: d = 810 nm, w_i = 600 nm, l_c = 1.5 μm. For the total width of the quasi 1D channel we used $2w_c$ = 600 nm. The current density at $z = l_c/2$ for VDS = 2 V, VGS = 0 is represented in Fig. 21. The dominant current flow is

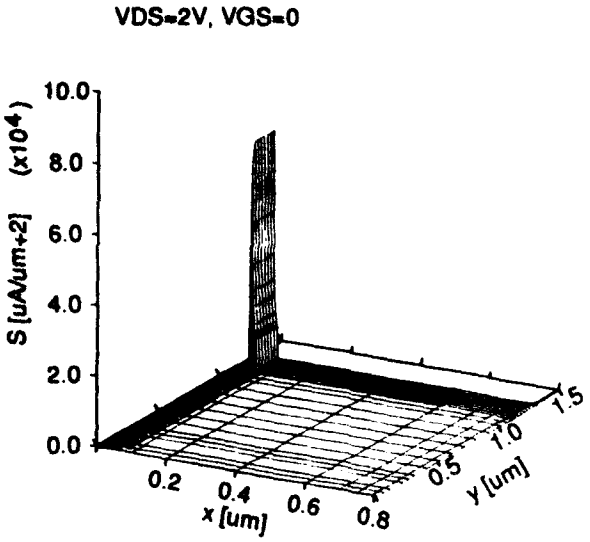

Fig. 21. Current density at $z = l_c/2$

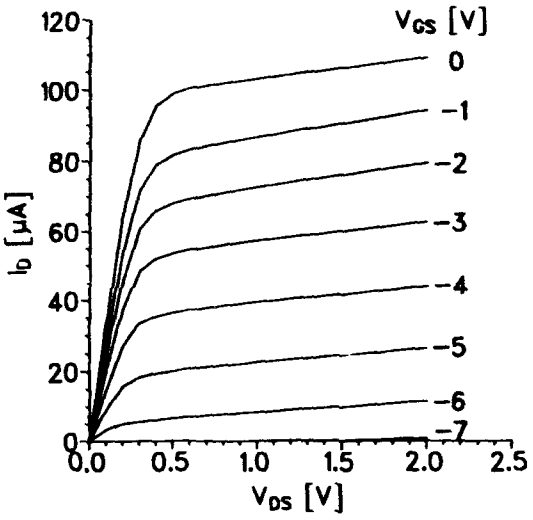

Fig. 22. Output characteristics

observed inside the channel region between the isolation lines at the GaAs/InGaAs heterojunction (x > 46 nm, y > 1.2 µm). An increasing negative gate to source voltage yields to an increasing lateral electric field and thus to an increase of the space charge layer within the n-channel region and therefore to a control of the drain current. The obtained output characteristics are shown in Fig. 22. A complete depletion of the 1DEG can be achieved at V_{GS} = -7.4 V. The corresponding transconductance is about 18 µS.

In the following we present results concerning the influence of the isolation line width w_i and the channel width w_c. An increasing isolation line width yields to a lower lateral electric field; therefore, the transconductance decreases and the drain current rises slightly (Fig. 23). With increasing channel width, the drain current increases proportionally and the transconductance goes into saturation (Fig. 24).

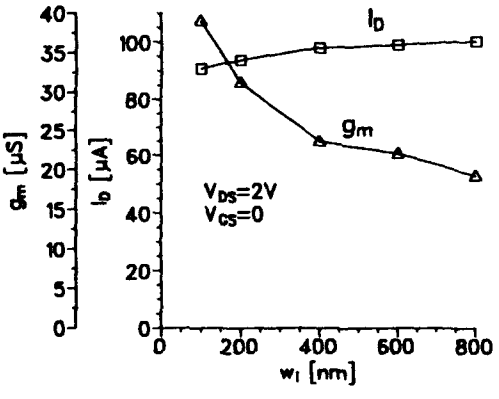

Fig.23. Transconductance and drain current versus isolation line width

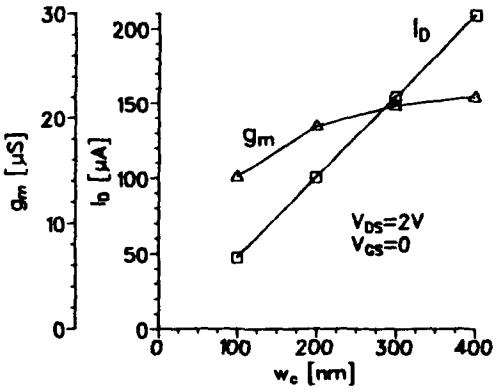

Fig.24. Transconductance and drain current versus channel width

4. Conclusions

After a brief overview about the different model levels of device simulation the current physical models and numerical methods of the 2D- and 3D-simulators SEMICO and SIMBA are represented. The results of the static and dynamic simulation of HEMT-, HBT- and IPG-structures show the efficiency of these simulation tools and yield contributions for the optimization of the devices.

Acknowledgement

The authors would like to thank H. Brugger and H. Leier from Daimler Benz Research Center Ulm and R. Dittmann from the TU Dresden for many helpful discussions.

References

[1] H. Elschner, W. Klix, M. Paßlack, R. Spallek and R. Stenzel: Simulation of small Si and GaAs devices. Proc. of NASECODE V, Dublin 1987, Boole Press Lim., pp. 19-30

[2] B. Zimmermann, J.F. Palmier, P. Caussignac and M. Ilegems: Self-consistent calculation of electron states in III-V-multilayer structures. Proc. of NASECODE V, Dublin 1987, Boole Press Lim., pp. 346-351

[3] L. Reggiani: Hot-electron transport in semiconductors. Topics in Applied Physics, vol. 58, Springer-Verlag 1985

[4] R. Brunetti: A Monte Carlo analysis of diffusion-noise properties in GaAs-AlGaAs quantum wells. ESSDERC 1987, Techn. Digest, pp. 181-184

[5] K. Blotekjer: Transport equation for electrons in two-valley semiconductors. IEEE Trans. ED, 17(1970), No. 1, pp. 38-47

[6] S. Selberherr: Analysis and simulation of semiconductor devices. Springer Verlag, 1984

[7] T. Wang and C.H. Hsieh: Numerical analysis of nonequilibrium electron transport in AlGaAs/InGaAs/GaAs pseudomorphic MODFETs. IEEE Trans. ED, 37(1990), No. 9, pp.1930-1938

[8] K. Tomizawa, Y. Awano and N. Hashizume: Monte Carlo simulation of AlGaAs/GaAs heterojunction bipolar transistors. IEEE-EDL, 5(1984), No. 9, pp. 362-364

[9] F. Fasching, S. Halama and S. Selberherr: Technology CAD systems. Springer-Verlag, 1993

[10] J.E. Sutherland and J.R. Hauser: A computer analysis of heterojunction and graded composition solar cells. IEEE Trans. ED, 24 (1977), No. 4, pp. 363-372

[11] D.M. Chaughey and R.E. Thomas: Carrier mobilities in silicon empirically related to doping and field. Proc. IEEE, 55(1967), pp. 2192-2193

[12] D.L. Scharfetter and H.K. Gummel: Large-signal analysis of a silicon read diode oszillator. IEEE Trans. ED, 16 (1969), pp. 64-77

[13] H.K. Gummel: A self-consistent iterative scheme for one-dimensional steady state transistor calculations. IEEE Trans. ED, 11(1964), pp. 455-465

[14] W. Klix and R. Reuter: Three-dimensional simulation of semiconductor devices using the IBM 3090 multiprocessor. IBM Scientific Center Heidelberg, Technical Report (in preparation)

[15] J.A. Meijerink and H.A. van der Vorst: An iterative solution method for linear systems of which the coefficient matrix is a symmetric M-matrix. SIAM J. Math. of Comp., 31(1977), No. 137, pp. 148-162

[16] I. Gustafsson: A class of 1st order factorization methods. BIT 18 (1978), pp. 142-156

[17] R. Fletcher: Conjugate gradient methods for indefinite systems. Proc. of the Dundee Biennal Conference on Numerical Analysis 1974, University of Dundee, Scotland, Springer-Verlag, New York 1975, pp. 73-89

[18] M. Driessen and H.A. van der Vorst: BiCGSTAB in semiconductor modeling. Simulation of Semiconductor Devices and Processes, Vol. 4, Zurich, Sept. 1991, pp. 56-54

[19] R. Schüffny, H. Elschner and K. Hoffmann: Analyse des Kleinsignalverhaltens statischer Anodendomänen in Gunn-Elementen. Zeitschrift für elektr. Informations- u. Energietechnik, 8(1978), No. 1, pp.3-13

[20] B. Pejcinovic, T.-W. Tang and D.H. Navon: High-frequency characterization of heterojunction bipolar transistors using numerical simulation. IEEE-ED, 36(1989), No.2, pp.233-239

[21] M. Berroth and R. Bosch: Broad-band determination of the FET small-signal equivalent circuit. IEEE-MTT, 38(1990), No. 7, pp. 891-895

[22] R. Stenzel and H. Leier: Heterobipolartransistoren - Simulation und experimentelle Ergebnisse. GME-Fachbericht 11, VDE-Verlag, 1993, pp.259-264

[23] A.D. Wieck and K. Ploog: In-plane-gated quantum wire transistor fabricated with directly written focused ion beams. Appl. Phys. Lett. 56 (1990), pp. 928-930

[24] R. Stenzel, W. Klix, R. Dittmann, C. Pigorsch, U. Meiners and H. Brugger (unpublished)

Signal-processing approach to robust time-domain modelling of electromagnetic fields

Alfred Fettweis, Ruhr-Universität Bochum, Germany

Summary: The paper offers an overview of a new method for numerically integrating the partial differential equations (PDEs) of field problems, placing particular emphasis on PDEs of electromagnetics. The method, which is applicable to a wide variety of linear and nonlinear physical problems, consists in finding robust algorithms for modelling the given physical system. It draws heavily from results in MD (multidimensional) circuit theory and MD digital signal processing.

93/1/0b

Numerical integration of PDEs by discrete passive modelling of physical systems

Goal: Find advantageous algorithms for numerically integrating partial differential equations (PDEs) by drawing maximum advantage from natural physical properties of original physical system, especially from passivity, losslessness, massive parallelism, full locality.

Solution: Model original physical system by a discrete multidimensional (MD) dynamical system behaving essentially like the original one except that it is described by difference equations instead of differential equations.

93/1/1

Basic idea

Model original system by a discrete MD-passive (multidimensionally passive) dynamical system.

Main advantages to be expected:

1. Massive parallelism. Nature is massively parallelel due to finiteness of propagation speed.
2. Full locality of all operations. Is realized in nature due to action at proximity. Thus:

- only local exchange of information,
- can accomodate arbitray changes of parameters,
- can accomodate arbitrary boundary shapes and conditions,
- nonlinear problems: need solve only local nonlinear equations.

3. Full robustness, i.e. property that can widely keep under control errors due to discretization of

- space and time coordinates (linear effects: sampling),
- values of field variables (nonlinear effects due to reformating, i.e. rounding / truncation and overflow correction).

For achieving robustness, recall that in nature fundamental laws govern conservation of energy and direction of its flow. Due to this, physical systems often are passive.

By appropriate MD (multidimensional) generalization, stored energy (energy density) can thus give rise to an MD Liapunov function (MD vector function!) which in turn can serve as basis for solving robustness problem.

4 Approximation in MD (multidimensional) frequency domain

(Note: Term "frequency" used here independently of physical nature of underlying coordinate, thus also for "wave number.")

Problem: How can such approximation be made meaningful?

Indeed, a formally good frequency-domain approximation has significance for the actual space-time behavior only if the system possesses suitable strict stability properties. For assuring these, make use of appropriate passivity property.

5. Such frequency-domain concepts are very helpful also for dealing with specific aspects off stiff equations.

6. The approach is well suited as basis for building specialized massively parallel computers.

93/1/3a

How achieve desired multidimensional (MD) modelling (simulation)?

1. Start from original system of PDEs, not from global PDE.

2. Physical systems usually passive, even incrementally passive.

   This true only with respect to time: physically passive.

   But required: multidimensionally passive (MD-passive).

   Therefore, suitable coordinate transformation (space-time!)

3. Represent transformed system by MD Kirchhoff cicuit.

4. For discretization, use preferably trapezoidal rule.

5. To ensure recursibility (computability), use wave quantities (instead of original field variables), as for scattering matrix.

   Ensures cause-to-effect relationship: incident ⟶ reflected waves.

6. Thus, use principles of MD wave digital filters (MD WDFs).

93/1/4

By using wave quantities (short: waves) instead of the original quantities (voltages, currents; electric / magnetic fields; pressure, velocity etc.), an explicitly computable (recursible) passive MD (multidimensional) simulation becomes feasible: MD-WDF principle (WDF = wave digital filter).

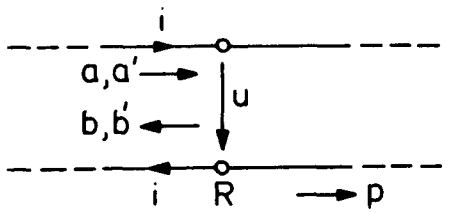

u = voltage, i = current,

R = port resistance,

a, b and a', b' = waves:

Voltage waves: $a' = u + Ri = 2\sqrt{R}\,a$, $b' = u - Ri = 2\sqrt{R}\,b$.

power waves: $a = (u + Ri)/2\sqrt{R}$, $b = (u - Ri)/2\sqrt{R}$.

a, a' = "flowing to the right", b, b' = "flowing to the left".

Power transmitted: $p = ui = a^2 - b^2 = (a'^2 - b'^2)/4R$.

93/1/5

Note: Description by waves and scattering matrix is of fundamental, universal physical importance:

input quantities ⟶ reflected and transmitted quantities,

cause ⟶ effect.

Closely related to this: ensuring explicit computability by use of waves.

Note: Voltage waves lead to simpler algorithms.

(current waves: similar results as voltage waves.)

Power waves: Needed if voltage waves do not allow us to guarantee robustness. Transition trivial:

$a' = 2\sqrt{R}\,a$, $b' = 2\sqrt{R}\,b$.

Hence, use voltage waves wherever possible, make transition where strictly required.

93/1/6

Applicability of the approach and further aspects:

1. Hyperbolic problems (finite propagation speed) feasible.
2. Elliptic problems: applicable only indirectly, i.e. as equilibrium state of hyperbolic problem (relaxation).
3. Parabolic problems: after suitably complementing PDEs.
4. Linear problems: applicability quite straightforward.
   Examples: acoustics, electrodynamics, elasticity.
5. Nonlinear problems:
   - quite straightforward if "corrective" nonlinearity,
   - also applicable if strongly nonlinear, e.g. fluid dynamics.
6. Can use multirate principles, multigrid principles.
7. Also: systems comprising active domains.

93/1/7

Motivation for defining multidimensional (MD) passivity

Classical concepts of passivity and losslessness are defined with respect to time only, i.e. by observing the energy supplied to the system during any time interval. We refer to this as physical passivity (of MD system). For obtaining full robustness of the final algorithm to be derived from the MD Kirchhoff circuit, need, however, passivity (possibly also losslessness) with respect to all k independent variables, say t_1 to t_k (later: t_1' to t_k' or $t_{k'}$). We refer to this as MD passivity, MD losslessness. Hence, require system, N, under consideration to be MD-passive (multidimensionally passive), partly MD-lossless.

93/1/8

How can concepts of multidimensional (MD) passivity and losslessness be properly defined?

Indeed, in theory of MD systems, so far only frequency domain has been considered, i.e. description of k-dimensional (k-D) system, N, in terms of k complex frequencies, say p_1 to p_k.

Then, extension of definition of positive functions, bounded functions etc. to k-D systems is quite straightforward for any dimensionality k.

Obviously, this is restricted to linear constant systems.

However, systems of particular interest may have varying parameters or may even be strictly nonlinear.

93/1/9

For recalling definition of physical passivity, consider k-D (k-dimensional) system N, with $k \geq 1$, during time interval $t_1 \leq t \leq t_2$.

Define: $p(t)$ = power supplied to N at t,

$W(t_1,t_2) = \int_{t_1}^{t_2} p(t)\,dt$ = energy supplied to N during $[t_1, t_2]$.

Then, N is said to be passive if there exists a function $W_S = W_S(t) \geq 0$ that is entirely determined by values of internal variables (state variables) of N at time t and is such that the following always holds:

$$W(t_1,t_2) \geq W_S(t_2) - W_S(t_1), \qquad (1)$$

$$\text{usually} \iff p(t) \geq dW_S(t)/dt. \qquad (2)$$

If in (1,2) equality holds in all cases, N is called lossless.

Note: $W_S(t)$ = (available) energy stored in N at t.

93/1/10

MD generalization of passivity, i.e. passivity with respect to k independent variables, say to $\underline{t}=(t_1,\dots,t_k)^T$. For this, consider:

G = any proper k-dimensional domain,

∂G = boundary of G, dF = boundary element of ∂G,

$\underline{n}$ = normal at ∂G, i.e., unit vector perpendicular to ∂G and directed towards the outside of G,

$p(\underline{t})$ = MD power supplied to system N at $\underline{t}$,

$W = \int_G p(\underline{t})\, d\underline{t}$ = total MD energy supplied to N.

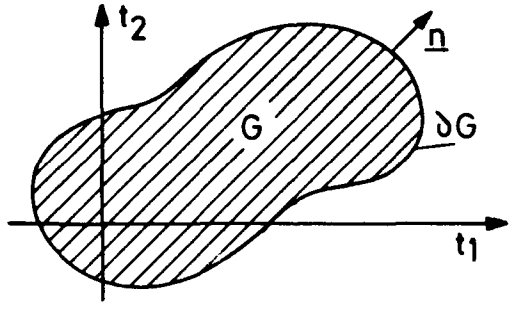

Note: In later use, will have to replace $\underline{t}$ by $\underline{t}'$.

(MD = multidimensional)

93/1/11

Generalized definition: The k-dimensional system N is called MD-passive if there exists a vector function, $\underline{W}_S(\underline{t})$, that is entirely determined by the values of internal variables (state variables) of N at $\underline{t}$ and that is such that

$$\underline{W}_S(\underline{t}) = (W_{S1}(\underline{t}),\dots, W_{Sk}(\underline{t}))^T \geq \underline{0}\,, \qquad \underline{t}=(t_1,\dots,t_k)^T\,,$$

and that for any domain G the following inequality holds:

$$W = \int_G p(\underline{t})\, d\underline{t} \geq \int_{\partial G} \underline{n}^T \underline{W}_S\, dF = \int_G \underline{D}^T \underline{W}_S\, d\underline{t}\,, \quad \underline{D}=(D_1,\dots,D_k)^T,\ D_\varkappa = \frac{\partial}{\partial t_\varkappa},\ \varkappa = 1 \text{ to } k.$$

thus usually $\Longleftrightarrow$ $p(\underline{t}) \geq \underline{D}^T \underline{W}_S$.

$\underline{W}_S(\underline{t})$ = energy density vector at $\underline{t}$ (MD-energy in N per (k-1)-dimensional volume) = MD vector Liapunov function!

$\underline{W}_{S1}(\underline{t}) + \dots + \underline{W}_{Sk}(\underline{t})$ = similar to a total energy density.

If for $\geq$ equality holds in all cases, N is MD-lossless.

93/1/12

Recall. For k-dimensional (k-D) system ($k \geq 1$):

1. Physical passivity / losslessness (t = time coordinate):

$$\int_{t_1}^{t_2} p(t)\,dt \geq W_S(t_2) - W_S(t_1) \Longleftrightarrow p(t) \geq \frac{dW_S(t)}{dt}\ ;\ W_S(t) \geq 0.$$

2. k-dimensional passivity / losslessness:

$$\int_G p(\underline{t})\,d\underline{t} \geq \int_{\partial G} \underline{n}^T \underline{W}_S\,dF \Longleftrightarrow p(\underline{t}) \geq \underline{D}^T \underline{W}_S(\underline{t})\ ;\ \underline{W}_S(\underline{t}) \geq \underline{0}.$$

Note: equivalence marked by $\Longleftrightarrow$ holds usually.

Conclude: For $k=1$, both concepts coincide, i.e.,

1-D passivity / losslessness = physical passivity / losslessness.

Obvious for differential form. For integral form:

$$\int_{\partial G} \underline{n}^T \underline{W}_S\,dF \longrightarrow -W_S(t_1) + W_S(t_2).$$

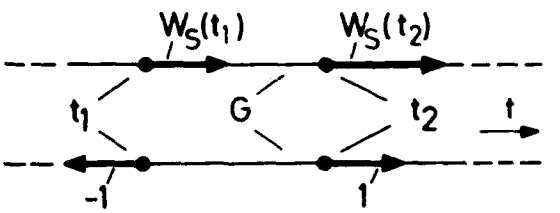

93/1/13

Inductance:

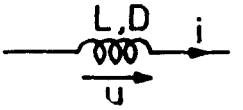

$u = \sqrt{L}\,D(\sqrt{L}\,i)$

$p(\underline{t}) = ui = D(\frac{1}{2}Li^2)$, where

$D = \underline{\alpha}^T \underline{D}$, $\underline{\alpha} = (\alpha_1, \ldots, \alpha_k)^T$ = const., $\|\underline{\alpha}\| = 1$, $\underline{D} = (D_1, \ldots, D_k)^T$, $D_\varkappa = \frac{\partial}{\partial t_\varkappa}$.

Thus, with $\underline{L} = \underline{\alpha} L$, is special case of more general

k-dimensional (k-D) inductance $\underline{L} = (L_1, \ldots, L_k)^T$,

defined by $u = \sum_{\varkappa=1}^{k} \sqrt{L_\varkappa}\,D_\varkappa(\sqrt{L_\varkappa}\,i)$.

Power absorbed: $p(\underline{t}) = ui = \underline{D}^T \underline{W}_s$ where

$\underline{W}_s = (W_{s1}, \ldots, W_{sk})^T$, $W_{s\varkappa} = \frac{1}{2} L_\varkappa i^2$, $\varkappa = 1$ to k.

Obviously, $p(\underline{t}) = \underline{D}^T \underline{W}_S$ always holds.

Hence, L is passive, even lossless, if $L_\varkappa \geq 0$, $\varkappa = 1$ to k.

Similarly: capacitances, coupled inductances.

93/1/14

Resistance: $u = Ri$, $R > 0$, $p(t) = ui = Ri^2 \geq 0$.

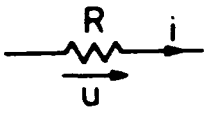

Have $p(t) \geq D^T W_S$ for $W_S = 0$.

Thus, passivity requirement satisfied with $W_S = 0$.

Ideal transformer of ratio m: $u_1 = mu_2$, $i_2 = -mi_1$.

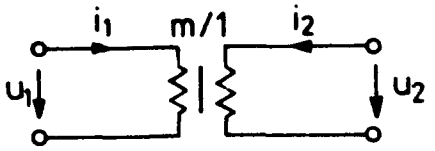

$p(t) = u_1 i_1 + u_2 i_2 = 0 \quad \forall t$.

Have $p(t) = D^T W_S$ for $W_S = 0$

Thus, is passive, even lossless, with $W_S = 0$.

Holds in particular, of course, for $m = -1$, as primarily needed in present context.

Note: Similar results for gyrator, circulators.

93/1/15

Consider Kirchhoff circuit with b branches, $\beta = 1$ to b.

To each branch β there belongs current i_β, voltage u_β.

Then, for every node: Kirchhoff current law holds,

for every loop: Kirchhoff voltage law holds.

Power absorbed by branch β: $u_\beta i_\beta$.

By a known fundamental theorem: $\sum_{\beta=1}^{b} u_\beta i_\beta = 0$, i.e., conservation of power guaranteed.

Hence, passivity of circuit is guaranteed as soon as all its elements are passive. (Similarly for losslessness.)

Consequently, MD Kirchhoff circuit is passive if all elements are passive. The latter is easy to check, e.g. by verifying that inductances, capacitances, resistances are ≥ 0.

93/1/16

How can we obtain an MD-passive system from a physically passive system N depending on spatial coordinates t_1 to t_{k-1} (thus x, y, ...) and time t?

1. Replace t by $t_k = t_k(t)$ having same dimension as t_1 to t_{k-1}, $v_k = dt_k/dt$ sufficiently large > 0. Simplest: $v_k = \text{const.} > 0$. Assume that N has finite propagation speed.
2. Apply coordinate transformation $\underline{t} \longrightarrow \underline{t}' = (t_1', \ldots, t_k')^T$ (simplest: rotation) such that original causality with respect to t becomes causality with respect to t_1' to t_k'; thus, for any movement taking place, then $d\underline{t}'/dt \geq \underline{0}$.
3. If N was physically passive, then after transformation will be passive with respect to all t_1' to t_k'.

93/1/17

Approach by coordinate transformation $\underline{t} \longrightarrow \underline{t}'$.

Original coordinates: $\underline{t} = (t_1, \ldots, t_k)^T$, $t_k = t_k(t)$, t = time.

New coordinates: $\underline{t}' = (t_1', \ldots, t_k')^T$, $\underline{t} = \underline{H}\,\underline{t}'$. $\quad v_k = \dfrac{dt_k}{dt} > 0$.

$\underline{H}$ = k x k matrix, preferably orthogonal.

t_k should be main diagonal of $\underline{t}'$-system of coordinates, i.e., all entries of last row of $\underline{H}$ should be equal to a same positive constant.

$D_\varkappa = \dfrac{\partial}{\partial t_\varkappa}$, $D_\varkappa' = \dfrac{\partial}{\partial t_\varkappa'}$, $\quad \varkappa = 1$ to k,

$\underline{D} = (D_1, \ldots, D_k)^T$, $\underline{D}' = (D_1', \ldots, D_k')^T$, $\underline{D}' = \underline{H}^T \underline{D}$.

For problems with 3 spatial coordinates plus time, have: $k = 4$, thus: $t_1 = x$, $t_2 = y$, $t_3 = z$, $t_4 = t_4(\underline{t})$.

93/1/18

Suitable choices for rotation / transformation matrix $\underline{H}$:

For $k = 2$: $\underline{H} = \frac{1}{\sqrt{2}} \begin{pmatrix} 1 & -1 \\ 1 & 1 \end{pmatrix}$

For $k = 3$: $\underline{H} = \begin{pmatrix} 1/\sqrt{2} & -1/\sqrt{2} & 0 \\ 1/\sqrt{6} & 1/\sqrt{6} & -\sqrt{2/3} \\ 1/\sqrt{3} & 1/\sqrt{3} & 1/\sqrt{3} \end{pmatrix}$

$$= \mathrm{diag}\left(\frac{1}{\sqrt{2}}, \frac{1}{\sqrt{6}}, \frac{1}{\sqrt{3}}\right) \cdot \begin{pmatrix} 1 & -1 & 0 \\ 1 & 1 & -2 \\ 1 & 1 & 1 \end{pmatrix}$$

For $k = 4$: $\underline{H} = \mathrm{diag}\left(\frac{1}{\sqrt{2}}, \frac{1}{\sqrt{6}}, \frac{1}{\sqrt{12}}, \frac{1}{2}\right) \cdot \begin{pmatrix} 1 & -1 & 0 & 0 \\ 1 & 1 & -2 & 0 \\ 1 & 1 & 1 & -3 \\ 1 & 1 & 1 & 1 \end{pmatrix}$

93/1/19

Simple possibility feasible for $k = 2^m$, $m \in \mathbb{N}$:

Use <u>Hadamard matrix</u>; always orthogonal.

Choose symmetric type, i.e. with $\underline{H} = \underline{H}^T = \underline{H}^{-1}$:

$k = 2$: $\underline{H} = \frac{1}{\sqrt{2}} \begin{pmatrix} -1 & 1 \\ 1 & 1 \end{pmatrix}$

$k = 4$: $\underline{H} = \frac{1}{2} \begin{pmatrix} 1 & -1 & -1 & 1 \\ -1 & 1 & -1 & 1 \\ -1 & -1 & 1 & 1 \\ 1 & 1 & 1 & 1 \end{pmatrix}$

Note: Hadamard matrices also exist for many cases where k = multiple of 4.

93/1/20

Example of a suitable orthogonal matrix $\underline{H}$ for any $k \geq 2$.

Define for this $\underline{H} = \underline{H}_{k-1}\, \underline{H}_{k-2} \cdots \underline{H}_1$

where $\underline{H}_\varkappa = \mathrm{diag}\,(\underline{H}_{\varkappa 1}, \underline{H}_{\varkappa 2}, \ldots, \underline{H}_{\varkappa,k-1})$, $\varkappa = 1$ to $k-1$

$$\underline{H}_{\varkappa\lambda} = \begin{cases} 1 & \text{for } \lambda \neq \varkappa \text{ (then, scalar)} \\ \dfrac{1}{\sqrt{\varkappa+1}} \begin{pmatrix} 1 & -\sqrt{\varkappa} \\ \sqrt{\varkappa} & 1 \end{pmatrix} & \text{for } \lambda = \varkappa \text{ (2×2 matrix).} \end{cases}$$

Find: $\underline{H} = (\!(H_{\varkappa\lambda})\!)$

where
$$H_{\varkappa\lambda} = \begin{cases} 1/\sqrt{\varkappa(\varkappa+1)} & \text{for } \lambda \leq \varkappa \leq k-1 \\ -\sqrt{\varkappa/(\varkappa+1)} & \text{for } \lambda = \varkappa+1 \\ 1/\sqrt{k} & \text{for } \varkappa = k \\ 0 & \text{otherwise.} \end{cases}$$

Obtain thus in particular $t_k = \dfrac{1}{\sqrt{k}}\,(t'_1 + t'_2 + \ldots + t'_k)$.

Hence, t_k is indeed the main diagonal of $\underline{t}'$-coordinates.

93/1/21

For discretization in space and time, use sampling raster generated by equal spacings along all t'_j to t'_k. This has added advantage that it leads to very efficient grid in actual spatial variables t_1 to t_{k-1}.

Examples: For $k-1=1$: Get 2 interleaved sets of points.

For $k-1=2$: Spatial grid points form equilateral triangles; in fact, 3 consecutive such grids are distinct but form on average again equilateral triangles, i.e. with altogether 3 times higher point density.

For $k-1=3$: Spatial grid points are centers of densest ball packing; 4 consecutive such grids are distinct, form on average again densest ball packing, 4 times denser.

93/1/22

Sampling raster obtained for k = 2 by 45° rotation:

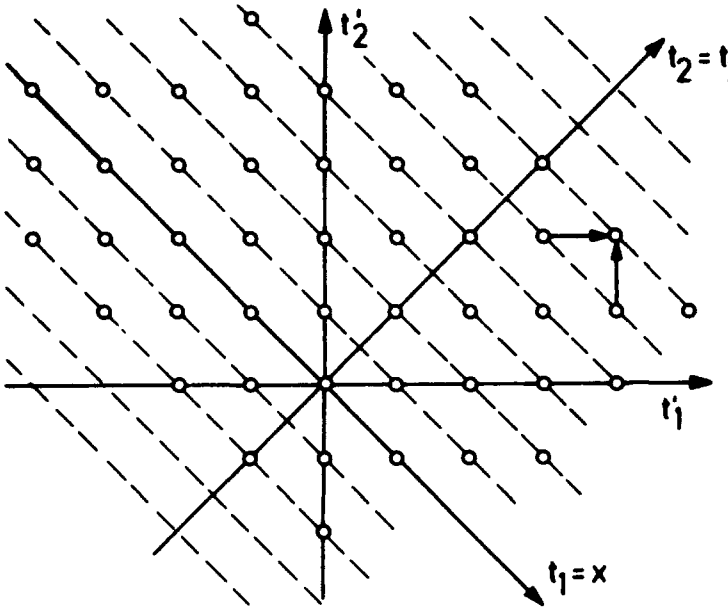

The computations for any point require only knowledge of results obtained for points on previous lines. Hence, all points on a same dashed line parallel to the t_1-axis can be computed in parallel: Massive parallelism available!

93/1/23

Alternative representation of sampling raster obtained for k = 2 after 45° rotation.

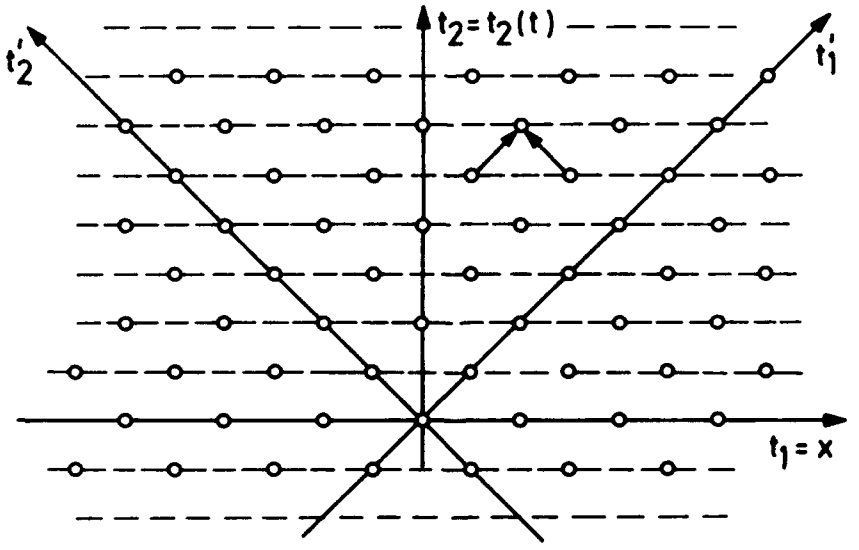

Observe t_2-axis ("time"-axis) is main diagonal of the new coordinate system $\underline{t'}$.

93/1/24

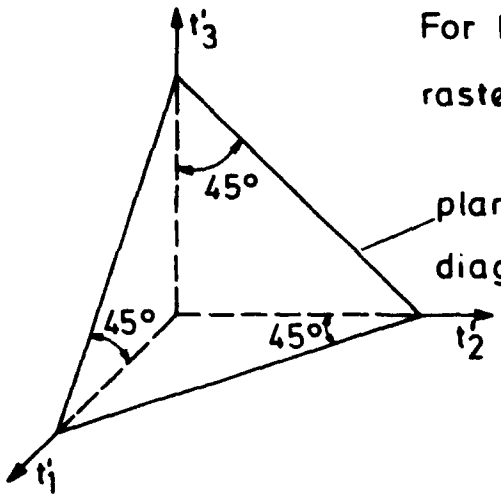

For k=3: Processing in 3-dimensional (3-D) raster after appropriate rotation.

plane perpendicular to main diagonal ("time" axis)

Computations for all points in planes parallel to the one shown can be carried out simultaneously.

Extends to any number of dimensions (hyperplanes!).

Thus, true massive parallelism available, i.e., extremely high speed achievable at expense of added hardware.

93/1/25

For k=3: Planes perpendicular to main diagonal ("time" axis).

In planes of same colour, the sampling pattern is the same.

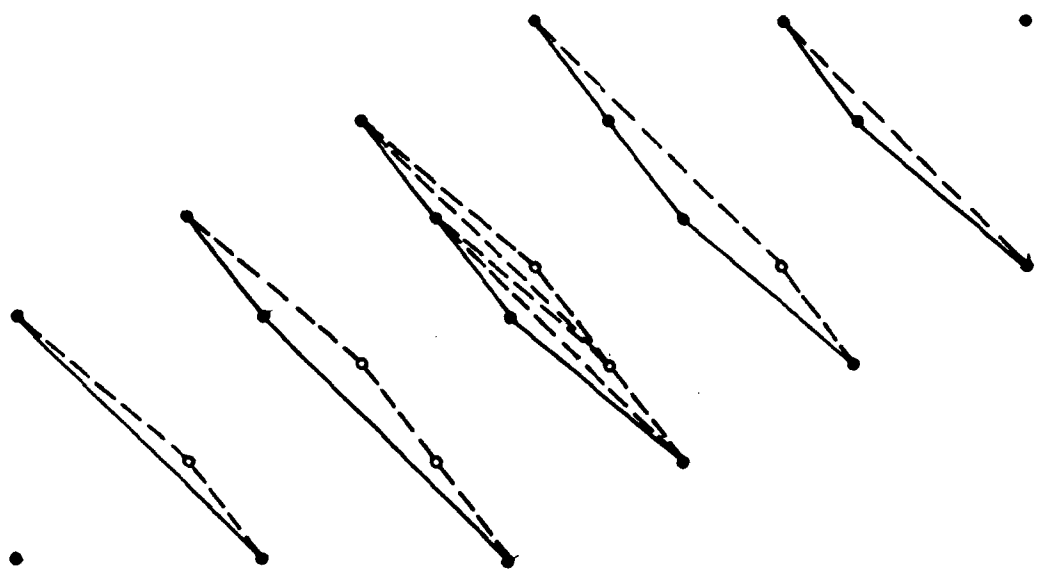

93/1/26

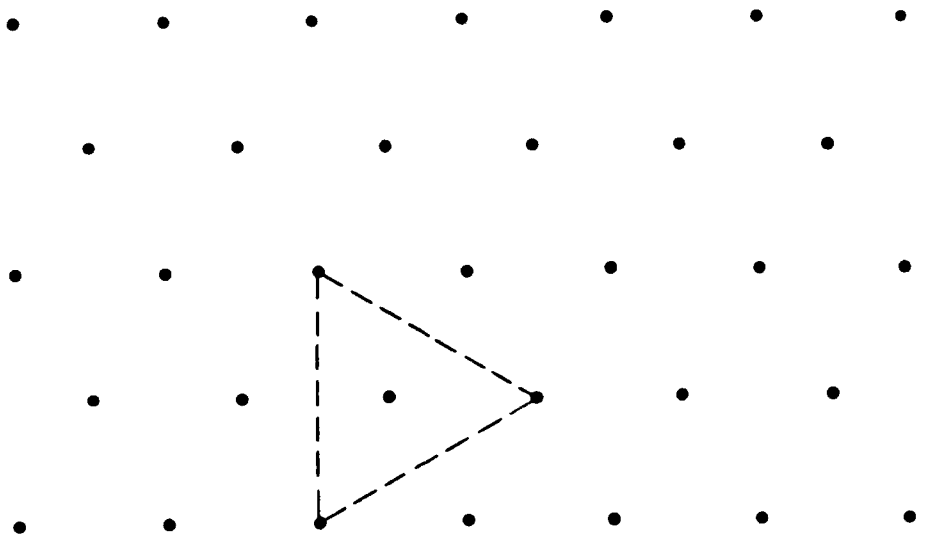

Sampling patterns existing in planes perpendicular to the diagonal ("time" axis). These patterns alternate between 3 distinct types of equilateral triangles marked in red, blue, green.

93/1/27

Generalized trapezoidal rule (constant-parameter case)

Given: $u = D(Li) = LDi$, where

$D = \underline{\alpha}^T \underline{D}$, $\underline{D} = (D_1, \ldots, D_k)^T$, $D_\varkappa = \partial / \partial t_\varkappa$, $\varkappa = 1$ to k,

$\underline{\alpha} = (\alpha_1, \ldots, \alpha_k)^T = \text{const.}$, $\|\underline{\alpha}\| = 1$, $T_o = \text{const.} > 0$.

Apply conventional trapezoidal rule in direction of $\underline{\alpha}$, i.e., writing $\underline{t} = \underline{\alpha}\tau$, apply it with respect to τ. Obtain

$u(\underline{t}) + u(\underline{t} - \underline{T}) = R\,(i(\underline{t}) - i(\underline{t} - \underline{T}))$, where $\underline{T} = \underline{\alpha} T_o$, $R = \frac{2L}{T_o}$,

i.e., in compact notation, $u = R\Delta(\underline{T})\{i\}$.

Define voltage waves, $a' = u + Ri$, $b' = u - Ri$

Find: $a'(\underline{t}) \circ\!\!-\!\!\boxed{\underline{T}}\!\!-^{-1}\!\!\circ\!\!-\!\!\circ\; b'(\underline{t}) = -a'(\underline{t} - \underline{T})$

Important: Holds for $R(\underline{t})$ if $R(\underline{\alpha}\tau)$ independent of τ.

Similar results for $\underline{t}'$, T_o', D', $\underline{D}'$, $D_\varkappa'$, $\underline{\alpha}'$, k', $\underline{T}'$.

93/1/28

Generalized trapezoidal rule (nonconstant case)

Given: $u = \sqrt{L}\, D(\sqrt{L}\, i)$, thus $\frac{u}{\sqrt{R}} = \frac{T_0}{2} D(\sqrt{R}\, i)$, $R = R(\underline{t}) = \frac{2L}{T_0}$

where $D = \underline{\alpha}^T \underline{D}$, $\underline{D} = (D_1, \ldots, D_k)^T$, $D_\varkappa = \partial / \partial t_\varkappa$, $\varkappa = 1$ to k.

$\underline{\alpha} = (\alpha_1, \ldots, \alpha_k)^T = \text{const.}$, $\|\underline{\alpha}\| = 1$, $\underline{T} = \underline{\alpha} T_0$, $T_0 = \text{const.} > 0$.

Apply conventional trapezoidal rule in direction of $\underline{\alpha}$, i.e., writing $\underline{t} = \underline{\alpha}\tau$ apply it with respect to τ. Obtain

$(u/\sqrt{R})(\underline{t}) + (u/\sqrt{R})(\underline{t} - \underline{T}) = (\sqrt{R}\, i)(\underline{t}) - (\sqrt{R}\, i)(\underline{t} - \underline{T})$,

i.e., in compact notation, $u/\sqrt{R} = \Delta(\underline{T})\{\sqrt{R}\, i\}$.

Define power waves, $a = \frac{u + Ri}{2\sqrt{R}}$, $b = \frac{u - Ri}{2\sqrt{R}}$.

Find: 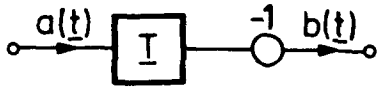

$b(\underline{t}) = -a(\underline{t} - \underline{T})$.

Similar for $\underline{t}'$, T_0', D', $\underline{D}'$, $D_\varkappa'$, $\underline{\alpha}'$, k', $\underline{T}'$.

93/1/29

More general coordinate transformation $\underline{t} \longrightarrow \underline{t}'$:

As before: $\underline{t} = (t_1, \ldots, t_k)^T$, $t_k = t_k(t)$, $v_k = \frac{dt_k}{dt} > 0$.

However: $\underline{t}' = (t_1', \ldots, t_{k'}')^T$, $k' \geq k$, $\underline{t} = \underline{H}\, \underline{t}'$,

where $\underline{H} = k \times k'$ matrix of rank k, $\underline{H}\, \underline{H}^{-R} = 1_k$,

$\underline{H}^{-R}$ a right inverse of $\underline{H}$, 1_k = unit matrix of order k.

Directions determined by t_1' to $t_{k'}'$ should have maximal symmetry with respect to the direction of t_k, thus of t.

All entries in last row of $\underline{H}$ must be positive.

There must be at least one $\underline{H}^{-R}$ such that all entries in last cotumn of this $\underline{H}^{-R}$ are positive.

Have: $D_\varkappa = \frac{\partial}{dt_\varkappa}$, $\varkappa = 1$ to k; $D_\varkappa' = \frac{\partial}{dt_\varkappa'}$, $\varkappa = 1$ to k',

$\underline{D} = (D_1, \ldots, D_k)^T$, $\underline{D}' = (D_1', \ldots, D_{k'}')^T$, $\underline{D}' = \underline{H}^T \underline{D}$.

93/1/30

Suitable matrices for more general transformation:

For $k=3$: $\quad \underline{H} = \begin{pmatrix} 1 & 0 & -1 & 0 & 0 \\ 0 & 1 & 0 & -1 & 0 \\ 1 & 1 & 1 & 1 & \delta \end{pmatrix}$

$$\underline{H}^{-R} = \underline{H}^{T} . \operatorname{diag}\left(\frac{1}{2} , \frac{1}{2} , \frac{1}{4+\delta^2} \right) , \quad \delta = 1 \text{ or } 2 .$$

For $k=4$: $\quad \underline{H} = \begin{pmatrix} 1 & 0 & 0 & -1 & 0 & 0 & 0 \\ 0 & 1 & 0 & 0 & -1 & 0 & 0 \\ 0 & 0 & 1 & 0 & 0 & -1 & 0 \\ 1 & 1 & 1 & 1 & 1 & 1 & \delta \end{pmatrix}$

$$H^{-R} = H^{T} . \operatorname{diag}\left(\frac{1}{2} , \frac{1}{2} , \frac{1}{2} , \frac{1}{6+\delta^2} \right) , \quad \delta = 1 \text{ or } 2 .$$

For $\delta = 1$, leads to standard (canonic) sampling,

For $\delta = 2$, leads to checkerboard sampling if $k=3$,

to generalization thereof if $k=4$.

Is easier to program, but less efficient than rotation.

93/1/31

Checkerboard sampling explained for $k=3$,

thus for t_1, t_2 = spatial coordinates (x, y), $t_3 = t_3(t)$.

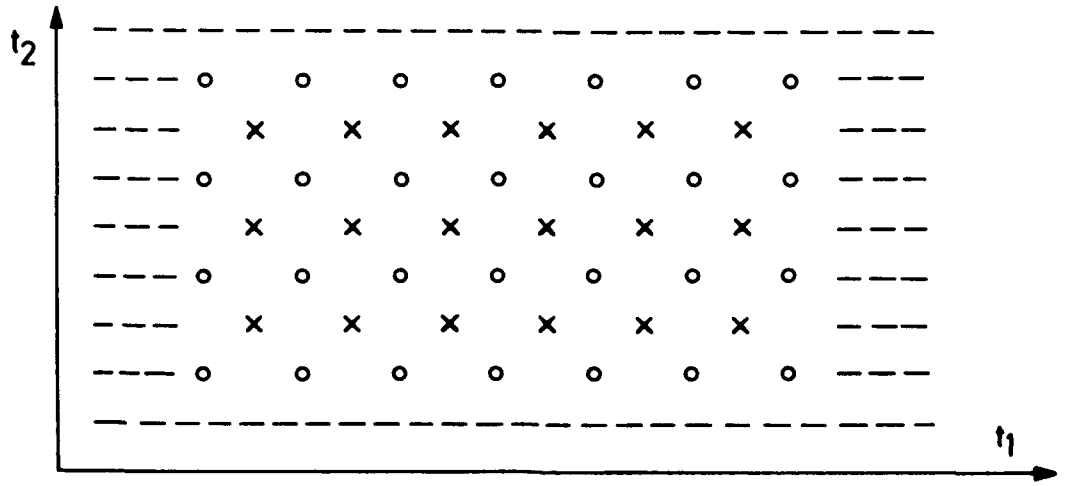

For consecutive time instants, use in (t_1, t_2)-plane (= actual spatial domain) alternately the points marked by "o" and those marked be "x".

93/1/32

Checkerboard sampling and generalization thereof:

For any k, have 2 distinct spatial sampling grids between which process switches back and forth in alternating time slots (like between black and white fields of a checkerboard). This is easier to program than for the grids in the rotational approach, but is less efficient (requires higher point density for same accuracy).

For k = 2, can be made identical to rotational approach.

For standard sampling in t_1' to $t_{k'}'$, obtain only one spatial sampling grid. Is even easier to program than checkerboard approach. Comparison of efficiency requires more detailed investigation.

93/1/33

For general transformations, all condiderations for obtaining MD causality and MD passivity hold as before if properly applied to t_1' to $t_{k'}'$ instead of t_1' to t_k'.

For discretization in space and time, use again the sampling raster generated by equal spacings along all new coordinates t_1' to $t_{k'}'$. This puts requirements on $\underline{H}$ in order to guarantee that obtain a consistent raster. The (discrete) values of the t_1' to $t_{k'}'$ fixing a given knot (sampling point) will then usually not be unique, but this is of no disadvantage.

For approximating the differential operators use trapezoidal rule in same way as before.

93/1/34

Examples, with $l>0$, $c>0$, $r\geq 0$, $g\geq 0$, $v_k = \text{const.} > 0$:

1. Transmission line, $k=2$, $\underline{t} = (t_1, t_2)^T$, $t_1 = x$, $t_2 = v_2 t$,

$$v_2 l \frac{\partial i}{\partial t_2} + ri + \frac{\partial u}{\partial t_1} = f_1(\underline{t}), \qquad v_2 c \frac{\partial u}{\partial t_2} + gu + \frac{\partial i}{\partial t_1} = f_2(\underline{t})$$

2. Two parallel conducting plates, $k=3$, $\underline{t} = (t_1, t_2, t_3)^T$,

$$v_3 l \frac{\partial i_\varkappa}{\partial t_3} + r i_\varkappa + \frac{\partial u}{\partial t_\varkappa} = f_\varkappa(\underline{t}), \quad \varkappa = 1, 2; \qquad t_1 = x, \quad t_2 = y$$

$$v_3 c \frac{\partial u}{\partial t_3} + gu + \frac{\partial i_1}{\partial t_1} + \frac{\partial i_2}{\partial t_2} = f_3(\underline{t}); \qquad t_3 = v_3 t$$

3. More generally, $k \geq 2$, $\underline{t} = (t_1, \ldots, t_k)^T$, $t_k = v_k t$,

$$v_k l \frac{\partial \underline{i}}{\partial t_k} + r\underline{i} + \nabla u = \underline{f}(\underline{t}), \qquad \underline{i} = (i_1, \ldots, i_k)^T$$

$$\nabla = \left(\frac{\partial}{\partial t_1}, \ldots, \frac{\partial}{\partial t_{k-1}} \right)^T$$

$$v_k c \frac{\partial u}{\partial t_k} + gu + \nabla^T \underline{i} = f_k(\underline{t}). \qquad \underline{f} = (f_1, \ldots, f_{k-1})^T$$

For $k=4$, equivalent to standard acoustics equations.

93/1/35

For $k=2$ (transmission line), assume

$l = l(t_1) > 0$, $c = c(t_1) > 0$, $r = r(\underline{t}) \geq 0$, $g = g(\underline{t}) \geq 0$,

$\underline{t} = (t_1, t_2)^T$, $t_1 = x$, $t_2 = v_2 t$, $v_2 = \text{const.} > 0$; $i_1 = i$, $i_2 = \frac{u}{r_o}$.

Find:

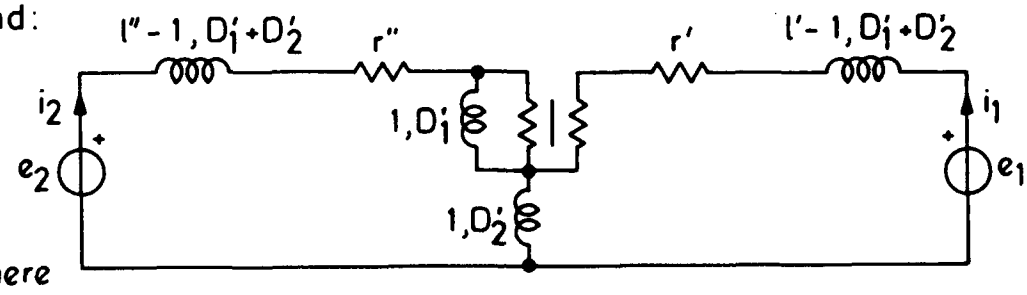

where

$\sqrt{2}\, D'_1 = D_2 - D_1$, $\sqrt{2}\, D'_2 = D_1 + D_2$, $e_1 = \sqrt{2}\, f_1(\underline{t})/r_o$, $e_2 = \sqrt{2}\, f_2(\underline{t})$,

$l' = v_2 l / r_o$, $l'' = v_2 c\, r_o$, $r' = \sqrt{2}\, r / r_o$, $r'' = \sqrt{2}\, g\, r_o$,

r_o being a constant such that $l' \geq 1$, $l'' \geq 1$.

Requires $1/v_2 c \leq r_o \leq v_2 l$, thus $v_2 \geq 1/\sqrt{l_{min} c_{min}}$

Then sufficient that, e.g., $r_o = \sqrt{l_{min}/c_{min}}$.

93/1/36

Applying uniform <u>discretization</u> steps T_o' in the t_1' and t_2' directions, the previous continuous-domain MD Kirchhoff circuit is transformed into the following <u>discrete-domain MD Kirchhoff circuit</u>:

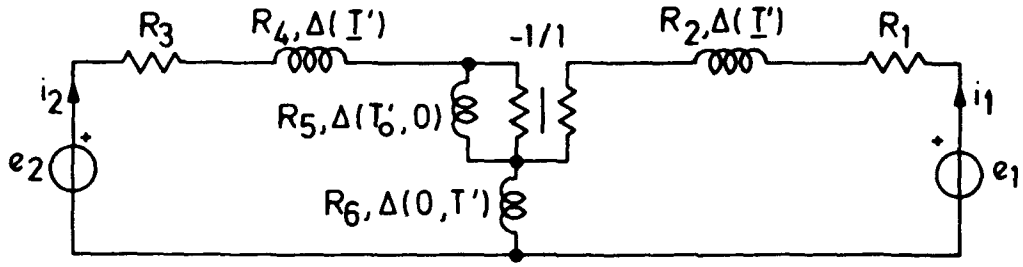

where $\underline{T}' = (T_o', T_o')^T = \underline{a}\sqrt{2}\,T_o'$, $\underline{a} = \frac{1}{\sqrt{2}}(1,1)^T$,

$R_1 = r'$, $R_3 = r''$, $R_5 = R_6 = 2/T_o'$

$R_2 = \sqrt{2}\,(l'-1)\,T_o'$, $R_4 = \sqrt{2}\,(l''-1)\,T_o'$, $l' \geq 1$, $l'' \geq 1$.

93/1/37

Applying the principles known from WDF theory, the MD Kirchhoff circuit gives rise to the following <u>signal-flow</u> (wave-flow) <u>diagram</u> (algorithm!):

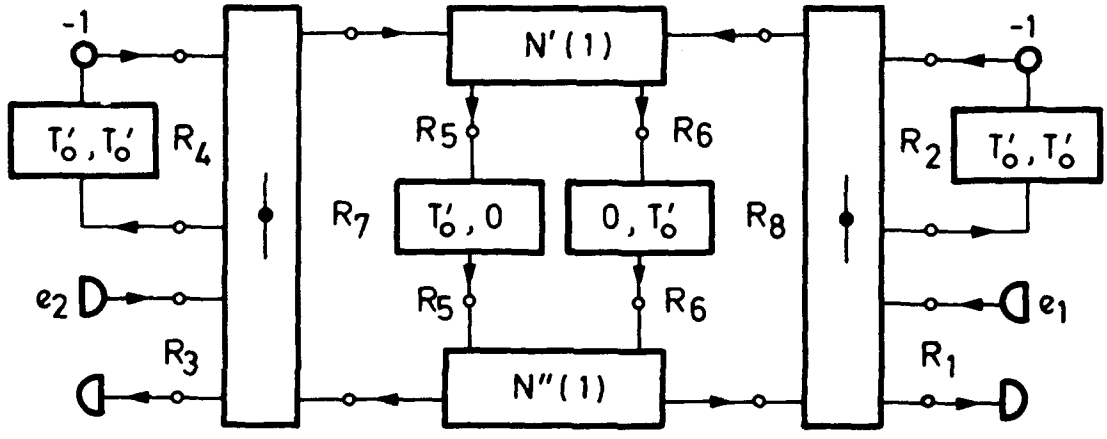

where R_1 to R_6 are as given previously

and where $R_7 = R_8 = 4/T_o'$.

93/1/38

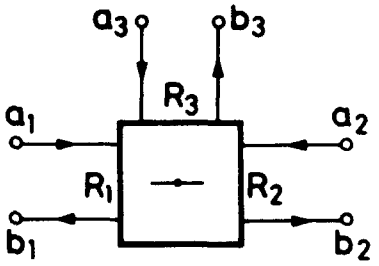

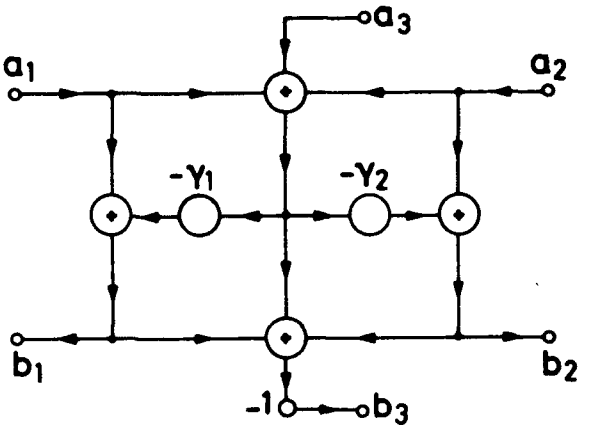

Three-port series adaptor and a corresponding signal-flow diagram (port 3 = dependent port).

$\gamma_1 = 2R_1/(R_1+R_2+R_3)$, $\gamma_2 = 2R_2/(R_1+R_2+R_3)$.

93/1/39

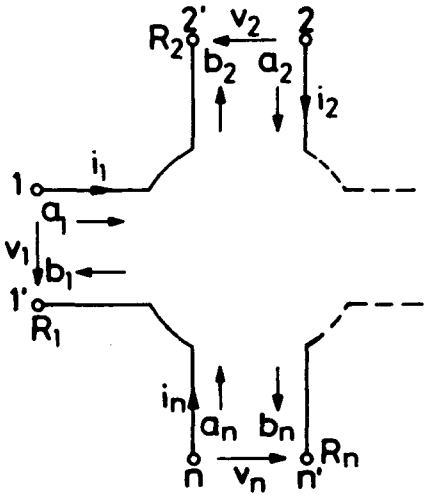

Series connection of

n ports (numbered v = 1 to n).

R_v = port resistance.

$v_1 + v_2 + \cdots\cdots + v_n = 0$

$i_1 = i_2 = \cdots\cdots = i_n$

$a_v = v_v + R_v i_v$, $b_v = v_v - R_v i_v$

Thus, have 3n equations in 4n variables.

Eliminate all v_v, i_v . Solve for the b_v :

$b_v = a_v - \gamma_v(a_1 + a_2 + \cdots\cdots + a_n)$, $\gamma_v = 2R_v/(R_1 + R_2 + \cdots\cdots + R_n)$

93/1/40

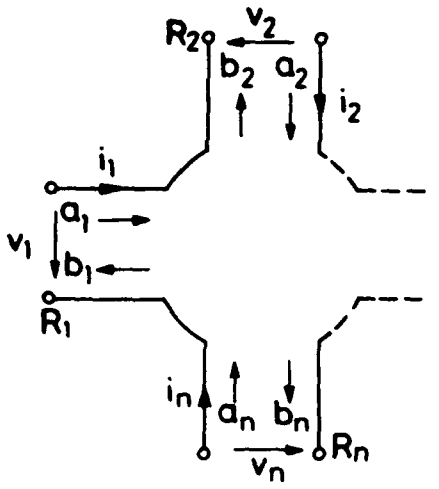

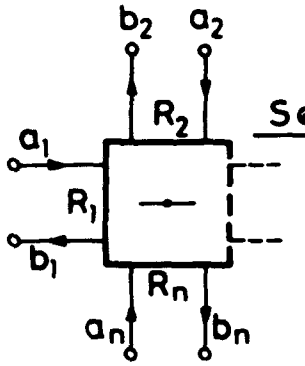

Series adaptor,

with n ports

v = 1 to n

$$b_v = a_v - \gamma_v (a_1 + a_2 + \cdots\cdots + a_n)$$

$\gamma_v = 2R_v/(R_1 + R_2 + \cdots\cdots + R_n)$, $\quad \gamma_1 + \gamma_2 + \cdots\cdots + \gamma_n = 2.$

Can choose one port as <u>dependent</u> port,

e.g. $v=1$: $\gamma_1 = 2 - \gamma_2 - \gamma_3 - \cdots\cdots - \gamma_n$. Thus, need

n-1 multipliers (not n^2) = number degrees of freedom.

93/1/41

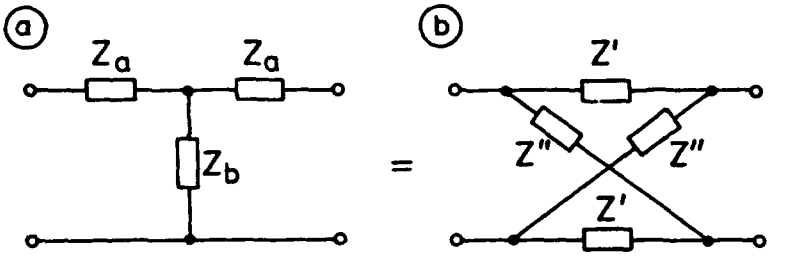

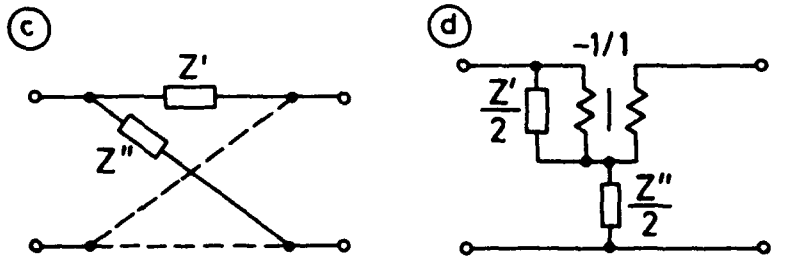

Symmetric two-port and various equivalent representations.

(a) T-configuration, (b) lattice configuration,

(c) simplified represention of (b), (d) Jaumann structure.

Z', Z" = canonic impedances, $Z' = Z_a$, $Z'' = Z_a + 2Z_b$.

93/1/42

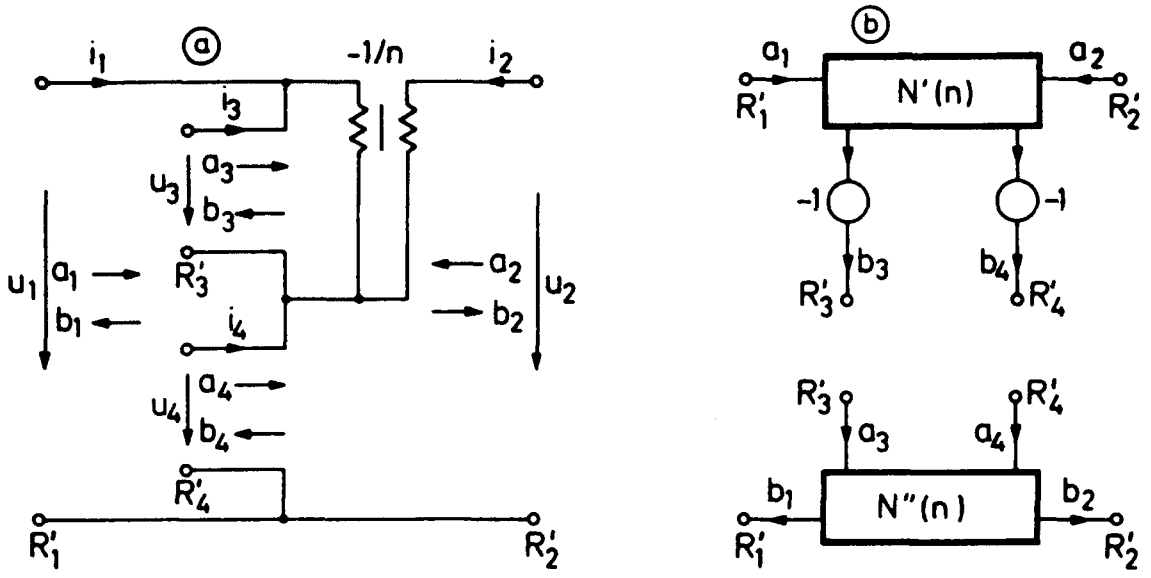

ⓐ A 4-port circuit involving an ideal transformer.

ⓑ Corresponding signal-flow (wave-flow) representation.

93/1/43

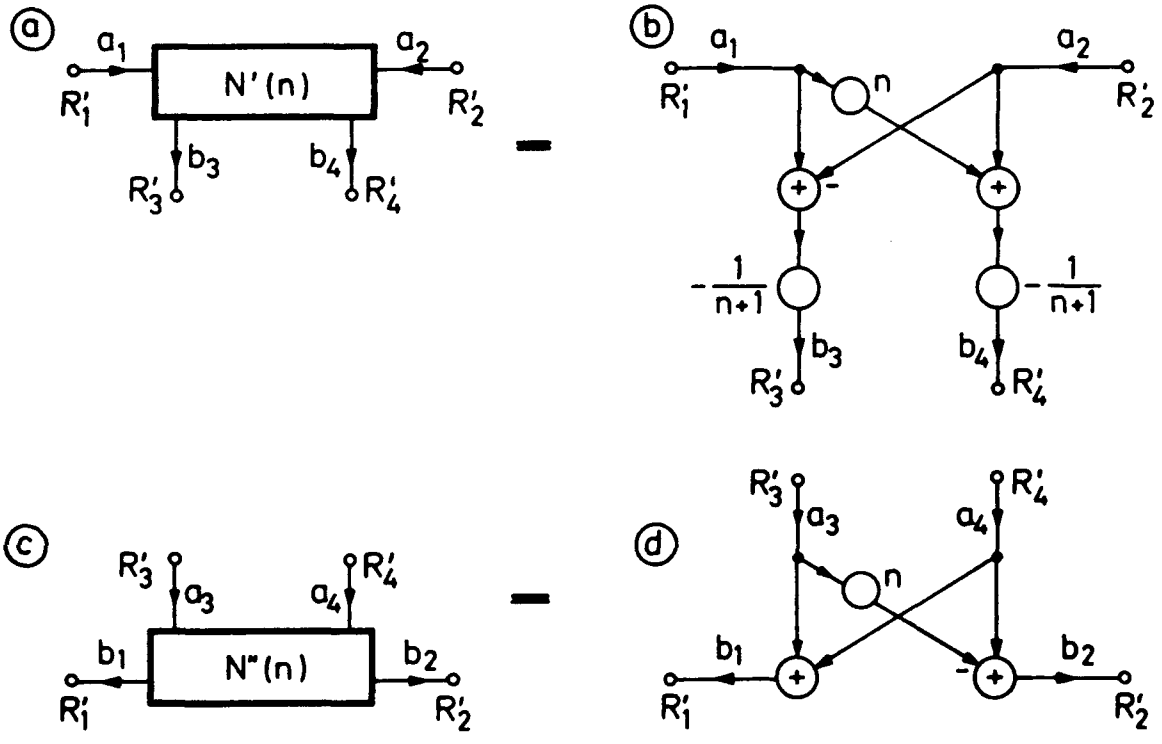

ⓐ and ⓒ Two adaptors needed for n=1 and n=2.

ⓑ and ⓓ Corresponding signal-flow diagrams.

93/1/44

Let now k=4 and l,c,r,g be not necessarily constant, i.e.,

$l = l(\underline{t})$, $c = c(\underline{t})$, $r = r(\underline{t})$, $g = g(\underline{t})$, $\underline{t} = (t_1, t_2, t_3, t_4)^T$,

although $l(\underline{t})$ and $c(\underline{t})$ independent of $t_4 = t_4(t)$, t=time.

Then:

$$D_4(li_1) + ri_1 + D_1(r_4 i_4) = e_1(\underline{t}) ,$$

$$D_4(li_2) + ri_2 + D_2(r_4 i_4) = e_2(\underline{t}) ,$$

$$D_4(li_3) + ri_3 + D_3(r_4 i_4) = e_4(\underline{t}) ,$$

$$D_1(r_4 i_1) + D_2(r_4 i_2) + D_3(r_4 i_3) + D_4(r_4^2 ci_4) + r_4^2 g i_4 = e_4(\underline{t}) ,$$

where

$$D_\varkappa = \frac{\partial}{\partial t_\varkappa} , \quad \varkappa = 1,2,3,4.$$

Note: If parameters not constant, there does not exist a steady-state with constant amplitudes.

93/1/45

For k=4, transformation approach becomes, with $\varkappa = 1$ to 4:

$$\underline{t} = (t_1, \ldots, t_4)^T , \quad \underline{D} = (D_1, \ldots, D_4)^T , \quad D_\varkappa = \frac{\partial}{\partial t_\varkappa} , \quad t_4 = t_4(t) ,$$

$$\underline{t}' = (t_1', \ldots, t_4')^T , \quad \underline{D}' = (D_1', \ldots, D_4')^T , \quad D_\varkappa' = \frac{\partial}{\partial t_\varkappa'} , \quad \underline{t} = \underline{H}\,\underline{t}' .$$

Simplest choice for $\underline{H}$:

Hadamard rotation, e.g. $\underline{H} = \underline{H}^T = \underline{H}^{-1} = \frac{1}{2}\begin{pmatrix} 1 & -1 & -1 & 1 \\ -1 & 1 & -1 & 1 \\ -1 & -1 & 1 & 1 \\ 1 & 1 & 1 & 1 \end{pmatrix}$

Then: $D_i = \frac{1}{2}(D_i'' - D_{i+3}'')$, $D_4 = \frac{1}{2}(D_i'' + D_{i+3}'')$, i = 1 to 3 ,

where $D_1'' = D_1' + D_4'$, $D_2'' = D_2' + D_4'$, $D_3'' = D_3' + D_4'$,

$D_4'' = D_2' + D_3'$, $D_5'' = D_1' + D_3'$, $D_6'' = D_1' + D_2'$,

Also: $D_1'' = D_4 + D_1$, $D_2'' = D_4 + D_2$, $D_3'' = D_4 + D_3$,

$D_4'' = D_4 - D_1$, $D_5'' = D_4 - D_2$, $D_6'' = D_4 - D_3$.

93/1/46

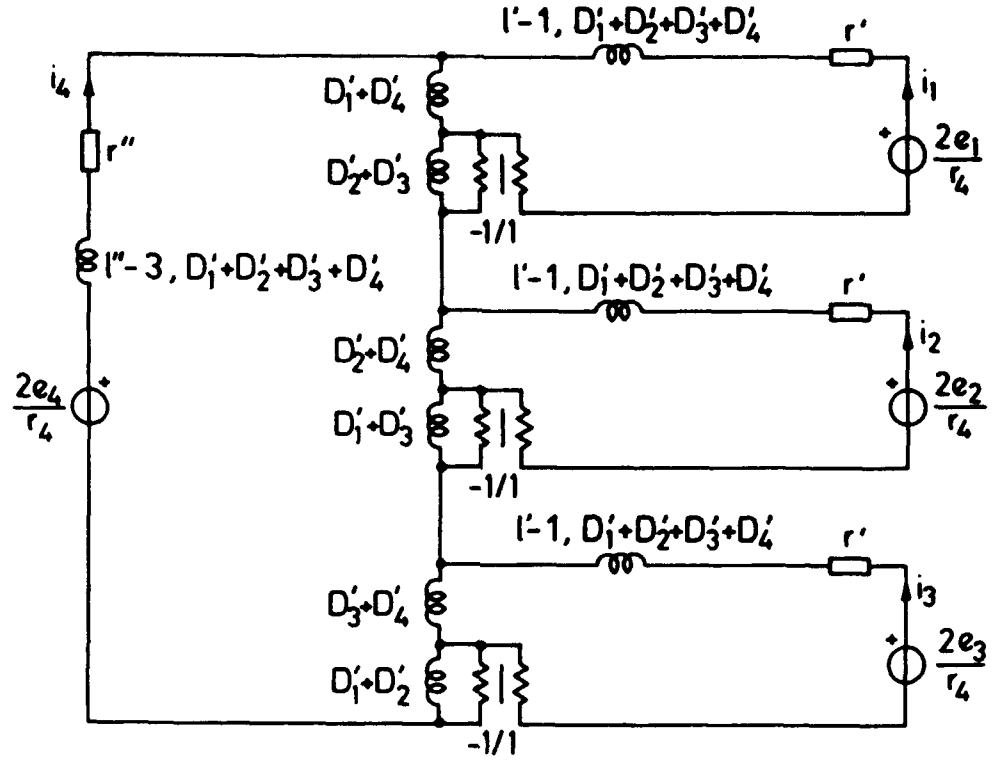

Circuit for k = 4, obtained by Hadamard rotation.

93/1/47

Applying Hadamard rotation to Maxwell's equations:

$$D''_7(\varepsilon' E_1) + (D''_5 - D''_2)\,E_6 + (D''_3 - D''_6)\,E_5 + \sigma' E_1 = 0$$

$$D''_7(\varepsilon' E_2) + (D''_6 - D''_3)\,E_4 + (D''_1 - D''_4)\,E_6 + \sigma' E_1 = 0$$

$$D''_7(\varepsilon' E_3) + (D''_4 - D''_1)\,E_5 + (D''_2 - D''_5)\,E_4 + \sigma' E_3 = 0$$

$$D''_7(\varepsilon'' E_4) + (D''_2 - D''_5)\,E_3 + (D''_6 - D''_3)\,E_2 = 0$$

$$D''_7(\varepsilon'' E_5) + (D''_3 - D''_6)\,E_1 + (D''_4 - D''_1)\,E_3 = 0$$

$$D''_7(\varepsilon'' E_6) + (D''_1 - D''_4)\,E_2 + (D''_5 - D''_2)\,E_1 = 0$$

where $\varepsilon' = 2r_o v_4 \varepsilon$, $\varepsilon'' = 2v_4 \mu / r_o$, $\sigma' = 2\sigma r_o$, $r_o = \text{const.} > 0$.

$D''_1 = D'_1 + D'_4$, $D''_2 = D'_2 + D'_4$, $D''_3 = D'_3 + D'_4$, $E_{3+i} = r_o H_i$, $i = 1$ to 3,

$D''_4 = D'_2 + D'_3$, $D''_5 = D'_1 + D'_3$, $D''_6 = D'_1 + D'_2$, $D''_7 = \frac{1}{2}(D'_1 + D'_2 + D'_3 + D'_4) = \frac{1}{v_4} D_4$.

Leads to structure with nonnegative elements if

$v_4 \geq 2/\sqrt{\varepsilon_{min}\mu_{min}}$ and, e.g., $r_o = \sqrt{\mu_{min}/\varepsilon_{min}}$.

93/1/48

Multidimensional Kirchhoff circuit representing Maxwell's equations.

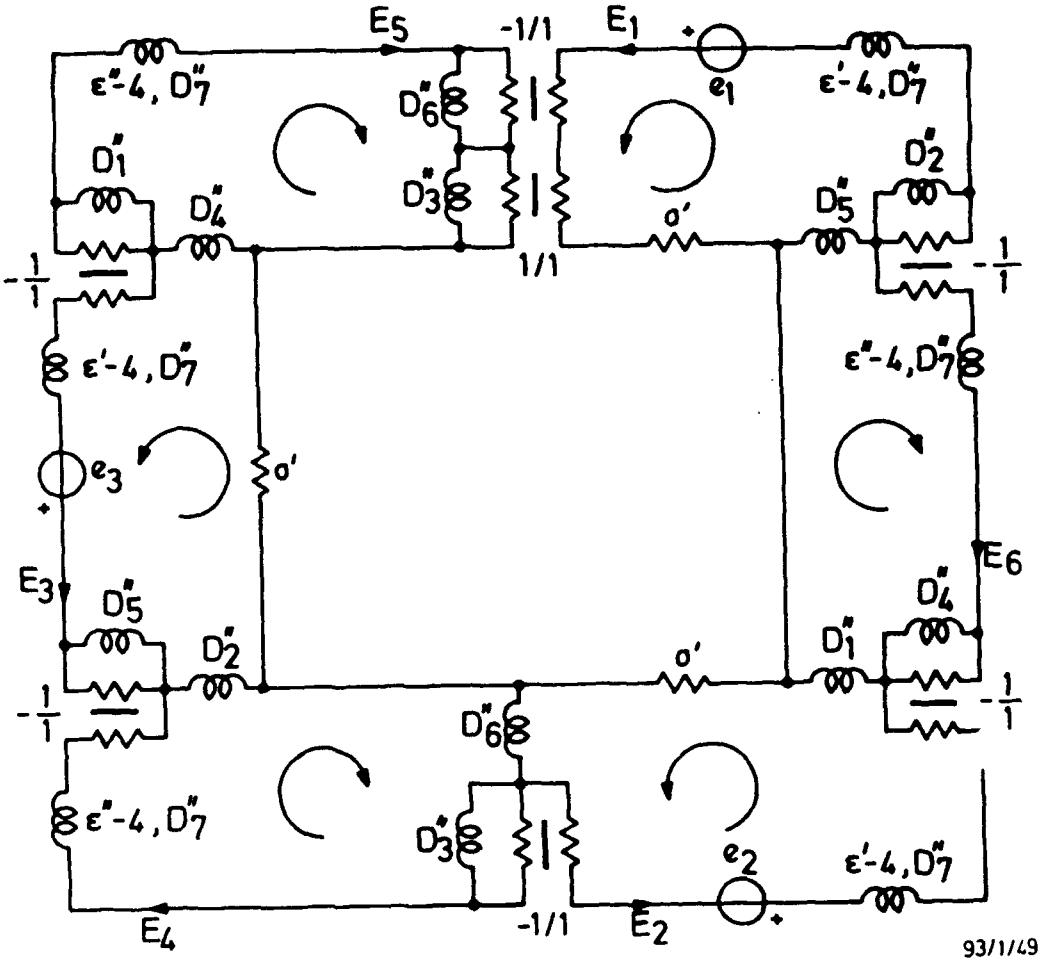

93/1/49

93/1/50

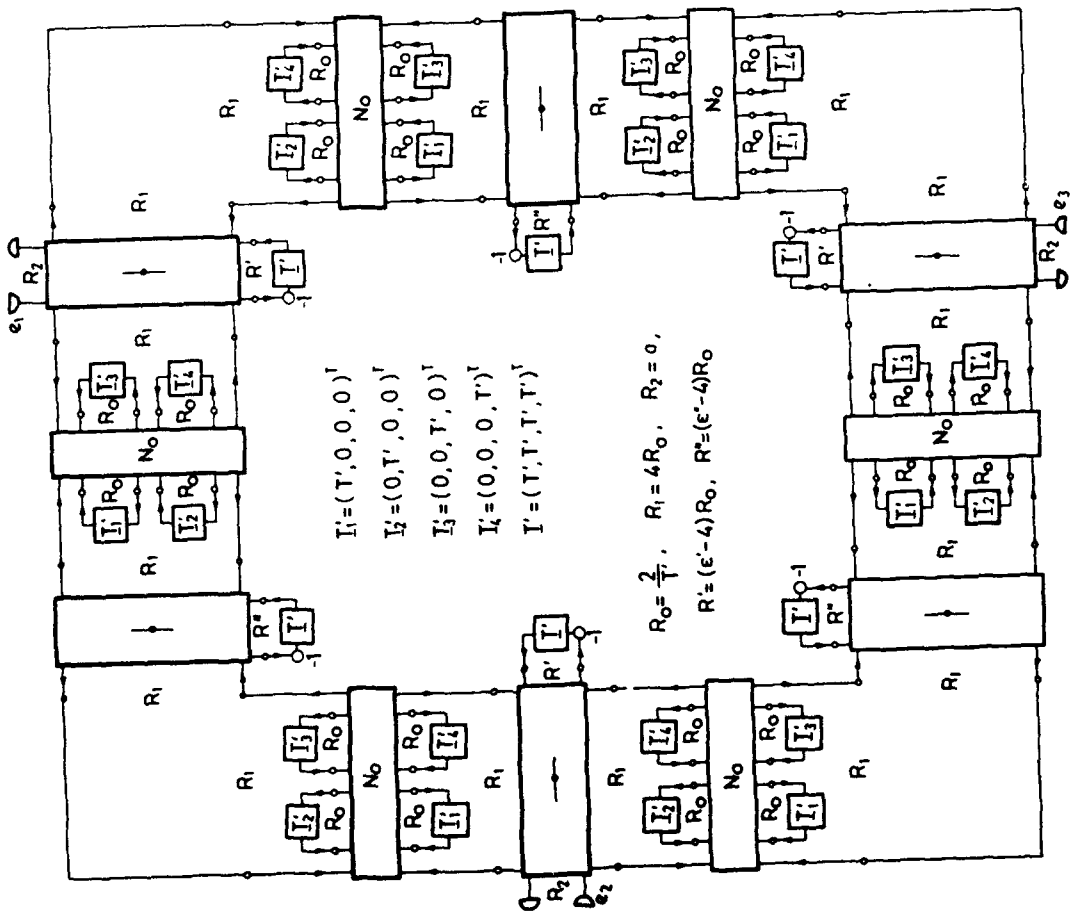

Signal-flow diagram representing the algorithm that models Maxwell's equations.

Definition of N_o in the signal-flow diagram obtained for Maxwell's equations, the shift operators being chosen, for illustration, as in the top part of that diagram:

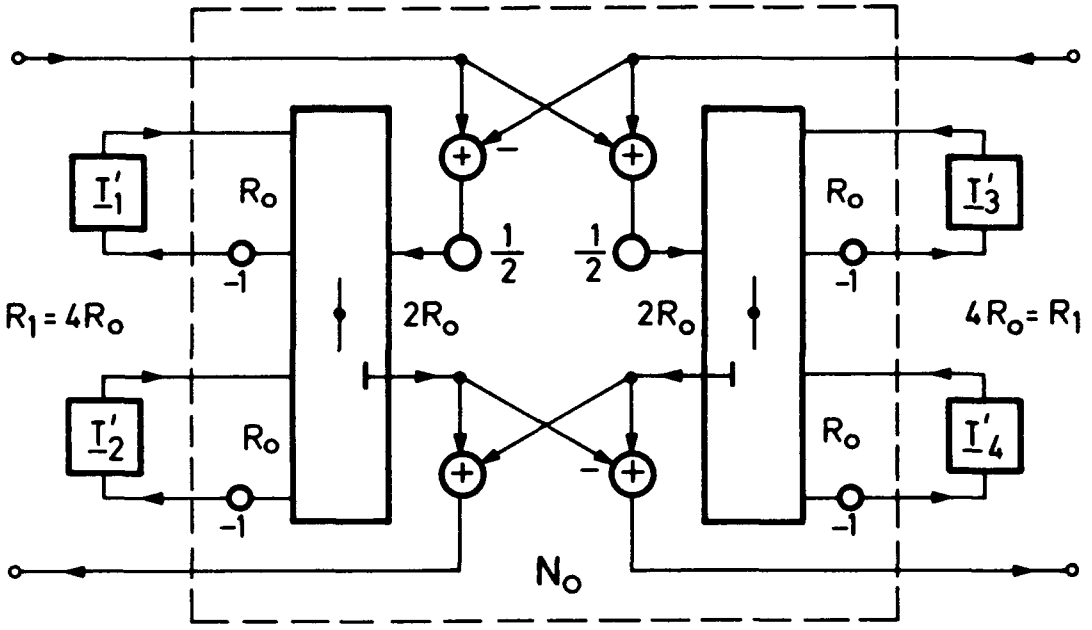

93/1/51

Nonlinearities in electromagnetic fields

1. Consider $\underline{\nabla} \times \underline{H} = \frac{\partial(\varepsilon \underline{E})}{\partial t} + \sigma \underline{E}$ (1), $\underline{\nabla} = \left(\frac{\partial}{\partial x}, \frac{\partial}{\partial y}, \frac{\partial}{\partial z} \right)^T$.

– Resistive nonlinearity, $\sigma = \sigma(\underline{E})$: no problem.

– Reactive nonlinearity, $\varepsilon = \varepsilon(|\underline{E}|)$

For W_E = stored electric energy, have

$$\frac{\partial W_E}{\partial t} = \underline{E}^T \cdot \frac{\partial(\varepsilon \underline{E})}{\partial t} = \frac{\partial}{\partial t}(\hat{\varepsilon} |E|^2) \quad \text{where} \quad \hat{\varepsilon} = \frac{W_E}{|E|^2}$$

Then, can rewrite (1) as follows:

$$\underline{\nabla} \times \underline{H} = \sqrt{\hat{\varepsilon}} \, \frac{\partial}{\partial t} (\sqrt{\hat{\varepsilon}} \, \underline{E}) + \sigma \underline{E}$$

Apply then known theory with power waves.

2. Similarly $\underline{\nabla} \times \underline{E} = -\mu \frac{\partial \underline{H}}{\partial t} = -\sqrt{\hat{\mu}} \, \frac{\partial}{\partial t} (\sqrt{\hat{\mu}} \, \underline{H})$.

3. Similarly for time dependencies, say $\varepsilon = \varepsilon(|\underline{E}|, t)$.

New results in transient analysis of crystal oscillators

Christof Schmidt-Kreusel and Wolfgang Mathis (IEEE/CAS, VDE/ITG)
Department of Electrical Engineering
University of Wuppertal
Fuhlrottstr. 10, D-42097 Wuppertal, Germany
Phone: +49-202-439 3008, Fax: +49-202-439 3040

Introduction

Invented during the 1920's, crystal oscillators are one of the most widely used circuits in electronics. There are a variety of applications in discrete and integrated technique, such as microprocessors, frequency standards, clocks, PLL's and others. In a sharp contrast to this until now no tool is available in the domain of computer-aided design and analysis which allows an accurate and fast simulation of such circuits. In general, this prevents optimization for a given application.

The approaches found in the literature to analyze oscillatory circuits can be subdivided in two classes:

1. analytical approaches for certain oscillator configurations, such as for the CMOS Pierce oscillator e.g. in [1], [2];
2. algorithms that compute the steady-state of nonlinear circuits with periodic response, based on harmonic balance techniques, newton methods [3], hybrid harmonic balance methods [4], extrapolation methods [5] and others.

Nevertheless the common approach in circuit simulation is the so called *brute force approach*, i.e. the numerical integration of the differential-algebraic system

$$\mathbf{F}(\mathbf{y}, \dot{\mathbf{y}}, t) = 0, \qquad \mathbf{y}_0 = \mathbf{y}(0)$$

with the n-dimensional vector of unknowns $\mathbf{y}$ arising from the circuit description for $t \in [0, t_{out}]$ until the transients have died out. It was shown in [2] that the start-up time of common Pierce oscillators takes a minimum of 1000 periods. So the brute force approach will be a very time consuming process in all cases.

Formulation of the problem

The task to be solved can easily be described, if we consider a result from common

transient analysis, given in figure 2, for the 16 MHz oscillator circuit as drawn in figure 1. The equivalent circuit for the quartz crystal is given in figure 3.

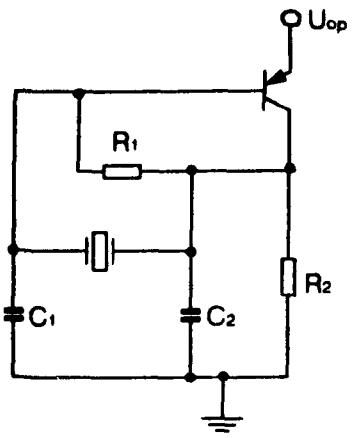

Figure 1

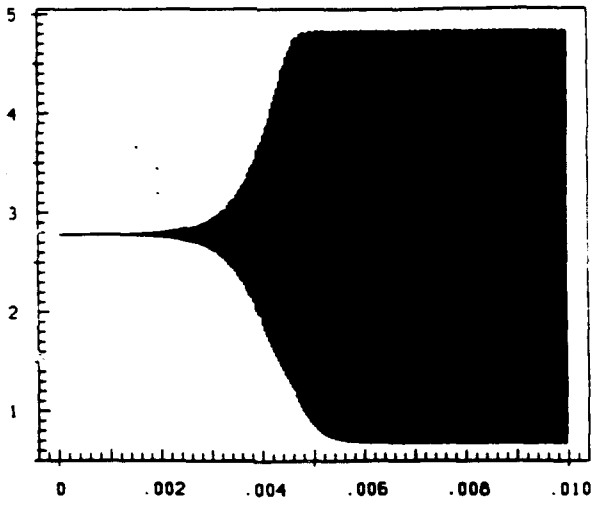

Figure 2

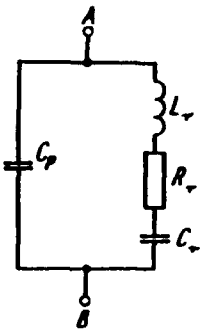

Figure 3

The development of the output voltage for a given set of parameters depicted in figure 2 was computed with integration formulaes based on trigonometric polynomials as proposed in [6], that are specially suited for this problem of a near-sinusoidal oscillator. It can be seen that approximately 160.000 periods were computed and as a result nearly 3 millions integration steps have to be performed. Even for this relatively small circuit the computation takes several hours on a high performance workstation. This is not acceptable. In contrast, the desired information, which allows a complete overview about start-up behaviour (including steady state), would consist of some sets of values for distinct time points t_i,

$$
\begin{aligned}
M_0 &= \{y_{1,0}, y_{2,0}, y_{3,0}, y_{4,0}, \ldots, y_{n,0}\} \\
M_1 &= \{y_{1,1}, y_{2,1}, y_{3,1}, y_{4,1}, \ldots, y_{n,1}\} \\
M_2 &= \{y_{1,2}, y_{2,2}, y_{3,2}, y_{4,2}, \ldots, y_{n,2}\} \\
M_3 &= \{y_{1,3}, y_{2,3}, y_{3,3}, y_{4,3}, \ldots, y_{n,3}\} \\
&\ldots \\
M_i &= \{y_{1,i}, y_{2,i}, y_{3,i}, y_{4,i}, \ldots, y_{n,i}\} \\
&\ldots \\
M_s &= \{y_{1,s}, y_{2,s}, y_{3,s}, y_{4,s}, \ldots, y_{n,s}\}
\end{aligned}
$$

separated Δt in time, which allows a reconstruction for every timepoint $t_i, i = 1, s$. Index s indicates the steady state. Without loss of generality we can add a suitable phase condition, e.g. $y_i = 0$ for some $i \in 1, \ldots, n$. Because of high redundancy, $\Delta t = t_{i+1} - t_i \gg T$, where T is the underlying period of oscillation. If it would be possible to calculate

exclusively only these sets of values, separated hundred of periods in time, our task would - in principle - be completed.

Some basics

That this is indeed possible, will be shown now. The approach we recommend is founded on several well known properties and describing models of quartz oscillators. These characteristics lead to a 'hierarchy of state variables' and can be effectively exploited in the numerical computation. A stringent mathematical foundation of our algorithm is not yet available, but is the topic of future work.

As described in [2], the crystals high quality factor Q has as a consequence that the current through the resonator, i_L, can be assumed to be sinusoidal, even if the voltage across it is strongly distorted. Therefore, under an energetical point of view, exchange of energy between the resonator (resp. its motional arm consisting of R_r, C_r and L_r) and the surrounding circuit takes pl. .e only on the fundamental frequency, ω_m, given by

$$\omega_m = \frac{1}{\sqrt{L_r C_r}}.$$

So the nonlinear circuit can be characterized by its impedance at the fundamental frequency [2],

$$Z_{c_1} = -\frac{V_1}{I_L}$$

were I_L is the complex value of i_L and V_1 is the fundamental component of the voltage across the resonator. Introducing p, the value of frequency pulling,

$$p = \frac{\omega - \omega_m}{\omega} \ll 1,$$

the impedance of the motional arm can be written as

$$Z_m = R_r + j\frac{2p}{\omega C_r}.$$

For start-up of oscillation, the relation

$$-Re\{Z_{c_1}\} > R_r$$

has to be fulfilled. The **fundamental** component of the voltage across the resonator, of current i_L and the voltage u_C across the capacitor C_r will therefore build up with the time constant

$$\tau = -\frac{2L_r}{Re\{Z_{c_1}\} + R_r}.$$

Hence

$$u_{C,max},\ i_{L,max} \sim e^{\frac{t}{\tau(t)}} = e^{-t\cdot\frac{Re\{Z_{c_1}\}+R_r}{2L_r}}$$

and the behaviour during start-up depends upon the motion of $Re\{Z_{c_1}\}$ in time. Because Z_{c_1} changes only slowly, it may be assumed that τ is local constant, while the global behaviour of τ can be approximated as piecewise linear. τ can be calculated in two ways: First it is possible to extract $Re\{Z_{c_1}\}$ by Fourier analysis and the second way consists of computing the logarithmic decrement, which is defined as the natural logarithm of the ratio of two maxima a period apart. Both methods are based on the results from the numerical integration. The details of this computation can not be explained here. It should be noted that both methods deliver the same result if we consider that the second one also includes the dc portion of the above mentioned signals and therefore increases τ to τ^*, which at all has no effect on the computation. At present, we use the second method; the rate of growth in interval $\Delta t = t_{i+1} - t_i$ is the averaged value

$$\overline{\tau^*} = \frac{\tau^*_{i+1} + \tau^*_i}{2}.$$

The values of τ^*_i can be used, if we consider that the 'figure of merit' Q of the quartz crystal

$$Q = \omega \cdot \frac{L_r}{R_r}$$

can be interpreted as the ability of the resonator to keep the stored (electrical) energy according to

$$\frac{decrease\ in\ energy\ per\ cycle}{Total\ energy} = \frac{2\pi}{Q}.$$

It is to be expected that this observable physical property is carried over into and can also be observed in the field of numerical integration. This is indeed the case. The results on several types of crystal oscillators (Pierce-, Colpitts-, Miller-, Emitter-coupled, Common base Oscillator) indicate that the variables which represent the energetic state (i_L and u_C) overwhelmingly dominate the behaviour of the circuit under (numerical) investigation.

In other words: If in a certain set of values of the state (and nonstate) variables

$$M_i = \{y_{1,i}, y_{2,i}, y_{3,i}, y_{4,i}, \ldots, y_{n,i}\}$$

one member (say $y_{1,i} = u_{C_1}$) is changed in its numerical value according to $y_{1,i} \hookrightarrow y^*_{1,i} \approx y_{1,i+1}$, then, after a certain amount of time (which has yet to be specified) necessary for possible adjustments, the circuit will enter the state

$$M_{i+1} = \{y_{1,i+1}, y_{2,i+1}, y_{3,i+1}, y_{4,i+1}, \ldots, y_{n,i+1}\}.$$

Therefore the transitions

$$M_i \rightsquigarrow M^*_i = \left\{y^*_{1,i}, y_{2,i}, y_{3,i}, y_{4,i}, \ldots, y_{n,i}\right\} \overset{\tau_c}{\rightsquigarrow} M_{i+1}$$

can be made. The second transition heavily depends on time constants inherent in the circuit, as indicated by τ_c. In the ideal case of a delay-less circuit, the new state M_{i+1} will be reached 'immediately', as will be seen in the next section. If there exist one or more $\tau_c > T$, the solution manifold associated with M_{i+1} will be reached according to and delayed by the dominating time constant.

Two examples

The algorithm based on the above considerations is a very simple one; in every step from M_i to M_{i+1} the value for $u_{C,i}$ is multiplied with a factor, whose value depends on the dynamics of u_C; the elapsed time $\Delta t = t_{i+1} - t_i$ can be estimated according to

$$\Delta t = \overline{\tau^*} \ln \frac{u_{C,i+1}}{u_{C,i}}.$$

if we consider that τ^* can be approximated as piecewise linear. This algorithm was implemented in an experimental version and several oscillators up to 25 nodes were investigated. In all cases the reduction of computation time was drastic; the results are accurate enough compared with ordinary transient analysis.

The first example represents the ideal case: an emitter-coupled oscillator (1 MHz) without any $\tau_c > T$, as given in figure 4.

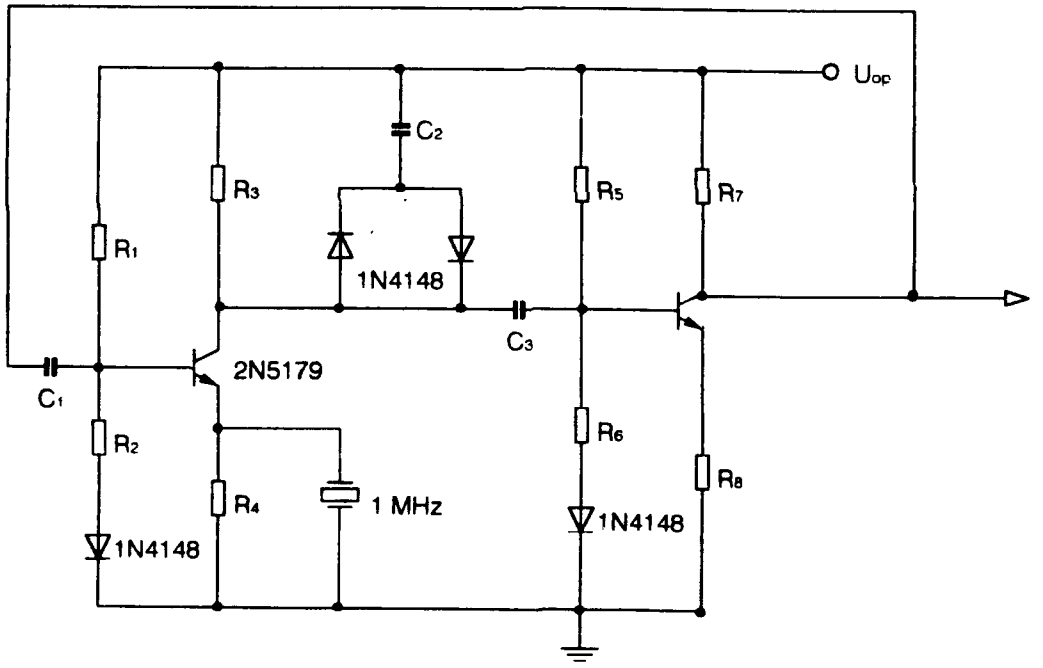

Figure 4: Emitter-coupled oscillator, 1 MHz

The results of the computations are depicted in figure 5 and 6. In figure 5 the envelope of u_C is drawn. in figure 6 we see the phase space representation (i_L (horizontal axis) vs. u_C). The total start-up takes approximately 266.000 periods. Our algorithm only computes 60 periods and the number of 'giant steps' (with a stepsize $H \gg T$) is 16. Here the transition from M_i to M_{i+1} takes places in about 4 periods in every step. The statistics say that on the average only 0.085 steps per period were performed, so that the

reduction compared to (the best possible) pure transient analysis is about a factor of 100. In figure 6, the performed jumps in phase space can be seen, in connection with the phase condition $i_L = 0$. The process of reaching the limit cycle is obvious and can equally be expressed by

$$\lim_{t\to\infty} -Re\{Z_{c_1}\} = R_r.$$

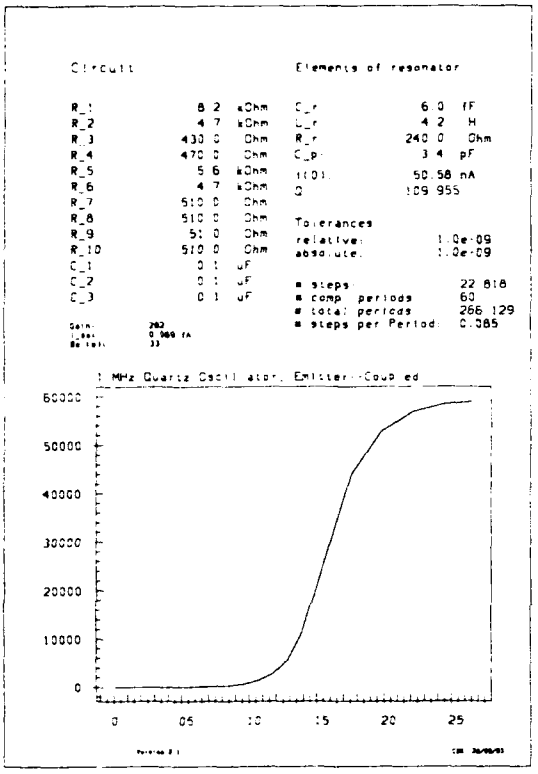

Figure 5

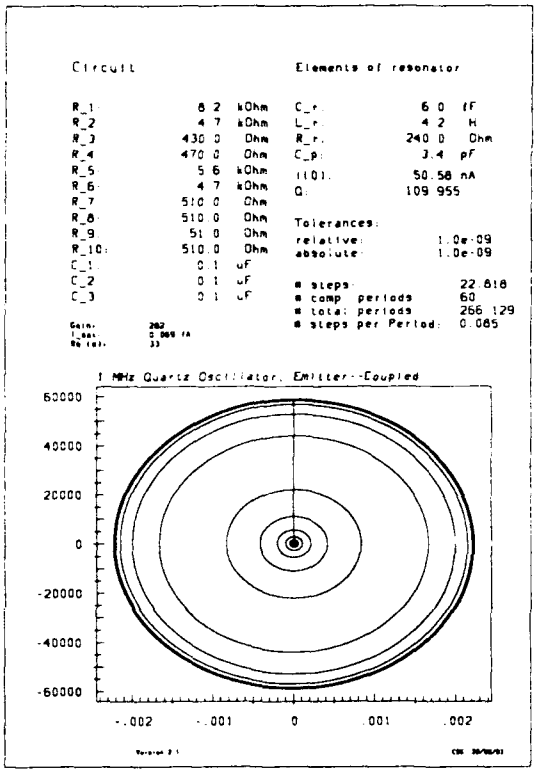

Figure 6

The second example shows the influence of time constants $\tau_c > T$. The oscillator in figure 1 has the dominating time constant $\tau_c = R_1 C_p$. The nominal value is $\tau_c \approx 22,4T$, which gives rise to a noticeable delay. The effect can be studied, if we start the integration with values y_0 except for u_C, which is initialized with the steady state value of $u_{C,max}$. Figure 7 shows the effect of various values of τ_c on the development of the output voltage. This voltage reaches its steady state value delayed in accordance to the time constant.

If we perform the start-up analysis, we see from table 1 that the number of periods computed during one giant step is proportional to the value of τ_c.

$\tau_c =$	$22.4 \cdot T$	$5.6 \cdot T$	$1.4 \cdot T$	$0.35 \cdot T$
# total periods	123.690	67.932	36.409	28.978
# steps	83.003	63.917	30.410	21.883
# comp. periods	396	299	145	104
# giant steps	17	17	14	14
# $\frac{periods}{giantstep}$	23.3	17.5	10.35	7.42

Table 1: Impact of τ_c on the no. of computed periods per giant step (averaged)

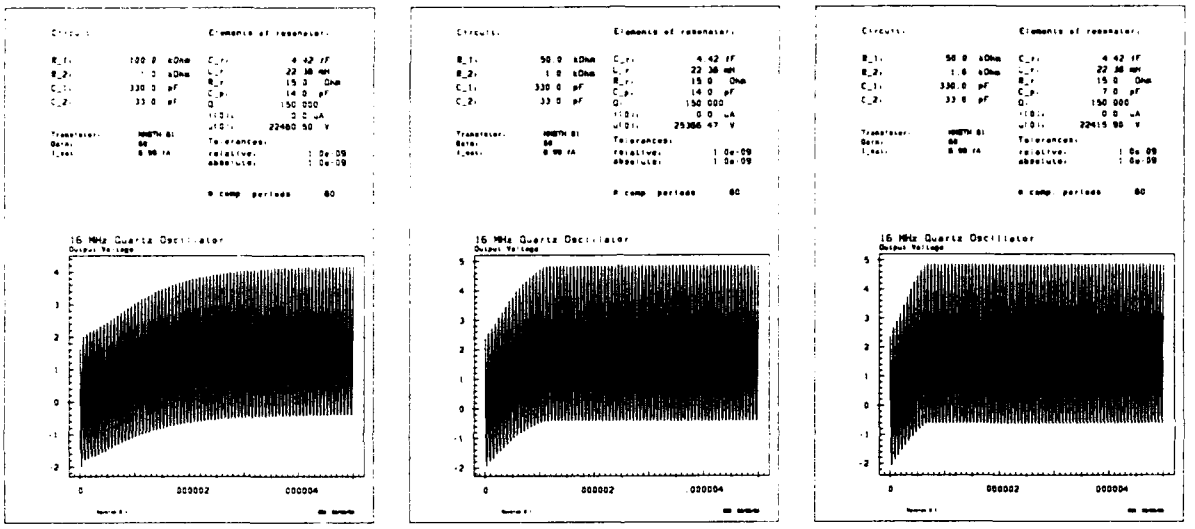

Figure 7: The effect of three different time constants $\tau_c = R_1 C_p$

Conclusions

We have shown that transient analysis of quartz crystal based oscillators is indeed possible by extracting only information from timepoints hundreds or thousands of periods apart in time. The characteristics of these oscillators, i.e.

- drastic differences between the timeconstants in the circuit and
- the typical behaviour of energy exchange between resonator and nonlinear circuit

can be exploited successfully in a numerical algorithm. Future work will concentrate on a strict mathematical foundation of the cited phenomena and on a more elaborated algorithm.

References

[1] *Rusznyak, A.*: Start-up time of CMOS oscillators; IEEE Transactions on Circuits and Systems, Vol. CAS-34, No. 3, pp. 259 - 268, March 1987

[2] *Vittoz, E.A.; Degrauwe M.G.R.; Bitz, S.*: High-performance crystal oscillator circuits: Theory and application; IEEE Journal of Solid-State Circuits, Vol. 23, No. 3, pp. 774 - 783, June 1988

[3] *Aprille, T.J.; Trick, T.N.*: Steady-state analysis of nonlinear circuits with periodic inputs; Proceedings of the IEEE, Vol. 60, No. 1, pp. 108 - 114, January 1972

[4] *Ushida, A.; Adachi, T.; Chua, L.O.*: Steady-state analysis of nonlinear circuits based on hybrid methods; IEEE Transactions on Circuits and Systems, Vol. CAS-39, No. 8, pp. 649 - 661, August 1992

[5] *Skelboe, S.*: Computation of the periodic steady-state response of nonlinear networks by extrapolation methods; IEEE Transactions on Circuits and Systems, Vol. CAS-27, pp. 161 - 175, March 1980

[6] *Gautschi, W.*: Numerical integration of ordinary differential equations based on trigonometric polynomials; Numerische Mathematik 3, 1961, pp. 381 - 397

Derivation of Stability Condition for the Time Domain Method of Moments Algorithms Using Functional Analysis Approach

Michał Mrozowski
Department of Electronics,
The Technical University of Gdańsk
80-952 Gdańsk, POLAND.

ABSTRACT

This contribution presents the derivation of the stability condition for time domain method of moment for linear hyperbolic differential equations The algorithm uses the method of moment approach for space variables and finite difference scheme for time. The stability condition of the algorithm is derived by investigating the properties of operators in suitably defined Hilbert spaces. The method discussed in this contribution has been developed in context of the time domain analysis of Maxwell's equations but the approach is general and can be used for other explicit algorithms.

INTRODUCTION

Functional analysis is one of the most powerful tools of the theoretical investigation of the basic properties of numerical methods. The methods of functional analysis are commonly used in the mathematical physics, numerical mathematics and computer science but seldom in engineering. At the same time the engineering creates demand for new more efficient numerical methods which would provide a sufficiently accurate solution as fast as possible. This results in the constant improvements of published algorithms by researchers who adapt them to their particular needs without investigation of the properties of modified algorithms. For instance, explicit algorithms for the solution of initial value problems have recently received much attention among researchers involved in the numerical analysis of electromagnetic fields. Two methods belonging to this class, known as finite difference-time

domain (FDTD) and transmission line matrix (TLM) algorithms have intensively been developed in the last decade. Their salient feature is that electromagnetic field is analyzed in the time domain and the samples of relevant physical quantities at nodes located at the discrete points in space are used to represent a physical continuum. These two methods are constantly being improved. The improvements include the application of graded meshes or non orthogonal cells, application of local approximations or extension of the basic algorithms to the new class of materials such as ferrites or dispersive media. Also new concepts of space representation of fields have been introduced. The sampling at discrete points can be replaced by the expansion into the series of basis functions and the expansion coefficients found by the method of moments procedure.

Recognizing the progress achieved in the recent years in the time domain analysis of electromagnetic fields, it should be noted, that the explicit algorithms underlaying these methods are not unconditionally stable and the improvements introduced to algorithms affect their stability. In this contribution we shall present how the effects of the algorithm modifications can be investigated using the functional analysis.

STABILITY ANALYSIS OF EXPLICIT TIME DOMAIN ALGORITHMS

Let us consider a hyperbolic differential equation

$$\frac{\partial^2}{\partial t^2} f + \mathbf{L} f = 0 \tag{1}$$

where $\mathbf{L}$ is a linear elliptic differential operator with positive coefficients. The hyperbolic equation of this type, supplemented by conditions at $t = 0$ can be solved for $t > 0$ using a classical finite difference explicit algorithm. For $\mathbf{L}$ being a Laplacian the stability criterion for the algorithm is known as the Courant condition. For other operators it is convenient to use the methods of functional analysis. In [2] such an approach was used for the case of finite difference representation of $\mathbf{L}$. The theorems used in that case are general so it is very instructive to show how they can be applied for other explicit algorithms.

To investigate the stability of a time marching algorithms for the hyperbolic equations it is useful to present a problem in a canonical form

$$(\mathbf{I} + \Delta^2 t\mathbf{R})\frac{\partial^2}{\partial t^2} f + \mathbf{A}f = 0 \tag{2}$$

Where $\mathbf{I}$ is the identity operator.
The time marching algorithm for the above problem is stable if the following conditions are fulfilled [2]:

$$\mathbf{A} = \mathbf{A}^* > 0, \quad \mathbf{R} = \mathbf{R}^* > 0 \tag{3}$$

$$\mathbf{R} - 0.5\mathbf{A} \geq 0 \tag{4}$$

In other words for the explicit algorithm to be stable it is sufficient that both operators $\mathbf{A}$ and $\mathbf{R}$ be self adjoint and positive and additionally the operator $\mathbf{R} - 0.5\mathbf{A}$ be nonnegative.
A linear operator $\mathbf{F}$ defined in a Hilbert space $(H, <\cdot,\cdot>)$ is self adjoint if for any $x, y \in H$

$$<\mathbf{F}x, y> = <x, \mathbf{F}y>^* \tag{5}$$

An operator $\mathbf{F}$ is positive $\mathbf{F} > 0$ (or nonnegative $\mathbf{F} \geq 0$) when for all $x \in H, x \neq 0$ we have

$$<\mathbf{F}x, x> > 0 \quad \text{or} \quad <\mathbf{F}x, x> \geq 0 \tag{6}$$

The canonical form (2) is obtained from (1) by simply multiplying it by 2 and writing the result as

$$(\mathbf{I} + \frac{\Delta^2 t}{\Delta^2 t}\mathbf{I})\frac{\partial^2}{\partial t^2} f + 2\mathbf{L}f = 0 \tag{7}$$

Comparing (7) with (2) we get $\mathbf{R} = \mathbf{I}/\Delta^2 t$ and $\mathbf{A} = 2\mathbf{L}$
If operator $\mathbf{L}$ is symmetric and positive than the stability condition is

$$||\frac{\mathbf{I}}{\Delta^2 t}|| \geq ||\mathbf{L}|| \tag{8}$$

or

$$\Delta t \leq \frac{1}{\sqrt{||\mathbf{L}||}} \tag{9}$$

It is seen that the stability depends on the norm of the operator $\mathbf{L}$. The norm of the operator depends on the space it acts in.

STABILITY ANALYSIS FOR THE TIME DOMAIN METHOD OF MOMENTS

Let us consider a one dimensional second order equation

$$\frac{\partial^2}{\partial t^2} f - b(x) \frac{\partial^2}{\partial x^2} f = 0 \tag{10}$$

$$f(x, t_0) = f_0(x), \quad f(x = 0) = f(x = a) = 0 \tag{11}$$

where $b(x) > 0$ is a time independent continuous function of x. Instead of using the finite difference representation of $\frac{\partial^2}{\partial x^2}$ let us combine the explicit algorithm with the method of moments. To this end we will use the finite differences for the approximation of time derivatives, expand the function $f(x)$ into series of sines

$$f(x) = \sum c_i \sin(i\pi x/a) \tag{12}$$

and use the inner product

$$< u, v >= \int_0^a uv \, dx \tag{13}$$

to find the expansion coefficient at any instance of time. (A detailed derivation of the time domain method of moments for Maxwell's equations can be found in [1])

It can easily be verified that operator

$$\mathbf{L} = -b(x) \frac{\partial^2}{\partial x^2} \tag{14}$$

is positive and self adjoint. This case was considered previously so we may conclude that the algorithm is stable if

$$\Delta t \leq \frac{1}{\sqrt{||\mathbf{L}||}} \tag{15}$$

At this point it is necessary to estimate the norm of $\mathbf{L}$. The problem is defined in the Hilbert space spanned over sine functions. The norm of $\mathbf{L}$ in such a space can be estimated as follows

$$||\mathbf{L}|| \leq ||\mathbf{L_M}|| = \frac{< \mathbf{L_M} x, x >}{||x||} = b_{max} \frac{(i\pi)^2}{a^2} \tag{16}$$

where b_{max} is the maximal value of $b(x)$ over the interval $0 < x < a$.

We may conclude that the explicit algorithm combined with the method of moment with sine series will be stable if the time step is chosen such that

$$\Delta t \leq \frac{a}{i\pi\sqrt{b_{max}}} \tag{17}$$

Note that maximal time step is inversely proportional to number of basis functions.

Obviously, the same procedure can be applied to other types of expansion functions, including for instance finite elements. It is important to note however that the time step in the explicit algorithm depends not only on the operator (equation) solved but also on the way the approximation of space is constructed.

CONCLUSIONS

The application of the functional analysis to the investigation of the stability of time domain algorithms has been presented. The method can easily be applied to the investigation of the properties of novel time domain schemes for Maxwell's equations such as the ones proposed in [1].

ACKNOWLEDGMENT

This research was supported by the Polish Committee of Scientific Research under contract KBN - 3 0687 91 01 and the US ARMY ERO under the contract DAJA45 - 92-C-0032

References

[1] M.Mrozowski, "Function expansion algorithms for the time domain analysis of shielded structures supporting electromagnetic waves", J. of Numerical Modelling, (accepted for publication)

[2] J.M. Jankowscy, M. Dryja, *Survey of numerical methods and algorithms vol.2*, (in Polish), WNT,Warsaw, 1982.

Second International Workshop on Discrete Time Domain Modelling of Electro-Magnetic Fields and Networks, Berlin, Germany, 28 - 29 October, 1993.

Stability Criteria for MAXEMOL - a Numerical Scheme for the Solution of Maxwell's Equations using the Method of Lines

Wai B. **Fu**, Ricky A.C. **Metaxas**
Electricity Utilisation Group
Engineering Department
Cambridge University
Trumpinton Street
Cambridge, UK
CB2 1PZ

ABSTRACT

We first outline the MAXEMOL scheme for the determination of the magnetic field. We then deduce the electric field and show some results of our calculations. We next derive the stability criteria which the scheme must satisfy and discuss their implications. Finally, the criteria are applied to a practical problem in the heating of foodlike materials in a microwave oven, and some typical power density distributions are shown.

INTRODUCTION

The Method of Lines (MOL) is a variant of the time domain finite difference scheme which is often employed to treat partial differential equations (PDEs). Normally, *all* the partial derivatives are replaced by their finite difference approximations, giving rise to a set of algebraic equations the solution of which requires the inversion of a large matrix. With the MOL, the derivatives along *one* chosen axis (spatial x,y,z or temporal t) are left untouched, resulting thereby in a system of ordinary differential equations (ODEs) which can be solved numerically by a standard procedure, or by a more sophisticated software package.

The MOL is a well-established technique for the solution of heat conduction problems of the *parabolic* type[1]. In the study of electromagnetism, its applications to *elliptic* steady state or time harmonic equations have been made[2]. It has been used to tackle transient problems of the *hyperbolic* type, e.g. absorption of microwave power by a dielectric material inside a multimode cavity applicator [3]. Here, we outline an MOL scheme for Maxwell's Equations in three spatial dimensions, and verify its validity by comparing our results with recently published work. We then derive and discuss the stability criteria which the scheme must satisfy.

NUMERICAL SCHEME

Our ultimate aim is to estimate, from a knowledge of the electromagnetic field intensities, the temperature distribution of a dielectric load inside a multimode applicator. Starting from Maxwell's Equations, we eliminate the electric field **E** to arrive at a hyperbolic PDE for the magnetic field **H** in non-dimensional form:

$$\epsilon' \, \partial^2 \mathbf{H}/\partial t^2 = \nabla^2 \mathbf{H} - \sigma^* \, \partial \mathbf{H}/\partial t \qquad (1)$$

Here, ϵ' is the real relative permittivity and σ^* an effective conductivity of the load, inclusive of the effective loss factor ϵ''_e. We then rewrite Equation (1) as a pair of first order equations:

$$\partial \mathbf{G}/\partial t = (\nabla^2 \mathbf{H} - \sigma^* \mathbf{G}) / \epsilon', \qquad \partial \mathbf{H}/\partial t = \mathbf{G} \qquad (2)$$

and apply discretization of the spatial derivatives in a three-dimensional mesh to obtain a system of first order ODEs:

$$d\mathbf{G}_{i,j,k}/dt = \mathbf{g}_{i,j,k} ([\mathbf{G}], [\mathbf{H}], t), \qquad d\mathbf{H}_{i,j,k}/dt = \mathbf{h}_{i,j,k} ([\mathbf{G}], [\mathbf{H}], t) \qquad (3)$$

where $\mathbf{g}_{i,j,k}$ and $\mathbf{h}_{i,j,k}$ denote the right hand sides of Equations (2) evaluated at grid point $\mathbf{r}(i,j,k)$ at time t, whereas [**G**] and [**H**] represent function values located in a small neighbourhood of the grid point.

Having determined **H**, we deduce **E** by integrating Ampere's Law as a first order ODE:

$$\mathbf{E}(\mathbf{r}, t) = P(t) \left(\mathbf{E}(\mathbf{r}, 0) + \int_0^t \{ K / [\epsilon' P(t)] \} \, \mathrm{curl}\, \mathbf{H} \, dt \right) \qquad (4)$$

where K is a constant, and $P(t) = \exp\left[- \int_0^t (\sigma^* / \epsilon') \, dt \right]$.

NUMERICAL RESULTS

The numerical scheme is implemented on a Sunsparc workstation as MAXEMOL (**MAX**well's Equations by the Method Of Lines) and is used first to model the propagation of microwaves through a dielectric-filled waveguide, for which an analytical solution is available. Our solutions are found to tend to a steady state in less than ten periods of the input microwaves. The magnetic field profile along the z-axis, the direction of propagation, is shown in Figure 1 together with the analytical result. The agreement is very good, even for a fairly coarse mesh of 9x9x9 internal grid points. The temporal variations of the electric field at the centre of the dielectric material are compared in Figure 2. It can be clearly seen that, as the mesh becomes finer and finer, the numerical results converge towards the analytical solution.

We have calculated the power density distributions within a two-layered dielectric (water inside a polystyrene container) placed near the centre of a cavity, an example of which is shown in Figure 3. There are good qualitative agreements with recent experimental data obtained by Jia[4]. We have also produced results for a slab of woodlike material placed near the top of a cavity (Figure 4), and found satisfactory comparisons with those obtained numerically by Jia and Jolly[5].

STABILITY CRITERIA

If the exact solution is denoted by **H** , then the numerical solution can be written as $\mathbf{H} + \xi$, where ξ is the numerical error given by the same wave equation as (1):

$$\epsilon' \partial^2 \xi / \partial t^2 = \nabla^2 \xi - \sigma^* \partial \xi / \partial t \qquad (5)$$

To show stability we let ξ be one of the components of ξ at grid point (i,j,k). Then, using the MOL as before, with central differences, we have

$$\epsilon' \partial^2 \xi / \partial t^2 + \sigma^* \partial \xi / \partial t + [\, 2/(\delta L)^2] \xi = R \qquad (6)$$

where

$$(1/\delta L)^2 = (1/\delta x)^2 + (1/\delta y)^2 + (1/\delta z)^2$$

δx, δy, δz being the local spatial step lengths in the x, y, z directions respectively; whereas R denotes the set of function values evaluated in a small neighbourhood surrounding but not including the grid point.

Let us consider a simple central difference ODE solver so that Equation (6) takes the form:

$$\xi_{k+1} - 2\xi_k + \xi_{k-1} + a(\xi_{k+1} - \xi_{k-1}) + b\,\xi_k = R\,(\delta t)^2 \qquad (7)$$

where ξ_k = value of ξ at the k'th time step, $a = \sigma^* \delta t / (2\epsilon')$, and $b = 2\,(\delta t / \delta L)^2 / \epsilon'$. For stability we only need to investigate the homogeneous part of Equation (7), i.e.

$$(1+a)\xi_{k+1} + (b-2)\xi_k + (1-a)\,\xi_{k-1} = 0 \qquad (8)$$

Its solution can be written as $\xi_k = A \exp(\gamma k)$, where A is a finite constant, and $u = \exp(\gamma)$, which may be complex, is given by:

$$(1+a)\,u^2 + (b-2)\,u + (1-a) = 0 \tag{9}$$

There is stability if $\| u \|$, the modulus of u, is such that $\| u \| \leq 1$, so that $\xi_k \rightarrow$ finite constant as $k \rightarrow \infty$, or $t \rightarrow \infty$.

Now let $\Delta = (2-b)^2 - 4(1-a^2)$, the discriminant of the quadratic. If $\Delta > 0$, then

$$(2\epsilon')^{1/2}\,\delta L < \delta t. \tag{10}$$

where δt. is the time step length. This contradicts the Courant condition for stability [6], that is,

$$\delta t \leq (\epsilon')^{1/2}\,\delta L \tag{11}$$

Hence we must have $\Delta \leq 0$, i.e.

$$(\delta L)^4 - (8\,\epsilon'/\sigma^{*2})\,(\delta L)^2 + 4(\delta t)^2/\sigma^{*2} \leq 0 \tag{12}$$

For real values of δL we require that

$$0 < \delta t \leq 2\,\epsilon'/\sigma^* \tag{13}$$

which is the same as $0 < a \leq 1$. Use of $\Delta \leq 0$ in the solution to Equation (9) then gives $\| u \| < 1$, as required.

Using the MOL, it is always possible to satisfy Inequality (13) with a very wide margin, so that

$$\delta t << 2\,\epsilon'/\sigma^* \tag{14}$$

The solution to Inequality (12) can then be expressed as:

$$\delta t\,/(2\,\epsilon')^{1/2} < \delta L < (8\,\epsilon')^{1/2}/\sigma^* \tag{15}$$

Incorporating the Courant Condition (11), which is a universal requirement for the treatment of wave propagation problems by numerical means, Inequality (15) becomes

$$\delta t\,/(\epsilon')^{1/2} \leq \delta L < (8\,\epsilon')^{1/2}/\sigma^* \tag{16}$$

The stability criteria for our MAXEMOL scheme can now be stated below:

$$\delta t << \min\,(2\,\epsilon'/\sigma^*) \tag{17a}$$

$$\max\,[\delta t\,/(\epsilon')^{1/2}] < \delta L < \min\,[\,(8\,\epsilon')^{1/2}/\sigma^*\,] \tag{17b}$$

where we have allowed for the temporal variations of the physical parameters ϵ' and σ^*.

In the traditional method, δL has to be quite small, typically a small fraction of the microwave wavelength λ in the material concerned, which means that δt must be even smaller, in order to satisfy the Courant Condition (11). In the MAXEMOL scheme, however, we have a much freer choice of δt, from Condition (17a). As a result, δL need not be small compared to λ in order to satisfy

Condition (17b). This represents a considerable advantage over the traditional method, especially for large microwave applicator systems.

Numerical Example

We have used the MAXEMOL program to predict three-dimensional power density distributions inside a joint of beef heated by microwaves (Figure 5). Some typical results are shown in Figures 6 - 8. To verify the stability of our results, we refer to Figure 5, and give the numerical data below:

Oven dimensions: a = 400mm, b = 380mm, d = 350mm;
Relative permittivity of raw beef = $\epsilon' - j\,\epsilon''_e$, where $\epsilon' = 48.0$, $\epsilon''_e = 15.0$;
Relative permittivity of polystyrene = 3.0 - j 0.0;
Input microwaves = $TE_{1,0}$ at f = 2450 MHz;
Time scale = 10/f = 4.082 ns;
Length scale = 1224 mm;
$\sigma^* = 942.5$ (non-dimensional).

With 400 time steps, $\delta t = 0.0025$ (10.2 ps), much smaller than the critical value of $2\epsilon'/\sigma^*$, (Equation (17a)), which is ≈ 0.1019 (416 ps).

For δL, the lower limit is $\delta t/(\epsilon')^{1/2} \approx 3.61 \times 10^{-4}$ (0.4mm), and the upper limit is $(8\epsilon')^{1/2}/\sigma^* \approx 0.0208$ (25.4mm). With 13 x 13 x 29 internal grid points, we have $\delta x = 0.0234$ (28.6mm), $\delta y = 0.0222$ (27.2mm) and $\delta z = 0.0095$ (11.6mm), so that $\delta L = 0.0082$ (10.0mm), which is quite large, about 56% of the dielectric wavelength λ (17.7mm), yet small enough to satisfy Condition (17b) with a good margin. We have therefore verified the stability of MAXEMOL in this particular example.

CONCLUDING REMARKS

The Method of Lines has been shown to be a versatile technique which is applicable *not only* to partial differential equations of the parabolic and elliptic types, as claimed by earlier workers, *but also* to problems of the hyperbolic type, to which belongs the absorption, reflection or transmission of microwave energy within a cavity. Our numerical results, obtained for a dielectric-filled waveguide, have been found to be in excellent quantitative agreement with the analytical solution. For the case of a microwave cavity, there are good qualitative agreements with recent experimental and numerical results.

We have derived and discussed the stability criteria which the MAXEMOL scheme must satisfy, and illustrated their use in a practical example, namely the heating of a joint of beef inside a microwave oven.

The convergence criteria for MAXEMOL have also been derived and will be the subject of a future paper.

REFERENCES

[1]. **Lawson**, J. and **Berzins**, M. (1992), in 'Computational Ordinary Differential Equations' (Eds. J.R. Cash and I. Gladwell). Clarendon Press, Oxford UK, 309-322.

[2]. **Pregla**, R. and **Kremer**, D. (1992), IEEE Microwave and Guided Wave Letters, 2, 6, 239-241.

[3]. **Fu**, W.B. and **Metaxas**, A.C. (1993), International Conference on Microwave and High Frequency, 28-30 September, Goteborg, Sweden.

[4]. **Jia**, X. (1993), Journal of Microwave Power and Electromagnetic Energy, 28, 1, 25-31.

[5]. **Jia**, X. and **Jolly**, P. (1992), Journal of Microwave and Electromagnetic Energy, 27, 1, 11-22.

[6]. **Cangellaris**, A.C. (1993), IEEE Microwave and Guided Wave Letters, 3, 1, 3-5.

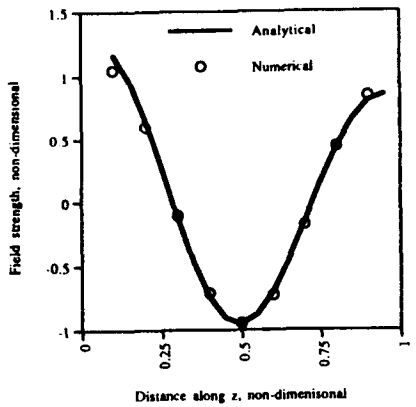

Fig. 1. Comparison of analytical and numerical results for the *magnetic* field profile inside a dielectric-filled waveguide with dimensions = 100mm x 50mm x 100mm; relative permittivity = 2.73 - j 0.34; microwave frequency = 2450 MHz; timestep = 10.2 ps and total number of grid points used = 9 x 9 x 9.

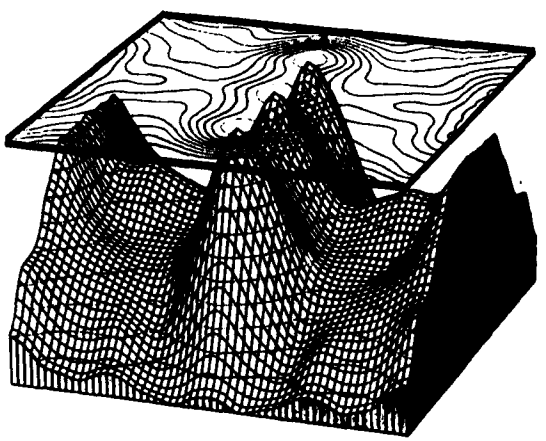

Fig. 3. Calculated power density distribution within a layer of water inside a polystyrene container placed *150*mm above the bottom of a cavity with dimensions = 400mm x 380mm x 350mm; relative permittivity of water = 77.7 - j 12.0; relative permittivity of polystyrene = 3.0; input frequency = 2450 MHz; timestep = 10.2 ps and total number of grid points = 13 x 13 x 29.

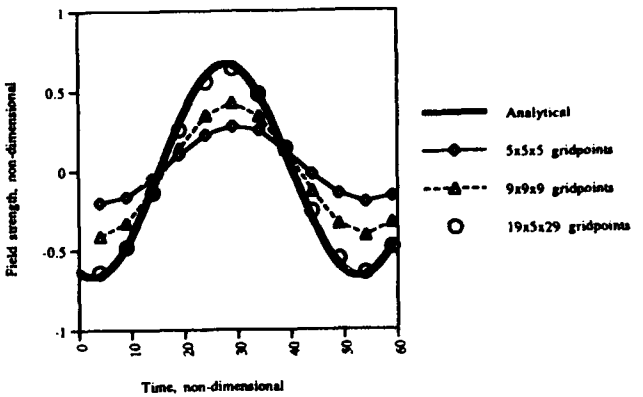

Fig. 2. Comparison of analytical and numerical results for the *electric* field history inside a dielectric-filled waveguide with dimensions = 100mm x 50mm x 100mm; relative permittivity = 2.73 - j 0.34; microwave frequency = 2450 MHz; timestep = 10.2 ps.

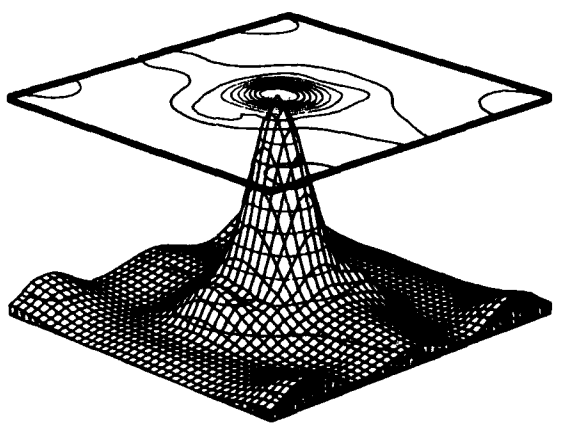

Fig. 4. Calculated power density distribution within a woodlike dielectric placed *220*mm above the bottom of a cavity with dimensions = 300mm x 280mm x 240mm; relative permittivity = 2.0 - j 0.5; input frequency = 2450 MHz; timestep = 10.2 ps and total number of grid points = 13 x 13 x 29.

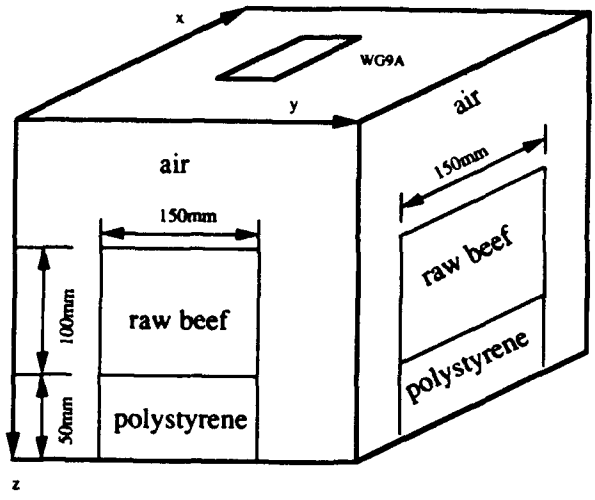

Fig. 5. Microwave Oven (400mm x 380mm x 350mm) inhomogeneously loaded with a joint of beef inside a polystyrene container with thick base and sides of negligible thickness. Power enters through a standard waveguide (86mm x 43mm) centrally located at the top of the oven.

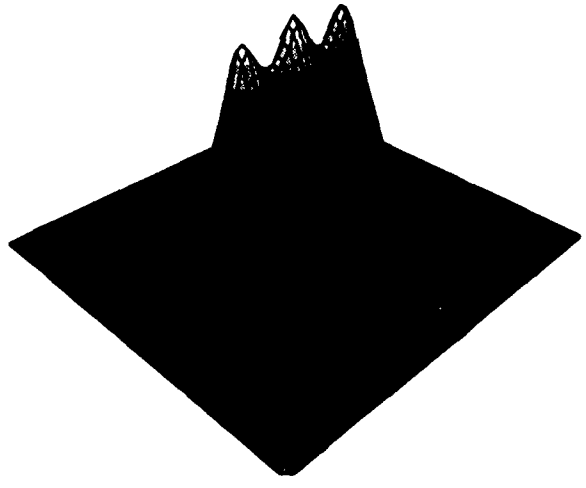

Fig. 6. Calculated power density distribution on a horizontal layer of beef near the *top* of the oven; relative permittivity of beef = 48.0 - j 15.0; relative permittivity of polystyrene = 3.0; input frequency = 2450 MHz; time step = 10.2 ps and total number of grid points = 13 x 13 x 29.

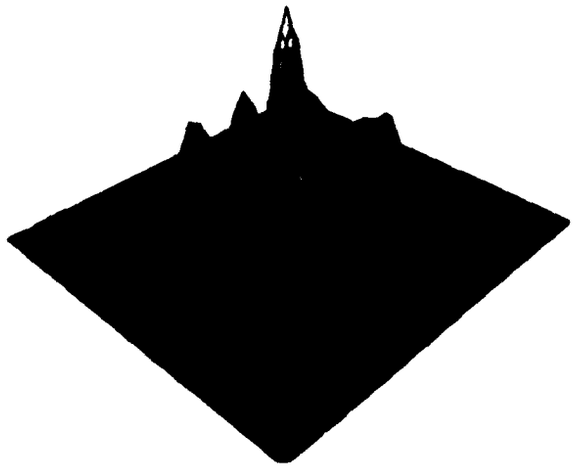

Fig. 7. Calculated power density distribution on a horizontal layer of beef near the *bottom* of the oven; relative permittivity of beef = 48.0 - j 15.0; relative permittivity of polystyrene = 3.0; input frequency = 2450 MHz; time step = 10.2 ps and total number of grid points = 13 x 13 x 29.

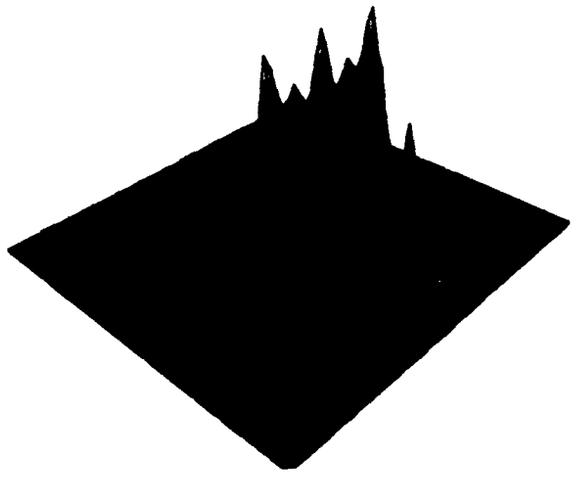

Fig. 8. Calculated power density distribution on a *vertical* layer of beef in the middle of the oven; relative permittivity of beef = 48.0 - j 15.0; relative permittivity of polystyrene = 3.0; input frequency = 2450 MHz; time step = 10.2 ps and total number of grid points = 13 x 13 x 29.

BROADBAND SIMULATION OF OPEN WAVEGUIDE BOUNDARIES WITHIN LARGE FREQUENCY RANGES

M.Dohlus, P.Thoma[1],T.Weiland

Technische Hochschule Darmstadt, FB 18, FG TEMF, Schloßgartenstr. 8, 64289 Darmstadt, Germany

SUMMARY

S-parameter computations in the time domain using the Finite Integration Technique (FIT) often require the simulation of infinitely long waveguides connected to the port planes. The approximation of open waveguide boundaries usually is accurate only for one particular frequency. Thus, multiple computation runs have to be performed to obtain the whole frequency dependency of the S-parameters within the specified frequency range.

In this paper we present a broadband waveguide boundary operator which leads to very low reflection factors within large frequency ranges. Using this operator the whole frequency dependency of the S-parameters can be obtained from only one calculation.

The basic idea is to separate the transversal field at the waveguide port into a superposition of waveguide modes. For each of these modes the infinitely long waveguide is represented by a lossy transmission line model. The parameters of the transmission line are determined in regard to obtain very low reflection factors down to <-110dB (for single precision calculations). The maximum stable timestep is not affected by the boundary field computation.

After giving a short introduction to the method we will present some examples which demonstrate the excellent accuracy as well as a large gain in calculation speed using this operator.

1. INTRODUCTION

The computation of S-parameters for microwave structures is of increasing importance for many technical applications. The computation of these parameters requires a termination of waveguide ports with minimized reflection. This can be obtained by "open" waveguide boundary operators simulating infinitely long waveguides connected to the port planes.

For homogeneously filled and lossfree waveguides these boundary operators can be implemented "broadband" which means that the open boundary condition is satisfied within large frequency ranges. Using broadband operators the whole frequency dependency of the S-parameters can be obtained from only one computation.

In this paper we present a new broadband boundary operator and its application to three problems. A comparison with a monochromatic operator which has been proven to be very accurate for many examples demonstrates the high precision of the new method and the large gain in computation speed.

The first example is a simple rectangular waveguide. The S-parameters of this structure are well-known which recommends this example for demonstrating the accuracy of the operator.

The next two examples show more practical structures. The first one is a 3dB power splitter which has been designed in regard to minimize input reflection for a high power application ($P = 150MW$). The results of a broadband calculation are compared with results of monochromatic computations at several frequency points.

The last example shows a filter consisting of a rectangular waveguide with metallic inserts. The results of a broadband computation are compared with measurements and results of a mode matching method.

[1]Work supported by GSI Darmstadt

2. THE METHOD

The Finite Integration Technique (FIT) ([1,2]) applied to two dimensional homogeneously filled and lossless waveguides yields an eigenvalue problem for the computation of transversal waveguide mode fields ([3]). The eigenvectors and thus the transversal electric mode fields are not frequency dependent within the restrictions mentioned above. If we assume the propagation constant β for the modes to be zero and consider that the eigenvalue problem can be transformed into a symmetric one ([4,5]) we can write:

$$M \cdot x = \omega_c^2 \, x \qquad , \quad M^T = M \tag{1}$$

with M being a real symmetric matrix depending on the discretization of the structure. The eigenvalues $\omega_{c,i}/2\pi$ are the cutoff frequencies corresponding to eigenvectors x_i which are normalized to be orthonormal. The transversal electric mode fields can be derived from these orthonormal eigenvectors x_i using a nonsingular real transformation matrix T:

$$e_i = T \cdot x_i \qquad , \quad e_i \in \mathcal{R} \tag{2}$$

We introduce a bilinear functional related to the transformation matrix T which represents an orthogonality relation for the modes:

$$< e_i, e_j >_T = e_i^T \cdot \left(T \cdot T^T\right)^{-1} \cdot e_j = \delta_{i,j} \qquad , \quad \delta_{i,j} = \begin{cases} 0 & : \quad i \neq j \\ 1 & : \quad i = j \end{cases} \tag{3}$$

We assume $\underline{e}(\omega)$ to be the Fouriertransform of the transversal electric field in an arbitary cross-section of the waveguide. This field can be written as a superposition of the transversal waveguidemode fields e_i:

$$\underline{e}(\omega) = \sum_k \underline{a}_k(\omega) \tilde{e}_k \qquad , \quad \underline{a}_k(\omega) \in \mathcal{C} \tag{4}$$

Transforming this equation into time domain and considering that the e_i do not depend on frequency we obtain:

$$e(t) = \sum_k a_k(t) \tilde{e}_k \tag{5}$$

The mode coefficients a_k in eq. (5) can be computed at an arbitary time t_0 using the orthogonality relation (3):

$$< e(t_0), \tilde{e}_j >_T = \sum_k a_k(t_0) < \tilde{e}_k, \tilde{e}_j >_T = a_j(t_0) \tag{6}$$

Using eq. (3) the transversal electric waveguide field can be separated into several waveguidemodes. For each of these modes the transversal electric field and the cutoff frequency are given by the solution of the eigenvalue problem.

In the following we consider the waveguide termination shown in Fig. 1. The coefficient a_1 of the regarded mode in plane 1 can be obtained from the transversal electric fields at this plane using eq. (6). The common leap-frog time integration scheme ([6]) needs the transversal electric field at the boundary plane 2 to compute the magnetic fields inside the computation domain. Now we will show how to obtain the electric field at the boundary plane 2 from the field at plane 1.

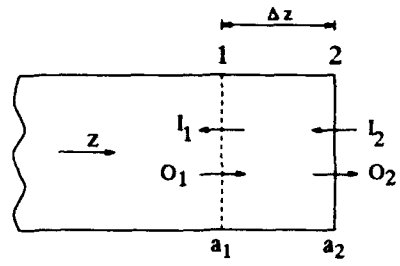

Figure 1: This picture shows the waveguide ending at the boundary plane 2. Plane 1 is the meshplane next to the boundary. a_1 and a_2 are the coefficients of the regarded mode at the planes 1 and 2, respectively. Each of these coefficients a_i can be split up into two parts propagating along $\pm z$-direction named I_i and O_i, respectively.

The mode coefficients can be separated into two parts according to waves propagating along $\pm z$ direction. The coefficients corresponding to a_i are named as I_i and O_i, respectively. Related to Fig. 1 we write the following set of equations:

$$I_1 = e^{-jk_z(\omega)\Delta z} I_2 \quad , \quad O_2 = e^{-jk_z(\omega)\Delta z} O_1 \tag{7}$$

$$a_1 = I_1 + O_1 \quad , \quad a_2 = I_2 + O_2 \tag{8}$$

Solving these equations yields the mode coefficient a_2 and thus the transversal electric field at the boundary plane from the mode coefficient a_1 and the incident mode amplitude I_2. Setting $I_2 \neq 0$ results in a stimulation of the fields by a waveguide mode. This kind of excitation is required for the computation of S-parameters.

The discrete dispersion relation which correlates the propagation constant k_z and the frequency $\omega/2\pi$ can be written as:

$$\left(\frac{sin(\omega\Delta t/2)}{c\Delta t/2}\right)^2 = \left(\frac{sin(\omega_c\Delta t/2)}{c\Delta t/2}\right)^2 + \left(\frac{sin(k_z\Delta z/2)}{\Delta z/2}\right)^2 \tag{9}$$

In the following we will derive a one dimensional discrete transmission line model for the waveguide. First we consider an infinitely long transmission line as shown in Fig. 2. The differential equations describing the concentrated elements of the model can be discretized by replacing the time derivations by a central discrete differential operator:

$$I_{1,i}^{n+1} = I_{1,i}^{n} + \frac{\Delta t}{L_1}\left(U_i^{n+1/2} - U_{i+1}^{n+1/2}\right) \quad , \quad I_{3,i}^{n+1} = I_{3,i}^{n} + \frac{\Delta t}{L_2} U_i^{n+1/2} \tag{10}$$

$$U_i^{n+1/2} = U_i^{n-1/2} + \frac{\Delta t}{C} I_{2,i}^{n} \tag{11}$$

Assuming k_z to be the propagation constant along the transmission line we can write:

$$U_{i+1}^{n+1/2} = U_i^{n+1/2} \cdot e^{-jk_z\Delta z} \quad , \quad I_{1,i}^{n} = I_{1,i-1}^{n} \cdot e^{-jk_z\Delta z} \tag{12}$$

The discrete dispersion relation for the model can be derived from eq. (10),(11) and (12) using the Z-transform:

$$cos(k_z\Delta z) = 1 + \frac{CL_1}{\Delta t^2}\left(cos(\omega\Delta t) + \frac{1}{2}\left(\frac{\Delta t^2}{CL_2}\right)\right) \tag{13}$$

The parameters L_1, L_2 and C can be choosen in order to fit the two dispersion relations (9) and (13). For this case the transmission line model is an exact one dimensional representation of the three dimensional waveguide.

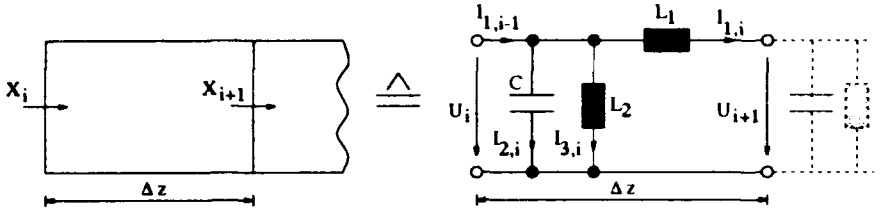

Figure 2: This picture shows the three dimensional waveguide and its one dimensional representation by a transmission line model. For both in fact infinitely long structures only a part of length Δz is considered.

The initial problem has been reduced to simulate an open boundary for the transmission line with minimized reflection. Now we consider the structure shown in Fig. 3.

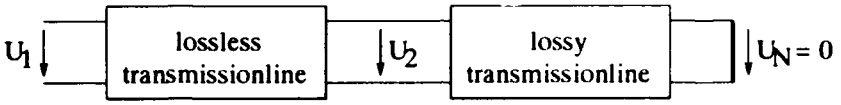

Figure 3: This picture shows the structure of the open waveguide boundary operator. The lossless transmission line is an exact one dimensional representation of the three dimensional waveguide. The lossy part of the model is needed for the termination of the lossless transmissionline with minimized reflection.

The waveguide part of length Δz is represented by the lossless part of the transmission line. The lossy part of the model is needed to obtain a low reflecting termination of the one dimensional waveguide representation. Two effects essentially contribute to the total reflection at the input of the structure:

- The reflection at the electric termination: This part can be reduced by increasing length and damping constant of the transmision line.
- Reflections at the transition of transmission line cells with different parameters: These reflections can be kept small by varying the parameters smoothly along the transmission line.

The damping can be introduced to the transmission line equations (10) and (11) by a factor K_i:

$$I_{1,i}^{n+1} = K_i\, I_{1,i}^{n} + \frac{\Delta t^2}{L_1 C}\left(U_i^{n+1/2} - U_{i+1}^{n+1/2}\right) \quad , \quad I_{3,i}^{n+1} = K_i\, I_{3,i}^{n} + \frac{\Delta t^2}{L_2 C} U_i^{n+1/2} \tag{14}$$

$$U_i^{n+1/2} = U_i^{n-1/2} + I_{2,i}^{n} \tag{15}$$

In these equations the voltage is normalized by $C/\Delta t$. The complex dispersion equation derived from eq. (14) and eq. (15) yields an approximation for the distribution of the propagation constant $k_z = \beta - j\alpha$ along the transmission line:

$$\beta_{i+1} = \beta_i + (K_{i+1} - K_i)\left(\frac{\Delta z}{2c\Delta t}\right)^2 \frac{2A_i sin^2(\omega\Delta t/2) + B_i sin(\omega\Delta t)}{A_i^2 + B_i^2} \tag{16}$$

$$\alpha_{i+1} = \alpha_i + (K_{i+1} - K_i)\left(\frac{\Delta z}{2c\Delta t}\right)^2 \frac{2B_i sin^2(\omega\Delta t/2) - A_i sin(\omega\Delta t)}{A_i^2 + B_i^2} \tag{17}$$

A_i and B_i are expressions depending on α_i, β_i and Δz. Using eq. (16) and (17) the correlation between the reflection factor r_i (at the transition from the i-th to the $(i+1)$-th cell) and the distribution of the damping constant K_i can be written as:

$$K_{i+1} = K_i + |r_i| \frac{|(z - K_i) f_1 (1/Q_i - Q_i)|}{|f_1(1 - Q_i) + f_2 + (z - K_i) f_1 Q_i (jC_i + D_i)|} \tag{18}$$

The parameters f_1, f_2 and z are constants depending on frequency, timestep, cut-off-frequency and discretization. C_i, D_i and Q_i additionally depend on the propagation constant according to the i-th transmission line cell.

The transmission line parameters can be computed from eq. (16), (17) and (18) in order keep the total input reflection below a specified limit. The length of the transmission line and thus the cpu-time and memory space required for the boundary simulation depends on the frequency range to be simulated as well as on the cutoff-frequency of the mode and the reflection factor limit.

A remarkable feature of this boundary operator is that the maximum stable timestep for the field computation is not affected by the open waveguide simulation.

3. EXAMPLES

Our first example is a simple rectangular waveguide as shown in Fig. 4. With this example we can test the accuracy of the boundary operator because the S-parameters of this structure are well-known.

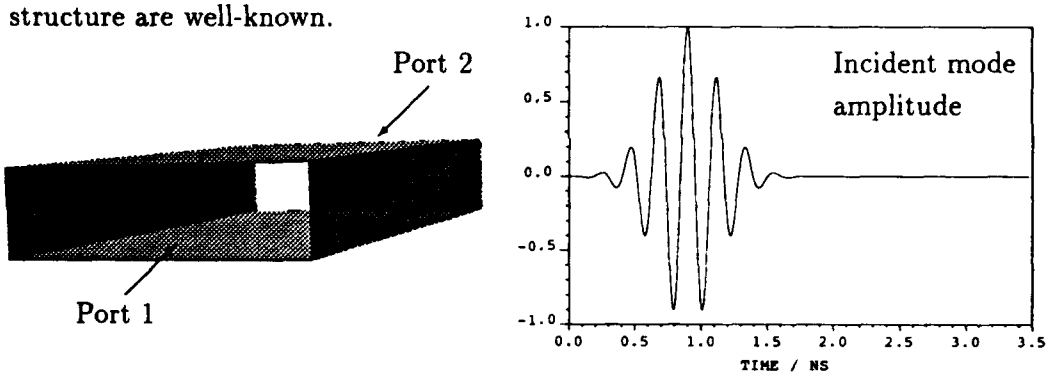

Figure 4: The geometry-plot shows the rectangular waveguide. The cross-section dimensions are 72.14mm x 34.04mm which results in a cutoff-frequency of 2.079 Ghz. The right plot shows the time function of the incident mode amplitude at port 1 (mean frequency 4.5 Ghz, bandwidth 5 Ghz).

The structure has been modeled using about 5000 mesh cells. Two computations have been performed with different upper limits for the reflection factor. In both cases the computation has been terminated when the output pulse at port 2 decreased to $4 \cdot 10^{-3}$ of its maximum amount. The computation time was about 47 cpu-seconds[1] for low reflection (10^{-6}) and about 41 cpu-seconds for medium reflection (10^{-4}).

Fig. 5 shows the results for low accuracy corresponding to an estimated reflection factor limit of 10^{-4}. The length of the transmission line was 523 cells for this case.

Fig. 6 shows the results for improved accuracy (reflection factor limit set to 10^{-6}). For this case the length of the transmission line was 3405 cells. The small difference between the two cpu-time requirements measures the additional numerical effort for the boundary operator.

[1]all cpu-times in this paper refer to a SUN SPARC SERVER 690 MP

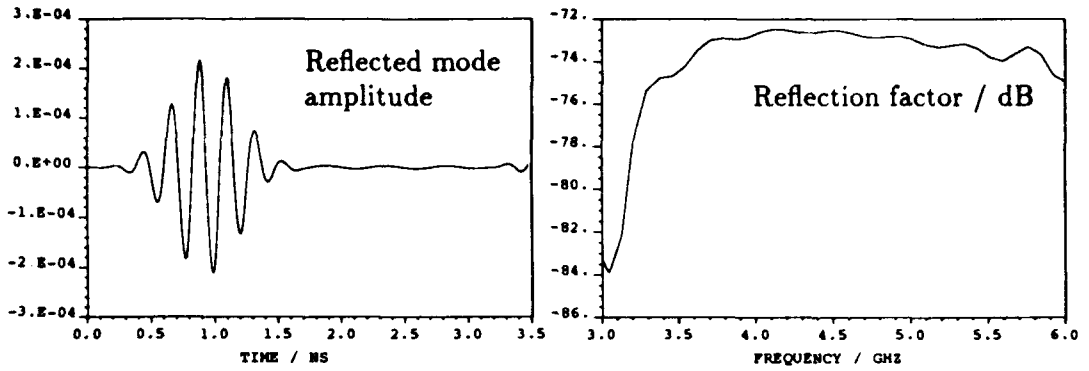

Figure 5: This picture shows the reflection at port 1 for an estimated reflection factor limit of 10^{-4}. The left plot shows the time signal of the reflected mode amplitude and the right plot shows the reflection factor versus frequency in dB.

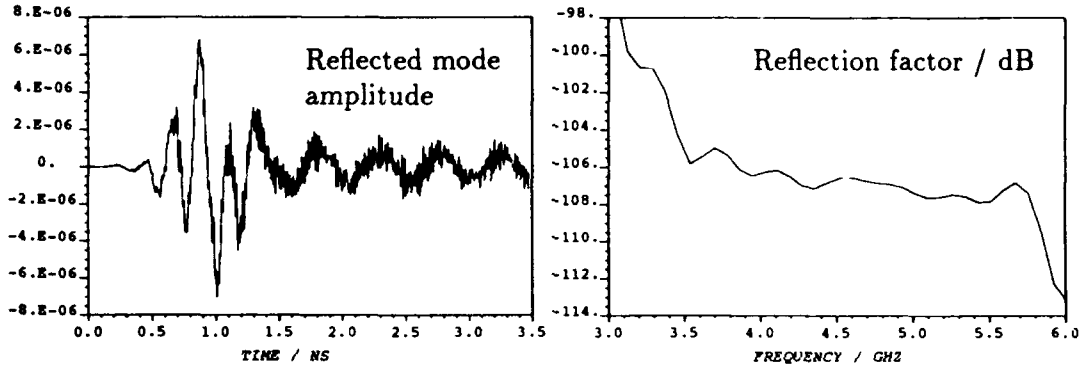

Figure 6: This picture shows the reflection at port 1 for an estimated reflection factor limit of 10^{-6}. The left plot shows the time signal of the reflected pulse and the right plot shows the reflection factor versus frequency in dB.

Both computations demonstrate that the actual reflection coefficient is of the same dimension as the specified limit. The computation with high accuracy shows that the reflected pulse can be limited down to the dimension of numerical noise.

The second example is a 3dB power splitter as shown in Fig. 7 which has been designed in regard to minimize the input reflection factor and to avoid large field strength values.

The structure has been modeled with about 20.000 mesh cells. Due to symmetries only one half of the structure has to be considered. The S-parameters have been computed using the broadband boundary operator and additionally at several frequencies using a monochromatic operator which has previously been proven to be very accurate ([6]). The cpu-time of about 1900 seconds needed for the broadband computation is equal to the time needed for one monochromatic computation. All calculations have been terminated when the pulses were decreased to $5 \cdot 10^{-3}$ of their highest amount.

Fig. 8 shows the excellent agreement between broadband and monochromatic computations within the accuracy limit of $-48dB$ given by the chosen termination error of $5 \cdot 10^{-3}$. This example demonstrates also a large gain in computation speed using the broadband operator.

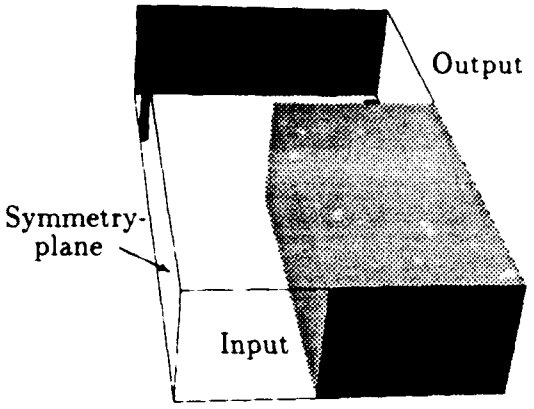

Figure 7: This picture shows the geometry of the 3dB power splitter modeled with about 20.000 mesh cells. Due to symmetries only one half of the structure has to be considered.

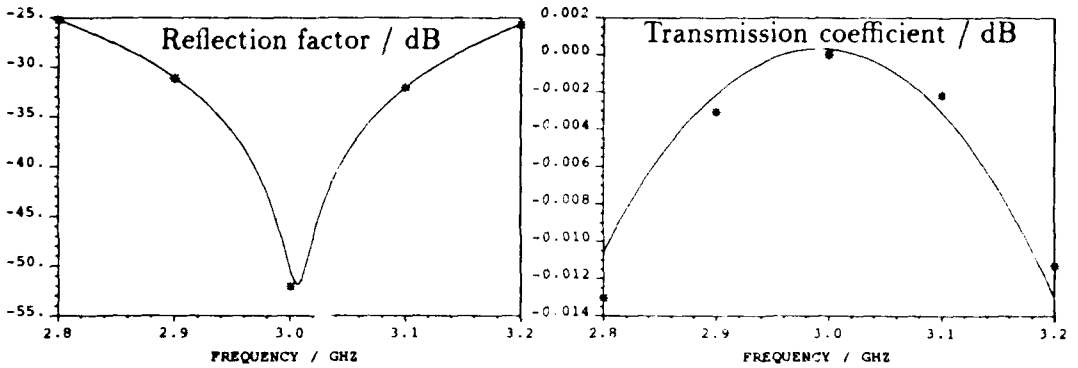

Figure 8: The left plot shows the input reflection coefficient versus frequency in dB. The right plot shows the frequency dependency of the transmission coefficient in dB. The solid lines are results of a broadband computation (173 samples within this frequency range). The marked points in both plots are results of monochromatic computations. The accuracy limit given by the termination error is $-48dB$ for all computations.

The last example is a waveguide filter shown in Fig. 9. For the discretization about 100.000 mesh cells have been used. The computation time for the broadband calculation was about 45 cpu-minutes. Due to symmetries only one half of the structure has to be considered.

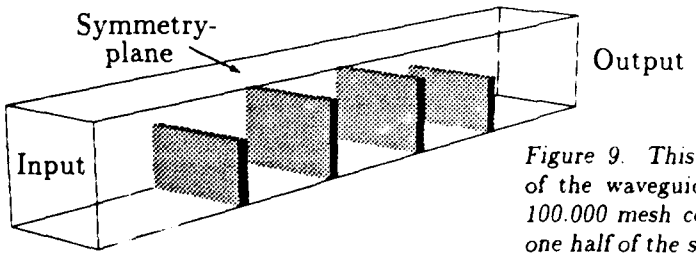

Figure 9. This picture shows the geometry of the waveguide filter modeled with about 100.000 mesh cells. Due to symmetries only one half of the structure has to be considered.

Fig. 10 compares the results for reflection factor and transmission coefficient with measurements and results of a mode matching computation. The agreement between all three results for the reflection factor is good within the interesting range above $-20dB$. The agreement between the results for the transmission factor obtained by the different methods is excellent. In all cases it is remarkable that the results of the broadband computation are closer to the measurement than the results of the mode matching method. The accuracy of the computations may be further improved by considering losses at the conducting material surfaces.

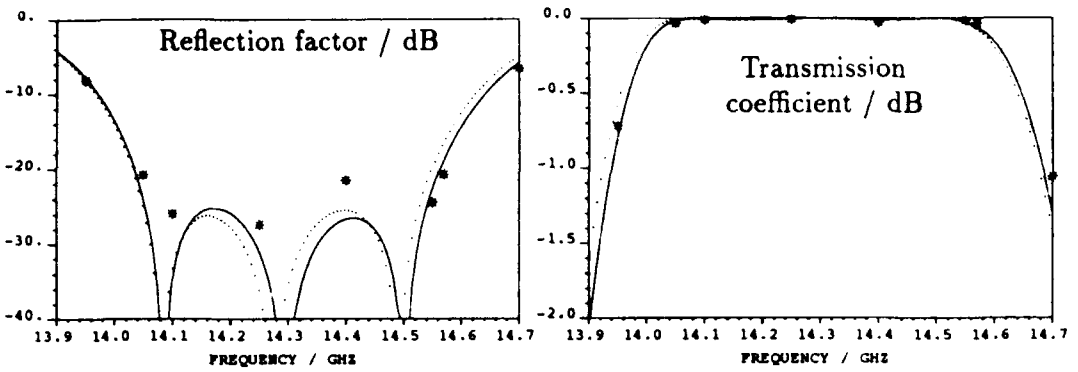

Figure 10: The left plot shows the input reflection coefficient versus frequency in dB. The right plot shows the frequency dependency of the transmission coefficient in dB. The solid lines are results of a broadband computation, the dotted lines are results of a mode matching method and the stars in both plots mark results of measurements (courtesy of Dr. Steffen Haffa, Hirschmann GmbH.).

4. CONCLUSION

In this paper we presented a new broadband operator for open waveguide boundaries which often are required e.g. for S-parameter computations.

The algorithm also allows the field-excitation by incident waveguide modes. The maximum stable timestep is not affected by the boundary simulation.

The essential advantage of the broadband operator in comparison to monochromatic operators is the enormous gain in computation speed.

For three examples the agreement with results obtained from computations using a monochromatic operator or a mode matching method as well as the agreement with measurements has been demonstrated.

REFERENCES

[1] Yee, K.S.: *Numerical solution of initial boundary value problems involving Maxwell's equations in isotropic media.* IEEE Transactions on antennas and propagation, vol. 17, 1966, p 585-589.

[2] Weiland, T.: *On the unique numerical solution of Maxwellian eigenvalue problems in three dimensions.* Particle accelerators, 1985, vol. 17, p 227-242.

[3] Weiland, T.: *A numerical method for the solution of the eigenvalue problem of longitudinally homogeneous waveguides.* Electronics and Communication (AEÜ), vol. 31, 1977, p 308.

[4] Schmitt, D.: *Zur numerischen Berechnung von Resonatoren und Wellenleitern.* Dissertation TH Darmstadt, to be published.

[5] Pröpper, T.: *Numerische Integration der Gittermaxwellgleichungen zur Lösung langsam veränderlicher Feldprobleme.* Dissertation, TH Darmstadt, to be published.

[6] Dohlus, M.: *Ein Beitrag zur numerischen Berechnung elektromagnetischer Felder im Zeitbereich.* Dissertation, TH Darmstadt, 1992, p 38-45.

ADAPTIVE DETECTION AND TRACKING OF ACTIVE SCATTERERS BY CASCADED NOTCH FILTERS

ZOUAK MOHCINE AND SAILLARD JOSEPH
S2HF-IRESTE La chantrerie, CP:3003, 44087, Nantes cedex 03,France
Phone (33) 40 68 30 09 ,Fax (33) 40 68 32 33

1. INTRODUCTION.

In the optics approximation, it is well known that the backscattered echo can be associated with a finite number of discrete sources. This leads to echo signals formed by a sum of independent elementary components [1]. The commonly used method to approximate this inverse scattering problem is to extract the scattering centers by a peak peaking procedure from an estimated time-domain profil. This is usually performed by an Inverse Discrete Fourier Transform operation on frequency-domain scattering measurements.

With recent developments in systems and materials design, the control of echo characteristics of targets that may fall in the beam of the radar becomes vitally important in a tactical point of view both in military and civilian applications. Electronic warfare and electronic countmeasures motivate the reduction and the control of military target's echo. Techniques like target masking, chaff (diversion system by clouds of metal particles), jamming (deliberate emission of signals) and echo reduction have been so developed. Cancelation methods (loading objects with specified elementary RCS) including passive and active cancelation are also used to reduce the target echo in spite of the difficulties in controlling self-oscillations, phase and amplitude of added antenna like elements.

On the other hand, it is well known from geometrical consideration that the physical scattering process have a specific dependency on the wavenumber ($k=2\pi/\lambda$) therefore on the frequency ($\lambda=c/f$). Moreover, based on loading discrete antennalike elements (dipoles, slots,..), on chaff or on jamming; electronic countermeasures may change all backscattered features including magnitudes, spatial frequencies, introduced phases and even the number of detected components. This make the target's echo frequency-dependent. Adaptive parametric methods are therefore more appropriate to the scatterings' center extraction problem. These techniques learn the required input (measurements) statistics and converge in a steady mode with permanent adjustment.

This paper investigates the identification and tracking of the scattering centers models associated with the frequency response of a frequency-dependent backscattered echo. The use of discrete scattering model is justified in section 2. To this purpose, we use a constrained adaptive Infinite Impulse Response (IIR) filter consisting of a cascade of notch sections to track the scatterers' range projected on the direction of propagation (Fig .1). Definition and properties of this structure are presented in section 3. This choice is explained on the basis of a time-domain and frequency-domain structures analysis. The combined detection-estimation operation is accomplished by the joint application of a

cascade of IIR notch filters and a recursive least square estimation (section 5). The elementary outputs' powers are used to determine the number of signal components.

2. PROBLEM STATEMENT:

Due to the lack of an exact RCS formulation of practical target, it is well known that under the high-frequency hypothesis (i.e. when the incident wavelength is significantly shorter than any characteristic target dimension), optics methods give very good approximations when the objects are as small as about two wavelengths. The target scattering is then often modelled as an array of n points-like scatterers and can be considered as a set of independent discrete scattering centers characterized by their RCS (σ_i) and by the introduced phases (ϕ_i). The backscattered field appears to emanate from a finite number of discrete sources residing at these scattering centers and occuring principally at geometrical discontinuities of a body [2].

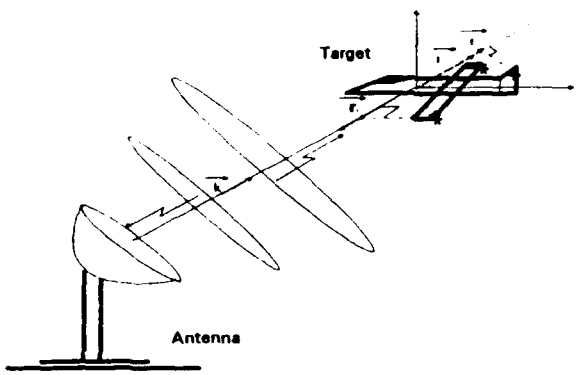

Figure 1:Monostatic, Fixed Polarisation System

With a monostatic polarized receiving antenna (fig.1), the backscattered field is decomposed into n elementary components each with a different phase and magnitude. The physics of the scattering process determines the relative magnitudes of each contribution, while the phase is dependent on the distance from the scattering center to the observation point.

$$H(f) = \sum_{i=1}^{n} A_i e^{jS_i(f)}$$

The received field H(f), can then be measured continuously over a frequency band as a sum of p complex sinusoids with additive noise v(f):

$$\sum_{i=1}^{n} A_i \exp(j(2\pi f_i f + \phi_i) + v(f)$$

For the targets' features tracking problem we assume A_i, ϕ_i, ω_i and n change slowly with respect to frequency f and hence the received signal should be denoted by a frequency-dependent model characterising the backscattered echo:

$$\sum_{i=1}^{n(f)} A_i(f)\exp(j(2\pi f_i(f)f + \phi_i(f)) + v(f)$$

The necessary format for digital-signal analysis is provided by a frequency sampling of the specified emission band (B) centred on f_O. This produces N equally spaced frequencies:

$$f_n = f_o + \left(k - \frac{N+1}{2}\right)\Delta f$$

$$\text{where} \quad \frac{f_0 - B}{2} \le f_0 \le \frac{B + f_0}{2} - \quad \text{and} \quad 0 \le k \le N-1$$

The discrete backscattered measurements will be used in identification and tracking of the scattering centers' features i.e. the amplitudes $A_i(k)$, the spatial frequencies $f_i(k)$ and the initial phases $\phi_i(k)$. The detection of the number of scattering centers n(k) is also investigated.

The signal format followed in this presentation is then:

$$y(k) = \sum_{i=1}^{n(k)} A_i(k)\exp(j\omega_i(k)k + \phi_i(k)) + v(k)$$

$$k = 0,1,.....N-1$$

As it had been shown [3,6], the estimation of the parameters of complex sinusoids is impractical to implement even in a stationary environment. The function to be minimized is highly nonlinear with respect to the unknown frequencies and require a search over a p-dimensional space. Iterative optimisation can be used, but convergence to global minimum is not guaranteed. Simplified methods for optimizing the maximum likelihood function were suggested by several numerical analysts and in the signal processing literature [4,5,6]. Recently, a number of IIR adaptive filters have been described that can be used for tracking sinusoidal features [8,9,11].

The independence of scattering centers, the study of maximum likelihood estimator and the suitablility of ANF in processing narrow band signals convince us to use this last structure in the inverse scattering problem [7].

3. NOTCH FILTER PARAMETRIZATION.

Many studies had shown that the N.F. appears to be the simplest natural way to eliminate sinusoidal signals. In fact, it had been shown from frequency-domain and time-domain analysis that this structure allows a perfect sinusoidal-in-noise representation [9]. As it is easy to show, the real (or imaginary) part of the signal y(k) obeys a homogenous difference equation of order n=2p. The coefficients of this equation form a monic symmetric polynomial with unit modulus roots. The observed process (signal+noise) has a structure of an ARMA(p,p) with a special symmetry in which the AR parameters are identical to the parameters of the MA portion of the model [7]. The proposed IIR model satisfy the miror symmetric form property so that the zeros of its transfer function lie on the unit circle. The poles are constrained to be on the same radial line as the zeros and slightly displaced towards the origin by the introduction of a debiasing parameter α. The closer α is to unity, the flatter the notch filter response will be, constraining the ARMA filter model to have identical AR and MA portions and making the bias smaller. Zeros and poles are then linked by a simple relation:

$$z_i = r_i \exp(j\omega_i) \quad \text{and} \quad p_i = \alpha z_i = \alpha r_i \exp(j\omega_i)$$
$$\text{for } i = 1,2,....2p \quad 0 \le \alpha \le 1 \quad \text{and} \quad 0 \le r \le 1$$

The general set of the sinusoidals' signals adapted IIR filters is of the form:

$$H(z^{-1}) = \frac{1 + b_1 z^{-1} + ... + b_p z^{-p} + ... + b_1 z^{-2p+1} + z^{-2p}}{1 + \alpha^1 b_1 z^{-1} + ... + \alpha^p b_p z^{-p} + ... + \alpha^{2p-1} b_1 z^{-2p+1} + \alpha^{2p} z^{-2p}} = \prod_{i=1}^{p} \frac{1 + a_i z^{-1} + z^{-2}}{1 + \alpha^1 a_i z^{-1} + \alpha^2 z^{-2}}$$

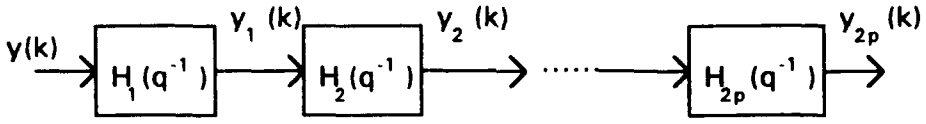

Figure 2: Cascaded Notch Filter Structure.

This last structure will present a great interest in the remaining of the investigation due to its following properties [7,8,9,11]:

1. The idependency relationship of differents elements.
2. Minimal parametrisation (one frequency ↔ one parameter).
3. Computational efficiency and numerical robustness.
4. Stability and rapid convergence.

4. RECURSIVE FREQUENCY ESTIMATION ALGORITHM:

The independence between backscattering centers implies independence of frequencies which lead to independence between the parameters in each elementary cell. Without loss of generality, we assume identical bandwith ($B=\pi(1-\alpha)$) for all the notchs. The j^{th} cell's ouput is then (Fig.2):

$$y_j(k) = \prod_{i=1}^{j} H_i(q^{-1}) y(k)$$

Where q^{-1} is the delay operator. The parameter adaptation algorithm can be applied to each cell independently of the others. We suppose that the first (j-1) filters have converged. The cascaded nature ensures that the signal components will be removed one by one in successive cells. The Recursive Maximum Likelihood Algorithm for the cascaded A.N.F. may then be summarized as the following:

For $j=1$ to p

$$\hat{y}_j(k) = \varepsilon_j = H_j(q^{-1})\hat{y}_{j-1}(k)$$

For $k=1$ to N,

$$\hat{a}_j(k) = \hat{a}_{j-1}(k) + F_j(k)\Psi_j(k-1)\varepsilon_j(k)$$

$$F_j(k) = \frac{F_j(k-1)}{\lambda + \Psi_j^T(k-1)F_j(k-1)\Psi_j(k-1)}$$

$$\Psi_j(k-1) = -\frac{d\varepsilon_j(k)}{d\hat{a}_j(k)} = \frac{y_j(k) - \alpha(k)\varepsilon_j(k-1)}{1 + \hat{a}_j(k-1)\alpha(k)q^{-1} + \alpha(k)^2 q^{-2}}$$

$$\alpha(k) = \alpha_0\alpha(k-1) + (1 - \alpha_0\alpha(N))$$

λ is a forgotten factor.

• SIMULATION RESULTS:

In the following, the notch frequencies were normalized with respect to the sampling frequency. The input data were a sum of two sinusoids in white noise with a Signal to Noise Ratio (SNR) of about 20 dB (Fig.3). A SNR is defined for the signal as the power of the sinusoids over the total noise power [7]. The input frequencies are 0.1 and 0.3 respectively for the 256 first samples after which the second frequency is step changed to 0.25. The frequencies of the notches are initialized to zero.

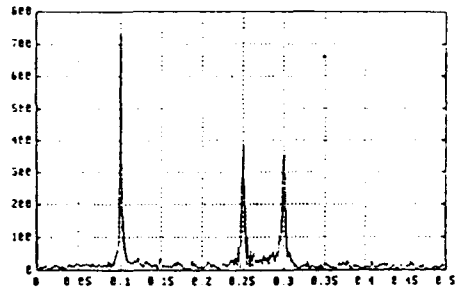

Figure 3: Input data periodogram.

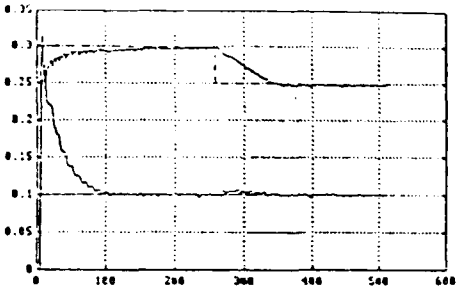

Figure 4: Estimated frequencies tracking.

It can be seen by referring to fig. 4 that both notches converged to the nominal values and we can observe the tracking ability of the adaptive algorithm. Moreover, it is interesting to note that the second-order system had a similar convergence time (about 100 samples). This adaptation period is a function of choice of the filter's parameters. Referring to figures 5 and 6, the two sinusoids are adequately notched:

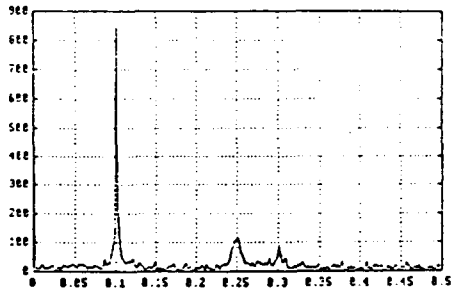

Figure 5: Periodogram at the first ouput.

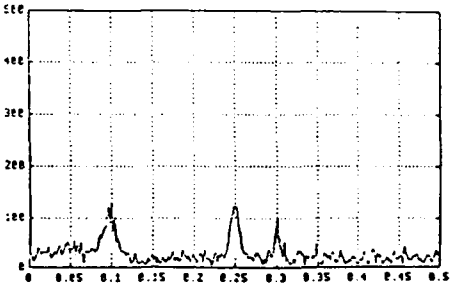

Figure 6: Periodogram at the second output

The remaining "trace" of the sinusoids' frequencies observed on the output periodograms are due to the filters parameters and to the size of the imput data. Better notching can be obtained with greater data size.

5. MAGNITUDES AND COMPONENTS' PHASE TRACKING:

The second step in this investigation is to estimate the scatterers magnitudes and phases by a Recursive Least Square (RLS) algorithm. Its tracking capabilities ensure the quality of the estimations. The analysis and performance evaluation of this algorithm can be found in the literature [10]. Using the following signal model, it can be seen that with an adequate problem formulation given by the trigonometric equality:

$$y(k) = \sum_{i=1}^{2p} A_i \sin(\omega_i k + \phi_i) + v(k) = \sum_{i=1}^{2p} A_i \left(\sin(\omega_i k)\cos(\phi_i) + \cos(\omega_i k)\sin(\phi_i)\right) + v(k)$$

we can obtain the standard adjustable predictor which can be time varying. In the following, we drop the time index for simplicity. The signal can then be expressed as

$$y(k) = \theta^T(k) w(k) \quad \text{where} \quad w(k) = \left[\cos(\hat{\omega}_1)\sin(\hat{\omega}_2) \ \ldots\ldots \ \cos(\hat{\omega}_{2p})\sin(\hat{\omega}_{2p})\right]^T$$

A linear least square formulation can be obtained if we consider the new parameters:

$$\theta_i^1 = A_i \cos(\phi_i) \qquad \theta_i^2 = A_i \sin(\phi_i) \qquad \text{for } i = 1,2, \ \ldots\ldots \ 2p$$

Many algorithms [10] may then be applied to minimize the square prediction error:

$$\text{minimum} \sum_{k=1}^{N} \left(y(k) - \sum_{i=1}^{2p} \hat{\theta}_i^1 \cos(\omega_i k) + \hat{\theta}_i^2 \sin(\omega_i k) \right)^2$$

The least square solution is so given by:

$$\hat{\theta} = \left[\hat{\theta}_1^1, \hat{\theta}_1^2, \ldots\ldots\ldots, \hat{\theta}_{2p}^2\right] = \frac{1}{N} \left\{ \sum_{k=1}^{N} W(k) W(k)^T \right\}^{-1} \left\{ \sum_{k=1}^{N} W(k) y(k)^T \right\}$$

where

$$\hat{A}_i = \sqrt{\hat{\theta}_i^1 + \hat{\theta}_i^2} \qquad \text{and} \qquad \hat{\phi}_i = \text{Arctg}(\hat{\theta}_i^1 / \hat{\theta}_i^2) \qquad \text{for } i = 1,2,\ldots.2p$$

- **SIMULATION RESULTS:**

For a three sinusoids signal, we let the frequencies be 0.1, 0.2 and 0.3 respectively. All the magnitudes are equal to one and the phases are initialized to 0.01, 0.02 and 0.03 for the first 100 sample points after which they are respectively step changed one after one at every 50 sample points (i.e. at 100th sample for the first, at 150th sample for the second and at 200th sample for the third frequency). The new phase values are the old ones increased by π (0.51,0.52 and 0.53) (Figure 7):

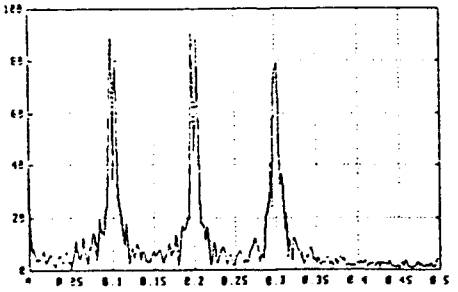

Figure 7: Input data periodogram

This periodogram of the simulated signal shows a dedoubled peak at all the frequencies and specially at the last two ones. This is attributed to the sinusoidal relationship of the periodogram at the nominal frequencies due to the π phase step change of the phases [7]:

$$|y(f)| = \frac{\sin(\pi(f - f_1)T)}{\pi(f - f_1)} \sin(\pi T(f - f_1)/2)$$

Figures 8 to 13 shows respectively the phases and magnitudes tracking obtained by an exponential forgotten RLS algorithm:

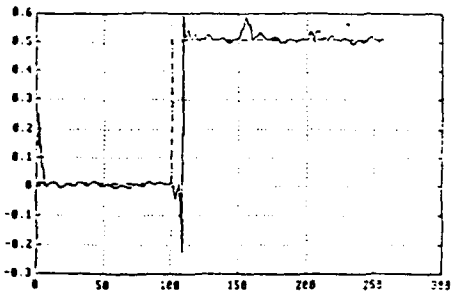

Figure 8:First phase estimation

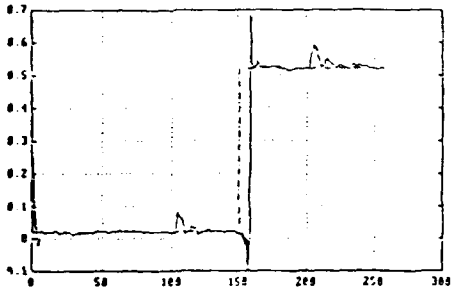

Figure 9:Second phase estimation

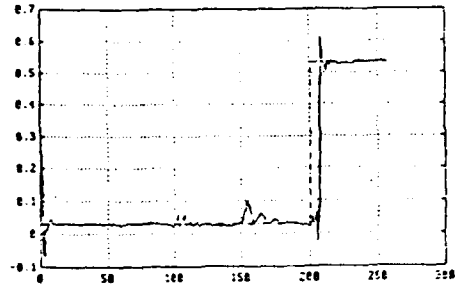

Figure 10:Third phase estimation

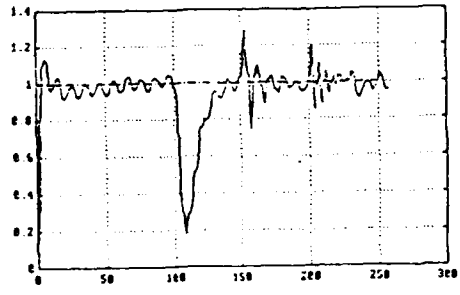

Figure 11:First magnitude estimation

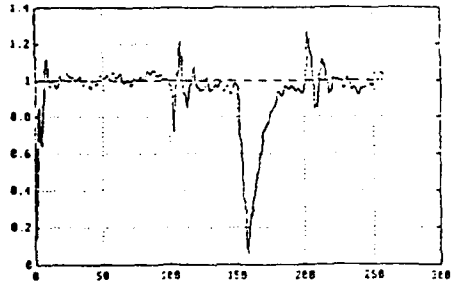

Figure 12:Second magnitude estimation

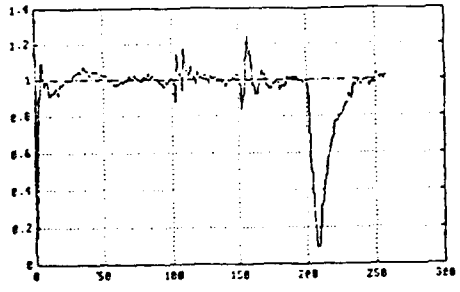

Figure 13:Third magnitude estimation

The π step phase changes was successfully tracked and the magnitudes was also adequately estimated. Others simulation results have been made [7].

6. DETECTION AND DISCREMINATION OF SCATTERING CENTERS.

The number of active components can now be estimated by using a sufficiently long chain of elementary N.F. cells and measuring the power of each output. When the normalized power of any ouput is equal to about the power of the previous cell we conclude that the number of contributors is equale to the previous cell's order. This can be summurised by the following steps:

- Assume an over-evaluated order, say n, and estimate the different frequencies .
- Filter the successive outputs through the resonant bandpass filters:

$$1 - \hat{H}_i(q^{-1}) \quad \text{for } 1 \le i \le n$$

- Measure the normalized power $\hat{E}_i / E$ where $\hat{E}_i = \hat{Y}_i^H \hat{Y}_i$ and $E = Y^H Y$. (Y is the input data vector), and compare them to conclud about the number of components.

The discrimination of the scatterers on active or passive is made on the basis of the estimated features. If the magnitude, frequency or the introduced phase is frequency varying, it corresponds to an active scatterer.

Example:

In the following we let the input data be a noisy sum of three sinusoids with unite magnitude and normalized frequencies 0.1, 0.2 and 0.3. The RSB is about 20 dB. With 5 N.F. cells, the computed powers are indicated on the following figure [7]:

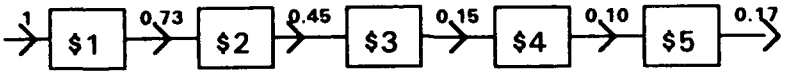

The comparison of the output power of successive cells traducte the notching effect. The stabilisation of the powers arround the noise power indicate that all the components have been rejected and we can conclude about the components' number. This method was tested under different signal-to-noise-ratios for well separated frequencies.

7. CONCLUSION: According to RCS signal analysis, the structure of the cascaded ANF has been proposed and associated to a *RLS* algorithm for the estimation of target backscattered echo features. It was shown that the structure can isolate and enhance individual components in the presence of noise. It is possible to determine the spatial frequencies of the received data directly without any root finding or transfer function evaluation. The number of scattering centers can also be determined by the notching property of the filters. Magnitudes and phases are obtained by adequate parametrisation by a RLS algorithm. It is expected that the proposed procedure will be especially practical in real RCS data and in real-time applications.

REFERENCES:

[1] M.Skolnik, Radar Handbook,Mc Graw-Hill, Second edition, 1990
[2] M.P.Hurst and R.Mittra, IEEE Trans. AP, VOl. 35, N°8, August 1987.
[3] P.Stoica, R.L.Moses, B.Friedlander and T.Soderstrom, IEEE Trans. ASSP-37, N°3,March 1989.
[4] I.Guttman, V.Peeyra and H.D.Scolnik, Technometrics, Vol-15,pp:209-218, May 1973.
[5] R. Kumaresan, L.L.Scharf and A.K.Shaw, IEEE ASSP, Vol.34, N°3, June 1986.
[6] S.M.Kay, Modern Spectral Estimation. Theory and Application, Prentice-Hall, 1988.
[7] M.Zouak and J.Saillard, S2HF-Report, N°929551400, Juillet 1993.
[8] N.K.M'Sirdi,Thèse d'état de L'Univ. Scientifique et Médicale de Grenoble, 1988.
[9] D.V.B.Rao and S.Y.Kung, IEEE Trans. ASSP-32, N°4, August 1984.
[10] L.Ljung and T.Soderstrom, Theory and practice of recursive identification,Cambridge, MA:MIT Press, 1983.
[11]A.Nehorai, IEEE Trans. ASSP, Vol 33, N°4, 1985.

Sub-mm Wave Circuit Characterization Using the Finite Difference Time Domain Method

Nihad Dib and Linda Katehi

Electrical Engineering and Computer Science Department
Radiation Laboratory
The University of Michigan
1301 Beal Ave.
Ann Arbor MI 48109-2122

Abstract — Sub-mm/THz monolithic circuit components made of a combination of layered dielectric waveguide and strip-ridge line are characterized using the Finite Difference Time Domain (FDTD) technique. The use of FDTD analysis allows for the characterization of these components in a very wide frequency range. The first structure analyzed with this method was a transition from a strip-ridge line to a layered dielectric waveguide. The transition is found to be very efficient over a wide frequency band which makes it useful for a variety of applications. Moreover, preliminary results for a sub-mm wave distributed directional coupler are presented. This coupler employs the above transition and consists of a section of a coupled layered dielectric waveguide.

1 INTRODUCTION

Millimeter wave dielectric waveguides have been extensively studied during the past two decades. Examples of these waveguides include dielectric image guides, strip dielectric guides, insulated image guides, inverted strip dielectric guides, cladded image guides and trapped image guides. These waveguides are constructed from combinations of layers and ridges of various permittivities in order to provide a region wherein the propagating power is well-confined. The widths of these lines approach one guided wavelength in order to maximize field confinement. Although there are several examples of the monolithic use of these dielectric lines in the literature [1], they have been generally considered hybrid in nature.

Recently, Engel and Katehi [2] suggested that development of monolithic sub-mm guiding structures be realized by considering variations of the early dielectric lines. The new waveguides are made of materials which are available in monolithic technology so that they are compatible with solid-state sources. The dimensions of these monolithic guides are fractions of a guided wavelength, so the new structures may be used not only as guiding media but as means of making passive components. Presently, limitations in the fabrication process and availability of III-V materials permit use of these lines at the high frequency end of the sub-mm-wave spectrum.

The successful integration of dielectric waveguides and power sources into a sub-millimeter wave or THz monolithic circuit relies on an effective transition. In particular, when layered ridged dielectric waveguides [2] are used, a transition to the waveguide may be realized with a short length of conductor on top of the ridge (Figs. 1-2) [3]. Of primary interest in evaluating a transition is the power transferred from the dominant mode in the strip-ridge structure to the dominant

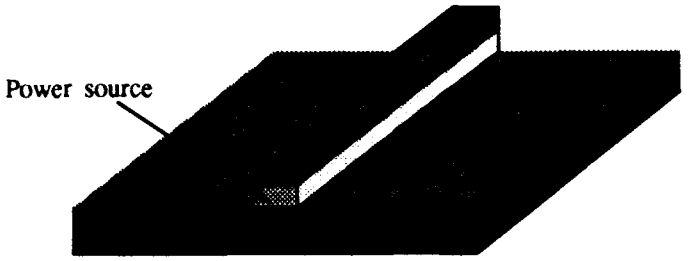

Figure 1: A transition between a power source and a layered ridged dielectric waveguide.

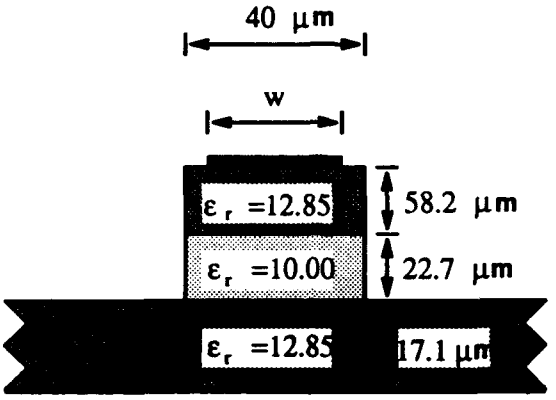

Figure 2: Cross-section of the strip-ridge structure. The dielectric waveguide structure is the same except w=0.

mode in the dielectric waveguide. If only the guiding properties of either region are desired, then two-dimensional analysis is sufficient and higher order modes are easily taken into account. If the properties of a transition are desired, then three-dimensional analysis is necessary. Previous work on the characterization of this transition was based on a hybrid full-wave integral equation-mode matching (IEMM) analysis technique and some preliminary results were presented in [4]. In addition, a detailed study of a shielded transition from a strip-ridge line to a dielectric waveguide in both the frequency and time domains is presented in [3]. In that study, difficulties arised in designing a shielding structure in which the dominant dielectric waveguide mode propagates and the first higher order strip-ridge mode does not.

In this paper, the same transition is analyzed in open environment using the FDTD technique. This is performed with the use of a combination of Absorbing Boundary Conditions (ABCs) around the structure instead of a perfectly electric conductor. In addition, preliminary results for a distributed directional coupler, which employs such a transition, made of a section of a coupled layered dielectric waveguide are presented.

2 THEORY

The FDTD method was first introduced by Yee [5] to solve electromagnetic scattering problems. In this method, Maxwell's curl equations are expressed in discretized space and time domains and are then used to simulate the propagation of an initial excitation in a "leapfrog" manner. Recently, the method has been successfully applied to characterize microstrip lines and discontinuities [6, 7, 8]. The interested reader may consult these references for a detailed description of the method.

The FDTD technique has the ability to determine accurately the broadband characteristics of sub-mm/THz monolithic circuit components by simulating the propagation of a Gaussian pulse through the circuit. In this research, the vertical electric field component at z=0 under the metal strip is excited and the magnetic wall source condition of [8] is used to compute the fields elsewhere in the plane z=0. The source distribution has been modified to take into account the discontinuity experienced by the vertical electric field [9].

The first order Mur boundary condition [10] is used in the left, right and top walls in order to simulate an open structure. On the other hand, the super-absorbing first-order Mur condition [11, 12] is utilized in the front and back cavity walls in order to simulate infinite lines. This absorbing boundary condition requires a choice for the incident velocity of the waves, or equivalently ϵ_{eff}. It has been found that an appropriate choice of $\epsilon_{r,eff}$ minimizes the effect of the absorbing boundary walls. For the transition shown in Figs. 1 and 2, the average between the *dc* relative effective dielectric constant of the strip-ridge line and that at the higher frequency limit has been used at the front wall. This can be obtained using either the 2D-FDTD [13] method or by simulating a propagating pulse on a strip-ridge through line [6]. For the dielectric ridge guide, it is found (using 2D-FDTD) that the cutoff frequency of the dominant mode is approximately 350 GHz. Thus, $\epsilon_{r,eff}$ at the back wall is chosen to be equal to the average between the relative effective dielectric constant of the dielectric guide at 350 GHz (i.e., 1) and that at the higher frequency end. The effectiveness of these choices has been checked by performing several numerical experiments with different values of $\epsilon_{r,eff}$.

3 RESULTS

As a first example, Fig. 3 shows $|S_{11}|$ for a transition completely shielded inside a rectangular waveguide of width 200 μm and height 250 μm in the frequency range 0-520 GHz [3] (see Figs. 1 and 2 for other dimensions). It is worth mentioning that the results agree with those obtained using the IEMM technique [3]. Figure 3 shows that the incident wave is totally reflected by the open end for frequencies below approximately 475 GHz. This is due to the fact that the shielded dielectric line cannot support any propagating mode in this frequency range [3].

Figures 4 and 5 show the dispersion curves of the dominant propagating modes of the strip-ridge line and the dielectric guide (both un-shielded), respectively. As mentioned above, the dielectric guide dominant mode has a cutoff frequency around 350 GHz (compared to 475 GHz for the shielded one).

Figure 6 shows $|S_{11}|$ for the transition in open environment. Due to the open nature of the transition, $|S_{11}|$ is not equal to one below the cutoff frequency of the dielectric guide (as was the case of the shielded transition). Almost 20% of the incident power is lost as radiation for frequencies between 100 and 300 GHz. The return loss is less than -10 dB for frequencies above 500 GHz. Thus, the transition is an efficient one for frequencies from 500 to 570 GHz, where 570 GHz is the cutoff frequency of the strip-ridge first higher order mode.

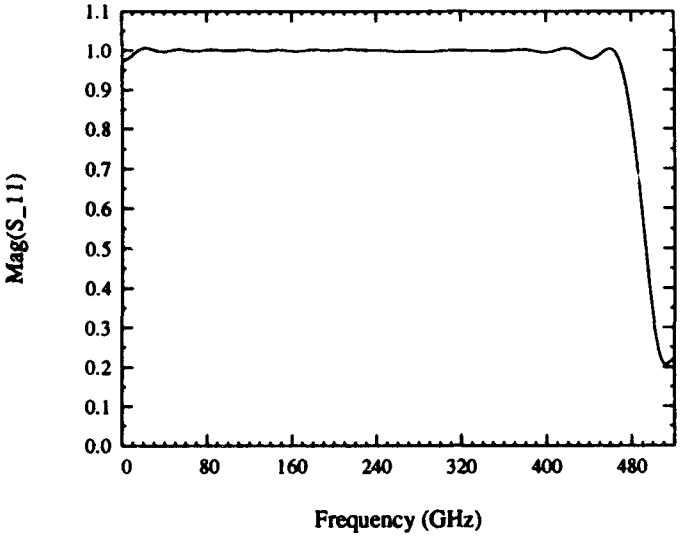

Figure 3: Magnitude of S_{11} for a shielded transition. (w=40 μm).

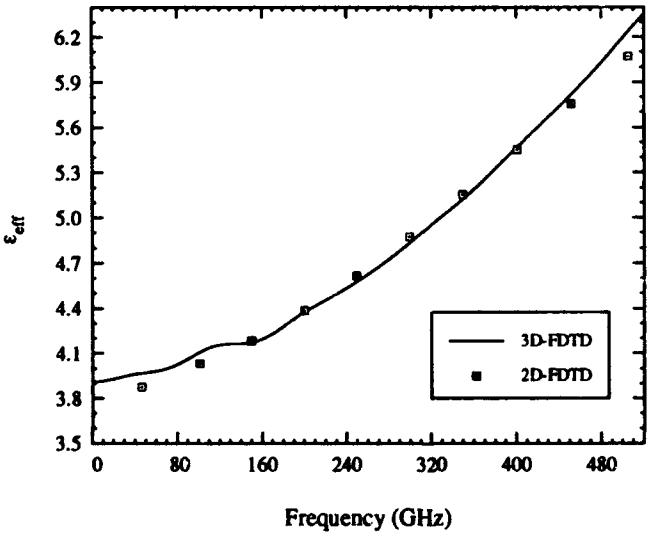

Figure 4: Dispersion diagram for the dominant mode of the strip-ridge line with w=20 μm. Other dimensions are as shown in Fig. 2.

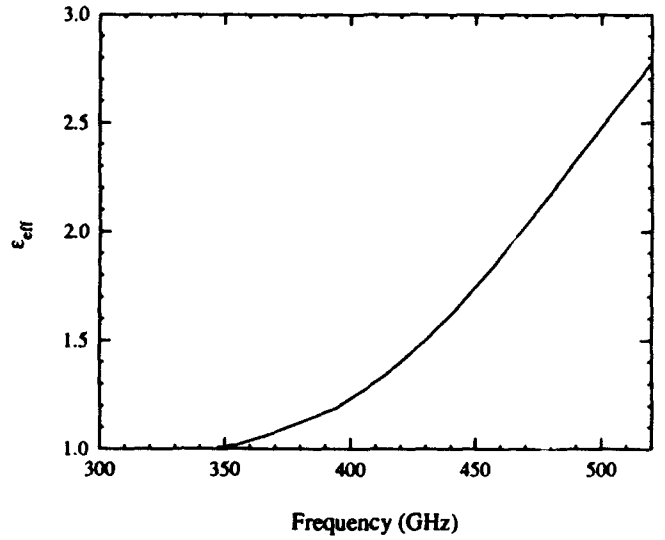

Figure 5: Dispersion diagram for the dominant mode of the layered dielectric line. Other dimensions are as shown in Fig. 2.

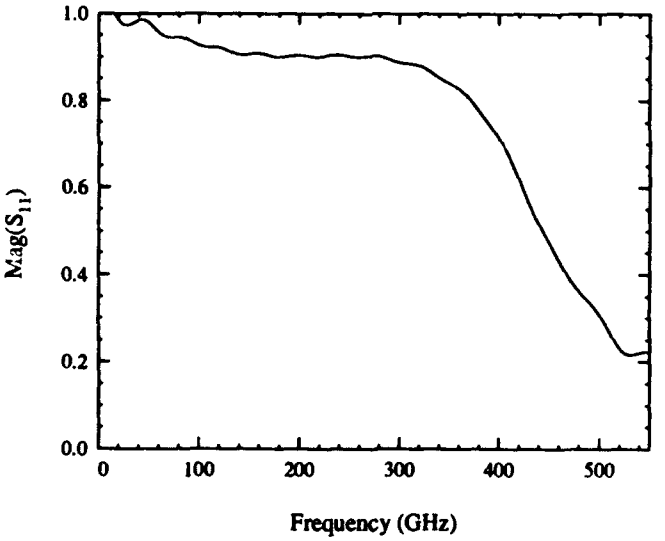

Figure 6: Magnitude of S_{11} for the transition in open environment. (w=20 μm)

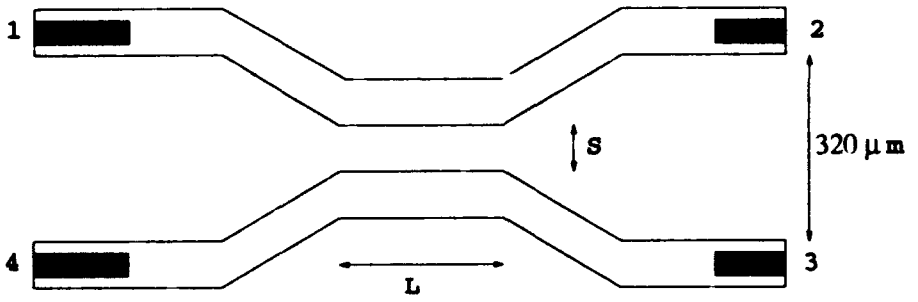

Figure 7: Top view of a distributed coupler made of the layered dielectric waveguide.

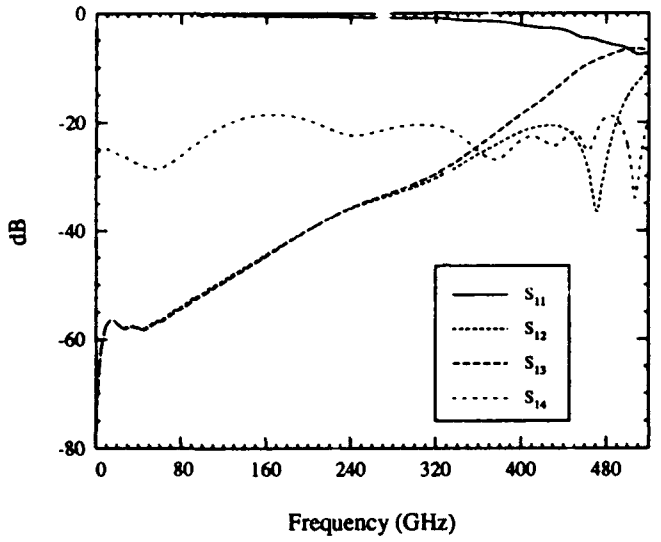

Figure 8: Scattering parameters of the coupler shown in Fig. 7.

Figure 7 shows a distributed directional coupler which employs the above studied transition and consists of a section of a coupled layered dielectric guide of length L=870 μm and separation S=160 μm. Assuming that the coupling due to the connecting guides is negligible, the length L is chosen such that a 3 dB-coupler is obtained with a center frequency of 500 GHz [14]. The tapered sections of the dielectric guide are modeled using the "staircase" approximation. The scattering parameters of such a coupler and the radiation loss factor are shown in Figs. 8 and 9, respectively. The sources of the discrepancy between the simulated results and the ideal response (i.e., both $|S_{12}|$ and $|S_{13}|$ should be equal to -3 dB at 500 GHz) are the effects of the junctions and the coupling between the connecting guides [14, 15]. 539. In conclusion, the above results are not indicative of optimum coupler performance due to the several junctions involved in the coupler. The optimization of the coupler performance, including the transition between the strip-ridge line and the layered dielectric guide, is a subject presently under study at the University of Michigan.

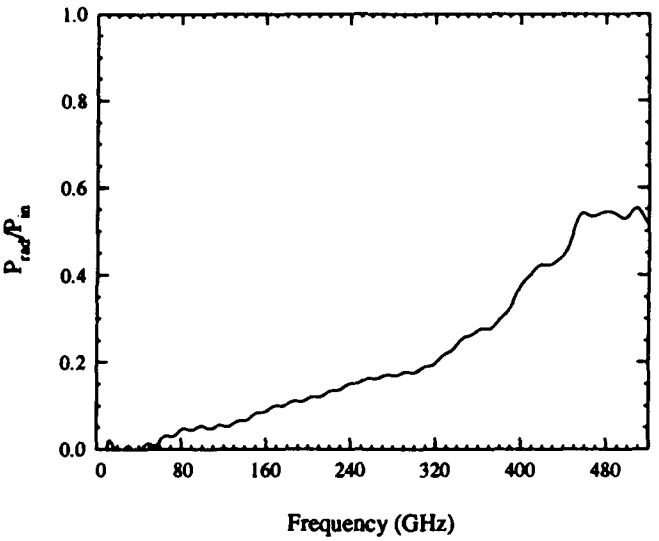

Figure 9: Radiation loss factor of the coupler shown in Fig. 7.

4 CONCLUSIONS

A transition from a microstrip-ridge to a layered ridged dielectric waveguide has been characterized using the FDTD technique. The variation of the S-parameters over frequency was shown, and the transition was found to be very efficient over a wide frequency band. Preliminary results for a distributed dielectric coupler have been presented too. As a future work, the transition and the coupler will be optimized by varying the dimensions of the dielectric layers involved in the structure.

5 ACKNOWLEDGMENT

This work was supported by Rome Laboratory, Hanscom AFB under contract # F19628-92-K-0027.

References

[1] T. Wang and S. Schwarz, "Design of Dielectric Ridge Waveguides for Millimeter Wave Integrated Circuits, " *IEEE Trans. MTT*, pp. 128-134, Feb. 1983.

[2] A. G. Engel, Jr. and P. B. Katehi, "Low-loss monolithic transmission lines for submillimeter and terahertz frequency applications," *IEEE Trans. MTT*, pp. 1847–1854, Nov. 1991.

[3] A. Engel, N. Dib and L. Katehi, "Characterization of a Shielded Transition to a Dielectric Waveguide, " accepted for publication in the *IEEE Trans. MTT.*

[4] A. G. Engel, Jr., and L. P. B. Katehi, "On the analysis of a transition to a layered ridged dielectric waveguide," *1992 IEEE MTT-S Intl. Microwave Symp. Dig.*, pp. 983–986.

[5] K. S. Yee, "Numerical solution of initial boundary value problems involving Maxwell's equations in isotropic media," *IEEE Trans. AP*, pp. 302-307, May 1966.

[6] X. Zhang, J. Fang, K. Mei and Y. Liu, "Calculation of the dispersive characteristics of microstrips by the time-domain finite difference method, " *IEEE Trans. MTT*, pp. 263–267, Feb. 1988.

[7] X. Zhang and K. Mei, "Time-domain finite difference approach to the calculation of the frequency-dependent characteristics of microstrip discontinuities, " *IEEE Trans. MTT*, pp. 1775–1787, Dec. 1988.

[8] D. Sheen, S. Ali, M. Abouzahra and J. Kong, "Application of the Three-Dimensional Finite-Difference Time-Domain Method to the Analysis of Planar Microstrip Circuits, " *IEEE Trans. MTT*, pp. 849–857, July 1990.

[9] L. Wu and H. Chang, "Analysis of dispersion and series gap discontinuity in shielded suspended striplines with substrate mounting grooves, " *IEEE Trans. MTT*, pp. 279–284, Feb. 1992.

[10] G. Mur, "Absorbing boundary conditions for the finite-difference approximation of the time-domain electromagnetic-field equations," *IEEE Trans. EMC*, pp. 377–382, Nov. 1981.

[11] K. Mei and J. Fang, "Superabsorbtion-A method to improve absorbing boundary conditions," *IEEE Trans. AP*, pp. 1001–1010, Sep. 1992.

[12] V. Betz and R. Mittra, "Comparison and Evaluation of Boundary Conditions for the Absorption of Guided Waves in an FDTD Simulation, " *IEEE MGWL*, pp. 499–501, Dec. 1992.

[13] N. Dib and L. Katehi, "Dispersion Analysis of Multilayer Planar Lines Containing Ferrite Regions Using an Extended 2D-FDTD Method, " *1993 IEEE AP-S International Microwave Symposium Digest*, pp. 842-845.

[14] R. Rudokas and T. Itoh, "Passive Millimeter-Wave IC Components Made of Inverted Strip Dielectric Waveguides, " *IEEE Trans. MTT*, pp. 978-981, Dec. 1976.

[15] J. Rodriguez and A. Prieto, "Wide-Band Directional Couplers in Dielectric Waveguide, " *IEEE Trans. MTT*, pp. 681-686, Aug. 1987.

FDTD Modelling of Wirebond Interconnects

E. Pillai, C. Bomkessel, W. Wiesbeck
University of Karlsruhe

Abstract

As the transmission rates for ultra wide band digital systems increases steadily due to world telecommunication demand, the occurrence of discontinuities in electronic packaging must be characterised. The wirebond interconnect is such a discontinuity and can cause signal degradation. The Finite Difference Time Domain (FDTD) method is now a well established powerful analytical tool, which is used here to provide insight into wirebond behaviour through the field distributions and scattering [S] parameters computed for variation of the material parameters associated with it. This can lead to recommending improved wirebond geometries. Comparison of FDTD results with measurement shows extremely good agreement and hence verification. In addition important considerations are provided with regard to discretisation schemes, which take into account the number of overall discretisation cells, numerical errors and computation time.

Introduction

The transmisson of light wave signals moves steadily into the ever increasing GHz range, requiring suitably designed multiplexor technology for rapid demodulation. As part of the development of this hardware, attention must be placed on the occurrence of signal track discontinuities in multi-layer printed circuit boards (PCB). Such discontinuities include via holes, coupling between lines, crossovers, line bends and wirebonds. It is possible to solve Maxwell's equations numerically for such structures and observe their behaviour. This can lead to not only avoiding effects such as dispersion, reflection, resonances, coupling and radiation, but also to the development of simpler models for the discontinuities to be implemented in computer aided design CAD [1].

The FDTD [2] is now a well established numerical method for solving microwave circuit structures. The versatility of the method lies in the number of physical features it incorporates. The FDTD method implemented here includes the ability to define non equidistant cartesian cells and variation from cell to cell of metal thickness, conductivity (σ), and dielectric constant (ε_r), including, additionally the presence of a Mur's first order absorbing boundary condition (ABC) [4]. For curved structures the staircase approximation is used, where sufficient discretisation causes minimal discrepancy. Here, the application of the FDTD to wirebonds is undertaken. A suitable discretisation scheme is derived for the microstrip based wirebond structure, which minimises numerical error, especially that which is caused by the homogeneously applied gaussian pulse below the microstrip line, known as the DC offset error [3]. The discretisation scheme chosen has also an effect on the computation time for the structure. In this respect it is mainly necessary to find a trade off between the maximum frequency to which S parameter information is desired (i.e.: the pulse width in time) and the corresponding discretisation step which can guarantee a stable computation. Once the appropriate computational parameters for the FDTD are determined, the material parameters linked to the wirebond are varied to investigate the wirebond behaviour. Structures are computed in the FDTD in a cartesian grid to obtain S parameter, field distribution at a time instant and continuous time field variation information. The S parameter results with respect to the length s (Fig.2) for two different dielectric constants, variation of the dielectric constant and variation of microstrip line

width are provided. Comparison of results with measurement shows the extremely accurate modelling offered by the FDTD. This provides a basis for the design and implementation of wirebonds.

Microstrip based Wirebond Discretisation and Computation Time

Discretisation is an important factor in the use of numerical techniques. As the number of discretisation steps is not limitless, there is a need to find optimum discretisation schemes when dealing with the FDTD algorithm. Moreover, over discretisation in some cases leads to numerical error. In the process of modelling these wirebond structures, observations made indicate that some simple discretisation rules can be used in order to produce the best results. These rules apply in general for microstrip based discontinuities.

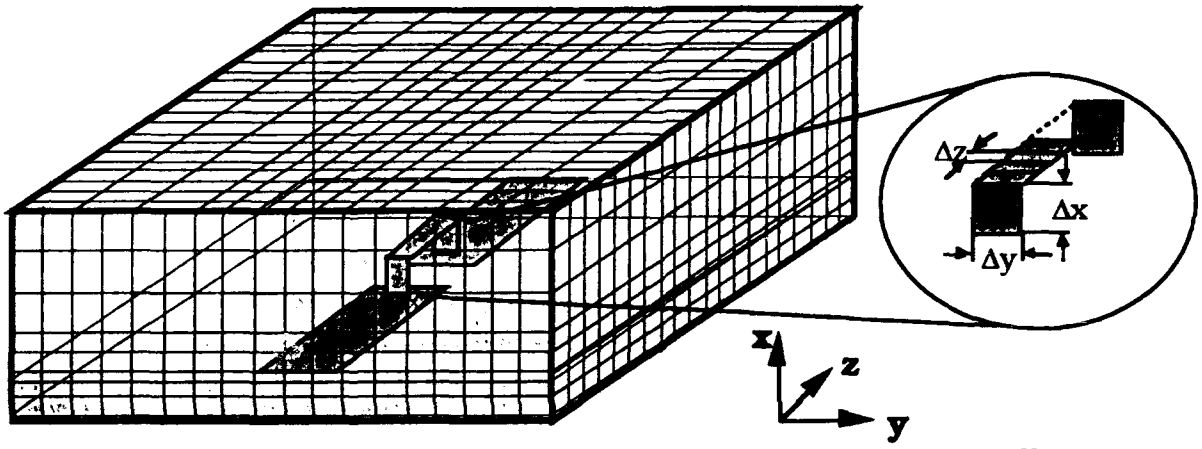

Fig. 1: Discretisation of the wirebond structure, including an expanded view of the wire geometry. Height and width modelled with one discretisation (Δx, Δy respectively), length with between 3 and 12 (Δz)

As seen in Fig. 1 the wirebond is approximated using three straight two dimensional sections. The wirebond height and width is modelled with 1 discretisation step in the x and y directions respectively. The horizontal section has between 3 and 12 discretisations depending on the length of the wirebond.

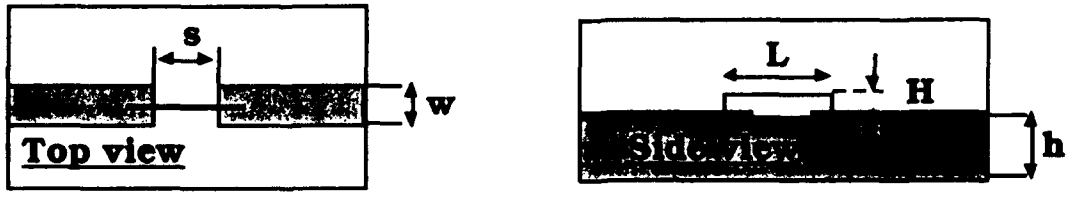

Fig. 2: Dimensions associated with the wirebond structure. (s = gap length, L = wire length, H = wire height, w = line width, h = substrate thickness)

The application of the gaussian excitation pulse homogeneously under the microstrip line [3], is known to produce a DC-offset error in the tangential magnetic field. The use of several discretisation steps for the x-direction (Fig.1) inside the substrate causes an increase of this error, as even more Electric Field E_x components are homogeneously treated. This error is especially exaggerated when the microstrip line width to substrate thickness w/h ratio drops below 1, as the homogeneity condition is even less true for the field below the microstrip line. Hence for wirebond structures here

with a w/h ratio of 0.8, only 4 or 5 discretisation steps in the substrate are taken. This reduces the number of overall discretisation steps as well as the DC offset error, which if not contained, produces the familiar Gibb's phenomena ripple in the frequency domain when computing the S parameters using the fast fourier transform (FFT). In some cases, the pulse can be truncated at the final zero crossing with negligible loss of information or a windowing function may be used.

The total number of discretisation steps in the three directions x, y, z produce a 20, 105, 90 mesh respectively, amounting to 190000 cartesian cells. As the Mur's first order ABC is used [4], about a 20h (h=substrate thickness) distance is required in the y direction to avoid surface wave reflections. With microstrip structures the number of discretisation steps in the x direction can be minimised to around 20 steps as here the reflection is always minimal. In the z direction the reflection is significant for high dielectric constant values, due to the use of a non dispersive ABC. With approximately 90 steps this reflection from the end wall however can be separated from the transmitted gaussian pulse, which is recorded under the second microstrip line $30\Delta z$ away from the end wall. One must make sure that the DC offset error of the output pulse is less than that of the input so that the transmission coefficient is not greater than one for low frequencies (the input pulse is recorded at $30\Delta z$ from the excitation plane, where a quasi TEM mode exists). The FDTD is used with a non-equidistant grid in order to increase the accuracy of modelling the wirebond dimensions. The results show that the FDTD performs at best, when a non equidistant grid can be used to discretise the structure in an exact manner dimensionally. Hence in the x direction Δx is varied between 0.14 and 0.16 mm, similarly Δy between 0.03 and 0.13mm and Δz between 0.125 and 0.13mm.

In accordance with the rules given in [3] these discretisations produce a Δt of 0.0544 picoseconds, which provides information up to about 70 GHz for the gaussian pulse. For these structures therefore with 4000 time steps, a CPU time of about 7 hours is attained on a HP9000/735 workstation. If an extension of this frequency range is required a smaller Δt can be chosen, this would require finer discretisation in the z direction such that the narrower time pulse still occupies the mandatory 20 space steps. This results not only in a greater mesh, but a larger number of time steps, as the oscillations from the shorter pulse need to decay. This can drastically increase the CPU time. Tests conducted on a Fujitsu 2600, 5 Gflop vectorised machine demonstrated that no saving in time could be achieved. This is due to the inherent suitability of the FDTD algorithm to parallel machines.

Capture of the Propagating Pulse

All pulses in this section are recorded for the E_x component of the electric field directly under the microstrip line. The propagation of the gaussian pulse is recorded at four different time instants for the case of $\varepsilon_r = 10.8$, w = 0.55, h = 0.635, s = 0.1mm, L = 0.35mm, H = 0.14mm shown in Fig. 3. The dimensional symbols are referenced according to Fig. 2.

In Fig. 3, at $t = 866\Delta t$ the initial launched pulse with an initial reflection beginning at the wirebond is shown. At $t = 1066\Delta t$ the reflected initial part of the pulse begins to travel into the still approaching pulse. At $t = 1266\Delta t$ the reflected and transmitted pulse separate and travel in opposite directions. At $t = 1666\Delta t$ trailing pulses are seen due to multiple reflections at the wire and microstrip open ends. An overlapping of pulses additionally occurs.

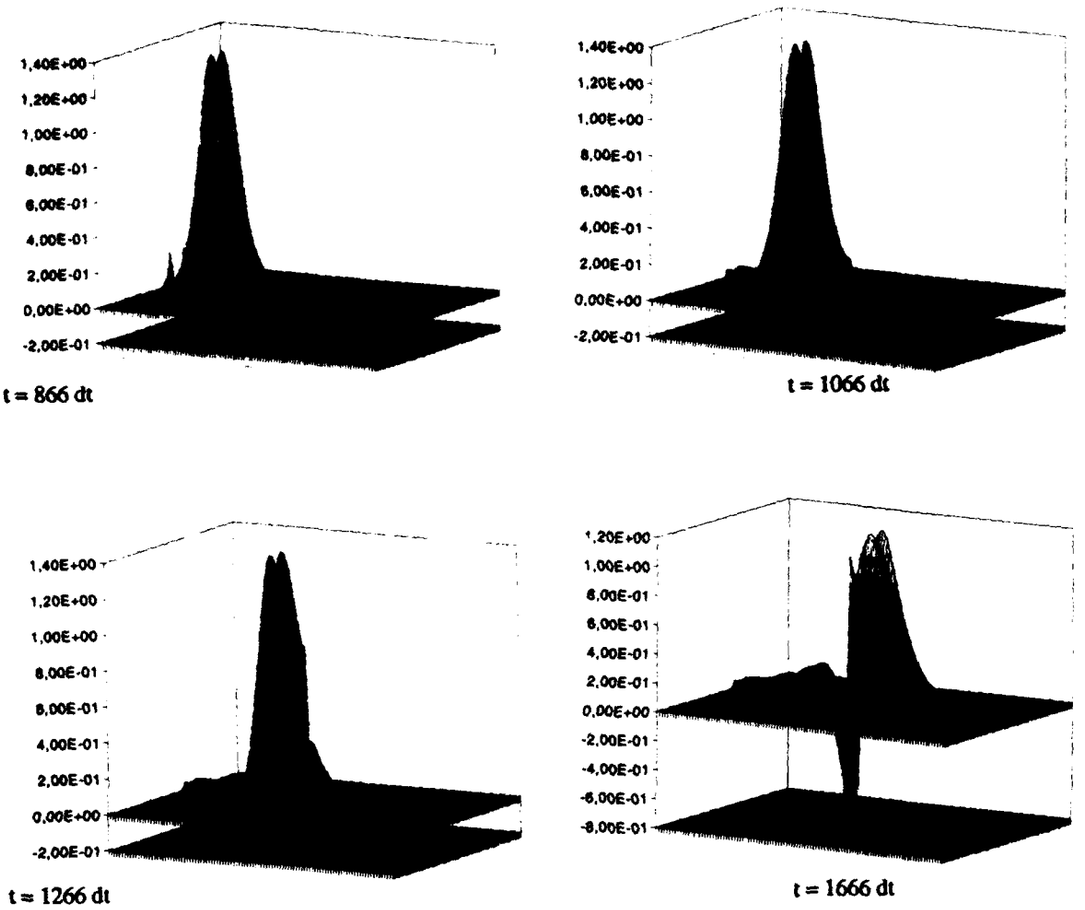

Fig. 3: Propagating pulse shown at four time instants. (E_x component plane directly below the microstrip line) For graphical purposes the end ABC is placed a few grid positions inside from the boundary.

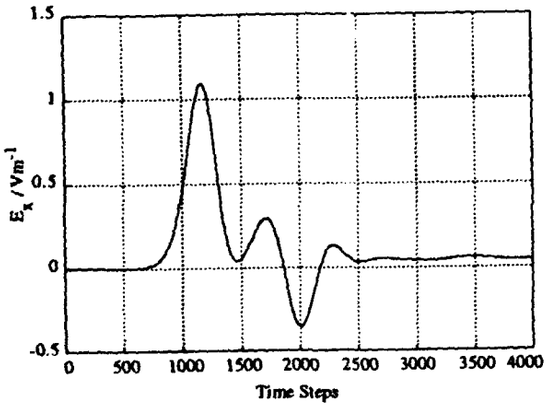

Fig. 4a: The total signal consisting of the incident pulse being reflected at the wirebond taken at 30 Δz from the excitation plane. (The centre E_x component under the microstrip line)

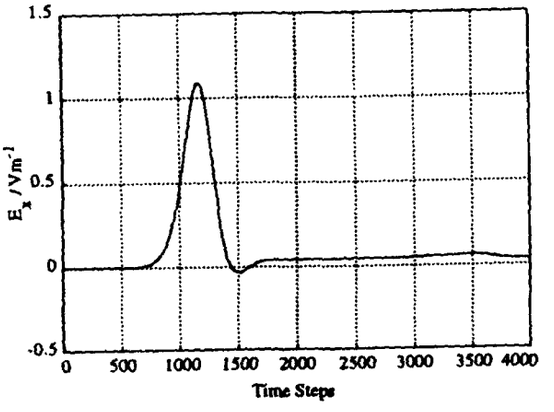

Fig. 4b: The input signal recorded at 30 Δz from the excitation plane. (The centre E_x component under the microstrip line)

For the case of ε_r = 10.8, w = 0.55, h = 0.635, s = 0.1mm, L = 0.35mm, H = 0.14mm time continuous signals for the total, input and output signals are shown in Figures 4a,b,c respectively. The total signal, the centre E_x component under the microstrip line, consists of the incident pulse being reflected at the wirebond taken at 30 Δz from the excitation plane. The input signal in a separate computation, is recorded at 30 Δz from the excitation plane for a length of microstrip line reaching the far ABC wall. The output signal is recorded at 30 Δz from the end wall. The reflected signal is obtained by subtracting the input from the total signal. These quantities with fourier transformation provide the necessary S parameters.

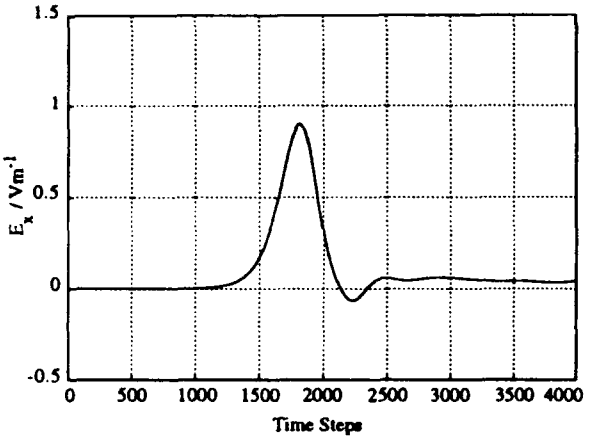

Fig. 4c: The output signal from the wirebond recorded at the 30 Δz from the end wall. (The centre E_x component under the microstrip line)

Measurements on Wirebonds

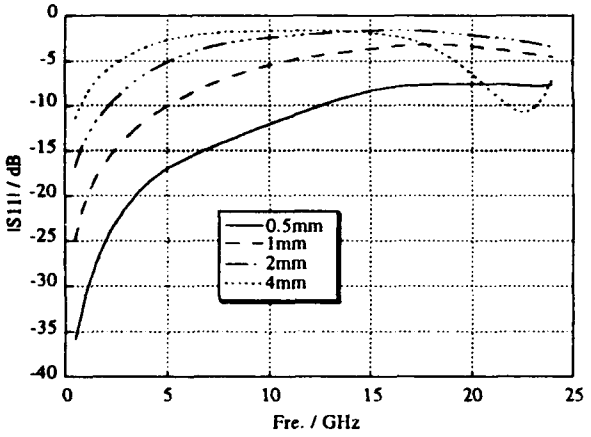

Fig. 5a: Measurement (gated) of $|S_{11}|$ for variation of s.

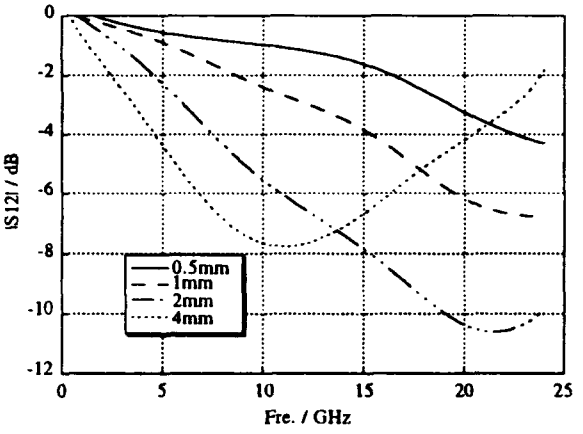

Fig. 5b: Measurement (gated) of $|S_{12}|$ for variation of s.

Several wirebond structures with variation of s shown in Fig. 2 for lengths of 0.5mm, 1mm, 2mm, and 4mm connecting microstrip lines on a duroid 6010 substrate (ε_r = 10.8, tanδ = 0.0024, w = 0.55, h = 0.635, H = 0.14mm) are measured using Thru Reflect Line TRL [5] techniques. The measurements in Fig. 5a,b shows the magnitude of reflection $|S_{11}|$ and transmission $|S_{12}|$ respectively. A rapid increase in reflection and decline in transmission is noticed as the wire length increases. In fact the wirebond shows a band stop filter behaviour, where the stop band moves down slowly in frequency as the wire length is increased. This indicates that in order to move the stop band further up in the frequency range and allow a low pass behaviour, wire lengths below around 0.5mm are required. Fig. 5c and 5d compare the FDTD with measurement for the 0.5mm and 2mm cases. The shaded area shows the measurement range. Here extremely good agreement is seen. Again the band stop pattern is seen for the 2mm case where the FDTD is able in addition to show the better transmission properties of the wirebond above 50 GHz. The 2mm structure's $|S_{12}|$ shows some

discrepancy between measurement and transmission. This is due to the use of a two dimensional approximation for the wirebond in the FDTD in contrast to the presence of a circumference for the wire. The 0.5mm structure's $|S_{12}|$ on the other hand shows practically no discrepancy, as the error clearly increases with the length of the wirebond. The above observations lead to focusing attention on modelling structures with s values below 0.5mm in the analysis which follows.

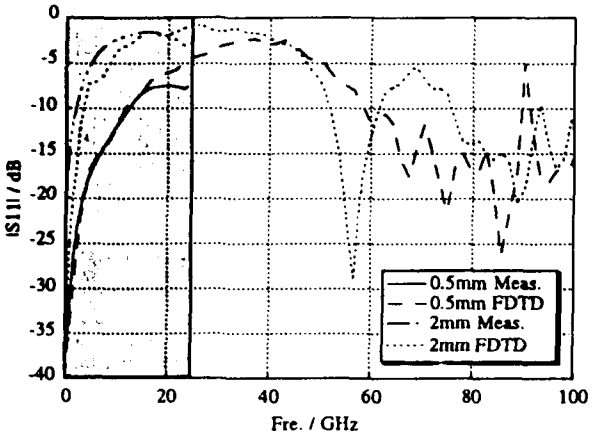

Fig. 5c: Comparison of FDTD and Measurement (TRL) $|S_{11}|$ for variation of s.

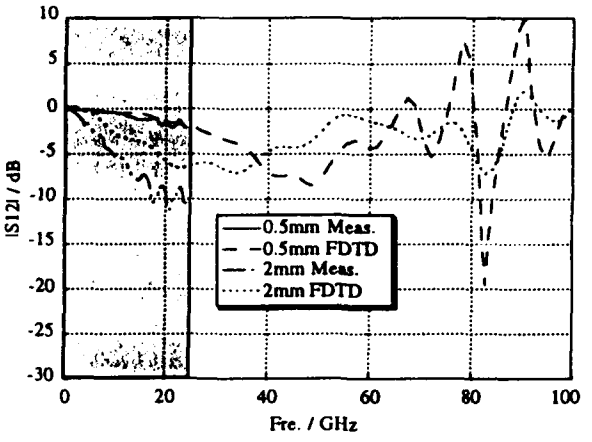

Fig. 5d: Comparison of FDTD and Measurement (TRL) $|S_{12}|$ for variation of s.

Variation of Wirebond Length s with $\varepsilon_r = 10.8$

Fig. 6a with w = 0.55, h = 0.635, L = 0.35mm, H = 0.14mm shows the magnitude of reflection $|S_{11}|$ for s variation. Here it is seen that the reflection increases with the length s. The transmission $|S_{12}|$ in Fig. 6b similarly is seen to suffer with the increase of s. The gradient of the curves however is inversely proportional to the length s and the shortest 0.1mm structure registers the lowest $|S_{12}|$ value. This effect is due to the dominating inductive behaviour of longer lengths of wirebond, which presents a higher overall impedance to the pulse in the frequency range. Yet the results show that both the reflection and transmission characteristics upto around 20 GHz make all three s lengths worthy of implementation. Further, above 60 GHz an improvement in the wirebond S parameters is seen, proving the band stop behaviour of the wirebond.

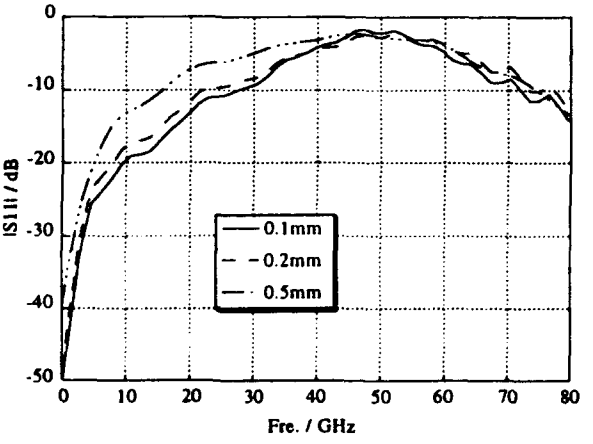

Fig. 6a: $|S_{11}|$ from FDTD for variation of s with $\varepsilon_r = 10.8$.

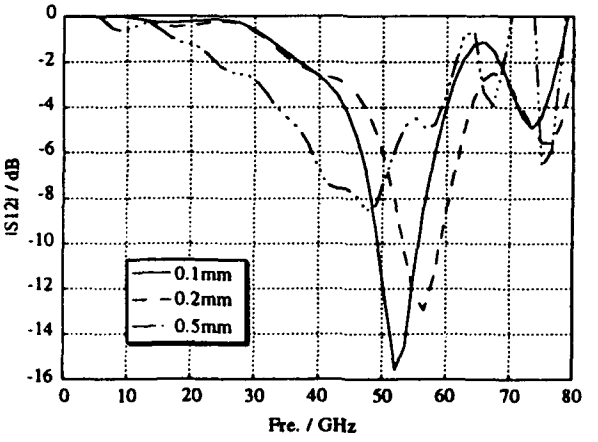

Fig. 6b: $|S_{12}|$ from FDTD for variation of s with $\varepsilon_r = 10.8$.

Variation of Wirebond Length s with $\varepsilon_r = 5$

The value $\varepsilon_r = 5$ is chosen here as it occurs in chip packages. The propagation characteristics shown in Fig. 7a and 7b for reflection $|S_{11}|$ and transmission $|S_{12}|$ respectively (w = 0.55, h = 0.635, L = 0.35mm, H = 0.14mm) provide similar information to the previous case, except for the transmission $|S_{12}|$ which does not show as big a change between s lengths. This means that with a lower dielectric constant, s lengths slightly longer than 0.5 mm can be used.

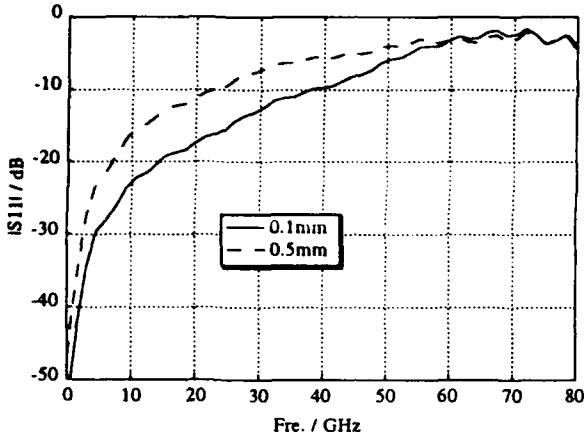

Fig. 7a: $|S_{11}|$ from FDTD for variation of s with $\varepsilon_r = 5$.

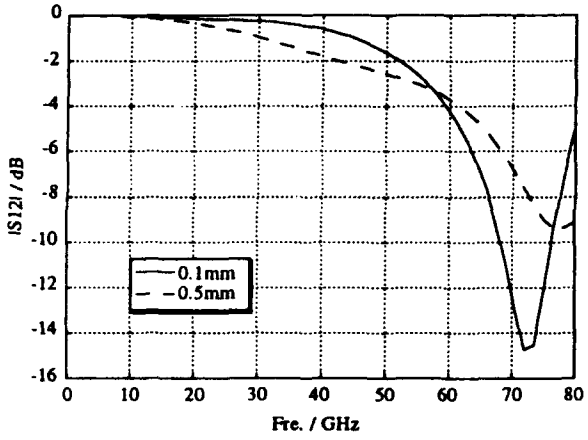

Fig. 7b: $|S_{12}|$ from FDTD for variation of s with $\varepsilon_r = 5$.

Variation of Wirebond Dielectric Constant ε_r

Fig. 8a and 8b show that $|S_{11}|$ and $|S_{12}|$ characteristics respectively are better for the lower value of dielectric material in the lower frequency range (w = 0.55, h = 0.635, s = 0.5mm, L = 0.35mm, H = 0.14mm). Yet at higher frequencies above 50 GHz, where the higher dielectric constant materials band stop behaviour ceases, the lower dielectric material's band remains closed up to around 80 GHz. Some ripple in the $|S_{11}|$ and $|S_{12}|$ values for $\varepsilon_r = 10.8$ is seen. This is, as mentioned earlier, due to the truncation of the DC offset error, which causes a ripple when the FFT is applied. Yet the exact curve can be thought of as following a path in the middle of the ripple.

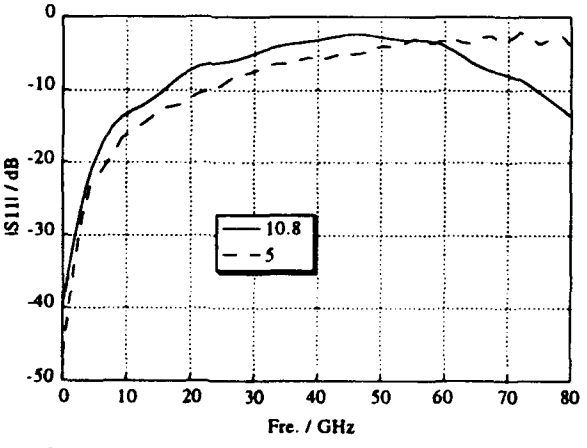

Fig. 8a: $|S_{11}|$ from FDTD for variation of ε_r

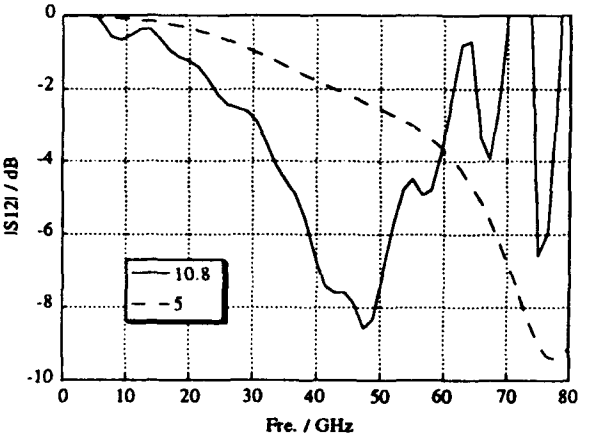

Fig. 8b: $|S_{12}|$ from FDTD for variation of ε_r

Variation of Wirebond Microstrip line Width w

The connecting lines can often vary in width, to this end two different line widths are chosen. With $\varepsilon_r = 5$, h = 0.635, s = 0.1mm, L = 0.35mm, H = 0.14mm, the results in Fig. 9a and 9b show that the effect of the discontinuity worsens with increase in the microstrip line width. The band stop for the 0.55mm width lies further up in the frequency range as for the 0.85mm line width.

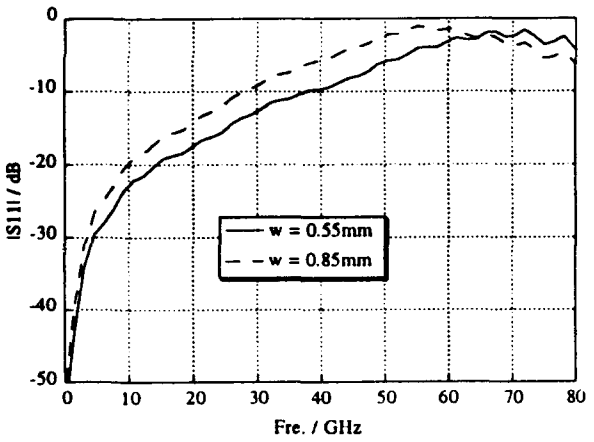

Fig. 9a: $|S_{11}|$ from FDTD for variation of w

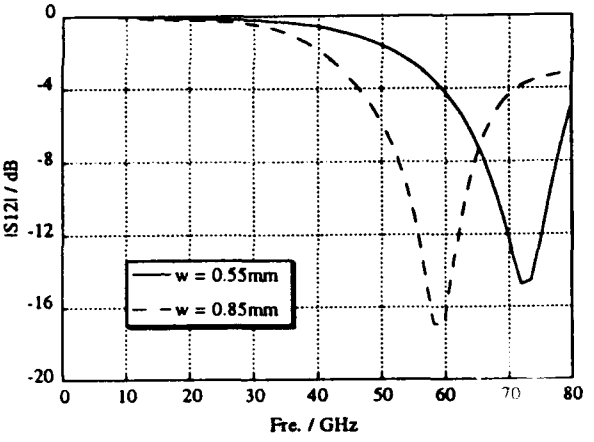

Fig. 9b: $|S_{12}|$ from FDTD for variation of w

Conclusion

The FDTD is used successfully to compute wirebond structures. This is verified through the good agreement achieved with measurement. The variation of the material parameters associated with the wirebond structure in the FDTD comprehensively analyses wirebond behaviour up to 80 GHz. Observations indicate that the capacitative effects caused by the two microstrip open ends connecting with the wirebond can compensate for the inductive behaviour of the wire and allow transmission at the lower GHz range continuing later into a band stop characteristic in the higher GHz range upto about 50 GHz, where the band stop ends and allows transmission again. For lengths of s above 0.5mm, the inductance dominates the impedance presented by the wirebond and indicates its unsuitability for implementation.

Acknowledgement: The authors wish to extend their appreciation to, Abt. VS/ETPE2, Alcatel SEL, Lorenzstr. 10, 70435 Stuttgart for funding this work.

References

[1] E. Pillai, F. Rostan and W. Wiesbeck, "Derivation of Equivalent Circuits for Via Holes from Full Wave Models," *IEE Electronics Letters*, vol. 29, No. 11, pp. 1026-1028, 27th May 1993.

[2] K. S. Yee, "Numerical Solution of Initial Boundary Value Problems involving Maxwell's Equations in Isotropic Media," *IEEE Trans. Antennas and Propagation*, vol. AP-14, pp. 302-307, May 1966.

[3] X. Zhang and K. K. Mei, "Time-Domain Finite Difference Approach to the Calculation of the Frequency-Dependent Characteristics of Microstrip Dicontinuities," *IEEE Trans. Microwave Theory Tech.*, vol. MTT-36, pp. 1775-1787, Dec. 1988.

[4] G. Mur, "Absorbing Boundary Conditions for the Finite-Difference Approximation of the Time-Domain Electromagnetic-Field Equations," *IEEE Trans. on Electromagnetic Compat.*, vol. EMC-23, pp. 377-382, Nov. 1981.

[5] G. F. Engen and C. A. Hoer, "Thru-Reflect-Line: An Improved Technique for Calibrating the Dual Six-Port Automatic Network Analyzer," *IEEE Trans. Microwave Theory Tech.*, vol. MTT-27, pp. 987-993, Dec. 1979.

SPACE AND TIME DISCRETISATION IN FIELD COMPUTATION USING TLM

C. Christopoulos and J.L. Herring
University of Nottingham

Abstract:

The implications for accuracy, resolution and computational demands of a range of meshing techniques used in the transmission-line modelling (TLM) method are described. Particular emphasis is placed on the effectiveness and accuracy of the multigrid technique. It is shown that it can be simply implemented and that it offers better spatial resolution and similar accuracy at low frequencies to other methods at a fraction of computational effort.

1. Introduction

Computation of electromagnetic fields and circuits by numerical means involves discretisation in space and in time. This process may be implemented in a variety of ways. In Transmission-Line Modelling (TLM) discretisation in space is achieved by using lumped circuit equivalents, and in time by describing lumped energy storage components by transmission line segments. Thus, field computation is reduced to solving transmission line networks. Time-discretisation may be applied in the same way to solve general lumped circuits. The discretisation process introduces dispersion and an upper frequency limit to the validity of the computation. The use of a finite number of modelling elements to describe fine features such as wires and plates introduces coarseness errors. Although these errors may be reduced by increasing the number of modelling elements, in practice this leads to unacceptably large computer requirements. The demands of simulating complex systems inevitably lead to the requirement for multigrid methods and graded mesh techniques better suited to particular problems.

The implementation of TLM in recent years is based on the three-dimensional symmetrical condensed node (SCN) pioneered by P.B. Johns[1]. The basic twelve-port node is useful for modelling cubical space blocks and uniform materials. The addition of open and short-circuit stubs introduces the flexibility of modelling inhomogeneous space (different ε_r and μ_r) and also non-cubical basic blocks (variable or graded mesh). The addition of stubs increases dispersion and also imposes a very small timestep. Both these disadvantages may be reduced by the hybrid symmetrical condensed node (HSCN)[2-4] where only open-circuit stubs are used, at the expenses of introducing three different link line impedances. In its most general form the HSCN with electric and magnetic lossy stubs can be used to model very general configurations[4]. In the modelling of wire-like structures or thin plate conductors it is advantageous to use the HSCN in a configuration based on long and thin basic nodes. However, the complexity of problems confronting the modeller is such that new more flexible approaches to space discretisation are necessary.

A decisive step in this direction may be taken if the problem space is divided into regions where space discretisation is done on the basis of the resolution required locally and not other global considerations. This development referred to as the multigrid or subgrid technique has been described in connection with TLM in [5,6]. The basic difficulty in such an approach manifests itself in TLM in the following form: If a different space-step is used on either side of the interface between two different regions, this inevitably leads to different time steps (loss of synchronism), and the loss of one-to-one correspondence between nodes on either side of the interface (loss of connectivity). It is evident that some form of space and time averaging is necessary at the interface. A pulse conversation scheme to be used at the interface was proposed in [5,6]. The scheme is based, ideally, on adherence to the following principles:

(i) conservation of energy
(ii) conservation of charge
(iii) no reflections and zero delays at interface

As is shown in the references already cited, it does not appear possible to meet all three requirements without increasing complexity to the extent that it neutralises any benefits of the multigrid mesh. The scheme which the authors have found to be most efficient is one in which energy conservation is not explicitly imposed. The implications of this are explored in this paper. In order to understand more fully energy relations in a multigrid mesh the situation is first explored in a uniform mesh.

2. Energy in a Uniform Mesh

The electric and magnetic fields can be calculated either at a node or on the link-lines connecting nodes. It is convenient to obtain the field at a node when several field components are required at the same point and it is appropriate to consider the field on link-lines when dealing with closed surfaces (e.g. when calculating the power flow through a surface surrounding an antenna). This last point is illustrated in Figure 1 where it is apparent that corner nodes have to be treated as a special case if node outputs are taken (Figure 1a) but link-line outputs can be processed in a uniform manner (Figure 1b). There is often found to be little difference between the two types of output beyond any expected spatial variation. The field at a node can be considered as an average value obtained from the voltage pulses (either incident or reflected) on the contributing transmission-lines. This has important implications when calculating the stored energy since, when several quantities are considered, the sum of the squares is not equal to the square of the sum. If high frequency energy is present then values of energy calculated from fields at a node can be very different to those calculated from fields on link-lines.

In the time-domain, for a single link-line with voltage pulses v_1 and v_2, the electric and magnetic fields are given by:

$$E = -\frac{1}{\Delta l}(v_1 + v_2) \quad \textit{and} \quad H = \pm\frac{1}{Z_o \Delta l}(v_1 - v_2)$$

The electric and magnetic energy densities, w_e and w_m are given by:

$$w_e = \frac{1}{2}\,\epsilon\, E^2 = \frac{\epsilon}{2\Delta l^2}(v_1 + v_2)^2 \quad \textit{and}$$

$$w_m = \frac{1}{2}\mu H^2 = \frac{\mu}{2Z_o^2 \Delta l^2}(v_1 - v_2)^2$$

The total energy density can then be written as:

$$w = \frac{1}{cZ_o \Delta l^2}(v_1^2 + v_2^2)$$

The total energy stored in the whole mesh is given by:

$$W = \frac{\Delta l}{cZ_o} \sum_n v_n^2$$

where the summation is taken over all ports on all nodes. The stored energy calculated from fields on link-lines is therefore proportional to the total energy of the individual voltage pulses and, because the scattering matrix is unitary for a system with no losses, this stored energy will be the same on successive timesteps. This condition is not met if the energy is calculated from fields at nodes. However, at low frequencies, where the field variation is small, similar results may be obtained from both link-line and node outputs.

To compare the values of energy obtained from the field at nodes and the fields on link-lines, a loss-free cubic cavity is considered. For node outputs, the short-circuit boundaries are placed at the mid-point of link-lines and for link-line outputs the boundaries are modelled with short-circuit nodes, thus avoiding the added complexity of including incomplete link-lines in the energy calculation. The system is excited by placing x-polarised voltage sources at the mid-point of two sets of link-lines - one parallel to the y-axis and the other parallel to the z-axis. This choice of excitation avoids the situation which occurs when only one set of link-lines is excited and voltage pulses are zero on alternate link-lines and during alternate timesteps and is thus representative of a real system.

For these comparisons, the factor $1/cZ_o$ is omitted and the node spacing is set to unity. The energy is calculated from one of the following expressions:

$$\sum_n v_n^2 \tag{1}$$

$$\sum_n E_{node_n}^2 + Z_o^2 \sum_n I_{node_n}^2 \tag{2}$$

$$\sum_n E_{line_n}^2 + Z_o^2 \sum_n H_{line_n}^2 \tag{3}$$

Figure 2a shows the value of expression (1) evaluated on each of 500 timesteps when an impulse excitation is applied and boundaries are placed at the mid-point of link-lines. The simulation was performed using single precision real numbers and this accounts for the very small perturbations about the nominal value. Some single precision implementations can cause a very slight increase in energy with time, but this is not a significant problem. Figure 2b shows the value of expression (2) over the same period. It is apparent that the energy is not constant with time and, more importantly, the nominal value is significantly less than the expected value of 8. The energy calculated from expression (3) is shown in Figure 2c. There are two orthogonal sets of link-lines for each polarisation and so the expected value is 16. Within the accuracy of single-precision numbers, the expected result is obtained.

The disadvantage of an impulse excitation is that it introduces energy at frequencies well above the accepted maximum working frequency of the mesh, which is generally taken to be that corresponding to a wavelength of 10 nodes. The calculation of energy within a more realistic frequency range can

be studied by replacing the impulse excitation with a Gaussian source. In discrete form, such a source function can be written as:

$$f[n] = \exp\left(-\frac{n^2}{2s^2}\right)$$

where s is the standard deviation expressed in terms of the timestep ($s = \sigma/\Delta t$). Choosing s as 10, injects a signal which is 0.7% of its d.c. value at a wavelength of 10 nodes and 29% at 20 nodes. The corresponding energy curves are shown in Figure 3, over a period of 500 timesteps after the Gaussian pulse has decayed to zero. The nodal energy varies between 98.60% and 99.34% of the expected value and, although an underestimate, the error is not that great. The link-line energy varies between 99.448% and 99.462%. The fact that this energy is consistently low can only be attributed to single precision arithmetic errors.

The calculation of energy in the presence of stubs can be illustrated for the same system by reducing the timestep. For example, if the hybrid node is used and the timestep is halved then the normalised link-line admittance must be 0.5 and open-circuit stubs of normalised admittance 6 must be added. Expression (1) must be modified to include the transmission-line admittance and voltage pulses on both link-lines and stubs must be included in the summation:

$$\sum_n \hat{Y}_n v_n^2 \qquad (4)$$

where $\hat{Y}_n$ is the normalised admittance. The total energy in the link-lines and in the stubs is shown separately in Figures 4a and 4b, respectively. The response is dominated by the first few resonances. The stub energy oscillates in sympathy with the electric field since open-circuit stubs are electric energy storage components. The oscillation of the link-line energy is similar to that of the magnetic field, although the link-lines also store electric energy. The total energy calculated from expressions (4), (2) and (3) is shown in Figure 5. In this case, the value of energy calculated from individual voltage pulses is twice the energy stored in the field. Reasonable estimates are obtained from both node and link-line outputs. The nodal energy varies between 99.335% and 99.763% of the expected value and the link-line energy varies between 99.565% and 100.007%. In the presence of stubs, the link-line energy would be expected to give a poorer estimate, since the stub voltages are not explicitly included, but this is not the case.

3. Energy in a Multigrid System

In a multigrid system, there is inevitably a loss of energy as pulses are converted from the fine mesh to the coarse mesh. Tests must be performed to ensure that this problem does not prevent useful results from being obtained. In this section, the system considered consists of a cubic cavity which is divided into two halves, both modelled with the same resolution, and Figure 6a shows the energy in each of the two halves, as well as the total energy, when an impulse excitation is applied in one half. The energy is calculated from the individual voltage pulses (expression (1)) and the graph is plotted over a period of 2000 timesteps. In the steady state there is approximately equal energy in each half. Figure 6b shows the corresponding curves when one half of the cavity is modelled with a 40x40x20 node fine mesh and the other is modelled with a 20x20x10 node coarse mesh in which the timestep is twice that of the fine mesh. The impulse excitation is applied in the fine mesh. It is apparent that the total energy is decaying exponentially and there is consistently more energy in the fine mesh. After 2000 fine mesh timesteps, the fine mesh contains 9.3% of the original energy and

the coarse mesh contains 3.2%. If the impulse excitation is applied in the coarse mesh then the curves shown in Figure 6c are obtained. Again, the excitation region contains consistently greater energy, but here, the total energy loss is reduced. The final values of energy are 11.6% in the fine mesh and 19.1% in the coarse mesh. When the excitation is applied in the coarse mesh, the excitation region contains proportionally less energy than when the excitation is applied in the fine mesh. This leads to the conclusion that, in a multigrid system, the fine mesh will tend to contain more high frequency energy than the coarse mesh. Also, there is some difficulty in transferring the high frequency energy introduced by the impulse excitation across the interface since, in both cases, the excitation region contains more energy than the other region.

The fact that energy is lost at high frequencies does not necessarily present a problem since it is usually only wavelengths above the 10 node limit which are of interest. Figure 7a shows the energy in the same multigrid system when a Gaussian pulse with a standard deviation of 20 fine mesh timesteps is applied in the fine mesh region. The response is dominated by the first few resonances but it can be seen that there is approximately equal energy in the fine and coarse mesh regions. The final energy is reduced to 88.6% of its initial value after 2000 timesteps. The slight oscillation in the total energy is due to the fact that some energy at the interface was not considered. The effect of different reduction ratios on the total energy is shown in Figure 7b. The standard 2:1 result is shown again as well as a 2:1 reduction in space only, in which the hybrid node is used to run the coarse mesh with the same timestep as the fine mesh. A 4:1 reduction in both space and time is also shown in which a coarse mesh of 10x10x5 nodes is used. As expected, the energy loss is greatest for the greatest reduction ratio. In general, the loss of energy will depend upon the system modelled, the location and extent of the interface and the reduction ratio. If the area of the interface can be reduced as far as possible, then the loss of energy will often be much less than indicated by the above results even for quite severe reduction ratios.

4. Example

In this section, two different meshing techniques are applied to a problem to demonstrate their relative efficiency and accuracy. The multigrid technique with a 7:1 reduction ratio is compared with a graded mesh using the hybrid node. The system under consideration consists of a 1m dipole placed centrally in a $1.1 \times 1.1 \times 2.0 m^3$ cavity. For the multigrid case, cubic nodes are used and a 21x21x112 0.476cm fine mesh is placed inside a 33x33x30 3.33cm coarse mesh. For the graded mesh case, the largest node dimension is 3.33cm and this is gradually reduced to model the dipole cross-section and to place a cubic node at the dipole centre. For a dipole in free-space there is negligible difference between the two methods but when many timesteps are performed in a closed system, the energy loss for the multigrid mesh can be observed. The current at the centre of the dipole is shown in Figures 8a and 8b for the multigrid and graded mesh methods, respectively. The resonant frequencies are in good agreement but there is a reduction in amplitude for the multigrid case, particularly for the 414MHz resonance. A comparison of the computer resources is shown in Table 1. The values for the uniform fine mesh have been estimated for obvious reasons.

Table 1

	mesh	storage	timesteps	cpu time
uniform fine	231x231x210	513 Mbyte	42000	>30 days
7:1 multigrid	33x33x30 coarse 21x21x112 fine	4.0 Mbyte	6000 coarse 42000 fine	213 min.
graded	69x69x51	19.5 Mbyte	42000	2189 min.

5. Discussion and Conclusions

The implications of different discretisations in parts of space were explored with emphasis on energy conservation. Undeniably, further work needs to be done to address in more detail issues raised and to propose alternative conversion schemes at the interface between regions described by a different mesh. It appears that the worst case is that of a problem in a loss-less cavity where any approximations in the conversion scheme have a more noticeable effect as signals suffer repeated passes through the interface. In contrast lossy or open-boundary problems are unlikely to be affected by such approximations. This is fortunate as it is with open-boundary problems where the need for multigrid techniques is the greatest. Resolution ratios as high as 9:1 have been implemented without instability but with a smaller energy loss. This energy is mainly associated with high-frequency signals, beyond the coarse mesh frequency cut off point, and it is therefore of little significance. Since the cut-off characteristics are not sharp, some care must be taken in applying multigrid techniques and in intercepting results. This is particularly true for high resolution ratios and at frequencies near the cut-off point. It appears that minimising the extent of the interface between regions of different resolution is a good practice and must be adhered to as far as possible.

6. References

1. Johns, P.B: "A symmetrical condensed node for the TLM method", IEEE Trans, MTT-35, 1987, pp370-377.

2. Scaramuzza, R.A. and Lowery, A.J: "Hybrid symmetrical condensed node for the TLM method", Electronics Letts, 26, 1990, pp1947-1949.

3. Scaramuzza, R.A. and Christopoulos, C: "Developments in transmission line modelling and its application in electromagnetic field simulation", Int.Jrnl. for Computation and Mathematics *in Electrical and Electronic Engineering*, 11, 1992, pp49-52.

4. Scaramuzza, R.A, Naylor, P.N. and Christopoulos, C: "Numerical simulation of field-to-wire coupling using transmission line modelling", Int.Conf. on Computation in Electromagnetics, 25-27 Nov. 1991, IEE, London, pp63-66.

5. Herring, J.L. and Christopoulos, C: "Multigrid transmission line modelling method for solving electromagnetic field problems", Electronics Letts, 27, 1991, pp1794-1795.

6. Christopoulos, C. and Herring, J.L: "Developments in the transmission line modelling (TLM) method", Proc. 8th Annual Rev. of Progress in Applied Computational Electromagnetics, Mar 16-20, 1992, NPS, Monterey, CA, USA, pp523-530.

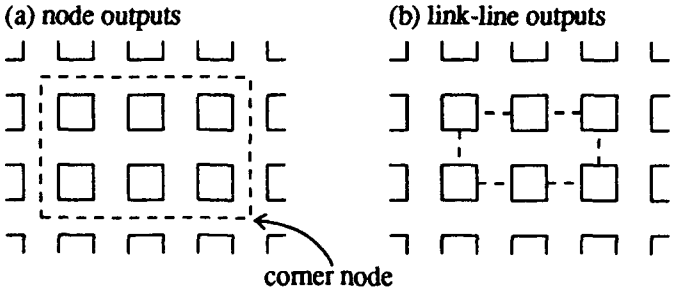

Figure 1 – Taking outputs on a closed surface

(a) Energy from voltage pulses

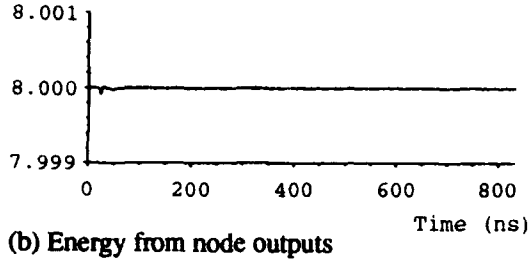

(b) Energy from node outputs

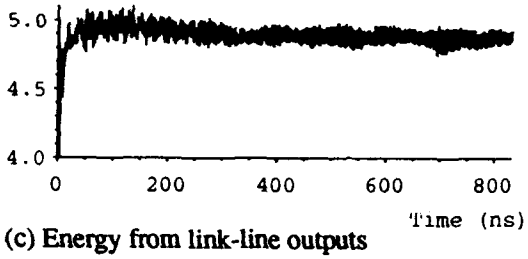

(c) Energy from link-line outputs

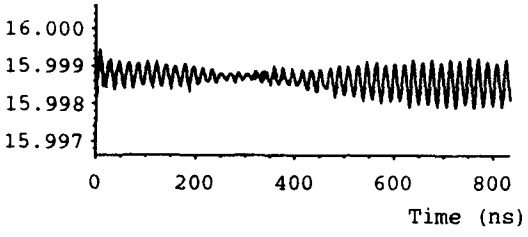

Figure 2 – Uniform mesh with impulse source

(a) Energy from voltage pulses

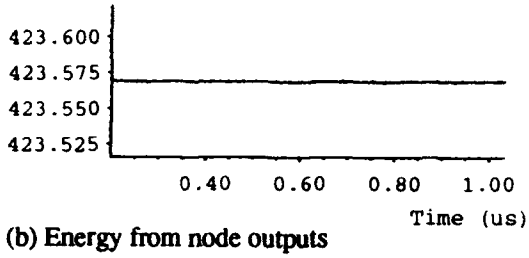

(b) Energy from node outputs

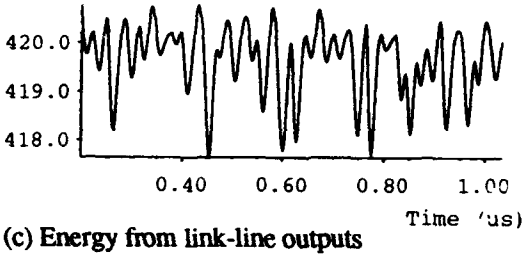

(c) Energy from link-line outputs

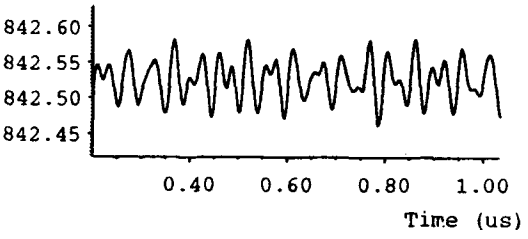

Figure 3 – Uniform mesh with Gaussian source

(a) Link-line energy

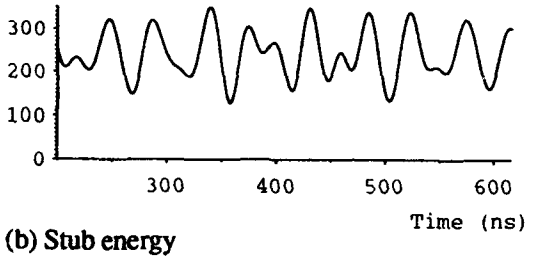

(b) Stub energy

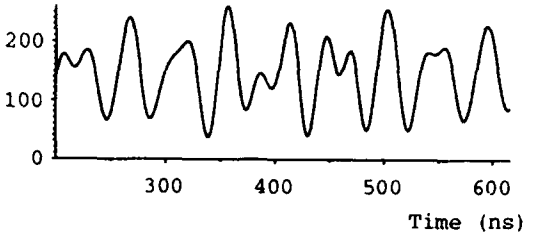

Figure 4 – Hybrid node with Gaussian source

(a) Energy from voltage pulses

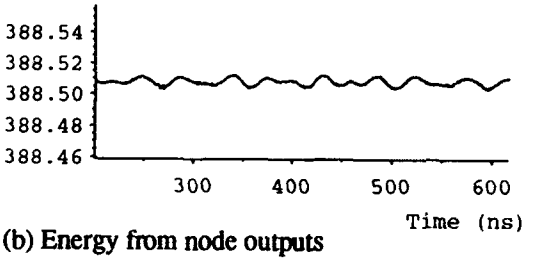

(b) Energy from node outputs

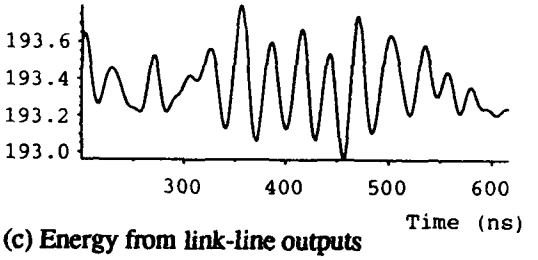

(c) Energy from link-line outputs

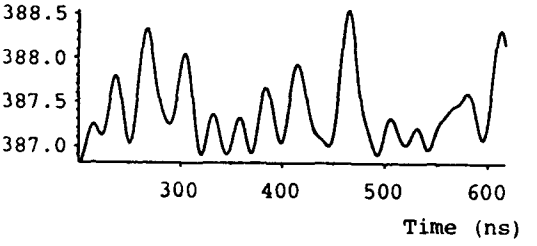

Figure 5 – Hybrid node with Gaussian source

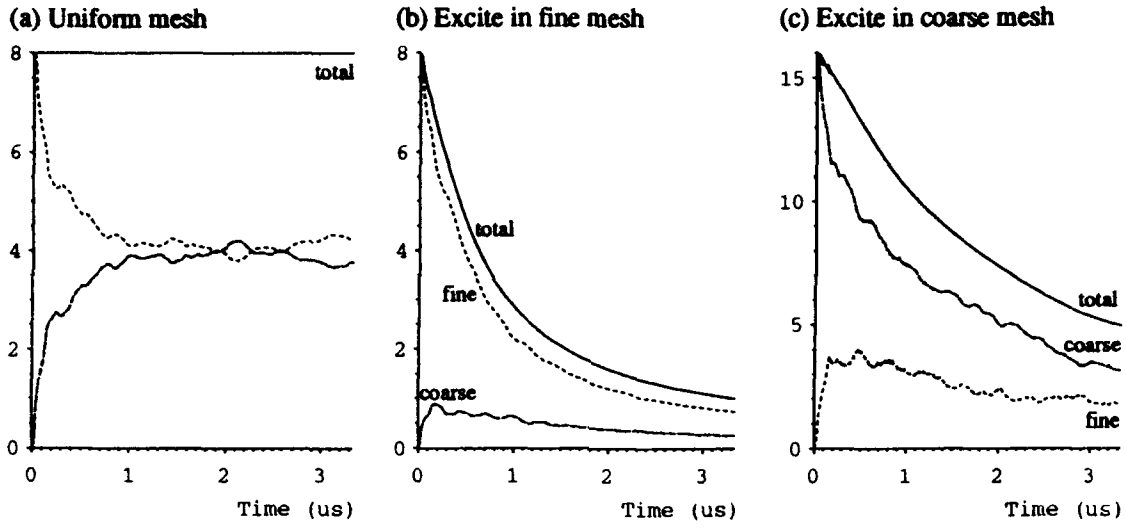

Figure 6 – Cavity with impulse source

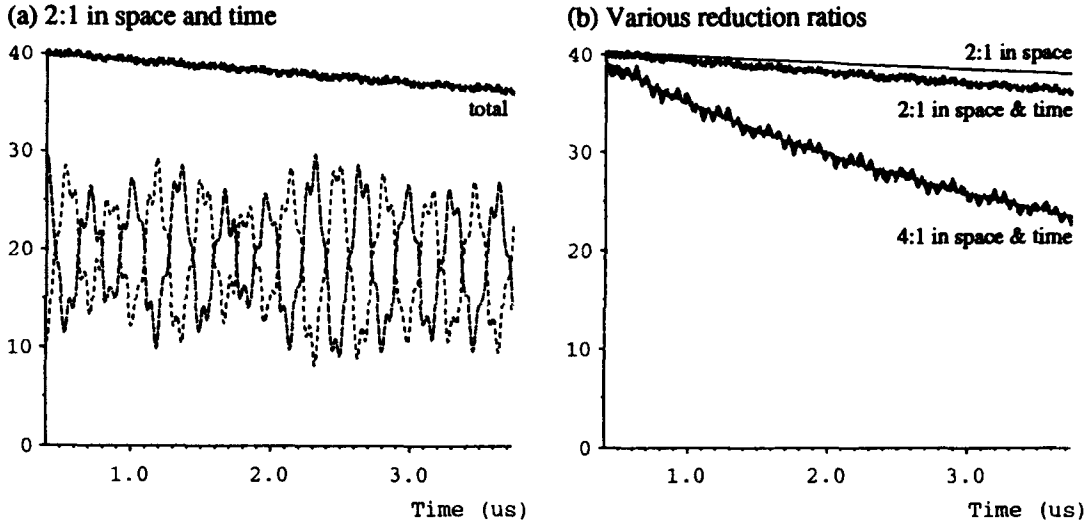

Figure 7 – Cavity with Gaussian source

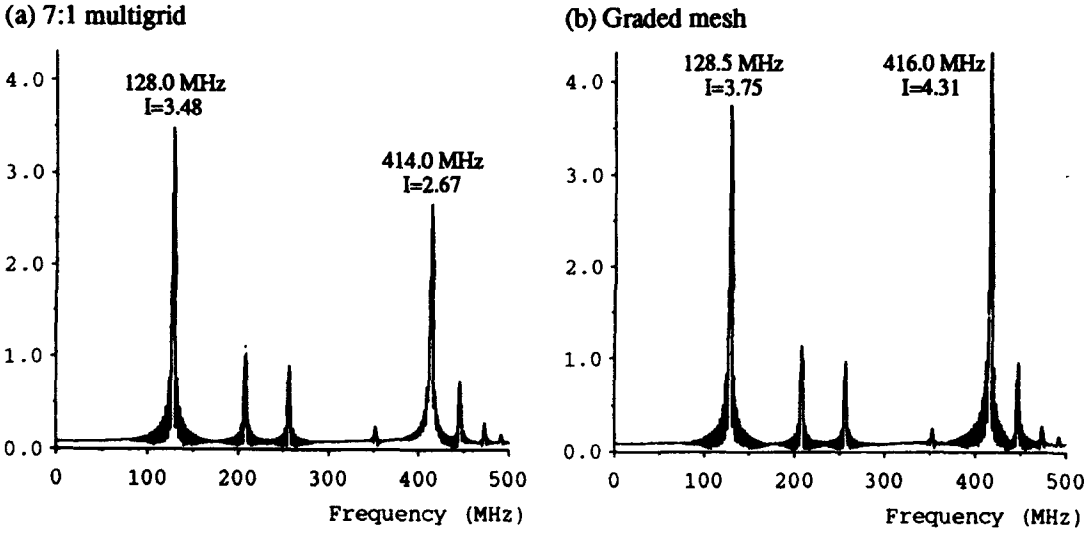

Figure 8 – Current at the centre of a dipole in a closed cavity

Distributed Computing for Transmission Line Matrix Method

Poman P.M. So and Wolfgang J.R. Hoefer

NSERC/MPR Teltech Research Chair in RF Engineering
Department of Electrical and Computer Engineering
University of Victoria, Victoria, B.C., Canada, V8W 3P6
Tel: (604) 721-6511
Fax: (604) 721-6230
E-Mail: Poman.So@ECE.UVic.CA

Abstract

Time domain methods such as TLM and FDTD are attractive numerical techniques, but they are also very computer time intensive. Therefore, techniques of computing must be developed to reduce the execution time for these methods so that they can be used routinely in commercial CAD software. Parallel computing is one possible approach; another procedure that can be employed together with parallel computing, is distributed computing. This paper addresses the basis of distributed computing techniques in the UNIX environment and then applies the technique to parallel TLM computation.

Introduction

The basis of distributed computing is a client-server communication protocol. The field simulation program must be broken down into a client module and one or more server modules. The client and server modules communicate with each other through a client-server communication protocol. Distributed computing can then be achieved by installing server modules on all the machines connected to a network, say internet. This idea can be implemented easily in the UNIX environment by using its *pipe*, *fork* and *execlp* commands.

UNIX Piping Technique

UNIX was designed for programs to work together seamlessly; *piping* is one of the techniques available to achieve this. This idea can be easily illustrated by the following command combination: `ps | sort`. The `ps` command prints information about processes associated with the current terminal. The | operator sends the output of the `ps` command to a sorting program `sort`. The fascinating thing, which is not obvious to the normal UNIX users, is that the `ps` and `sort` commands are executed concurrently; the data produced by the `ps` command are sent directly to the `sort` command via the internal memory of UNIX. Therefore, no temporary file is needed and transfer of data between the two programs is very fast. This is a uni-directional *piping* example: `ps` can send data to `sort` but `sort` has no means to send data back to `ps`. This is only a limitation of the command interpreter, or *shell* as it is called, not that of the UNIX operating system.

```
#include <fstream.h>

class Pipes{
public:
        Pipes(char *child_program, char *arg1="", char *arg2="");
       ~Pipes(){ifs.close(); ofs.close();}
  void  flush() {ofs.flush(); }
  int   okay()  { return (ifs && ofs)?1:0;}
  //---------------------
  //   Input Operators
  //---------------------
  Pipes &operator>>(char   &c){ ifs>>c;  return *this; }
  Pipes &operator>>(char   *s){ ifs>>s;  return *this; }
  Pipes &operator>>(int    &i){ ifs>>i;  return *this; }
  Pipes &operator>>(float  &f){ ifs>>f;  return *this; }
  Pipes &operator>>(double &d){ ifs>>d;  return *this; }
  Pipes &operator>>(long   &l){ ifs>>l;  return *this; }
  //----------------------
  //   Output Operators
  //----------------------
  Pipes &operator<<(char   c){ ofs<<c<<' '; return *this; }
  Pipes &operator<<(char   *s){ ofs<<s<<' '; return *this; }
  Pipes &operator<<(int    i){ ofs<<i<<' '; return *this; }
  Pipes &operator<<(float  f){ ofs<<f<<' '; return *this; }
  Pipes &operator<<(double d){ ofs<<d<<' '; return *this; }
  Pipes &operator<<(long   l){ ofs<<l<<' '; return *this; }
protected:
  ifstream ifs;
  ofstream ofs;
};//--- Pipes ---//
```

(a) Pipes.h

```
#include "Pipes.h"
#include <sys/unistd.h>
#include <stdio.h>
#include <stdlib.h>

Pipes::Pipes(char *child_program, char *arg1, char *arg2):ifs(),ofs(){
int p1[2],p2[2];
  //---------------------
  //   Create pipe-one
  //---------------------
  if (pipe(p1)){
    cerr << "Pipes::Pipes --- Cannot Create pipe-one!" << endl;
    exit(1);
  }
  //---------------------
  //   Create pipe-two
  //---------------------
  if (pipe(p2)){
    cerr << "Pipes::Pipes --- Cannot Create pipe-two!" << endl;
    exit(2);
  }
  if (fork()){
  //------------------------
  //   The parent process
  //------------------------
    if (fdopen(p1[0],"r")==NULL){
      cerr << "Pipes::Pipes --- Cannot open pipe two for input!" << endl;
      exit(3);
    }
    ifs.attach(p1[0]);
    close(p1[1]);
    if (fdopen(p2[1],"w")==NULL){
      cerr << "Pipes::Pipes --- Cannot open pipe for output!" << endl;
      exit(4);
    }
    ofs.attach(p2[1]);
    close(p2[0]);
  }
  else{
    //-----------------------
    //   The child process
    //-----------------------
    close(1); dup(p1[1]); close(p1[1]); close(p1[0]);
    close(0); dup(p2[0]); close(p2[0]); close(p2[1]);
    execlp(child_program,child_program,arg1,arg2,NULL);
    cerr << "Pipes::Pipes --- Cannot load " << child_program << "!" << endl;
    exit(5);
  }
}//--- Pipes::Pipes ---//
```

(b) Pipes.C

Listing 1 **A C++ implementation of a bi-directional pipe. Knowledge in C++, [1], and UNIX, [2], is needed in order to fully understand the listing. Computational practitioners only need to know how to use this object in their C++ programs.**

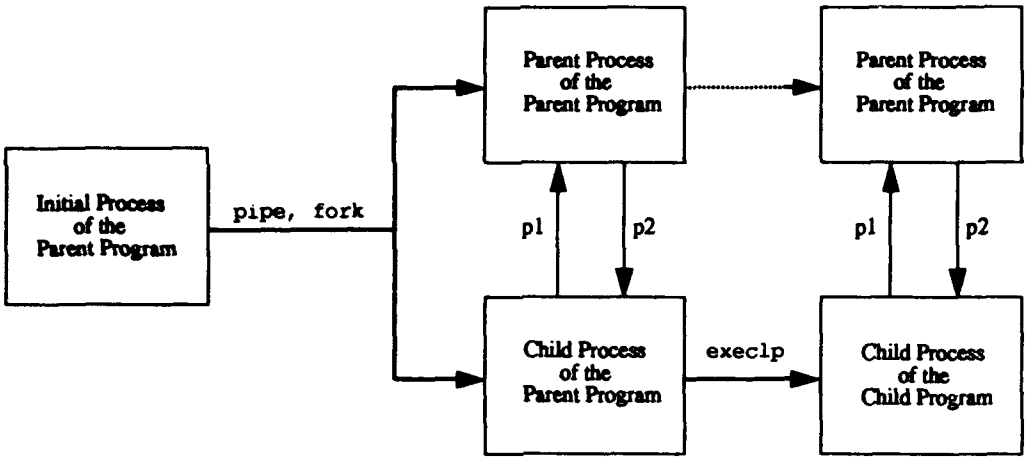

Figure 1 The sequence of events that take place when the `pipe`, `fork` and `execlp` commands are executed.

Listing 1 shows a C++ implementation of a bi-directional pipe *object*[1], `Pipes`. Knowledge in C++, [1], and UNIX, [2], is needed in order to fully understand the listing. Computational practitioners only need to know how to use this object in their C++ programs. A brief explanation for this object is:

- The constructor[2] of this object creates two pipes, `p1` and `p2`, using the `pipe` command.
- The process[3] that calls this constructor is split into two identical processes, a parent and a child process of the same parent program[4] by the `fork` command.
- The parent process attaches the output-end of `p1` and the input-end of `p2` to its input and output file streams (`ifs` and `ofs`), respectively.
- The child process attaches the input-end of `p1` and the output-end `p2` to its standard output and input streams, respectively.
- The child process transforms itself into a new program, `child_program`, by using the `execlp` command.
- After the constructor of this object has been executed, there will be two different processes of two different programs running on the system. The parent process can use the input, >>, and output, <<, operators of the `Pipes` object to communicate with the child process. The child process can use the standard input and output functions[5] of the language in which the child program is implemented to communicate with the parent process.

The above ideas are illustrated in Figure 1.

---

1. In object oriented programming, a collection of data and functions is called an object.
2. The function having the same name as the object; in this case it is `Pipes`.
3. A running instance of a program.
4. It is very important to distinguish between a program and its process.
5. For C, they are the `scanf` and `printf` functions. For Fortran, they are the `read` and `write` subroutines.

```
enum MESSAGES {
  ERROR,                    /* An error hand-shaking message.                    */
  OKAY,                     /* A normal hand-shaking message.                    */

  BYE,                      /* ------------------------------------------->> BYE */

  MPP_NXPROC,
  MPP_NYPROC,

  SIM_FORWARD,              /* num_it                                            */

  MESH_CREATE,              /* x_size,y_size,delta_l  ---------------------->> mesh */
  MESH_DESTROY,             /* mesh                                              */
  MESH_SET_VOLTAGES,        /* mesh,v                                            */
  MESH_SET_VY,              /* mesh,x,y,vy                                       */
  MESH_GET_VY,              /* mesh,x,y ------------------------------------>> vy */
  MESH_WALL,                /* mesh                                              */

  ANALYZER_CREATE,          /* mesh,x,y,num_t,num_f,f_min,fmax ------->> analyzer */
  ANALYZER_DESTROY,         /* analyzer                                          */
  ANALYZER_SET_FREQ,        /* analyzer                                          */
  ANALYZER_GET_FREQ_RES,    /* analyzer --------->> num_f,rf1,rf2,.....,rfn      */
  ANALYZER_GET_TIME_RES,    /* analyzer --------->> num_t,rt1,rt2,.....,rtn      */
};
```

Listing 2 An example TLM client-server communication protocol. The first two messages, ERROR and OKAY are used for handshaking purposes. For every message the client process sends to the server process, the server process must reply with the appropriate return values, if there are any, terminated by one of the above two messages.The use of this protocol will be illustrated in detail later in this paper.

A TLM Client-Server Communication Protocol

Figure 1 depicts a parent and a child process linked together by a bi-directional pipe object. These two processes[1] must communicate with each other through a pre-defined protocol. Listing 2 depicts an example TLM client-server communication protocol. The first two messages, `ERROR` and `OKAY` are used for handshaking purposes. For every message the client process sends to the server process, the server process must reply with the appropriate return values, if there are any, terminated by one of the above two messages. The use of the other messages will be illustrated in detail later in this paper.

A TLM Client Program

Listing 3 shows a client TLM C++ program. The most important part of this program from the distributed computing point of view is the `MPP`[2] object. This object is derived from the `Pipes` object, Listing 1, therefore it has all the properties of the `Pipes` object. There are five new member functions in the `MPP` object: `Nx_Proc` and `Ny_Proc` are used to enquire about the dimensions of the processor array of the DECmpp 12000 on which the TLM server is running. The `check` and `okay` member functions are for software handshaking between the client and server processes. Finally, the `Forward` function is used to initiate a forward TLM simulation. See "A Simulation Example" for a detailed explanation of the `main` function.

The constructor of the `MPP` object creates a bi-directional communication pipe between the local TLM client process and the remote `2d-tlm-server` process by using the UNIX `remsh`[3] command. Once such a pipe is set up, the client and server processes can communicate with each other via the communication protocol in Listing 2. For example, in line 3 of the `main` function the `mpp.Nx_Proc` function is called. This function sends the `MPP_NXPROC` message to the server process, reads the returned values from the server process, then returns the value to the calling function.

---

1. From now on, the parent and child processes will be called the client and server processes, respectively.
2. MPP stands for Massively Parallel Processor.
3. This is the HPUX implementation; the command name for other UNIX implementations is `rsh`.

```
#include "Analyzer.h"
#include "Mesh.h"
#include <Stopwatch.h>

class MPP: public Pipes{
public:
       MPP():Pipes("remsh","eagle.bcsc.gov.bc.ca","/usr/.../2d-tlm-server"){}

       ~MPP(){*this << BYE;   okay();}
  int  Nx_Proc(){
         int nxproc;
         *this << NXPROC;   flush();
         *this >> nxproc;   check();
         return nxproc;
       }//--- Nx_Proc ---//

  int  Ny_Proc(){
         int nyproc;
         *this << NYPROC;   flush();
         *this >> nyproc;   check();
         return nyproc;
       }//--- Ny_Proc ---//

  void check(){
       int status;
         *this >> status;
         if (status!=OKAY){
           cerr << "MPP piping error!";
           exit(status);
         }
       }//--- check ---//

  void okay(){ flush();  check(); }

  void Forward(int num){ *this << SIM_FORWARD << num;    okay();}
};//--- MPP ---//

/*  1 */ void main(){
/*  2 */ MPP       mpp;
/*  3 */ Mesh      mesh(&mpp,mpp.Nx_Proc(),mpp.Ny_Proc(),7.112e-3/(mpp.Nx_Proc()-1));
/*  4 */ Analyzer  analyzer(&mpp,&mesh,64,32,8000,101,40.0e9,60.0e9);
/*  5 */ Stopwatch sw1,sw2,sw3;

/*  6 */ mesh.Wall(-1.0,   0, 0,127, 0);        // Set up waveguide boundaries
/*  7 */ mesh.Wall(-1.0,   0,63,127,63);
/*  8 */ mesh.Wall(-1.0,   0, 0,  0,63);
/*  9 */ mesh.Wall(-1.0,127, 0,127,63);

/* 10 */ sw1.start();                           // Start the stopwatches
/* 11 */ sw2.start();
/* 12 */ sw3.start();
/* 13 */ mesh.Set_Vy(20,20,1);                  // Inject signal
/* 14 */ mpp.Forward(8000);                     // Forward simulation
/* 15 */ sw1.stop();                            // Stop stopwatch-1
/* 16 */ mpp.Nx_Proc();                         // Purposely block the client process so that
                                                // stopwatch-2 would record the CPU time for
                                                // the 8000 iterations.
/* 17 */ sw2.stop();                            // stop stopwatch-2
/* 18 */ analyzer.Get_Freq_Response();          // Get frequency response
/* 19 */ sw3.stop();                            // stop stopwatch-3
                                                // The difference in time between stopwatch-3 and
                                                // stopwatch-2 is the time required to get the
                                                // frequency response from the server.

/* 20 */ analyzer.Print_Freq_Response(cout);    // Print frequency response

/* 21 */ cout << "Stopwatch-1" << endl;         // Output stopwatch-1 data
/* 22 */ cout << "real    " << sw1.real()    << endl;
/* 23 */ cout << "user    " << sw1.user()    << endl;
/* 24 */ cout << "system " << sw1.system() << endl << endl;
/* 25 */ cout << "Stopwatch-2" << endl;         // Output stopwatch-2 data
/* 26 */ cout << "real    " << sw2.real()    << endl;
/* 27 */ cout << "user    " << sw2.user()    << endl;
/* 28 */ cout << "system " << sw2.system() << endl << endl;
/* 29 */ cout << "Stopwatch-3" << endl;         // Output stopwatch-3 data
/* 30 */ cout << "real    " << sw3.real()    << endl;
/* 31 */ cout << "user    " << sw3.user()    << endl;
/* 32 */ cout << "system " << sw3.system() << endl;
/* 33 */}//--- main ---//
```

Listing 3 A TLM client program. The most important part of this program from the distributed computing point of view is the `MPP` object. This object is derived form the `Pipes` object, Listing 1, therefore it has all the properties of the `Pipes` object plus some of its own. There are five new member functions in the `MPP` object: `Nx_Proc` and `Ny_Proc` are used to enquire about the dimensions of the processor array of the DECmpp 12000 on which the TLM server is running. The `check` and `okay` member functions are for software handshaking between the client and server process. Finally, the `Forward` function is used to initiate a forward TLM simulation. The `Mesh` and `Analyzer` objects in line 3 and 4 of the `main` function are implemented using the same message protocol. See "A Simulation Example" for a detailed explanation of the `main` function.

```
/*=========================================================================
    Supporting Functions
=========================================================================*/
inline void Okay()          { printf(" %d ", OKAY ); fflush(stdout); }
inline void Error()         { printf(" %d ", ERROR); fflush(stdout); }
inline void Bye()           { Okay(); }
inline int  Get_int (int *i){ return scanf (" %d ", i); }
inline void NxProc()        { printf(" %d ", nxproc); Okay(); }

void Abort(char *msg){
  fprintf(stderr,"Server Aborted: %s!\n",msg);
  exit(ERROR);
}/*--- Abort ---*/

int GetMessage(int *in){
int okay;
  okay = Get_int(in);
  if (okay)
    return okay;
  else
    Abort("Invalid Input --- Bye!\n");
}/*--- GetMessage ---*/

/*=========================================================================
    Main Function
=========================================================================*/
void main(){
int message;
  while (GetMessage(&message) && message!=BYE) {
    switch (message) {
    /*--- MPP Specific Functions ---*/
    case MPP_NXPROC:            NxProc();           break;
    case MPP_NYPROC:            NyProc();           break;

    /*--- Simulation Functions ---*/
    case SIM_FORWARD:           SimForward();       break;

    /*--- Mesh Function ---*/
    case MESH_CREATE:           MeshCreate();       break;
    case MESH_DESTROY:          MeshDestroy();      break;
    case MESH_SET_VOLTAGES:     MeshSetVoltages();  break;
    case MESH_SET_VY:           MeshSetVy();        break;
    case MESH_GET_VY:           MeshGetVy();        break;
    case MESH_WALL:             MeshWall();         break;

    /*--- Analyzer Function ---*/
    case ANALYZER_CREATE:       AnalyzerCreate();   break;
    case ANALYZER_DESTROY:      AnalyzerDestroy();  break;
    case ANALYZER_GET_FREQ_RES: AnalyzerGetFreqRes(); break;
    case ANALYZER_GET_TIME_RES: AnalyzerGetTimeRes(); break;

    /*--- Unknown Request ---*/
    default:                    Error();
    }
  }
  Bye();
}/*--- main ---*/
```

Listing 4 Code segment from `2d-tlm-server.m`, an MPP implementation of our TLM server.

The `Mesh` and `Analyzer` objects in line 3 and 4 of the `main` function are implemented using the same message protocol. The algorithms for these objects are published in [3] and [4], therefore they are not repeated here. The major difference between the algorithms in the server program and the published ones is that the ordinary function calls are replaced by sending and receiving messages.

A Parallel TLM Server Program

Listing 4 is an exerpt from our parallel TLM server program, `2d-tlm-server.m`, which is written in MPL, a C-like language. The main function of this program is just a message loop which keeps polling data from its standard input stream. This stream is connected to the output file stream of the client program via a `Pipes` object, see Figure 1. Once a message is received, the `switch` statement determines what message it is and calls the corresponding function.

For instance, if the incoming message is `MPP_NXPROC`, then the `NxProc` function is called. This function sends the value of `nxproc` to the standard output stream terminated with an `OKAY` message so that the client process can verify that the request was indeed completed successfully.

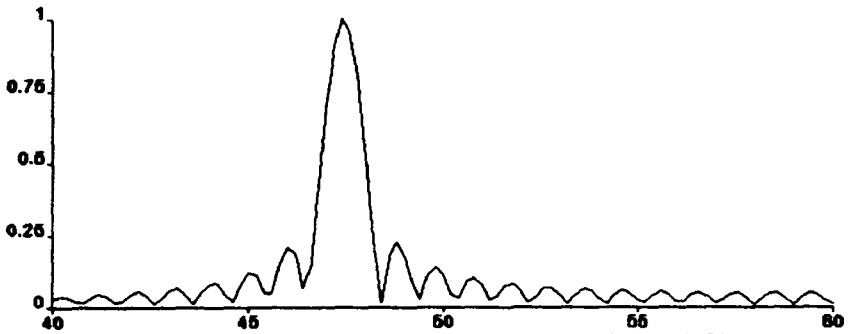

	stopwatch 1	stopwatch 2	stopwatch 3
real	0.03	13.84	14.08
user	0.00	0.00	0.01
system	0.00	0.00	0.00

Figure 2 The frequency response of a WR28 waveguide cavity obtained from Listing 3. The peak represents the TM_{202} resonant frequency of the cavity. The table below the graph shows the time of the three stopwatches at the end of the simulation.

A Simulation Example

The main function in Listing 3 simulates a WR28 rectangular waveguide cavity. The purpose of this example is to illustrate the use of this distributed computing technique, not the correctness or other properties of the TLM method.

Line 2 of the `main` function creates a `MPP` object, which is a parallel TLM server running in a remote site on the network. Lines 3 and 4 declare a `Mesh` and an `Analyzer` object. The `Mesh` object represents a cross-section of a WR28 rectangular waveguide; the mesh size is 128×64, and Δl is 0.056mm[1]. The `Analyzer` object specifies that the signal is to be sampled at node (64,32)[2], 8000 iterations are needed, and 101 equally spaced frequency points from 40.0 GHz to 60.0 GHz are chosen for the Fourier transform operation. These two objects communicate with the `MPP` objects to perform TLM and Fourier transform computations.

Line 5 declares three stopwatches which will be used to time the execution of the client process in various locations of the program. Lines 6 to 9 set up the boundaries of the waveguide wall. Lines 10 to 12 start the stopwatches.

Lines 13 to 15 inject a signal into the mesh at node (20,20), ask the server to perform 8000 iterations and stop the first stopwatch. For a normal process, line 15 would not be executed until the 8000 iterations have been finished. In this client process, line 15 is executed as soon as an `OKAY` handshaking message is returned. Stopwatch-1 in the table of Figure 2 confirms this behaviour. This feature allows the client process to communicate with a number of server processes with minimum delay so that they can work concurrently to solve large problems.

Line 16 blocks the client process so that stopwatch-2 records the CPU time required for the 8000 iterations. The time difference between stopwatch-3 and stopwatch-2 is the time required to retrieve the frequency response.

The remaining lines in the listing are self-explanatory. The output of this program is summarized in Figure 2.

---

1. The dimension of the processor array of the MPP available to us is 128×64.
2. XY co-ordinate normalized to Δl.

Applications of Distributed Computing Technique to Computational Electromagnetics

The previous example illustrated the use of distributed computing in TLM computation. The technique introduced in this paper, in particular the bi-directional `Pipes` object in Listing 1, is very general, . Therefore, all CPU time intensive frequency and time domain methods, such as FDTD, MOM, etc., can use this technique.

Optimization, especially hybrid frequency/time domain optimization [5], is an area to which distributed computing techniques can be readily applied. The basis of all optimization programs is repetitive iteration — i.e. computation of the response of the structure to be optimized based on some strategic approaches with a large number of different values for a set of variables, and the selection of a combination of values that give the best response. The speed of this operation can be greatly increased if these unrelated simulations can be executed on separate computers and solved concurrently. The table in Figure 2 shows that network delay[1] is negligible[2] even compared with the short parallel computation CPU time. Therefore the increase in performance would be linearly[3] proportional to the number of available stations[4].

Conclusion

In this paper, we have addressed the basis of distributed computing and given a complete C++ implementation of a bi-directional pipe object. This pipe object allows computational practitioners to use distributed computing techniques to solve complex electromagnetics problems. Program segments from our TLM client and MPP server programs are given and used to illustrate the distributed computing technique. A detailed sample program is also presented with a thorough explanation. Optimization, especially hybrid frequency/time domain optimization, of microwave and millimeter wave circuits is one of the areas to which this distributed computing technique can be readily applied.

References

[1] Bjarne Stroustrup, *The C++ Programming Language*, second Edition, October 1992, Addison-Wesley.

[2] John J. Valley, *UNIX Programmer's Reference*, 1991, Que.

[3] W. Hoefer and P. So, *The Electromagnetic Wave Simulator*, John Wiley, 1991.

[4] Poman P.M. So, Eswarappa Channabasappa and Wolfgang J.R. Hoefer, *Transmission Line Matrix Method on Massively Parallel Processor Computers*, in 9th Annual Review of Progress in Applied Computational Electromagnetics Digest, pp.467-474, March 1993, Monterey, CA.

[5] P.P.M. So, W.J.R. Hoefer, J.W. Bandler, R.M. Biernacki and S.H. Chen, *Hybrid Frequency/Time Domain Field Theory Based CAD of Microwave Circuits*, in 23rd European Microwave Conference Digest, pp. 218-219, September 1993, Madrid, Spain.

---

1. The time difference between stopwatch-3 and stopwatch-2.
2. The client process should retrieve as little data as possible from the server process. Therefore, Fourier transform and other data processing should be done on the server side, only the frequency response or S-parameters should be fetched back to the client process.
3. It should be linear as long as the number of stations is within a practical limit, say less than 50.
4. The stations should be of similar speed, otherwise special steps must be carried out to prevent the slow station to slow down the client and other server processes.

TLM: Order of Accuracy Enhancement

A. Soulos (a), D. de Cogan (a) & P. Enders (b)

(a) School of Information Systems, University of East Anglia, Norwich NR4 7TJ, UK
(b) Stendaler Straße 126, D-12627 Berlin, FRG

The transmission-line matrix modelling method (TLM) has several advantages over other time-domain finite-difference (TD-FD) algorithms, such as being one-step explicit and, at least when applied to diffusion processes, unconditionally stable. But its order of accuracy is not higher, than that of the conventional TD-FD method, *viz*, $O(\Delta t+\Delta x^2)$ and $O(\Delta t^2+\Delta x^4)$, respectively, depending on the circuit parameter values used. It will be shown, that stubs can be used to increase the order of accuracy without loosing the freedom in the choice of Δt, when the stubs involves also a free resistive element.

1. INTRODUCTION

Within transmission-line matrix modelling (TLM), field propagation is mapped onto travelling voltage pulses on a mesh of lossless transmission lines and lumped resistors [1]. Use is made of known analogies between the field variables and the circuit variables. The conceptual and computational simplicity attracts an increasing number of applicants. Nevertheless, the accuracy of this algorithm has been tested by comparison of more or less specific numerical results, rather than generally investigated. This contribution undertakes a first attempt considering the case of 1D overdamped waves. However, the approach proposed can easily be extended to weekly and undamped wave propagation as well as to higher space dimensions.

The basic parameter is here the order of accuracy. It measures, how the discretization error vanishes, when the mesh is refined. It turns out, that the freedom in the choice of Z cannot be used to enhance the order of accuracy. For this, stubs are included, where, following an idea which the late Peter Johns proposed to one of the authors (D. de C.), the stub transmission line, Z_S, is complemented by a stub resistor, R_S. As Z_S represents a distributed capacity, such a stub is closer to the unity of resistive conduction and capacitive storage, which is characteristic for diffusion-like propagation. R_S should proof to be crucial for the purpose of this investigation.

This network will be examined, starting with the derivation of the corresponding TLM difference equations in section 2. In section 3, consistency and accuracy of this new routine will be considered. The new algorithm will be tested by means of a standard problem, where the exact analytical solution is known.

2. 1D NETWORK WITH RESISTIVE STUB

2.1. Scattering of currents

Consider Figure 1. Introducing left-to-right and right-to-left running pulses as usually, one has incident from the left and right, and from the stub, respectively, the pulses

$$I_L^i;\quad V_L^i = Z\cdot I_L^i;\quad I_R^i;\quad V_R^i = Z\cdot I_R^i;\quad I_s^i;\quad V_s^i = Z_s\cdot I_s^i \qquad (1)$$

(I^i_L and V^i_L correspond to I^i and V^i in Figure 1). The outgoing ("scattered") currents are connected with those *via* a "scattering matrix" S_I as

$$\begin{pmatrix} I_L^s \\ I_R^s \\ I_S^s \end{pmatrix} = \begin{pmatrix} \rho & 1-\rho-\tau' & \frac{1}{2}(1-\rho_s) \\ 1-\rho-\tau' & \rho & \frac{1}{2}(1-\rho_s) \\ \tau' & \tau' & \rho_s \end{pmatrix} \begin{pmatrix} I_L^i \\ I_R^i \\ I_S^i \end{pmatrix} \underset{\text{def}}{=} \mathbf{S}_I \begin{pmatrix} I_L^i \\ I_R^i \\ I_S^i \end{pmatrix} \tag{2}$$

where the reflection coefficients for the link lines and the stub, respectively, are

$$\rho = 1-\tau = \frac{2R(R_s+Z_s)+(R+Z)(R-Z)}{(R+Z)(R+Z+2R_s+2Z_s)}; \qquad \rho_s = 1-\tau_s = \frac{Z+R+2R_s-2Z_s}{Z+R+2R_s+2Z_s} \tag{3a}$$

τ' denotes that part of the incident current being first transmitted from the link line to the node and then flowing into the stub,

$$\tau' = 1-\rho' = \frac{R+Z}{R+Z+R_s+Z_s}\cdot\tau = \frac{2Z}{R+Z+2R_s+2Z_s} \tag{3b}$$

Substance/charge conservation is guaranteed due to the fact, that the matrix elements of each column sum up to unity,

$$\sum_i (S_I)_{ij} = 1 \qquad \text{for all } j \tag{4}$$

2.2. The incoming voltages and the node voltage

Consider now the voltage propagation in more detail; first, from the incidence along the transmission lines up to before meeting the node point. Due to the impedance discontinuities, fractions V^ρ of the voltages of the incoming pulses, V^i, eq.(1), are backscattered at the ends of the transmission lines,

$$V_{L,R}^\rho = \rho V_{L,R}^i = \rho Z I_{L,R}^i; \qquad V_S^\rho = \rho_s V_S^i = \rho_s Z_s I_S^i \tag{5a}$$

That pulses that are forward scattered, *ie*, transmitted towards the node, carry the voltages

$$V_{L,R}^t = (1+\rho)V_{L,R}^i = (1+\rho)ZI_{L,R}^i; \qquad V_S^t = (1+\rho_s)V_S^i = (1+\rho_s)Z_s I_S^i \tag{5b}$$

Passing the resistors, these voltages are diminuished by a voltage drop of RI_L^t, RI_R^t, and RI_S^t, respectively. The resulting pulses incoming at the node, $V_{L,R,S}^n$, constitute the node voltage,

$$\begin{aligned} V^n &= V_L^n + V_R^n + V_S^n = V_L^t - RI_L^t + V_R^t - RI_R^t + V_S^t - R_s I_S^t \\ &= (1+\rho)ZI_L^i - R(1-\rho)I_L^i + (1+\rho)ZI_R^i - R(1-\rho)I_R^i + (1+\rho_s)Z_s I_S^i - R_s(1-\rho_s)I_S^i \end{aligned} \tag{5c}$$

2.3. The outgoing (scattered) voltages

Second, the current pulses leaving the node point carry voltages according to the resistances and impedances of the branches. However, not the total node voltage, V^n, causes the branch currents leaving the node point, but only the forward-scattered voltages from the correspondingly other branches, *viz*,

$$I_L^s - \rho I_L^i = (\tau - \tau')I_R^i + \tfrac{1}{2}\tau_s I_S^i = \frac{1}{R+Z}\left[(1+\rho)ZI_R^i - \tau R I_R^i + (1+\rho_s)Z_s I_S^i - \tau_s R_s I_S^i\right] \quad (6a)$$

$$I_R^s - \rho I_R^i = (\tau - \tau')I_L^i + \tfrac{1}{2}\tau_s I_S^i = \frac{1}{R+Z}\left[(1+\rho)ZI_L^i - \tau R I_L^i + (1+\rho_s)Z_s I_S^i - \tau_s R_s I_S^i\right] \quad (6b)$$

$$I_S^s - \rho_s I_S^i = \tau' I_L^i + \tau' I_R^i = \frac{1}{R_s+Z_s}\left[(1+\rho)ZI_L^i - R\tau I_L^i + (1+\rho)ZI_R^i - R\tau I_R^i\right] \quad (6c)$$

Then, there is a voltage drop of $R\left(I_L^s - \rho I_L^i\right)$, $R\left(I_R^s - \rho I_R^i\right)$, and $R_s\left(I_S^s - \rho_s I_S^i\right)$, respectively. On the transmission lines, the reflected pulses, $V_{L,R,S}^{\rho}$, add, such that, finally, the scattered pulses carry the voltages

$$V_L^s = (R+Z)\left(I_L^s - \rho I_L^i\right) - R\left(I_L^s - \rho I_L^i\right) + Z\rho I_L^i = ZI_L^s \quad (7a)$$

$$V_R^s = (R+Z)\left(I_R^s - \rho I_R^i\right) - R\left(I_R^s - \rho I_R^i\right) + Z\rho I_R^i = ZI_R^s \quad (7b)$$

$$V_S^s = (R_s+Z_s)\left(I_S^s - \rho I_S^i\right) - R_s\left(I_S^s - \rho I_S^i\right) + Z_s\rho_s I_S^i = Z_s I_S^s \quad (7c)$$

Therefore, despite of the different scattering rule for voltages and currents at impedance discontinuities, the relation between the scattered voltages and the scattered currents is the same as between the incoming ones (*ie*, Ohm's law; see eq.(1)), as to be expected. In summary, the voltage scattering can be described by means of a scattering matrix, S_V,

$$\begin{pmatrix} V_L^s \\ V_R^s \\ V_S^s \end{pmatrix} = \begin{pmatrix} \rho & 1-\rho-\tau' & \frac{Z}{2Z_s}(1-\rho_s) \\ 1-\rho-\tau' & \rho & \frac{Z}{2Z_s}(1-\rho_s) \\ \frac{Z_s}{Z}\tau' & \frac{Z_s}{Z}\tau' & \rho_s \end{pmatrix} \begin{pmatrix} V_L^i \\ V_R^i \\ V_S^i \end{pmatrix} \underset{\text{def}}{=} S_V \begin{pmatrix} V_L^i \\ V_R^i \\ V_S^i \end{pmatrix} = S_I{}^t \begin{pmatrix} V_L^i \\ V_R^i \\ V_S^i \end{pmatrix} \quad (8)$$

where $S_I{}^t$ denotes the transpose of S_I, eq.(2). Without the stub variables, this is the scattering matrix given by Johns [2].

2.4. The TLM difference equations

As noted above, the representation of the cell capacitance by transmission lines renders the time discrete, the time step, Δt, being fixed by the pulse travel time on these lines. Hence, the pulse scattered at time step k at node i are, at time step k, incident at the neighbouring nodes, i±1, or at the same node (after reflection at the stub end). Thus, the TLM difference equations for the voltages read

$$\underset{k}{\begin{pmatrix} V_L^s(i) \\ V_R^s(i) \\ V_S^s(i) \end{pmatrix}} = S_V \underset{k}{\begin{pmatrix} V_L^i(i) \\ V_R^i(i) \\ V_S^i(i) \end{pmatrix}} = \underset{k+1}{\begin{pmatrix} V_R^i(i-1) \\ V_L^i(i+1) \\ V_S^i(i) \end{pmatrix}} \quad (9)$$

Eliminating the scattered pulses and introducing node number shift operators $\mathbf{x}$ and $\bar{\mathbf{x}}$ as $\mathbf{x}V(i)=V(i+1)$ and $\bar{\mathbf{x}}V(i)=V(i-1)$, equations (9) become

$$\begin{pmatrix} V_L^i \\ V_R^i \\ V_S^i \end{pmatrix}_{k+1} = \begin{pmatrix} (1-\rho-\tau')\bar{\mathbf{x}} & \rho\bar{\mathbf{x}} & \tau'\bar{\mathbf{x}} \\ \rho\mathbf{x} & (1-\rho-\tau')\mathbf{x} & \tau'\mathbf{x} \\ \frac{1}{2}\tau_s & \frac{1}{2}\tau_s & \rho_s \end{pmatrix}_k \begin{pmatrix} V_L^i \\ V_R^i \\ V_S^i \end{pmatrix} \tag{10}$$

These coupled partial difference equations are easily diagonalized by means of the Caley-Hamilton theorem. This states that a matrix fulfills its own eigenvalue equation. Consequently, each component of the voltage vector in eq.(10) obeys the equation

$$\begin{aligned} {}_{k+3}V_M^i = &\left[\rho_s + (\tau-\tau')\mathbf{X}\right]_{k+2}V_M^i - \left\{\left[(\tau-\tau')\rho_s - \tfrac{1}{2}\tau'\tau_s\right]\mathbf{X} + (\tau-\tau')^2 - \rho^2\right\}_{k+1}V_M^i \\ &+ \left\{\left[(\tau-\tau')^2 - \rho^2\right]\rho_s + \tau'\tau_s(\rho-\tau+\tau')^2\right\}_k V_M^i; \quad \mathbf{X} \equiv \mathbf{x} + \bar{\mathbf{x}}; \quad M = L,\ R,\ \text{or } S \end{aligned} \tag{11}$$

In contrast to the stub-free case, the scheme (11) is <u>three</u>-step, and the number of mesh points which enter the calculation of ${}_kV$ is significantly higher (as to be expected from an algorithm of - potentially - higher accuracy), see Figure 2. Since the field variables are linear combinations of these voltages, it is sufficient to consider in what follows just one of these equations (11).

3. CONSISTENCY AND ACCURACY

3.1. Continuum limit of the discrete diffusion equation (11)

The continuum limit of formula (11) is

$$V(x,t) = \sum_{r=0}^{4}\sum_{s=0}^{4} a_{r,2s}\frac{\Delta t^r \Delta x^{2s}}{r!(2s)!}\frac{\partial^{r+2s}}{\partial t^r \partial x^{2s}}V(x,t) + O\left(\Delta t^5 + \Delta x^{10}\right) \tag{12}$$

Due to $a_{00}=1$, the 0th-order terms, V(x,t), cancel. The 1st-order terms form the diffusion equation, since

$$-\frac{a_{02}}{a_{10}} = \frac{ZZ_s}{R(Z+2Z_s)} = D\frac{\Delta t}{\Delta x^2} \tag{13}$$

where D denotes a diffusivity. Notice, that R_s does *not* enter this relation. Therefore, the scheme (11) is consistent with the diffusion equation up to the order $O(\Delta t^2+\Delta x^4)$.

3.2. Numerical investigation of the accuracy

As a standard problem with known analytical solution, the temperature diffusion in an 1D infinite copper bar ($D=1.17 cm^2 s^{-1}$) excited with a single impulse of strength 3 at its centre (x=0) is considered. The network of Figure 1 is excited with ${}_0V_L^i(i)={}_0V_R^i(i)={}_0V_S^i(i)=\delta_{i0}$. The relative error of the numerical results when compared with the analytical solution,

$$ {}_kA(i) = \frac{3}{\sqrt{4\pi Dk\Delta t}} \exp\left\{ -\frac{i^2\Delta x^2}{4Dk\Delta t} \right\} \tag{14} $$

is observed, at the centre node i=0, to behave as

$$ {}_k\varepsilon_{rel} \equiv \frac{{}_kV(0) - {}_kA(0)}{{}_kA(0)} \propto \frac{\varepsilon_{as}}{k} \tag{15} $$

The asymptotics $\propto k^{-1}$ holds exactly in the stubless case [3]. ε_{as} depends on the network parameters. Figure 3 shows an early result of ε_{as} as function of Z and R_S; the other parameters being $\Delta x=1.0$, $\Delta t=0.1$, $R=0.125$. It is suggested that the contour $\varepsilon_{as}=0$ indicates parameter values with small error for large k-values. It should be noted, however, that this region exhibits larger errors for small k-values. This region has to be investigated in finer detail and over a wider range of R_S and Z.

4. DISCUSSION

The TLM algorithm is proposed to be extended by a series resistor R_S in the (capacitive or inductive) stub. In the case considered, this additional element does not affect the relation between the mesh and the propagation constant, but can be chosen to minimize the discretization error. The computational effort is not increased, once the scattering coefficients are calculated. In inhomogeneous materials, R_S may vary properly as a function of the mesh coordinate.

Evidence has been obtained, that this stub allows for a systematic improvement of accuracy. Further studies should relate the vanishing of ε_{as} with the order of accuracy and extend this optimization to the relation between the initial pulses on the link lines and on the stub line.

Subsequent work should be devoted to the extension of this approach to other problems and to the question, whether the order of accuracy can be further increased, to $O(\Delta t^3+\Delta x^6)$, by properly chosing Z_S.

Acknowledgement. These investigations have been started during the visit of UEA by the third author. He would like to thank the colleagues of the School of Information Systems for their hospitality and support.

REFERENCES

[1] P. B. Johns, 'Simulation of Electromagnetic Wave Interactions by Transmission-Line Modelling (TLM)', *Wave Motion* 10 (1988) 597-610.

[2] P. B. Johns, 'A simple explicit and unconditionally stable numerical routine for the solution of the diffusion equation', *Int. J. Num. Meth. Engin.* 11 (1977) 1307-1328.

[3] P. Enders & D. de Cogan, 'The Efficiency of Transmission-line Matrix Modelling - Rigorous Viewpoint', *Int. J. Num. Modell.* 6 (1993) 2, 109-126.

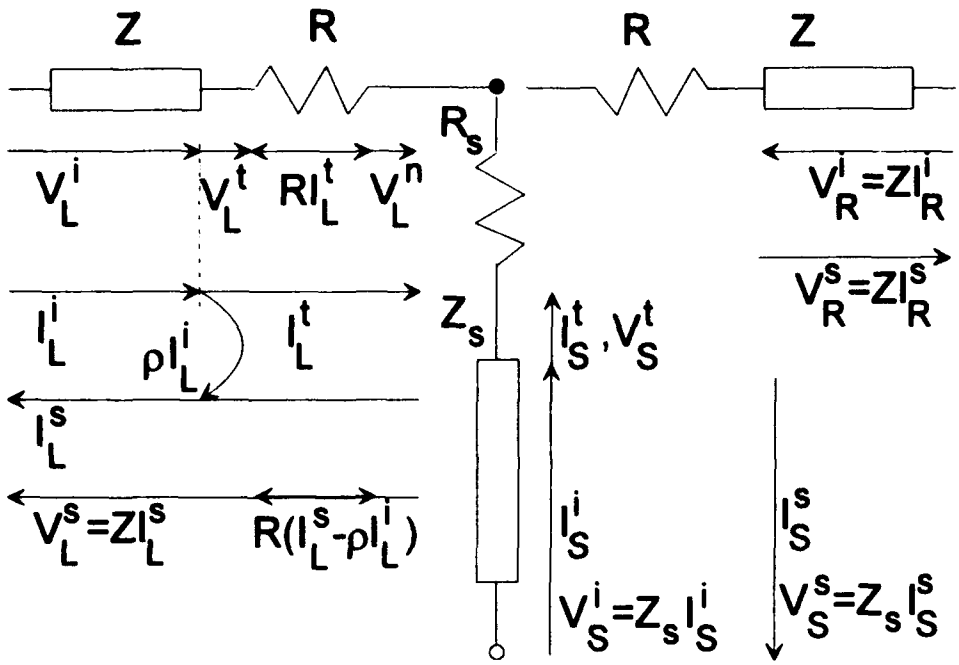

Figure 1. One-dimensional node with stub; the pulse variables of the right branch being completely analogous to those of the left branch are not shown

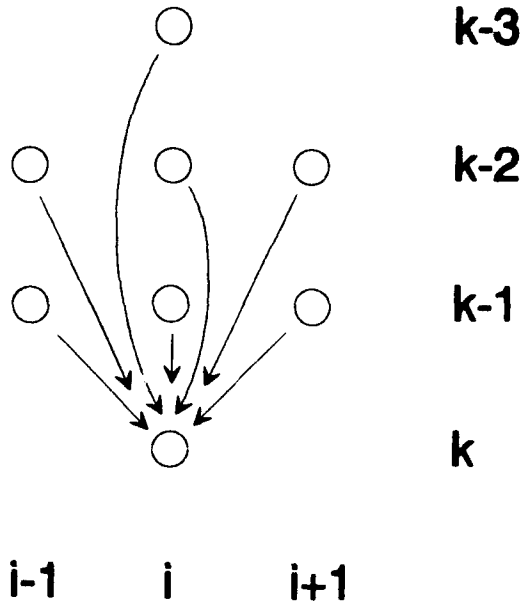

Figure 2. Scheme of mesh points which enter the calculation of V(k,i)

$$\varepsilon_{as} = \begin{bmatrix} -0.490 & -0.478 & -0.462 & -0.445 & -0.398 \\ -0.561 & -0.346 & -0.124 & -0.107 & -0.353 \\ -0.599 & -0.213 & 0.292 & 0.621 & 1.077 \\ -0.635 & -0.114 & 0.441 & 1.036 & 1.683 \end{bmatrix}$$

numerical results from $\varepsilon_{rel} \to \varepsilon_{as}/k$ as $k \to \infty$

$\varepsilon_{as} = k_{max} * \varepsilon_{max}$ vs. Z_S and R_S:

surface plot

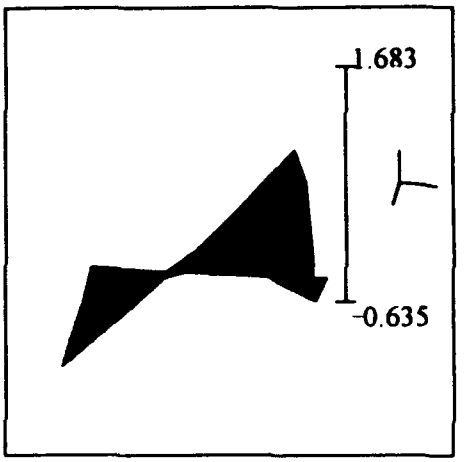

ε_{as}

contour plot

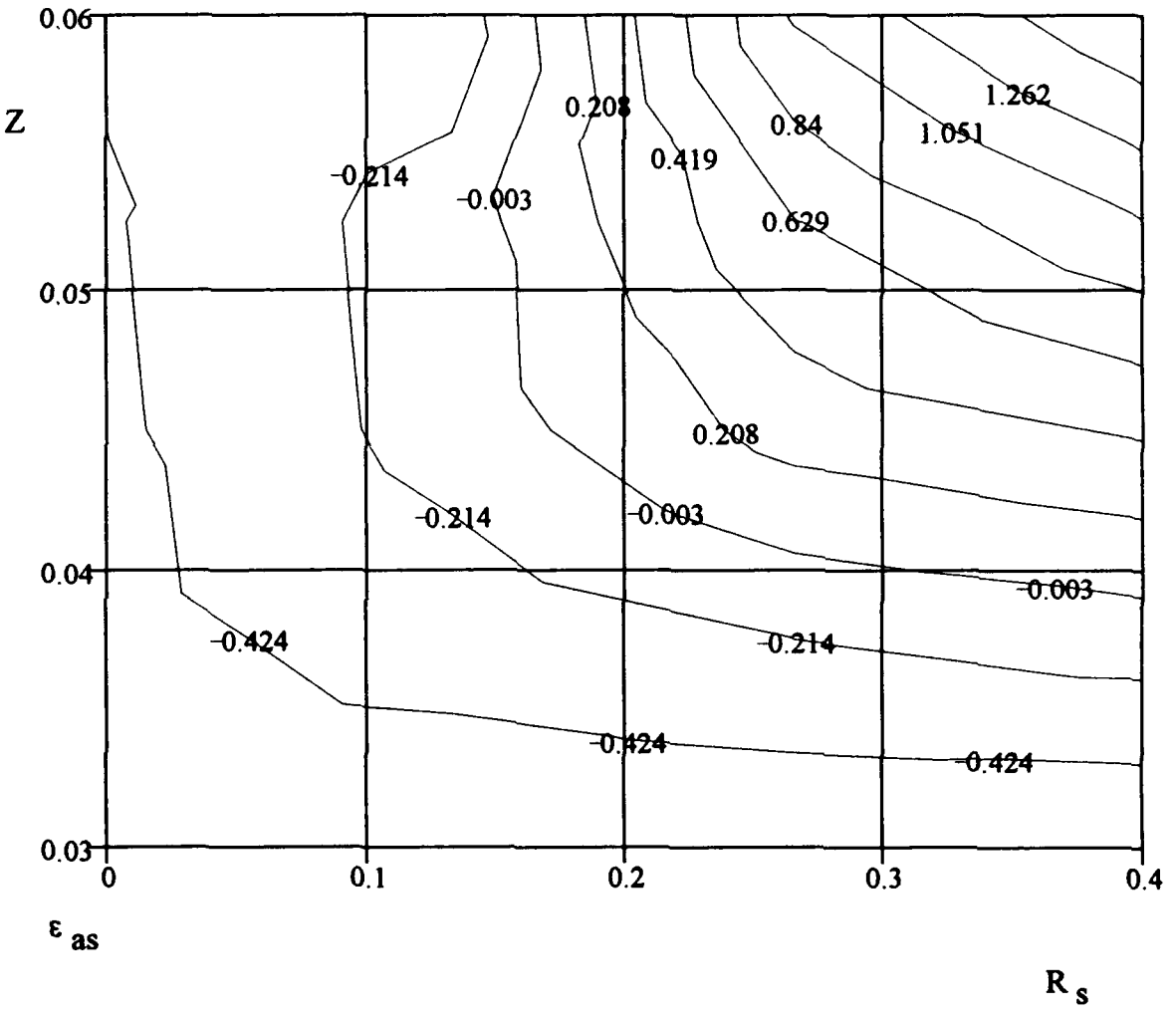

Figure 3. Asymptotic behaviour of the relative error as function of R_S and Z

Rigorous and Fast Computation of Modal Johns Responses

M.Mongiardo^, M.Righi°, R.Sorrentino^· W.J.R. Hoefer°

^Istituto di Elettronica, Università di Perugia, I-06100 Perugia, ITALY

°NSERC/MPR Teltech Research Chair in RF Engineering, Department of Electrical and Computer Engineering, University of Victoria, Victoria, B.C., CANADA

Abstract

A technique is introduced for the analytical computation of the impulse response (Johns' streams) of dispersive structures from frequency domain expressions. This technique, combined with a procedure which converts the TLM field quantities into the modes of the outer region, allows to dramatically reduce the computational burden. In this communication the analytically calculated Johns' stream are compared with the numerical one and several interesting features are pointed out. The new Johns streams are also used in actual TLM computations; results obtained via the numerical and the analytical Johns responses are also presented demonstrating the effectiveness of the proposed approach.

Introduction

Since its introduction [1] the TLM method has been extensively used for solving complex boundary value problems [2,3]. The TLM makes use of discretized field quantities in a given volume of space. As for similar numerical methods, problems arise when in the domain of interest becomes infinite. In this case it is necessary to truncate the mesh and to introduce a suitable scheme to account this truncation. To this end the diakoptic procedure has been introduced in [4]. The diakoptic approach solves rigorously the problem of absorbing boundary conditions (abc). However, the considerable numerical effort involved in the application of such an approach prevents its application in practical cases. The sources of the numerical burden are essentially the following [5]:

- for each node on the boundary the Johns matrix must be calculated in advance;
- during the TLM simulation the incident waves at each node must be convolved with the appropriate term of the Johns matrix.

In order to reduce the computational burdens several simplifications have been devised. The simplest arises when the incident wave is a TEM wave. In this case it is possible to terminate the TLM mesh directly in a resistance of proper value. Moreover, since the closing element is purely resistive, convolution is not necessary.

Another significant simplification has been introduced in [6] for homogenous waveguide. In that paper it has been observed that, inside a waveguide supporting only the fundamental mode, it is not necessary to perform the convolution at each point of the boundary. In fact the value of the field at the various points of the boundary are related in as simple way.

A rigorous abc for homogenous waveguide which accounts for higher order and evanescent modes, has been recently introduced [7]. This abc is based on representing the fields arising from TLM computation as a sum of frequency independent modes with appropriate amplitude coefficients. The amplitude of each mode is separately convolved with the corresponding modal Johns response. Afterward, the TLM fields are retrieved from the modal amplitudes.

Several advantages, and dramatical numerical improvements are obtained by using these new ABC. To cite just a few of these advantages, the new abc provides:

- absorbing boundaries for multi-modal propagation;
- the possibility to consider also evanescent waves at the boundary;
- the reduction of the size of the TLM computational domain;
- a considerable reduction of the numerical effort, with respect to classical diakoptics (typically two order of magnitude)

Nevertheless, the major source of numerical burden still are the convolutions and the calculations of the modal Johns responses. In fact, the latter are generally pre-calculated by rather lengthy simulations.

In this work we show how to avoid these TLM simulations, by analytically calculating the modal Johns responses.

Analytic computations of the modal Johns responses

Let us consider a parallel plate waveguide where only the TEM mode is present. We can describe this structure by its TLM mesh as shown in Fig. 1.

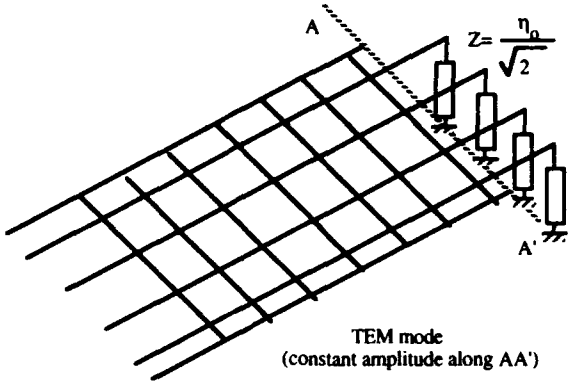

Fig. 1 TLM description of a parallel-plate waveguide using a 2-D mesh terminated at the reference plane AA'

We want to terminate our structure at the right of the plane AA'. It is well known that we must truncate each TLM transmission line in the characteristic impedance $\frac{Z_0}{\sqrt{2}}$, therefore obtaining an impulse reflection coefficient given by [9]:

$$\Gamma_i = \frac{\frac{Z_0}{\sqrt{2}} - Z_0}{\frac{Z_0}{\sqrt{2}} + Z_0} = -0.17157 \tag{1}$$

This amounts to a matched load for a TEM wave traveling in the mesh in a direction normal to the boundary.

If we are now considering a parallel plate waveguide with just the fundamental TE mode present we have again the TLM mesh on the left, while on the right we must terminate each TLM transmission line in $\frac{Z_{TE}}{\sqrt{2}}$ where Z_{TE} is

$$Z_{TE} = \frac{\omega\mu}{\beta} \qquad \beta = \sqrt{k^2 - k_c^2} \qquad \text{above cut-off}$$

$$Z_{TE} = \frac{j\omega\mu}{\beta} \qquad \beta = \sqrt{k_c^2 - k^2} \qquad \text{below cut-off} \tag{2}$$

As a consequence we get the following impulse reflection coefficient in the frequency domain:

$$\Gamma_i(\omega) = \frac{\frac{Z_{TE}(\omega)}{\sqrt{2}} - Z_0}{\frac{Z_{TE}(\omega)}{\sqrt{2}} + Z_0} \tag{3}$$

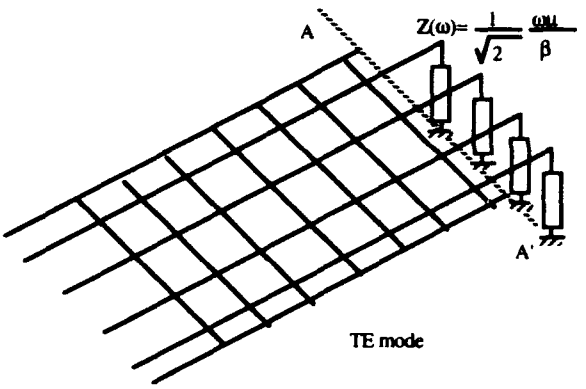

Fig.2 2-D mesh with single mode propagation terminated with Z_{TE}

This amounts to a match at the frequency ω for a TE wave traveling in the mesh toward the boundary. Fig. 3a and 3b show the Γ(ω) calculated analytically.

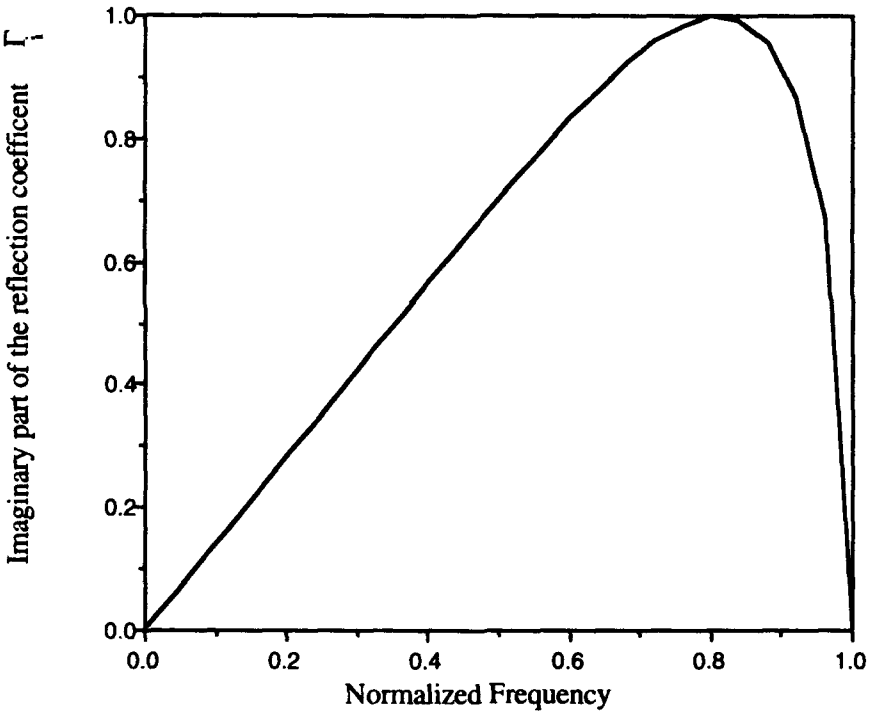

Fig. 3a Imaginary part of the impulse reflection coefficient Γ_i

The normalized frequency is the frequency divided by the cut-off frequency. Observe the different ranges of the normalized frequency on the two graphs.

For transformation from the frequency domain to the time domain it is necessary that our function satisfies:

$$\begin{aligned} \mathrm{Re}[\ \Gamma(\omega)\ ] &= \mathrm{Re}\ [\ \Gamma(-\omega)\ ] \\ \mathrm{Im}[\ \Gamma(\omega)\ ] &= -\ \mathrm{Im}\ [\ \Gamma(-\omega)\ ] \end{aligned} \qquad (4)$$

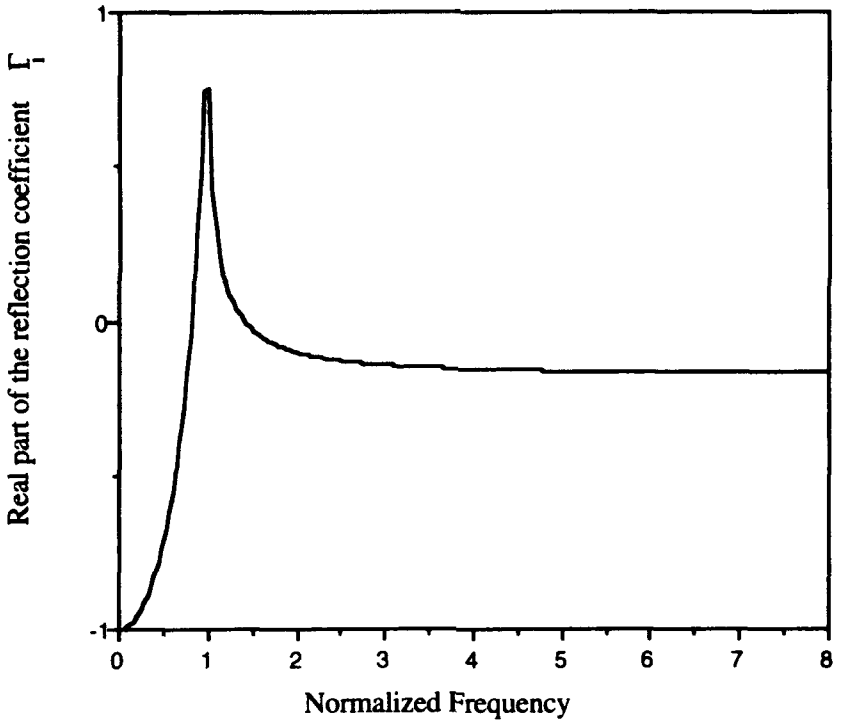

Fig. 3b Real part of the impulse reflection coefficient Γ_i

Moreover, after consideration of the Z_{TE} asymptotic behavior for $\omega \rightarrow \infty$ it is also convenient to separate our reflection coefficient into two different parts:

i) a constant, which is equal to $c_1 = -0.17157$

ii) a function going to zero at high frequency.

The transform of the constant is a delta function and corresponds to the high frequency content traveling along the guide as a TEM wave which is absorbed. The transform of the remaining part is calculated numerically. In fact, by introducing

$$\Gamma'(\omega) = \Gamma(\omega) - c_1 \tag{5}$$

and by applying (4) we have:

$$\Gamma'(t) = \int_{-\infty}^{\infty} \Gamma'(\omega)\, e^{j\omega t}\, d\omega = \int_{-\infty}^{\infty} \{ \mathrm{Re}[\Gamma'(\omega)] + j\, \mathrm{Im}[\Gamma'(\omega)] \} \{\cos \omega t + j \sin \omega t\}\, d\omega$$

and therefore, since the integral of the product between an even and an odd function is zero we get:

$$\Gamma'(t) = 2 \{ \int_{0}^{\infty} \{ \mathrm{Re}[\Gamma'(\omega)] \cos \omega t\, d\omega - \int_{0}^{\infty} \mathrm{Im}[\Gamma'(\omega)] \sin \omega t\, d\omega \} \tag{6}$$

After subtraction of the constant c_1 the reflection coefficient becomes band-limited in the frequency domain. While its imaginary part remains unchanged, its real part becomes the function shown in Fig. 4.

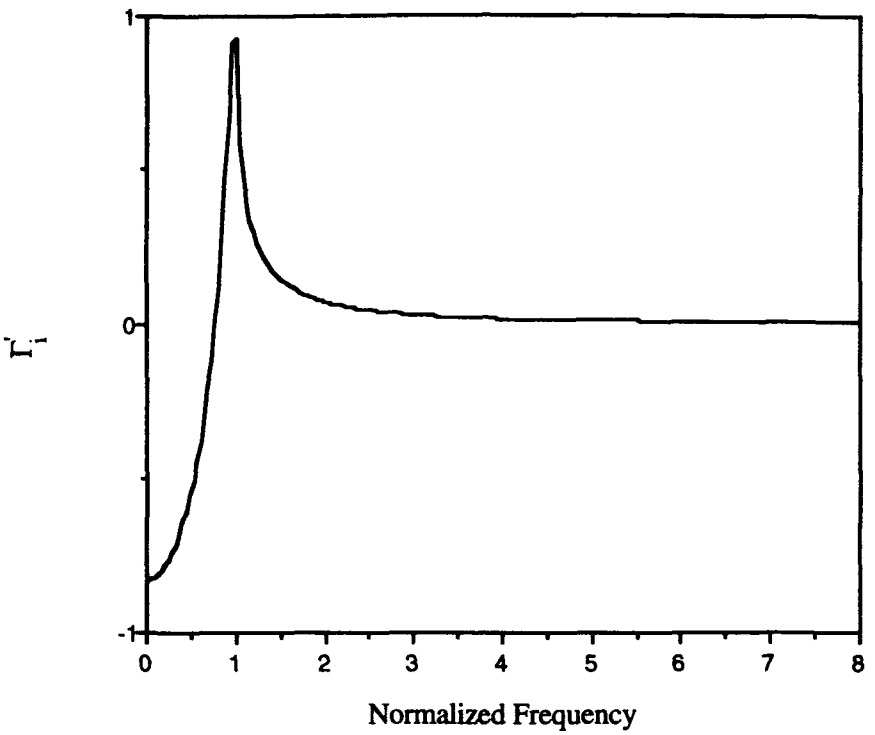

Fig. 4 Re[$\Gamma(\omega)$] as function of the normalized frequency

Since the signal in the frequency domain is limited to a relatively narrow band, it is expected that its time domain transform is spread out in time. The frequency domain energy content is essentially due to the components near and below cut-off. The signals just above cut-off propagate very slowly, giving rise to a very long tail in the time domain. The signal below cut-off corresponds to evanescent waves going back and forth near the excitation point. These waves remain trapped near the excitation point since they are prevented from traveling along the guide.

We can now separately Fourier transform the signal and the constant c_1. In this way we obtain the Johns response shown in Fig. 5. Note that this signal is composed of a Dirac pulse plus a long lasting time signal. The pulse corresponds to the constant c_1 and takes into account the very high frequency content of our impulsive excitation. This part of the signal is absorbed like a TEM wave in the parallel plate waveguide. Fig. 5

It is important to observe that the integral of the signal must be equal to - 1.

Note that a similar approach, in which frequency domain data are transformed into the time domain, has also been used in [8] (i.e. a TLM analysis of very thin resistive sheets) leading to a different procedure. In particular, in [8], the data have been considered as periodical in the frequency domain. While this approach is appropriate for that problem, it is not convenient when calculating the Johns response.

Comparison between the analytical and numerical modal Johns responses

It is now interesting to compare the results obtained in the previous paragraph with those obtained from TLM simulations. An example of such a comparison is reported in Fig. 5. It is apparent that, apart from the initial transient, the numerical Johns response and the analytical one are almost identical (it is impossible to distinguish between the two curves).

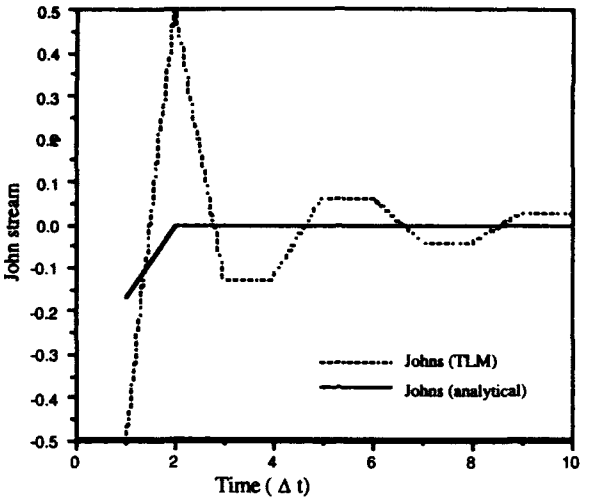

Fig. 5a Comparison of the early terms of the Johns matrix computed via TLM simulation and via analytical formulation

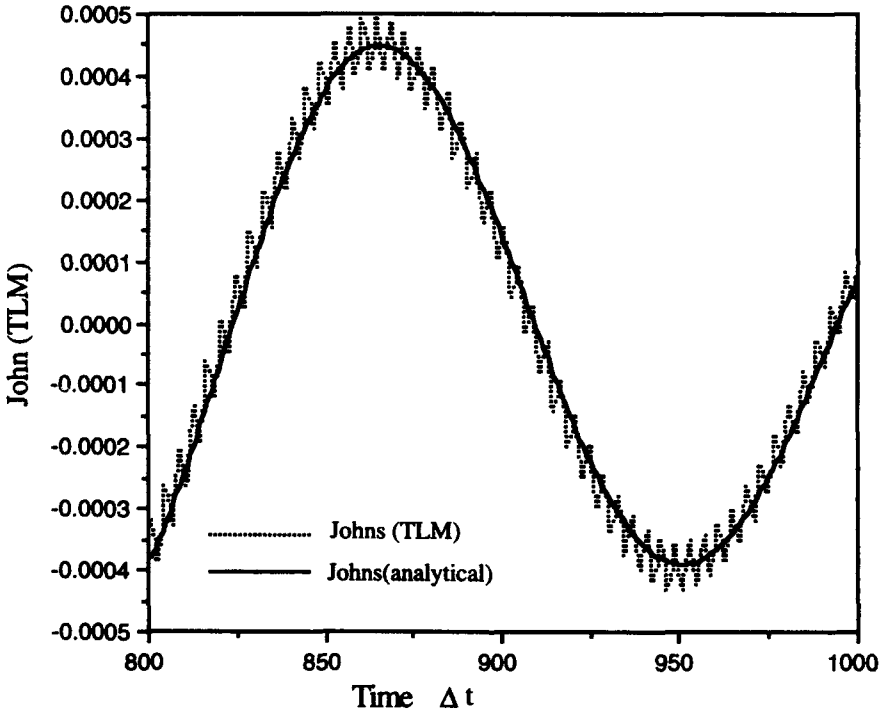

Fig. 5b Comparison of the late terms of the Johns matrix computed via TLM simulation and via analytical formulation

However, the initial difference is to be expected. In fact, the TLM simulations are only valid up to a certain frequency. Since the early response is mainly due to the high frequency content of the signal it is trivial that, in this region, some differences exist between the TLM response and the analytical one.

It is also worthwhile to note that even for the case of TEM propagation inside a parallel plate waveguide the same differences are present. In this case it is well-known that a rigorous absorbing boundary condition can be obtained by terminating the mesh in the proper resistance as already shown in Fig. 1. However if we apply the diakoptic procedure we get a different result. In fact the TLM impulse response will show an initial transient different from the physical one.

Fig. 5b shows the comparison between $\Gamma(t)$ calculated analytically and that obtained from the numerical Johns response.

To further investigate the behavior of the numerical Johns response it is convenient to compare its Fourier transform with the analytical reflection as calculated from (3).

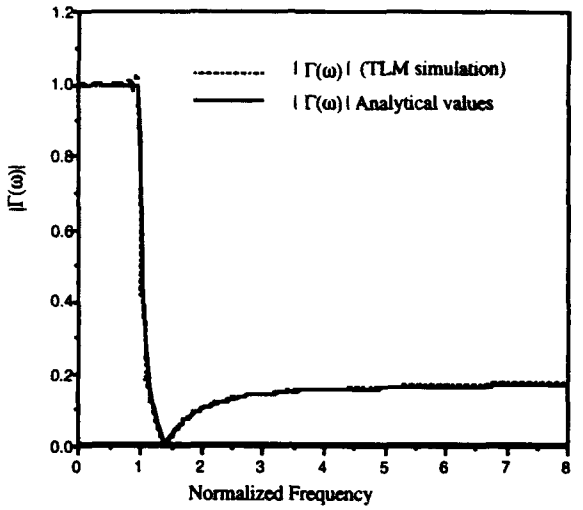

Fig. 6. Comparison between the Fourier transform of the numerical Johns response and the reflection coefficient calculated analytically

Numerical results

However, the analytically computed Johns modal response can be used in subsequent computations providing fairly accurate results. A symmetric and an asymmetric thick iris in a WR (28) waveguide have been analyzed. The mesh has been terminated λ/20 from the discontinuity. Results are compared with those obtained using the Johns matrix computed via TLM.

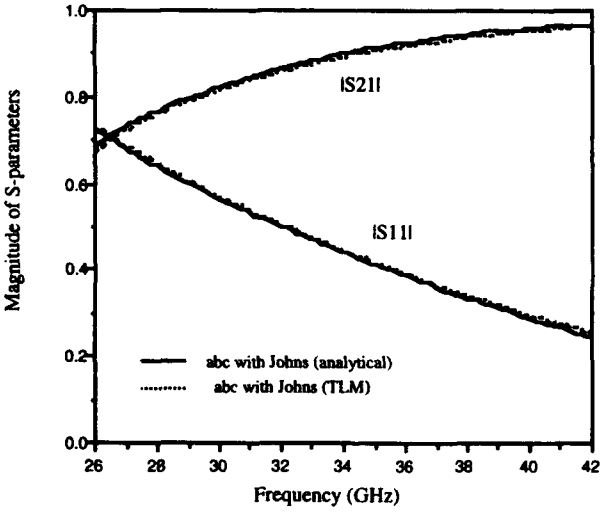

Fig. 7 Magnitude of S-parameters for an inductive iris in a WR 28 waveguide (aperture: 2/3a, thickness a/6)

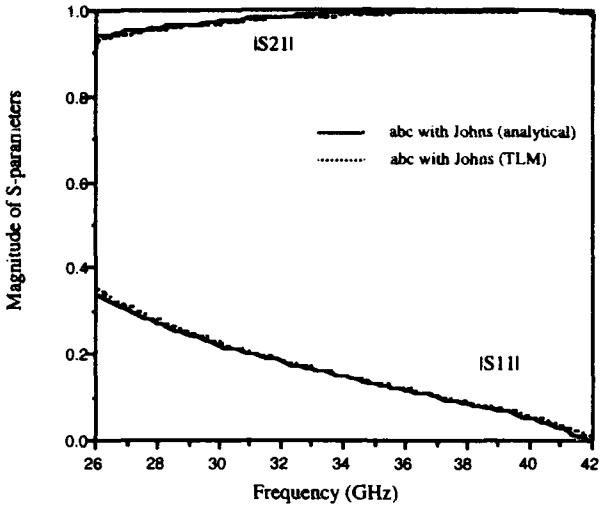

Fig. 8 Magnitude of S-parameters for an asymmetric inductive iris in a WR (28) waveguide (aperture 5/6a , thickness a/6)

Conclusions

The scattering impulse response (Johns' streams) of dispersive structures has been calculated from the frequency domain expression. By considering the impedance of the TLM mesh and by separately transforming the asymptotic term, it has been possible to calculate the Johns' stream for the fundamental mode as well as for higher order modes.In this way a dramatical reduction the computational effort has been realized.

The analytically calculated Johns' stream have been compared with the numerical one and several interesting features have been pointed out. The new Johns streams have also been used in actual TLM computations providing results almost identical to those obtained via the numerical responses.

References

[1] P.B. Johns, R.L. Beurle, "Numerical Solution of 2-Dimensional Scattering Problems using a Transmission Line Matrix", Proc. Inst. Elec. Eng., vol. 118, pp.1203-1208, Sept. 1971

[2] W.J.R. Hoefer, "The Transmission Line Matrix Method-Theory and Application", IEEE Trans. Microwave Theory and Tech., vol. 33, pp.882-893, Oct 85

[3] P. So, C. Eswarappa, W.J.R. Hoefer, "A Two-Dimensional TLM Microwave Field Simulator using New Concepts and Procedures", IEEE Trans. Microwave Theory and Tech., vol. 37, pp.1877-1883, Dec. 89

[4] P.B. Johns, A. Akhtarzad, "The use of Time Domain Diakoptics in Time Discrete Models of Fields", Int. J. Numer. Methods Eng., vol. 18, pp. 1361-1373, 1982

[5] W.J.R. Hoefer, "The Discrete Time domain Green's Function of Johns Matrix- A Powerful Concept in Transmission Line Modeling", Int. J. Numer. Modeling: Electronic and Networks, Devices and Fields., vol. 2, n. 4, pp. 215-225, 1990

[6] C. Eswarappa, G.J. Costache, W.J.R. Hoefer, "TLM Modeling of Dispersive Wideband Absorbing Boundaries with Time Domain Diakoptics for S-Parameters Extraction", IEEE Trans. Microwave Theory and Tech., vol. 38, pp.379-386, Apr.90

[7] M. Righi, M. Mongiardo, R. Sorrentino, W.J.R. Hoefer, "Efficient TLM Diakoptics for Separable Structures", IEEE MTT-Symposium Digest, pp. 425-428, 1993

[8] Z. Chen, W.J.R. Hoefer, M. Ney, "A new Procedure for Interfacing the Transmission Line Matrix Method with Frequency Domain Solutions", IEEE Trans. Microwave Theory and Tech., vol. 38, pp.1788-1792, Oct. 91

[9] W.J.R. Hoefer, P.P.M. So, "The electromagnetic wave simulator", John Wiley & Sons, 1991

Transmission-Line Matrix Modelling and Huygens' Principle or The Range of Applicability of TLM

PETER ENDERS

Stendaler Str. 126, D-12627 Berlin, FRG

Abstract. As natural processes take place in space and time, a time-domain approach may be closer to the physical reality, than other ones. Huygens' principle (HP) is a very general law for propagation. In the sense of action-by-proximity (Faraday) and superposition of secondary wavelets (Huygens' construction), it will be applied to the field propagator (Green's function). Mathematical expression of HP is now the Chapman-Kolmogorov equation. This new formulation leads to a unified representation of not only damped and undamped waves, but of virtually all phenomena being tractable by means of explicit differential and difference equations, respectively. Numerical algorithms which realize HP in discrete form provide a universal tool for the computation of such processes. The transmission-line matrix modelling method is such an algorithm; the Johns matrix being the appropriate Green's function. The principles of a monolithic TLM model of electromagnetic field, current carrier, and heat dynamics and their interaction in semiconductor devices will be outlined.

1. Introduction

TLM involves a discrete formulation of Huygens' principle (HP). This relationship is usually demonstrated by means of the 2D scalar TLM mesh (Johns 1974). One of the goals of this contribution is to establish it for the TLM method as a whole using Green's functions (GF). GF represent one of the most powerful and, at once, most beautiful and clear (propagator!) tools of Mathematical Physics at all. Thus, another goal is to show, that certain GF *themselves* may provide an *exact and clear, because immediate* formulation of Huygens' construction. It is aimed at a formulation of HP which contains no assumptions or simplifications, but even extends the application to virtually all propagation processes, which obey the principle of action-by-proximity and can be treated by means of explicit transport equations.

A discrete treatment quickly leads to random walks and related problems of probability theory. A rigorous treatment requires measure theory. This is much more, than necessary for the understanding of "common" physical propagation processes. But it may proven useful for later generalizations [*eg*, fractals for the description of wave propagation in disordered media, West (1992)]. The use of GF within such considerations is not new. However, this contribution concentrates on a *new representation of HP through GF* and *not* on a discussion of the probabilistic questions behind such approaches.

In order to avoid confusion, section 2 starts with Hadamard's notion of HP being the most exact one known to us. The superposition of secondary waves will be represented by means of general field propagators. Huygens' construction then means that these propagators (GF) obey the Chapman-Kolmogorov equation, the equation of motion of Markov processes. This leads to a description of wave motion, which overcomes certain difficulties in the interpretation of GF and of Kirchhoff's formula. Section 3 illustrates these ideas through discrete examples and discusses implications for practical computations, in particular, the fascinating perspectives for treating complex systems, such as lasers and semiconductor devices. Section 4, finally, condenses these results into thesis for the formulation of such a generalized HP and concludes this paper.

2. Huygens' principle and Green's functions

2.1. Hadamard's notion of Huygens' principle

It is preferable to follow Hadamard's exact representation of HP in form of a syllogism (Hadamard 1953, § 33):

(A) *Major premise*: "The action of phenomena produced at the instant t=0 on the state of matter at the time $t=t_0$ takes place by the mediation of every intermediate instant t=t' ...";

(B) *Minor premise*: "The propagation of light pulses proceeds without deformation (spreading, tail building) of the pulse";

(C) *Conclusion*: "In order to calculate the effect of our initial luminous phenomenon produced at ω_0 at t=0, we may replace it by a proper system of disturbances taking place at t=t' and distributed over the surface of the sphere with centre ω_0 and radius c(t'-t)."

Proposition (A) is the *principle of action-by-proximity*, proposition (C) is essentially *Huygens' construction*. Proposition (B), in contrast, holds less generally, namely for some special cases only. Well known examples are the lossless wave equation (d'Alembert's equation) in odd space dimensions and the distortion-free special case of the 1D telegrapher's equation (Heaviside, Pupin): "...when a source irradiates waves within a time interval Δt, then this stream of waves should affect the receiver within the same time interval Δt, *ie*, the speed of propagation of the waves should not depend on the oscillation frequency of the source and during whole the propagation process, the waves should suffer not any deformation through smearing or wake building" (Ivanenko & Sokolov 1953, p. 78). Here, "for the validity of H.P. it is necessary and sufficient that the Greens' function of d'Alembert's equation is proportional to the delta-function $\delta(R-cT)$ or to its derivatives" (Naas & Schmidt 1974, p. 767). The construction of equations the solutions to which are non-spreading sharp wave fronts has been developed to a special topic of its own (Günther 1988). These results may be useful for the design of dispersionless transmission systems.

Discarding the practical consequencies of (B) for signal transmission, we will adopt the use of the term HP also for the case that only (A) and (C) apply. This notion includes the generalization, that the secondary sources belong not necessarily to a *sharp* wave front. It extends unexpectedly widely the applicability of Huygens' basic idea of propagation as ordered sequence of intermediate excitations and irradiations within infinitesimal space-time intervals. Then, (B) just follows for the special cases mentioned above.

Thus, having this in mind, we will call Huygens's principle (HP) the combination of action-by-proximity ("elastic waves in ether" in Huygens' pictural imagination) and superposition of secondary wavelets (Huygens' construction).

2.2. Huygens' construction and Greens' functions

Figure 1 illustrates Huygens' construction by means of, for the present, general field propagators, $G(\mathbf{r},t|\mathbf{r}_0,t_0)$. $G(\mathbf{r},t|\mathbf{r}_0,t_0)$ is assumed to describe the propagation of all necessary information about the field considered from the space-time point $(\mathbf{r}_0,t_0)$ to $(\mathbf{r},t)$. Huygens' construction may then be expressed as follows,

$$(1) \qquad G(\mathbf{r},t|\mathbf{r}_0,t_0) = \iiint G(\mathbf{r},t|\mathbf{r}_1,t_1)G(\mathbf{r}_1,t_1|\mathbf{r}_0,t_0)d\mathbf{r}_1; \qquad t_0 < t_1 < t$$

This equation is isomorphic with the Chapman-Kolmogorov equation, the equation of motion of Markov processes. Since $t-t_0$ can be infinitesimally small, it is, moreover, an *alternative mathematical formulation* of HP in the sense of action-by-proximity and superposition of secondary wavelets (obviously, these are not necessarily sharp fronts!).

GF which represent HP in that sense and obey with respect to **r** the boundary conditions of the field variables are proposed to be termed *Huygens propagator*.

It follows at once, that, (i), wave propagation is a Markov process and, (ii), HP in that sense holds true for diffusion processes as well.

2.3. Problems of interpretation of Kirchhoff's formula and of Green's functions

Within classical wave theory, the mathematical problem of wave propagation is usually reduced to the solution of the wave equation for the field amplitude, while its time derivative is considered to be secondary. The GF is its solution for unit sources; *eg*, in 3D free (infinite, homogeneous, linear) space the expanding impulsive spherical wave

$$(2) \qquad g_f(\mathbf{r},t;\mathbf{r_0},t_0) = \frac{\delta(R/c - t)}{4\pi R};\ R \equiv |\mathbf{r_0} - \mathbf{r}|,\ \tau \equiv t - t_0$$

It obeys the Minor Premise, but does *not* fulfill the Chapman-Kolmogorov equation (1). Indeed, eq.(1) is obeyed by functions being the solution to partial differential equations of *first* order in time. For wave and other propagation processes of higher order in time one has, obviously, to "return" to systems of first-order equations. Remarkably enough, these are, in general, the *fundamental* relations, *viz*, constitutive equation(s) and law(s) of conservation, such as the Maxwell equations supplemented by appropriate constitutive relations.

Huygens propagators contain the *common* propagation of $\psi(\mathbf{r},t)$ *and* $\partial\psi(\mathbf{r},t)/\partial t$ [or $\nabla\psi(\mathbf{r},t)$] as *independent dynamical variables*. This lifts the conceptual difficulties of "building derivations in the nature" (Johns 1974) and of the "occurrence of different sources" in Kirchhoff's formula (Miller 1991). Sharp wave fronts correspond to δ-functions in the GF, which reduce the integrals over volumes to integrals over surfaces, so that diffraction at screens is treated in a manner resembling Kirchhoff's formula. The treatment of the common propagation of $\psi(\mathbf{r},t)$ and $\partial\psi(\mathbf{r},t)/\partial t$ [or $\nabla\psi(\mathbf{r},t)$] as independent dynamical variables is the *fundamental difference* between this interpretation of HP and previous ones, but Hadamard (1953) and Feynman (1948).

3. Discrete modelling

3.1. Markov chains

In *one*-step Markov chains each *two* subsequent states, $\mathbf{u_k} \equiv (u_{k,1}, u_{k,2}, \ldots)$ and $\mathbf{u_{k+1}}$, where the second index may label spatial cells, are connected through a transition matrix, **P**,

$$(3) \qquad \mathbf{u_{k+1}} = \mathbf{P}\cdot\mathbf{u_k},\quad u_{k+1,i} = \Sigma\, P_{ij} u_{k,j}$$

For k-independent **P** one obtains

$$(4) \qquad \mathbf{u_k} = \mathbf{P^k u_0} = \mathbf{P^{k-1} u_1} = \mathbf{P^{k-1}}(\mathbf{P}\cdot\mathbf{u_0}) \quad \text{etc.}$$

Thus, the evolution of such chains is describes by the Chapman-Kolmogorov equation(s)

$$(5) \qquad \mathbf{P^k} = \mathbf{P^{k-1}}.\mathbf{P} = \mathbf{P^{k-m}}.\mathbf{P^m};\quad 0 \le m \le k$$

This is just the *discrete analogue* to eq.(1) and describes too the *superposition of secondary "wavelets"*, despite of that one-step Markov processes are diffusion-like (overdamped waves).

In the discrete case, the principle of action-by-proximity means, that during a single

time interval, no cells can be reached, but the next-neighbour ones. Pascal's triangle is a simple example of such Markovean "number diffusion" obeying Huygens' recipe of construction.

For first-order processes, the Huygens propagator proves to be identical with the GF of the difference equation, while the GF of a multi-step equation of motion does, in general, not. This perfectly parallelizes the continuum case. Again, one has "to return" to a system of one-step equations of motion for a complete set of independent dynamical variables. As an example, consider the partial difference equation of 2nd order

$$V_{k+2,i} = \tau(V_{k+1,i-1}+V_{k+1,i+1}) + (\rho^2-\tau^2)V_{k,i} \tag{6}$$

being a discrete analogue to the telegraph equation (Goldstein 1951). For $\rho=0$, one gets the Lax scheme (Lax 1954) for hyperbolic equations of first order [see eqs.(7) below]. It also describes travelling voltage pulses on a network of lossless transmission lines and resistors (Johns 1977). The corresponding GF is *not* a Huygens propagator.

However, following d'Alembert, the scalar wave field **V** may be decomposed into a left-running part, **R**, and a right-running part, **L**,

$$V_{k,i} = L_{k,i} + R_{k,i}; \qquad L_{k+1,i} = \rho R_{k,i-1} + \tau L_{k,i-1}; \qquad R_{k+1,i} = \rho L_{k,i+1} + \tau R_{k,i+1} \tag{7}$$

(Johns 1977, Zauderer 1989). In matrix form,

$$\begin{pmatrix} \mathbf{L}_{k+1} \\ \mathbf{R}_{k+1} \end{pmatrix} = \begin{pmatrix} \tau\Delta_- & \rho\Delta_- \\ \rho\Delta_+ & \tau\Delta_+ \end{pmatrix} \begin{pmatrix} \mathbf{L}_k \\ \mathbf{R}_k \end{pmatrix} \equiv \mathbf{D} \begin{pmatrix} \mathbf{L}_k \\ \mathbf{R}_k \end{pmatrix}; \quad \Delta_\pm L_{k,i} \equiv L_{k,i\pm1} \tag{8}$$

This is the two-step analogue to eq.(6), and the "Johns matrix" (Hoefer 1989) $\mathbf{G}_{k,i;k',i'}=(\mathbf{D}^{k-k'})_{i,i'}$ is the corresponding Huygens propagator. For constant ρ and τ, one has

$$\mathbf{D}^2 = \tau(\Delta_-+\Delta_+)\mathbf{D} + (\rho^2-\tau^2)\mathbf{1} \tag{9}$$

It is proposed to term Huygens propagators like **D** *proper* or *irreducible*, since elements of them obey the multi-step equation of motion, too. The corresponding eigenvalue equation diagonalizes the first-order equations of motion to a physically relevant equation.

3.2. Monolithically modelling semiconductor devices

Semiconductor devices work due to intriguing interactions of different force fields. Since carrier and heat diffusion as well as electromagnetic and matter waves are subject to HP, it should be possible to construct monolithic device models which overcome the drawbacks of the conventional computing of the subsystems using different algorithms together with inefficient data sweeps. An example is given in Fig. 2. Of course, for optical frequencies, one has to separate the fast optical oscillations (they will apear as pseudo-sources in Maxwell's equations). The use of *first*-order equations within TLM makes slowly varying envelope *approximations* not *a priori* necessary, however. The time-domain (TD) character of TLM makes this approach appealing, in particular, for fast transient processes. The carrier momentum (intra-band relaxation!) can be included on equal footing opening promising alternatives to numerically cumbersome Monte Carlo techniques. Dispersion is relaxation and thus can be treated within the TD as well (Hoefer 1989). Techniques of diakoptics allow for a separation of time scales in devices with slow and fast parts. Closed-form solutions for the Johns matrix facilitate the inclusion of free-space propagation, *eg*, in external resonators.

4. Discussion

The following thesis are proposed as a base for an extension of the application of HP in the generalized sense mentioned above to all propagation phenomena, which can be described by means of explicit differential and difference equations, respectively:

1. Propagation through action-by-proximity proceeds such, that the field excites secondary sources, which re-irradiate the field accordingly to the actual boundary and continuity conditions. Topologically, this principle applies on structures with next-neighbour interaction (local theories; cellular automata; certain coupled maps).
2. The field is represented by a complete set of N independent dynamical variables, where N is equal to the number of time derivations in the governing equations; in general, there are several such sets. A complete set obeys a system of N differential and difference equations of first order, respectively. N may be lowered by symmetry.
3. The Greens (matrix) function (GF) of such a system contains the propagation of that complete set. It represents HP in the sense of action-by proximity and superposition of secondary wavelets by means of the Chapman-Kolmogorov equation, cf. Fig. 1. In order to avoid perturbing boundary terms and to completely represent the propagation problem under consideration, the GF should fulfill the boundary conditions for the field variables in appropriate form. For such GF the name Huygens propagator is proposed.
4. The elimination of backward motion and the conservation of sharp fronts during propagation are special cases which evolve naturally from the governing equations and do not need additional assumptions.

The representation and interpretation of HP proposed here unifies the description of propagation processes modeled by parabolic and hyperbolic differential equations; it is the same one for Geometrical and for Wave Optics, the former being a limit case, but without *ad-hoc* assumptions. Anisotropy (birefringence - Huygens 1690) is included as well as nonlinearities and fluctuating propagation conditions (Vanneste et al. 1992), audio-holography (Illenyi & Jessel 1991), the states in electrical power systems (Vasin 1990). The difficulties discussed by Johns (1974) and Miller (1991) are lifted. The GF of the TLM equations is a proper Huygens propagator exhibiting the modelling and computational advantages described. Johns' (1987) symmetric condensed node obeys even Huygens'-Hadamard's Minor Premise (Johns & Enders 1992).

The discrete modelling of wave propagation in d dimensions is connected with a 2d-step Markov chain. This suggest the hypothesis, that the dynamics of any locally interacting system with 2d degrees of freedom can be mapped on a d-dimensional TLM mesh. Thus, difference equations representing a discrete HP are directly suited for computing all propagation processes that can be described through explicit differential and/or difference equations. This should enable the simultaneous and self-consistent computation of interacting fields of different type, *eg*, heat diffusion and electromagnetic waves in lasers and in microwave ovens, or carrier transport and electromagnetic fields in semiconductor devices. Advantages are expected, in particular, for the study of fast switching and modulation processes. The carrier momentum can be included on equal footing, this yields an interesting routine for the Boltzmann equation. Within explicit schemes, self-consistency can be achieved at every (time) step, whereby convergency is considerably accelerated (Hoefer 1989). Delsanto and coworkers (1992) have argued that such an approach to simulation using local interactions is favorized by three practical advantages: (i), extremous speed due to immediate parallelizability; (ii), complex problems can be treated in a simple manner, since the local internodal connections are arbitrarily variable; (iii), the same code can be used for quite different problems, since the iterations (difference equations) are principally, *ie*, up the the values of the coefficients, identical. Such algorithms belong to the class of cellular automata (Toffioli 1984, Vichniac 1984), but there is no limitation for the state set of the nodes. In other words, they are inherently parallel.

Acknowledgement. These investigations have been started during a visiting fellowship at the University of East Anglia, Norwich, UK. I would like to thank the UK SERC and the colleagues of the School of Information Systems, in particular Donard de Cogan, for organizing this stay and for the fruitful collaboration. I am also indebted to Prof. H. Paul, Dr. R. Güther, M. Krumpholz, Prof. W. Ebeling, and Dr. R. Müller for useful discussions.

References

DELSANTO, P.P., CHASKELIS, H.H., MIGNOGNA, R.B., WHITCOMBE, T.V. & SCHECHTER, R.S. 1992 Connection Machine Simulation of Ultrasonic Wave Propagation: Two Dimensional Case. *Rev. Progr. Quant. Nondestr. Eval.* **11** (Eds. D.O. Thompson & D.E. Chimenti), Plenum Press, New York, p. 113-120; KANIADAKIS, G., DELSANTO, P.P. & SCALERANDI, M. 1992 Propagation of Electromagnetic Pulses in Stratified Media. *Physics Computing '92*, Prague, Aug. 24-28 (Eds. R. A. de Groot & J. Nadrchal), World Scientific, Singapore 1993, p. 364-365.

ENDERS, P. 1992 The Chapman-Kolmogorov Equation as Representation of Huygens' Principle and the Monolithic Self-Consistent Numerical Modelling of Lasers. *Physics Computing '92*, Prague, Aug. 24-28 (Eds. R. A. de Groot & J. Nadrchal), World Scientific, Singapore 1993, p. 328-329.

FEYNMAN, R.P. 1948 Space-Time Approach to Non-Relativistic Quantum Mechanics. *Rev. Mod. Phys.* **20**, 367-387.

GOLDSTEIN, S. 1951 On diffusion by discontinuous movements, and on the telegraph equation, *Quart. Journ. Mech. and Appl. Math.* **IV**, 129-156.

GÜNTHER, P. 1988 *Huygens' Principle and Hyperbolic Equations*. Academic Press, New York.

HADAMARD, J. 1953 *The Cauchy Problem and the Linear Hyperbolic Partial Differential Equations*. Dover, New York 1953.

HOEFER, W.J.R. 1989 Linear and Nonlinear Field Modelling in the Time Domain with the Transmission Line Matrix (TLM) Method, *Alta Frequenza* **LVIII** (5-6) 541-549.

HOEFER, W.J.R. 1991 Huygens and the Computer - A Powerful Allianz in Numerical Electromagnetics. *Proc. IEEE* **79**, 1459-1471.

HUYGENS, CHR. 1690 *Traité de la lumiere*. Pierre van der Aa, Leiden.

ILLENYI, A. & JESSEL, M. 1991 Holographics, a spread-out of the basic ideas on holography into audio-acoustics. In: Holography, Commemorating the 90th Anniversary of the Birth of Dennis Gabor, Tatabanya, H, 2-5 June 1990; SPIE Institutes for Advanced Optical Technologies, Vol. **IS 8** (1991). Bellingham: SPIE Optical Engineering Press, pp. 39-52.

IWANENKO, D.I. & SOKOLOW, A. 1953 *Klassische Feldtheorie*. Akademie-Verlag, Berlin.

JOHNS, D.P. & ENDERS, P. 1992 Wave Optics Computing by a Network-Based Vector Wave Automaton. *Physics Computing '92*, Prague, Aug. 24-28 (Eds. R. A. de Groot & J. Nadrchal), World Scientific, Singapore 1993, p. 359-361.

JOHNS, P.B. 1974 A new mathematical model to describe the physics of propagation. *The Radio and Electronic Engin.* **44**, 657-666.

JOHNS, P.B. 1977 A simple explicit and unconditionally stable numerical routine for the solution of the diffusion equation. *Int. J. Numer. Meth. Engin.* **11**, 1307-1328.

JOHNS, P.B. 1987 A Symmetrical Condensed Node for the TLM Method. *IEEE Trans. Microwave Theory Tech.* **MTT-35**, 370-377.

LAX, P.D. 1954 Week solutions of Nonlinear Hyperbolic Equations and Their Numerical Computation. *Comm. Pure Appl. Math.* **7**, 159-193.

MILLER, D.A.B. 1991 Huygens's wave propagation principle corrected. *Optics Lett.* **16**, 1370-1372.

NAAS, J. & SCHMID, H.L. 1974 *Mathematisches Wörterbuch*. Akademie-Verlag, Berlin, and Teubner, Leipzig, 3rd ed., Vol. I.

TOFFIOLI, T. 1984 Cellular Automata as an Alternative to (Rather Than an Approximation of) Differential Equations in Modeling Physics. *Physica* **10D**, 117-127.

VANNESTE, C., SEBBAH, P. & SORNETTE, D. 1992 A Wave Automaton for Time-Dependent Wave Propagation in Random Media. *Europhys. Lett.* **17**, 715-720.

VASIN, V. P. 1990 Methods of global analysis of electric power systems' states of operation. *Power Engineering (New York)* **28**, 22-34

VICHNIAC, G.Y. 1984 Simulating Physics with Cellular Automata. *Physica* **10D**, 96-116.

WEST, B.C. 1992 The use of fractals in optical wave propagation through random media. *Proc. Conf. Lasers and Electro-Optic CLEO'92*, 10.-15.05.1992, Anaheim, CA, S. 506.

ZAUDERER, E. 1989 *Partial Differential Equations of Applied Mathematics*, Wiley, New York.

Huygens' construction

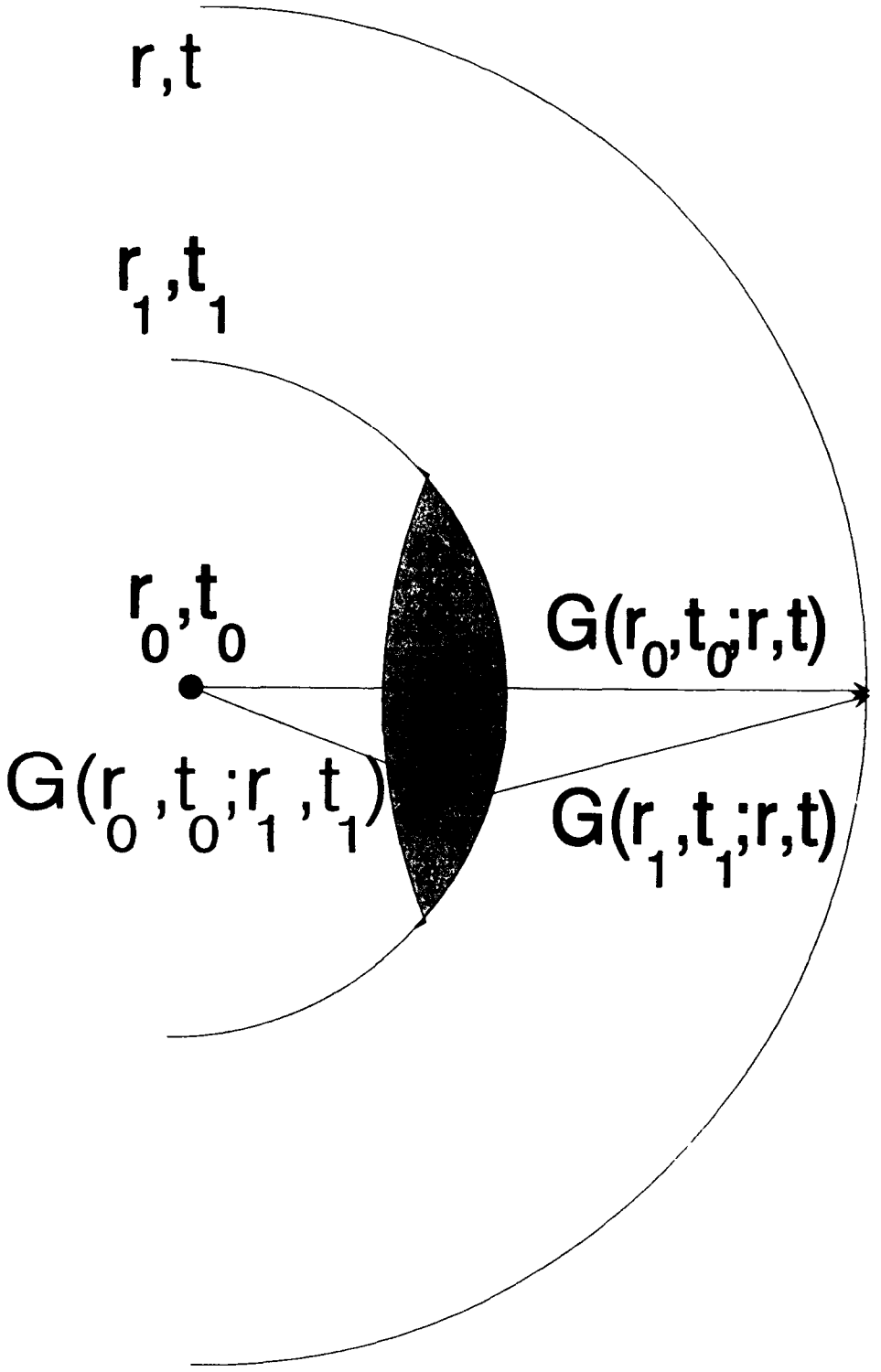

Figure 1

Monolithic TLM program paket

Modelling all subsystems of a laser with the same network algorithm (TLM): temperature, stress and optical field are computed concurrently and self-consistently

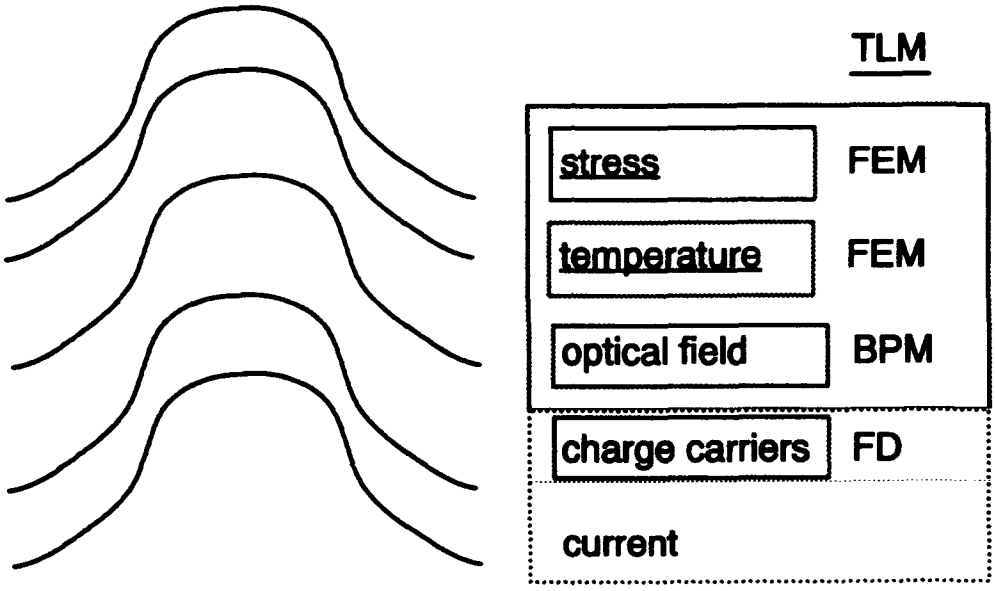

TLM: Transmission line matrix method
FEM: Finite element method
BPM: Beam propagation method
FD : Finite differences for carrier diffusion

Figure 2

TOWARDS BETTER UNDERSTANDING OF THE SCN TLM METHOD FOR INHOMOGENEOUS PROBLEMS

Malgorzata Celuch - Marcysiak

Institute of Radioelectronics, Warsaw University of Technology,
Nowowiejska 15/19, 00-665 Warsaw, Poland.
tel./fax: (+48 22) 255248, e-mail: czarekm@ire.pw.edu.pl

Abstract: Properties of the SCN TLM method for inhomogeneous problems are studied via the dispersion relations of the stub-loaded condensed node. It is originally demonstrated that these relations emulate the physical solution in the form of two dispersion surfaces. Consequently, errors of the SCN TLM depend on the intrinsic impedance of the modelled medium and on wave polarization, which does not happen in case of the classical expanded node. Included is the comparison of computer effort required by the condensed node and expanded node modelling for equal values of dispersion limits and ranges in the analysis of inhomogeneous problems.

1. INTRODUCTION.

Since the proposal of the symmetrical condensed node (SCN) [1], the SCN TLM method has been gaining a prominent place in science and engineering. In application to homogeneous electromagnetic problems, the properties of the SCN TLM have been investigated by Allen et al.[2], Nielsen and Hoefer [3] and Krumpholz and Russer [4], showing enhanced accuracy in comparison with the classical expanded node (ExpN) models. In application to inhomogeneous problems however, the SCN introduces numerical effects which have not been theoretically predicted, and which may in some cases deteriorate overall performance of the method. In recent papers Celuch and Gwarek [5][6] have revealed the effect of bilateral dispersion - meaning the coexistence of positive and negative dispersion errors within the SCN model of one circuit. Rationale behind this contribution is to provide a more diverse insight into the performance of the SCN TLM for inhomogeneous problems.

We shall begin by formulating dispersion relations of the stub-loaded SCN. From the physical viewpoint, dispersion relations describe how an arbitrary plane wave is distorted as it propagates through each homogeneous subregion of the model. Thus, they serve to estimate overall accuracy of the SCN TLM in application to inhomogeneous circuits of fairly regular geometry, such that additional errors due to imperfect representation of spatial discontinuities can be neglected.

Numerical phenomena deduced from the dispersion relations will be demonstrated in several examples. The notions of *dispersion limit* and *dispersion range* will be put forward, as criteria for evaluating the accuracy of the SCN TLM. Concluding, comparison of the SCN with the ExpN will be conducted, in terms of computer resources required by the two models to provide equal dispersion limits and ranges for various classes of electromagnetic problems.

2. DISPERSION RELATIONS FOR THE STUB-LOADED SCN.

A basic form of the condensed node is capable of representing only one medium in a circuit. For clarity, we shall consider this reference medium to be vacuum. Dielectric or magnetic filling in subregions of the circuit is then modelled at appropriate nodes by means of additional open or short stubs, respectively [1]. Scattering at the stub-loaded node is given by:

$$\underline{\underline{S}}\ \underline{V}^{i} = \underline{V}^{r} \qquad (1)$$

where $\underline{V}^{r}$ and $\underline{V}^{i}$ are vectors of reflected and incident pulses on 12 link lines and 6 stubs, and the 18x18 matrix $\underline{\underline{S}}$ can be found in [1].

Pulses reflected from one node on lines 1..12 are incident at the neighbouring nodes at the next time-step. Pulses reflected on stubs 13..18 return to the same node. These relationships can be formally described by a sparse connection matrix $\underline{\underline{C}}$:

$$\underline{\underline{C}}\ \underline{V}^{r} = \underline{V}^{i} \qquad (2)$$

Consider a plane wave supported by the SCN model, with frequency f and propagation constant $\underline{B}$:

$$\underline{B} = (\beta_x, \beta_y, \beta_z) \qquad (3)$$

In this case, the nonzero elements of $\underline{\underline{C}}$ become exponential functions of $f\Delta t$, $\beta_x a$, $\beta_y a$, $\beta_z a$, for example:

$$C_{2,9} = C_{4,8} = \exp(j\beta_x a - j2\Pi f\Delta t)$$

where a, Δt are the discretization steps of space and time, respectively.

Complete formal description of the SCN TLM simulation is given by:

$$\underline{\underline{C}}\ \underline{\underline{S}}\ \underline{V}^{i} = \underline{V}^{i} \qquad (4)$$

Nontrivial solutions of (4) exist if:

$$\det(\underline{\underline{C}}\ \underline{\underline{S}} - \underline{\underline{I}}) = 0 \qquad (5)$$

where $\underline{\underline{I}}$ is an 18x18 identity matrix. Equation (5) will be referred to as a general dispersion relation of the SCN TLM method.

The SCN TLM method produces solutions to the Maxwell equations as linear combinations of eigenmodes of (5). For each eigenmode the relation between f and $\underline{B}$ is defined by the corresponding eigenvalue of (5). In this way the eigenvalues and eigenmodes of (5) determine fundamental properties of the SCN TLM method. Generally, we must consider two aspects:

1. existence of spurious modes,
2. errors in approximating physical modes.

Spurious modes are eigenmodes of relation (5) which do not satisfy the Maxwell equations. Although spurious modes will not be discussed in this contribution, it is worth mentioning that observations previously made for the SCN without stubs [3][4][5] extend also to the stub-loaded case.

For physical modes the relation between f and $\underline{B}$ given by the eigenvalue of (5) approaches the dispersion relation of the analytic Maxwell solution in the infinitisimal limit of $a, \Delta t \rightarrow 0$. For $a, \Delta t > 0$ however there is a discrepancy between the analytical and numerical dispersion relation which we shall call a dispersion error of the SCN TLM.

Let us recall that for the ExpN modelling numerical dispersion relations within an arbitrary medium are given by:

$$-r^2 \sin^2 \frac{2\pi f \Delta t}{2} + \sin^2 \frac{\beta_x a}{2} + \sin^2 \frac{\beta_y a}{2} + \sin^2 \frac{\beta_z a}{2} = 0 \qquad (6)$$

where $r = \dfrac{a}{c\,\Delta t\,\sqrt{\mu_r\,\varepsilon_r}}$

and for stability, everywhere in the model $r \geq \sqrt{2}$ in 2D ($\beta_z = 0$) and $r \geq \sqrt{3}$ in 3D.

Unfortunately, extraction of an equally simple formula for the stub-loaded SCN from (5) seems a cumbersome task. So far, this has been achieved for the case of 2D propagation [5][6]. For the mode comprising H_z, E_x, E_y field components in a dielectric ($\mu_r = 1$) we have obtained:

$$-\left[\cos(2\pi f\,\Delta t) - (1 - 1/\varepsilon_r)\sin^2 \frac{\beta_x a}{2}\right]\left[\cos(2\pi f\,\Delta t) - (1 - 1/\varepsilon_r)\sin^2 \frac{\beta_y a}{2}\right] + \qquad (7)$$

$$+ \left[\cos \frac{\beta_x a}{2} \cos \frac{\beta_y a}{2}\right]^2 = 0$$

Similarly for the $E_z H_x H_y$ - mode in a magnetic medium ($\varepsilon_r = 1$):

$$-\left[\cos(2\pi f\,\Delta t) - (1 - 1/\mu_r)\sin^2 \frac{\beta_x a}{2}\right]\left[\cos(2\pi f\,\Delta t) - (1 - 1/\mu_r)\sin^2 \frac{\beta_y a}{2}\right] + \qquad (8)$$

$$+ \left[\cos \frac{\beta_x a}{2} \cos \frac{\beta_y a}{2}\right]^2 = 0$$

For all other cases we study the dispersion errors by numerically plotting the eigenvalues of (5).

3. INTERPRETATION OF DISPERSION ERRORS.

Dispersion errors contaminate the SCN TLM simulation in two ways:

In *eigenvalue problems* $\underline{B}$ is enforced correctly by the boundary conditions. The computed value of f is such that it satisfies the numerical dispersion relation (5) or (8), and it is generally different from the physical value f_{ph}. We define a relative frequency error as:

$$\delta f = (f - f_{ph}) \,/\, f_{ph} \qquad (9)$$

By $\overline{\delta f}$ we shall denote a value of δf corresponding to the discretization of $a/\lambda = 0.1$.

In *deterministic problems* a wave of a particular frequency f is excited in the model, and it propagates with wavelength λ different from the analytical value of λ_0. We define a relative wavelength error as:

$$\delta\lambda = (\lambda - \lambda_0) \,/\, \lambda_0 \qquad (10)$$

To verify the conclusions drawn from the dispersion relations, we shall consider cubic resonators appropriately closed by electric or magnetic walls. A relative error of resonant frequency computed for mode (p,q,r) must be equal to the error predicted for the (p,q,r) direction of propagation.

4. Splitting of the SCN eigenmodes in dielectrics.

Let us begin by considering the SCN models of isotropic dielectrics. By numerically plotting (5) we detect two eigensolutions, both reducing the physical dispersion relation for $a,\Delta t \to 0$ and to the same numerical dispersion relation for $\varepsilon_r=1$. Dispersion errors associated with the two eigensolutions are presented in Fig. 1. Clearly, a single dispersion surface of the basic SCN splits into two dispersion surfaces as a result of stub-loading. The two surfaces overlap along axial and 3D diagonal directions.

In case of propagation in the xy-plane the two corresponding eigenmodes have a physical interpretation of the $H_z E_x E_y$-mode (*S1* in Fig. 1, described by (7)) and the $E_z H_x H_y$-mode (*S2* in Fig. 1).

Note that for the ExpN models a single dispersion surface is maintained within any medium (Fig. 1).

5. Dispersion as a function of impedance.

For the ExpN modelling, dispersion errors depend on wave velocity within a particular medium (see (6)); for the SCN, they additionally depend on intrinsic impedance. Considering a magnetic medium in place of a dielectric, we obtain the same dispersion surfaces as shown in Fig. 1, but with reversed physical interpretation of eigenmodes *S1*, *S2*. This is confirmed by duality of relations (7) and (8).

To demonstrate this property of the SCN, we compute cutoff frequencies of the H_{10} and H_{11} modes in square waveguides homogeneously filled with media of various ε_r,μ_r. Results are shown in Fig. 2 versus errors predicted by (5), (7).

6. Dispersion as a function of wave polarization.

In the stub-loaded SCN a single dispersion surface is maintained only for media of unit normalized impedance ($\varepsilon_r=\mu_r$). In all other media, we detect two dispersion surfaces corresponding to two orthogonal polarizations.

analytic f_{ph}[GHz]	mode	calculated f [GHz]	δf [%]
1.500	H_{10}	1.509	0.61
2.121	H_{11} E_{11}	2.091 2.130	-1.43 0.41
3.354	H_{12} E_{12}	3.311 3.408	-1.29 1.61

Tab. 1.: Cutoff frequencies in a square waveguide 50x50mm, filled with a dielectric of ε_r=4. Cell size in the SCN model is a=10mm.

An appealing consequence for eigenvalue problems consists in splitting the cutoff frequencies of H_{mn} and E_{mn} waveguide modes (Tab.1). In deterministic problems involving dual polarization, we detect change of polarization of waves propagating along other than axial or 3D diagonal directions, as exemplified in Fig.3.

7. METHOD OF COMPARISON WITH EXPN.

Hitherto the SCN and ExpN have been compared by relating their dispersion errors for a particular discretization which (in case of homogeneous circuits) appears advantageous for the SCN [2][3]. On the other hand, it is known that the SCN TLM requires more computer effort per cell per iteration than the ExpN FDTD [5]. Thus, meaningful comparison of the two models will be via computer effort required by each of them for equal overall accuracy.

It has been proposed [6] to compare the accuracy of two spatial models by means of two parameters:

δf_{max} - dispersion limit (maximum absolute value of the dispersion error),

δf_{int} - dispersion range (difference between the highest and lowest dispersion error in the model).

In many linear applications, average value of the dispersion error can be treated as a systematic error and a posteriori eliminated from the results; then, δf_{int} is of main interest.

$\varepsilon_r\mu_r$		1	2	4	9	16
ExpN	δf_{max}	1.11	1.37	1.51	1.58	1.60
	δf_{int}^{hom}	1.11	1.10	1.10	1.09	1.09
	δf_{int}^{inh}	1.11	1.37	1.51	1.58	1.60
SCN $\mu_r=1$	δf_{max}	0.62	0.62	0.71	0.75	0.76
	δf_{int}^{hom}	0.62	1.03	1.32	1.47	1.51
	δf_{int}^{inh}	0.62	1.03	1.32	1.47	1.51
SCN $\mu_r=\varepsilon_r$	δf_{max}	0.62	0.62	1.30	1.84	2.20
	δf_{int}^{hom}	0.62	1.05	1.45	1.66	1.82
	δf_{int}^{inh}	0.62	1.24	1.92	2.46	2.82

Tab.2.: Normalized (a/λ=0.1) dispersion limits and dispersion ranges [%] for the 3D SCN and ExpN models.

δf_{int}^{hom}: dispersion range within an individual medium

δf_{int}^{inh}: dispersion range in a circuit comprising this medium and

In Tab.2 we summarize the values of dispersion
and ExpN in various media. In
dispersion, we distinguish
unit normalized impedance

The data of Tab.2 should be related to the diagrams of the SCN and ExpN computer effort presented Fig.4.

8. CONCLUSIONS.

It has been shown that the dispersion relations of the stub-loaded SCN define two dispersion surfaces approximating the physical solution. For propagation in a coordinate plane the two corresponding eigenmodes of the SCN TLM have simple physical meaning of TE and TM waves. Practical consequence is that the dispersion errors of the SCN TLM method depend on the polarization of emulated fields and on the intrinsic impedance of the modelled medium. These numerical effects do not contaminate the ExpN modelling.

Interesting observations are made by relating the accuracy of the ExpN and SCN models to the required computer effort. Only in application to homogeneous circuits advantages of the SCN as claimed by previous authors [2][3] are unambigously confirmed.

In the presence of inhomogeneitites, computer effort increases more rapidly for the SCN than for the ExpN. Also the dispersion range of the SCN increases faster and may exceed that of the ExpN in problems involving significant differences of media parameters. However, the dispersion limit of the SCN will typically remain smaller than that of the ExpN, except for the theoretical case of media with $\varepsilon_r \approx \mu_r$. Summarizing, the ExpN appears promising for 2D and vector 2D problems which include in particular full-wave analysis of dispersive transmission lines [7][8][9]. For general inhomogeneous 3D problems there appears to be good compensation between lower dispersion limit of the SCN and higher efficiency of the ExpN.

REFERENCES:

[1] P.B.Johns, "A Symmetrical Condensed Node for the TLM Method", *IEEE Trans. on MTT*, vol.MTT-35, April 1987, pp.370-377.

[2] R.Allen, A.Mallik, P.Johns, "Numerical Results for the Symmetrical Condensed TLM Node", *IEEE Trans. on MTT*, vol.MTT-35, April 1987, pp.378-382.

[3] J.S.Nielsen, W.J.R.Hoefer, "Effect of dispersion in the 3-D condensed node TLM mesh", *IEEE MTT-S Digest*, Albuquerque 1992, pp.853-855.

[4] M.Krumpholz, P.Russer, "A generalised method for the calculation of TLM dispersion relations", *Proc.23rd Eur.Microwave Conf.*, Madrid 1993, pp.287-289.

[5] M.Celuch-Marcysiak, W.K.Gwarek, "On the aspects of selecting the symmetrical condensed node or the expanded node modelling for electromagnetic simulations", *Proc.22nd Eur.Microwave Conf.*, Helsinki 1992.

[6] M.Celuch-Marcysiak, W.K.Gwarek, "On the Effect of Bilateral Dispersion in Inhomogeneous Symmetrical Condensed Node Modelling", accepted for publication in *IEEE Trans. on MTT*.

[7] C.Mroczkowski, W.K.Gwarek, "Microwave circuits described by two-dimensional vector wave equation and their analysis by FD-TD method", *Proc.21st Eur.Microwave Conf.*, Stuttgart 1991, pp.199-204.

[8] H.Jin, R.Vahldieck, S.Xiao, "A full-wave analysis of arbitrary guiding structures using a two-dimensional TLM mesh", *Proc.21st Eur.Microwave Conf.*, Stuttgart 1991, pp.205-210.

[9] M.Celuch-Marcysiak, W.K.Gwarek, "Time-Domain Analysis of Dispersive Transmission Lines", *Journal de Physique III*, France, March 1993, pp.581-591.

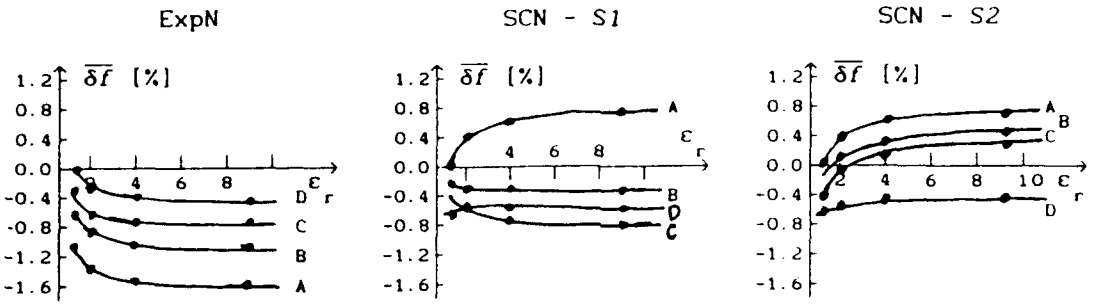

Fig.1.: Frequency errors of ExpN (single dispersion surface) and SCN (two eigensurfaces) in a dielectric (μ_r=1), for a/λ=0.1 and four directions of propagation: A - (1,0,0), B - (1,2,0), C - (1,1,0), D - (1,1,1).
——— errors predicted from relations (5),(6) and (8)
• errors detected in eigenvalue analysis of cubic resonators.

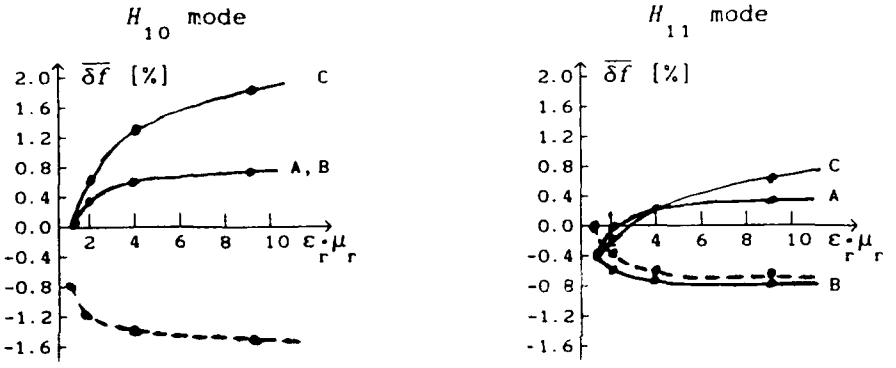

Fig.2.: Errors of calculated cutoff frequencies of modes in square waveguides homogeneously filled with various media:
—— predicted for SCN, for A: $Z = Z_0\sqrt{\mu_r}$; B: $Z = Z_0/\sqrt{\varepsilon_r}$; C: $Z = Z_0$,
--- predicted for ExpN, for arbitrary Z,
• detected in computation.

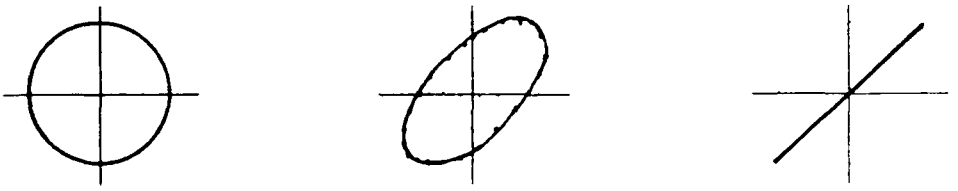

$l = 0$ $l = 10\ \lambda_0$ $l = 23.1\ \lambda_0$

Fig.3.: Change of polarization of waves of analytic wavelength λ_0, travelling distance l along the direction (1,1,0) in the SCN model of a dielectric (ε_r=9).

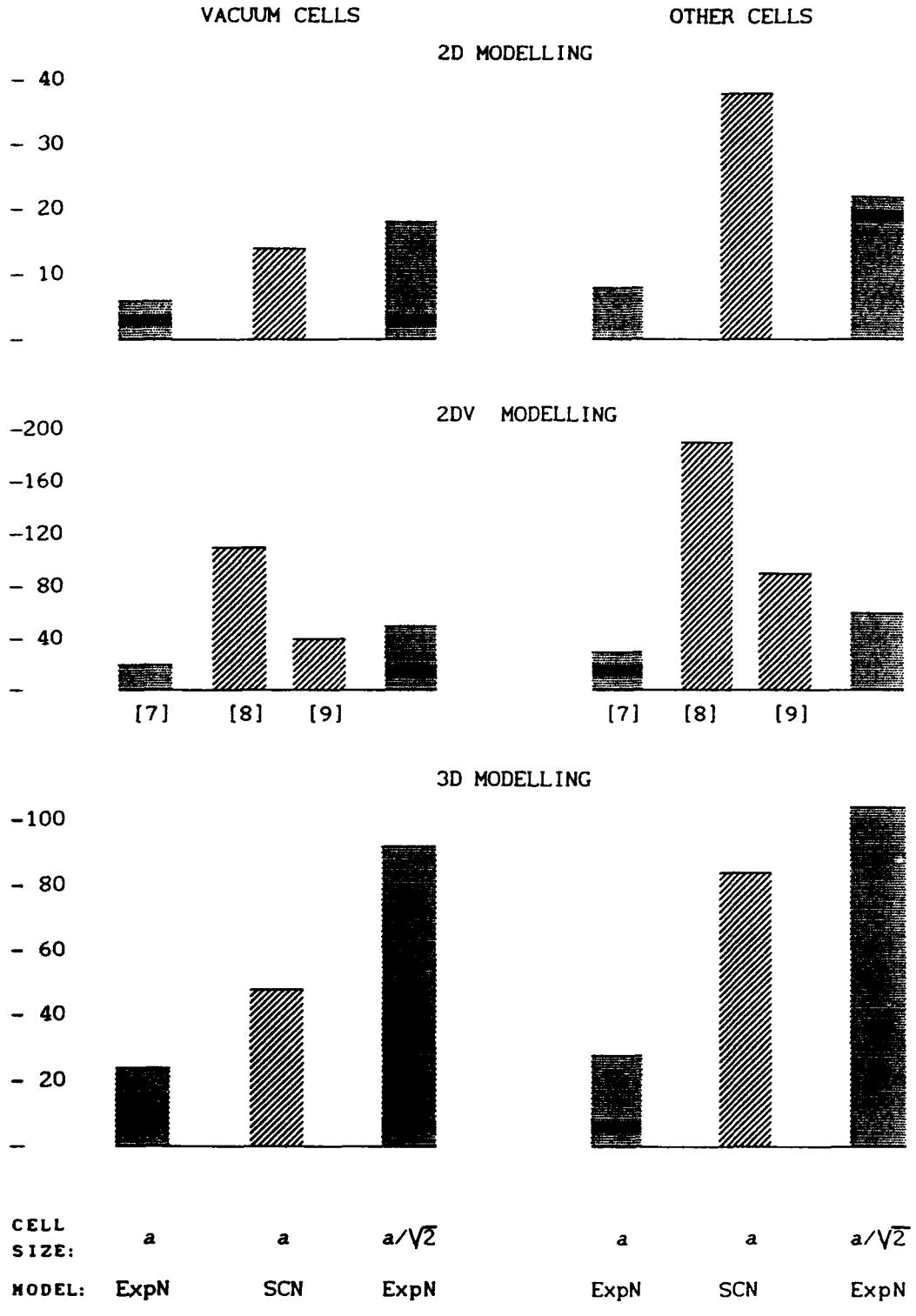

Fig. 4.: Efficiency of SCN and ExpN: number of FLOPs per circuit area a^2 in 2D (volume a^3 in 3D), per simulated time $\Delta t = a/2c$.

GENERATION OF LUMPED ELEMENT MODELS OF DISTRIBUTED MICROWAVE CIRCUITS

Peter Russer

Ferdinand-Braun-Institut für Höchstfrequenztechnik
Rudower Chaussee 5, 12489 Berlin, Germany
and Lehrstuhl für Hochfrequenztechnik Technische Universität München
Arcisstrasse 21 D-80333 München, Germany

Mario Righi
Chabanasappa Eswarappa
Wolfgang J.R. Hoefer
NSERC/MPR Teltech Research Chair in RF Engineering,
Department of Electrical and Computer Engineering
University of Victoria, Victoria, V8W 3P6 B.C., Canada

Abstract

A method for generation of lumped element equivalent circuits and the corresponing systems of ordinary differential equations for distributed microwave circuits is presented. Starting with a TLM analysis of a distributed multiport circuit the impulse response functions for reflection and transmission between the ports are computed. After Laplace–transforming the impulse functions numerically the poles are extracted within a specified domain of the complex frequency plane. From these poles canonical equivalent circuits representing the branches of the lumped element equivalent circuit are derived directly. By this way the topology as well as the parameters of the lumped element equivalent circuit are determined. Also the system of first order differential state equations is generated. The method is demonstrated in modeling of distributed one–port and multiport circuits.

1 Introduction

The transmission line matrix (TLM) method is a powerful method for modeling distributed microwave circuits [1]. Analyzing the pulse transmission and reflection behaviour in time domain provides the complete frequency domain information for a broad frequency band after Fourier or Laplace transformation Diakoptics allows the analysis of complex distributed circuits by subdividing the circuit into subcircuits [2]. The set of all the impulse reflection and transmission responses constitutes the complete description of the subcircuit. In the traditional application of time domain diakoptics in TLM the connection of the subcircuits requires the convolution of the response functions. The storage of the response functions in numerical form requires large memory, and performing the numerical convolutions requires considerable computing time. This problem is encountered especially in cases where the subcircuits exhibit a high Q factor and the impulse responses, consequently, decay slowly with time.

An alternative way to describe the subcircuits is to find an equivalent system of equations or an equivalent subcircuit exhibiting, within a specified range of frequencies, the same signal transmission behaviour as the subcircuit to be modeled. The restriction of the model to a finite range of frequencies allows to model the subcircuit by a system of ordinary differential equations or by a lumped element circuit. Lumped element modeling has already been introduced in TLM [3, 4] and has been extended to discrete state equation description [5, 6].

2 The Modeling of a Linear Reciprocal Lossless One–Port

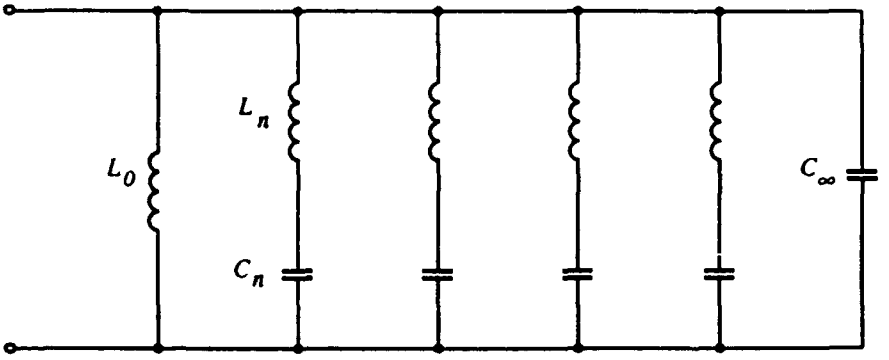

Figure 1: Equivalent Circuit of the Impedance $Y(p)$.

In the following we restrict our considerations to time–invariant linear passive lossless one–ports. In order to establish a lumped element equivalent circuit for the one–port we first calculate the impulse response by TLM simulation. From this the impedance or admittance function is calculated by Laplace transformation. After determining the location of the poles a lumped element equivalent circuit is determined by fitting of the location and residue values of the poles.

We start with the TLM calculation of the impulse response function in terms of voltage and current. The impedance or admittance representation may be chosen. We discuss the method for admittance modeling. For the impedance modeling the way to proceed follows from the principle of duality. The admittance response function $y(t)$ constitutes the relation

$$i(t) = \int_{-\infty}^{\infty} y(t_1 - t)u(t_1)dt_1 \tag{1}$$

The admittance representation can be obtained directly from TLM computations if input short circuit conditions are used. In the case of lossless circuits or circuits with high Q value the response functions corresponding to the impedance representation or the admittance representation should be determined directly from simulation under short circuit or open circuit conditions, respectively. This allows a more accurate determination of the poles than the simulation under reflection–free termination.

From the response function $y(t)$ or $z(t)$, respectively, the admittance $Y(p)$ or the impedance $Z(p)$ is calculated by Laplace transform:

$$Y(p) = \mathcal{L}\{y(t)\} = \int_0^{\infty} y(t)e^{-pt}dt \tag{2}$$

The Laplace Transform is performed numerically. In the following we restrict our considerations to the modeling of the admittance $Y(p)$. The corresponding rules for impedance modeling follow by the principle of duality. The poles p_i of the Laplace transform $Y(p)$ are determined within a specified region of the complex frequency plane $p = \sigma + j\omega$. This may be done by methods of optimization as for example by a gradient search strategy.

The next step is the synthesis of the linear passive lossless time–invariant one–port. We use the canonical Foster realization [7]. The admittance $Y(p)$ of any linear passive lossless time–invariant one–port may be represented by

$$Y(p) = \frac{A_0}{p} + \sum_{n=1}^{N} \frac{A_n p}{p^2 + \omega_n^2} + A_\infty p \tag{3}$$

From this expansion we may determine the equivalent circuit directly. Each term in the sum eq. (3) corresponds to an admittance. All these admittances are connected in parallel. The equivalent circuit of $Y(p)$ is depicted in Fig. (1). In eq. (3) A_0 and A_1 correspond to a conductor and to a capacitor, respectively. The coefficients A_n describe RL series circuits for real α_n and RLC series resonant circuits for pairs of complex conjugate α_n and α_n^*.

- The term A_0 corresponds to an inductor L_0

$$L_0 = \frac{1}{A_0} \tag{4}$$

- The term A_∞ corresponds to a capacitor C_∞

$$C_\infty = A_\infty \tag{5}$$

- For a pair of poles on the imaginary axis at $-j\omega$ and at $j\omega$ we obtain a series resonant circuit with

$$L_n = \frac{1}{A_n} \tag{6}$$

$$C_n = \frac{A_n}{\omega_n^2} \tag{7}$$

3 The Modeling of a Linear Reciprocal Lossless Multiport

Let us determine a lumped element rectance multiport which models a distributed linear rectance multiport within a specified range of frequency. We start again with TLM simulation of the impulse transmission behaviour of the circuit. From the pulse transmission functions $y_{kl}(t)$ we determine by Laplace transpormation the elements

$$Y_{kl}(p) = \mathcal{L}\{y_{kl}(t)\} \tag{8}$$

of the admittance matrix $\boldsymbol{Y}(p)$. The matrix elements Y_{kl} of the admittance matrix of a reactance multiport may be represented by

$$\boldsymbol{Y}(p) = \frac{\boldsymbol{A}^{(0)}}{p} + \sum_{n=1}^{N} \frac{\boldsymbol{A}^{(n)} p}{p^2 + \omega_n^2} + \boldsymbol{A}^{(\infty)} p \tag{9}$$

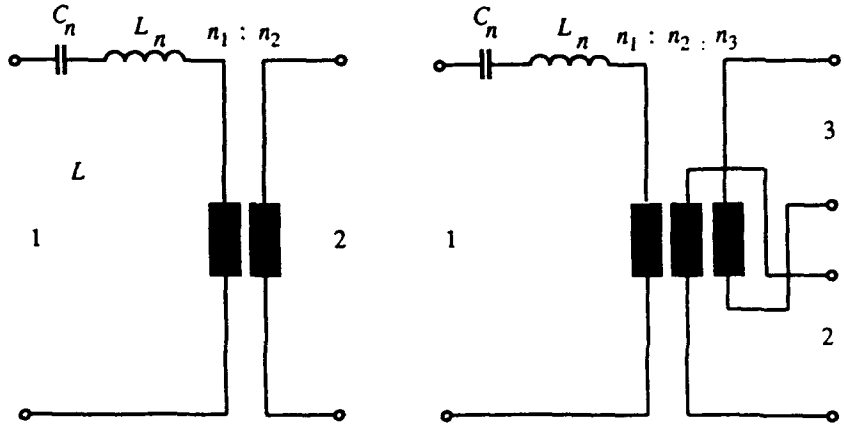

Figure 2: Compact two–port and three–port elements.

where the $\boldsymbol{A}^{(n)}$ are real, symmetric and positive semidefinite matrices. The proof is given for two–ports in [8] and holds also for multiports. Each of the matrices $\boldsymbol{A}^{(n)}$ may be represented as a sum real symmetric

matrices of rank 1. These diagonal matrices of rank 1 contribute multiport elements as depicted in Fig. 2, consisting of L, C and an ideal transformer. The turns ratio of the two transformers in Fig. 2 is given by $n_1 : n_2$ and $n_1 : n_2 : n_3$ respectively. The three-port circuit in Fig. 2 for example contributes

$$\frac{\boldsymbol{B}_i^{(n)} p}{p^2 + \omega_n^2} = \frac{1}{L_i^{(n)}} \frac{p}{p^2 + \omega_n^2} \begin{pmatrix} 1 & \frac{n_1}{n_2} & \frac{n_1}{n_3} \\ \frac{n_1}{n_2} & \frac{n_1^2}{n_2^2} & \frac{n_1^2}{n_2 n_3} \\ \frac{n_1}{n_3} & \frac{n_1^2}{n_2 n_3} & \frac{n_1^2}{n_3^2} \end{pmatrix} \tag{10}$$

4 The Equivalent System of Differential Equations

In the most general case our equivalent circuit will have one conductor G_0, one capacitor C_1, M RL–circuits and N $RLCG$–circuits in parallel. Using the currents of the inductors and the voltages of the capacitors as the state variables we obtain the following first–order differential equations:

1. The conductor G_0 is described by
$$i_0 = G_0 u \tag{11}$$
2. The capacitor C_1 is described by
$$i_1 = C_1 \frac{du}{dt} \tag{12}$$
3. The M RL–circuits are described by
$$\frac{di_m}{dt} = -\frac{R_m}{L_m} i_m + \frac{1}{L_m} u \tag{13}$$
for $m = 2$ to $m = M + 1$
4. The $RLCG$–circuits are described by
$$\frac{di_n}{dt} = -\frac{R_n}{L_n} i_n + \frac{1}{L_n} (u - u_{cn}) \tag{14}$$
$$\frac{du_{cn}}{dt} = \frac{1}{C_n} i_n - \frac{G_n}{C_n} u_{cn} \tag{15}$$
for $n = M + 2$ to $m = M + N + 1$

The total current i flowing through the equivalent circuit is given by

$$i = \sum_{n=0}^{M+N+1} i_n \tag{16}$$

5 Examples

As an example for modeling a one–port we have chosen the iris-coupled rectangular waveguide cavity resonator depicted in Fig. 3. The resonator is based on a WR 28 rectangular waveguide.

The resonator admittance Y was computed by TLM simulation and Fourier transformation of the impulse response. In the case of modeling lossless circuits or low loss circuits Fourier transformation instead of Laplace transformation can be used. The poles and the parameters of the lumped element equivalent circuit summarized in Table 1 were determined by optimization. The coefficients A_n were obtained by least-square fitting at 20 points between consecutive poles. The imaginary part $\Im\{Y\}$ of the admittance computed using TLM analysis as well as the admittance of the lumped element equivalent circuit are plotted in Fig. 4a. A comparison of the phase of the S-parameters of an iris-coupled waveguide cavity computed directly from the TLM analysis and via the lumped element model is given in Fig. 4b.

Table 1:

Poles and Lumped Element Parameters					
n	1	2	3	4	5
f_n	0.	28.14	29.76	42.77	46.93
A_n	6.16 10^7	2.26 10^7	2.26 10^7	3.96 10^7	4.0327 10^7
L_n/nH	16.24	22.11	22.17	12.63	12.40
C_n/fF	—	1.44	1.29	1.09	0.927

As an example of a two–port we consider an inductive iris in a rectangular waveguide WR 28 as shown in Fig. 5. The Y–parameters computed for this two–port using TLM analysis are plotted in Figs. 6a and 6b.

Fig. 6c gives a comparison of magnitude of S-parameters of the inductive iris. The element values obtained for the shunt admittance (based on $A_o/p + A_1 p$ approximation) are $L = 2.738$ nH and $C = 6.291$ fF. The element value obtained for the series admittance (based on A/p approximation) is L = 1.357 nH. Fig. (7) shows the lumped element equivalent circuit for the inductive iris in the rectangular waveguide.

6 Conclusion

We have presented a new method for computer aided generation of lumped element equivalent circuits for linear reciprocal distributed microwave circuits. The method is based on a field theoretical analysis of the distributed multiport circuit. It allows to generate the topology as well as the parameters of the lumped element equivalent circuit after specifying an arbitrary but finite interval of frequencies for the lumped element equivalent circuit.

References

[1] W.J.R. Hoefer, "The Transmission Line Matrix (TLM) Method", Chapter 8 in "Numerical Techniques for Microwave and Millimeter Wave Passive Structures", edited by T. Itoh, J. Wiley, New York, 1989, pp. 496-591.

[2] W.J.R. Hoefer, "The Time-Domain Green's Function or Johns Matrix - A New Powerful Concept in TLM," Intl. Journal of Numerical Modelling; Vol. 2; No. 4 Dec. 1989, pp. 215-225.

[3] P. Russer, P. P. M. So., W. J. R. Hoefer, "Modeling of Nonlinear Active Regions in TLM." *IEEE Microwave and Guided Wave Letters*, Vol. 1 No. 1, pp. 10-13, 1991.

[4] W.J.R. Hoefer, B. Isele, P. Russer, "Modelling of Nonlinear Active Devices in TLM," in: *IEE Int. Conf. Computation in Electromagnetics*, (London), Nov. 25-27, 1991.

[5] B. Isele, P. Russer, "Modelling of Nonlinear Dispersive Elements in TLM," *IEEE-MTT-S International Microwave Symposium 1992*, (Albuquerque, New Mexico)). 1-5 Juni, 1992, pp. 1217-1220.

[6] B. Isele, P. Russer, "State Variable Representation of Nonlinear Active Elements in TLM," *URSI Int. Symposium on Electromagnetic Theory 1992*, (Sydney), August 17-20 1992, pp. 227-229.

[7] V. Belevitch, "Classical Network Theory," Holden-Day, San Francisco, 1968.

[8] R. Unbehauen, "Synthese elektrischer Netzwerke und Filter." Oldenbourg, München 1988.

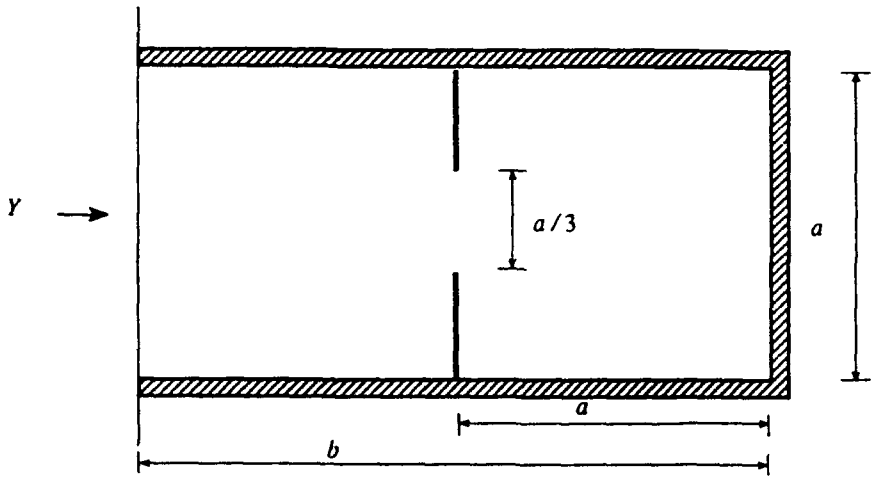

Figure 3: Resonator with iris-coupling to waveguide.

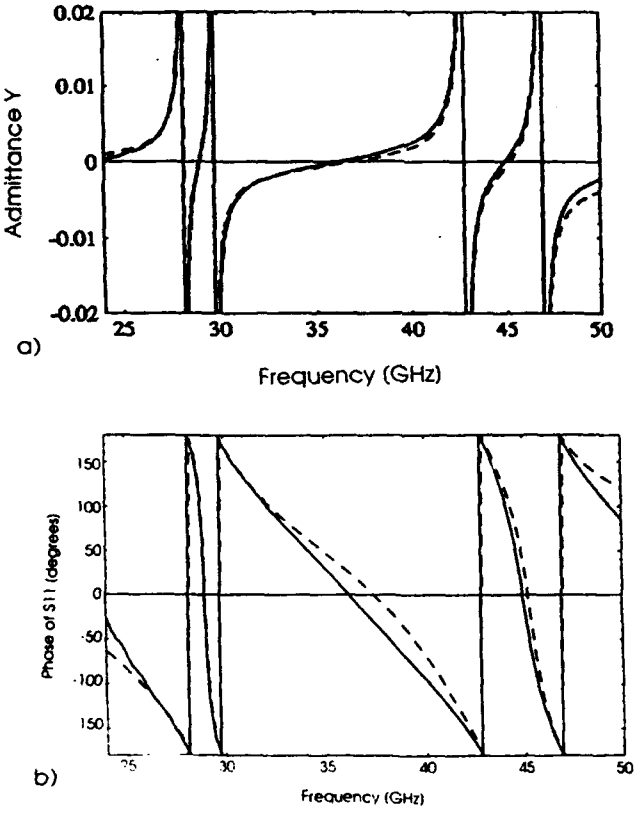

Figure 4: (a) Imaginary part $\Im\{Y\}$ of the admittance of the one–port cavity.
— TLM analysis, - - via lumped element model.
(b) Comparison of S-parameters of an iris-coupled waveguide cavity.
— TLM analysis, - - via lumped element model.

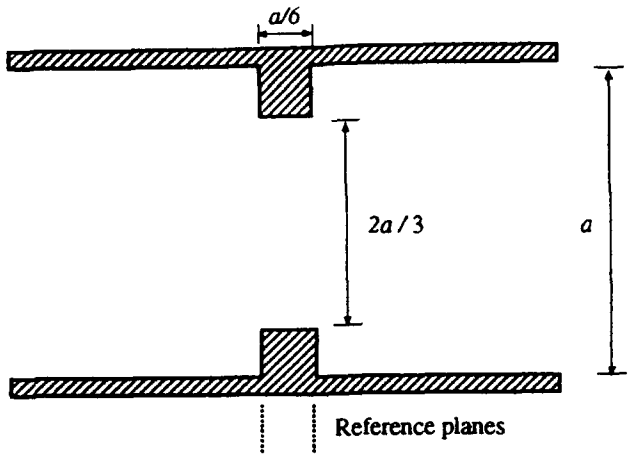

Figure 5: Inductive iris in rectangular waveguide.

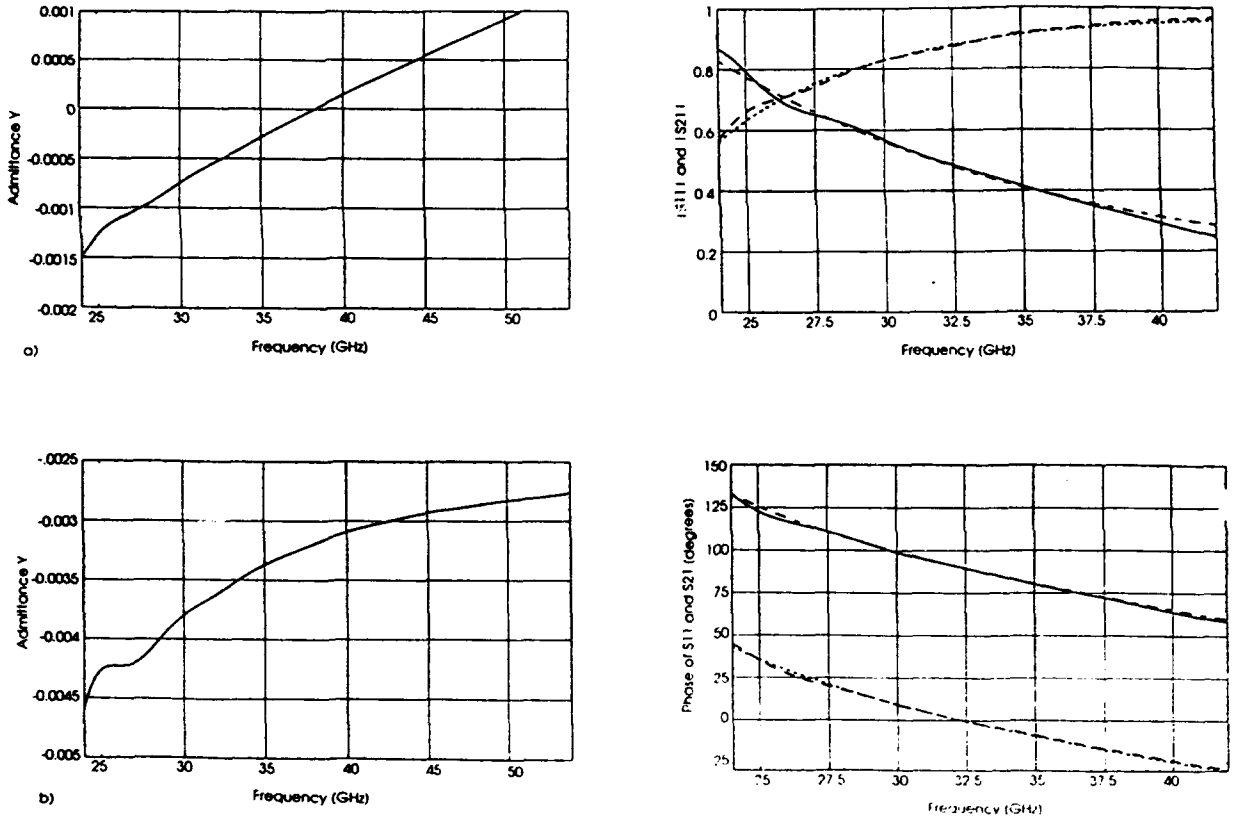

Figure 6: Imaginary parts of the shunt admittance (a) and series admittance (b) of the iris discontinuity. Comparison of magnitude of S-parameters of the inductive iris: - S11 (TLM), - . S11 (lumped element model), - - S21 (TLM), ... S21 (lumped element model)

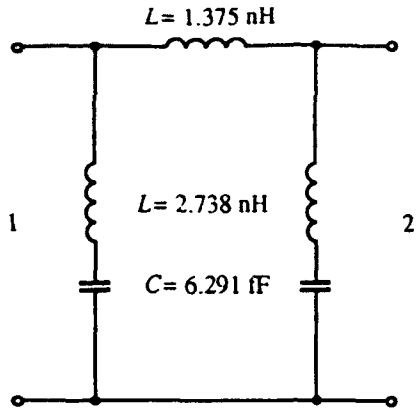

Figure 7: Equivalent circuit for the inductive iris in the rectangular waveguide.

Towards Exactly Modelling Open/Absorbing Boundaries

P. ENDERS (a) & A. J. WLODARCZYK (b)

(a) Stendaler Straße 126, D-12627 Berlin, FRG
(b) Kimberley Communications Consultants
104 GPT Business Park, Beeston, Nottingham NG9 2ND, UK

Open/absorbing boundaries can be modelled exactly by means of Green's functions (GF) which describe the genuine field propagation properties of the domain considered. In many cases, the laborous space-time iteration usually necessary for calculating the GF can be avoided by means of closed-form solutions of the difference equations of the numerical routine used. A general approach for obtaining such solutions will be described and closed-form solutions for the 2D scalar wave mesh and for the symmetrical condensed node routine of the transmission-line matrix modelling method will be presented.

1. INTRODUCTION

The numerical simulation of open/absorbing boundaries is an old challenge of computing. The correct description of the reflection of waves at arbitrary angles of incidence requires to account for the complete reaction of the physical space behind the mathematical boundary. This response behaviour is contained in the so-called Green's function (GF). The GF $G(\mathbf{r},t;\mathbf{r}_0,t_0)$ describes the field propagation from the space-time point $(\mathbf{r}_0,t_0)$ to the point $(\mathbf{r},t)$. It is, thus, a clear concept and, moreover, one of the most powerful tools of mathematical physics. Its full capabilities have not yet been employed in computing. The application to the present problem has been investigated by Hoefer (1989) and by Krumpholz and Russer (1993) within the transmission-line matrix modelling method (TLM).

The GF is the solution to the field equations with unit source. Hence, its computation requires usually to perform the complete space-time iterations of the numerical routine. In many cases, however, it is possible to circumvent this time-consuming procedure by applying closed-form solutions to the difference equations of the numerical routine. This contribution presents a simple approach to obtain such solutions for explicit FD algorithms, *ie*, for cellular automata with infinite state space of the nodes. Other applications of such non-iterative formulae consist in their general information on the accuracy of the method (Goldstein 1951, Enders & de Cogan 1993) and due to the tight connection of GF with the transfer functions.

Cellular automata (Farmer *et al* 1984) are network structures, where the state of a cell depends only on the states of its neighbouring cells. Consequently, they are predestined to yield discrete models of processes for which the principle of action-by-proximity holds, *ie*, virtually *all* physical propagation. Such structures are highly interesting from several points of view. In particular, transputer arrays are able to realize such topological structures and, thus, to materialize the "computing space" (Zuse 1969). The next-neighbour interaction structure favours *parallel* information processing (*eg*, Johns 1988, Vanneste et al. 1992). This is a distinctive advantage of explicit algorithms when compared with implicit ones. Moreover, within explicit routines, diakoptic methods are much easier to implement and, for nonlinear problems, self-consistency can be reached at each (time) step.

To be specific, in this contribution, the TLM difference equations for the 2D free space and for the symmetrical condensed node will be considered.

2. 2D SCALAR WAVES

For the incident pulses, the governing equations (Johns 1974) read in condensed form

$$\begin{pmatrix} \mathbf{W} \\ \mathbf{S} \\ \mathbf{E} \\ \mathbf{N} \end{pmatrix}_{k+1} = \frac{1}{2} \begin{pmatrix} \bar{x} & \bar{x} & -\bar{x} & \bar{x} \\ \bar{y} & \bar{y} & \bar{y} & -\bar{y} \\ -x & x & x & x \\ y & -y & y & y \end{pmatrix} \equiv \boldsymbol{H} \begin{pmatrix} \mathbf{W} \\ \mathbf{S} \\ \mathbf{E} \\ \mathbf{N} \end{pmatrix}_{k} \tag{2.1}$$

where $\pm xW(i,j)=\pm W(i+1,j)$, $\pm \bar{x}W(i,j)=\pm W(i-1,j)$ etc. are short-hand notations for step operators acting on the space coordinates. The reflected pulses have been eliminated from the original equations as they are irrelevant for this investigation. The space considered is thus the product space of the 4D vector space of the travel directions, W...N ("direction space"), of the 2D vector space of the (i, j) coordinates ("coordinate space"), and of the 1D vector space of the time axis. Vectors and matrices of the product space will be designed by bold italic capitals (***H***), those of the direction space - by italic capitals (*J*), and those of the coordinate space - by bold capitals (**W**).

The Johns matrix, ***J***, yielding the general solution of these equations as function of the initial values is defined as

$$\begin{pmatrix} \mathbf{W} \\ \mathbf{S} \\ \mathbf{E} \\ \mathbf{N} \end{pmatrix}_{k;i,j} = \sum_{i',j'} {}^{k-k'}\boldsymbol{J}_{i,j;i,j'} \begin{pmatrix} \mathbf{W} \\ \mathbf{S} \\ \mathbf{E} \\ \mathbf{N} \end{pmatrix}_{k';i',j'} ; \qquad \boldsymbol{J} = \begin{pmatrix} \mathbf{J}^{WW} & \mathbf{J}^{WS} & \mathbf{J}^{WE} & \mathbf{J}^{WN} \\ \mathbf{J}^{SW} & \mathbf{J}^{SS} & \mathbf{J}^{SE} & \mathbf{J}^{SN} \\ \mathbf{J}^{EW} & \mathbf{J}^{ES} & \mathbf{J}^{EE} & \mathbf{J}^{EN} \\ \mathbf{J}^{NW} & \mathbf{J}^{NS} & \mathbf{J}^{NE} & \mathbf{J}^{NN} \end{pmatrix} \tag{2.2}$$

The difference to eq.(5) of Hoefer's (1989) paper results from the fact that there, the "incident pulses" are treated as excitations by an external source. From eq. (2.1) one obtains

$${}^{k-k'}J_{i,j;i',j'} = \boldsymbol{H}^{k-k'}\delta_{ii'}\delta_{jj'} \tag{2.3}$$

where each matrix element of the operator $\boldsymbol{H}^{k-k'}$ acts on the initial Kronecker distribution $\delta_{ii'}\times\delta_{jj'}$. Thus, ***J*** can be calculated by first diagonalizing ***H*** and then transforming back the powered diagonal form. The following steps of calculation are equivalent to this method, but, moreover, yield the solution of the system (2.1) for other initial conditions as well (*eg*, ${}_0\mathbf{W}...{}_3\mathbf{W}$ given). First, ***H*** will be diagonalized in the direction space, then, the resulting partial difference equation in the coordinate-time space will be solved algebraically by simple means.

First step. The eigenvalue equation to ***H*** reads

$$0 = \lambda^4 - P(\lambda^3 - \lambda) - 1 = (\lambda^2 - 1)(\lambda^2 - P\lambda + 1); \qquad P \equiv \tfrac{1}{2}(\bar{x} + x + \bar{y} + y) \tag{2.4}$$

According to the Caley-Hamilton theorem, ***H*** obeys its own eigenvalue equation, *ie*,

$$\boldsymbol{H}^4 - P(\boldsymbol{H}^3 - \boldsymbol{H}) - \boldsymbol{1} = \boldsymbol{0} \tag{2.5}$$

(***H*** and *P* commute; *P* is not a vector). Applying this operator equation on eq.(2.1) yields

$$ {}_{k+4}\begin{pmatrix} \mathbf{W} \\ \mathbf{S} \\ \mathbf{E} \\ \mathbf{N} \end{pmatrix} = P\ {}_{k+3}\begin{pmatrix} \mathbf{W} \\ \mathbf{S} \\ \mathbf{E} \\ \mathbf{N} \end{pmatrix} - P\ {}_{k+1}\begin{pmatrix} \mathbf{W} \\ \mathbf{S} \\ \mathbf{E} \\ \mathbf{N} \end{pmatrix} + {}_{k}\begin{pmatrix} \mathbf{W} \\ \mathbf{S} \\ \mathbf{E} \\ \mathbf{N} \end{pmatrix} \qquad (2.6) $$

In other words, each component, $\mathbf{U}_M$, of the four-vector $\boldsymbol{U}=(\mathbf{W}, \mathbf{S}, \mathbf{E}, \mathbf{N})^t$ obeys the fourth-order partial difference equation

$$ {}_{k+4}\mathbf{U}_M = \tfrac{1}{2}(\bar{x}+x+\bar{y}+y)({}_{k+3}\mathbf{U}_M - {}_{k+1}\mathbf{U}_M) + {}_{k}\mathbf{U}_M; \qquad M = W,S,E,N \qquad (2.7) $$

Such multi-step, but decoupled equations are often easier to solve algebraically, than systems like (2.1).

Second step. In contrast to the scalar eigenvalue equation (2.4), the "eigenoperator" equation (2.5) does *not* factorize, since the matrix $(\boldsymbol{H-1})$ is singular. In fact,

$$ \boldsymbol{\Delta \equiv H^2 - PH + 1} = \begin{bmatrix} 1 & -\frac{1+\bar{x}z}{2} & \frac{\bar{z}+z\bar{x}}{2} & -\frac{1+\bar{x}\bar{z}}{2} \\ -\frac{1+x\bar{z}}{2} & 1 & -\frac{1+\bar{x}\bar{z}}{2} & \frac{\bar{x}+x}{2}\bar{z} \\ \frac{z+\bar{z}}{2}x & -\frac{1+xz}{2} & 1 & -\frac{1+x\bar{z}}{2} \\ -\frac{1+xz}{2} & \frac{\bar{x}+x}{2}z & -\frac{1+\bar{x}z}{2} & 1 \end{bmatrix} \neq \boldsymbol{0} \qquad (2.8) $$

Moreover, there are *four* initial value sets, ${}_0\mathrm{W}(i,j)\ldots{}_0\mathrm{N}(i,j)$, which only specify the solution of the system (2.1). However, the matrix $\boldsymbol{\Delta}$ has a two-fold eigenvalue zero. This means, that there is a 2D subspace of the direction space, where $\boldsymbol{\Delta U=0}$. The vectors of this subspace are special solutions to eq. (2.6). Their explicit form is

$$ \begin{pmatrix} \mathbf{D1} \\ x\frac{z-x}{1-x^2}\mathbf{D1} + \frac{1-xz}{1-x^2}\mathbf{D3} \\ \mathbf{D3} \\ x\frac{\bar{z}-x}{1-x^2}\mathbf{D1} + \frac{1-x\bar{z}}{1-x^2}\mathbf{D3} \end{pmatrix}; \qquad \mathbf{D1}, \mathbf{D3} \text{ arbitrary} \qquad (2.9) $$

The operators $(1-x^2)^{-1}$ makes these solutions inconvenient for practical computations, however. - Nevertheless, the solutions of the equation

$$ {}_{k+2}\mathbf{U}^S = \tfrac{1}{2}(\bar{x}+x+\bar{y}+y)_{k+1}\mathbf{U}^S - {}_k\mathbf{U}^S \qquad (2.10) $$

are special solutions to eq. (2.7). We first solve this equation and then construct more general ones from appropriate linear combinations of these solutions.

Third step. The 2D simple random walk has the solution ${}_kT_{i,j} = {}_kT_{i+j} \cdot {}_kT_{i-j}$, where ${}_kT_j = 2^{-k}\binom{k}{(k-j)/2}$ for $(k-j)\geq 0$ even, and ${}_kT_j=0$ otherwise, is the solution to the symmetric Bernoulli trial or 1D simple random walk, ${}_{k+1}T_j = \tfrac{1}{2}({}_kT_{j+1} + {}_kT_{j-1})$, with Kronecker initial data, ${}_0T_j = \delta_{0j}$. Unfortunately, eq.(2.9) cannot be factorized in terms of rotated coordinates. But it can be solved by means of the same simple GF technique (successive iteration of the equivalent

integral equation; cf. Duhamel's principle, Zauderer 1989) which has been applied to the 1D case (Enders & de Cogan 1993). The result is the special solution

$$ {}_k\mathbf{U}^s_{i,j} = 2^k \sum_{m=0} (-4)^{-m} \binom{k-m}{m} {}_{k-2m}\mathbf{T}_{i,j}; \qquad k - 2m \geq |i| + |j| \tag{2.11} $$

Fourth step. More general solutions to eq. (2.7) can be constructed by convolution with a function which adjusts the initial values prescribed, ${}_{0\ldots3}\mathbf{U}^p$. It is impossible to form from $\mathbf{U}^s$ a *f*undamental solution $\mathbf{U}^f$ which, due to

$$ {}_0\mathbf{U}^f = {}_0\mathbf{T}; \qquad {}_1\mathbf{U}^f = {}_2\mathbf{U}^f = {}_3\mathbf{U}^f = \mathbf{0} \tag{2.12} $$

would be the ideal starting distribution. But one may use the "*b*asic solution"

$$ {}_k\mathbf{U}^b = 2^{-k}\,{}_k\mathbf{U}^s + 2^{-2}\,{}_{k-2}\mathbf{U}^s \tag{2.13} $$

having much simpler initial distributions, than $\mathbf{U}^s$, *viz*,

$$ {}_k\mathbf{U}^b = {}_k\mathbf{T}; \qquad k = 0,1,2,3 \tag{2.14} $$

Therefore, the ansatz

$$ {}_k\mathbf{U}_{i,j} = \sum_{k'=k-3}^{k} \sum_{i',j'} c_{i-i',j-j',k-k'} \times {}_{k'}\mathbf{U}^b_{i',j'}; \qquad c_{i,j,k} = 0 \quad \text{for} \quad k < 0 \tag{2.15} $$

is proposed, where the coefficients, $c_{i,j,k}$, can be expressed in terms of the shift operators $x \ldots \bar{y}$ and calculated from a simple system of 4 linear equations,

$$ \sum_{k'=0}^{k} c_{k-k'}(x, \bar{x}, y, \bar{y})\,{}_{k'}\mathbf{T}(i,j) = {}_k\mathbf{U}^p(i,j); \qquad k = 0,1,2,3 \tag{2.16} $$

The compatibility of $\mathbf{U}^p$ with eq. (2.7) guarantees that of the solution (2.15).

3. 3D ELECTROMAGNETIC WAVES

For three-dimensional electromagnetic waves, the TLM mesh is favourably build with the SCN (Johns 1974). It has become the standard node here; corresponding software is commercially available. The SCN contains 12 pairs of lines for 12 travelling voltage pulses, $V_{1\ldots12}$ (3 dimensions × forward & backward motion × 2 polarizations) corresponding to the 12 field variables in Maxwell's equations. Often one can eliminate 6 of them (eg, **D** and **B**). Then, the treatment of 6 degrees of freedom (6 first-order in time differential equations for the remaining field variables, eg, **E** and **H**) by means of 12 (first-order in the time step) difference equations leads to the known ambiguities in the relationships between the TLM voltage pulses and the electromagnetic field variables. Here, Johns' (1987) original relations together with the transformation to diagonal ports proposed by Wlodarczyk (1992) will be used; the latter representation of the SCN is conceptually and computationally simpler.

The scattering of the voltage pulses is described through a 12×12 matrix, S_a, that gives the 12 outgoing (reflected) pulses, ${}_kV^r{}_{1\ldots12}={}_kV^r{}_{1\ldots12}(l,m,n)$ at node (l,m,n), in terms of the 12 incoming pulses, ${}_kV^i{}_{1\ldots12}$. At the next time step, k→k+1, the reflected pulses become incident pulses at the neighbouring nodes. We will diagonalize a modified scattering matrix, which connects ${}_kV^i{}_{1\ldots12}(l,m,n)$ with ${}_{k+1}V^i{}_{1\ldots12}(l',m',n')$, where the nodes (l,m,n) and (l',m',n') are neighbours. The solution of the resulting difference equation for one of the voltage pulses, *eg*, ${}_kV^i{}_2$, yields closed expressions for all values of ${}_kV^i{}_{1\ldots12}(l,m,n)$ in terms of any set of previous distributions, ${}_{k'}V^i{}_{1\ldots12}(l',m',n')$, k'<k, k' fixed, and in dependence upon any (external) sources, ${}_{k'}V^{ext}{}_{1\ldots12}(l',m',n')$, 0≤k'<k. As the electromagnetic field variables are linear combinations of the incident voltage pulses, we obtain immediately solutions for those, after properly accounting for the initial conditions.

The diagonal port representation (Wlodarczyk 1992) of the SCN yields a 6×6 block diagonalization of $\mathbf{S}_a$. Eliminating the reflected pulses, the diagonal port scattering matrix, $\mathbf{S}_d$, yields ${}_{k+1}\mathbf{V}^i=\mathbf{S}_{12}*{}_k\mathbf{V}^i$, ${}_k\mathbf{V}^i=({}_kV^i_1, \ldots, {}_kV^i_{12})^t$. The 12×12 matrix $\mathbf{S}_{12}{}^2$ is block-diagonal, such that the equation ${}_{k+2}\mathbf{V}^i=\mathbf{S}_{12}{}^2*{}_k\mathbf{V}^i$ decays in two 6×6 systems (decoupling of polarizations). The one reads

$$\begin{bmatrix}1\\2\\3\\4\\5\\6\end{bmatrix}^i_{k+2} = \frac{1}{4}\begin{bmatrix}0 & X & X'\\ Y' & 0 & Y\\ Z & Z' & 0\end{bmatrix}^2 \begin{bmatrix}1\\2\\3\\4\\5\\6\end{bmatrix}^i_{k}; \quad X=\begin{pmatrix}\bar{x} & \bar{x}\\ -x & -x\end{pmatrix}\ ;\ xV(l,m,n,)=V(l+1,m,n) \quad X'=\begin{pmatrix}-\bar{x} & \bar{x}\\ -x & x\end{pmatrix}\ ;\ \bar{x}V(l,m,n,)=V(l-1,m,n) \tag{3.1}$$

This system is diagonalized as above. Its eigenvalue equation reads

$$(1-\lambda)^2(\lambda^2-Q\lambda+1)^2=0; \qquad Q\equiv\tfrac{1}{4}(XY+XZ+YZ-4); \qquad X\equiv x+\bar{x}\ etc \tag{3.2}$$

Hence, for each component of the vector ${}_k\mathbf{V}$ a partial difference equation of quasi sixth order in k is obtained,

$$\begin{aligned}{}_{k+12}\mathbf{V} &= (2+2Q)_{k+10}\mathbf{V} - (3+4Q+Q^2)_{k+8}\mathbf{V} + (4+4Q+2Q^2)_{k+6}\mathbf{V}\\ &\quad - (3+4Q+Q^2)_{k+4}\mathbf{V} + (2+2Q)_{k+2}\mathbf{V} - {}_k\mathbf{V}\end{aligned} \tag{3.3}$$

The voltages at odd k-values are calculated using the original scattering matrix, $\mathbf{S}_{12}$.

Special solutions to eq.(3.3) can be obtained by exploiting the factorization of the eigenvalue equation (3.2). For instance, each solution to the equation

$${}_kV(l,m,n) = Q\,{}_{k-2}V(l,m,n) - {}_{k-4}V(l,m,n) \tag{3.4}$$

is a special solution to eq. (3.3). Eq. (3.4) is much simpler, but it requires that the initial conditions exhibit some symmetry, see below.

The two-step Markov chain (3.4) is similar to that for the node voltage within the 1D TLM diffusion model and thus may be calculated in the same manner (Enders & de Cogan 1993). First, consider the simpler partial difference equation

$${}_kV^0(l,m,n) = Q\,{}_{k-2}V^0(l,m,n) \tag{3.5}$$

A cubic-isotropic solution of this equation is

$$ {}_kV^0(l,m,n) = \sum_{\substack{p+q+r=0 \\ p,q,r\le k/2}}^{k;even} c^k_{pqr} T_p(l) T_q(m) T_r(n); \qquad c^k_{pqr} = (-1)^{\frac{k}{2}} (-3)^{\frac{p+q+r}{2}} \binom{k/2}{(p+q+r)/2} \quad (3.6) $$

Other solutions are possible, such as quasi-1D waves, ${}_kV(l,m,n)={}_kV(l)$, for instance. Note, that such a discrete wave (3.4) when emitted by a Kronecker source forms a cubic octahedron (Archimedean body).

Second, the solution to eq.(3.4) is developed into a series of the solution (3.6) yielding

$$ {}_k\mathbf{V}^i = \sum_{k'=0}^{[k/4]} (-1)^{k'} \binom{k/2-k'}{k'}_{k-4k'} \mathbf{V}^0; \quad [k/4] \equiv \text{integer part of } (k/4) \qquad (3.7) $$

This completes the solution to eq.(3.4); the voltages for odd k-values and ${}_k\mathbf{V}^i{}_{7\ldots12}$ are to be calculated from the original equations.

4. SUMMARY AND CONCLUSIONS

A simple, but quite general method for calculating closed algebraic solutions to TLM difference equations has been described. This method applies to virtually all explicit one-step (FD) algorithms. It should be interesting to extend it to other algorithms, too, in particular, to ones for the very electromagnetic fields (*eg*, Chen *et al* 1991). It is more direct, than the Fourier and Laplace transform techniques applied by Goldstein (1951) and by Russer & Krumpholz (1993), respectively. From such solutions, many other formulae for various applications can be derived in a simple way. Among others, applications are seen in the following areas:

- modelling radiative and dispersive boundary conditions more exactly;
- computing the Green's function (Johns matrix) and related (transfer) functions more effectively (note that the usual treatment of Huygens' construction and principle, respectively, by means of Kirchhoff's formula yields no algorithm for actual computations, *eg*, Zauderer 1989);
- saving iterations over the spatial mesh, the application of graded meshes and other sophistications which are difficult to implement into general-purpose software;
- examination of general properties of the algorithm (accuracy, convergency *etc*);
- improvement of routines for solving stationary problems basing on approaches like probabilistic potential theory (cf. Johns & Rowbotham 1981).

Acknowledgement: We are indebted to M. Krumpholz for useful discussions and making his manuscripts available to us prior publication.

References

Chen, Zh., Ney, M. M. & Hoefer, W. J. R. 1991: 'A New Finite-Difference Time-Domain Formulation and its Equivalence with the TLM Symmetrical Condensed Node, IEEE Trans. Microwave Theory Tech. 39 (12) 2160-2169

De Cogan, D. 1992. 'Error Optimisation in TLM Algorithms', Internal Report, University of East Anglia, Norwich (UK)

Enders, P. & de Cogan, D. 1993: 'On the transmission-line matrix modelling method - a rigorous viewpoint', Int. J. Num. Modell. 6 (2) 109-126

Farmer, D., Toffoli, T., & Wolfram, S. (Eds.) 1984: 'Cellular Automata', In: Physica 10D (1984) Nos. 1&2

Goldstein, S. 1951: 'On diffusion by discontinuous movements, and on the telegraph equation', Quart. Journ. Mech. Appl. Math. IV, 129-156

Hoefer, W. J. R. 1989: ' The Discrete Time Domain Green's Function or Johns Matrix - a New Powerful Concept in Transmission Line Modelling', Int. J. Num. Modell. 2 (4) 215-225

Johns, P.B. 1987: 'A symmetrical condensed node for the TLM method', IEEE Trans. MTT-35 (4) 370-377

Johns, P.B. 1988: 'Simulation of Electromagnetic Wave Interaction by Transmission-Line Modelling (TLM)', Wave Motion 10, 597-610

Johns, P.B. & Rowbotham, T.R. 1981: 'Solution of resistive meshes by deterministic and Monte Carlo transmission-line modelling', IEE Proc. 128, Pt.A, 453-462

Russer, P. & Krumpholz, M. 1993: 'The Hilbert Space Formulation of the TLM Method', Int. J. Num. Modell. 6 (1) 29-45; Krumpholz, M. & Russer, P. 1993: 'Discrete Time-Domain Greens Functions for Three-Dimensional TLM Modelling of the Radiating Boundary Conditions', submitted for publication

Vanneste, C., Sebbah, P. & Sornette, D. 1992: 'A Wave Automaton for Time-Dependent Wave Propagation in Random Media', Europhys. Lett. 17, 715-720.

Wlodarczyk, A.J. 1992: 'Representation of Symmetrical condensed TLM node', El. Lett. 28 (18) 1686-1687

Zauderer, E. 1989: 'Partial Differential Equations of Applied Mathematics', Wiley, New York

Zuse, K. 1969: 'Rechnender Raum', Vieweg, Braunschweig.